

# **Methods in Computational Physics**

*Advances in Research and Applications*

- 1 STATISTICAL PHYSICS**
- 2 QUANTUM MECHANICS**
- 3 FUNDAMENTAL METHODS IN HYDRODYNAMICS**
- 4 APPLICATIONS IN HYDRODYNAMICS**
- 5 NUCLEAR PARTICLE KINEMATICS**
- 6 NUCLEAR PHYSICS**
- 7 ASTROPHYSICS**
- 8 ENERGY BANDS OF SOLIDS**
- 9 PLASMA PHYSICS**
- 10 ATOMIC AND MOLECULAR SCATTERING**
- 11 SEISMOLOGY: SURFACE WAVES AND EARTH OSCILLATIONS**
- 12 SEISMOLOGY: BODY WAVES AND SOURCES**

# METHODS IN COMPUTATIONAL PHYSICS

*Advances in Research and Applications*

*Series Editors*

**BERNI ALDER**

*Lawrence Livermore Laboratory  
Livermore, California*

SIDNEY FERNBACH

MANUEL ROTENBERG

*Lawrence Livermore Laboratory  
Livermore, California*

*University of California  
La Jolla, California*

## Volume 12 Seismology: Body Waves and Sources

*Volume Editor*

**BRUCE A. BOLT**

*Seismographic Station  
Department of Geology and Geophysics  
University of California  
Berkeley, California*

AN  
ACADEMIC PRESS  
REPLICA REPRINT

1972



**ACADEMIC PRESS**

A Subsidiary of Harcourt Brace Jovanovich, Publishers

**New York London Toronto Sydney San Francisco**

---

This is an Academic Press Replica Reprint reproduced directly from the pages of a title for which type, plates, or film no longer exist. Although not up to the standards of the original, this method of reproduction makes it possible to provide copies of books which otherwise would be out of print.

---

COPYRIGHT © 1972, BY ACADEMIC PRESS, INC.

ALL RIGHTS RESERVED

NO PART OF THIS BOOK MAY BE REPRODUCED IN ANY FORM,  
BY PHOTOSTAT, MICROFILM, RETRIEVAL SYSTEM, OR ANY  
OTHER MEANS, WITHOUT WRITTEN PERMISSION FROM  
THE PUBLISHERS.

ACADEMIC PRESS, INC.  
111 Fifth Avenue, New York, New York 10003

*United Kingdom Edition published by*  
ACADEMIC PRESS, INC. (LONDON) LTD.  
24/28 Oval Road, London NW1

LIBRARY OF CONGRESS CATALOG CARD NUMBER: 63-18406

PRINTED IN THE UNITED STATES OF AMERICA

82 9 8 7 6 5 4 3 2

# Contributors

Numbers in parentheses indicate the pages on which the authors' contributions begin.

Z. ALTERMAN, *Department of Environmental Science, Tel Aviv University, Ramat-Aviv, Israel* (33)

ARI BEN-MENAHEM, *Department of Applied Mathematics, The Weizmann Institute of Science, Rehovot, Israel* (299)

C. H. CHAPMAN, *Institute of Earth and Planetary Physics, Department of Physics, University of Alberta, Edmonton, Alberta, Canada* (165)

FREEMAN GILBERT, *Institute of Geophysics and Planetary Physics, University of California, San Diego, La Jolla, California* (231)

F. HRON, *Institute of Earth and Planetary Physics, Department of Physics, The University of Alberta, Edmonton, Alberta, Canada* (1)

LEONARD E. JOHNSON,\* *Institute of Geophysics and Planetary Physics, University of California, San Diego, La Jolla, California* (231)

D. LOEWENTHAL, *Department of Environmental Science, Tel Aviv University, Ramat-Aviv, Israel* (35)

R. A. PHINNEY, *Department of Geological and Geophysical Sciences, Princeton University, Princeton, New Jersey* (165)

M. J. RANDALL, *Geophysics Division, Department of Scientific and Industrial Research, Wellington, New Zealand* (267)

SARVA JIT SINGH,† *Department of Applied Mathematics, The Weizmann Institute of Science, Rehovot, Israel* (299)

\* Present address: Cooperative Institute for Research in Environmental Sciences, University of Colorado, Boulder, Colorado.

† On leave from the Department of Mathematics, Kurukshetra University, Kurukshetra, India.

# Preface

THIS VOLUME, LIKE ITS companion Volume 11, deals with recent seismological research in which advanced computational analysis has played a critical role. In this volume the numerical solution of some central problems on seismic body wave propagation and generation in the Earth are covered.

A major aim in seismology is to infer the minimum set of properties of the earthquake source and of the Earth, which will explain in detail the recorded wave trains. By the end of the 1950s this geophysical interpretation of earthquake observations was limited severely by the laborious arithmetic needed to solve the theoretical models, yet great technical improvement occurred in the worldwide network of seismographic observatories. The impasse was broken with the application of the high speed computer. A clear example is given by F. Hron in his discussion of the power of the computer to trace out detailed seismic response by means of ray theory. Hron brings together for the first time some important but rather inaccessible work from the Soviet Union and the Continent. A different numerical procedure of generating synthetic seismograms to allow comparison with observations is set out in detail by Z. Alterman and D. Loewenthal. Correspondence with the ray theoretical results is pointed out.

Chapman and Phinney have made an important contribution to the problem of the diffraction of seismic waves by the sharp boundary of the Earth's liquid core, a phenomenon which has been known for about sixty years. However, no numerical solutions for the diffraction of elastic spherical waves propagating through an inhomogeneous medium were available until their work.

The basic seismological input to knowledge of the structure of the Earth is to provide times of travel of seismic body waves from one point to another on the surface. Given the empirical times, numerical integration is required to infer a seismic velocity distribution with depth which will satisfy the times within the measurement uncertainties. This optimal constraint formulation is typical of a general class of inverse geophysical problems. Johnson and Gilbert describe a method for the travel-time inversion problem including an assessment of uniqueness.

The final two chapters describe the latest methods of analysis of earthquake mechanisms. Randall shows how discrimination between source mechanisms is possible using the amplitudes of seismic waves as well as the direction of initial motion, which has traditionally been used since its development by P. Byerly of the University of California. The major review

by Ben-Menahem and Sarva Jit Singh is designed to acquaint physicists and geoscientists with the application of elastic dislocation theory to investigations of earthquake sources. Important computer applications to the study of faulting dynamics and the line spectra of terrestrial eigen vibrations are also considered.

# Numerical Methods of Ray Generation in Multilayered Media

F. HRON

INSTITUTE OF EARTH AND PLANETARY PHYSICS  
DEPARTMENT OF PHYSICS  
THE UNIVERSITY OF ALBERTA, EDMONTON, ALBERTA, CANADA

I. Introduction . . . . .	1
II. Notation and Identification of Phases . . . . .	2
III. Groups of Kinematic and Dynamic Analogs . . . . .	5
A. Unconverted Waves . . . . .	5
B. Kinematic and Dynamic Analogs of Simply Converted Waves . . . . .	11
C. Kinematic and Dynamic Analogs of Head Waves . . . . .	14
IV. Flow Charts of Subroutines . . . . .	19
A. Flow Chart of Subroutine Creating Symbols for Kinematic and Dynamic Analogs of Unconverted Waves . . . . .	19
B. Flow Chart of Subroutine Creating Codes of Representative Waves for Groups of Dynamic Analogs of Unconverted Waves . . . . .	26
V. Numerical Examples . . . . .	28
Appendix A. Number of Arrangements of $n_2$ Identical Balls into $n_1$ Pockets, Some of Which Can Be Empty . . . . .	32
Appendix B. Number of Arrangements of $n_2$ Identical Balls into $n_1$ Pockets, None of Which Can Be Empty . . . . .	33
References . . . . .	33

## I. Introduction

ALTHOUGH THE INCREASING NUMBER of publications dealing with the computation of synthetic (theoretical) seismograms for layered media has been due mainly to the rapidly developing computing facilities of universities and geo-physical research centers, the first few quite acceptable agreements between synthetic seismograms and field records (Helmberger, 1968; Helmberger and Morris, 1969) suggest that synthetic seismograms could play an important role in interpreting field materials in the near future. After evaluating results, it becomes obvious that a ray theory, which decomposes the displacement field into contributions attributed to the individual rays, is one of the most efficient methods that could be used for computation of synthetic seismograms.

To date, two different approaches within ray theory can be distinguished.

The first one, often called a generalized ray theory (or exact ray theory, method of generalized reflection and refraction coefficients), was used for the calculation of synthetic seismograms, for example, by Spencer (1965), Červený (1965, 1966), Helmberger (1968), Müller (1968a,b, 1970), and Helmberger and Morris (1969). Special attention should be given to Müller's last paper, where a list of all important publications dealing with generalized ray theory is given. The second approach, called here an asymptotic ray theory (or a ray method in most of the Russian literature), has been used quite recently for the calculation of synthetic seismograms by Hron and Kanasewich (1971), who also give an outline of this theory.

As both generalized and asymptotic versions of ray theory furnish well established methods of evaluating the displacement contribution attributed to the individual rays, the main problem which was encountered during the computation of synthetic seismograms lay in the selection of rays used for their construction. The crucial importance of the selection of rays becomes clear if one realizes that the "quality" or, in other words, the "reliability" of synthetic seismograms depends very strongly on the family of rays which are selected from the infinite number of rays existing between source and receiver for the calculation of synthetic seismograms. Until recently such selections were performed mostly manually according to human experience and that is why interpretations which were drawn from synthetic seismograms could only be inconclusive.

It is obvious that any practical solution of this problem cannot be achieved without using computers which would replace human judgment by an appropriate algorithm based on strictly defined criteria. In order to do this, some rules, by which significant rays could be selected, cataloged, and their contribution to a synthetic seismogram calculated, have to be determined.

One possible approach to the solution of this task is outlined in Sections II and III of this article, which are based on a recently published paper of the author (Hron, 1971). Then, flow charts of two subroutines, which perform automatic ray generation and create codes of so-called "representative waves," are given in Section IV while the corresponding numerical examples can be found in Section V.

## II. Notation and Identification of Phases

Suppose the medium consists of  $I + 1$  layers including a half-space. Then, according to ray theory, an infinite number of rays propagate from an arbitrarily placed source to a receiver at any other location. In this article, both the source and receiver will be restricted to the surface as this corresponds to a commonly used geometry in deep seismic sounding or refraction studies. For

simplicity, the medium will be considered to consist of homogeneous layers separated by plane interfaces parallel to the earth's surface. The object of this article is to describe rules by which phases with significant energy are selected, cataloged, and their contribution to a synthetic seismogram determined.

Those waves which travel from the source to the receiver along different paths but with identical travel time curves are kinematically equivalent and are called "kinematic analogs." The groups of kinematic analogs may be further divided into subgroups of waves whose amplitude curves are identical. The members belonging to each of these subgroups of phases may be called "dynamic analogs." The advantage of the distinction between dynamic and kinematic analogs is evident. For example, if we know the number of all dynamic analogs in the subgroup and multiply that number by the amplitude of one of them, we obtain the total dynamic effect of the subgroup.

This classification is only efficient in media with plane layers whose properties do not change in the direction parallel to interfaces. Another factor which can influence the efficiency of this distinction is the number of conversions from P- to S-waves and vice versa. The method is effective only for waves with few conversions.

The surface of the layered media will be called the zeroth interface while the top of the half-space will be the  $I$ th interface. The properties of the layers are described by the elastic wave velocities, density, and thickness as follows:

$\alpha_i$ —compressional or P-wave density,

$\beta_i$ —shear or S-wave velocity,

$\rho_i$ —density,

$h_i$ —thickness,

$i = 1, 2, \dots, I, I + 1$ , —layer index.

Every ray travels in a straight line through each layer and the ray may be divided into  $k = 1$  to  $K$  segments which always connect points where the ray changes its direction after reflection or refraction. Compressional and shear waves are identified in each segment by a code  $C_k$  as follows

$C_k = 1$ , compressional or P-wave in the  $k$ th segment,

$C_k = 2$ , shear or S-wave in the  $k$ th segment.

A ray is completely specified by  $K$  contiguous pairs of integers as follows

$$\{C_k, i_k\}, \quad k = 1, \dots, K. \quad (1)$$

The computing code used for the ray in Fig. 1 is

$$1, 1; 2, 2; 2, 2; 1, 2; 1, 3; 2, 3; 2, 2; 2, 1. \quad (2)$$

In more conventional notation the ray would be specified by

$$P_1, S_2, S_2, P_2, P_3, P_3, S_2, S_2, S_1. \quad (3)$$

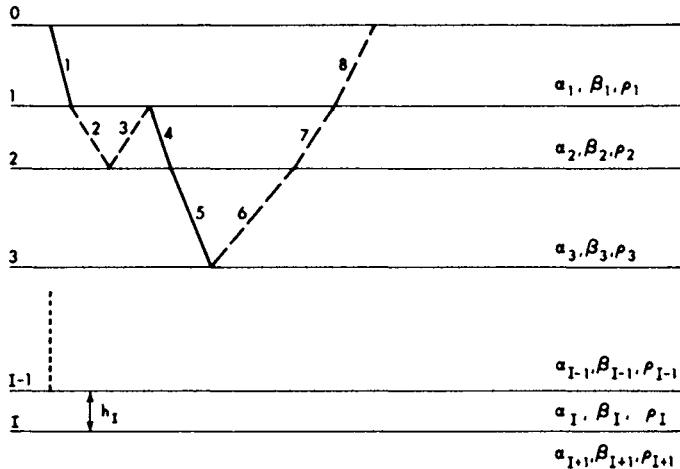


FIG. 1. A ray for the wave with the code  $P_1, S_2, S_2, P_2, P_3, S_3, S_2, S_1$  in a medium with  $I$  plane interfaces parallel to the surface. The segments of the ray are numbered sequentially from 1 to 8.

If a ray has no phase conversions a sequence of  $K$  integers may be used in place of the code (1):

$$\{i_k\}, k = 1, \dots, K. \quad (4)$$

Such a wave is described as an "unconverted" wave. Two waves are different if their code as given by Eq. (1) or (4) is different.

When the source and receiver are on the surface the number of segments in each layer is even. There will be  $n_i$  downgoing waves and  $n_i$  upgoing waves in each layer  $i$ . A "coupled segment" is defined as consisting of one downgoing and the next nearest upgoing segment in a layer. There are  $n_i$  coupled segments in each layer. In Fig. 1 the second and third segments constitute the first couple in the second layer while the fourth and seventh segments constitute the second couple.

An "element of the  $j$ th class" is defined to be the continuous chain of segments commenced and terminated by a coupled segment in the  $j$ th layer. The symbol  $J$  will be given to the deepest layer traversed by the ray. Elements of the  $j$ th class do not overlap and are numbered  $1, \dots, n_j$  along the ray in the direction of propagation. For example, in Fig. 1 the first element of the second class consists of segments 2 and 3 while the second element is composed of segments 4, 5, 6 and 7. If an element consists of only 2 segments, as in the first case, it is called a "trivial element." The second case is an example of a "normal element" which consists of at least one coupled segment in the  $(j+1)$ th layer.

Head waves are diffractions from a surface and have segments of rays that are parallel to an interface. The symbol "H" will be given to these waves

which have been critically refracted. Waves which suffer reflections or refractions without being critically refracted will be called "R"-waves. Further details concerning H-waves will be given in Section III, C.

### III. Groups of Kinematic and Dynamic Analogs

#### A. UNCOVERTED WAVES

##### 1. Kinematic Analogs

At the beginning of the previous section, the group of kinematic analogs was defined as the group of waves which were kinematically equivalent. If  $J$  is the number of the deepest layer through which the R-wave passes, the arrival time  $T$  at epicentral distance  $r$  is given by

$$T = \sum_{j=1}^J 2n_j \frac{h_j}{v_j(1 - p^2 v_j^2)^{1/2}}. \quad (5)$$

$2n_j$  is the number of segments of the ray lying in the  $j$ th layer,  $h_j$  is a thickness of the  $j$ th layer, and  $v_j$  is the velocity of the wave in the  $j$ th layer. Parameter  $p$  at epicentral distance  $r$  can be obtained from

$$r = \sum_{j=1}^J 2n_j h_j v_j \frac{p}{(1 - p^2 v_j^2)^{1/2}}. \quad (6)$$

We can see that the necessary and sufficient condition for kinematic equivalence of two different unconverted R-waves is that both waves must have an equal number of segments in each layer along their paths. In other words, the parameters of the group of kinematic analogs are  $J$  integers and we let the symbol of the group be

$$\{n_1, n_2, \dots, n_J\}, \quad (7)$$

where  $n_j$  is an integer equal to half the segments in layer  $j$ .

The next problem is to find the number of waves  $N_k(n_1, \dots, n_J)$  of the rays with  $2n_j$  segments in each layer  $j = 1, \dots, J$ . The required continuity of the chain of segments is satisfied if at least one element of the  $j$ th class,  $j = 1, \dots, J-1$ , is normal so that the segments in the  $j$ th and  $(j+1)$ th layers are connected. Moreover, all elements of the  $(j+1)$ th class within the element of the  $j$ th class must be linked together. Constructing the rays of all kinematic analogs we always have to proceed from  $n_1$  elements of the first class that should be linked together. If  $J = 1$ , there is only one possible way of creating a ray from  $n_1$  trivial elements of the first class. Then

$$N_k(n_1) = 1. \quad (8)$$

If  $J = 2$ , the number of all different rays built from  $2n_1$  segments in the first layer and  $2n_2$  segments in the second layer is equal to the number of all possibilities of distributing  $n_2$  trivial elements of the second class among  $n_1$  elements of the first class. According to Eq. (52), Appendix A, this number is

$$N_k(n_1, n_2) = \frac{(n_1 + n_2 - 1)!}{n_2!(n_1 - 1)!} = C_{n_2}^{n_1+n_2-1}. \quad (9)$$

Therefore, we obtain  $N_k(n_1, n_2)$  different rays from the original ray with  $n_1$  trivial elements of the first class. The new rays differ in the distribution of the  $n_2$  elements of the second class to the  $n_1$  elements of the first class. It is apparent that the number of these distributions is independent of the kind of elements of the second class. If  $J = 3$ , there are  $C_{n_3}^{n_2+n_3-1}$  different ways of binding  $n_3$  trivial elements of the third class to each of  $N_k(n_1, n_2)$  rays of kinematic analogs from the group  $\{n_1, n_2\}$ . The number of kinematic analogs in the group  $\{n_1, n_2, n_3\}$  is

$$N_k(n_1, n_2, n_3) = N_k(n_1, n_2) \cdot C_{n_3}^{n_2+n_3-1}. \quad (10)$$

In general, the number of waves belonging to the group of kinematic analogs  $\{n_1, n_2, \dots, n_J\}$ ,  $J \geq 2$ , is expressed by the relation

$$N_k(n_1, \dots, n_J) = \prod_{j=1}^{J-1} C_{n_{j+1}}^{n_j+n_{j+1}-1}. \quad (11)$$

$C_{n_{j+1}}^{n_j+n_{j+1}-1}$  is the number of all combinations of the  $(n_{j+1})$ th class from  $(n_j + n_{j+1} - 1)$  elements and represents the number of all possible connections between segments in the  $j$ th and  $(j+1)$ st layers. Equation (11) is identical with the one deduced by Vavilova and Petrashen (1966). If we apply (11) to a calculation of the number of kinematic analogs in the group  $\{2, 2, 1\}$  we get  $N_k(2, 2, 1) = C_2^3 \cdot C_1^2 = 6$ . All six waves of this group are drawn in Fig. 2.

## 2. Dynamic Analogs

Dynamic analogs are groups of rays with both identical travel time and amplitude curves. One group of kinematic analogs may consist of several different subgroups of dynamic analogs. Therefore it is evident that all the numbers  $n_1, \dots, n_J$  in Eq. (7) have to appear as parameters in symbols of all dynamic analogs that form the group specified by (7). The other parameters that would describe the group of dynamic analogs uniquely will be given after an examination of the formula for the complex amplitude of R-waves.

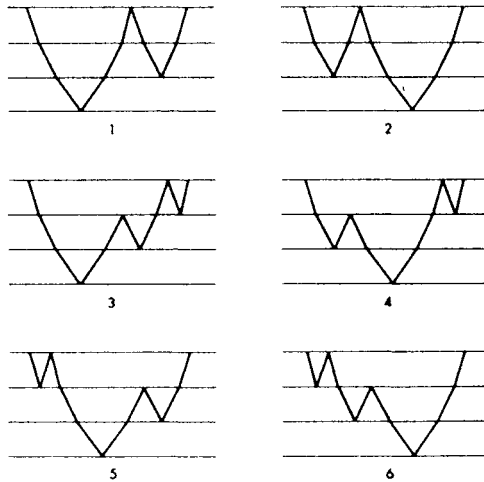


FIG. 2. Six phases from the group of kinematic analogs with symbol  $\{2, 2, 1\}$ . They can be divided into two groups of dynamic analogs with symbols  $\{2, 2, 1; 0, 1\}$  and  $\{2, 2, 1; 1, 1\}$ . Phases 1 and 2 belong to the first and phases 3, 4, 5, 6 to the second group of dynamic analogs.

According to asymptotic ray theory (Petrashen, 1959; Hron, 1968; Hron and Kanasewich, 1971; Červený and Ravindra, 1971), the complex amplitude of R-waves is

$$W = \frac{G_0^{\mu_0} D_J^{m_J}}{Q} \prod_{j=1}^{J-1} D_j^{m_j} E_j^l F_j^{\lambda_j} G_j^{\mu_j}, \quad (12)$$

where  $J$  is the number of the deepest layer (assume  $J \geq 2$ ),  $m_j$  is the number of reflections from the  $j$ th interface when the incident wave is in the  $j$ th layer,  $l_j$  is the number of transmissions from the  $j$ th to  $(j+1)$ th layer,  $\mu_j$  is the number of reflections from the  $j$ th interface when the incident wave is in the  $(j+1)$ th layer,  $\lambda_j$  is the number of transmissions from the  $(j+1)$ th to the  $j$ th layer,  $\mu_0$  is the number of reflections from the surface, and  $m_J$  is the number of reflections from the  $J$ th interface.  $D_j$ ,  $G_j$ ,  $E_j$ ,  $F_j$  are complex reflection and refraction coefficients of the plane wave incident with the same angle and on the same side of the  $j$ th interface as the ray of the R-wave being considered.  $Q$  is the geometrical spreading factor for the ray tube of the R-wave being considered.

Within the given medium  $Q$  is a function of the epicentral distance  $r$  and numbers  $n_1, \dots, n_J$ , and therefore within a single group of kinematic analogs  $Q$  changes only with respect to  $r$ . The choice of integers  $\lambda_j$ ,  $\mu_j$ , and  $l_j$ ,

$j = 1, \dots, J - 1$ , and  $m_j, j = 1, \dots, J$ , is restricted by the claim for continuity in the chain of segments that form the ray and by the assumption that both the source and receiver are on the surface. It is required that

$$\mu_0 = n_1 - 1, \quad m_J = n_J, \quad (13)$$

$$\text{Max}(0, n_j - n_{j+1}) \leq m_j \leq n_j - 1, \quad 1 \leq j \leq J - 1. \quad (14)$$

Vavilova and Pugach (1966) showed that the remaining numbers  $l_j$ ,  $\lambda_j$ , and  $\mu_j$  in (12) can be expressed as follows:

$$l_j = \lambda_j = n_j - m_j, \quad \mu_j = n_{j+1} - \lambda_j = n_{j+1} - n_j + m_j, \quad 1 \leq j \leq J - 1. \quad (15)$$

The sequence of  $2J - 1$  numbers

$$\{n_1, n_2, \dots, n_J; m_1, m_2, \dots, m_{J-1}\} \quad (16)$$

uniquely determines the amplitude curve of the R-wave that has  $2n_j$  segments in the  $j$ th layer and that suffers  $m_j$  reflections from the  $j$ th interface,  $j = 1, \dots, J$ . The sequence (16) and the numbers  $n_j, m_j$  may be called the symbol and the parameters for the group of dynamic analogs, respectively. It is apparent that the number of waves in the group of dynamic analogs (16) is equal to the number of all possible continuous chains of all segments that form the rays with the following properties: the rays should have  $2n_j$  segments in the  $j$ th layer and should be reflected  $m_j$  times,  $j = 1, \dots, J$ , from the  $j$ th interface. To ensure the continuity of the rays we have to submit the constructed rays to the following procedure: we split each ray of the group

$$\{n_1, \dots, n_j; m_1, \dots, m_{j-1}\}, \quad 1 \leq j \leq J - 1 \quad (17)$$

into  $M$  different rays of dynamic analogs from the group

$$\{n_1, \dots, n_j, n_{j+1}; m_1, \dots, m_{j-1}, m_j\} \quad (18)$$

by distributing  $n_{j+1}$  trivial elements of the  $(j+1)$ th class into  $n_j$  elements of the  $j$ th class leaving  $m_j$  of them trivial. The new rays from (18) are  $m_j$  times reflected from the  $j$ th interface as they have  $m_j$  trivial elements of the  $j$ th class.  $M$  can be written as

$$M = M_1 \cdot M_2,$$

where

$$M_1 = \frac{n_j!}{m_j!(n_j - m_j)!} = C_{m_j}^{n_j}$$

is the number of all possible choices of  $m_j$  trivial elements of the  $j$ th class from their total number  $n_j$ ,

$$M_2 = \frac{(n_{j+1} - 1)!}{(n_{j+1} - n_j + m_j)!(n_j - m_j - 1)!} = C_{n_j - m_j - 1}^{n_{j+1} - 1}$$

is the number of all possible distributions of  $n_{j+1}$  trivial elements of the  $(j+1)$ th class among the remaining  $n_j - m_j$  elements of the  $j$ th class. The number  $M_2$  is equal to the number of all possible arrangements of  $n_{j+1}$  identical balls into  $n_j - m_j$  pockets not leaving any of them empty, and its derivation is given in Appendix B (see Eq. 53).

If  $N_d(n_1, \dots, n_j; m_1, \dots, m_{j-1})$  is the number of the waves in the group (17) the number of dynamic analogs in the group (18) is

$$N_d(n_1, \dots, n_{j+1}; m_1, \dots, m_j) = C_{m_j}^{n_j} \cdot C_{n_j - m_j - 1}^{n_{j+1} - 1} \cdot N_d(n_1, \dots, n_j; m_1, \dots, m_{j-1}).$$

The expression

$$N_d(n_1, \dots, n_J; m_1, \dots, m_{J-1}) = \prod_{j=1}^{J-1} C_{m_j}^{n_j} C_{n_j - m_j - 1}^{n_{j+1} - 1} \quad (19)$$

is the general formula for the calculation of a number of single waves in the group of dynamic analogs with symbol

$$\{n_1, \dots, n_J; m_1, \dots, m_{J-1}\}. \quad (20)$$

Each  $m_j$ ,  $j = 1, \dots, J - 1$ , has to satisfy relation (14). Equation (19) is identical with the formula for the number of dynamic analogs derived by Vavilova and Petrashen (1966).

The application of the equation (19) can be demonstrated in the example shown in Fig. 2. The group of kinematic analogs symbolized by  $\{2, 2, 1\}$  can be divided into two groups of dynamic analogs with symbols  $\{2, 2, 1; 0, 1\}$  and  $\{2, 2, 1; 1, 1\}$ . According to (19) the number of waves in the first group is

$$N_d(2, 2, 1; 0, 1) = C_0^2 \cdot C_1^1 \cdot C_1^2 \cdot C_0^0 = 2,$$

and the number of waves in the second group is

$$N_d(2, 2, 1; 1, 1) = C_1^2 \cdot C_0^1 \cdot C_1^2 \cdot C_0^0 = 4.$$

In Fig. 2, the rays that belong to the first group have numbers 1 and 2 and those belonging to the second group have numbers 3, 4, 5, and 6. There are only two groups of dynamic analogs because only two different combinations of numbers,  $m_1$  and  $m_2$ , satisfy condition (14).

Amplitude-distance characteristics for the vertical component of both groups of dynamic analogs of unconverted S-waves calculated for the Alberta model (see Table I) are shown in Fig. 3.

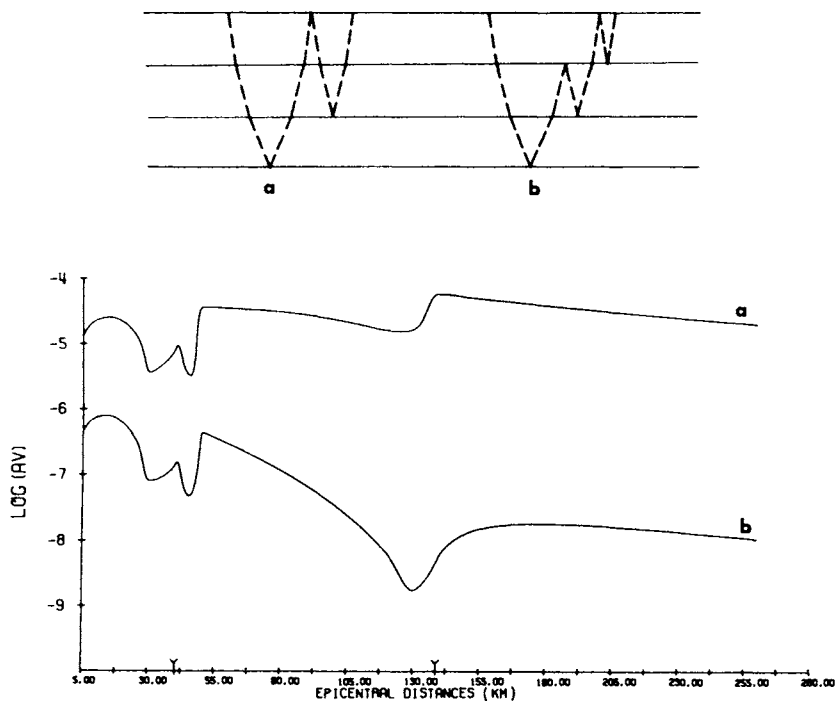


FIG. 3. Amplitude-distance characteristics for the vertical component of two unconverted S-phases calculated for the Alberta model. Small arrows indicate the positions of the first and second critical points.

It is obvious from the picture that the vertical component of the dynamic analogs from the group {2, 2, 1; 0, 1} is much stronger than that from the group {2, 2, 1; 1, 1}, and therefore the dynamic effect of all dynamic analogs from the second group can be neglected with respect to that from the first group at almost all epicentral distances.

TABLE I  
PARAMETERS OF THE ALBERTA MODEL<sup>a</sup>

Layer	$\alpha$ (km/sec)	$\beta$ (km/sec)	$\rho$ (g/cm <sup>3</sup> )	h(km)
1	2.31	1.33	2.04	1.105
2	3.06	1.77	2.21	1.097
3	6.50	3.75	2.73	31.198
4	7.15	4.13	3.20	9.800
Half-space	8.08	4.66	3.45	$\infty$

<sup>a</sup> According to Cumming and Kanasewich (1966).

## B. KINEMATIC AND DYNAMIC ANALOGS OF SIMPLY CONVERTED WAVES

A "simply converted wave" is defined as one that is converted only in the first reflection or refraction. This corresponds to the simplest use of converted waves when the type of source—P or S—and consequently even the mode of the first segment differ from the rest of the ray. If the phase of the first segment is changed in all waves given by (7) we obtain the group kinematically equivalent to simply converted waves with the symbol

$$\{\bar{n}_1, n_2, \dots, n_J\}. \quad (21)$$

The bar above  $n_1$  in (21) indicates that the first segment in each ray has a different phase than the rest of the ray. The number of kinematic analogs of simply converted waves is

$$N_k(\bar{n}_1, \dots, n_J) = \prod_{j=1}^{J-1} C_{n_{j+1}}^{n_j + n_{j+1} - 1}. \quad (22)$$

The group of dynamic analogs of simply converted R-waves is analyzed next. When the phase of the first segment of the ray is changed, the group of dynamic analogs in (16) divides into two subgroups of simply converted R-waves. If a wave is transmitted through the first interface at its first encounter, it is placed in a subgroup A. Alternatively, if it is reflected, it is placed in a subgroup B. Generally, the coefficient of reflection differs from the coefficient of refraction and therefore the complex amplitudes of the waves in A are different from those in B. Clearly, the number of waves in A must be equal to the number of such waves from (16) whose first element of the first class is normal. If  $J \geq 3$  their number is

$${}_A N_d(\bar{n}_1, \dots, n_J; m_1, \dots, m_{J-1}) = C_{m_1}^{n_1 - 1} \cdot C_{n_1 - m_1 - 1}^{n_2 - 1} \cdot \prod_{j=2}^{J-1} C_{m_j}^{n_j} \cdot C_{n_j - m_j - 1}^{n_{j+1} - 1} \quad (23)$$

because  $C_{m_1}^{n_1}$ , which gives the number of possible ways of choosing  $m_1$  trivial elements from  $n_1$  elements of the first class in (19), can be divided into two parts if  $m_1 > 0$ :

$$C_{m_1}^{n_1} = C_{m_1-1}^{n_1-1} + C_{m_1-1}^{n_1-1}. \quad (24)$$

Here  $C_{m_1-1}^{n_1-1}$  determines the number of all possible selections of  $m_1$  trivial elements from the  $n_1$  elements of the first class provided that the first element is not in the selection. If  $m_1 > 0$  the number of waves in subgroup B is given by

$$\begin{aligned} {}_B N_d(\bar{n}_1, \dots, n_J; \bar{m}_1, \dots, m_{J-1}) \\ = C_{m_1-1}^{n_1-1} \cdot C_{n_1-m_1-1}^{n_2-1} \cdot \prod_{j=2}^{J-1} C_{m_j}^{n_j} \cdot C_{n_j-m_j-1}^{n_{j+1}-1}. \end{aligned} \quad (25)$$

The symbol for subgroup A of dynamic analogs of simply converted R-waves is

$$\{\bar{n}_1, \dots, n_J; m_1, \dots, m_{J-1}\}. \quad (26)$$

For subgroup B the symbol is

$$\{\bar{n}_1, \dots, n_J; \bar{m}_1, \dots, m_{J-1}\}. \quad (27)$$

The bar above  $m_1$  indicates a change in phase after the first reflection of the wave from the first interface. For  $J < 3$  Eq. (23) becomes

$${}_A N_d(\bar{n}_1, n_2; m_1) = C_{m_1}^{n_1-1} \cdot C_{n_1-m_1-1}^{n_2-1}, \quad J = 2; \quad (23a)$$

$${}_A N_d(\bar{n}_1) = 0, \quad J = 1. \quad (23b)$$

Similarly, Eq. (25) becomes

$${}_B N_d(\bar{n}_1, n_2; \bar{m}_1) = C_{m_1-1}^{n_1-1} \cdot C_{n_1-m_1-1}^{n_2-1}, \quad J = 2; \quad (25a)$$

$${}_B N_d(\bar{n}_1) = 1, \quad J = 1. \quad (25b)$$

It is obvious that there is no wave within the group B of dynamic analogs of simply converted waves for the case  $m_1 = 0$ .

It is clear that a single conversion can also be achieved if the last segment of the ray of unconverted waves changes its mode. Because the code of these waves can be obtained by reversing the order of the sequence in the code

(1) of previously defined "simply converted waves," the formulas for the number of dynamic analogs of simply converted waves can be applied to both situations although the amplitudes will be different.

The application of Eqs. (23) and (25) is illustrated in Fig. 4 for the kinematic group  $\{\bar{2}, 2, 1\}$  of simply converted R-waves. The original group of unconverted waves,  $\{2, 2, 1\}$ , was shown in Fig. 2. According to (23) and (25)

$${}_A N_d(\bar{2}, 2, 1; 0, 1) = C_0^1 \cdot C_1^1 \cdot C_1^2 \cdot C_0^0 = 2,$$

$${}_A N_d(\bar{2}, 2, 1; 1, 1) = C_1^1 \cdot C_0^1 \cdot C_1^2 \cdot C_0^0 = 2,$$

$${}_B N_d(\bar{2}, 2, 1; \bar{1}, 1) = C_0^1 \cdot C_0^1 \cdot C_1^2 \cdot C_0^0 = 2.$$

The simply converted R-waves from group A are shown in diagrams 1, 2, 3, and 4 in Fig. 4 while the waves from group B are shown in diagrams 5 and 6.

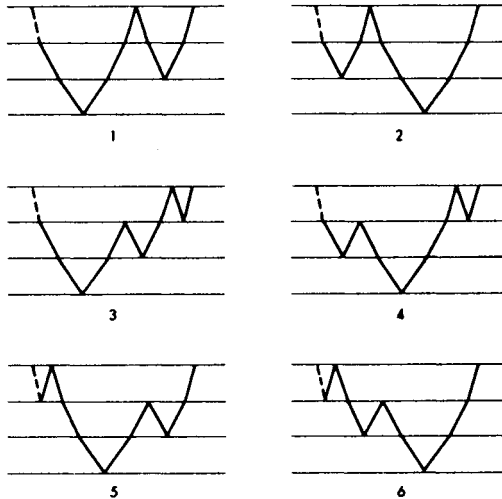


FIG. 4. Simply converted R-waves that arose from the group of kinematic analogs of unconverted R-waves with symbol  $\{2, 2, 1\}$ . Phases 1 and 2 belong to subgroup A with symbol  $\{\bar{2}, 2, 1; 0, 1\}$  while those with numbers 3 and 4 belong to subgroup A with symbol  $\{\bar{2}, 2, 1; 1, 1\}$ . Phases 5 and 6 belong to subgroup B with symbol  $\{\bar{2}, 2, 1; \bar{1}, 1\}$ . The solid line represents P-wave segments, while the dashed one represents S-wave segments.

Amplitude-distance characteristics for the vertical component of simply converted P-waves from both groups are shown in Fig. 5, where they are displayed together with the amplitude-distance curve for unconverted P-waves. The computations were performed for the Alberta model given in Table I.

It should be noted that in the case of simple layered media different approaches can be used. For example, Spencer (1965) developed a method of

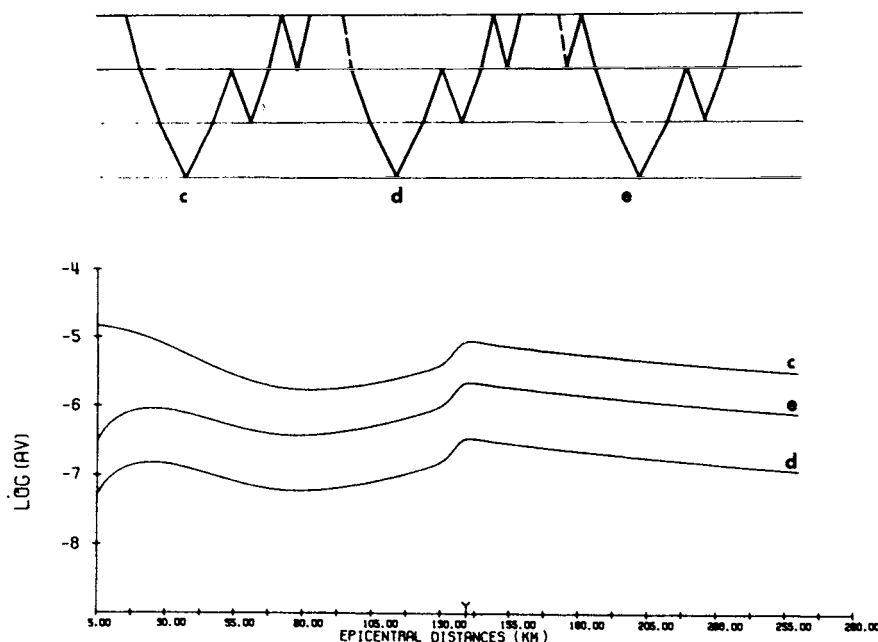


FIG. 5. Amplitude-distance characteristics for the vertical component of three different phases calculated for the Alberta model. The solid line represents P-wave segments; the dashed one stands for S-wave segments.

computing the dynamic effect of multiply reflected converted phases propagating in a high-speed layer which was embedded in an infinite medium. Unfortunately, Spencer's method, which considered all possible converted phases, cannot be applied to a more complicated layered medium.

### C. KINEMATIC AND DYNAMIC ANALOGS OF HEAD WAVES

Head waves can propagate under certain conditions in a layered medium with plane interfaces and are denoted by the symbol H. Although there are several groups of head waves, differentiated according to their mode of generation (i.e., whether the ray of the incident wave is critically reflected or refracted) and to the direction of their propagation (i.e., whether they propagate from the interface in the direction of reflected or refracted waves), we will pay our attention only to the group of so called basic head waves (classification according to Petrashen, 1959). These head waves, which are generated by the critical refraction of incident waves and which propagate from the interface in the direction of reflected waves, play an important role

in applied seismology and, moreover, represent the most numerous group of head waves. The following example demonstrates their generation from R-waves.

Consider an R-wave from the group of dynamic analogs characterized by the symbol

$$\{n_1, n_2, \dots, n_{J-1}, 1; m_1, \dots, m_{J-1}\}. \quad (28)$$

This wave has one trivial element of the  $J$ th class in the deepest layer and undergoes one refraction on the  $(J-1)$ th interface. If the velocity  $v_j > \text{Max}(v_j)$   $j = 1, \dots, J-1$ , the original R-wave may be critically refracted on the  $(J-1)$ th interface. Then the wave propagates along this interface with velocity  $v_j = v_H$  until it returns into the slower layer above (see Fig. 6). This

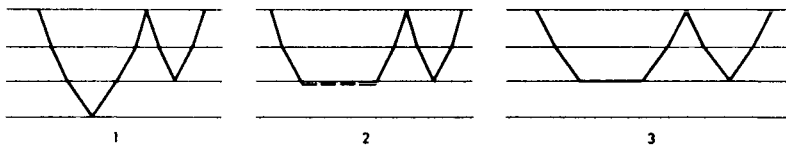


FIG. 6. An example of a part of the family of phases generated from the unconverted R-phase with symbol  $\{2, 2, 1\}$  (first diagram). Phase 1. One member of an unconverted R-wave with symbol  $\{2, 2, 1\}$ . Phase 2. An S-head wave  $\{2, 2; v_s\}$  generated by critical refraction of the wave in Phase 1. Phase 3. A P-head wave  $\{2, 2; v_p\}$  also generated by critical refraction of the wave in Phase 1.

critically refracted R-wave is usually called a basic head wave. The path length of the head wave along the  $(J-1)$ th interface is

$$L = r - \sum_{j=1}^{J-1} \frac{2n_j v_j h_j}{(v_H^2 - v_j^2)^{1/2}}, \quad (29)$$

where  $r$  is the epicentral distance of the receiver,  $h_j$  is the thickness of the  $j$ th layer, and  $v_j$  is the propagation velocity of the H-wave in the  $j$ th layer. According to Petrashen (1959), Hron (1968), and Červený and Ravindra (1971), the arrival time  $T_H$  and the complex amplitude  $W_H$  of a head wave derived from an unconverted R-wave with symbol (28) are

$$T_H = \frac{r}{v_H} + \sum_{j=1}^{J-1} 2h_j n_j \left( \frac{1}{v_j^2} - \frac{1}{v_H^2} \right)^{1/2}, \quad (30)$$

$$W_H = \frac{-i}{2\pi f(1/v_1^2 - 1/v_H^2)^{1/2}} \frac{H_{J-1} D_{J-1}^{m_{J-1}} G_0^{\mu_0}}{(rL^3)^{1/2}} \prod_{j=1}^{J-2} D_j^{m_j} E_j^l F_j^{\lambda_j} G_j^{\mu_j}, \quad (31)$$

where  $f$  is the dominant frequency of the wave,  $i = \sqrt{-1}$ ,  $H_{J-1}$  is the amplitude coefficient of the head wave. The symbols  $G_j$ ,  $D_j$ ,  $E_j$ ,  $F_j$ ,  $G_j$  and  $\mu_0$ ,  $m_j$ ,  $l_j$ ,  $\lambda_j$  were defined in (12).

Equation (30) reveals that the kinematic properties of head waves arising from unconverted R-waves from the group of kinematic analogs (32)

$$\{n_1, n_2, \dots, n_{J-1}, 1\} \quad (32)$$

are described uniquely by the numbers  $n_{J_1}, \dots, n_{-1}$  and the velocity  $v_H$ . These are defined to be *H-waves of the first kind*. The velocity  $v_H$  may be either a P- or S-wave velocity in the  $J$ th layer as the only condition imposed is that

$$v_H > \max(v(j(k))), \quad k = 1, \dots, K, \quad j \neq J, \quad (33)$$

where  $v(j(k))$  is the velocity of the  $k$ th segment of the ray in the  $j$ th layer. The symbol for H-waves of the first kind is

$$\{n_1, n_2, \dots, n_{J-1}; v_H\}. \quad (34)$$

The number of waves within the group of kinematic analogs (34) must be equal to the number of R-waves in (32), and for  $J \geq 3$  it is

$$\begin{aligned} N_k(n_1, n_2, \dots, n_{J-1}; v_H) &= \prod_{j=1}^{J-1} C_{n_{j+1}}^{n_j + n_{j+1} - 1} \\ &= n_{J-1} \cdot \prod_{j=1}^{J-2} C_{n_{j+1}}^{n_j + n_{j+1} - 1}. \end{aligned} \quad (35)$$

For  $J = 2$

$$N_k(n_1; v_H) = n_1. \quad (35a)$$

Equation (31) shows that the amplitudes of head waves of the first kind are uniquely determined by  $v_H$  and  $n_1, \dots, n_{J-1}, m_1, \dots, m_{J-2}$  as  $m_{J-1} = n_{J-1} - 1$ . Therefore the symbol for the group of dynamic analogs of H-waves of the first kind generated by R-waves (28) is

$$\{n_1, n_2, \dots, n_{J-1}; m_1, \dots, m_{J-2}; v_H\}. \quad (36)$$

The number of waves contained in this group has to be equal to the number of waves in (28). If  $J \geq 3$  this is

$$\begin{aligned} N_d(n_1, n_2, \dots, n_{J-1}; m_1, \dots, m_{J-2}; v_H) &= \prod_{j=1}^{J-1} C_{m_j}^{n_j} \cdot C_{n_j - m_j - 1}^{n_{j+1} - 1} \\ &= n_{J-1} \cdot \prod_{j=1}^{J-2} C_{m_j}^{n_j} \cdot C_{n_j - m_j - 1}^{n_{j+1} - 1}. \end{aligned} \quad (37)$$

For  $J = 2$

$$N_d(n_1; v_H) = n_1. \quad (37a)$$

Typical amplitude-distance characteristics for the vertical components of head waves of the first kind calculated for the Alberta model are given in Fig. 7.

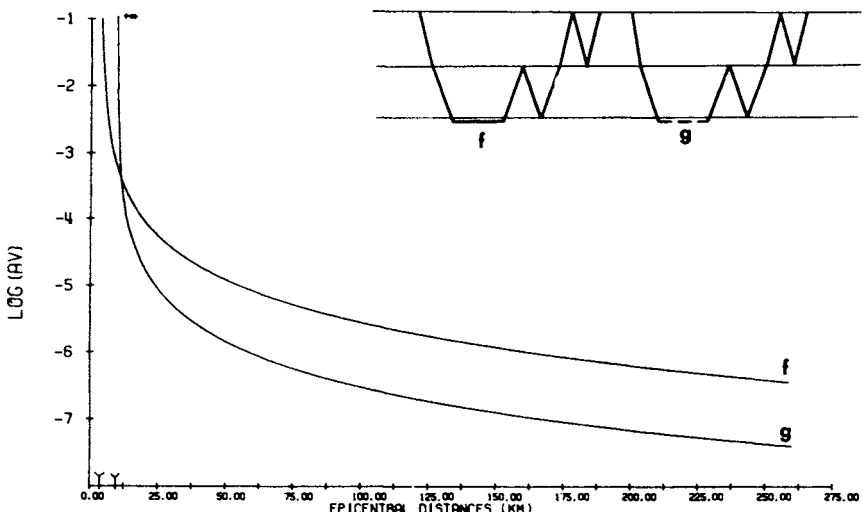


FIG. 7. Typical amplitude-distance characteristics for the vertical component of head waves calculated for the Alberta model.

*H-waves of the second kind* arise from critically refracted simply converted waves. The family of simply converted kinematic analogs of R-waves which are specified by the symbol

$$\{\bar{n}_1, n_2, \dots, n_{J-1}, 1\} \quad (38)$$

suggests that there is a family of H-waves of the second kind with the symbol

$$\{\bar{n}_1, n_2, \dots, n_{J-1}; v_H\}. \quad (39)$$

The number of phases in each group of kinematic analogs is given by

$$N_k(\bar{n}_1, n_2, \dots, n_{J-1}; v_H) = n_{J-1} \cdot \prod_{j=1}^{J-2} C_{n_j+n_{j+1}-1}^{n_j+n_{j+1}-1}, \quad J \geq 3; \quad (40)$$

$$N_k(\bar{n}_1; v_H) = n_1, \quad J = 2. \quad (40a)$$

Head waves derived from simply converted R-waves, subgroup A with symbol

$$\{\bar{n}_1, n_2, \dots, n_{J-1}, 1; m_1, \dots, m_{J-1}\} \quad (41)$$

are defined to be subgroup A of dynamic analogs for H-waves of the second kind:

$$\{\bar{n}_1, n_2, \dots, n_{J-1}; m_1, \dots, m_{J-2}; v_H\}. \quad (42)$$

The number of waves in (42) is

$$\begin{aligned} {}_A N_d(\bar{n}_1, n_2, \dots, n_{J-1}; m_1, \dots, m_{J-2}; v_H) &= C_{m_1-1}^{n_1-1} \cdot C_{n_1-m_1-1}^{n_2-1} \cdot n_{J-1} \\ &\cdot \prod_{j=2}^{J-2} C_{m_j}^{n_j} \cdot C_{n_j-m_j-1}^{n_{j+1}-1}, \quad J \geq 4; \end{aligned} \quad (43a)$$

$${}_A N_d(\bar{n}_1, n_2; m_1; v_H) = C_{m_1-1}^{n_1-1} \cdot C_{n_1-m_1-1}^{n_2-1} \cdot n_2, \quad J = 3; \quad (43b)$$

$${}_A N_d(\bar{n}_1; v_H) = 1, \quad J = 2. \quad (43c)$$

The critically refracted simply converted R-waves from the subgroup B in (44)

$$\{\bar{n}_1, n_2, \dots, n_{J-1} | 1; \bar{m}_1, \dots, m_{J-1}\}, \quad m_1 \neq 0 \quad (44)$$

suggest that there is also a subgroup B of dynamic analogs of H-waves of the second kind with symbol

$$\{\bar{n}_1, n_2, \dots, n_{J-1}; \bar{m}_1, \dots, m_{J-2}; v_H\}. \quad (45)$$

The number of waves within this subgroup is

$$\begin{aligned} {}_B N_d(\bar{n}_1, n_2, \dots, n_{J-1}; \bar{m}_1, \dots, m_{J-2}; v_H) &= C_{m_1-1}^{n_1-1} \cdot C_{n_1-m_1-1}^{n_2-1} \cdot n_{J-1} \\ &\cdot \prod_{j=2}^{J-2} C_{m_j}^{n_j} \cdot C_{n_j-m_j-1}^{n_{j+1}-1}, \quad J \geq 4; \end{aligned} \quad (46a)$$

$${}_B N_d(\bar{n}_1, n_2; \bar{m}_1; v_H) = C_{m_1-1}^{n_1-1} \cdot C_{n_1-m_1-1}^{n_2-1} \cdot n_2, \quad J = 3; \quad (46b)$$

$${}_B N_d(\bar{n}_1; v_H) = n_1 - 1, \quad J = 2. \quad (46c)$$

Equations (1) to (46) constitute a portion of an algorithm used to compute synthetic seismograms for models determined from deep seismic sounding programs. Results of the calculation are presented for example in Hron and Kanasewich (1971) or, to a lesser extent, in Section V.

#### IV. Flow Charts of Subroutines

##### A. FLOW CHART OF SUBROUTINE CREATING SYMBOLS FOR KINEMATIC AND DYNAMIC ANALOGS OF UNCONVERTED WAVES

From the previous sections it is obvious that the subroutine creating symbols for groups of kinematic and dynamic analogs should constitute the most important part of each algorithm which is used for the economic computation of synthetic seismograms in layered media. Since it was demonstrated in Sections III, B and III, C that the kinematic and dynamic analogs of both simply converted and head waves can be obtained quite easily from the kinematic and dynamic analogs of unconverted waves, only a flow chart of the subroutine for creating symbols of kinematic and dynamic analogs is presented in this section.

As we can see from the flow chart displayed in Fig. 8 a matrix  $N(I, L)$ , whose rows represent groups of kinematic analogs, is produced in the first part of the subroutine. After each new row of the matrix is computed, kinematic characteristics (such as the time of arrival at individual epicentral distances) may be calculated for corresponding groups of kinematic analogs. If the arrival time agrees with the required time window, for which a synthetic seismogram is being computed, the creation of symbols for groups of dynamic analogs is performed and their amplitudes are calculated. If the arrival time does not agree, the next row of matrix  $N(I, L)$  is calculated and a new group of kinematic analogs examined.

The computations of matrix  $N(I, L)$  are based on the idea that both the source and receiver are placed very close to the surface so that the number of segments in the rays of R-waves has to be even in each layer. If HSG is half the number of all segments in a ray and LBT is the number of the deepest layer traversed by the ray, there are as many different groups of kinematic analogs as there are possibilities of different distributions of HSG coupled segments of the rays into LBT upper layers not leaving any of them empty. According to Eq. (53), Appendix B, this number is

$$M(LBT, HSG) = C_{LBT-1}^{HSG-1} = \frac{(HSG-1)!}{(LBT-1)!(HSG-LBT)!}. \quad (47)$$

If LAY stands for number of layers in the medium (excluding a half-space) and HSG changes within the interval

$$1 \leq \text{HSG} \leq \text{HMS}, \quad (48)$$

the total number  $M_t$  of all different groups of kinematic analogs, satisfying Eq. (48) and propagating in the medium, would be

$$\begin{aligned} M_t(\text{LAY}, \text{HMS}) &= \sum_{\text{HSG}=1}^{\text{HMS}} \sum_{L=1}^{\text{LM}} M(L, \text{HSG}) \\ &= C_0^0 + C_0^1 + C_1^1 + \cdots + C_{\text{LMX}-2}^{\text{LMX}-1} + C_{\text{LMX}-1}^{\text{LMX}-1}, \end{aligned} \quad (49)$$

where

$$\text{LM} = \text{MIN}(\text{HSG}, \text{LAY}), \quad \text{LMX} = \text{MIN}(\text{HMS}, \text{LAY}).$$

Evidently,  $M_t(\text{LAY}, \text{HMS})$  represents the sum of up to LMX first numbers (or less, if the number of items in the row is less than LMX) in each of HMS upper rows in Pascal's triangle.

For example, adding up to 4 numbers in each of the 6 upper rows in Pascal's triangle in Table II (in other words, adding together all numbers in the area marked out by straight lines), we find out that the total number of all groups of kinematic analogs of unconverted R-waves with a maximum number of segments equal to 12, propagating in a 4-layer medium, is 56.

As  $M_t(\text{LAY}, \text{HMS})$  in Eq. (49) represents the total number of all events which one can distinguish in the computed seismograms for every epicentral distance, some values of  $M_t$  are given in Table III for  $\text{HMS} = \text{LAY}$ .

The fact that Eq. (49) gives us the expression for the row dimension of matrix  $N(I, L)$ , combined with the well-known feature of Pascal's triangle, whose each consecutive row can be computed with the aid of the previous one, suggests that the algorithm for computation of  $N(I, L)$  should be based on formula (49).

In order to visualize such an algorithm let us examine the last eight rows of matrix  $N(I, L)$ , which can be determined from the symbols for groups of dynamic analogs given in the numerical example in Section V. These rows represent 8 different groups of kinematic analogs consisting of rays with 8 segments. Since the column dimension of  $N(I, L)$  is equal to LMX, the above mentioned rows can be written in the way used in Table IV.

TABLE II

## **THE USE OF PASCAL'S TRIANGLE FOR THE DETERMINATION OF THE NUMBER OF GROUPS FOR KINEMATIC ANALOGS**

The figure illustrates the relationship between HMS (Horizontal Mutual Support) and LMX (Leader-Member Exchange) across 12 levels. The HMS scale (Y-axis) ranges from 1 to 12, with an arrow pointing downwards. The LMX scale (X-axis) ranges from 1 to 12, with an arrow pointing upwards. A diagonal line connects corresponding values, with points labeled 1 through 12.

HMS	LMX
1	1
2	1
3	1
4	2
5	1
6	3
7	3
8	1
9	4
10	6
11	10
12	12

TABLE III

## NUMBERS OF GROUPS OF KINEMATIC ANALOGS FOR HMS = LAY

LAY	1	2	3	4	5	6	7	8	9	10	11	12
$M_i(\text{LAY}, \text{HMS})$	1	3	7	15	31	63	127	255	511	1023	2047	4095

Looking at the fourth row of Pascal's triangle in Table II, we can see that all rows in Table IV can be divided into four groups, I-IV, with respect to the value LBT (note that in our particular case HSG = 4 in Eq. 49). Moreover, we can see that all three rows in the second group were obtained from row number 8 by subtracting integer values SN from the first column and adding them to the second one (the corresponding values of SN were 1, 2, 3, respectively, and LBT, the number of the column from which the SN was subtracted, was equal to 1). Similarly, row 12 was created from row 10

TABLE IV

DEMONSTRATION OF AN ALGORITHM FOR THE CREATION OF  
SYMBOLS FOR KINEMATIC ANALOGS

Row number	Row vector	LBT	$M(LBT, 4)$
8	4,0,0,0} I	1	1
9	3,1,0,0}		
10	2,2,0,0}	II	2
11	1,3,0,0}		3
12	2,1,1,0}		
13	1,2,1,0}	III	3
14	1,1,2,0}		3
15	1,1,1,1} IV	4	1

( $SN = 1, LBT = 2$ ) and rows 13 and 14 were obtained from row 11 using  $SN = 1, SN = 2$ , respectively ( $LBT = 2$  for both cases). Finally, the last row, number 15, was created from row 14 with the aid of  $SN = 1, LBT = 3$ .

From this very simple example we can also judge that the actual row dimension of the matrix  $N(I, L)$ , which is equal to  $M$ , in Eq. (49), can be reduced considerably during computation to the value

$$DIM = 2 * \text{MAX} \left( \frac{(HMS - 1)!}{(L - 1)!(HMS - L)!} \right), \quad 1 \leq L \leq \text{MIN}(HMS, LAY). \quad (50)$$

Some of these values are displayed in Table V, for  $HMS = LAY$ .

TABLE V  
REDUCED ROW DIMENSION OF MATRIX  $N(I, L)$ , FOR  $HMS = LAY$ 

LAY	2	3	4	5	6	7	8	9	10	11	12
DIM	2	4	6	12	20	40	70	140	252	504	924

The rest of the subroutine, whose flow chart is displayed in Fig. 8, deals mainly with the computations of all possible combinations of numbers

$$M_1, M_2, \dots, M_{L-1}, \quad (51)$$

which constitute the second part of the symbols for dynamic analogs. All these numbers have to satisfy condition (14) in Section III, A and there are as many groups of dynamic analogs within one group of kinematic analogs as there are different combinations of numbers (51) satisfying condition (14).

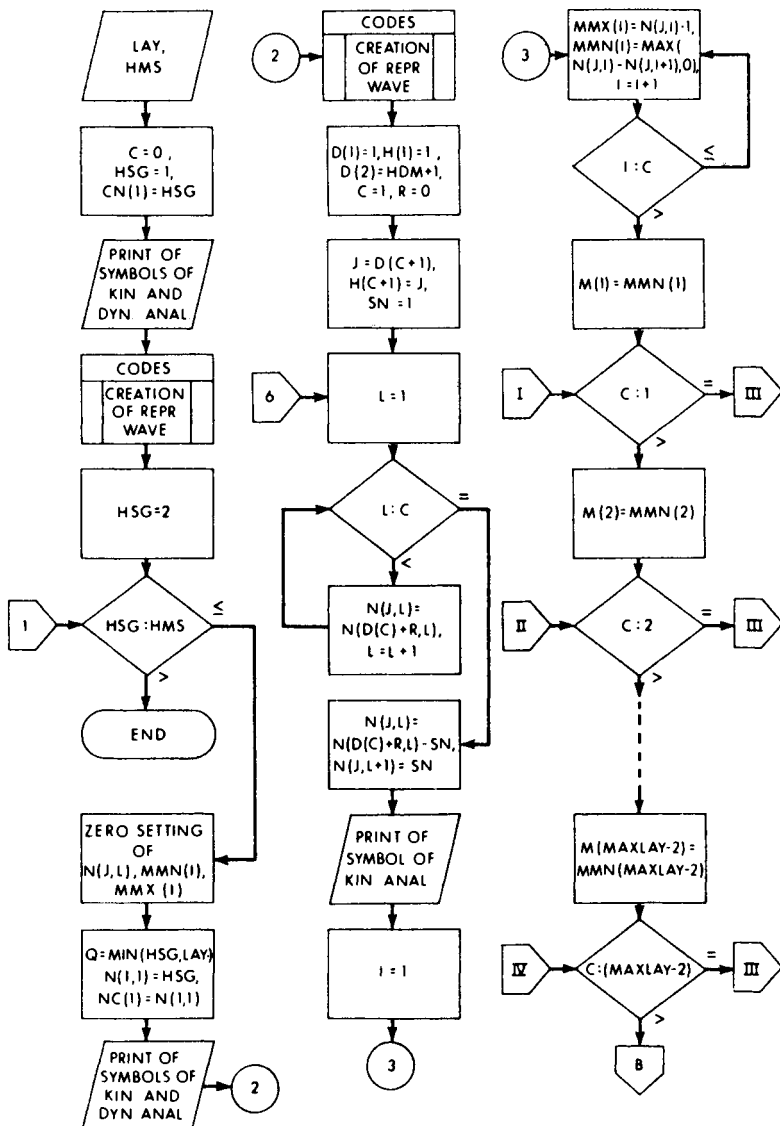


Fig. 8a. See caption on page 25.

Using the numerical results given in Section V, we can see, for example, that the original group of 3 kinematic analogs with symbol  $\{2, 2\}$  split into 2 different groups of dynamic analogs with symbols  $\{2, 2; 0\}$  and  $\{2, 2; 1\}$ , respectively, because there were only two values of  $M_1$  satisfying condition (14).

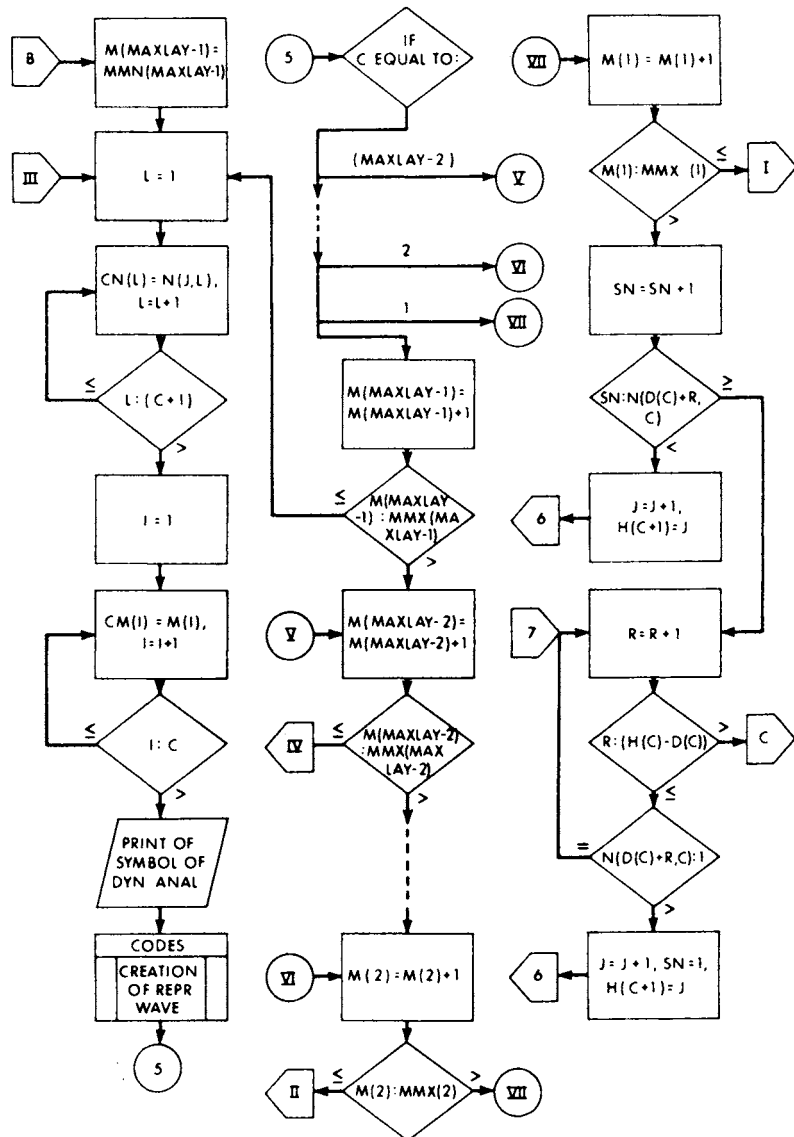


FIG. 8b. See caption on page 25.

The actual algorithm for creating groups of numbers (5!), which is based on nested DO loops, is outlined in the flow chart in Fig. 8 and does not need any further explanation.

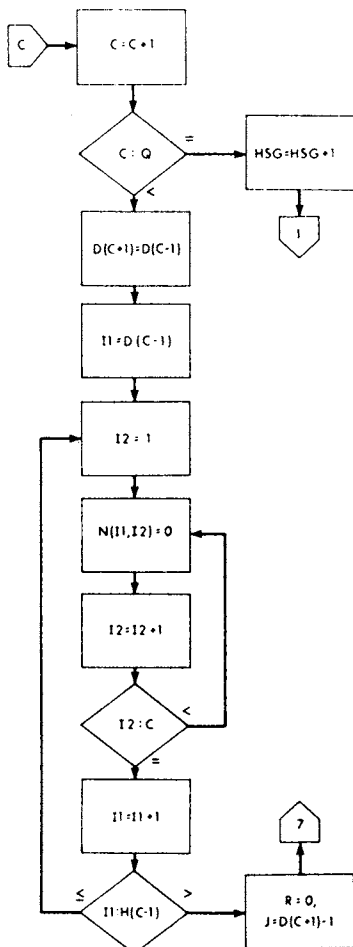


FIG. 8c

FIG. 8 a-c. Flow chart of subroutine creating symbols for kinematic and dynamic analogs of unconverted waves.

#### *List of Symbols Used in the Flow Chart in Fig. 8*

HMS—half the maximum number of segments in rays which are to be generated by the subroutine (HMS is an input value).

HSG—half the current number of all segments in the rays being generated. The range is  $1 \leq HSG \leq HMS$ .

LAY—number of layers in the medium (excluding a half space). The range is  $1 \leq LAY \leq MAXLAY$  (LAY is an input value).

MAXLAY—maximum admissible number of layers in the medium, for which computations can still be carried out using a current version of the program (see nested DO loops in the flow chart which depend on the parameter MAXLAY).

$N(I, L)$ —matrix, whose rows represent symbols for the groups of kinematic analogs. The ranges are  $1 \leq I \leq 2^*HDM$ ,  $1 \leq L \leq \text{MIN(HMS, LAY)}$ .  $HDM$ —half of the reduced row dimension of matrix  $N(I, L)$ , whose value has to be obtained from Eq. (50).

$M(\Lambda)$ —number of reflections of the ray from the  $\Lambda$ th interface. The ranges are  $\text{MMN}(\Lambda) \leq M(\Lambda) \leq \text{MMX}(\Lambda)$ ,  $1 \leq \Lambda \leq C$ , where  $\text{MMN}(\Lambda)$  and  $\text{MMX}(\Lambda)$  are obtained from Eq. (14).

$C$ —position of the last nonzero element in the row  $I$  of matrix  $N(I, L)$ . If  $N(I, C) > 1$ , a new row  $J$  of the matrix is computed by copying the first  $(C - 1)$  elements of  $N(I, L)$  (i.e.,  $N(J, K) = N(I, K)$ ,  $1 \leq K < C$ , subtracting SN from  $N(I, C)$  (i.e.,  $N(J, C) = N(I, C) - SN$ ), and creating a new  $(C + 1)$ st element of the  $J$ th row of the value SN (i.e.,  $N(J, C + 1) = SN$ ). The range is  $1 \leq C < \text{MIN(HSG, LAY)}$ .

$D(C)$ —number of the first row in the array  $N(I, L)$ , whose  $C$ th element is the last one different from zero [i.e.,  $N(D(C), L) \neq 0$ , for  $1 \leq L \leq C$ ;  $N(D(C), L) = 0$  for  $C < L \leq \text{MIN(HMS, LAY)}$ ].  $D(C)$  has either the value 1 or  $HDM + 1$ .

$H(C)$ —the position of the last row in  $N(I, L)$ , whose  $C$ th element is the last one different from zero. The range is  $H(C) - D(C) \leq HDM - 1$ .

$R$ —position of the row in  $N(I, L)$  from which a new row  $N(J, L)$  is being computed (see more details in definition of variable  $C$ ). The position indicator  $R$  is related to the row with number  $D(C)$  for which  $R = 0$ . Range is  $0 \leq R \leq H(C) - D(C)$ .

$SN$ —value of the  $(C + 1)$ st element of the newly calculated row  $N(J, L)$ . The range is  $1 \leq SN \leq N(D(C) + R, C) - 1$ .

{CN(1), CN(2), ..., CN( $C$ ), CN( $C + 1$ )}—symbol for a group of kinematic analogs, corresponding to the newly created row  $N(J, L)$ ,  $1 \leq L \leq C + 1$ .

{CN(1), CN(2), ..., CN( $C + 1$ ); CM(1), ..., CM( $C$ )}—symbols for the groups of dynamic analogs which belong to the family of kinematic analogs mentioned above.

## B. FLOW CHART OF SUBROUTINE CREATING CODES OF REPRESENTATIVE WAVES FOR GROUPS OF DYNAMIC ANALOGS OF UNCONVERTED WAVES

Although a symbol for the group of dynamic analogs contains all quantities which are necessary for the evaluation of the total dynamic effect of the group and kinematic features of its members (see Eq. 5 for arrival time, Eq. 12 for amplitude, and Eq. 19 for the number of different phases in the group), sometimes it is useful to know the code of one phase from the group, which could demonstrate both the kinematic and dynamic properties of all its members. For example, if we know the amplitude of this phase, which will be called a "representative wave," and multiply it by the number of dynamic analogs given by Eq. (19), we get the total dynamic effect of the group.

The knowledge of the code of a representative wave is especially useful during the final stages of interpretation of synthetic seismograms, when they are being compared with field measurements.

Although each of the phases from the group can serve as a representative wave, and in some cases its code can be written immediately following the "try and see" rule, in most cases such an approach becomes tedious and time consuming, especially where the number of segments in the ray is large.

Having considered the above mentioned reasons, a subroutine for creating the codes of representative waves has been written and its flow chart is displayed in Fig. 9.

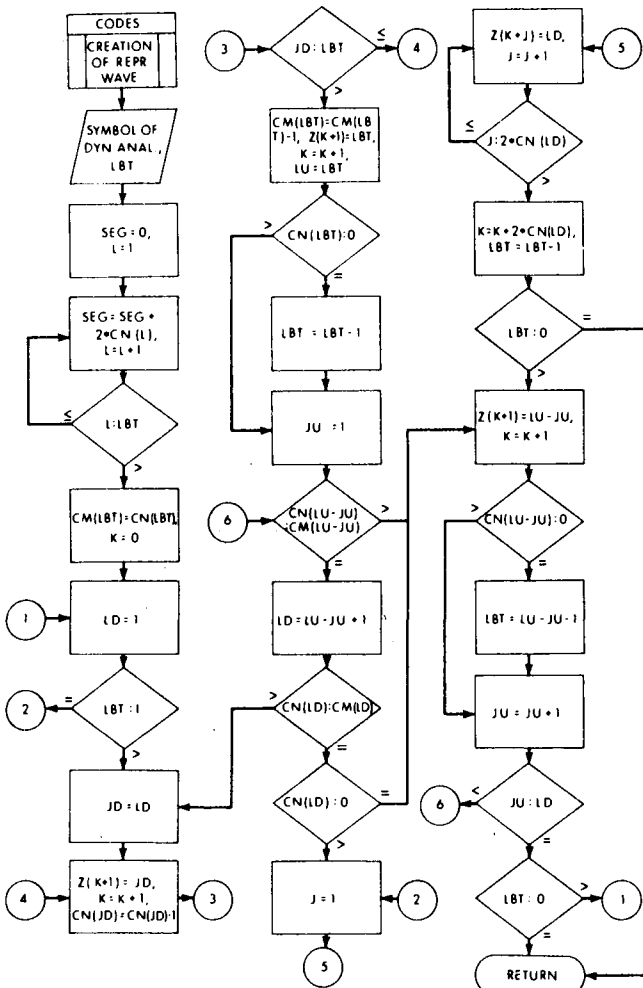


FIG. 9. Flow chart of subroutine creating codes for representative waves for any dynamic analog.

The algorithm for the subroutine, which is based on the knowledge of the symbol for the group of dynamic analogs, is so simple that it does not need any other explanation beside its flow chart. After observing a few codes of representative waves produced by this subroutine, it can be seen that each ray is constructed in such a way that each downgoing part of the ray attempts to reach the deepest possible layer before returning to the surface. The result is that the depth at which downgoing parts of the ray return to the surface does not increase while proceeding to the end of the ray.

*List of Symbols Used in the Flow Chart in Fig. 9*

- CN( $L$ )—half the current number of remaining segments in the  $L$ th layer, which have not yet been used for the construction of the ray of representative waves. [Input values CN( $L$ ),  $1 \leq L \leq (C + 1)$ , constitute the first part of the symbol of dynamic analogs.]
- C—parameter which is transferred to the subroutine from the calling program (see Section IV,B for more details).
- CM( $L$ )—current number of reflections from the  $L$ th interface, which must be undertaken by the rest of the ray that has not been constructed. [Input values CM( $L$ ),  $1 \leq L \leq C$ , constitute the second part of the symbol for dynamic analogs.]
- SEG—total number of segments in a ray.
- LBT—number of the deepest layer for which CN( $L$ )  $\neq 0$  holds at the moment of computation [i.e., CN(LBT)  $\neq 0$ , CN(LBT + 1) = 0]. The input value of LBT, LBT =  $C + 1$ , is equal to the number of the deepest layer traversed by the representative wave.
- Z( $K$ )—number of the layer in which the  $K$ th segment of the ray lies ( $K = 1$  corresponds to the segment which comes out from the source). The range is  $1 \leq Z(K) \leq C + 1$  for  $1 \leq K \leq \text{SEG}$ .
- LD—number of the layer from which the constructed branch of the ray starts going down. (JD is a variable of the corresponding DO loop.)
- LU—number of the layer from which the constructed branch of the ray starts going up (variable of corresponding DO loop is JU).

## V. Numerical Examples

Typical results of the program, which is based on two subroutines described in Section IV, are presented in this section. The program was modified in order to demonstrate the possibility of generating other groups of dynamic

analogs, provided that a symbol for the group of dynamic analogs of unconverted waves is known. The program follows strictly the method of derivation of these symbols as outlined in Section III.

The computations were carried out for an Alberta model (see Table I) and a point source which generated P-waves. The maximum number of segments in the rays was 8. The results are given in Table VI in the same form as they were printed in the actual output.

We can see from the table that there are 15 groups of kinematic analogs, which split into 16 groups of dynamic analogs numbered by roman figures. Note that only the tenth group of kinematic analogs consists of 2 groups of dynamic analogs with numbers X and XI, while the remainder contain only 1 group of dynamic analogs. The symbols for groups of dynamic analogs, which were produced by the subroutine described in Section IV, A, served as the input for the subroutine creating the code of a representative wave for the group of unconverted dynamic analogs. Once having the code of the unconverted wave, the remaining groups of dynamic analogs and their representative waves were created in the same order as they are printed in Table VI.

To visualize this process in greater detail we shall take a look at the family of 9 groups of dynamic analogs and their representative waves, as they were created from symbol XIII. It is seen that the group 37, consisting of two dynamic analogs, was created first. The number of analogs within this group,  $N = 2$ , was calculated according to Eq. (19). Keeping only the mode of the first segment in the ray, the code number 38 of a new wave, representing the subgroup A of simply converted dynamic analogs, was obtained. Equation (23) gave  $N = 1$  for this group. Then the representative waves for the groups of dynamic analogs of head waves of the first kind with numbers 39, 40 and those of the second kind, type A, with numbers 41, 42 were created. The numbers of dynamic analogs in both groups were determined by Eqs. (37) and (43b), respectively. Just reversing the order in the sequence  $\{Z(K)\}$  (an output of the subroutine in Section IV,B), which represents the sequence of the layers traversed by the representative wave number 36, we obtain the ray that was used for the code of the representative wave for the subgroup B of simply converted waves. The number of this group is 43 and Eq. (25) determines the number of its analogs. Finally, the representative waves 44 and 45 belong to the groups of head waves of the second kind, type B, and their numbers were calculated using Eq. (46b).

The usefulness of the classification of rays into groups of kinematic and dynamic analogs as well as the efficiency of both subroutines described in Section IV is demonstrated in Fig. 10. The synthetic seismogram was computed for an epicentral distance of 220 km and an eleven-layer model (Table VII), as interpreted by Dr. I. P. Kosinskaya for a particular portion of the

TABLE VI

TYPICAL OUTPUT OF THE PROGRAM WHICH IS BASED ON SUBROUTINES  
DESCRIBED IN SECTION IV<sup>a</sup>

Group symbol:		I				{1}	
$N = 1;$	1	P1	P1				
$N = 1;$	2	P1	S1				
Group symbol:		II				{2}	
$N = 1;$	3	P1	P1	P1	P1		
$N = 1;$	4	P1	S1	S1	S1		
Group symbol:		III				{1, 1; 0}	
$N = 1;$	5	P1	P2	P2	P1		
$N = 1;$	6	P1	S2	S2	S1		
$N = 1;$	7	P1	P2	P1			
$N = 1;$	8	P1	P2	S1			
Group symbol:		IV				{3}	
$N = 1;$	9	P1	P1	P1	P1	P1	P1
$N = 1;$	10	P1	S1	S1	S1	S1	S1
Group symbol:		V				{2, 1; 1}	
$N = 2;$	11	P1	P2	P2	P1	P1	P1
$N = 1;$	12	P1	S2	S2	S1	S1	S1
$N = 2;$	13	P1	P2	P1	P1	P1	
$N = 1;$	14	P1	S1	S1	S2	S2	S1
Group symbol:		VI				{1, 2; 0}	
$N = 1;$	15	P1	P2	P2	P2	P2	P1
$N = 1;$	16	P1	S2	S2	S2	S2	S1
Group symbol:		VII				{1, 1, 1; 0, 0}	
$N = 1;$	17	P1	P2	P3	P3	P2	P1
$N = 1;$	18	P1	S2	S3	S3	S2	S1
$N = 1;$	19	P1	P2	S3	P2	P1	
$N = 1;$	20	P1	P2	P3	P2	P1	
$N = 1;$	21	P1	S2	S3	S2	S1	
$N = 1;$	22	P1	S2	P3	S2	S1	
Group symbol:		VIII				{4}	
$N = 1;$	23	P1	P1	P1	P1	P1	P1
$N = 1;$	24	P1	S1	S1	S1	S1	S1
Group symbol:		IX				{3, 1; 2}	
$N = 3;$	25	P1	P2	P2	P1	P1	P1
$N = 1;$	26	P1	S2	S2	S1	S1	S1
$N = 3;$	27	P1	P2	P1	P1	P1	P1
$N = 2;$	28	P1	S1	S1	S1	S2	S2
$N = 2;$	29	P1	S1	S1	S1	P2	S1
Group symbol:		X				{2, 2; 0}	
$N = 1;$	30	P1	P2	P2	P1	P1	P1
$N = 1;$	31	P1	S2	S2	S1	S1	S1
Group symbol:		XI				{2, 2; 1}	
$N = 2;$	32	P1	P2	P2	P2	P1	P1
$N = 1;$	33	P1	S2	S2	S2	S1	S1
$N = 1;$	34	P1	S1	S1	S2	S2	S1
Group symbol:		XII				{1, 3; 0}	
$N = 1;$	35	P1	P2	P2	P2	P2	P1
$N = 1;$	36	P1	S2	S2	S2	S2	S1

TABLE VI—*continued*

Group symbol:		XIII				{2, 1, 1; 1, 0}		
$N = 2;$	37	P1	P2	P3	P3	P2	P1	P1
$N = 1;$	38	P1	S2	S3	S3	S2	S1	S1
$N = 2;$	39	P1	P2	S3	P2	P1	P1	P1
$N = 2;$	40	P1	P2	P3	P2	P1	P1	P1
$N = 1;$	41	P1	S2	S3	S2	S1	S1	S1
$N = 1;$	42	P1	S2	P3	S2	S1	S1	S1
$N = 1;$	43	P1	S1	S1	S2	S3	S3	S2
$N = 1;$	44	P1	S1	S1	S2	S3	S2	S1
$N = 1;$	45	P1	S1	S1	S2	P3	S2	S1
Group symbol:		XIV				{1, 2, 1; 0, 1}		
$N = 2;$	46	P1	P2	P3	P3	P2	P2	P1
$N = 2;$	47	P1	S2	S3	S3	S2	S2	S1
$N = 2;$	48	P1	P2	S3	P2	P2	P2	P1
$N = 2;$	49	P1	P2	P3	P2	P2	P2	P1
$N = 2;$	50	P1	S2	S3	S2	S2	S2	S1
$N = 2;$	51	P1	S2	P3	S2	S2	S2	S1
Group symbol:		XV				{1, 1, 2; 0, 0}		
$N = 1;$	52	P1	P2	P3	P3	P3	P2	P1
$N = 1;$	53	P1	S2	S3	S3	S3	S2	S1
Group symbol:		XVI				{1, 1, 1, 1; 0, 0, 0}		
$N = 1;$	54	P1	P2	P3	P4	P4	P3	P2
$N = 1;$	55	P1	S2	S3	S4	S4	S3	S2
$N = 1;$	56	P1	P2	P3	P4	P3	P2	P1
$N = 1;$	57	P1	S2	S3	S4	S3	S2	S1
$N = 1;$	58	P1	S2	S3	P4	S3	S2	S1

<sup>a</sup> Computations were carried out for the Alberta model given in Table I.

TABLE VII  
PARAMETERS FOR AN ELEVEN-LAYER MODEL<sup>a</sup>

Layer	$\alpha$ (km/sec)	$\beta$ (km/sec)	$\rho$ (g/cm <sup>3</sup> )	h(km)
1	3.0	1.73	2.20	5
2	6.1	3.54	2.80	2
3	6.0	3.47	2.75	5
4	6.4	3.69	2.90	2
5	6.0	3.47	2.75	5
6	6.8	3.93	3.00	2
7	6.5	3.75	2.90	5
8	7.2	4.16	3.10	2
9	6.5	3.75	2.90	5
10	7.4	4.28	3.15	2
11	6.5	3.75	2.90	5
Half-space	8.0	4.62	3.35	$\infty$

<sup>a</sup> According to a personal communication from Kosminskaya (1970).

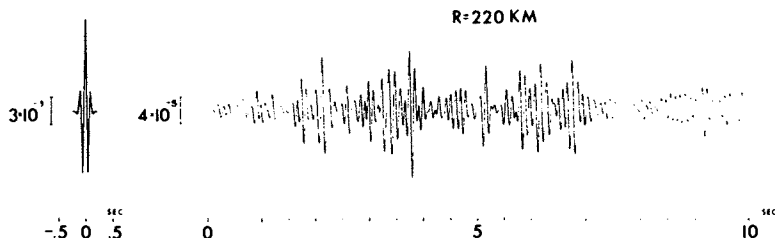


FIG. 10. Synthetic seismogram calculated for an eleven-layer medium (see Table VII) and epicentral distance 220 km. The point source, placed near the surface, generated an impulse which is displayed at the left. During computation over 150,000 individual phases, split into 21,650 groups of dynamic analogs, were generated and their contribution to the seismogram calculated.

continental crust in the U.S.S.R.. During the computation, which was carried out by IBM 360-67 computer, 21,650 groups of dynamic analogs representing over 150,000 individual waves were examined and their displacement contribution evaluated on the basis of asymptotic ray theory outlined by Hron and Kanasewich (1971). The execution time of the run, including interpretation of the most significant waves and the computation of data, which were necessary for an automatic display of the seismogram by a Calcomp plotter, was less than 10 min. Some other examples of using an automatic ray generation described in this article for the computation of synthetic seismograms can be found in the paper written by Hron and Kanasewich (1971).

#### Appendix A. Number of Arrangements of $n_2$ Identical Balls into $n_1$ Pockets, Some of Which Can Be Empty

Consider an arbitrary distribution of  $n_2$  identical balls into  $n_1 \geq 1$  pockets separated by  $(n_1 - 1)$  inner walls. Each such distribution can be visualized as a sequence of  $(n_1 - 1 + n_2)$  items represented by  $n_2$  balls and  $(n_1 - 1)$  inner boundaries, as illustrated in Fig. 11 for  $n_1 = 4$ ,  $n_2 = 5$ . From this diagram, we can see that three inner walls occupy, in the sequence of eight elements,

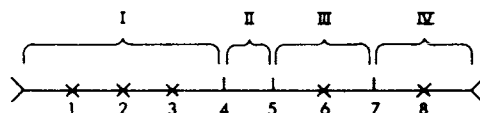


FIG. 11. One of 56 possible distributions of 5 balls into 4 pockets. The balls are represented by x marks, while inner boundaries are indicated by | marks.

the fourth, fifth, and seventh positions so that there are 3 balls in the first pocket, the second pocket is left empty, and there is 1 ball in pockets III and IV.

Because individual distributions differ from each other only in the selection of  $(n_1 - 1)$  positions occupied by inner boundaries, the number,  $M_1$ , of distributions of  $n_2$  balls into  $n_1$  pockets, some of which can be left empty, is equal to the number of all possible selections of  $(n_1 - 1)$  positions from the total number  $(n_1 - 1 + n_2)$ . Obviously, this is equal to

$$M_1(n_1, n_2) = C_{n_1-1}^{n_1+n_2-1} = C_{n_2}^{n_1+n_2-1} = \frac{(n_1 + n_2 - 1)!}{(n_1 - 1)! n_2!}. \quad (52)$$

There  $C_{n_1-1}^{n_1+n_2-1}$  is the number of all combinations of the  $(n_1 - 1)$ th class from  $(n_1 + n_2 - 1)$  elements.

### **Appendix B. Number of Arrangements of $n_2$ Identical Balls into $n_1$ Pockets, None of Which Can Be Empty**

Distributions of this kind can be performed only if  $n_2 \geq n_1$ . Then the problem can be transformed easily to the problem resolved in the previous section if we separate from  $n_2$  balls  $n_1$  so-called "fixed balls" by distributing them into  $n_1$  pockets, none of them leaving empty. Then the number  $M_2$  has to be equal to the number of arrangements of the remaining  $(n_2 - n_1)$  "movable balls" into  $n_1$  pockets provided that some of them may not contain any movable ball. Using Eq. (52) we get immediately

$$M_2(n_1, n_2) = M_1(n_1, n_2 - n_1) = C_{n_1-1}^{n_2-1} = \frac{(n_2 - 1)!}{(n_1 - 1)! (n_2 - n_1)!}, \quad (53)$$

where  $M_2(n_1, n_2)$  is the number of all arrangements of  $n_2$  identical balls into  $n_1$  pockets leaving none of them empty.

#### **ACKNOWLEDGMENTS**

This research was supported by funds from the National Research of Canada.

I express my appreciation to Professor E. R. Kanasewich from the University of Alberta, who read the manuscript and helped me with final arrangements of the text.

#### **REFERENCES**

- ČERVENÝ, V. (1965). *Trav. Inst. Géophys. Acad. Tchécosl. Sci.* **22**, 135.
- ČERVENÝ, V. (1966). *Geophys. J. Roy. Astron. Soc.* **11**, 139.
- ČERVENÝ, V., and RAVINDRA, R. (1971). "Theory of Seismic Head Waves." Univ. of Toronto Press, Toronto.

- CUMMING, G. L., and KANASEWICH, E. R. (1966). "Crustal Structure in Western Canada," Final report, Project Vela Uniform, Contract No. AF 19(628)-2835, Project No. 8652, Task No. 865202. Advanced Research Projects Agency.
- HELMBERGER, D. V. (1968). *Bull. Seismol. Soc. Amer.* **58**, 179.
- HELMBERGER, D. V., and MORRIS, G. B. (1969). *J. Geophys. Res.* **74**, 483.
- HRON, F. (1968). "Introduction to the Ray Theory in a Broader Sense: Application to Seismology," Textbook of Laboratoire de Physique de l'École Normale Supérieure. University of Paris, Paris.
- HRON, F. (1971). *Bull. Seismol. Soc. Amer.* **61**, 765.
- HRON, F., and KANASEWICH, E. R. (1971). *Bull. Seismol. Soc. Amer.* **61**, 1169.
- KOSMINSKAYA, I. P. (1970) Personal communication.
- MÜLLER, G. (1968a). *Z. Geophys.* **34**, 15.
- MÜLLER, G. (1968b). *Z. Geophys.* **34**, 147.
- MÜLLER, G. (1970). *Geophys. J. Roy Astron. Soc.* **21**, 261.
- PETRASHEN, G. I. (1959). In "Problems in Dynamic Theory of Seismic Wave Propagation" (G. I. Petrashen, ed.), Vol. III, p. 11. Leningrad Univ. Press, Leningrad (in Russian).
- SPENCER, T. W. (1965). *Geophysics*. **30**, 369.
- VAVILLOVA, T. I., and PETRASHEN, G. I. (1966). In "Problems in Dynamic Theory of Seismic Wave Propagation" (G. I. Petrashen, ed.), Vol. VIII, p. 48. Nauka, Moscow and Leningrad (in Russian).
- VAVILLOVA, T. I., and PUGACH, A. D. (1966). In "Problems in Dynamic Theory of Seismic Wave Propagation" (G. I. Petrashen, ed.), Vol. VIII, p. 30. Nauka, Moscow and Leningrad (in Russian).

# Computer Generated Seismograms

Z. ALTERMAN and D. LOEWENTHAL

DEPARTMENT OF ENVIRONMENTAL SCIENCE

TEL AVIV UNIVERSITY

RAMAT-AVIV, ISRAEL

I. Introduction . . . . .	35
II. Methods of Solution . . . . .	36
A. Finite Differences . . . . .	36
B. Normal Modes and Ray Analysis Methods . . . . .	58
III. Computed Seismograms and Their Analysis . . . . .	81
A. A Pulse in a Quarter Plane, Three-Quarter Plane, and in Two Welded Quarter Planes . . . . .	81
B. Shear Crack in a Plane and in a Half Plane . . . . .	106
C. Seismograms for the Layered Half Space . . . . .	110
D. Seismograms for the Layered Sphere . . . . .	126
E. Results for the Laterally Heterogeneous Sphere . . . . .	153
Appendix. Equations for the Layered Sphere . . . . .	157
References . . . . .	162

## I. Introduction

COMPUTER GENERATED SEISMOGRAMS HAVE become a tool with numerous possibilities of application. Only a limited number of years ago the state of the art was such that only the simplest models could be considered.

However, today complete seismograms can be computed for a layered plane or spherical earth, and also for heterogeneous media with various kinds of sources. Mathematical tools have been widely developed and very good results obtained despite the complexity of equations and boundary conditions—obviously the result of the use of computers.

Finite difference methods have been introduced into solid earth geophysics, which proved to widen essentially the scope of solvable problems. Moreover, the finite difference calculations proved to be much faster than previous calculations, i.e., consuming less computer time, and made it possible to obtain complete and accurate theoretical seismograms beginning with the onset and continuing through the reflection and diffraction phases and the various modes of surface waves. Consequently, it has proved practical to solve by finite differences not only problems for which analytic methods had been previously unsuccessful but also problems in which the analytic expressions were lengthy.

This article exposes the finite difference methods employed to obtain complete theoretical seismograms for a source in a layered half-space, in wedges, and in a sphere (Section II,A). Normal mode solutions for a source in a sphere and the ray expansion method are discussed in Section II, B. Seismograms have been computed for these models, with samples and interpretations presented in Section III.

## II. Methods of Solution

### A. FINITE DIFFERENCES

#### 1. Equations of Motion

The solutions for most of the interesting problems in theoretical seismology cannot be obtained in a closed analytic form. Even those problems which possess analytic solutions have in most cases a very complicated form and much labor is required to obtain the explicit numerical or graphical result.

In this section a numerical method is described consisting mainly of finite difference techniques which yield fast explicit solutions. The efficiency of the method is demonstrated by a few examples which have a closed analytic solution and by problems where no analytic solution can be obtained, i.e., cases where no separation of variables can be performed.

In most of the examples we consider an elastic medium which can be divided into a number of homogeneous isotropic elastic regions.

The equation of motion which governs the elastic displacement vector  $\mathbf{U}$  in an isotropic homogeneous elastic medium is given by

$$\rho \partial^2 \mathbf{U} / \partial t^2 = (\lambda + 2\mu) \operatorname{grad} \operatorname{div} \mathbf{U} - \mu \operatorname{rot} \operatorname{rot} \mathbf{U}, \quad (1)$$

where  $\rho$  is the density and  $\lambda, \mu$  are the Lamé elastic parameters of the medium. The boundary conditions usually require the free surface of the elastic medium to be stress free.

Denoting by  $\tau$  the stress tensor, by  $\mathbf{n}$  the unit vector perpendicular to the free surface, and by  $\mathbf{t}$  the unit vector parallel to the free surface, the normal and tangential components of stress satisfy

$$\tau_{nn} = \tau_{nt} = 0 \quad (2)$$

on the free surface.

On the interface between two elastic media, superscripted as 1 and 2, respectively, we require that both the displacements and the stresses be continuous:

$$\begin{aligned} U^1 &= U^2, \\ \tau_{nn}^1 &= \tau_{nn}^2, \\ \tau_{nt}^1 &= \tau_{nt}^2. \end{aligned} \quad (3)$$

## 2. Finite Difference Formulation for the Layered Half-Space

a. *Equations of Motion in Cylindrical Coordinates.* The layered half-space problem as treated by Alterman and Karal (1968) may serve as an illustration of the finite difference technique in cylindrical coordinates. Here we wish to determine the motion of the surface and of the interior of a homogeneous isotropic elastic layer overlying a homogeneous half-space when a pressure pulse is emitted from a point source situated in the layer. The thickness of the layer is  $h$  and the source is located inside the layer at a depth  $d$ .

Since the system has axial symmetry it is convenient to use cylindrical coordinates  $(r, z)$  with the  $z$  axis passing through the source and directed positively downwards. (See Fig. 1.<sup>1</sup>)

The displacement vector  $\mathbf{U} = \begin{bmatrix} u_r \\ u_z \end{bmatrix}$  is denoted as

$$\begin{aligned} u_r(r, z, t) &= A(r, z, t) = A, \\ u_z(r, z, t) &= B(r, z, t) = B, \end{aligned} \quad (4)$$

where  $A$  and  $B$  are the radial and normal components of displacement.

The equations of motion in three space dimensions and time may be written in finite difference form by replacing the various derivatives by their centered finite difference approximations. In cylindrical coordinates let  $r = m\Delta r$  and  $z = n\Delta z$ , where  $\Delta r$  and  $\Delta z$  are incremental lengths along the  $r$  and  $z$  axes, and let  $t = p\Delta t$ , where  $\Delta t$  is an increment in time. Equation (1) may be written as follows:

$$\begin{aligned} A_{m,n,p+1} &= 2A_{m,n,p} - A_{m,n,p-1} + r_p^2 \epsilon_1^2 [A_{m+1,n,p} - 2A_{m,n,p} + A_{m-1,n,p}] \\ &\quad + \frac{1}{2} r_p^2 \epsilon_1^2 (1/m) [A_{m+1,n,p} - A_{m-1,n,p}] - r_p^2 \epsilon_1^2 (1/m^2) A_{m,n,p} \\ &\quad + \frac{1}{4} \epsilon_1 \epsilon_2 [r_p^2 - r_s^2] [B_{m+1,n+1,p} - B_{m+1,n-1,p} - B_{m-1,n+1,p} \\ &\quad + B_{m-1,n-1,p}] + r_s^2 \epsilon_2^2 [A_{m,n+1,p} - 2A_{m,n,p} + A_{m,n-1,p}], \end{aligned} \quad (5)$$

<sup>1</sup> Figures 1-11 appear on pages 77-81.

$$\begin{aligned}
B_{m,n,p+1} = & 2B_{m,n,p} - B_{m,n,p-1} + v_p^2 \varepsilon_2^2 [B_{m,n+1,p} - 2B_{m,n,p} + B_{m,n-1,p}] \\
& + \frac{1}{2} \varepsilon_1 \varepsilon_2 [v_p^2 - v_s^2] (1/m) [A_{m,n+1,p} - A_{m,n-1,p}] \\
& + \frac{1}{4} \varepsilon_1 \varepsilon_2 [v_p^2 - v_s^2] [A_{m+1,n+1,p} - A_{m+1,n-1,p} - A_{m-1,n+1,p} \\
& + A_{m-1,n-1,p}] + \frac{1}{2} v_p^2 \varepsilon_1^2 (1/m) [B_{m+1,n,p} - B_{m-1,n,p}] \\
& + v_s^2 \varepsilon_1^2 [B_{m+1,n,p} - 2B_{m,n,p} + B_{m-1,n,p}].
\end{aligned} \tag{6}$$

Here  $\varepsilon_1 = \Delta t / \Delta r$  and  $\varepsilon_2 = \Delta t / \Delta z$ .

The notation  $A_{m,n,p+1}$  indicates the value of the radial displacement at the point  $(m \Delta r, n \Delta z)$  at the time  $(p+1) \Delta t$ . Similar meanings apply to other subscripts attached to the displacement components  $A$  and  $B$ .  $m$ ,  $n$ , and  $p$  take on nonnegative integral values only. All derivatives appearing in Eqs. (5) and (6) are correct to second order in the increments appearing in the denominators [e.g.,  $\partial^2 A / \partial t^2$  is correct to order  $(\Delta t)^2$ ,  $\partial^2 B / \partial r \partial z$  is correct to order  $(\Delta r)^2$ ,  $(\Delta z)^2$ , or  $(\Delta r \Delta z)$ , whichever is largest, etc.]. Equations (5) and (6) are explicit difference equations. Note that when values of the displacement components  $A$  and  $B$  are known at time levels  $p-1$  and  $p$ , it is possible to compute the displacement at the next time level  $p+1$ . The calculation stencil for Eqs. (5) and (6) is shown in Fig. 2.

Equations (5) and (6) apply to either medium so long as the stencil does not overlap the free surface or the interface and the axis of symmetry is excluded ( $m \neq 0$ ). Along the axis of symmetry ( $m = 0$ ), Eqs. (5) and (6) are undefined because of the presence of  $m$  in the denominator. Valid equations along the axis of symmetry are easily derived, however, by using independent arguments. Due to continuity of the elastic media, the radial displacement  $A$  is zero along the axis of symmetry. Hence

$$A_{0,n,p+1} = 0. \tag{7}$$

The normal displacement  $B$  is more complicated. The troublesome terms in the equation for  $B$  are  $(1/r)(\partial A / \partial z)$  and  $(1/r)(\partial B / \partial r)$ . By using L'Hopital's rule, the term  $(1/r)(\partial A / \partial z)$  can be replaced by  $\partial^2 A / \partial r \partial z$  and  $(1/r)(\partial B / \partial r)$  can be replaced by  $\partial^2 B / \partial r^2$ . These, in turn, can be replaced by their finite difference approximations.  $A$  and  $B$  are defined for  $r \geq 0$  only. Due to their regularity near  $r = 0$  they can be continued to  $r < 0$  by using the symmetry conditions

$$\begin{aligned}
A_{-1,n,p} &= -A_{1,n,p}, \\
B_{-1,n,p} &= +B_{1,n,p}.
\end{aligned} \tag{8}$$

If we make these new substitutions in the equation of motion for  $B$ , then we have

$$\begin{aligned} B_{0,n,p+1} = & 2B_{0,n,p} - B_{0,n,p-1} + v_p^2 \epsilon_2^2 [B_{0,n+1,p} - 2B_{0,n,p} + B_{0,n-1,p}] \\ & + \epsilon_1 \epsilon_2 [v_p^2 - v_s^2] [A_{1,n+1,p} - A_{1,n-1,p}] \\ & + 4v_s^2 \epsilon_1^2 [B_{1,n,p} - B_{0,n,p}]. \end{aligned} \quad (9)$$

Equations (5)–(7) and (9) are the basic formulas used in the computations.

b. *Surface Boundary Conditions.* The finite difference equations (5)–(7) and (9) cannot be applied at the free surface  $z = 0$  and at the interface  $z = h$  because the equations involve indefinite quantities. In order to calculate the displacements on these special surfaces, it is necessary to use the boundary conditions that must be satisfied there. Consider first the case of the free surface. The boundary conditions that must hold on this surface are given by conditions (2) which are expressed in this case as

$$\begin{aligned} \tau_{zz} = & (\lambda + 2\mu) \left[ \frac{\partial A}{\partial r} + \frac{1}{r} A + \frac{\partial B}{\partial z} \right] - 2\mu \left[ \frac{1}{r} A + \frac{\partial A}{\partial r} \right] = 0, \\ \tau_{rz} = & \mu \left[ \frac{\partial B}{\partial r} + \frac{\partial A}{\partial z} \right] = 0. \end{aligned} \quad (10)$$

By replacing all derivatives in Eq. (10) with their central finite difference approximations, and assuming the surface  $z = 0$  corresponds to the values of  $n = 0$ , we obtain

$$\begin{aligned} B_{m,-1,p}^1 = & B_{m,1,p}^1 + \left( \frac{\Delta z}{\Delta r} \right) \left[ 1 - 2 \left( \frac{v_{s1}}{v_{p1}} \right)^2 \right] [A_{m+1,0,p}^1 - A_{m-1,0,p}^1] \\ & + 2 \left( \frac{\Delta z}{\Delta r} \right) \left[ 1 - 2 \left( \frac{v_{s1}}{v_{p1}} \right)^2 \right] \frac{1}{m} A_{m,0,p}^1 \end{aligned} \quad (11)$$

and

$$A_{m,-1,p}^1 = A_{m,1,p}^1 + \left( \frac{\Delta z}{\Delta r} \right) [B_{m+1,0,p}^1 - B_{m-1,0,p}^1]. \quad (12)$$

Note that the values of  $A$  and  $B$  given on the left-hand side of Eqs. (11) and (12) are for  $n = -1$  and therefore correspond to a fictitious line above the actual physical surface at  $n = 0$ . See Fig. 3.

A complication arises on the axis of symmetry ( $m = 0$ ) and special treatment is required. Due to continuity and cylindrical symmetry,

$$A_{0, -1, p}^1 = 0 \quad (13)$$

as in Eq. (7).

An expression for  $B_{0, -1, p}^1$  can be found by using Eq. (10) for  $\tau_{zz} = 0$  and replacing the troublesome term  $(1/r)A^1$  by  $\partial A^1 / \partial r$  in the same way as was done for the equations of motion. Then

$$B_{0, -1, p}^1 = B_{0, 1, p}^1 + 4(\Delta z / \Delta r)[1 - 2(v_s/v_p)^2]A_{1, 0, p}^1, \quad (14)$$

using the symmetry condition  $A_{-1, n, p}^1 = -A_{1, n, p}^1$ . Equations (11)–(14) make it possible at any given time level to compute values of  $A$  and  $B$  on the fictitious line  $n = -1$ . Knowing values on this line, it is then possible to use the equations of motion (5)–(7) and (9) up to and on the actual physical surface  $n = 0$ .

c. *Interface Boundary Conditions.* The boundary conditions that must be satisfied at the interface  $z = h$  can be derived from Eqs. (3) which have here the form

$$\begin{aligned} & \left[ \frac{\partial A}{\partial r} + \frac{1}{r} A^1 + \frac{\partial B^1}{\partial z} \right] - 2 \left( \frac{v_{s1}}{v_{p1}} \right)^2 \left[ \frac{1}{r} A^1 + \frac{\partial A^1}{\partial r} \right] \\ &= \left( \frac{\rho_2}{\rho_1} \right) \left( \frac{v_{p2}}{v_{p1}} \right)^2 \left[ \frac{\partial A^2}{\partial r} + \frac{1}{r} A^2 + \frac{\partial B^2}{\partial z} \right] - 2 \left( \frac{\rho_2}{\rho_1} \right) \left( \frac{v_{s2}}{v_{p1}} \right)^2 \left[ \frac{1}{r} A^2 + \frac{\partial A^2}{\partial r} \right], \end{aligned} \quad (15)$$

$$\left[ \frac{\partial B^1}{\partial r} + \frac{\partial A^1}{\partial z} \right] = \left( \frac{\mu_2}{\mu_1} \right) \left[ \frac{\partial B^2}{\partial r} + \frac{\partial A^2}{\partial z} \right], \quad (16)$$

$$\begin{aligned} A^1 &= A^2, \\ B^1 &= B^2. \end{aligned} \quad (17)$$

In order to obtain an explicit finite difference computational scheme, we first add a fictitious line to medium 1 by extending the  $z$  grid beyond the interface at  $z = h$ . A fictitious line is not introduced in medium 2. The media have the interface  $z = h$  in common. In medium 1, however, the interface is the next-to-last line in that medium while the fictitious line is the last line. In medium 2, the interface is the first line of the  $z$  grid in that medium (see Fig. 4a). We now illustrate the procedure for Eq. (16). Replace the  $r$ -derivatives

with a centered (two-sided) finite difference approximation and the  $z$ -derivatives with an asymmetrical (one-sided) finite difference approximation. Equation (16) then becomes

$$\begin{aligned} \frac{1}{2\Delta r} [B_{m+1, N, p}^1 - B_{m-1, N, p}^1] + \frac{1}{\Delta z} [A_{m, N+1, p}^1 - A_{m, N, p}^1] \\ = \left( \frac{\mu_2}{\mu_1} \right) \left[ \frac{1}{2\Delta r} (B_{m+1, 1, p}^2 - B_{m-1, 1, p}^2) + \frac{1}{\Delta z} (A_{m, 2, p}^2 - A_{m, 1, p}^2) \right]. \quad (18) \end{aligned}$$

The notation involving the second subscript on  $A$  and  $B$  is important. In medium 1, the subscripts  $N$  and  $N+1$  indicate the interface and fictitious line, respectively. In medium 2, the subscripts 1 and 2 indicate the interface and next line beyond the interface extending into medium 2. From Eq. (17), which requires the continuity of displacement across the interface, we have

$$\begin{aligned} A_{m, 1, p}^2 &= A_{m, N, p}^1, \\ B_{m \pm 1, 1, p}^2 &= B_{m \pm 1, N, p}^1. \end{aligned} \quad (19)$$

Substituting into Eq. (18) and solving for  $A^1$  on the fictitious line, we obtain

$$\begin{aligned} A_{m, N+1, p}^1 &= \left[ 1 - \frac{\mu_2}{\mu_1} \right] A_{m, N, p}^1 + \left( \frac{\mu_2}{\mu_1} \right) A_{m, 2, p}^2 \\ &\quad - \frac{1}{2} \left( \frac{\Delta z}{\Delta r} \right) \left[ 1 - \left( \frac{\mu_2}{\mu_1} \right) \right] \left[ B_{m+1, N, p}^1 - B_{m-1, N, p}^1 \right]. \quad (20) \end{aligned}$$

In a similar way, the other interface condition (Eq. 15) gives

$$\begin{aligned} B_{m, N+1, p}^1 &= \left[ 1 - \left( \frac{\rho_2}{\rho_1} \right) \left( \frac{v_{p2}}{v_{p1}} \right)^2 \right] B_{m, N, p}^1 + \left( \frac{\rho_2}{\rho_1} \right) \left( \frac{v_{p2}}{v_{p1}} \right)^2 B_{m, 2, p}^2 \\ &\quad - \frac{1}{2} \left( \frac{\Delta z}{\Delta r} \right) \left\{ \left[ 1 - 2 \left( \frac{v_{s1}}{v_{p1}} \right)^2 \right] - \left( \frac{\rho_2}{\rho_1} \right) \left[ \left( \frac{v_{p2}}{v_{p1}} \right)^2 - 2 \left( \frac{v_{s2}}{v_{p1}} \right)^2 \right] \right\} \\ &\quad \times \left[ A_{m+1, N, p}^1 - A_{m-1, N, p}^1 + \frac{2}{m} A_{m, N, p}^1 \right]. \quad (21) \end{aligned}$$

Along the axis of symmetry ( $m = 0$ ) the values of  $A$  and  $B$  on the fictitious line become

$$A_{0, N+1, p}^1 = 0 \quad (22)$$

and

$$\begin{aligned}
 B_{0, N+1, p}^1 = & \left[ 1 - \left( \frac{\rho_2}{\rho_1} \right) \left( \frac{v_{p2}}{v_{p1}} \right)^2 \right] B_{0, N, p}^1 + \left( \frac{\rho_2}{\rho_1} \right) \left( \frac{v_{p2}}{v_{p1}} \right)^2 B_{0, 2, p}^2 \\
 & - 2 \left( \frac{\Delta z}{\Delta r} \right) \left\{ \left[ 1 - 2 \left( \frac{v_{s1}}{v_{p1}} \right)^2 \right] - \left( \frac{\rho_2}{\rho_1} \right) \left[ \left( \frac{v_{p2}}{v_{p1}} \right)^2 \right. \right. \\
 & \left. \left. - 2 \left( \frac{v_{s2}}{v_{p1}} \right)^2 \right] \right\} A_{1, N, p}^1. \tag{23}
 \end{aligned}$$

Note that the determination of  $A^1$  and  $B^1$  on the fictitious line  $N+1$  at time  $p$  means that we can compute  $A^1$  and  $B^1$  on the interface at the next time step  $p+1$  by using the equations of motion for medium 1. Also, since we can compute  $A^1$  and  $B^1$  on the interface (denoted by  $n=N$  in medium 1), we know  $A^2$  and  $B^2$  on the interface (denoted by  $n=1$  in medium 2) by continuity of displacements [Eq. (17)]. Hence we can find  $A^2$  and  $B^2$  at the next time step  $p+1$  using the equations of motion for medium 2.

Equations (20), (21), and (23) contain the ratios  $(\mu_2/\mu_1)$  and  $(v_{p2}/v_{p1})^2 \times (\rho_2/\rho_1)$ . If the constants characterizing the two media are quite different, then these ratios may be large. The effect of these large ratios is to introduce serious errors and (sometimes) instabilities in the calculations. The reason this occurs is because the one-sided derivative in  $z$  introduces an asymmetry in the boundary conditions. If we had used a two-sided or centered derivative in  $z$ , the finite difference equations for the boundary conditions would be symmetrical. However, the calculation scheme across the interface would no longer be explicit. When the ratios  $(\mu_2/\mu_1)$  and  $(v_{p2}/v_{p1})^2(\rho_2/\rho_1)$  are large, we add the fictitious line to medium 2 (rather than medium 1) and then derive results for  $A^2$  and  $B^2$  along this fictitious line. See Fig. 4b. Proceeding in the same manner as before, we obtain the following results when  $m \neq 0$ :

$$\begin{aligned}
 A_{m+1, p}^2 = & \frac{1}{2} \left( \frac{\Delta z}{\Delta r} \right) \left( 1 - \frac{\mu_1}{\mu_2} \right) [B_{m+1, N, p}^1 - B_{m-1, N, p}^1] \\
 & + \left( 1 - \frac{\mu_1}{\mu_2} \right) A_{m, N, p}^1 + \frac{\mu_1}{\mu_2} A_{m, N-1, p}^1 \tag{24}
 \end{aligned}$$

$$\begin{aligned}
 B_{m+1, p}^2 = & \left[ 1 - \left( \frac{\rho_1}{\rho_2} \right) \left( \frac{v_{p1}}{v_{p2}} \right)^2 \right] B_{m, N, p}^1 + \left( \frac{\rho_1}{\rho_2} \right) \left( \frac{v_{p1}}{v_{p2}} \right)^2 B_{m, N-1, p}^1 \\
 & + \frac{1}{2} \left( \frac{\Delta z}{\Delta r} \right) \left\{ \left[ 1 - 2 \left( \frac{v_{s2}}{v_{p1}} \right)^2 \right] - \left( \frac{\rho_1}{\rho_2} \right) \left[ \left( \frac{v_{p1}}{v_{p2}} \right)^2 - 2 \left( \frac{v_{s1}}{v_{p2}} \right)^2 \right] \right\} \\
 & \times \left[ A_{m+1, N, p}^1 - A_{m-1, N, p}^1 + \frac{2}{m} A_{m, N, p}^1 \right]. \tag{25}
 \end{aligned}$$

Along the axis of symmetry ( $m = 0$ ) we have

$$A_{0,1,p} = 0, \quad (26)$$

$$\begin{aligned} B_{0,1,p}^1 &= \left[ 1 - \left( \frac{\rho_1}{\rho_2} \right) \left( \frac{v_{p1}}{v_{p2}} \right)^2 \right] B_{0,N,p}^1 + \left( \frac{\rho_1}{\rho_2} \right) \left( \frac{v_{p1}}{v_{p2}} \right)^2 B_{0,N-1,p}^1 \\ &+ 2 \left( \frac{\Delta z}{\Delta r} \right) \left\{ \left[ 1 - 2 \left( \frac{v_{s2}}{v_{p2}} \right)^2 \right] - \left( \frac{\rho_1}{\rho_2} \right) \left[ \left( \frac{v_{p1}}{v_{p2}} \right)^2 - 2 \left( \frac{v_{s1}}{v_{p2}} \right)^2 \right] \right\} A_{1,N,p}^1. \end{aligned} \quad (27)$$

In comparing Eqs. (20)–(23) with Eqs. (24)–(27) we see that the effect of changing the fictitious line from medium 1 to medium 2 is to invert the ratios  $(\mu_2/\mu_1)$  and  $(v_{p2}/v_{p1})^2(\rho_2/\rho_1)$  into  $(\mu_1/\mu_2)$  and  $(v_{p1}/v_{p2})^2(\rho_1/\rho_2)$ , respectively. In the computational work the set of equations is used for which the ratios are least.

### 3. The Finite Difference Technique for Wedge Problems

Wedge problems have drawn much attention since Lapwood's (1961) investigation of the problem [see, e.g., the references in Fuchs (1965) and Alterman and Rotenberg (1969)].

However, the complete motion of a quarter plane due to an impulsive line source in its interior has so far not been obtained by analytic means. This seems to be due to two main reasons: Separation of variables is inapplicable for a quarter plane with free surfaces, and the integral equation or integral transform formulations are so involved that only first- or second-order approximations were obtained.

A finite difference solution, as given by Alterman and Rotenberg (1969) and by Alterman and Loewenthal (1970), is discussed here, which gives the complete motion of an elastic quarter plane due to an impulsive line source emitting compressional waves. Other corner problems such as the three-quarter plane, the two welded half planes, and crack problems were treated similarly (see Alterman and Loewenthal, 1969, 1970; Loewenthal and Alterman, 1972).

The method of finite differences as applied to corner problems is general enough to solve the equations of seismic wave propagation in a wide variety of additional problems which have not been solved by the classical analytical tools. Several problems of this kind have been solved by Boore (1970). The solution to some of them is given in the sequel to this study.

a. *Equations of Motion in Cartesian Coordinates.* In this problem we wish to determine the motion of the two-dimensional elastic homogeneous isotropic quarter plane  $x \geq 0, y \geq 0$  (90° wedge), caused by an impulsive point source located inside it (see Fig. 5a). [See Alterman and Rotenberg (1969) and Alterman and Loewenthal (1970).] The two perpendicular boundaries are assumed to be stress free.

The equations of motion (1) can be written for this case in Cartesian coordinates in the form:

$$\frac{\partial^2 \mathbf{U}}{\partial t^2} = A \frac{\partial^2 \mathbf{U}}{\partial x^2} + B \frac{\partial^2 \mathbf{U}}{\partial x \partial y} + C \frac{\partial^2 \mathbf{U}}{\partial y^2}. \quad (28)$$

Here  $\mathbf{U} = (u, v)$  is the displacement vector and  $A, B, C$  are the following matrices:

$$A = \begin{pmatrix} v_p^2 & 0 \\ 0 & v_s^2 \end{pmatrix}, \quad B = \begin{pmatrix} 0 & v_p^2 - v_s^2 \\ v_p^2 - v_s^2 & 0 \end{pmatrix}, \quad C = \begin{pmatrix} v_s^2 & 0 \\ 0 & v_p^2 \end{pmatrix}.$$

For the finite difference formulation of this problem the derivatives which appear in Eq. (28) are approximated by centered finite differences and

$$\begin{aligned} \mathbf{U}(x, y, t + \Delta t) &= 2\mathbf{U}(x, y, t) - \mathbf{U}(x, y, t - \Delta t) \\ &\quad + A\varepsilon_1^2 [\mathbf{U}(x + \Delta x, y, t) - 2\mathbf{U}(x, y, t) + \mathbf{U}(x - \Delta x, y, t)] \\ &\quad + \frac{B}{4} \varepsilon_1 \varepsilon_2 [\mathbf{U}(x + \Delta x, y + \Delta y, t) - \mathbf{U}(x + \Delta x, y - \Delta y, t) \\ &\quad - \mathbf{U}(x - \Delta x, y + \Delta y, t) + \mathbf{U}(x - \Delta x, y - \Delta y, t) + C\varepsilon_2^2 \\ &\quad \times [\mathbf{U}(x, y + \Delta y, t) - 2\mathbf{U}(x, y, t) + \mathbf{U}(x, y, -\Delta y, t)]] \end{aligned} \quad (29)$$

Here

$$\varepsilon_1 = \Delta t / \Delta x, \quad \varepsilon_2 = \Delta t / \Delta y.$$

As in Eqs. (5) and (6) all finite difference approximations appearing in Eq. (29) are correct to second order in the increments. Equation (29) is an explicit difference equation. When values of the displacement components  $u$  and  $v$  are known at time  $t - \Delta t$  and  $t$ , the displacement at the next time level can be computed.

By choosing the source to be equidistant from the two boundary lines, i.e., on the main diagonal from the corner, and for a source which is circularly symmetric, there is symmetry about the main diagonal. Then at any point in the plane  $u(x, y, t) = v(y, x, t)$ , and it is not necessary to reserve storage for both the  $u$  and  $v$  arrays. Instead only one array is used and the values of  $u$  stored therein, the values of  $v$  being obtained from the symmetry relationship.

b. *Boundary Conditions for the Quarter Plane.* The following boundary conditions are derived from Eq. (2):

$$\begin{aligned}\tau_{xx} &= \rho \left[ v_p^2 \frac{\partial u}{\partial x} + (v_p^2 - 2v_s^2) \frac{\partial v}{\partial y} \right] = 0, \\ \tau_{xy} &= \rho v_s^2 \left[ \frac{\partial u}{\partial y} + \frac{\partial v}{\partial x} \right] = 0, \quad \text{on } x = 0, y \geq 0\end{aligned}\quad (30)$$

$$\begin{aligned}\tau_{yy} &= \rho \left[ (v_p^2 - 2v_s^2) \frac{\partial u}{\partial x} - v_p^2 \frac{\partial v}{\partial y} \right] = 0, \\ \tau_{xy} &= \rho v_s^2 \left[ \frac{\partial u}{\partial y} + \frac{\partial v}{\partial x} \right] = 0, \quad \text{on } y = 0, x \geq 0.\end{aligned}\quad (31)$$

In the sequel let us consider a grid of spacing  $\Delta x = \Delta y = h$ .

To satisfy the boundary conditions for the quarter plane the lines of mesh points at  $x = -h$  and  $y = -h$  are added to the array as special lines. On these lines the displacement components  $u$  and  $v$  are determined such that boundary conditions in Eqs. (30) and (31) are satisfied on the lines  $x = 0, y > 0$  and  $y = 0, x > 0$ . As before (see Section II,A,2) better results are obtained when derivatives perpendicular to the boundary are approximated by uncentered differences and derivatives parallel to the boundary are approximated by centered differences.

On  $x = 0$  the equations are

$$\mathbf{U}(-h, y, t) = \mathbf{U}(0, y, t) + F[\mathbf{U}(0, y + h, t) - \mathbf{U}(0, y - h, t)]. \quad (32)$$

and on  $y = 0$

$$\mathbf{U}(x, -h, t) = \mathbf{U}(x, 0, t) + G[\mathbf{U}(x + h, 0, t) - \mathbf{U}(x - h, 0, t)], \quad (33)$$

with

$$F = \begin{pmatrix} 0 & \frac{1}{2} - (v_s/v_p)^2 \\ \frac{1}{2} & 0 \end{pmatrix} \quad \text{and} \quad G = F^T = \begin{pmatrix} 0 & \frac{1}{2} \\ \frac{1}{2} - (v_s/v_p)^2 & 0 \end{pmatrix}. \quad (34)$$

They determine  $\mathbf{U}$  on the special lines  $y = -h$  and  $x = -h$ .

For a source on the diagonal of the quarter plane there is symmetry and one condition is sufficient. For a source at an arbitrary location we need also the second boundary condition.

c. *Corner Conditions.* A special situation exists at the corner (see Fig. 6). If we set  $x = y = 0$ , Eq. (29) involves the point  $(-h, -h)$  which has not

been obtained by the boundary conditions (32) and (33). An additional equation has to be derived to satisfy the boundary conditions at the corner. Within the accuracy of the grid spacing, the location of the corner is at some point in the square  $(0, 0); (0, -h); (-h, 0); (-h, -h)$ , i.e., the grid determines the location of the corner to an accuracy given by  $h$ . Within this square, the boundary at the corner may be approximated by a smooth curve, such that the tangent to the boundary at the point  $x = y = -h/2$  is at an angle of  $45^\circ$  to both axes. The normal and tangential stresses at this point,  $\tau_{nn}$  and  $\tau_{nt}$ , are given by

$$\tau_{nn} = \frac{1}{2}\tau_{xx} + \tau_{xy} + \tau_{yy}, \quad (35)$$

$$\tau_{nt} = \frac{1}{2}(\tau_{yy} - \tau_{xx}). \quad (36)$$

Vanishing of these stresses is expressed by the two equations

$$(v_p^2 - v_s^2)\left(\frac{\partial u}{\partial x} + \frac{\partial v}{\partial y}\right) + v_s^2\left(\frac{\partial u}{\partial y} + \frac{\partial v}{\partial x}\right) = 0 \quad (37)$$

and

$$\frac{\partial u}{\partial x} - \frac{\partial v}{\partial y} = 0. \quad (38)$$

The finite difference form for (37) and (38) is obtained by substituting the approximation

$$(1/2h)[u(0, -h, t) - u(-h, -h, t) + u(0, 0, t) - u(-h, 0, t)] \quad (39)$$

for  $\partial u / \partial x$  and

$$(1/2h)[u(-h, 0, t) - u(-h, -h, t) + u(0, 0, t) - u(0, -h, t)] \quad (40)$$

for  $\partial u / \partial y$ .

Similar expressions approximate  $\partial v / \partial x$  and  $\partial v / \partial y$ . Thus  $u$  and  $v$  at  $(-h, -h)$  are determined by

$$\begin{aligned} u(-h, -h, t) &= u(0, 0, t) + [(v_p^2 - v_s^2)/v_p^2][u(0, -h, t) - u(-h, 0, t)] \\ &\quad - (v_s^2/v_p^2)[v(-h, 0, t) - v(0, -h, t)], \end{aligned} \quad (41)$$

$$\begin{aligned} v(-h, -h, t) &= v(0, 0, t) - (v_s^2/v_p^2)[u(0, -h, t) - u(-h, 0, t)] \\ &\quad + [(v_p^2 - v_s^2)/v_p^2][v(-h, 0, t) - v(0, -h, t)]. \end{aligned} \quad (42)$$

A very simple condition results at the corner if we impose at  $x = y = 0$  the boundary conditions (30) and (31) simultaneously. From the first equation in (30) and the second equation in (31) we find

$$\partial u / \partial x = \partial v / \partial y = 0 \quad (43)$$

and determine

$$u(-h, -h) = u(0, -h), \quad (44)$$

$$v(-h, -h) = v(-h, 0). \quad (45)$$

Calculations for several grid sizes show that the two sets of boundary conditions lead to the same results. For example, when the source is on the diagonal at  $x = y = d$  so that by symmetry  $u(x, y) = v(y, x)$  and in a grid of  $21 \times 21$  divisions in the square between the source and corner, the maximum value of  $u$  at the corner was found to be  $1.937d$  according to the condition in Eq. (41) and  $1.944d$  according to Eq. (44). When the number of grid points is doubled in each direction the value of  $u$  is  $1.938d$  and  $1.935d$  in the two cases, respectively.

Similar boundary conditions are also encountered in the problem of a  $270^\circ$  wedge in the three-quarter plane problem depicted in Fig. 5b and in the problem of the two welded quarter planes shown in Fig. 5c.

#### 4. The Equations of Motion in a Heterogeneous Medium and Their Finite Difference Approximation

a. *Equations of Motion in Spherical Coordinates.* Let us consider here the motion of a solid elastic sphere caused by an impulsive point source. The sphere is assumed to be radially and laterally heterogeneous. This case was investigated by Alterman and Aboudi (1970). It demonstrates both the use of finite difference techniques for solving nonhomogeneous problems and the formulation of difference schemes in spherical coordinates.

The equation of motion for a heterogeneous elastic medium can be written in the form

$$\begin{aligned} \rho \partial^2 \mathbf{U} / \partial t^2 &= (\lambda + 2\mu) \operatorname{grad} \operatorname{div} \mathbf{U} - \mu \operatorname{rot} \operatorname{rot} \mathbf{U} \\ &+ \operatorname{div} \mathbf{U} \cdot \operatorname{grad} \lambda + 2 (\operatorname{grad} \mu \cdot \mathcal{E}). \end{aligned} \quad (46)$$

Here  $\mathcal{E}$  is the strain tensor. In the system of spherical coordinates  $(R, \theta, \phi)$  and for motions having cylindrical symmetry for which also  $u_\phi = 0$ , let us denote  $\mathbf{U} = (u_R, u_\theta)$  and

$$\mathcal{E} = \begin{bmatrix} \frac{\partial u_R}{\partial R} & \frac{1}{2} \left[ \frac{\partial u_\theta}{\partial R} - \frac{u_\theta}{R} + \frac{1}{R} \frac{\partial u_R}{\partial \theta} \right] \\ \frac{1}{2} \left[ \frac{\partial u_\theta}{\partial R} - \frac{u_\theta}{R} + \frac{1}{R} \frac{\partial u_R}{\partial \theta} \right] & \frac{1}{R} \left[ \frac{\partial u_\theta}{\partial \theta} + u_R \right] \end{bmatrix}. \quad (47)$$

Introducing the vector

$$\mathbf{V} = R\mathbf{U} \quad (48)$$

of components

$$F = Ru_R, \quad G = Ru_\theta, \quad (49)$$

Eq. (46) can be written as

$$\begin{aligned} \frac{\partial^2 \mathbf{V}}{\partial t^2} = A \frac{\partial^2 \mathbf{V}}{\partial R^2} + \frac{B}{R} \frac{\partial^2 \mathbf{V}}{\partial R \partial \theta} + \frac{C}{R^2} \frac{\partial^2 \mathbf{V}}{\partial \theta^2} \\ + \frac{D}{R} \frac{\partial \mathbf{V}}{\partial R} + \frac{E}{R^2} \frac{\partial \mathbf{V}}{\partial \theta} + \frac{H}{R^2} \mathbf{V} + \left[ M \frac{\partial \mathbf{V}}{\partial R} + \frac{N}{R} \frac{\partial \mathbf{V}}{\partial \theta} + \frac{Q}{R} \mathbf{V} \right]. \end{aligned} \quad (50)$$

Here

$$A = \begin{pmatrix} v_p^2 & 0 \\ 0 & v_s^2 \end{pmatrix}, \quad B = \begin{pmatrix} 0 & v_p^2 - v_s^2 \\ v_p^2 - v_s^2 & 0 \end{pmatrix}, \quad C = \begin{pmatrix} v_s^2 & 0 \\ 0 & v_p^2 \end{pmatrix}, \quad (51)$$

$$\begin{aligned} D = \begin{pmatrix} 0 & (v_p^2 - v_s^2) \cotg \theta \\ 0 & 0 \end{pmatrix}, \quad E = \begin{pmatrix} v_s^2 \cotg \theta & -2v_p^2 \\ v_p^2 + v_s^2 & v_p^2 \cotg \theta \end{pmatrix}, \\ H = \begin{pmatrix} -2v_p^2 & -2v_p^2 \cotg \theta \\ 0 & -2v_p^2 / \sin^2 \theta \end{pmatrix}, \end{aligned} \quad (52)$$

$$\begin{aligned} M = \frac{1}{\rho} \begin{bmatrix} \frac{\partial \lambda}{\partial R} + 2 \frac{\partial \mu}{\partial R} & \frac{1}{R} \frac{\partial \mu}{\partial \theta} \\ \frac{1}{R} \frac{\partial \lambda}{\partial \theta} & \frac{\partial \mu}{\partial R} \end{bmatrix}, \quad N = \frac{1}{\rho} \begin{bmatrix} \frac{1}{R} \frac{\partial \mu}{\partial \theta} & \frac{\partial \lambda}{\partial R} \\ \frac{\partial \mu}{\partial R} & \frac{1}{R} \left[ \frac{\partial \lambda}{\partial \theta} + 2 \frac{\partial \mu}{\partial \theta} \right] \end{bmatrix}, \\ Q = \frac{1}{\rho} \begin{bmatrix} \frac{\partial \lambda}{\partial R} - 2 \frac{\partial \mu}{\partial R} & \left[ \frac{\partial \lambda}{\partial R} - \frac{2}{R} \frac{\partial \mu}{\partial \theta} \right] \cotg \theta \\ \frac{1}{R} \left[ \frac{\partial \lambda}{\partial \theta} + 2 \frac{\partial \mu}{\partial \theta} \right] & \left[ \frac{1}{R} \frac{\partial \lambda}{\partial \theta} - 2 \frac{\partial \mu}{\partial R} \right] \cotg \theta \end{bmatrix}. \end{aligned} \quad (53)$$

The matrices  $A$ ,  $B$ ,  $C$  defined in Eq. (51) are identical to the matrices used in Cartesian coordinates (Eq. 28). The matrices  $M$ ,  $N$ ,  $Q$  defined in Eq. (53) are zero for a homogeneous medium.

b. *Finite Difference Approximation.* A finite difference approximation to Eq. (50) is obtained by replacing all derivatives by central finite differences. The finite difference equation can then be solved, expressing  $\mathbf{V}$  at the time  $t + \Delta t$  in terms of  $\mathbf{V}$  at the time  $t$  and  $t - \Delta t$ . The result is

$$\begin{aligned} \mathbf{V}(R, \theta, t + \Delta t) = & \varepsilon_1^2 [A + D(\Delta R/2R) + M(\Delta R/2)]\mathbf{V}(R + \Delta R, \theta, t) \\ & + \varepsilon_1^2 [A - D(\Delta R/2R) - M(\Delta R/2)]\mathbf{V}(R - \Delta R, \theta, t) \\ & + 2[1 - A\varepsilon_1^2 + (H/2)\varepsilon_1^2(\Delta R/R)^2 - C\varepsilon_2^2 + (QR/2) \\ & \times \varepsilon_1^2(\Delta R/R)^2]\mathbf{V}(R, \theta, t) \\ & + \varepsilon_2^2 [C + E(\Delta\theta/2) + N(R \Delta\theta/2)]\mathbf{V}(R, \theta + \Delta\theta, t) \\ & + \varepsilon_2^2 [C - E(\Delta\theta/2) - N(R \Delta\theta/2)]\mathbf{V}(R, \theta - \Delta\theta, t) \\ & + \frac{1}{4}\varepsilon_1\varepsilon_2 B[\mathbf{V}(R + \Delta R, \theta + \Delta\theta, t) + \mathbf{V}(R - \Delta R, \theta - \Delta\theta, t) \\ & - \mathbf{V}(R + \Delta R, \theta - \Delta\theta, t) - \mathbf{V}(R - \Delta R, \theta + \Delta\theta, t)] \\ & - \mathbf{V}(R, \theta, t - \Delta t). \end{aligned} \quad (54)$$

Here

$$\varepsilon_1 = \Delta t/\Delta R, \quad \varepsilon_2 = \Delta t/R \Delta\theta. \quad (55)$$

Equation (57) is valid for  $0 < \theta < \pi$ . For  $\theta = 0$  and  $\theta = 180^\circ$  the coefficients  $D$ ,  $E$ ,  $H$ , and  $Q$  in Eqs. (52) and (53) become infinite. In this case the corresponding terms are evaluated taking into account that due to symmetry

$$u_\theta = 0, \quad \partial u_R / \partial \theta = 0 \quad \text{at } \theta = 0 \text{ and } \pi, \quad (56)$$

and also

$$\partial u_\theta / \partial R = \partial^2 u_\theta / \partial R^2 = 0 \quad \text{at } \theta = 0 \text{ and } \theta = \pi. \quad (57)$$

Following L'Hopital's rule  $(\partial u_R / \partial \theta) \cot \theta$  is replaced by  $\partial^2 u_R / \partial \theta^2$ , and  $u_\theta / \sin^2 \theta$  by  $[\partial^2 u_\theta / \partial \theta^2] / 2$ . The finite difference expression is then modified to

$$\begin{aligned}
F(R, 0, t + \Delta t) = & \varepsilon_1^2 v_p^2 [F(R + \Delta R, 0, t) + F(R - \Delta R, 0, t)] \\
& + \varepsilon_1^2 \frac{\Delta R}{2\rho} \left( \frac{\partial \lambda}{\partial R} + 2 \frac{\partial \mu}{\partial R} \right) [F(R + \Delta R, 0, t) - F(R - \Delta R, 0, t)] \\
& + 4v_s^2 \varepsilon_2^2 F(R, \Delta \theta, t) \\
& + \left[ 2 - 2v_p^2 \varepsilon_1^2 - 2v_p^2 \varepsilon_1^2 \left( \frac{\Delta R}{R} \right)^2 - 4\varepsilon_2^2 v_s^2 \right. \\
& \left. + \varepsilon_1^2 \frac{(\Delta R)^2}{\rho R} \left( \frac{\partial \lambda}{\partial R} - 2 \frac{\partial \mu}{\partial R} \right) \right] F(R, 0, t) \\
& + (v_p^2 - v_s^2) \varepsilon_1 \varepsilon_2 [G(R + \Delta R, \Delta \theta, t) - G(R - \Delta R, \Delta \theta, t)] \\
& + \left[ \frac{2}{\rho} \left( R \frac{\partial \lambda}{\partial R} - \frac{\partial \mu}{\partial \theta} \right) - 4v_p^2 \right] G(R, \Delta \theta, t) - F(R, 0, t - \Delta t)
\end{aligned} \tag{58}$$

A similar expression holds for  $F(R, \pi, t + \Delta t)$ . In the latter case the signs of  $\Delta \theta$  are interchanged. Equations (54) and (58) have a singularity also at  $R = 0$ . However, as explained in the sequel, the finite difference equations are not applied at this point.

c. *Boundary Conditions.* In the case of a free boundary, the vanishing of the normal and tangential component of stress is required. Equation (2) becomes here

$$\tau_{RR} = \lambda \operatorname{div} \mathbf{U} + 2\mu \frac{\partial u_R}{\partial R} = 0, \tag{59}$$

at  $R = a$

$$\tau_{R\theta} = \mu \frac{\hat{\partial} u_\theta}{\hat{\partial} R} + \frac{1}{R} \frac{\hat{\partial} u_R}{\hat{\partial} \theta} - \frac{u_\theta}{R} = 0. \tag{60}$$

At the interface of two different elastic media the boundary conditions express the fact that the displacement vector and the normal and tangential stress components are continuous across the interface,  $R = d$  (Eq. 3). The finite difference expressions for the boundary conditions are readily obtained. Whenever normal derivatives occur, a fictitious line is added to the grid, extending one of the media. As an example, let us assume that an interface between medium 1 of constants  $\mu_1, \lambda_1$  and medium 2 of constants  $\mu_2, \lambda_2$  occurs at  $R = d$ . Figure 7 shows the grid at and near the interface. The regular grid points are denoted by  $x$ . Additional fictitious grid points, denoted by

circles, extend medium 1 from  $R \geq d$  to  $R < d$ . From Eq. (3) of continuity of stresses we then determine  $u_{R_1}$  and  $u_{\theta_1}$  on the fictitious line  $R = d - \Delta R$ . They are denoted by  $u_R$  and  $u_\theta$  and are given by

$$\begin{aligned} (\lambda_1 + 2\mu_1)u_R(d - \Delta R) &= (\lambda_1 + 2\mu_1)u_R(d) + (2\Delta R/d)(\lambda_1 - \lambda_2)u_R(d) \\ &\quad + (\lambda_1 - \lambda_2)u_\theta(d) \cotg \theta(\Delta R/d) + (\Delta R/\Delta\theta) \\ &\quad \times [(\lambda_1 - \lambda_2)/2d][u_\theta(\theta + \Delta\theta) - u_\theta(\theta - \Delta\theta)] \\ &\quad + (\lambda_2 + 2\mu_2)[u_R(d) - u_R(d - \Delta R)], \end{aligned} \quad (61)$$

$$\begin{aligned} \mu_1u_\theta(d - \Delta R) &= \mu_1u_\theta(d) + [(\mu_1 - \mu_2)/2d](\Delta R/\Delta\theta) \\ &\quad \times [u_R(\theta + \Delta\theta) - u_R(\theta - \Delta\theta)] \\ &\quad + [(\mu_2 - \mu_1)/d]\Delta Ru_\theta - \mu_2[u_\theta(d) - u_\theta(d - \Delta R)]. \end{aligned} \quad (62)$$

The choice of one-sided and two-sided difference expressions for the derivatives with respect to the space coordinates has been made as explained for the cylindrical coordinates. The other boundary conditions are treated similarly.

### 5. Stability Conditions

a. *Stability Analysis for Cartesian Coordinates.* For simplicity we determine first stability conditions in cartesian coordinates. The equations of motion in their finite difference form are given in Eq. (29).

In order to find the conditions for stability of Eq. (29) let us consider the propagation of a disturbance  $\eta$  in the displacement

$$\eta = \eta_0 e^{i(ma\Delta x + nb\Delta y)} \zeta^p \quad \zeta = e^{c\Delta t}. \quad (63)$$

Here  $\eta_0$  is a constant vector,  $\eta_0 = (\eta_1, \eta_2)$ , and  $x = m\Delta x$ ,  $y = n\Delta y$ . Inserting  $\eta$  in Eq. (29) and rearranging terms, we obtain

$$\begin{bmatrix} 2D_1 - \zeta - \frac{1}{\zeta} & -\sqrt{D_3} \\ -\sqrt{D_3} & 2D_2 - \zeta - \frac{1}{\zeta} \end{bmatrix} \begin{pmatrix} \eta_1 \\ \eta_2 \end{pmatrix} = \begin{pmatrix} 0 \\ 0 \end{pmatrix}. \quad (64)$$

Here

$$\begin{aligned} D_1 &= 1 - 2\varepsilon^2(X + \gamma\delta Y), \\ D_2 &= 1 - 2\varepsilon^2(\delta X + \gamma Y), \\ D_3 &= 4(1 - \delta)^2\gamma\varepsilon^4 XY(1 - X)(1 - Y), \end{aligned} \quad (65)$$

and

$$\gamma = (\Delta x / \Delta y)^2, \quad \delta = (v_s / v_p)^2, \quad \varepsilon = v_p \Delta t / \Delta x,$$

$$X = \sin^2(a \Delta x / 2), \quad Y = \sin^2(b \Delta y / 2).$$

For nonzero solutions the determinant of coefficients of  $\eta_0$  must vanish, so that

$$(\zeta^2 - 2D_1\zeta + 1)(\zeta^2 - 2D_2\zeta + 1) - D_3\zeta^2 = 0,$$

which can be written as

$$(\zeta^2 - 2A_1\zeta + 1)(\zeta^2 - 2A_2\zeta + 1) = 0. \quad (66)$$

Here

$$\begin{aligned} A_1 &= \frac{1}{2}[D_1 + D_2 + \{(D_1 - D_2)^2 + D_3\}^{1/2}] \\ &= 1 - \varepsilon^2(1 + \delta)(X + \gamma Y) + \varepsilon^2(1 - \delta)\sqrt{s}, \\ A_2 &= \frac{1}{2}[D_1 + D_2 - \{(D_1 - D_2)^2 + D_3\}^{1/2}] \\ &= 1 - \varepsilon^2(1 + \delta)(X + \gamma Y) - \varepsilon^2(1 - \delta)\sqrt{s}, \end{aligned} \quad (67)$$

and

$$s = (X - \gamma Y)^2 + 4\gamma XY(1 - X)(1 - Y).$$

For stability  $|\zeta| \leq 1$  and according to Eq. (66) this implies that

$$|A_1| \leq 1 \quad \text{and} \quad |A_2| \leq 1.$$

Equation (67) and  $|A_1| \leq 1$  imply that

$$-1 \leq 1 - \varepsilon^2(1 + \delta)(X + \gamma Y) + \varepsilon^2(1 - \delta)\sqrt{s} \leq 1,$$

which is equivalent to

$$0 \leq \varepsilon^2(1 + \delta)(X + \gamma Y) - \varepsilon^2(1 - \delta)\sqrt{s} \leq 2. \quad (68)$$

Equation (67) and  $|A_2| \leq 1$  imply

$$-1 \leq 1 - \varepsilon^2(1 + \delta)(X + \gamma Y) - \varepsilon^2(1 - \delta)\sqrt{s} \leq 1,$$

or

$$0 \leq \varepsilon^2(1 + \delta)(X + \gamma Y) + \varepsilon^2(1 - \delta)\sqrt{s} \leq 2. \quad (69)$$

From  $0 \leq X \leq 1$ ,  $0 \leq Y \leq 1$ ,  $0 \leq \delta < 1$ , and  $\gamma \geq 0$ , it follows that  $s$  is positive and that the left-hand side inequalities in (68) and (69) are satisfied for all values of  $\varepsilon$ .

By using the estimate  $\sqrt{s} \geq |X - \gamma Y|$  in the right-hand side inequality condition of (68),

$$\varepsilon^2(1 + \delta)(X + \gamma Y) - \varepsilon^2(1 - \delta)\sqrt{s} \leq \varepsilon^2(1 + \delta)(X + \gamma Y) - \varepsilon^2(1 - \delta)|X - \gamma Y|,$$

and (68) is satisfied if the right-hand side is less than or equal to 2. Hence

$$\varepsilon^2 \leq \frac{2}{(1 + \delta)(X + \gamma Y) - (1 - \delta)|X - \gamma Y|} = \begin{cases} 1/(X + \gamma \delta Y) & X \leq \gamma Y, \\ 1/(\delta X + \gamma Y) & X \geq \gamma Y. \end{cases} \quad (70)$$

The strongest condition for  $\varepsilon$  occurs when  $X = Y = 1$ . In this case

$$\varepsilon^2 \leq \min[1/(1 + \gamma \delta), 1/(\gamma + \delta)] = \begin{cases} 1/(1 + \gamma \delta) & \gamma \leq 1, \\ 1/(\gamma + \delta) & \gamma \geq 1. \end{cases} \quad (71)$$

An upper bound for  $\sqrt{s}$  is given by

$$\sqrt{s} \leq \begin{cases} X + \gamma Y - 2\gamma XY & \gamma \leq 1, \\ X + \gamma Y - 2XY & \gamma \geq 1, \end{cases}$$

and is applied to the expression in Eq. (69):

$$\begin{aligned} \varepsilon^2(1 + \delta)(X + \gamma Y) + \varepsilon^2(1 - \delta)\sqrt{s} &\leq \\ &\begin{cases} \varepsilon^2(1 + \delta)(X + \gamma Y) + (1 - \delta)(X + \gamma Y - 2\gamma XY) & \gamma \leq 1, \\ \varepsilon^2(1 + \delta)(X + \gamma Y) + (1 - \delta)(X + \gamma Y - 2XY) & \gamma \geq 1. \end{cases} \end{aligned} \quad (72)$$

The right-hand inequality in Eq. (69) is satisfied if the last expression in Eq. (72) is less than or equal to 2, or

$$\varepsilon^2 \leq \begin{cases} \{\gamma Y + X[1 - (1 - \delta)\gamma Y]\}^{-1} & \gamma \leq 1, \\ \{\gamma Y + X[1 - (1 - \delta)Y]\}^{-1} & \gamma \geq 1. \end{cases} \quad (73)$$

In Eq. (73) the strongest condition for  $\varepsilon$  occurs when  $X = Y = 1$ . Inserting these values of  $X$  and  $Y$  in Eq. (73) we get the same results as in Eq. (71) which can be expressed in the original notation by

$$v_p \Delta t \leq \begin{cases} \Delta x [1 + (v_s^2/v_p^2)(\Delta x^2/\Delta y^2)]^{-1/2} & \Delta x/\Delta y \leq 1, \\ \Delta y [1 + (v_s^2/v_p^2)(\Delta y^2/\Delta x^2)]^{-1/2} & \Delta x/\Delta y \geq 1. \end{cases} \quad (74)$$

For equal grid spacing in the  $x$  and  $y$  direction,  $\Delta x = \Delta y = h$ , condition (74) reduces to

$$v_p \Delta t \leq h/[1 + (v_s^2/v_p^2)]^{1/2}. \quad (75)$$

b. *Stability Analysis for Spherical Coordinates.* In spherical coordinates the stability analysis is more involved because of the nonconstant coefficients of the equations of motion. Some of them tend to infinity at the origin. An indication of stability can be obtained by considering the homogeneous case for points which are far enough from the origin so that  $R \gg \Delta R$ . For this case the analysis proceeds in a similar fashion as for Cartesian coordinates since terms with nonconstant coefficients can be neglected, and the stability criterion given in Eq. (74) applies also for this case after a change of notation is made as follows:

$$\Delta x \rightarrow \Delta R, \quad \Delta y \rightarrow R \Delta \theta.$$

An indication of stability near the origin of a homogeneous sphere is obtained by letting  $R \sim \Delta R$ . From Eq. (54) one finds that for this case the dominant terms are those which are multiplied by the matrix  $C$  (Eq. 51) and the equation becomes

$$\begin{aligned} V(R, \theta, t + \Delta t) - 2V(R, \theta, t) + V(R, \theta, t - \Delta t) \\ = \varepsilon_2^2 C[V(R, \theta + \Delta \theta, t) - 2V(R, \theta, t) + V(R, \theta - \Delta \theta, t)]. \end{aligned} \quad (76)$$

Expressing  $V$  by Eq. (63), Eq. (76) reduces to

$$\{-4C\varepsilon_2^2 \sin^2(bR \Delta \theta/2) + I[-\zeta + 2 - (1/\zeta)]\}V(R, \theta, t) = 0. \quad (77)$$

Equation (77) can be satisfied if the determinant of the coefficients vanishes or if

$$\begin{aligned} [\zeta^2 - 2\zeta(1 - 2\varepsilon_2^2 v_s^2 \sin^2(bR \Delta \theta/2)) + 1] \\ \times [\zeta^2 - 2\zeta(1 - 2\varepsilon_2^2 \sin^2(bR \Delta \theta/2)) + 1] = 0, \end{aligned} \quad (78)$$

and the condition for  $|\zeta| \leq 1$  becomes

$$\begin{aligned}-1 &\leq 1 - 2\epsilon_2^2 v_s^2 \sin^2(bR \Delta\theta/2) \leq 1, \\ -1 &\leq 1 - 2\epsilon_2^2 \sin^2(bR \Delta\theta/2) \leq 1.\end{aligned}\quad (79)$$

It implies

$$\epsilon_2 \leq 1. \quad (80)$$

Finally, the time step is determined by the stronger condition which has to hold near the origin.

$$\Delta t \leq \Delta R \Delta\theta/v_p. \quad (81)$$

The stability condition in Eq. (81) requires a small  $\Delta t$  near the origin. In order to avoid extremely small time steps, the first interval  $\Delta R$  in  $R$  can be chosen larger than the following intervals, for which the less stringent condition holds.

In cylindrical coordinates a similar stability analysis can be performed. However, special analysis must be performed near the  $z$  axis.

## 6. Source Conditions

General definitions of sources have been given by Archambeau (1968) and others. As a first step in computing theoretical seismograms a very simple and homogeneous kind of source was preferred. The impulsive P-wave cylindrical line source (Alterman and Rotenberg, 1969) and the symmetric point source (Alterman and Karal, 1968) were chosen.

As a next step extended sources defined over a given area or volume and of more involved characteristics, including also surface forces, were considered (Alterman and Aboudi, 1970).

a. *The Impulsive Line Source.* At time  $t = 0$  an impulsive line source starts to emit compressional waves in a radial direction. Let us first consider a source as defined by Garvin (1956),

$$s(r, t) = \begin{cases} 0 & t < r/a, \\ At/2r(t^2 - r^2/v_p^2)^{1/2} & t \geq r/a, \end{cases} \quad (82)$$

where  $s$  is the radial displacement at a distance  $r$  from the source at time  $t$  and  $A$  is a constant with dimensions of area. This source describes an initial compressional P-wave pulse and is a solution of Eq. (1) in a homogeneous infinite medium. S-waves develop only on reflection at the boundary.

The initial pulse in Eq. (82) has two singularities. At  $r = 0$ ,  $s$  is infinite at all times. At every other point,  $s$  is infinite at  $t = r/v_p$  and the very large values of  $s(r, t)$  near this point lead to numerical errors in finite difference schemes. In addition, whereas the Garvin source is a useful one for obtaining certain analytical solutions, the singularity at the front lacks physical meaning. Instead of using the source function  $s(r, t)$  as given by (82), a function is used which is derived from  $s(r, t)$  by integrating it  $n$  times with respect to  $t$  and taking the  $n$ th time difference of this integral. The value chosen here for  $n$  is 2, thus ensuring continuity of the displacement and of its derivative. The integrals are standard:

$$G_1(r, t) = \int_0^t s(r, \tau) d\tau = \begin{cases} 0 & t < r/v_p, \\ (A/2v_p)\sqrt{(tv_p/r)^2 - 1} & t \geq r/v_p, \end{cases} \quad (83)$$

and

$$\begin{aligned} G_2(r, t) &= \int_0^t G_1(r, \tau) d\tau, \\ &= \begin{cases} 0 & t < r/v_p, \\ \frac{rA}{4v_p^2} \left[ \frac{v_p t}{r} \left[ \left( \frac{tv_p}{r} \right)^2 - 1 \right]^{1/2} - \log \left( \frac{v_p t}{r} + \left[ \left( \frac{v_p t}{r} \right)^2 - 1 \right]^{1/2} \right) \right] & t \geq r/v_p. \end{cases} \end{aligned} \quad (84)$$

By differencing Eq. (84) we get a new source term as follows:

$$S(r, t) = \begin{cases} 0 & t < r/v_p, \\ (1/\Delta^2)[G_2(r, t) - 2G_2(r, t - \Delta) + G_2(r, t - 2\Delta)] & t \geq r/v_p, \end{cases} \quad (85)$$

where  $\Delta$  is arbitrary and designates a smoothing parameter.  $S(r, t)$  differs from  $s(r, t)$  in several respects. In the first place  $S(r, t)$  is nowhere infinite (for  $r \neq 0$ ) and in fact is zero at  $t = r/v_p$ . Furthermore,  $S(r, t)$  has its maximum (for  $r \neq 0$ ) near  $t = r/v_p + 4\Delta/3$ ; thus the maximum of the pulse  $S$  is displaced with respect to that of  $s$ . Also  $S(r, t)$  varies less rapidly in time than  $s(r, t)$  and can be adjusted to fit any desired range of pulse duration. In the present calculations  $\Delta$ , which has the dimension of time, is chosen to be of the order of a few time steps. A larger  $\Delta$  gives a pulse with a large risetime (from zero to the maximum), a situation which can make discrimination between pulses difficult if several waves arrive at a receiver close together.

b. *The Impulsive Point Source.* We select a disturbance satisfying the elastic equations of motion (1) and having the appropriate singularity at the source. The source starts at the time  $t = 0$ , causes a variation in stress during a finite

time interval, and then leads to a constant displacement for each particle in the medium for large time ( $t \rightarrow \infty$ ). In order to have a smooth enough source displacement, the displacement potential is defined as the  $n$ th finite difference of an  $n$ th-order polynomial. The displacement potential of the source is defined by

$$\Phi_0(t) = \frac{1}{\Delta^n} \sum_{i=0}^n (-1)^i \binom{n}{i} f_0(t - i\Delta), \quad (86)$$

with

$$f_0(t) = -\frac{A}{n!} \left( t - \frac{R}{v_p} \right)^n H\left(t - \frac{R}{v_p}\right). \quad (87)$$

Here  $R$  is the distance from the source,  $A$  is an amplitude factor (dimension of length),  $H$  is the Heaviside unit function, and  $\Delta$  is a constant measuring the sharpness of the pulse. The spherically symmetric displacement  $\mathbf{U}$  is given by

$$\mathbf{U} = \text{grad } \Phi_0. \quad (88)$$

Usually  $n = 4$  or  $n = 3$  is chosen. For  $n = 4$  the source causes a quartic increase in radial displacement up to a maximum value  $(u_R)_{\max}$ , which is then followed by a quartic decrease down to a constant value  $(u_R)_{\text{const}}$ , which is obtained after a time  $4\Delta$ . The maximum occurs at the time  $t_{\max} = R/v_p + 2\Delta$ . In the limit of vanishing  $\Delta$ ,  $\Phi_0(t)$  approaches the Heaviside unit function, and  $u_R(t)$  becomes a delta function followed by a finite step. See Fig. 8.

Other smoothed sources suitable for the finite difference techniques are derived in a similar fashion.

c. *Separation of the Source Term.* The line source displacement is unbounded near  $r = 0$ . The finite difference scheme cannot be used at  $r = 0$  as well as at a few points in its neighborhood. This difficulty is overcome by subtracting  $S(r, t)$  from the total displacement  $\mathbf{U}(r, t)$  and applying the finite difference scheme to the remaining displacement  $\mathbf{U}_R$ .

$$\mathbf{U}_R(r, t) = \mathbf{U}(r, t) - S(r, t). \quad (89)$$

By linearity, the finite difference equation for  $\mathbf{U}_R$  is identical to the finite difference equation which  $\mathbf{U}$  satisfies. However the boundary conditions are changed. The method of calculation of the reflected field only is utilized also for the point source and for extended sources.

## B. NORMAL MODES AND RAY ANALYSIS METHODS

### 1. Formal Solution for a Source in a Sphere

a. *Operational Solution.* The problem of a source in a radially stratified sphere lends itself to solution by normal mode analysis.

As a first illustration, let us assume, according to Alterman and Abramovici (1965), that an impulsive point source is applied at point B located at distance  $b$  from the center of a homogeneous elastic sphere of radius  $a$  ( $a > b$ ) (see Fig. 9). We wish to find the subsequent disturbance at any point on the surface of the sphere and at an angular distance  $\theta$  from OB.

The displacement potential of the source is similar to that defined in Eq. (86) except that here we assume that smoothing is obtained by three integrations ( $n = 3$ ). It is denoted by  $\Phi_0$ .

Using the spherical system of coordinates  $(R, \theta, \phi)$  the radial component of displacement  $u_R$  is given by

$$u_R = \frac{\partial \Phi}{\partial R} - \frac{1}{R} \Lambda M, \quad (90)$$

$$\Lambda = \frac{1}{\sin \theta} \frac{\partial}{\partial \theta} \left( \sin \theta \frac{\partial}{\partial \theta} \right), \quad (91)$$

and the tangential components by

$$u_\theta = \frac{\partial}{\partial \theta} \left( \frac{\Phi}{R} + \frac{M}{R} + \frac{\partial M}{\partial R} \right), \quad (92)$$

$$u_\phi = 0. \quad (93)$$

The compressional and shear potentials  $\Phi$  and  $M$  satisfy the equations

$$(\nabla^2 - h^2)\Phi = 0, \quad h^2 = p^2/v_p^2, \quad (94)$$

and

$$(\nabla^2 - k^2)M = 0, \quad k^2 = p^2/v_s^2, \quad (95)$$

where  $p$  is the operator  $\partial/\partial t$ . The source stems from the potential  $\Phi_0$ , while the shear waves represented by  $M$  are generated after the P-wave from  $\Phi_0$  reaches the surface of the sphere.

A solution of the wave equations (94) and (95) for  $0 \leq R \leq a$  and  $t \geq 0$  is required, which includes the primitive disturbance  $\Phi_0$  and satisfies the boundary condition of zero radial and tangential stresses at the surface  $R = a$ . These conditions are expressed in Eqs. (59) and (60). As representative of the source potential  $\Phi_0$  we consider initially only the first term  $f_0(t)$  in Eq. (86) and later derive the solution corresponding to the complete pulse by taking third-order differences.  $f_0$  is expanded in spherical coordinates in the form

$$f_0(p) = -\frac{\pi A^3}{p^3(Rb)^{1/2}} \sum_{n=0}^{\infty} (n + \frac{1}{2}) K h_{n+1/2}(hR) I_{n+1/2}(hb) P_n(\cos \theta), \quad r > b. \quad (96)$$

Here  $A$  is an amplitude factor,  $P_n(\cos \theta)$  is the Legendre polynomial, and  $Kh$ ,  $I$  are Bessel functions of imaginary argument as defined by Jeffreys and Jeffreys (1956).

#### Secondary disturbances

$$\Phi_1 = \frac{\pi A^3}{p^3(RB)^{1/2}} \sum_{n=0}^{\infty} (n + \frac{1}{2}) A_n I_{n+1/2}(hR) P_n(\cos \theta) \quad (97)$$

and

$$M_1 = \frac{A^3}{p^3(Rb)^{1/2}} \sum_{n=1}^{\infty} (n + \frac{1}{2}) B_n I_{n+1/2}(kr) P_n(\cos \theta) \quad (98)$$

for  $0 \leq R \leq a$  are added to  $f_0$ , and the coefficients  $A_n$  and  $B_n$  are determined by inserting the expansions (96), (97), and (98) in Eqs. (90) and (92) for the displacements, and then in Eqs. (59) and (60) for the boundary conditions. We obtain the following sets of linear equations

$$\begin{aligned} g(I_{n+1/2}, ha) A_n + n(n + 1) f(I_{n+1/2}, ka) B_n \\ = g(Kh_{n+1/2}, ha) I_{n+1/2}(hb) \quad n = 0, 1, 2, \dots, \end{aligned} \quad (99)$$

and

$$\begin{aligned} f(I_{n+1/2}, ha) A_n + [g(I_{n+1/2}, ka) + f(I_{n+1/2}, ka)] B_n \\ = f(Kh_{n+1/2}, ha) I_{n+1/2}(hb) \quad n = 0, 1, 2, \dots \end{aligned} \quad (100)$$

Here

$$f(I_{n+1/2}, ya) = -3I_{n+1/2}(ya) + 2I'_{n+1/2}(ya)ya, \quad (101)$$

$$g(I_{n+1/2}, ya) = I_{n+1/2}(ya)[k^2 a^2 + 2(n^2 + n + 1)] - 4ayI'_{n+1/2}(ya), \quad (102)$$

with similar definitions for  $Kh_{n+1/2}$  instead of  $I_{n+1/2}$ .

For  $n = 0$ ,  $A_0$  is determined by the first boundary condition, Eq. (99) alone,

$$A_0 = \frac{g(Kh_{1/2}, ha)}{g(I_{1/2}, ha)} I(hb) = \frac{Kh_{1/2}(ha)(k^2 a^2 + 2) - 4ahKh'_{1/2}(ah)}{I_{1/2}(ha)(k^2 a^2 + 2) - 4ahI'_{1/2}(ah)} I_{1/2}(hb) \quad (103)$$

for  $n > 0$ ,

$$A_n = (D_A/D_n) I_{n+1/2}(hb), \quad (104)$$

$$B_n = (D_B/D_n) I_{n+1/2}(hb). \quad (105)$$

Here

$$\begin{aligned} D_n &= g(I_{n+1/2}, ha)[g(I_{n+1/2}, ka) + f(I_{n+1/2}, ka)] \\ &\quad - n(n+1)f(I_{n+1/2}, ha)f(I_{n+1/2}, ka), \end{aligned} \quad (106)$$

$$\begin{aligned} D_A &= g(Kh_{n+1/2}, ha)[g(I_{n+1/2}, ka) + f(I_{n+1/2}, ka)] \\ &\quad - n(n+1)f(Kh_{n+1/2}, ha)f(I_{n+1/2}, ka), \end{aligned} \quad (107)$$

$$\begin{aligned} D_B &= g(I_{n+1/2}, ha)f(Kh_{n+1/2}, ha) - f(I_{n+1/2}, ha)g(Kh_{n+1/2}, ha) \\ &= -(4/\pi)[a^2 k^2 + 2(n^2 + n - 2)]. \end{aligned} \quad (108)$$

Equation (108) follows from the identity

$$I'_v(x)Kh_v(x) - I_v(x)Kh'_v(x) = 2/\pi x. \quad (109)$$

By Eqs. (96) and (97), the P-wave potential

$$\Phi = f_0 + \Phi_1 = \frac{\pi A^3}{p^3(Rb)^{1/2}} \sum_{n=0}^{\infty} (n + \frac{1}{2}) P_n \frac{I_{n+1/2}(hb)}{D_n} G_n(R), \quad (110)$$

where

$$G_n(R) = D_A I_{n+1/2}(hR) - D_n Kh_{n+1/2}(hR). \quad (111)$$

The derivative

$$\frac{\partial \Phi}{\partial R} = \frac{\pi A^3}{p^3(ab)^{1/2}} \sum_{n=0}^{\infty} (n + \frac{1}{2}) p_n \frac{I_{n+1/2}(hb)}{D_n} \left[ -\frac{1}{2a} G_n(R) + G'_n(R) \right], \quad (112)$$

where

$$\begin{aligned} -\frac{1}{2a} G_n(a) + G'_n(a) &= \frac{2}{\pi a} f(I_{n+1/2}, ka) \{a^2 k^2 + 4n(n+1)\} \\ &\quad + \frac{2}{\pi a} g(I_{n+1/2}, ka) \{a^2 k^2 + 2(n^2 + n)\}. \end{aligned} \quad (113)$$

From Eq. (98), at  $R = a$  one gets

$$-\frac{1}{a} \Lambda M_1 = -\frac{\pi A^3}{p^3(ab)^{1/2}} \sum_{n=0}^{\infty} (n + \frac{1}{2}) p_n (\cos \theta) \frac{I_{n+1/2}(hb)}{D_n} \frac{n(n+1)}{a}. \quad (114)$$

Inserting Eqs. (112) and (114) in (90), we obtain the operational solution for the radial displacement at the surface of the sphere,

$$\begin{aligned} u_R &= \frac{A^3}{ap^3(ab)^{1/2}} \sum_{n=0}^{\infty} (2n+1) P_n(\cos \theta) \frac{I_{n+1/2}(hb)}{D_n} \\ &\quad \times \{f(I_{n+1/2}, ka)(a^2 k^2 + 4n^2 + 4n) + g(I_{n+1/2}, ka) \\ &\quad \times (a^2 k^2 + 2n^2 + 2n) - 2I_{n+1/2}(ka)n(n+1)(a^2 k^2 + 2n^2 + 2n - 4)\}, \end{aligned} \quad (115)$$

and inserting the expressions for  $f$  and  $g$  as given in Eqs. (101) and (102), we have

$$\begin{aligned} u_R(ka) &= \frac{aA^3}{v_s^2 p(ab)^{1/2}} \sum_{n=0}^{\infty} (2n+1) P_n(\cos \theta) \frac{I_{n+1/2}(hb)}{D_n} \\ &\quad \times \{(a^2 k^2 + 2n^2 + 2n - 1)I_{n+1/2}(ak) - 2ak I'_{n+1/2}(ak)\}. \end{aligned} \quad (116)$$

The tangential displacement is obtained by inserting the expansions for  $\Phi$  and  $M$  in Eq. (92):

$$\begin{aligned} u_\theta(ka) &= \frac{2aA^3}{v_s^2 p(ab)^{1/2}} \sum_{n=0}^{\infty} (2n+1) \frac{d}{d\theta} P_n(\cos \theta) \frac{I_{n+1/2}(hb)}{D_n} \\ &\quad \times \{(1-n)I_{n+1/2}(ka) - ka I'_{n+3/2}(ka)\}. \end{aligned} \quad (117)$$

b. *Time-Dependent Solution.* The operational inverse of (116) is obtained by evaluating

$$\frac{1}{2\pi i} \int_{\gamma-i\infty}^{\gamma+i\infty} u_R(z) e^{\tau z} \frac{dz}{z}. \quad (118)$$

Here

$$\tau = v_s t/a, \quad z = ka. \quad (119)$$

Inserting Eq. (116) in (118) and interchanging the order of summation and integration for a finite number of terms, we have

$$u_R(\tau) = \frac{A^3 a^2}{v_s^3 (ab)^{1/2}} \sum_{n=0}^N (2n+1) P_n(\cos \theta) \frac{1}{2\pi i} \int_{\gamma-i\infty}^{\gamma+i\infty} f_n(z) \frac{e^{\tau z}}{z^3} dz, \quad (120)$$

where

$$f_n(z) = \frac{\{[z^2 + 2(n^2 - 1)]I_{n+1/2}(z) - 2zI_{n+3/2}(z)\}I_{n+1/2}(hz/ka)}{D_n(z)} \quad (121)$$

and

$$\begin{aligned} D_n(z) = & z[z^2 + 2(2n+1)(n-1)]I_{n+1/2}(hz/k)I_{n+1/2}(z) \\ & - 2[z^2 + 2n(n+2)(n-1)]I_{n+1/2}(hz/k)I_{n+3/2}(z) \\ & - 4(h/k)[z^2 + (n+2)(n^2-1)]I_{n+3/2}(hz/k)I_{n+1/2}(z) \\ & - 4(h/k)z(n+2)(n-1)I_{n+3/2}(hz/k)I_{n+3/2}(z). \end{aligned} \quad (122)$$

The Bromwich integral appearing in (120) can be evaluated as a sum of residues at the poles of the integrand. All the poles are situated on an imaginary axis.

The residue at  $z = 0$  is found by expanding the integrand into a power series in  $z$ . The result is

$$\text{res}_0 = \text{res}[f_n(z)e^{\tau z}/z^3]_{z=0} = (b/a)^{n+1/2} [c_0 \frac{1}{6}\tau^3 + c_1 \tau]. \quad (123)$$

where, for  $n \neq 1$ ,

$$c_0 = \frac{(n+1)(2n+3)}{(2n^2 + 4n + 3) - 2(n+2)(n+1)(h/k)^2} \quad (124)$$

and

$$c_1 = \frac{(n^2 - 1)[(bh/ka)^2 + 1] + (2n + 1)}{2[(n-1)2n^2 + 4n + 3] - 2(n+2)(n^2 - 1)(h/k)^2]} \\ - \frac{(n+1)(2n+3)[n(n^2 + 5n + \frac{9}{4}) - (n + \frac{5}{2})(3n + 1)]}{(h/k)^2 - (n+2)(n^2 - 1)(h/k)^4} \frac{(h/k)^4}{(2n+5)[(n-1)(2n^2 + 4n + 3) - 2(n+2)(n^2 - 1)(h/k)^2]} \\ \frac{[(2n^2 + 4n + 3) - 2(n+2)(n+1)(h/k)^2]}{(125)}$$

and, for  $n = 1$ ,

$$c_0 = \frac{3}{3 - 4(h/k)^2} \quad (126)$$

$$c_1 = \frac{12[5 - 7(b/a)^2](h/k)^2 + 63(b/a)^2 - 79}{70[3 - 4(h/k)^2]^2} (h/k)^2. \quad (127)$$

The nonzero poles of the integrand in Eq. (120) are of the form

$$z = \pm iy_{jn} \quad j = 1, 2, \dots, \quad (128)$$

where  $y_{jn}$  are simple zeros of

$$D = y[-y^2 + 2(2n+1)(n-1)]J_{n+1/2}(hy/k)J_{n+1/2}(y) \\ - 2[-y^2 + 2n(n+2)(n-1)]J_{n+1/2}(hy/k)J_{n+3/2}(y) \\ - 4(h/k)[-y^2 + (n+2)(n^2 - 1)]J_{n+3/2}(hy/k)J_{n+1/2}(y) \\ + 4(hy/k)(n+2)(n-1)J_{n+3/2}(hy/k)J_{n+3/2}(y) \\ = 0. \quad (129)$$

The residue corresponding to  $z = iy_{jn}$  is

$$\text{res}_{y_{jn}} = \text{res} \left[ f_n \frac{e^{zy}}{z^3} \right]_{z=iy_{jn}} = iB_{jn} e^{iy_{jn}}, \quad (130)$$

where

$$B_{jn} = \frac{\{[-y_{jn}^2 + 2(n^2 - 1)]J_{n+1/2}(y_{jn}) + 2y_{jn}J_{n+3/2}(y_{jn})\}J_{n+1/2}(bh y_{jn}/ak)}{y_{jn}^3 D'} \quad (131)$$

and  $D'$  is proportional to the derivative of  $D_n(z)$  with respect to  $z$ , at  $z = iy_{jn}$ , the constant factor  $e^{(n+1/2)\pi i}$  being omitted, as it cancels with a similar factor in the numerator. The derivatives of the Bessel functions are eliminated by using well-known recurrence formulas. The final expression for  $D'$  is

$$\begin{aligned} D' = & 2\{-[1 + n - 2(h/k)^2]y^2 + 2(n-1)[(n^2+n+1) \\ & - (h/k)^2(n+1)(n+2)]\}J_{n+1/2}(hy/k)J_{n+1/2}(y) \\ & + (h/k)y[y^4 + 2(3n-1)y^2 + 4(n+2)(n^2-1)]J_{n+3/2}(hy/k)J_{n+1/2}(y) \\ & + (1/y)\{y^4 - 2[(2n^2-n-2) - 2(h/k)^2(n+2)(n-1)]y^2 \\ & + 4n(n+2)(n-1)\}J_{n+1/2}(hy/k)J_{n+3/2}(y) \\ & + (2h/k)[-3y^2 - 2(n+2)(n-1)]J_{n+3/2}(hy/k)J_{n+3/2}(y). \end{aligned} \quad (132)$$

The sum of residues at  $y = +y_{jn}$  and  $y = -y_{jn}$  equals

$$-2B_{jn} \sin \tau y_{jn}. \quad (133)$$

The radial displacement for the actual source corresponding to the potential  $\phi_0(t)$ , as defined in Eq. (86) ( $n = 3$ ), is obtained by taking the third finite divided difference of

$$u_R(\tau) = \frac{A^3 a^2}{v_s^3 (ab)^{1/2}} \sum_{n=0}^N (2n+1) P_n(\cos \theta) \left[ \text{res}_0 + \sum_j (\text{res}_{y_{jn}} + \text{res}_{-y_{jn}}) \right]. \quad (134)$$

For  $\tau > 3\delta$ ,  $\delta = v_s \Delta/a$ , the result is

$$\begin{aligned} w = & \frac{A^3}{a^2} \sum_{n=0}^N (2n+1) P_n(\cos \theta) \\ & \times \{(b/a)^n c_0 + [16/(b/a)^{1/2}] \sum_j \cos[(\tau - 1.5\delta)y_{jn}] B_{jn} \delta^{-3} \sin^3(\delta y_{jn}/2)\}. \end{aligned} \quad (135)$$

$c_0$  is given by Eqs. (124) and (126).

The angular component of the displacement,  $u_\theta(\tau)$ , is derived in a similar fashion from  $u_\theta$ , Eq. (117). For  $\tau > 3\delta$  the result of taking the third divided difference of  $u_\theta(\tau)$  is

$$\begin{aligned} q = & -\frac{A^3}{a^2} \sin \theta \sum_{n=0}^N (2n+1) P_n' \\ & \times \{(b/a)^n d_0 - [32/(b/a)^{1/2}] \sum_j \cos[(\tau - 1.5\delta)y_{jn}] C_{jn} \delta^{-3} \sin^3(\delta y_{jn}/2)\}, \end{aligned} \quad (136)$$

where  $P'_n$  is the derivative of the Legendre polynomial  $P_n(\cos \theta)$  with respect to  $\cos \theta$  and

$$C_{jn} = [(1 - n)J_{n+1/2}(y_{jn}) + y_{jn}J_{n+3/2}(y_{jn})]J_{n+1/2}(bh y_{jn}/ak)/y_{jn}^3 D', \quad (137)$$

$$d_0 = \begin{cases} -\frac{2n+3}{2n^2+4n+3-2(n+2)(n+1)(h/k)^2} & \text{for } n \neq 1, \\ -\frac{2}{3-4(h/k)^2} & \text{for } n = 1. \end{cases} \quad (138)$$

By using normal modes it is possible to obtain also a solution for the impulsive force which acts as before at the point  $R = b$ ,  $\theta = 0$ ,  $\phi = 0$  inside a homogeneous sphere of radius  $R = a$ . (See Fig. 9). The source condition is then given by specifying a jump in radial stress at  $r = b$  in the form

$$\tau_{RR_1} - \tau_{RR_2} = (A/2\pi b^2)\delta(\theta)f(t)H(t). \quad (140)$$

Here  $A$  is a constant measuring the strength of the source,  $\delta(\theta)$  is the Dirac delta function,  $H(t)$  the unit step function, and  $f(t)$  designates the time variation of the source. The subscripts 1 and 2 designate the regions  $0 \leq R < b$  and  $b < R \leq a$ , respectively. The equations and displacement of the sphere for this case are derived in Alterman and Abramovici (1967).

A similar analysis applies for a layered sphere (Alterman and Aboudi, 1969). A summary of the equations is given in the Appendix.

Using a similar normal mode analysis a study was made on torsional and spheroidal motions for a homogeneous sphere (Satô *et al.*, 1962; Usami and Satô, 1964; Alterman and Kornfeld, 1965) and for a homogeneous mantle over a homogeneous fluid core (Satô *et al.*, 1963; Satô and Usami, 1964; Alterman and Kornfeld, 1966). Theoretical seismograms were obtained by a similar method also for more realistic models as the Gutenberg-Bullen A earth model (Satô *et al.*, 1967; Usami and Satô, 1970). While the summations in the first two articles (Alterman and Abramovici, 1967; Alterman and Aboudi, 1969) were carried out to obtain complete and accurate seismograms as shown in the figures, the latter articles generally do not sum more than 10 to 60 normal modes, and the results constitute a long wave approximation to the complete seismograms.

## 2. Ray Analysis

a. *Reflected Rays.* In the previous section we have shown the theoretical solution for the displacement of a solid homogeneous sphere due to an impulsive point source as obtained by normal mode analysis. Even though it

represents a complete solution the analytic form of the solution does not indicate the different reflected rays. It is possible to perform a separation of terms in Eq. (115) so that each term will represent a different ray. By computing the individual contribution of each term a better understanding of the ray solution is obtained.

In the case of an impulsive P-source at the center of the sphere,  $b = 0$ , only successive reflected P-waves occur. When the source is off the center,  $b \neq 0$ , the primary P-wave yields on reflection at the surface both P- and S-waves. A multiply-reflected ray will be characterized by specifying the number  $\alpha$  of chords it has passed as P and the number  $\beta$  of chords it has passed as S up to arrival at the point of observation. The complete theoretical seismograms include all possible reflections. For comparison the exact formal expression for the radial displacement, Eq. (116), will now be decomposed according to  $\alpha$  and  $\beta$ , and in the shortwave limit the contribution of the reflected rays will be obtained.

According to Alterman and Abramovici (1965) let us first rewrite Eq. (116) for  $u_R(ka)$  with the notations

$$x = x(\Phi) = \frac{R}{\Phi} \frac{\partial \Phi}{\partial R} - 1, \quad (141)$$

$$y = y(M) = \frac{2R}{M} \frac{\partial M}{\partial R} - 2 - m^2, \quad (142)$$

$$m^2 = 2(n + 2)(n - 1) + k^2 R^2, \quad (143)$$

as used by Scholte (1956). In this notation, according to Eqs. (90) and (96)–(98),

$$u_R(kR) = \frac{-\pi A^3 h}{p^3} \sum_{n=0}^{\infty} (n + \frac{1}{2}) \frac{x(\Phi_n) + 1}{R} \Phi_n + \frac{\pi A^3 h}{p^3} \sum_{n=0}^{\infty} (n + \frac{1}{2}) \frac{n(n + 1)}{R} M_n. \quad (144)$$

Here

$$\Phi_n = [1/n(Rb)^{1/2}] [kh_n(hR)I_{n+1/2}(hb) - A_n I_{n+1/2}(hR)]P_n(\cos \theta), \quad (145)$$

$$M_n = [1/h(Rb)^{1/2}]B_n I_{n+1/2}(kR)P_n(\cos \theta). \quad (146)$$

In terms of spherical modified Bessel and Hankel functions

$$i_n(z) = (1/\sqrt{z})I_{n+1/2}(z), \quad (147)$$

$$kh_n(z) = (1/\sqrt{z})Kh_{n+1/2}(z), \quad (148)$$

and

$$i_n(z) = \frac{1}{2}[h_n(z) - (-1)^n kh_n(z)], \quad (149)$$

Eqs. (145) and (146) become

$$\Phi_n = [kh_n(hR)i_n(hb) - (1/\sqrt{hb})A_n i_n(hR)]P_n(\cos \theta), \quad (150)$$

$$M_n = (\sqrt{k/h}\sqrt{b})B_n i_n(kr)P_n(\cos \theta). \quad (151)$$

Taking into account the linearity of  $\Phi_x(\Phi)$  in  $\Phi$ , the radial displacement at the surface can now be written

$$u_R(ka) = -\frac{\pi A^3 h}{ap^3} \sum_{n=0}^{\infty} (n + \frac{1}{2}) F_n P_n(\cos \theta), \quad (152)$$

$$\begin{aligned} F_n &= [x(kh_n) + 1]kh_n(ah)i_n(hb) - \frac{1}{2} \frac{D_A}{D_n} i_n(hb)h_n(ah) \\ &\times \left[ x(h_n) + 1 - (-1)^n[x(kh_n) + 1] \frac{kh_n(ah)}{h_n(ah)} \right] \\ &- n(n+1) \frac{\sqrt{k}}{2\sqrt{h}} \frac{D_B}{D_n} i_n(hb)h_n(ak) \left[ 1 - (-1)^n \frac{kh_n(ak)}{h_n(ak)} \right]. \end{aligned} \quad (153)$$

Similarly the determinants  $D_A$ ,  $D_B$ , and  $D_n$  (Eqs. 106–108) will be rewritten in the form

$$\frac{1}{a(hk)^{1/2}} D_A = \frac{1}{2} h_n(ah)h_n(ak) \left[ D_{k,h} \frac{kh_n(ah)}{h_n(ah)} - (-1)^n D_{k,k} \frac{kh_n(ah)}{h_n(ah)} \frac{kh_n(ak)}{h_n(ak)} \right], \quad (154)$$

$$(1/ah)D_B = h_n(ah)kh_n(ah)m^2[x(kh_n) - x(h_n)], \quad (155)$$

$$\begin{aligned} \frac{1}{a(hk)^{1/2}} D_n &= \frac{1}{4} h_n(ah)h_n(ak) \\ &\times \left[ D_{h,h} - (-1)^n D_{h,k} \frac{kh_n(ak)}{h_n(ak)} \right. \\ &\left. - (-1)^n D_{k,h} \frac{kh_n(ah)}{h_n(ah)} + D_{k,k} \frac{kh_n(ah)}{h_n(ah)} \frac{kh_n(ak)}{h_n(ak)} \right]. \end{aligned} \quad (156)$$

Here

$$D_{s,t} = [4x(s) - m^2]y(t) - 2n(n+1)[y(t) + m^2]x(s). \quad (157)$$

The spherical reflection coefficients are defined (Bremmer, 1949; Scholte, 1956) as follows; for longitudinal reflection:

$$(ll) = D_{h,h}/D_{h,h}, \quad (158)$$

transverse-transverse reflection:

$$(tt) = D_{h,k}/D_{h,h}, \quad (159)$$

longitudinal-transverse reflection:

$$(lt) = \frac{2nm^2[x(h_n) - x(kh_n)]}{D_{h,h}} e^{\pi i/2}, \quad (160)$$

transverse longitudinal reflection:

$$(tl) = \frac{(n+1)m^2[y(h_n) - x(kh_n)]}{D_{h,h}} e^{-\pi i/2}. \quad (161)$$

In terms of the reflection coefficients, Eq. (156) for  $D_n$  becomes

$$\begin{aligned} \frac{1}{a(hk)^{1/2}} D_n &= \frac{1}{4} h_n(ah) h_n(ak) D_{h,h} \\ &\times \left\{ 1 - \left[ (-1)^n (ll) \frac{kh_n(ah)}{h_n(ah)} + (-1)^n (tt) \frac{kh_n(ak)}{h_n(ak)} \right. \right. \\ &\quad \left. \left. + \{(lt)(tl) - (ll)(tt)\} \frac{kh_n(ah)}{h_n(ah)} \frac{kh_n(ak)}{h_n(ak)} \right] \right\}. \quad (162) \end{aligned}$$

We now proceed to the expansion according to the different reflected rays.

The reciprocal of (162) can be developed formally into the power series

$$\frac{a(hk)^{1/2}}{D_n} = \frac{4S}{h_n(ah)h_n(ak)D_{h,h}} \quad (163)$$

$$S = \sum_{s=0}^{\infty} \{(ll)L_h + (tt)L_k + (dlt)L_h L_k\}^3. \quad (164)$$

Here

$$L_h = \frac{kh_n(ah)}{h_n(ah)} (-1)^n, \quad L_k = \frac{kh_n(ak)}{h_n(ak)} (-1)^n, \quad (165)$$

and

$$(dlt) = (lt)(tl) - (ll)(tt). \quad (166)$$

$S$  can be written in the form

$$S = \sum_{s=0}^{\infty} \sum_{s_1+s_2 \leq s} \frac{s!}{s_1! s_2! (s-s_1-s_2)!} (dlt)^{s-s_1-s_2} (ll)^{s_2} (tt)^{s_1} L_h^{s-s_1} L_k^{s-s_2}. \quad (167)$$

Let

$$\alpha = s - s_1, \quad \beta = s - s_2; \quad (168)$$

then

$$S = \sum_{s=0}^{\infty} \sum_{\alpha+\beta=s}^{2s} \frac{s!}{(s-\alpha)!(s-\beta)!(\alpha+\beta-s)!} (dlt)^{\alpha+\beta-s} (ll)^{s-\beta} (tt)^{s-\alpha} L_h^{\alpha} L_k^{\beta}. \quad (169)$$

Taking now  $\alpha$  and  $\beta$  as the summation indices, we have

$$S = \sum_{\alpha, \beta=0}^{\infty} U_1(\alpha, \beta) L_h^{\alpha} L_k^{\beta}, \quad (170)$$

where

$$U_1(\alpha, \beta) = \sum_{s=\max(\alpha, \beta)}^{\alpha+\beta} \frac{s!}{(s-\alpha)!(s-\beta)!(\alpha+\beta-s)!} (dlt)^{\alpha+\beta-s} (ll)^{s-\beta} (tt)^{s-\alpha}. \quad (171)$$

Substituting Eqs. (158)–(161) and (165) in (155) and (156) gives

$$[1/a(hk)^{1/2}] D_A = \frac{1}{2} h_n(ah) h_n(ak) D_{h, h} [(ll)L_h + (dlt)L_h L_k] (-1)^n \quad (172)$$

$$(1/ah) D_B = -h_n(ah) kh_n(ah) (lt) (D_{h, h}/2n) e^{-\pi i/2}. \quad (173)$$

Inserting expressions (163), (172), and (173) for  $D_n$ ,  $D_A$ , and  $D_B$  in (153) gives

$$\frac{F_n}{i_n(bh)kh_n(ah)} = [x(kh_n) + 1] - \{(ll) + (dlt)L_k\}[x(kh_n) + 1] \\ - (x(kh_n) + 1)L_n] - (n+1)(lt)e^{-\pi i/2}[1 - L_k]S. \quad (174)$$

Rearranging the last term in (174) according to powers of  $L_h$  and  $L_k$ ,

$$F_n = i_n(bh)kh_n(ah) \left[ x(kh_n) + 1 + \sum_{\alpha, \beta=0}^{\infty} U_2(\alpha, \beta)L_h^\alpha L_k^\beta \right], \quad (175)$$

where

$$U_2(\alpha, \beta) = [-(ll)(x(kh_n) + 1) + (n+1)(lt)e^{-(\pi i/2)}]U_1(\alpha, \beta) \\ + (ll)[x(kh_n) + 1]U_1(\alpha - 1, \beta) \\ - [(dlt)(x(kh_n) + 1) + (n+1)(lt)e^{-(\pi i/2)}]U_1(\alpha, \beta - 1) \\ + (dlt)(x(kh_n) + 1)U_1(\alpha - 1, \beta - 1) \quad (176)$$

and

$$U_1(\alpha, \beta) = 0 \quad \text{unless both } \alpha \text{ and } \beta \text{ are } \geq 0. \quad (177)$$

Finally the radial displacement as a sum over  $\alpha, \beta$  is given by Eqs. (152) and (175) or

$$u_R(ka) = - \frac{\pi A^3 h}{ap^3} \sum_{n=0}^{\infty} (n + \frac{1}{2}) i_n(bh) kh_n(ah) \sum_{\alpha, \beta} U_{n+1/2}(\alpha, \beta) L_h^\alpha L_k^\beta P_n(\cos \theta), \quad (178)$$

where

$$U_{n+1/2}(\alpha, \beta) = [x(kh_n) + 1]\delta_{0, \alpha+\beta} + U_2(\alpha, \beta) \quad (179)$$

and  $\delta_{0, \alpha+\beta}$  is the Kronecker delta.

b. *Steepest Descent Approximation.* The sum of waves in (178) reduces, in the limit of infinite frequency, to the expressions for the reflected rays. We shall now obtain the surface displacement due to each reflected ray at the time it arrives.

Replacing the series of spherical harmonics (178) by a finite sum up to  $n = N$  and inverting the order of summations, we get

$$u_R(ka) \simeq -\frac{\pi A^3 h}{ap^3} \sum_{\alpha, \beta} \bar{l}_{\alpha, \beta}. \quad (180)$$

Here

$$\begin{aligned} \bar{l}_{\alpha, \beta} = & \frac{1}{4} \sum_{n=0}^N (2n+1) U_{n+1/2}(\alpha, \beta) kh_n(ah)[h_n(hb) - (-1)^n kh_n(hb)] \\ & \times L_h^\alpha L_k^\beta P_n(\cos \theta). \end{aligned} \quad (181)$$

We follow the well-known procedure of replacing the sum over  $n$  in (181) by the Watson integral and residues at poles of the integrand.

The Watson integral is

$$\bar{l}_{\alpha, \beta} = \frac{1}{4i} \int_W \frac{\zeta}{\cos \zeta \pi} U_\zeta(\alpha, \beta) [H - K] d\zeta, \quad (182)$$

where

$$\begin{aligned} H = & kh_{\zeta-1/2}(ha)h_{\zeta-1/2}(hb)P_{\zeta-1/2}\{\cos[\theta - (\alpha + \beta + 1)\pi]\} \\ & \times \frac{kh_{\zeta-1/2}(ah)^\alpha}{h_{\zeta-1/2}(ah)^\alpha} \frac{kh_{\zeta-1/2}(ak)^\beta}{h_{\zeta-1/2}(ak)^\beta} \end{aligned} \quad (183)$$

and

$$\begin{aligned} K = & kh_{\zeta-1/2}(ha)kh_{\zeta-1/2}(hb)P_{\zeta-1/2}\{\cos[\theta - (\alpha + \beta + 2)\pi]\} \\ & \times \frac{kh_{\zeta-1/2}(ah)^\alpha kh_{\zeta-1/2}(ak)^\beta}{h_{\zeta-1/2}(ah)^\alpha h_{\zeta-1/2}(ak)^\beta}. \end{aligned} \quad (184)$$

Using the integral representation of the Legendre function,

$$P_{\zeta-1/2}\{\cos[\theta - (\alpha + \beta + 1)\pi]\} = (1/2\pi) \int_0^\pi \{\exp(E_1) + \exp(E_2)\} d\phi, \quad (185)$$

where

$$E_1 = (\zeta - \frac{1}{2}) \ln\{\cos[\theta - (\alpha + \beta + 1)\pi] + i \sin[\theta - (\alpha + \beta + 1)\pi] \cos \phi\}, \quad (186)$$

$$E_2 = (\zeta - \frac{1}{2}) \ln \{\cos[\theta + (\alpha - \beta - 1)\pi] - i \sin[\theta + (\alpha + \beta - 1)\pi] \cos \phi\}. \quad (187)$$

The integrand in (182) splits into four terms. The first term, taking into consideration (165), is, in terms of Hankel functions,

$$l_{1:\alpha, \beta} = \frac{1}{h(ab)^{1/2} 8\pi i} \int_W \int_0^\pi \frac{U_\zeta(\alpha, \beta) K h_\zeta^{2\alpha+1}(ha) K h_\zeta^{2\beta}(ka) H_\zeta(hb)}{\{K h_\zeta(ha) H_\zeta(ha)\}^\alpha \{K h_\zeta(ka) H_\zeta(ka)\}^\beta \cos \zeta \pi} \times \zeta \exp(E_1) d\phi d\zeta. \quad (188)$$

In the notation introduced by Jeffreys and Lapwood (1957) for a fluid sphere, replacing the Hankel functions in the numerator of (188) by their integral representation

$$K h_\zeta(z) = \frac{i}{\pi} \int_{i\infty}^{-i\infty} e^{-z \cos \tau + i\zeta \tau} d\tau, \quad (189)$$

$$H_\zeta(z) = \frac{1}{\pi} \int_{i\infty - \pi}^{-i\infty + \pi} e^{z \cos \sigma - i\zeta \sigma} d\sigma, \quad (190)$$

and with

$$\frac{1}{\cos \zeta \pi} = 2 \sum_{m=0}^{\infty} e^{[(2m+1)\zeta + m]\pi i}, \quad \text{for } \operatorname{Im}(\zeta) > 0, \quad (191)$$

the  $m$ th term in Eq. (188) for  $l_1$  is

$$l_{1m:\alpha, \beta} = \int_W d\zeta \int d\tau_1 \cdots \int d\tau_{2\alpha+1} \int d\bar{\tau}_1 \cdots \int d\bar{\tau}_{2\beta} \int d\sigma \int G(\zeta) e^{g_1(\phi, \zeta, \sigma, \tau, \bar{\tau})} d\phi, \quad (192)$$

where

$$G(\zeta) = \frac{(-1)^{\alpha+\beta} \zeta U_\zeta(\alpha, \beta)}{4h(ba)^{1/2} \{K h_\zeta(ha) H_\zeta(ha)\}^\alpha \{K h_\zeta(ka) H_\zeta(ka)\}^\beta \pi^{2(\alpha+\beta)+3}} \quad (193)$$

and

$$g_1(\phi, \zeta, \sigma, \tau, \bar{\tau}) = [(2m+1)\zeta + m]\pi i + \sum_{j=1}^{2\alpha+1} (-ha \cos \tau_j + i\zeta \tau_j) + \sum_{l=1}^{2\beta} (-ka \cos \bar{\tau}_l + i\zeta \bar{\tau}_l) + (hb \cos \sigma - i\zeta \sigma) + E_1. \quad (194)$$

At saddlepoints, the following equations are satisfied:

$$(2m+1) + \sum_{j=1}^{2\alpha+1} \tau_j + \sum_{l=1}^{2\beta} (\bar{\tau}_l - \sigma) \pm [\theta - (\alpha + \beta + 1)\pi] = 0 \quad (195)$$

and

$$hb \sin \sigma = ha \sin \tau_j = ka \sin \bar{\tau}_j = -i\zeta. \quad (196)$$

Denoting

$$\tau_j = \pm \frac{1}{2}\pi - \gamma, \bar{\tau}_l = \pm \frac{1}{2}\pi - \bar{\gamma}, \sigma = \pm \frac{1}{2}\pi - \delta, \quad (197)$$

(196) and (195) become, respectively,

$$hb \cos \delta = ha \cos \gamma = ka \cos \bar{\gamma} = \pm i\zeta \quad (198)$$

and

$$(2\alpha + 1)\gamma + 2\beta\bar{\gamma} - \delta = 2m\pi + \theta. \quad (199)$$

c. *Arrival Time of Reflected Rays.* In  $I_{1m; \alpha, \beta}$  the value of  $g_{10}$  of the exponent (194) at the saddlepoint is

$$g_{10} = i\{m\pi - \frac{1}{2}[\theta - (\alpha + \beta + 1)\pi]\} - [ha(2\alpha + 1) \sin \gamma + 2\beta ka \sin \bar{\gamma} - hb \sin \delta], \quad (200)$$

so that the arrival time of the corresponding ray is

$$t_0 = (a/r_p)(2\alpha + 1) \sin \gamma + (a/r_s)2\beta \sin \bar{\gamma} - (b/r_p) \sin \delta, \quad (201)$$

and the length of path is

$$d_0 = a(2\alpha + 1) \sin \gamma + 2\beta a \sin \bar{\gamma} - b \sin \delta. \quad (202)$$

For the second term in  $I_{\alpha, \beta}$ ,

$$(2\alpha + 1)\gamma + 2\beta\bar{\gamma} - \delta = 2m\pi + 2\pi - \theta, \quad (203)$$

the travel time and distance are unchanged and given by Eqs. (201) and (202). For the third term,  $I_{3m; \alpha, \beta}$ :

$$(2\alpha + 1)\gamma + 2\beta\bar{\gamma} + \delta = 2m\pi + \theta, \quad (204)$$

$$t_0 = (a/r_p)(2\alpha + 1) \sin \gamma + (a/r_s)2\beta \sin \bar{\gamma} + (b/r_p) \sin \delta, \quad (205)$$

$$d_0 = (2\alpha + 1)a \sin \gamma + 2\beta \gamma \sin \bar{\gamma} + b \sin \delta. \quad (206)$$

For the fourth term,  $I_{4m; \alpha, \beta}$ :

$$(2\alpha + 1)\gamma + 2\beta\bar{\gamma} + \delta = 2m\pi + 2\pi - \theta. \quad (207)$$

Arrival time and distance are given by Eqs. (205) and (206).

Figures 10 and 11 show the geometric interpretation of  $\gamma$ ,  $\bar{\gamma}$ ,  $\delta$ . Here  $\gamma$ ,  $\bar{\gamma}$  are half the central angle of the chord transversed by the ray after reflection

TABLE I

THE NUMBER  $N$  OF REFLECTED RAYS EMITTED FROM A SOURCE AT  $b/a = 7/8$ , REACHING A POINT AT THE SURFACE AT ANGULAR DISTANCE  $\theta^a$

$\alpha$	$\beta$	$N$ for $0 < \theta < \theta_0$	$\theta_0$	$N$ for $\theta_0 < \theta < \pi$
0	1	1	138	3
0	2	3	98	1
0	3	1	21	3
1	0	1	81	3
1	1	3	158	1
1	2	5	39	3
1	3	3	82	5
2	0	3	146	5
2	1	5	99	3
2	2	3	21	5
2	3	5	140	7
3	0	5	159	3
3	1	7	39	5
3	2	5	80	7
3	3	7	161	5

<sup>a</sup>  $\alpha$  Denotes the number of reflections as P and  $\beta$  the number of reflections as S.  $\theta_0$  is the critical angle of transition.

TABLE II

ARRIVAL TIMES  $\tau + 1.5\delta$ , FOR  $\delta = 0.01$ , OF REFLECTED AND DIFFRACTED WAVES AT DISTANCES  $0 < \theta < \pi^a$

Ray	<i>m</i>	<i>i</i>	$0^\circ$	$10^\circ$	$45^\circ$	$60^\circ$	$90^\circ$	$135^\circ$	$170^\circ$	$180^\circ$
$P_2$	0	1					0.88	1.15	1.24	1.24
	0	3		0.12D	0.47D	0.61D	0.88	1.26	1.53	1.60
	0	4	2.25	2.25	2.21	2.18	2.08	1.88	1.67	1.60
PS	0	1							2.08	2.09
	0	3		0.19D	0.78D	1.02D	1.44D		2.21	2.29
	0	4	3.10	3.09	3.04	3.00	2.89	2.63	2.37	2.29
$P_3$	0	2	2.40	2.39	2.35	2.32	2.21	1.99	1.77	1.69
	0	1			0.47D	0.62D	0.91D	1.33D	1.62	1.69
	0	3		0.12D					1.63	1.72
	0	4	2.95	2.90	2.71	2.62	2.42	2.08	1.80	1.72
	1	3	2.95	3.00	3.15	3.20	3.29	3.38	3.41	3.41
$P_2S$								1.91D	2.25D	2.31D
	0	2	3.24	3.24	3.18	3.14	3.01	2.73		
	0	4	3.73	3.67	3.45	3.34	3.12	2.74	2.44D	2.38D
	1	3	3.73	3.78	3.95	4.02	4.12	4.22	4.25	4.25
					.80D	1.06D	1.57D	2.31D	2.86D	2.96D
					5.20D	5.14D	4.78D	4.62D	4.26D	3.67D
$PS_3$	1	1	5.27D	5.32D	{5.61	5.71	5.87	6.03	6.08	6.09
	1	3			{5.63	5.76	6.00	6.33	6.54	6.60
	1	4	7.10	7.10	7.07	7.04	6.97	6.81	6.65	6.60
$P_2$	1	2	4.71	4.70	4.68	4.67	4.62	4.50	4.39	4.35
	0	2	3.33	3.25	2.98	2.86	2.61}			
	0	4	3.37	3.29	3.00	2.87	2.61}	2.21	1.89D	1.76D
	1	3	3.37	3.45	3.72	3.83	4.05	4.35	4.57	4.63
	1	1	3.33	3.40	3.64	3.73	3.91	4.15	4.31	4.35
	1	4	5.44	5.41	5.28	5.22	5.10	4.88	4.69	4.63
	2	3	5.44	5.47	5.56	5.59	5.65	5.70	5.72	5.72
$P_4S$	1	2	5.55	5.55	5.53	5.51	5.45	5.32	5.19	5.15
	1	1	4.02	4.10	4.36	4.47	4.67	4.93	5.11	5.15
	0	2	4.02	3.93}						
	0	4	4.03	3.94}	3.64D	3.50D	3.23D	2.80D	2.46D	2.39D
	1	3	4.03	4.11	4.40	4.52	4.75	5.08	5.32	5.38
	1	4	6.26	6.22	6.09	6.03	5.89	5.65	5.44	5.38
	2	3	6.26	6.29	6.39	6.43	6.49	6.54	6.56	6.56

<sup>a</sup> The arrival of diffracted waves is marked by D. The source is at  $b/a = 7/8$ .

at the surface of the sphere as P or S, respectively;  $\delta$  is defined similarly to  $\gamma$  but in a concentric sphere of radius  $b$ ;  $m$  denotes the number of complete circuits of the ray;  $\alpha$  is the number of reflections as P;  $\beta$  is the number of reflections as S;  $i$  shows the location of the first reflection from the surface as indicated in Fig. 9. The intersection of sphere and diametral plane in Fig. 9 is divided into four arcs denoted by  $i = 1$  or 2 above the source to its right or to its left, respectively, and by  $i = 3$  or 4 below the source to its right or left. Table II shows for a source at  $b/a = \frac{7}{8}$  the arrival time of rays of given  $\alpha, \beta$  for distances  $\theta < \theta_0$  and for  $\theta > \theta_0$ .  $\theta_0$  is the critical distance at which the number of rays changes, and is listed in Table I. For example, for the once-reflected PP,  $\alpha = 1, \beta = 0, \theta_0 = 81^\circ$ . For  $\theta > \theta_0$  there are three such rays, namely, pP and two PP, whereas for  $\theta < \theta_0$  only a single once-reflected ray exists. When  $\alpha = 0, \beta_i = 1$  the situation is similar, but now the transition occurs at  $\theta_0 = 138^\circ$ . The reflected pS and the two PS arrive only at a distance larger than  $138^\circ$  from the source. Their paths are drawn in Fig. 11. Let us consider now the three types of twice-reflected rays:  $P_3(\alpha = 2, \beta = 0)$ ,  $P_2S(\alpha = 1, \beta = 1)$ , and  $PS_2(\alpha = 0, \beta = 2)$ . Table I shows that three  $P_3$  rays arrive at distances  $\theta < 146^\circ$ , while five  $P_3$  rays arrive when  $\theta > 146^\circ$ . Three  $P_2S$  waves arrive at distances  $\theta < 158^\circ$ ; however, at a larger distance, only one  $P_2S$  ray exists. A similar change from three rays to one possible ray occurs at  $98^\circ$  for the  $PS_2$ . Figure 10 shows the three possible ray paths at  $\theta = 45^\circ$  for each of  $P_3$ ,  $P_2S$ , and  $PS_2$ . The two variants of  $P_2S$ , namely, PSP and PPS, are considered as one ray. In Fig. 11,  $\theta = 170^\circ$ , and all three-times reflected rays consist of five  $P_3$ , one  $P_2S$ , and one  $PS_2$ . Arrival times for all possible rays up to  $\alpha + \beta = 5$  are entered in Table II.

The problem of the layered half-space can be treated by a similar method of ray analysis, e.g., by evaluating the solution in a series of terms where each term represents certain reflections and the total summation gives the complete seismogram (see Abramovici and Alterman, 1965). For further analysis of the layered media problem and for an extensive list of references, see Müller (1967, 1970) and Ewing *et al.*, (1957).

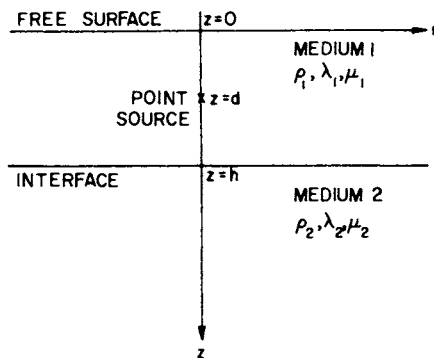


FIG. 1. A point compressional source located at depth  $z = d$  inside an elastic layer of thickness  $z = h$  overlying a homogeneous elastic half-space.

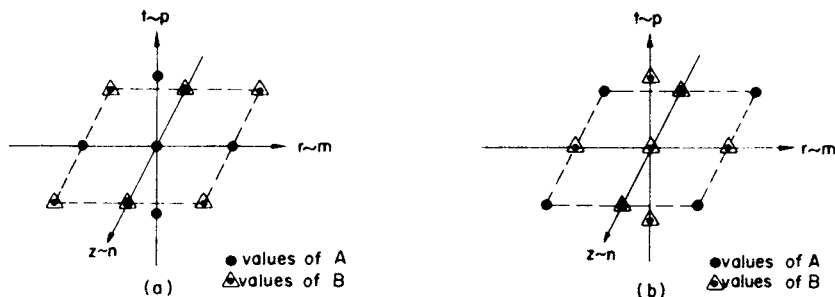


FIG. 2. Calculation stencils for the displacement components. Part (a) shows the grid points used in calculating  $A$ , and part (b) shows the grid points used in calculating  $B$ .

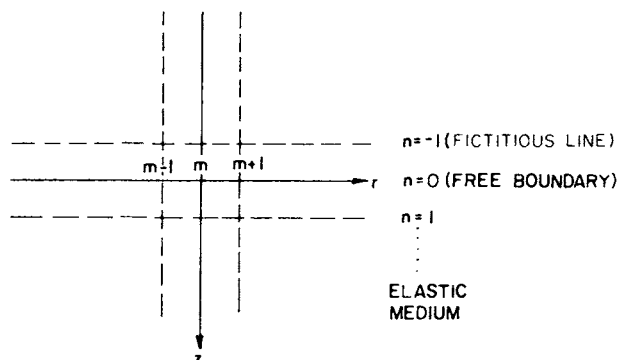


FIG. 3. Grid arrangement at the surface  $z = 0$  showing the fictitious line and free boundary.

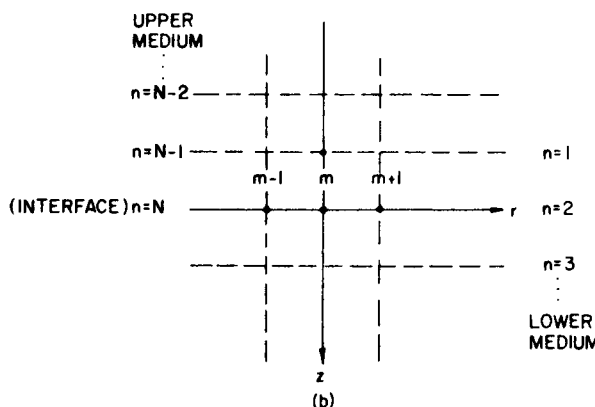
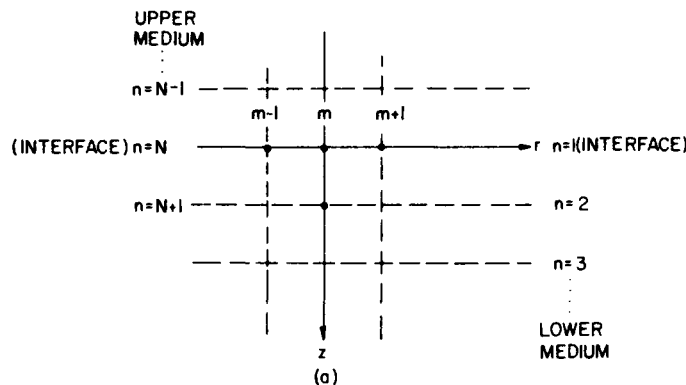


FIG. 4. Grid arrangement at the interface  $z = h$ . (a) shows the grid points used when the upper medium is extended to include an additional fictitious line below the interface, and (b) shows the grid points used when the lower medium is extended to include an additional fictitious line above the interface.

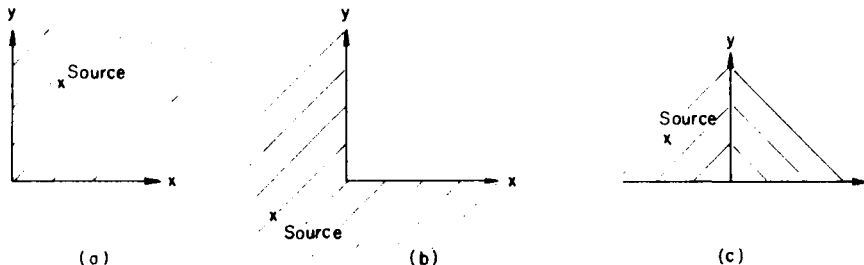


FIG. 5. The quarter plane (a), the three-quarter plane (b), and the two welded quarter planes (c).

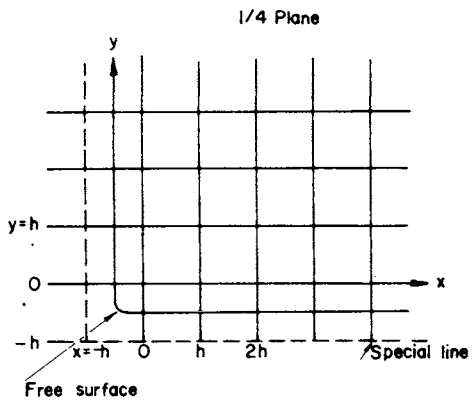


FIG. 6. The quarter plane with the superimposed grid for the finite difference scheme.

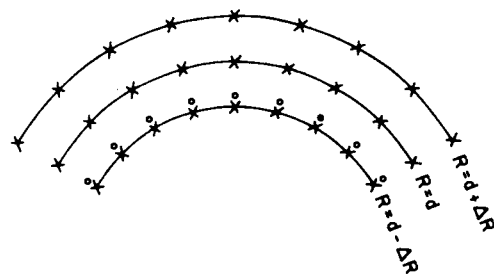


FIG. 7. Grid points at the interface  $R = d$  of the solid elastic sphere. The regular grid points are denoted by  $X$ . Additional fictitious grid points, denoted by circles, extend medium 1 from  $R \geq d$  to  $R < d$ .

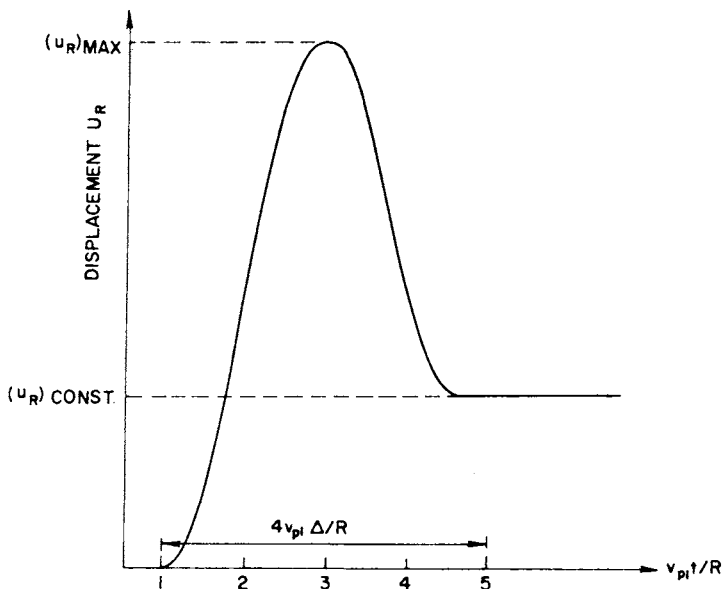


FIG. 8. Time variation of the radial displacement  $u_R$  for a point compressional smoothed source in a homogeneous elastic medium.

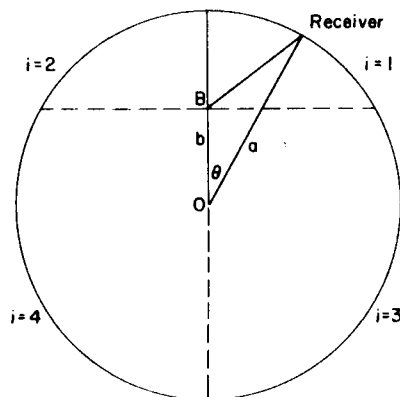


FIG. 9. Rays from a point source at B in a sphere. Observer at a point on the surface at an angular distance  $\theta$  from the source.

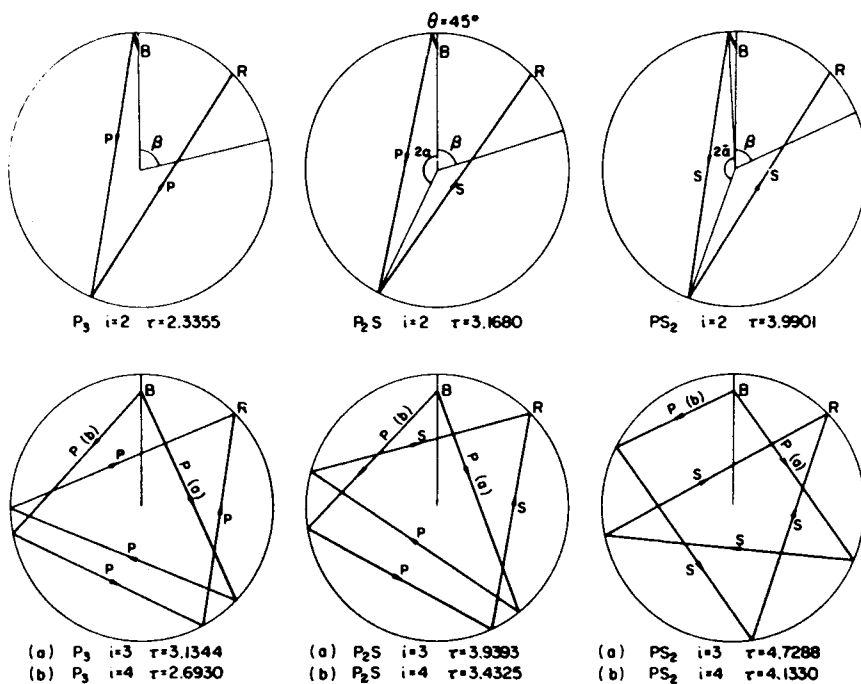


FIG. 10. The three types of twice-reflected rays  $P_3$ ,  $P_2S$ , and  $PS_2$  arriving at the surface at an angular distance  $\theta = 45^\circ$ .

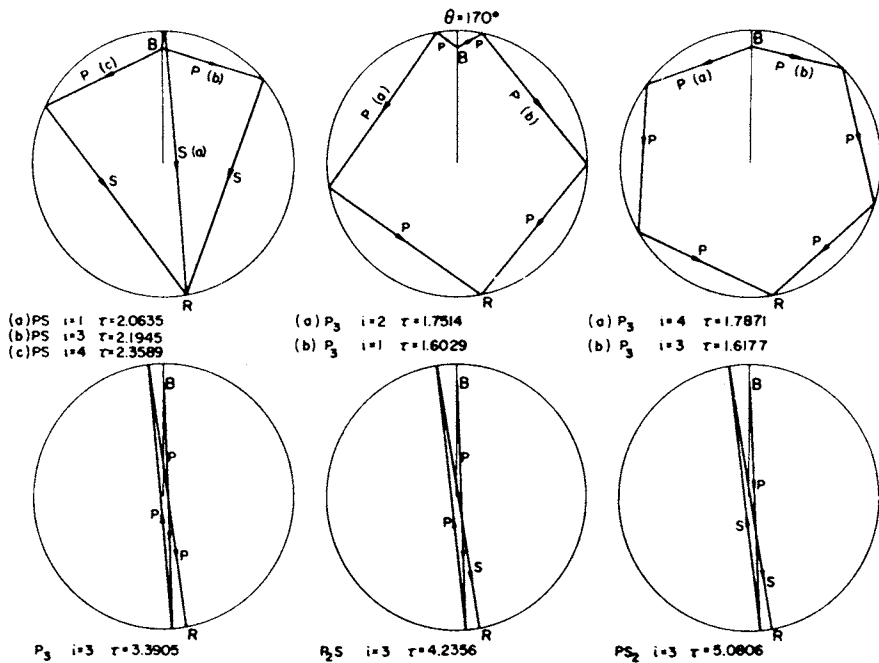


FIG. 11. The three once-reflected PS, the five  $P_3$ , and the single  $P_2S$  and  $PS_2$  arriving at  $\theta = 170^\circ$ .

### III. Computed Seismograms and Their Analysis

#### A. A PULSE IN A QUARTER PLANE, THREE-QUARTER PLANE, AND IN TWO WELDED QUARTER PLANES

##### 1. Description of the Problems

Let us analyze the motion of the two-dimensional isotropic and elastic quarter plane and of the three-quarter plane with stress-free surfaces, caused by an impulsive line source acting inside the medium or by an external force applied at the surface and perpendicular to it. The two-dimensional problem of the two welded quarter planes is also treated on the assumption that on the interface the usual condition, given by Eq. (3), of continuity of displacements and stresses holds.

The seismograms are obtained by the finite difference technique of Section II. A. We choose Cartesian coordinates with the origin at the corner of the medium and take its boundary lines as:  $x = 0, y \geq 0$ ;  $y = 0, x \geq 0$  for the quarter plane (Fig. 5a); and  $x = 0, y \leq 0$ ;  $y = 0, x \geq 0$  for the three-quarter

plane (Fig. 5b). The free surfaces of the two welded quarter planes are along the lines  $y = 0, x \leq 0$ ;  $y = 0, x \geq 0$  and the interface is along the line  $x = 0, y \geq 0$  (Fig. 5c).

In the subsequent discussion of results several figures show the components of displacement of a point in the elastic medium as a function of the dimensionless time parameter  $r_p t/d$  where  $d$  is the characteristic length of the problem, usually taken to be the distance from the source to one of the free surfaces.

## 2. Accuracy of the Finite Difference Calculation

In order to demonstrate the accuracy and convergence of the finite difference schemes we examine a few examples. We check first the convergence of the scheme for the problem of the quarter plane with an impulsive source defined by Eq. (85) of Section II, A, 6 and located at equal distances from the free surfaces, at  $x = y = d$ . The source constant is chosen to be  $A = d^2$ .

The finite difference calculations are performed for several grid sizes. In the region between the corner and the source,  $0 \leq x \leq d, 0 \leq y \leq d$ , where the reflection and diffraction phenomena are of interest, the narrow, peaked pulse of  $\Delta = 0.25d/r_p$  is applied. Results are obtained in a coarse, medium, and fine grid of  $\Delta x = d/21, d/42$ , and  $d/84$ . The upper part of Fig. 12<sup>2</sup> gives an example of the accuracy obtained in the three grids. It shows the  $v$ -component of displacement at the observation point  $x/d = 4/21, y = 0$  of an elastic quarter plane where  $r_s/r_p = 0.55$ . We see that the dashed and dotted curves for the medium and fine grids, respectively, are close. The solid curve for the coarse grid shows slightly different values at the minimum and maximum of the pulse. The curves are slightly displaced with respect to each other, so that the peak of the pulse in the fine grid arrives first, in the medium grid it is second, and in the coarse grid it is last. According to the choice of one-sided boundary conditions in Eqs. (32) and (33) the boundary should be considered as located in the middle between the lines  $x = 0, x = -h$  on one boundary line, and  $y = 0, y = -h$  on the second boundary. With decreasing  $h$  the distance between source and boundary decreases and the pulse is reflected earlier than for large  $h$ .

At a larger distance from the source, we considered a wider pulse of  $\Delta = 1.04d/r_p$  for the investigation of surface waves. The grid sizes are chosen as  $\Delta x = \Delta y = h = d/10$  and  $h = d/5$ . The second graph in Fig. 12 shows the  $v$ -component of displacement at a horizontal distance of  $5d$  from the source in a three-quarter plane—at the point  $x = -4d, y = d$ . In this example the source is located as before at  $x = y = d$  and the elastic parameters satisfy  $r_s/r_p = 0.55$ . The results for the coarser grid (dashed curve) are near enough

<sup>2</sup> Figures 12-38 appear on pages 93-105.

to the results for the fine grid (solid curve) to conclude that for an analysis of the motion at distance points of the order of  $5d$  away from the source, a coarse grid of  $h = d/5$  is sufficient. Near the source, calculations were performed for the grid  $h = d/42$  with occasional checking of results obtained with the other grids.

Another way of checking the accuracy of the finite difference method is to compare results obtained by this method with known analytic solutions. Analytic solutions are known for the two-dimensional half plane and the two welded half planes. These problems are in fact limiting cases of the problems of the quarter plane and the two quarter planes, respectively, and they are obtained by moving the source far away from one of the free surfaces of the medium.

The analytic solutions for the half plane and the two welded half planes are obtained by using Garvin's method. The source is located at a distance  $d$  from the boundary. For reasons of simplicity the calculation of the analytic solution was done only for the unsmoothed source expressed in Eq. (82).

Figure 13 shows the displacements for the two welded half planes  $y \leq 0$  and  $y \geq 0$  obtained from the analytic solution (solid line). They are compared with results obtained by the finite difference technique (dashed line) for observation points  $x/d = 4, y/d = 0$  and  $x/d = 4, y/d = 1$ . The source is located at  $x/d = 0, y/d = 1$ .

The elastic constants are

$$v_{s1}/v_{p1} = 0.58, \quad v_{s2}/v_{p2} = 0.60, \quad \rho_2/\rho_1 = 0.2.$$

Here index 1 designates the upper half plane  $y \geq 0$  in which the source is located, and index 2 designates the other half plane  $y \leq 0$ .

In the finite difference calculation it was possible to introduce the more realistic smoothed source defined in Eq. (85), which emits a wave of finite amplitude and has a smoothing parameter  $\Delta = 0.25d/v_p$ . In order to identify the different waves which appear in this figure and in most of the following figures, small arrows which designate the theoretical arrival time of each wave are drawn. By comparing the analytic and numerical results it is seen that very good matching is obtained in the interface waves, or Stonely waves (denoted by  $S_i$ ), while for the body waves  $P, P_1P_1, P_1S_1$  the matching is not as good. This is explained by the fact that the unsmoothed source applied in the analytical solution involves very high frequencies which are not included in the smoothed solution applied in the numerical calculations, and thus the body waves obtained by finite differences appear more spread out in time, while the surface waves which naturally involve only the lower frequencies show a very similar shape which clearly indicates the accuracy of the numerical results.

A similar situation arises in Figs. 14 and 15 where a comparison of results obtained by the two methods in a half plane is made at observation points located at  $x/d = 2, y/d = 1$  and  $x/d = 5, y/d = 3/5$ , respectively. The elastic parameters satisfy  $v_s/v_p = 0.55$  and the smoothing parameter used for the source applied in the finite difference method is as before,  $\Delta = 0.25d/v_p$ .

It is of interest to note that the  $v$ -component in Fig. 14 does not show any  $P$ -wave. This is as expected for an observation point which is located at the same depth as the source so that the vertical component of the direct  $P$ -wave vanishes. The reflected PS which arrives shortly before the Rayleigh wave has infinite amplitude in the analytic solution.

In both figures excellent matching is obtained in the surface Rayleigh waves (denoted by R).

### 3. The Displacement at the Corner. Effect of $v_s/v_p$

In this section and in Sections III,A,4 and 5 which follow, we study the motion of the quarter and three-quarter plane, caused by a source located on the diagonal at  $x = y = d$ .

The displacement at the corner is of special interest. It shows a single large maximum at the arrival of the direct pulse, and then decreases to zero. This maximum is larger than the maximum of the initial pulse and includes the effect of reflection at the surface and of diffraction at the corner.

Figure 16 shows the displacement at the corner of the quarter plane and of the three-quarter plane as compared with the motion in a homogeneous medium at the same distance. The ratio of shear to compressional wave velocity  $v_s/v_p$  varies from 0.50 to 0.70. One sees that for  $v_s/v_p = 0.55$  at the corner of a quarter plane the maximum displacement is about three times the maximum in the homogeneous medium (or of the incident wave). At the corner of a three-quarter plane the maximum is only about 1.5 times the initial value.

Let us consider the form of the slowly varying part of the curves for  $t \geq 2.5d/v_p$ . In the three-quarter plane it is similar to the form of the initial wave. In the quarter plane the curvature is different—a Rayleigh wave arrives from 3 to 4 time units after the maximum of the direct pulse. The arrival times of all other waves, including reflected and diffracted waves, coincide with the arrival time of the direct pulse, and simply change its amplitude.

Considering the displacement at the corner of the quarter plane for several values of  $v_s/v_p$ , one sees that the amplitude decreases with decreasing  $v_s/v_p$ . It is interesting to note that in a three-quarter plane the dependence on  $v_s/v_p$  is different. The maximum of the displacement at the corner increases with decreasing  $v_s/v_p$ .

#### 4. Diffraction Effects

The effect of diffraction at the corner is found clearly in the curves which describe the motion of the three-quarter plane. At points near to the corner the arrival times of direct and diffracted pulse are close and the two pulses are superposed. Subtracting the direct pulse, the residual displacement  $\mathbf{U}_R$  shows the diffracted P(D) and S(D) pulses. In order to separate between P(D) and S(D) let us calculate the components of  $\mathbf{U}_R$  in polar coordinates  $(r, \theta)$  with origin  $r = 0$  at the corner and  $\theta = 0$  on the positive  $x$  axis. Except for spherical-wave effects, P(D) occurs in the  $r$ -component, and S(D) in the  $\theta$ -component.

Consider the maximum values of P(D) and S(D) with and without filtering of zero frequency at several points  $(r, \theta)$ , we find that P(D) depends mainly on the distance  $r$  from the corner. It decreases linearly with increasing  $r$  in the range  $0 \leq r/d < \frac{1}{2}$ , and the amplitude of P(D) at  $r$ ,  $A(r)$ , is given in terms of the amplitude  $A_0 = A(0)$  at the corner,  $r = 0$ , by

$$A(r) = A_0(1 - 0.88r/d). \quad (208)$$

Here  $A_0 = 0.45d$ . The variation in  $\theta$  has only a secondary effect.

S(D) varies mainly with  $\theta$ . It is zero at  $\theta = 45^\circ$  and its amplitude  $B$  increases linearly with  $\theta$ . In the range  $20^\circ \leq \theta \leq 100^\circ$ ,

$$B(\theta) = (\theta - 45^\circ)B(90^\circ). \quad (209)$$

Here  $\theta$  is measured in degrees.  $B(\theta)$  is negative for  $\theta < 45^\circ$  and positive for  $\theta > 45^\circ$ .  $B(90^\circ) = 0.005d$ .

Figure 17 shows the lines  $A(r)$  and  $B(\theta)$  together with the result for amplitudes of diffracted pulses. The dependence of P(D) on  $\theta$  is indicated by the spreading of points around the line for  $A(r)$ . The points for S(D) are close to the line  $B(\theta)$  for  $\theta < 100^\circ$ . For  $\theta > 100^\circ$  the amplitude of S(D) increases more rapidly. Figure 17 shows also the variation in amplitude of P(D) and S(D) after filtering of the lowest frequencies.

#### 5. Surface Waves

In addition to the Rayleigh waves which occur in a half-space, there are surface waves associated with reflection or transmission of Rayleigh waves at the corner  $R_c R$ , and surface waves due to diffraction of the initial pulse at the corner,  $P_c R$ . Their occurrence in a quarter plane has been discussed by Alterman and Rotenberg (1969). Let us compare the surface waves in the quarter and three-quarter plane with results for the same source in a half plane.

At a point on the surface of the half plane at a horizontal distance of  $5d$  from the source the maximum of the direct P arrives at  $r_p t/d = 6.48$  and is followed by a Rayleigh wave. The dashed curves in Fig. 18 show the  $u$ - and  $v$ -components of P and of R in the half-space. The solid curve shows the motion

in the three-quarter plane. The Rayleigh wave,  $R$ , is preceded by  $P_c R$ ; and has in both  $u$ - and  $v$ -components an amplitude which is less than one-half of the amplitude of  $R$  in a half plane. The particle motion in Fig. 19 is retrograde elliptic in the half plane, and similar elliptic motion occurs in the three-quarter plane. It is more involved, does not complete a full cycle, and has a larger eccentricity. In the three-quarter plane the elliptic particle trajectory consists of two parts. The first part is the  $P_c R$  wave alone, the second part includes  $R$  and the continuation of  $P_c R$ . For large time the  $u$ -components coincide and converge to the stationary value  $-0.28d$ . The  $v$ -component tends to  $-0.05d$  in the half plane, while  $v$  in the three-quarter plane stays positive at  $0.15d$ . Figure 20 shows a similar comparison to that given in Fig. 18 when the observer is at the depth of the source,  $y = d$ , and at  $5d$  horizontal distance from the source. The attenuation of the surface waves with depth is clearly found. The  $u$ -component of the Rayleigh wave is near zero both in the half plane and in the three-quarter plane. The decrease in the  $v$ -component amounts to  $1/10$  of the surface amplitude in the half plane. The decrease of  $v$  in the three-quarter plane is more pronounced—being one fifth of the surface amplitude. The analytic solution for a source in a half plane is given for comparison (see Garvin, 1956; Alterman and Loewenthal, 1969). In this analytic solution the time constant of the source is  $\Delta = 0$ . The direct P-pulse and the reflected pulses have infinite amplitude at their respective arrival times; however, the Rayleigh wave has finite amplitude. The dashed curves in Figs. 18 and 20 show the motion of the half plane as caused by this source. Except for a small phase shift the Rayleigh waves for both sources in the half plane have the same form on the surface.

Figures 21 and 22 show a comparison between the motion of the quarter plane and the half plane. Here, the  $v$ -components of the Rayleigh waves in the two geometries are similar while the largest difference occurs in the  $u$ -components. The  $u$ -component of the Rayleigh wave in the quarter plane is more than twice as large as in the half plane. After the arrival of the various waves,  $u$  in the quarter plane tends to zero while in the half plane it tends to  $0.28d$ . The  $v$ -component in Fig. 21 shows that  $P_c R$  and  $R_c R$  have larger amplitude than the direct P-pulse. They arrive at  $r_p t/d > 12$ . A comparison with Fig. 22 shows the attenuation of these surface waves with depth.

In conclusion, the  $u$ -component of motion in the three-quarter plane is similar to the  $u$ -displacement in the half plane. The motion differs for the  $v$ -components. A comparison of the quarter and half planes shows the opposite; here the  $v$ -components (which are perpendicular to the free surface) are similar, and the main difference is in the  $u$ -components—i.e., parallel to the surface near which the observer is located.

The surface waves are largest in the quarter plane, less in the half plane, and have the smallest amplitude in the three-quarter plane. The particle

motion in the surface waves of the quarter plane shows the separate elliptic paths of  $R$ ,  $P_c R$ , and  $R_c R$  (see Fig. 19). A comparison of surface waves at several distances from the source confirms the known result that in a half plane the amplitude of the Rayleigh wave does not change with distance. A phase shift with distance is found. Figure 22 shows the  $v$ -components of displacement at distance  $3d$ ,  $4d$ , and  $5d$  from the source. The surface wave in the quarter plane is almost unchanged, except for interference with reflected waves and a slight increase in amplitude with distance. The surface wave in the three-quarter plane shows some decrease in amplitude and a phase shift. The corner-generated  $P_c R$  and  $R_c R$  are indicated in Fig. 23.

### 6. Source Off-Diagonal

For simplicity we have considered up to now a source located on the diagonal axis of symmetry. However the same analysis applies also when the source is located at an arbitrary point in the elastic medium.

Let us consider the motion at the corner of the quarter plane when the source is moved away from the diagonal. Figure 24 shows the horizontal and vertical displacements  $u$  and  $v$  at the corner when the source is at  $x = d$  and at  $y/d = 17/21$  and  $y/d = 13/21$  as compared with  $y = d$ .

Let us consider first the amplitude of the direct P-pulse. As expected, the maximum of the  $u$ -component,  $A(u)$ , increases with decreasing distance from the surface  $y = 0$ , while the maximum  $A(v)$  of  $v$  decreases. However, on comparing the total amplitude  $A = (A(u)^2 + A(v)^2)^{1/2}$  with the amplitude of the incident wave,  $A_i$ , we find that  $A/A_i$  is constant, independent of the location of the source. Several additional source locations in the range  $0 \leq y \leq d$  were checked and in all cases  $A/A_i = 2.9$ . One sees that the displacement at the corner has about three times the amplitude of the incident pulse (for elastic constants  $v_s/v_p = 0.55$ ) and that this result is independent of the location of the source.

In the curve for  $y/d = 13/21$ , when the source is nearest to the surface we clearly observe the arrival of a Rayleigh wave. Its amplitude  $A$  is five times as large as the amplitude  $B$  of a Rayleigh wave at the same point in a half-space. When the source is even nearer to the surface both  $A$  and  $B$  increase. Table III shows the variation of  $A$  and  $B$  with depth of source. One sees that  $A/B$  decreases when the source nears the surface, i.e., the attenuation of the corner generated surface waves is smaller than the attenuation of the Rayleigh wave in a half-space. Figure 25 shows the particle motion. The upper curves are for the half plane and show the elliptic particle paths. The major axis of the ellipses is in the  $v$  direction or near to it. The lower curves are for the quarter plane. They show the larger amplitude of the elliptic particle motion and an inclination of  $45^\circ$  between the major axes and the  $u$  and  $v$  directions.

TABLE III

THE MAJOR AXIS OF THE PARTICLE  
ELLIPSE:  $A$  IN QUARTER PLANE;  $B$  IN  
HALF PLANE

Location of source $y/d$	$A/d$	$B/d$	$A/B$
13/21	0.5	0.1	5.2
11/21	0.8	0.2	3.3
9/21	1.2	0.4	2.9
8/21	1.6	0.6	2.7
5/21	3.4	1.2	2.8

### 7. Results for a Quarter Plane with a Force Applied on Its Surface

The problem of the quarter plane when a force is applied on one of the free surfaces is solved by a similar finite difference method as described in Section II, A, 3. In the mathematical formulation we have now a nonhomogeneous boundary condition instead of the source condition.

Let us assume that a force acts on the free surface  $y = 0$ ,  $x \geq 0$  and perpendicular to it, at a distance  $d$  from the corner, so that the normal component of stress on  $y = 0$  is given by

$$\tau_{yy}(x, 0, t) = -A\delta(t)\delta(x - d) = Z. \quad (210)$$

Here  $A$  is a constant having the dimension of stress and  $\delta$  is the Dirac delta function. In the numerical scheme the singularities of the  $\delta$  functions are removed by using a similar smoothing device to that discussed in Section II, A, 6. All other boundary conditions remain the same as in Eqs. (30) and (31). This problem was first investigated by Lapwood (1961). He gave an iterative solution from which he was able to derive first approximations for the parts of the displacement field which describe the Rayleigh pulse incident at the corner and the pulse transmitted round the corner. It is of interest to note that although the force is applied to the quarter plane on one of its boundaries, the numerical solution converges rapidly on refining the grid. This is in contrast with the poor numerical convergence encountered when an impulsive compressional source is located very near to the free boundary of an elastic quarter plane (see Alterman and Loewenthal, 1970).

As the applied force acts directly on the free boundary, the surface waves and the derived diffracted waves have large amplitudes and thus are easy to analyze near the corner.

Figure 26 shows the horizontal and vertical components of displacement at the corner of the quarter plane. The first wave to arrive there is the direct P-wave which has a horizontal component only. It has a negative sign and is found in the upper part of Fig. 26. The second wave is the S-wave which contributes to the vertical component  $v$  and is seen in the lower part of Fig. 26. The direct Rayleigh wave arrives later. The particle motion in the Rayleigh wave at the corner is retrograde with the major axis at an angle of  $45^\circ$  to the  $x$  axis. The same result was obtained at the corner of a quarter plane excited by a compressional impulsive source when the source is near one of the free surfaces (see Section III, A, 6). Figure 27 shows the particle motion in the two cases. The source coefficient  $A$  is adjusted so that the amplitudes of the surface waves are equal in both cases.

As described by Lapwood (1961), a Rayleigh wave travels along the surface  $y = 0$ , arrives at the corner, and propagates along the second surface  $x = 0$ . We distinguish between three kinds of Rayleigh waves which are generated at the corner.

1. A Rayleigh wave which propagates along the surface on which the force is applied arrives at the corner, and proceeds to travel as a Rayleigh wave along the free surface. We denote this wave as  $R_cR$ .

2. A compressional wave produced by the applied force reaches the corner, and by diffraction a surface wave propagates along the free surface  $x = 0$ . This wave is denoted by  $P_cR$ .

3. A shear wave produced by the applied force reaches the corner and by diffraction a surface wave propagates along the free surface  $x = 0$ . This wave is denoted by  $S_cR$ .

At  $x/d = 0$ ,  $y/d = \frac{1}{2}$  we note two separate parts of two ellipses (see Fig. 28). The first ellipse describes the particle motion in the direct Rayleigh wave. Its arrival time is indicated by an arrow. The other part of the motion is due to the combined effect of the  $R_cR$ ,  $P_cR$ , and  $S_cR$  surface waves which start another ellipse.

Figure 29 shows the motion of points on the surface  $y = 0$  on which the force is applied. A similar situation as before occurs. The particle motion in the direct R-wave is elliptic with the major axis perpendicular to  $y = 0$ , while the combined motion of  $P_cR$ ,  $R_cR$ ,  $S_cR$  produces an ellipse with a major axis parallel to  $y = 0$ . For points near and above the location of the applied force the direct R-wave has zero amplitude. This is found in the particle motion at the point  $x/d = 1$ ,  $y/d = 0$ , at the location of the applied force in Fig. 29, and also in Fig. 30 which shows the horizontal and vertical components of displacement and the particle motion at  $x/d = 1$ ,  $y/d = \frac{1}{2}$ . On  $y = 0$  the horizontal component  $u$  of the Rayleigh wave has the form  $\phi$ , where  $\phi$  is the time

dependence of the applied stress  $Z$  which in our case is the smoothed  $\delta$  function, denoted as  $\delta_\Delta(t)$ . The  $v$ -component has the form  $\phi'$ —the Hilbert transform of  $\phi$  or the allied function of  $\phi$  defined as

$$\phi'(t) = \frac{1}{\pi} \int_{-\infty}^{\infty} \frac{\phi(\tau)}{t - \tau} d\tau. \quad (211)$$

The allied function of  $\delta_\Delta(t)$  is given by

$$\begin{aligned} \delta_\Delta(t) = \frac{1}{4\pi\Delta^3} & [(t + 2\Delta)^2 \log|t + 2\Delta| - 2(t + \Delta)^2 \log|t + \Delta| \\ & + 2(t - \Delta)^2 \log|t - \Delta| - (t - 2\Delta)^2 \log|t - 2\Delta|]. \end{aligned} \quad (212)$$

Figure 31 shows  $\phi$  and  $\phi'$  as given by Eq. (212). On the free surface  $y = 0$  at  $x/d = \frac{1}{2}$  the S-wave, which is the only wave to arrive near the arrival time of the Rayleigh wave, has zero  $u$ -component and only a small  $v$ -component. Thus the main contribution at this time is that of the Rayleigh wave which, as Fig. 32 shows, has exactly the form mentioned above. The Rayleigh waves pass the corner, so that on the boundary  $x = 0$  at  $y/d = \frac{1}{2}$  the displacement has changed its form in a way such that  $u$  now has a time dependence similar to  $\phi'$  and  $v$  a form similar to  $\phi$  (see Fig. 32). Thus a  $90^\circ$  phase shift is caused in the surface waves which travel round the corner. This is the same result as De Bremaecker (1958) obtained in his experiments.

The phase shift is noticed more clearly at a location far from the corner, Figure 33 shows the particle motion at the two surfaces for an observer located at distance  $3d$  from the corner. At  $x = 3d$ ,  $y = 0$  we find concentric ellipses which belong to the particle motion in the direct Rayleigh wave, in  $P_cR$ ,  $S_cR$ , and  $R_cR$ . In all of these waves the direction of propagation is the positive  $x$  direction and the elliptic motion is retrograde. At the point  $x = 0$ ,  $y = 3d$ , one finds after the arrival of body waves the elliptic motion in  $P_cR$ ,  $S_cR$ , and  $R_cR$ . The surface waves propagate in the direction of the positive  $y$  axis and we find again the retrograde particle motion. The major axis is perpendicular to the free surface as expected for Rayleigh waves in a half space. At the corner it is the sum of the motions on the two surfaces and the result is the elliptic motion depicted in Fig. 27, which has an inclination of  $45^\circ$  to the axes.

### 8. Numerical Results for the Two Welded Quarter Planes

As the welded quarter planes problem is a generalization both of the quarter plane and the half plane problems, it is of interest to study the motion of the two quarter planes as a perturbation of the quarter plane or the half plane problems.

Figure 34 shows the components of displacement at the corner  $(0, 0)$  when the densities  $\rho_1, \rho_2$  of the quarter planes are assumed to satisfy  $\rho_2/\rho_1 = 0, 0.1, 0.2, 0.4$ , and all other elastic parameters are assumed to be equal in both media. The impulsive line source is located inside medium 1 at point  $(-d, 4d)$ . When  $\rho_2 = 0$  the solution of the quarter plane problem is obtained. When  $\rho_2$  differs from zero a strong decay in the amplitudes of the surface waves is noticed. A smaller decay in amplitude occurs also in the body waves. The motion at the corner for the above cases is given in the upper part of Fig. 35, and in its lower part the respective motions in the two welded half planes  $x \geq 0, x \leq 0$  are given.

By comparing the elliptical paths of the corner  $x = 0, y = 0$  it is noticed that while in the two half planes the major axes of the ellipses are always perpendicular to the interface  $x = 0$ , the inclination in the two quarter planes increases rapidly from  $45^\circ$ , when  $\rho_2/\rho_1 = 0$ , to  $90^\circ$ , when  $\rho_2/\rho_1 = 0.4$ .

A decay of the amplitude with increasing ratio  $\rho_2/\rho_1$  occurs in the two quarter planes as well as in the two half planes. For  $\rho_2 = 0$  we get the surface Rayleigh waves. When  $\rho_2$  differs from zero Stoneley waves appear. Their domain of existence is narrow, their amplitude decreases with increasing density ratio  $\rho_2/\rho_1$ , and they disappear completely when  $\rho_2/\rho_1 > 0.5$ . A similar effect occurs also in the two quarter planes. The source being very near to the interface, the dominant contribution to the motion arises from Stoneley waves similar to those of the two half planes.

Figures 36–38 show results for perturbations of the half plane. The source is located near the free surface  $y = 0$  of medium 1 at point  $(-4d, d)$  and the observation points are at  $(d, 0), (0, 0)$ , and  $(-d, 0)$ , respectively. The elastic parameters were chosen to satisfy  $v_{p1} = v_{p2}$  and  $v_{s1}/v_{p1} = v_{s2}/v_{p2} = 0.55$ , and results are obtained for the following density ratios:  $\rho_2/\rho_1 = 0.8$  (dashed line),  $\rho_2/\rho_1 = 1$  (solid line), and  $\rho_2/\rho_1 = 1.2$  (dotted line). The solid line, where  $\rho_2 = \rho_1$ , shows the motion of the elastic and homogeneous half plane  $y \geq 0$ . Rayleigh waves are clearly observed just after the arrival time of the body waves. When  $\rho_2 \neq \rho_1$  a similar motion is obtained and the observed surface waves are Rayleigh waves which travel along the free surface of medium 1 and are transmitted through the corner at  $(0, 0)$  to the free surface of medium 2. Transmission coefficients were calculated for the same problem by McGarr and Alsop (1967) utilizing a variational method. McGarr and

Alsop chose the two cases of  $v_{p2}/v_{p1} = 1.26$ ,  $\rho_2/\rho_1 = 1.13$ ,  $v_{s1}/v_{p1} = v_{s2}/v_{p2} = 0.58$  and of  $v_{p2}/v_{p1} = 0.86$ ,  $\rho_2/\rho_1 = 0.89$ ,  $v_{s1}/v_{p1} = v_{s2}/v_{p2} = 0.58$ , and obtained transmission coefficients of  $W_2/W_1 = 0.83$  and  $1.16$ , respectively. Here  $W_i$  denotes the amplitude in medium  $i$  ( $i = 1, 2$ ). The authors checked these results by experiment using a technique described by Oliver *et al.* (1954) and obtained  $W_2/W_1 = 0.85 \pm 0.05$  and  $W_2/W_1 = 1.17 \pm 0.04$ , respectively. By using a finite difference method Loewenthal (1970) obtained for those cases  $W_2/W_1 = 0.82$  and  $W_2/W_1 = 1.15$ , respectively, which are in good agreement with the previous results.

---

FIG. 12. The vertical component of displacement,  $v$ , in a coarse mesh (solid line), medium mesh (dashed line), and a fine mesh (dotted line) in a quarter plane (a) and in the three-quarter plane (b).

FIG. 13. Comparison between the components of displacements in the two welded half planes as obtained analytically (in solid line) and numerically, by finite differences (in dashed line) for observation points  $x/d = 4$ ;  $y/d = 0$  (left) and  $x/d = 4$ ;  $y/d = 1$  (right).  $\rho_2/\rho_1 = 0.2$ .

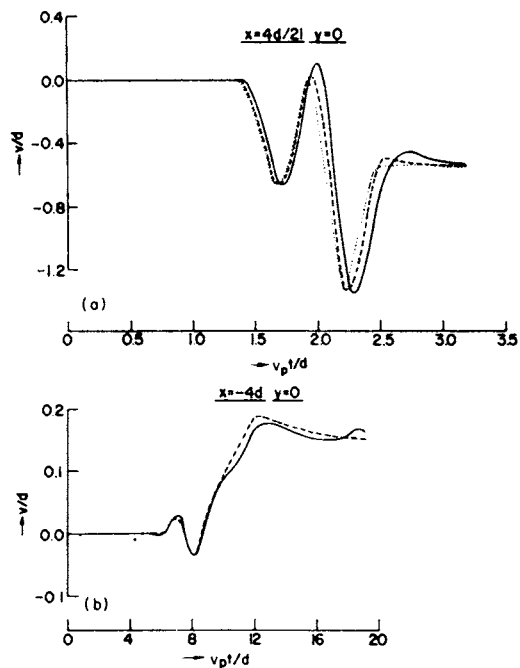


FIG. 12

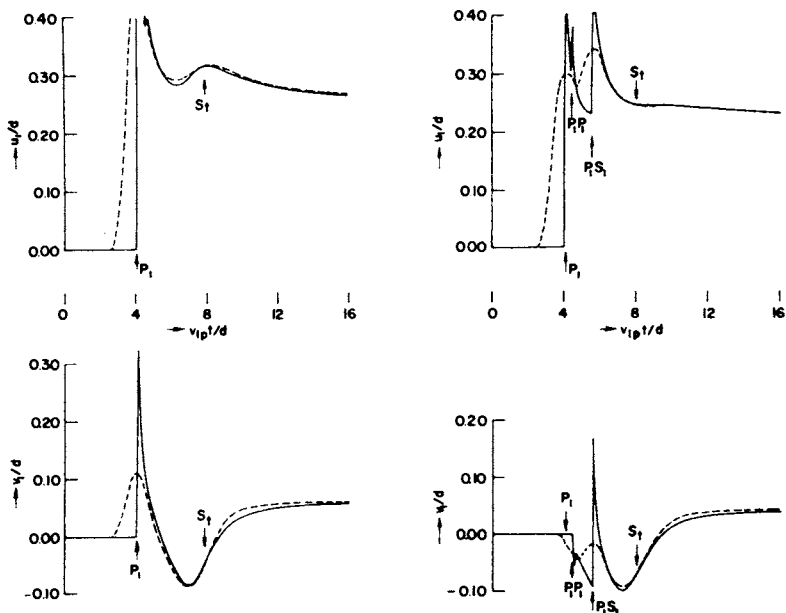


FIG. 13

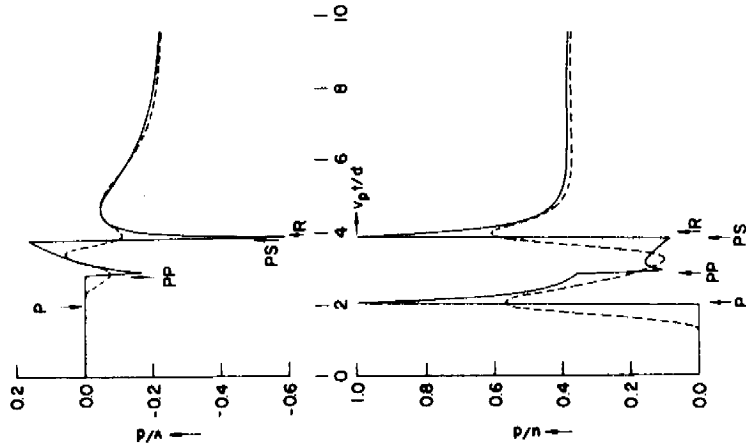


FIG. 14. Horizontal and vertical displacements  $u, v$  obtained analytically (solid line) compared with results obtained by the finite difference scheme (dashed line) for observation point  $x/d = 2, y/d = 5$ , and for  $v_s/v_p = 0.55$ .

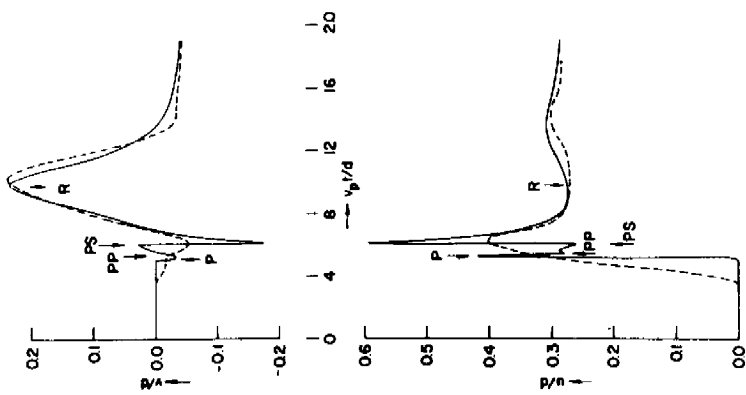


FIG. 15. Horizontal and vertical displacements  $u, v$  obtained analytically (solid line) compared with results obtained by the finite difference scheme (dashed line) for observation point  $x/d = 5, y/d = 3/5$ , and for  $v_s/v_p = 0.55$ .

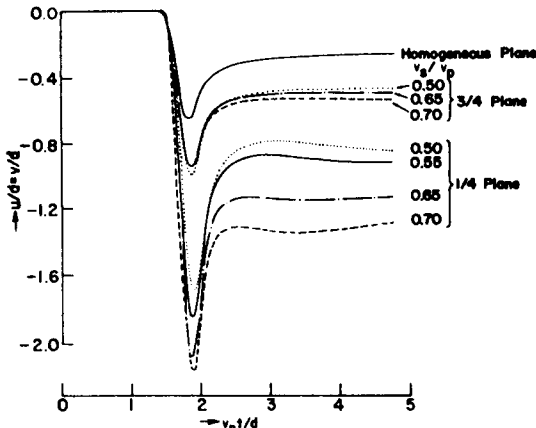


FIG. 16. The displacement components  $u, v$  at the corner of a quarter plane and of a three-quarter plane having elastic constants  $v_s/v_p = 0.50, 0.55, 0.65, 0.70$ .

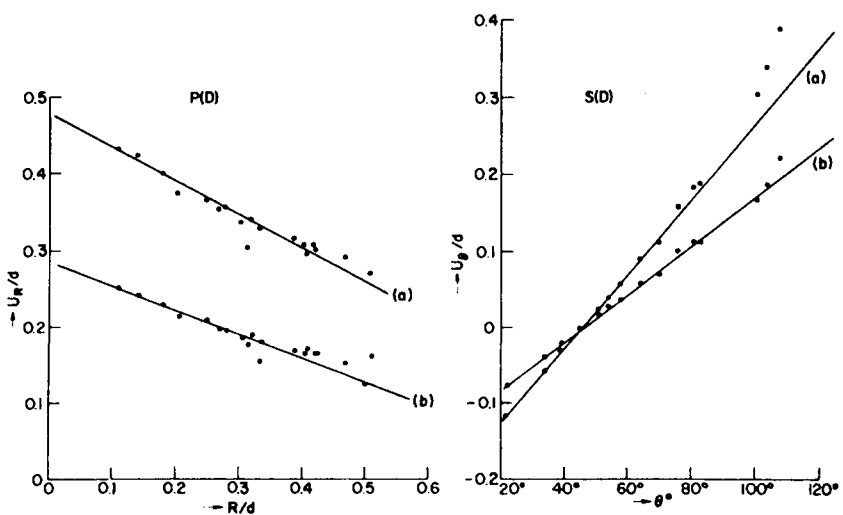


FIG. 17. Diffraction at the corner of a three-quarter plane; the amplitude of the diffracted P as function of distance  $R$  from the corner, and the amplitude of the diffracted S as a function of  $\theta$ , (a) without filtering, (b) with filtering.

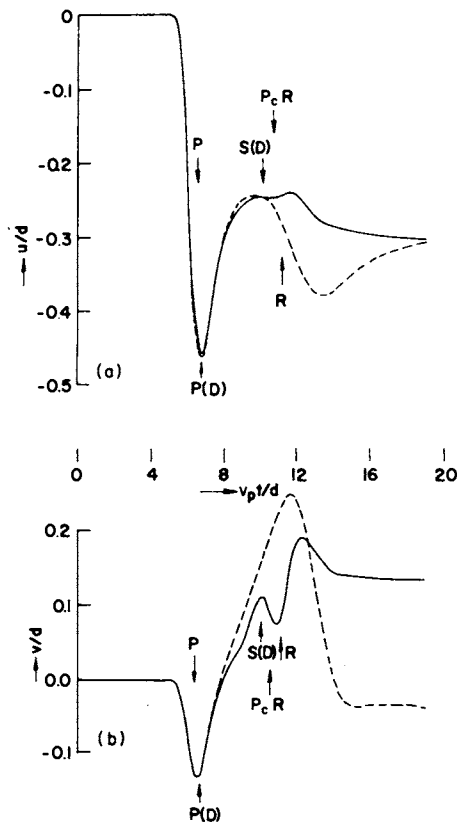


FIG. 18. The horizontal  $u$  (a) and vertical  $v$  (b) components of displacement in a three-quarter plane (solid line) compared with results obtained for a half plane (dashed line), for an observer located on the free boundary at distance  $5d$  from the source.

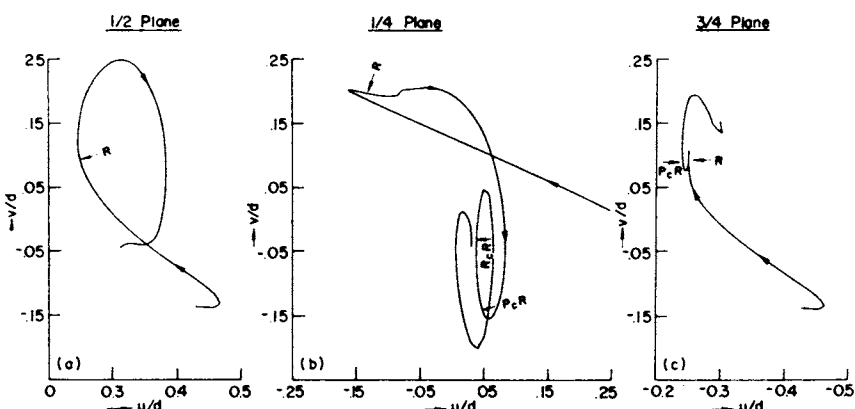


FIG. 19. Elliptic particle motion at the corner of a quarter plane (b) and a three-quarter plane (c) as compared with the particle motion in a half plane (a).

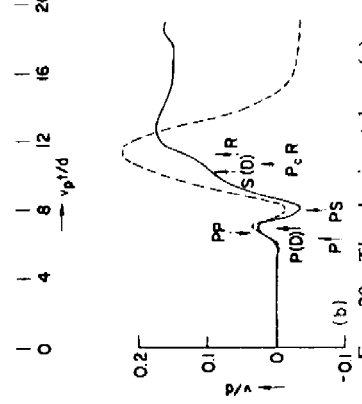
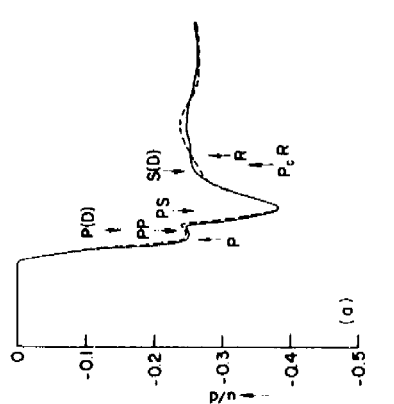


FIG. 20. The horizontal  $u$  (a) and vertical  $v$  (b) components of displacement in a three-quarter plane (solid line) compared with results obtained for a half plane (dashed line). The observer is located at the depth of the source at a distance  $5d$  from the source.

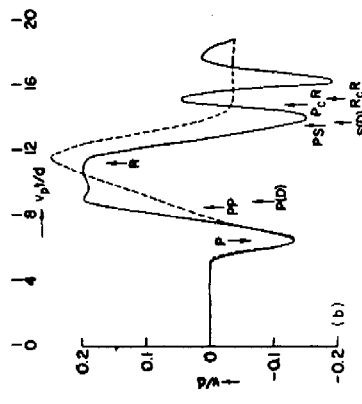
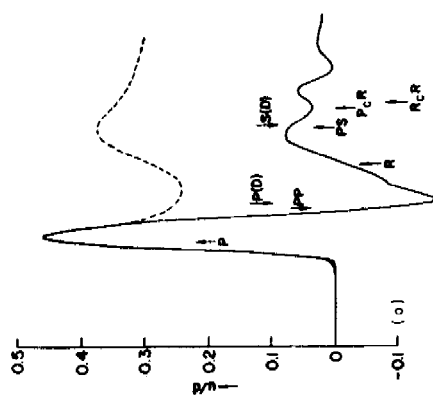


FIG. 21. The horizontal  $u$  (a) and vertical  $v$  (b) components of displacement in a quarter plane (solid line) and in a half-plane (dashed line) for an observer located at the depth of the source and at a distance  $5d$  from the source.

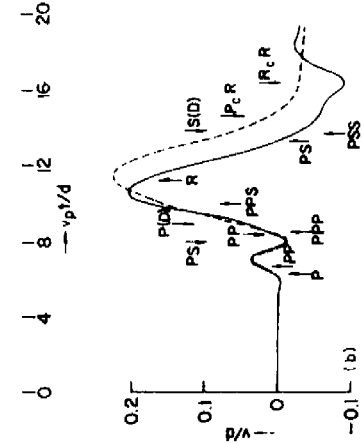
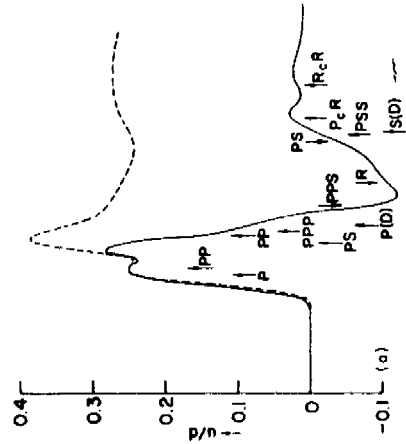


FIG. 22. The horizontal  $u$  (a) and vertical  $v$  (b) components of displacement in a quarter plane (solid line) and in a half-plane (dashed line) for an observer located at the depth of the source and at a distance  $5d$  from it.

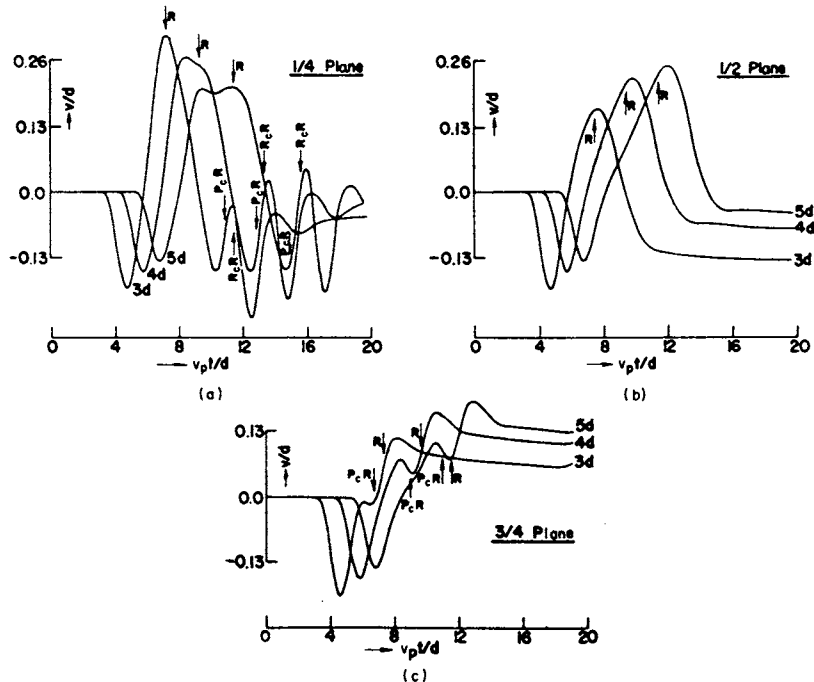


FIG. 23. Verticle component of displacement at a horizontal distance of  $3d$ ,  $4d$ , and  $5d$ , from the source, on the surface of a quarter plane (a), half plane (b), and a three-quarter plane (c).

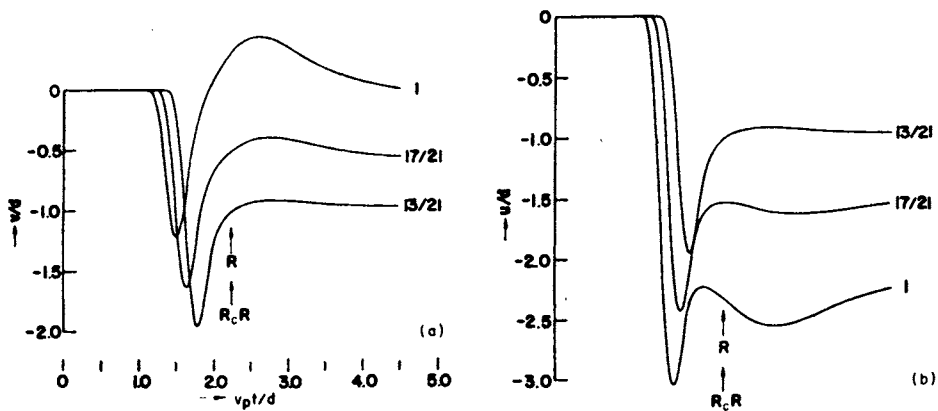


FIG. 24. Vertical  $v$  (a) and horizontal  $u$  (b) components of displacement at the corner of a quarter plane. The source is at a distance  $d$  from the free surface  $x = 0$  and at distances  $d$ ,  $17d/21$ , and  $13d/21$  from the second free surface  $y = 0$ .

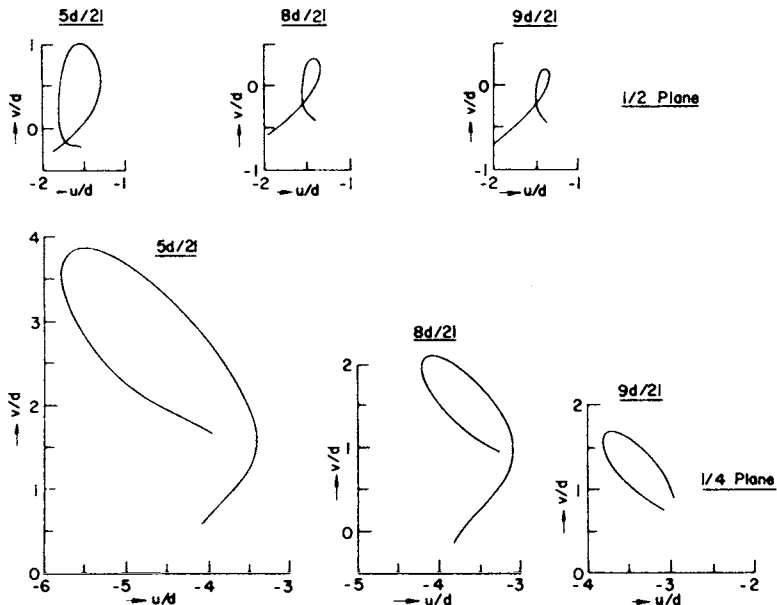


FIG. 25. Particle motion at the corner  $x = y = 0$  of a quarter plane for sources at horizontal distance  $d$  from the free surface  $x = 0$  and at vertical distances  $5d/21$ ,  $8d/21$ ,  $9d/21$  from the free surface  $x = 0$  (below), compared with the particle motion at  $x = y = 0$  for the same sources in a half plane (above).

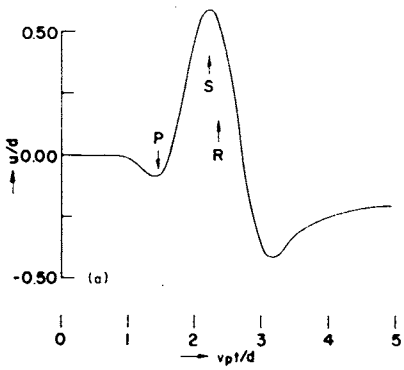
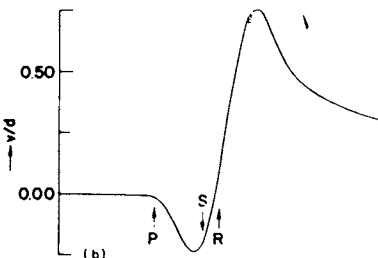


FIG. 26. The horizontal (a) and vertical (b) components of displacement at the corner.  $x/d = 0$ ;  $y/d = 0$ .



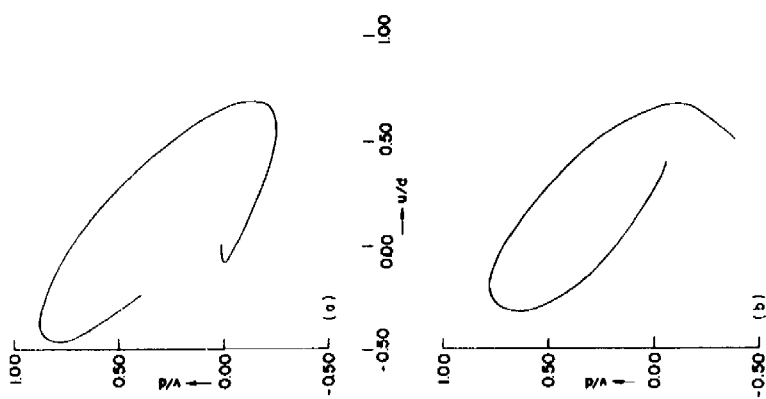


FIG. 27. Particle motion at the corner caused by a perpendicular force applied on  $y = 0$  (a) compared with particle motion at the corner due to an internal source (b),  $x/d = 0$ ;  $y/d = 0$ .

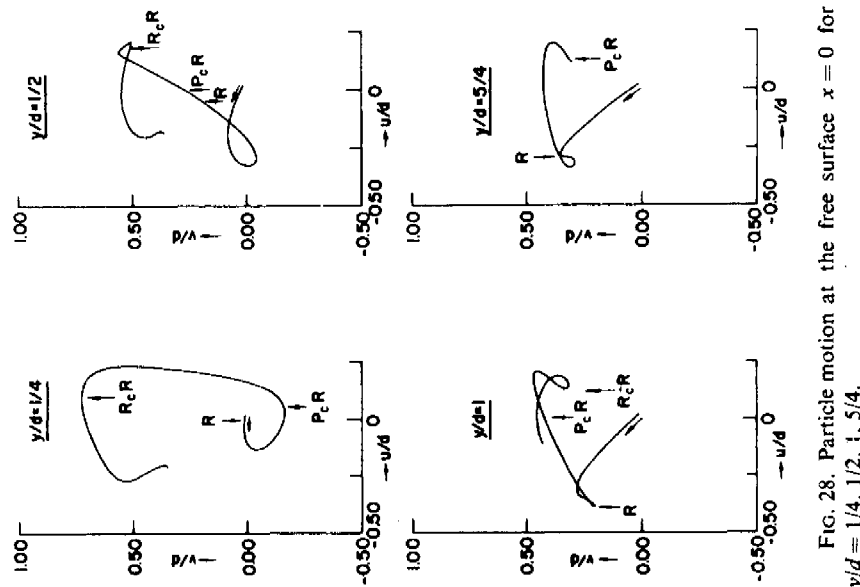


FIG. 28. Particle motion at the free surface  $x = 0$  for  $y/d = 1/4, 1/2, 1, 5/4$ .

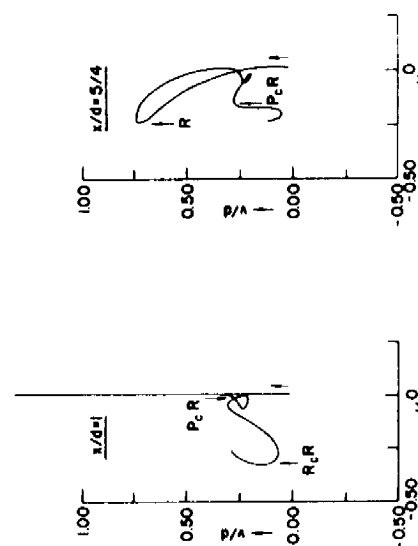
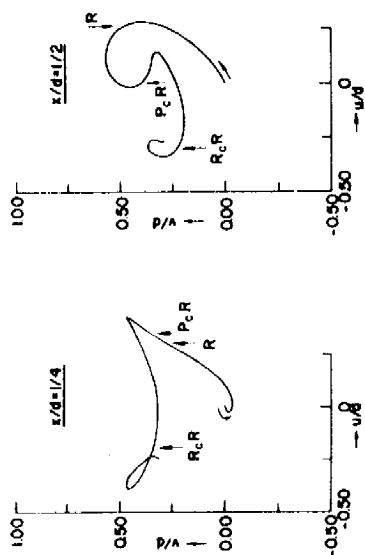


FIG. 29. Particle motion at the free surface for  $x/d = 1/4, 1/2$ .

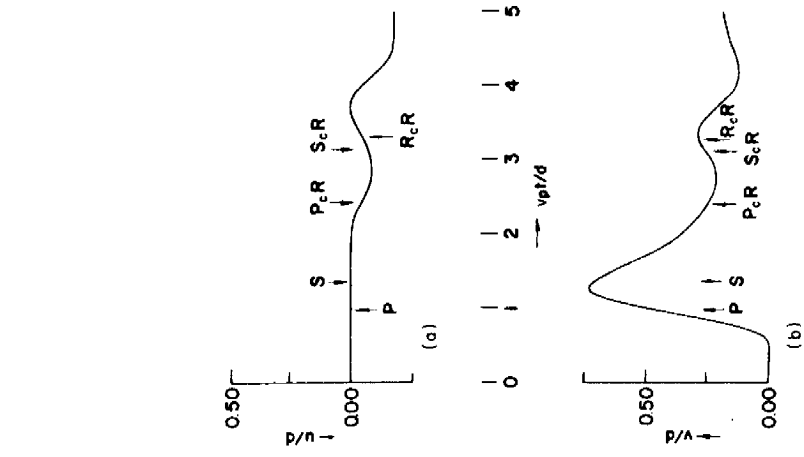


FIG. 29. Particle motion at the free surface for  $x/d = 1, y/d = 1/2$ .

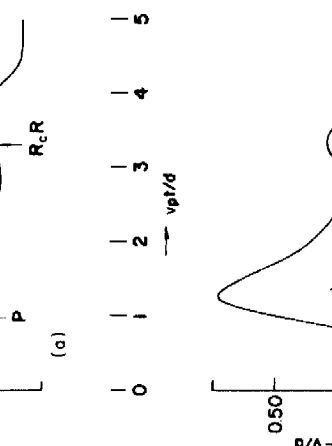
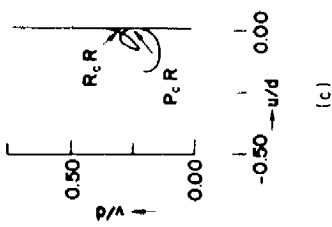


FIG. 30. The horizontal  $u$  (a) and vertical  $v$  (b) components of motion and the (c) particle motion at  $x/d = 1, y/d = 1/2$ .

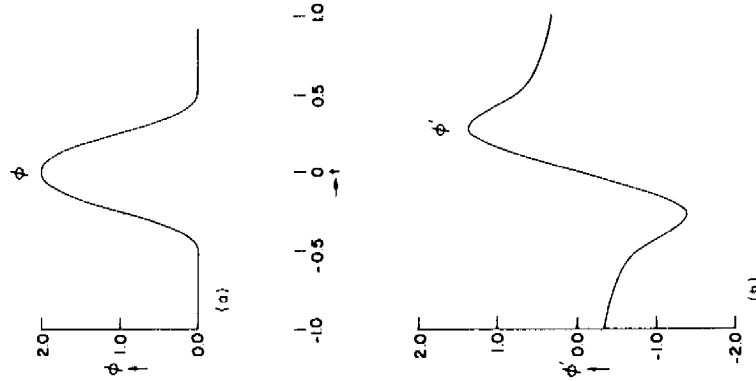


FIG. 31. The smoothed delta function  $\delta_{\Delta}(t)$  (a) and its allied function (b) ( $\Delta = 0.25d/v_p$ ).

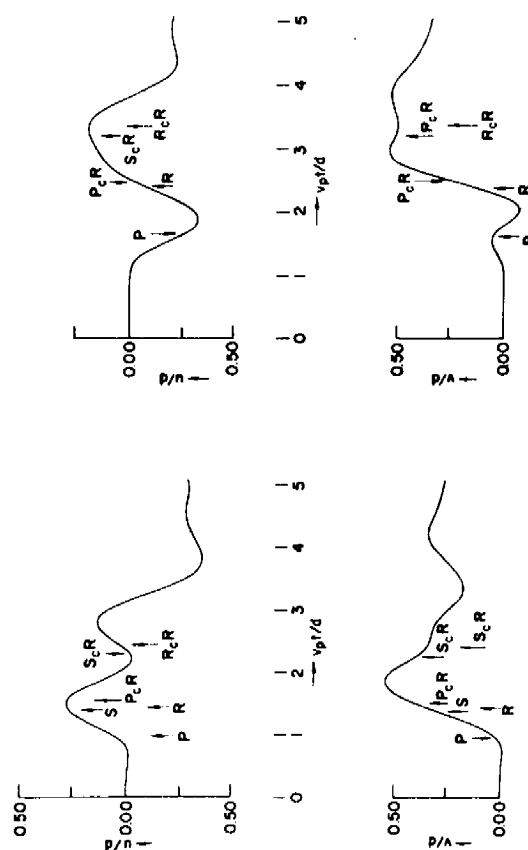


FIG. 32. The horizontal and vertical components of motion on the free surface  $y = 0$  at  $x/d = 1/2$  (left-hand curves) and on the free surface  $x = 0$  at  $y/d = 1/2$  (right-hand curves).

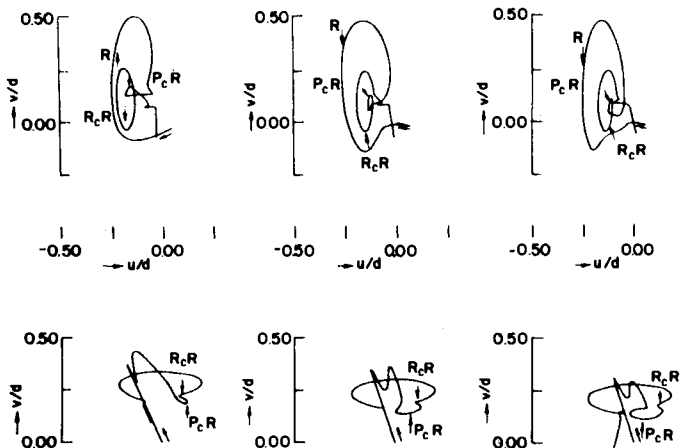


FIG. 33. Particle motion on the two surfaces  $x = 0$  and  $y = 0$  at a distance of  $2d$ ,  $3d$ , and  $4d$  from the corner.

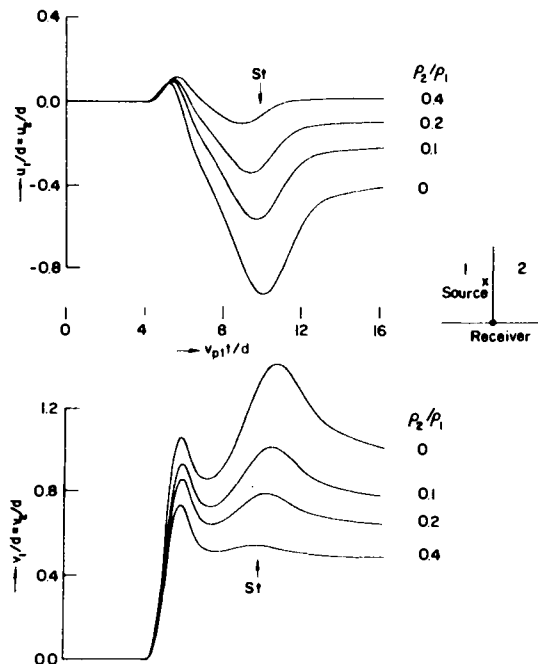


FIG. 34. Components of displacement at the corner  $(0, 0)$  of the two welded quarter planes for the following density ratios:  $\rho_2/\rho_1 = 0, 0.1, 0.2, 0.4$ . The source is located at  $(-d, 4d)$ .

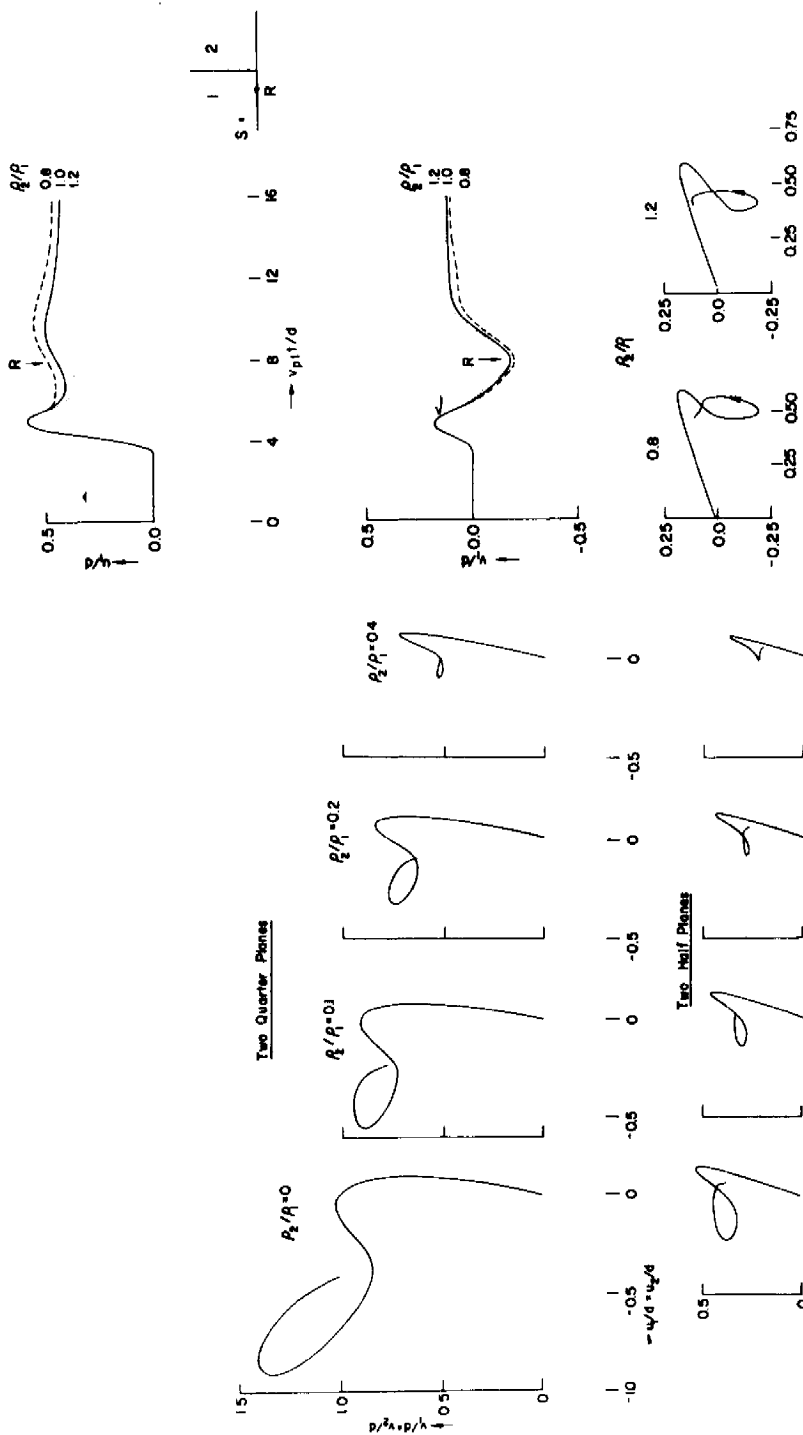


FIG. 35. The motion of a particle at the point  $(0, 0)$  located at the corner of the two welded quarter planes (upper curves) compared with the motion obtained at the point  $(0, 0)$ , located on the interface of the two welded half planes (lower curves) for the following density ratios:  $p_2/p_1 = 0, 0.1, 0.4$ . The source is located at point  $(-d, 4d)$ .

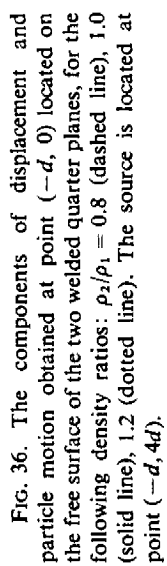


FIG. 36. The components of displacement and particle motion obtained at point  $(-d, 0)$  located on the free surface of the two welded quarter planes, for the following density ratios:  $p_2/p_1 = 0.8$  (dashed line), 1.0 (solid line), 1.2 (dotted line). The source is located at point  $(-d, 4d)$ .

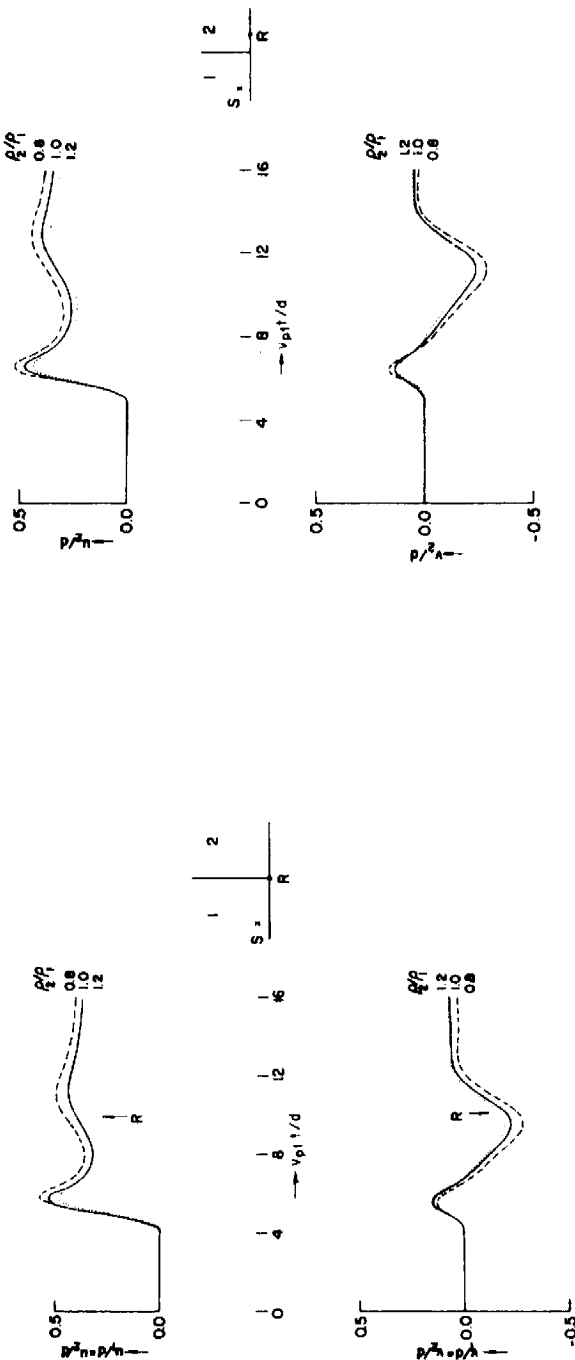


FIG. 37. The components of displacement and particle motion obtained at the point  $(0, 0)$  located at the corner of two welded quarter planes, for the following density ratios:  $\rho_2/\rho_1 = 0.8$  (dashed line), 1.0 (solid line), 1.2 (dotted line). The source is located at point  $(-4d, d)$ .



FIG. 38. The components of displacement and particle motion obtained at point  $(d, 0)$  located on the free surface of the two welded quarter planes for the following density ratios:  $\rho_2/\rho_1 = 0.8$  (dashed line), 1.0 (solid line), 1.2 (dotted line). The source is located at point  $(-4d, d)$ .

## B. SHEAR CRACK IN A PLANE AND IN A HALF PLANE

### 1. Crack in the Plane (Deep Focus Earthquake)

a. *The Physical Problem.* The problems of cracks are of much interest in the study of models of earthquakes. They can be solved numerically by using finite difference techniques which are very similar to those applied for corners. Let us consider a crack caused by shearing stresses, which occupies a straight line of constant length  $2d$ . At time  $t_0$  the crack becomes perfectly lubricated so that the time dependence of the stress drop across the crack faces is  $H(t - t_0)$ , where  $H$  is the Heaviside function and  $t_0$ , which will be taken henceforth as zero, is the time of occurrence of the crack.

This model was investigated by Alterman *et al.* (1971). It may be considered as a simple model of a deep focus earthquake.

b. *Mathematical Formulation for the Crack in the Plane.* Let the  $x, y$  plane be stationary, stressed by a constant shearing stress  $\hat{\tau}$  and with a field of displacements  $\hat{\mathbf{U}} = \begin{pmatrix} u \\ v \end{pmatrix}$ . At time  $t = 0$  a crack occurs in the region  $y = 0$  and  $|x| \leq d$ . (See Fig. 39.<sup>3</sup>)

The total stress tensor for  $t \geq 0$  is denoted  $\tau'$  and the displacement field  $\mathbf{U}' = \begin{pmatrix} u' \\ v' \end{pmatrix}$ . To find the net effect of the crack,  $\mathbf{U}$  and  $\tau$ , we subtract the initial stresses and displacements

$$\mathbf{U} \equiv \begin{pmatrix} u \\ v \end{pmatrix} = \mathbf{U}' - \hat{\mathbf{U}}, \quad \tau = \tau' - \hat{\tau}. \quad (213)$$

Choosing the components of the initial stress tensor to be

$$\hat{\tau}_{xy} = \rho v_p^2, \quad \hat{\tau}_{xx} = \hat{\tau}_{yy} = 0,$$

it is easily seen that it satisfies the equations of motion given in Section II, A, 3, a), Eq. (28), and that its displacement field is given by

$$\hat{\mathbf{U}} = \frac{v_p^2}{2v_s^2} \begin{pmatrix} y \\ x \end{pmatrix},$$

where  $\rho$  is the density of the elastic medium and  $v_p, v_s$  are the velocities of P- and S-waves, respectively. This solution possesses a special symmetry: it is antisymmetric in  $\hat{u}$  and symmetric in  $\hat{v}$  with respect to the  $x$  axis and it is also antisymmetric in  $\hat{v}$  and symmetric in  $\hat{u}$  with respect to the  $y$  axis.

After the occurrence of the crack, the dynamic stress  $\tau'$  satisfies

$$\tau'_{yy} = \tau'_{xy} = 0 \quad (|x| \leq d, y = 0). \quad (214)$$

<sup>3</sup> Figures 39–56 appear on pages 116–125.

This is because the faces of the crack have now become free surfaces. We shall now demand of  $\mathbf{U}'$  the same conditions of symmetry that  $\hat{\mathbf{U}}$  satisfies (except for the region  $|x| \leq d, y = 0$ ), and therefore  $\mathbf{U} = \mathbf{U}' - \hat{\mathbf{U}}$  will also have the same symmetry. Thus:

$$u(x, -y, t) = -u(x, y, t), \quad v(x, -y, t) = v(x, y, t), \quad (215)$$

$$u(-x, y, t) = u(x, y, t), \quad v(-x, y, t) = -v(x, y, t), \quad (216)$$

for all  $x, y$  except in the region  $|x| \leq d, y = 0$ .

The continuity of displacements in Eqs. (215) and (216) implies that

$$u(x, 0, t) = 0 \quad \text{on} \quad |x| > d, y = 0, \quad (217)$$

and

$$v(0, y, t) = 0 \quad \text{on} \quad x = 0. \quad (218)$$

Thus we are able to solve the problem by considering the quarter plane  $x \geq 0, y \geq 0$  with boundary conditions which are summarized as

$$\begin{aligned} \tau_{xy} &= -\rho v_p^2 H(t), & 0 \leq x \leq d, & y = 0, \\ \tau_{yy} &= 0, & x \geq 0, & y = 0, \\ u &= 0, & x \geq d, & y = 0, \\ \tau_{xx} &= 0, & y \geq 0, & x = 0, \\ v &= 0, & y \geq 0, & x = 0. \end{aligned} \quad (219)$$

*c. Analytic Solutions.* A complete analytic solution to the problem of the crack in the plane is not known. However, the solution of the corresponding static problem was given by Starr (1928). By defining a stress function and using elliptic coordinates he obtained simple boundary conditions on the crack and found the static solution. Bringing the displacements at infinity to zero and transforming back into Cartesian coordinates we get for the crack

$$u = \frac{r_p^4}{2v_s^2(r_p^2 - v_s^2)} (d^2 - x^2)^{1/2} \quad (|x| \leq d, y = 0). \quad (220)$$

We find that the dynamic displacements near the crack tend to their static value for  $t > 10 d/v_p$  (see Fig. 40).

In order to obtain an analytic solution for brief periods near the middle of the crack, let the length of the crack tend to infinity. Two half-spaces

separated by the crack then occur. The boundary conditions on  $y = 0$  are in this case

$$\tau_{xy} = -\rho v_p^2 H(t) \quad \text{and} \quad \tau_{yy} = 0. \quad (221)$$

Because of the homogeneous initial and boundary conditions and of the infinite length of the crack this problem does not depend on  $x$  but on  $y$  and  $t$  only. Trying a solution with  $v \equiv 0$ , the equations of motion reduce to

$$u_{tt} = v_s^2 u_{yy}, \quad (222)$$

with initial conditions

$$u(y, 0) = \partial u / \partial t (y, 0) = 0, \quad (223)$$

and boundary conditions on  $y = 0$ :

$$\frac{\partial u}{\partial y} = \frac{-v_p^2}{v_s^2} H(t). \quad (224)$$

Equation (222) admits a general solution

$$u = f[t - (y/v_s)] + g[t + (y/v_s)]. \quad (225)$$

But  $g = 0$  by (223). Substituting in (224) gives

$$(1/v_s)f'(t) = (v_p^2/v_s^2)H[t - (y/v_s)]. \quad (226)$$

and so by integration

$$u(y, t) = (v_p^2/v_s)[t - (y/v_s)]H[t - (y/v_s)]. \quad (227)$$

Indeed we find in the results for the finite crack that  $u(y, t)$  is given by (227) up to the time of arrival of disturbances from the end of the crack (see Fig. 41).

d. *Results for the Crack in the Plane.* By virtue of Eq. (227) each point on the crack emits S-waves which travel parallel to the  $y$  axis with velocity  $v_s$ . The particle motion in an S-wave is perpendicular to the direction of motion, and we find horizontal displacements  $u$  only. According to Eq. (227), the horizontal displacement increases linearly with time. This happens for an infinitely long crack. Because of the finite length of the crack, disturbances occur due to the diffracted waves P(D), S(D) emitted from the two ends of the crack at  $x = -d$  and  $x = d$  on the  $x$  axis.

In the middle of the crack, i.e., at point  $(0, 0)$  the first diffracted wave is P(D) which travels with velocity  $v_p$ . Assuming  $v_s/v_p = 1/\sqrt{3}$  the first disturbance occurs at  $t = d/v_p$ . Figures 40 and 41 clearly show the linear increase of the horizontal component  $u$  up to  $t = d/v_p$  when waves start to arrive and

cause a decrease in the rate of change of  $u$  in time. At  $t = d/v_s$ , S(D) waves begin to reach the point  $(0, 0)$  and a short time afterwards the displacements stabilize to their static form. Because of the symmetry conditions imposed at  $x = 0$  the vertical component  $v$  vanishes until S(D) waves start to arrive from the ends of the crack. S-waves generated at the crack and which are propagating parallel to the  $y$  axis, as well as diffracted P-waves from the end of the crack, do not affect this component of displacement because particle motion due to these waves is parallel to the crack. The horizontal displacement is affected by the diffracted P-wave and by the S-wave generated at the crack but not from the diffracted S-wave. Figure 41 also gives a comparison with results obtained by Burridge (1969) who used a numerical method which consists of discretization of kernel functions. Excellent matching is found.

## 2. Crack in a Half Plane (Dip Slip on a Vertical Fault Which Breaks the Free Surface)

a. *Mathematical Formulation of the Crack in the Half Plane.* The displacements caused by a crack when a shearing stress acts on the half plane  $x \geq 0$  are found by a method similar to that given in Section III, B, 1, a (Alterman *et al.*, 1971). It is assumed that at  $t = 0$  a crack occurs along the segment  $y = 0$ ,  $0 \leq x \leq d$  (see Fig. 39). This may be taken to be a simple model for a dip slip on a vertical fault which breaks the free surface. As before, we are concerned with the net displacement  $\mathbf{U}$  caused by the crack. We assume the initial shearing stress to be  $\hat{\tau}_{xy} = \rho v_p^2 x$ ,  $\hat{\tau}_{yy} = -\rho v_p^2 y$ ,  $\hat{\tau}_{xx} = 0$ , which satisfies the equations of motion as well as the requirement of vanishing stresses at the free boundary  $x = 0$ . We require as before that  $\hat{\mathbf{U}}$  should be antisymmetric in  $\hat{x}$  and symmetric in  $\hat{v}$  with respect to the  $x$  axis. After the crack occurs, i.e., for  $t \geq 0$ , we denote as before the total stress tensor by  $\tau'$  and the displacement field by  $\mathbf{U}'$ . We shall require that  $\mathbf{U}'$  satisfy the same condition of symmetry as  $\hat{\mathbf{U}}$ . Substituting  $\mathbf{U} = \mathbf{U}' - \hat{\mathbf{U}}$ ,  $\tau = \tau' - \hat{\tau}$  we see that  $\mathbf{U}$  also possesses the same symmetry as  $\hat{\mathbf{U}}$  and  $\mathbf{U}'$  and therefore we can limit our calculation to the quarter plane  $x \geq 0$ ,  $y \geq 0$  with the appropriate boundary condition, and by a similar procedure to that used in the previous section we get

$$\begin{aligned} \tau_{yy} &= 0, & y &= 0, & x &\geq 0, \\ \tau_{xy} &= -\rho v_p^2 XH(t), & y &= 0, & 0 &\leq x \leq d, \\ u &= 0, & y &= 0, & x &> d, \\ \tau_{xx} &= \tau_{xy} = 0 & x &= 0, & y &\geq 0. \end{aligned} \quad (228)$$

b. *Results in the Half Plane.* Figure 42 shows the motion at  $x = y = 0$  on the crack in the half plane. In order to see clearly the arrival of various waves, Fig. 43 shows the time derivative of the previous result. This is obviously equivalent to applying a  $\delta(t)$  function load in Eq. (228). In order to

use the  $\delta$  function in the finite difference scheme a discretization of this function was made by using a smoothing device similar to that applied for the point source (see Section II, A, 6, b).

The first waves to arrive are the waves diffracted at the edge  $(d, 0)$ . The diffracted P(D) wave is found only in the horizontal component of displacement  $u$  while the S(D) wave is found only in the vertical component  $v$ . This is clearly seen in Figs. 42 and 43. Long period waves with a period of  $t = 8d/v_p$ , which decay very slowly are also seen. This time period suggests that these are Rayleigh waves which originate at the end of the crack, travel along the crack, and bounce back from the free surface. In the present case the velocity of Rayleigh waves is about  $0.5 v_s$  and the size of the crack is  $d$ , therefore it takes 4 time units for the wave to reach the same point again by diffraction. But it returns with a  $180^\circ$  phase shift and so only after 8 time units does it reach the same point again with the initial phase.

Figure 42 also shows results at the point  $x = 0, y = d/2$  (dashed line) and at  $x = 0, y = d$  (dotted line), which are located above the crack on the free surface. Similar surface waves are clearly visible for these points too. Figures 44 and 45 show the particle motion for different points on and near the crack. The elliptical motions, which are characteristic for surface waves, are seen very clearly. But instead of one ellipse caused by the Rayleigh waves traveling along a free surface, there are many ellipses which become smaller and smaller with time, each ellipse having a period of about 8 time units. The elliptical paths are drawn for  $t \geq 3.2d/v_p$ , after the arrival of the body waves.

The surface waves are mainly connected to the free surface along the  $y$  axis. These waves propagate along  $x = 0$  and decay perpendicular to this direction. The decay of the  $u$  component, which is normal to the free surface  $x = 0$ , is much smaller than the decay in the other component. This is similar to the decay of  $u$  and  $v$  in a half plane (see Alterman and Loewenthal, 1969).

In conclusion it seems that the crack in the half plane behaves differently from the crack in the plane, mainly due to the strong effect of the surface waves on the free surface of the half space and to the diffraction effect of the crack. Due to these waves the stationary solution is not reached in a short time ( $t < 20 d/v_p$ ). From a seismological point of view it is interesting to notice the strong tendency for the crack which breaks the free surface to generate Rayleigh waves.

### C. SEISMOGRAMS FOR THE LAYERED HALF-SPACE

#### 1. Comparison with Earlier Results

One would like first to establish that the finite difference equation scheme derived in Section II, A, 2 gives accurate and reliable results. The simplest way of doing this is to compare the numerical results with those obtained by a different method for the same problem. Fortunately this is possible, since

theoretical seismograms for a compressional point source lying inside a layered half-space have been obtained by Alterman and Abramovici. The computational technique pertaining to the problem is given in Alterman and Abramovici (1965) and the graphs appear in Abramovici (1965). The method used by these investigators was to evaluate numerically the exact solution obtained by splitting the Laplace transform of the solution into rays and using Cagniard's technique for taking the inverse of the transform. Their method, which is entirely different from the finite difference technique of Section II, A, 4, offers an excellent independent means for checking the calculations.

Figure 46 contains the theoretical seismograms obtained by finite differences for a compressional source located midway between the surfaces and having pulse widths given by  $4\Delta = 1.2$  and  $4\Delta = 1.6$  time units. Here all time values in the theoretical seismograms, unless otherwise specified, are expressed in terms of the dimensionless variable  $t(v_{s1}/d)$ , where  $v_{s1}$  is the shear velocity in the layer,  $d$  is the depth of the source below the surface (or above the interface), and  $t$  is real time. For purposes of comparison with the graphs of Abramovici it is assumed that the properties for the surface layer and lower medium are  $\lambda_1 = \mu_1$ ,  $\rho_2 = (2/1.21)\rho_1$ ,  $v_{p2} = 1.1v_{p1}$ , and  $v_{s2} = 1.1v_{s1}$ . Hence  $v_{p2} > v_{p1} > v_{s2} > v_{s1}$ . The observation point is taken on the surface at a distance of five layer thicknesses measured from the epicenter. Figure 47 contains the results of the analytic solution. Note that the time values are expressed in terms of the dimensionless variable  $t(v_s/h)$ , where  $h$  is the thickness of the layer and  $h = 2d$ . Hence the time values in Fig. 47 should first be multiplied by 2 before making any comparison between the two sets of theoretical seismograms. The physical problem solved by the two different methods is identical except for the analytical form of the input pulse. In the finite difference calculation the potential function representing the input pulse was a quartic, as defined before in Section II, A, 6, b by Eqs. (86) and (87) where  $n = 4$ , while in the work of the previously mentioned investigators, the input pulse was a quadratic  $n = 2$  in Eq. (86). In the finite difference solution the quartic pulse was preferred since it can be used with a much coarser grid. In making the comparison, the input displacements were adjusted so that the pulse widths are the same and the maxima occur at the same time. The shape of the curves differs slightly at points intermediate between the initial, maximum, and end points. The agreement between the theoretical seismograms obtained by the two different methods is excellent.

## 2. Rayleigh Wave Series

Figures 48 and 49 show a series of curves for six different observation points located along the free surface of a homogeneous half space. The properties assumed for the half-space are  $v_{p1} = \sqrt{3}v_{s1}$ . A point source of

compressional waves emitting a pulse of width  $4\Delta = 0.8$  is located below the surface. The observation points in Fig. 48 are located on the surface at the epicenter, and at distances of two and four source depths measured from the epicenter. The observation points in Fig. 49 are located on the surface at distances of six, eight, and ten source depths away from the epicenter. The development of the Rayleigh wave is evident as the observation point is moved along the surface. Note that the ratio of  $A$  to  $B$  (i.e., the ratio of horizontal to vertical particle displacement) is approximately 0.68, the correct theoretical value. Also, the motion is seen to be elliptically retrograde on comparing amplitudes of horizontal and vertical displacement. Furthermore, the relative amplitude of the surface wave to the direct wave increases as expected since the surface wave spreads in two dimensions and the other in three. In the first curve in Fig. 48, which gives the displacement at the epicenter, a wave appears after the direct wave, which is due entirely to the presence of the surface. This is a result of the complete solution of the equations of elasticity. According to Nakano (1925), who gave the solution for high frequencies, this wave occurs before the minimum distance at which the Rayleigh wave is supposed to exist (Altermann and Karal, 1968). See also the curves for  $r/h = 0.28$  ( $\theta = 2^\circ$ ) given in Fig. 24 of the paper by Altermann and Abramovici (1966). The observation point in this case is very near the epicenter. Finally, we notice that the first curve in Fig. 49 can be used as an additional check on the finite difference equation scheme. It is the same as the vertical and horizontal solid curves for  $r/h = 6.28$  ( $\theta = 45^\circ$ ) given in Fig. 24 of the paper by Altermann and Abramovici (1966). The agreement is excellent.

Figures 50 and 51 show the effect of depth and pulse width on the appearance of the Rayleigh wave. In both figures the horizontal distance of the observation point is held fixed at a distance of six source depths from the source. The first curve shows the observation point on the surface, the second curve shows the observation point at a distance of one-half the source depth below the surface, and the third curve shows the observation point at one source depth below the surface. Figure 50 shows the variation with depth when the pulse width is  $4\Delta = 0.8$ , and Fig. 51 shows the variation with depth when the pulse width is  $4\Delta = 1.6$ . Note that the series in Fig. 50 has higher frequencies than the series in Fig. 51 since  $\Delta$  is smaller. Consequently, the Rayleigh wave at the same depth gets more damped for the higher frequencies. The damping of the Rayleigh wave depends both on the depth of source and the depth of observer. Therefore, the ratio of the amplitude of the Rayleigh wave to the direct wave on the surface is larger for large  $\Delta$  than for small  $\Delta$ . Compare the first curves in Figs. 50 and 51. Next observe that the amplitude of the direct wave in the first curve is larger than in the other two because it contains the reflected wave in addition. In the other two, the reflected peak appears separately. For fixed  $\Delta$  the amplitude of the Rayleigh wave decreases

with depth. We notice, however, that the horizontal component of the Rayleigh wave decreases faster with depth than the vertical component. By continuing the depth series to larger depths, one finds a change from retrograde to prograde motion. The third curves in Figs. 50 and 51 show that the vertical component of the direct wave is zero (as expected for the horizontal path of the direct wave). The vertical component in the second curve in Fig. 50 is small, and the second curve in Fig. 51 is only slightly noticeable due to the overlapping with the reflected pulse.

### 3. Refraction Series

Figures 52 and 53 show a series of curves for five different observation points located along the surface of a layered half-space when the shear and compressional speeds in the lower medium are much larger than in the layer. The properties assumed for the surface layer and lower medium are  $\lambda_1 = \mu_1$ ,  $\rho_2 = 1.5\rho_1$ ,  $v_{p2} = 3v_{p1}$ , and  $v_{s2} = 3v_{s1}$ . Hence  $v_{p2} > v_{s2} > v_{p1} > v_{s1}$ . A point source of compressional waves with a pulse width of  $4\Delta = 0.8$  is located midway between the surface and interface. The observation points in Fig. 52 are located at the epicenter and on the surface at a distance of one layer thickness away from the epicenter. The observation points in Fig. 53 are located on the surface at distances of two-, three-, and/or four-layer thicknesses away from the epicenter. The two figures together form a series showing the development of the refraction arrival. With increasing distance of observer from the source, the refracted wave  $P_1P_2P_1$  becomes more clearly separated from the later arriving waves. (Subscripts 1 or 2 attached to either P or S denote the medium in which the ray propagates.) In the last two curves of Fig. 53 it is completely separated from the later arriving direct wave and from other refracted and reflected waves. In the present model all the refracted waves, including  $P_1P_2S_1$ ,  $P_1S_1P_1$ , and  $P_1S_2S_1$ , exist. However, their arrival times are too close one to another and to the arrival of the direct and reflected pulses to be noticed separately. The arrival times of pulse maxima are indicated in the figures by arrows. In order to see more clearly the refraction arrival traveling at the shear speed in the lower medium, we consider the same layered half-space as before but place the observation points on the interface. Figure 54 contains a series of three curves with observation points located on the interface at distances of one-, two-, and three-layer thicknesses away from the point directly below the source. In the last two curves of Fig. 54,  $P_1S_2$  arrives now far earlier than the direct  $P_1$  and is found separately. Whereas both components of  $P_1P_2$  are positive and similar in form to the initial pulse, the vertical component of  $P_1S_2$  is negative and of the same form as the input. The vertical component of  $P_1S_2$  shows a phase change of  $90^\circ$ . Other arrivals, such as  $P_1$ ,  $P_1P_1$ ,  $P_1S_1$ , and  $P_1P_1P_2$ , are indicated on the theoretical seismograms for purposes of comparison.

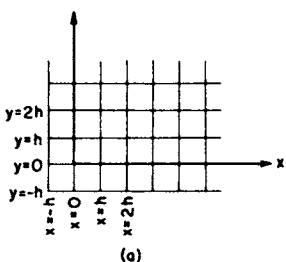
#### 4. Interface Wave Series

Figures 55 and 56 show a series of theoretical seismograms at a fixed observation point located on the interface between two semi-infinite media. A point source of compressional waves emitting a pulse of width  $4\Delta = 0.8$  is located in the upper medium. The observation point is located on the interface at a distance equal to four times the height of the source above the interface. This distance is measured from a point on the interface directly below the source. The properties assumed for the upper and lower media are  $\lambda_1 = \mu_1$ ,  $v_{p2} = (1.05v_{p1})^{1/2}$  and  $v_{s2} = (1.05v_{s1})^{1/2}$ . Hence  $v_{p2} > v_{p1} > v_{s2} > v_{s1}$ . The density contrast  $\rho_2/\rho_1$  between the two media is permitted to take on the values 0, 0.2, 0.4, 1.0, 1.4, 2.0, 3.0, and 5.0. Figure 55 shows a series of theoretical seismograms for density contrasts given by 0, 0.2, 0.4, and 1.0. Figure 56 is a continuation of the series for density contrasts given by 1.4, 2.0, 3.0, and 5.0. When  $\rho_2/\rho_1 = 0$ , which is the special case of a free surface, we again find the Rayleigh wave. As  $\rho_2$  increases, the interface wave continues and arrives at times expected for either the Stoneley wave or the "second surface wave."<sup>4</sup> Since the phase velocity of Stoneley waves is very nearly  $v_{s1}$ , and that for the "second surface wave" is exactly  $v_{s1}$ , the pulses overlap and are not resolved. As  $\rho_2/\rho_1$  increases up to 1.0, the amplitudes of the horizontal and vertical components of the interface waves decrease. At  $\rho_2/\rho_1 = 1$  the amplitudes are zero and no interface wave is found. Recall that these are still different media with different velocities. The horizontal component decreases more rapidly than the vertical component as the density contrast increases from 0 to 1. For the Rayleigh wave the ratio of the horizontal to the vertical component is approximately 0.68 while for the interface wave the ratio is smaller. For  $\rho_2/\rho_1$  larger than 1 and increasing, the amplitude of the interface wave increases again and it appears mainly in the vertical component. Notice that there is a phase change of  $180^\circ$  in this component in passing through the value  $\rho_2/\rho_1 = 1$ .

The phase velocity of Stoneley waves is a root of an equation originally derived by him (Stoneley, 1924). The region in which these roots exist is given in the book by Ewing *et al.* (1957, see p. 113) and also in the book by Cagniard [1939, see Figs. 4-6, p. 49. In this figure the vertical scale is incorrect and should be changed to  $q = (s/s')^2$ .] Stoneley's equation was also solved independently in order to determine whether Stoneley roots exist in the present problem. The theoretical seismograms given in Figs. 55 and 56 show interface waves in all cases for which  $\rho_2/\rho_1 \neq 1$  and show no interface wave when  $\rho_2/\rho_1 = 1$  (still different media). Interface waves exist on the theoretical seismograms even in cases when the physical parameters of the problem lie outside the region

<sup>4</sup> A name used by Cagniard (1962) for the surface wave that travels along the interface with the shear velocity  $v_s$ .

indicated on the graphs given by Ewing *et al.* and Cagniard (e.g., for density contrasts  $\rho_2/\rho_1 = 1.4, 2.0, 3.0$ ). The appearance of Stoneley-like pulses for values of the elastic parameters outside this region has also been noted by Gilbert and Laster (1962). The interface wave may also include the "second surface wave." However, it should be remembered that in those cases where the Stoneley equation does not have solutions (and hence the Stoneley wave should not exist), other solutions do exist provided different Riemann sheets are permitted. Also, as mentioned by Roever *et al.* (1959), the pole causing the Stoneley wave in the first place may still influence the solution even though it slips onto some other Riemann sheet as the physical parameters in the problem change. We remark that when  $\rho_2/\rho_1 = 1$ , we do not find any interface wave in our theoretical seismograms and also there are no roots on any of the possible Riemann sheets in Stoneley's equation.



(a)

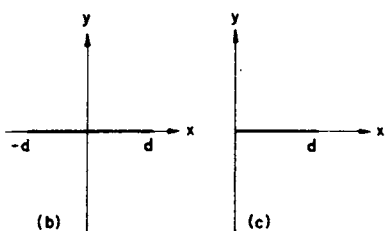


FIG. 39. (a) The grid for the finite difference scheme applied for solving the problems of the crack in the plane and in the half plane. (b) The geometry of the crack in the plane. (c) The geometry of the crack in the half plane.

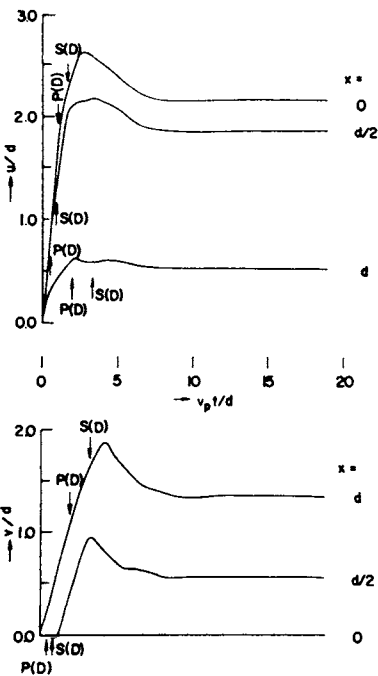


FIG. 40. The components of displacement  $u$  and  $v$  calculated for a long time up to  $t = 20d/v_p$  obtained by a coarse mesh ( $h = d/10$ ) for observation points located on the crack at  $x = 0$ ,  $d/2$ ,  $d$ .

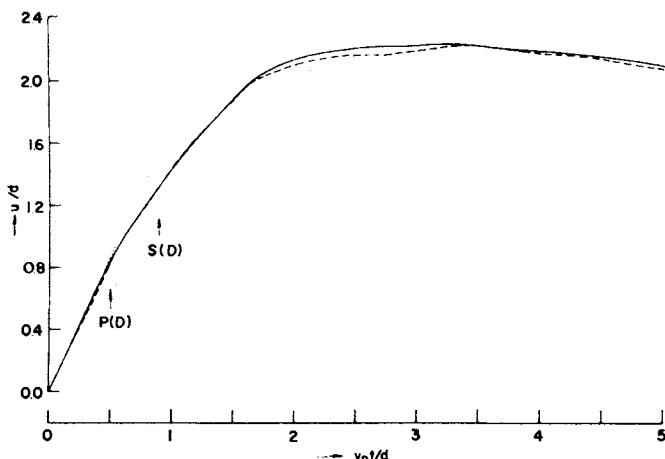


FIG. 41. The horizontal component of displacement  $u$  at the center of the crack in the plane as obtained by the kernel discretization method (solid line), by finite differences (dashed line), and by the known analytic solution for the initial displacement (dotted line).  $x = d/2$ ;  $y = 0$ .

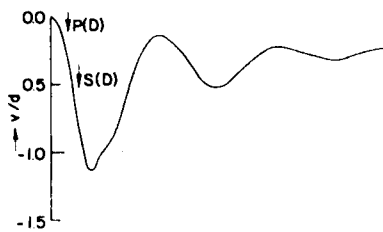
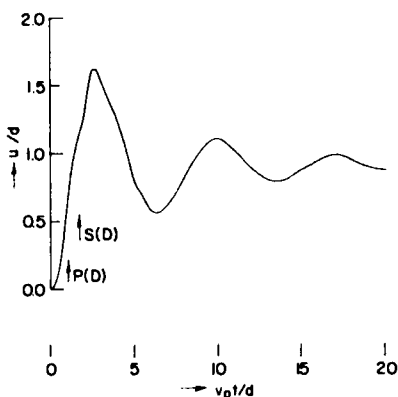


FIG. 42. The components of displacement  $u$  and  $v$  in the half plane, on the crack at the point  $x = 0, y = 0$ .

FIG. 44 (below). Particle motion of the crack in the half plane at  $x = 0$ , and  $y = 0$  (a),  $y = d/2$  (b), and  $y = d$  (c). A delta function stress is applied.

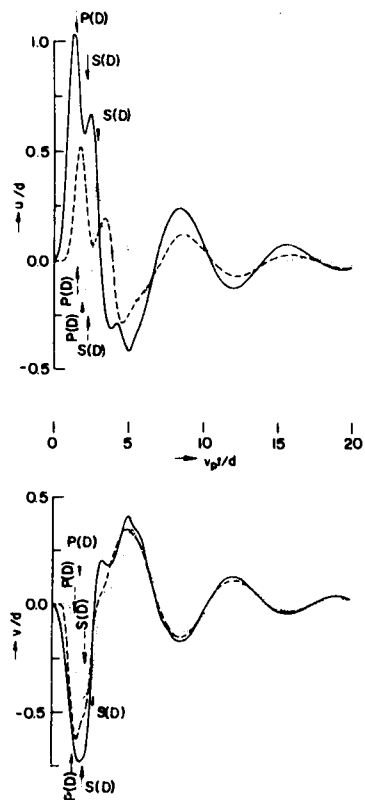
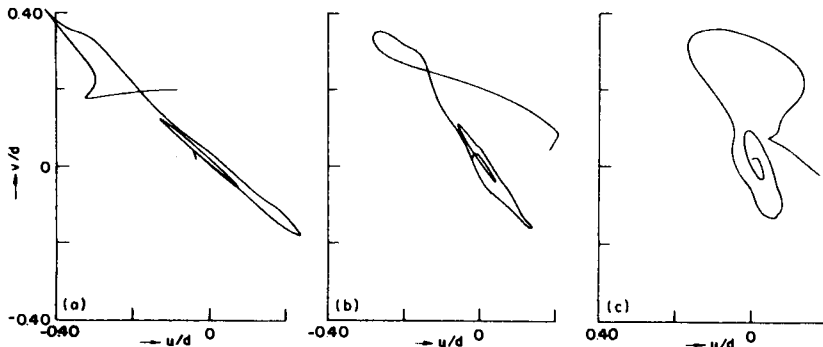


FIG. 43. Horizontal and vertical components of displacement for the delta function stress, at observation points located on the free surface in the half plane on the crack at  $x = 0, y = 0$  (solid line), and above it at  $y = d/2$  (dashed line), and at  $y = d$  (dotted line). Smoothing parameter for  $\delta(t)$  is  $\Delta = 0.25d/v_p$ .



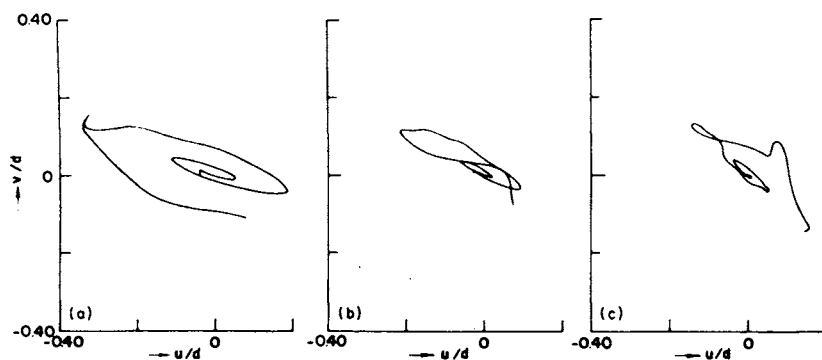


FIG. 45

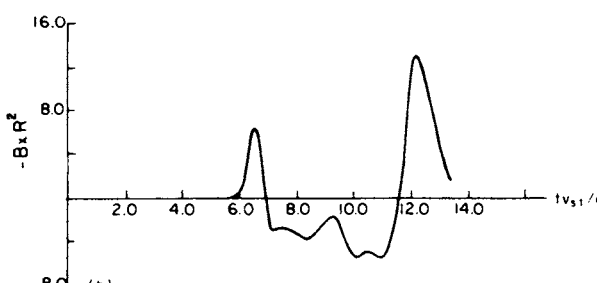
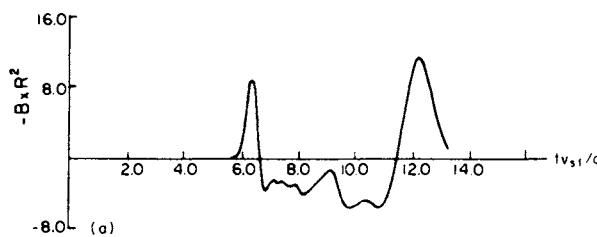


FIG. 46

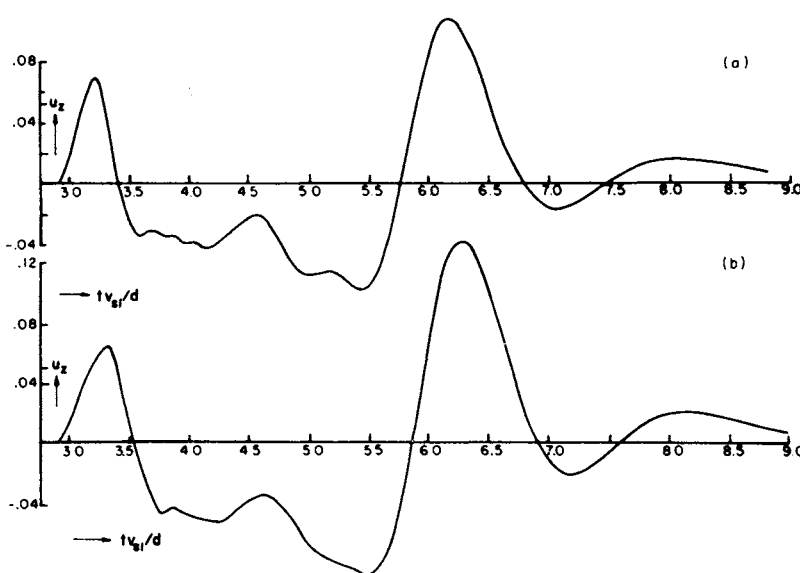


FIG. 47

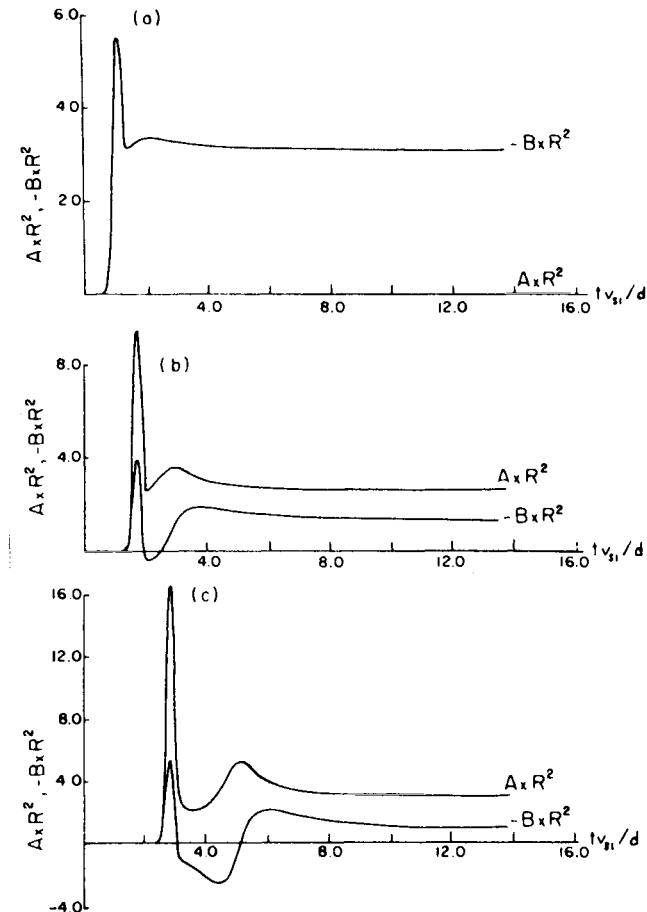


FIG. 48. Horizontal and vertical displacements on the surface of the elastic half-space. The three curves are for observation points located on the surface at the epicenter (a) and at distances of two (b) and four (c) source depths from the epicenter ( $v_{p1}/v_{s1} = \sqrt{3}$ ).

FIG. 45. Particle motion of the crack in the half plane for delta function stress at  $x = d/2$ , and  $y = 0$  (a),  $y = d/2$  (b), and  $y = d$  (c).

FIG. 46. Vertical displacement on the surface of the layered half space, obtained by finite differences. The source is located midway between the surface and interface. ( $\rho_2/\rho_1 = 2/1.21$ ;  $v_{p2}/v_{p1} = 1.1$ ;  $v_{s2}/v_{s1} = 1.1$ .) The observation point is on the surface at a distance of five layer thicknesses from the epicenter, for pulse widths of 1.2 (a) and 1.6 time units (b).

FIG. 47. Vertical displacement on the surface of the layered half-space obtained by the analytic solution (Abramovici, 1965). The source is located midway between the surface and interface. ( $\rho_2/\rho_1 = 2/1.21$ ;  $v_{p2}/v_{p1} = 1.1$ ;  $v_{s2}/v_{s1} = 1.1$ .) The observation point is on the surface at a distance of five layer thicknesses from the epicenter, for pulse widths of 1.2 (a) and 1.6 time units (b).

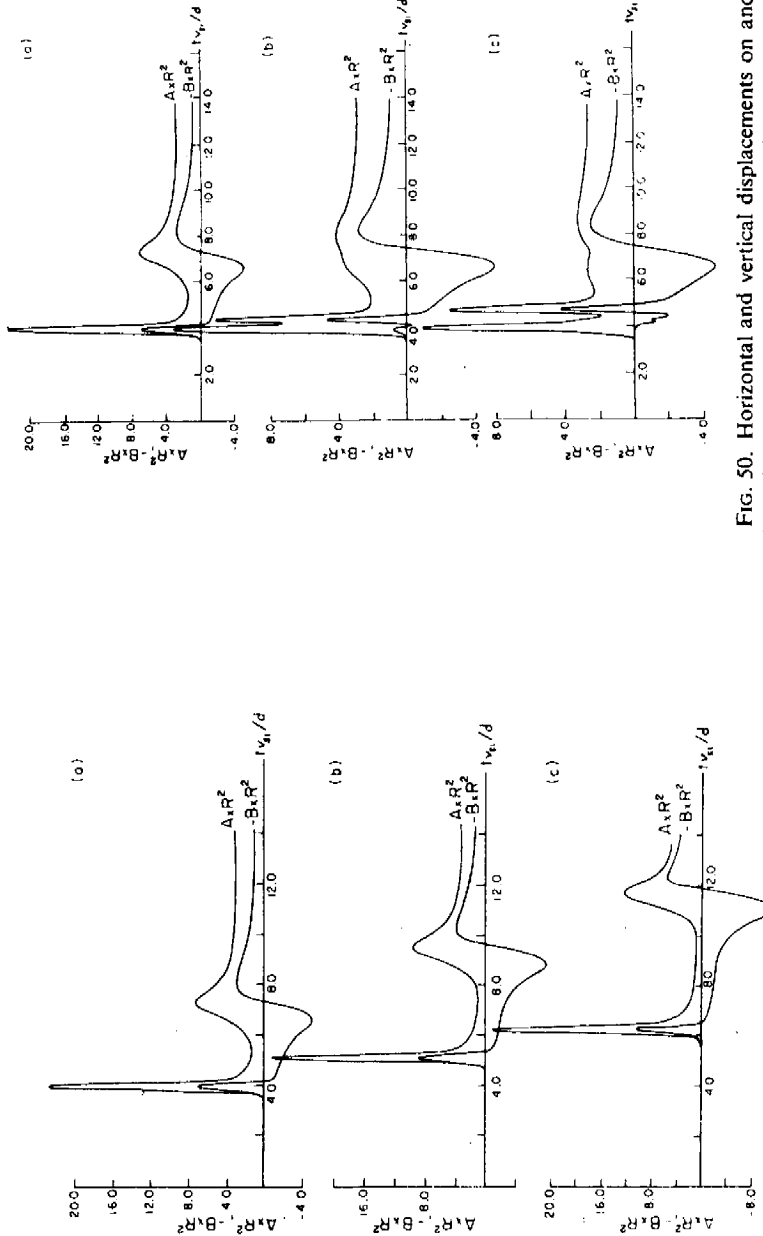


FIG. 49. Horizontal and vertical displacements on the surface of the elastic half-space. The three curves are for observation points located on the surface (a), and at distances of one-half source depth (b), and one source depth (c) below the surface. The horizontal distance of the observation point from the epicenter is equal to a distance of six source depths.

FIG. 50. Horizontal and vertical displacements on and below the surface of an elastic half-space. A compressional point source of pulse width 0.8 is located below the surface ( $v_{p1} = \sqrt{3}v_s$ ). The three curves are for observation points located on the surface (a), and at distances of one-half source depth (b), and one source depth (c) below the surface. The horizontal distance of the observation point from the epicenter is equal to a distance of six source depths.

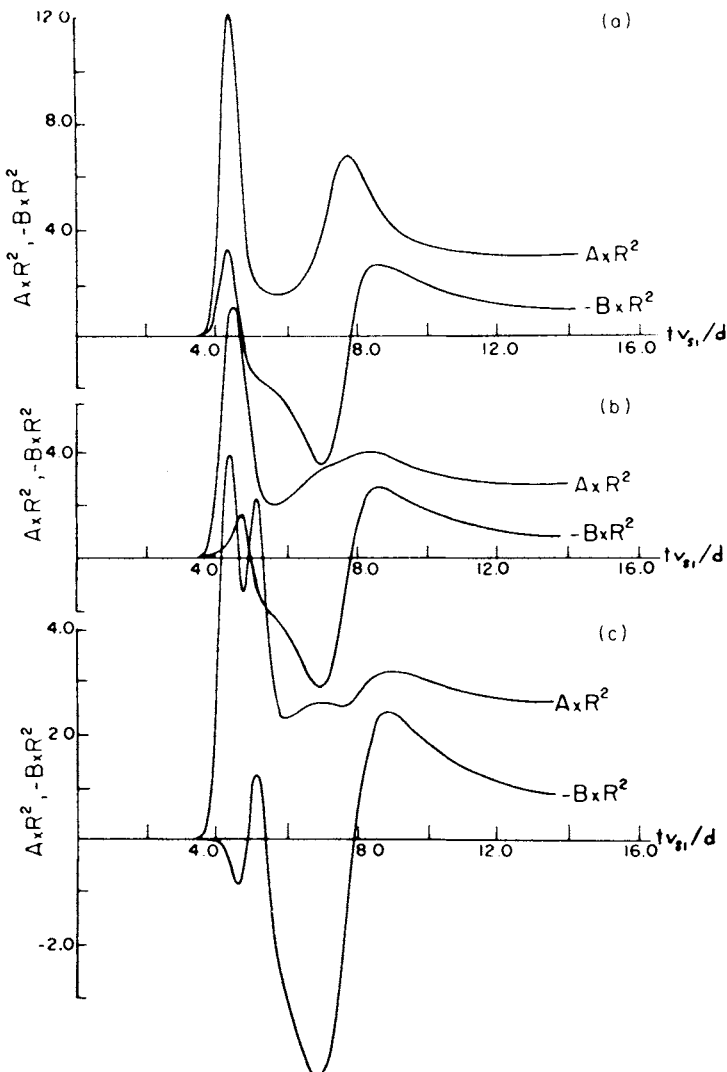


FIG. 51. Horizontal and vertical displacements on and below the surface of an elastic half-space. A compressional point source of pulse width 1.6 is located below the surface ( $v_{p1} = \sqrt{3}v_{s1}$ ). The three curves are for observation points located on the surface (a), and at distances of one-half source depth (b) and one source depth (c) below the surface. The horizontal distance of the observation point from the epicenter is equal to a distance of six source depths.

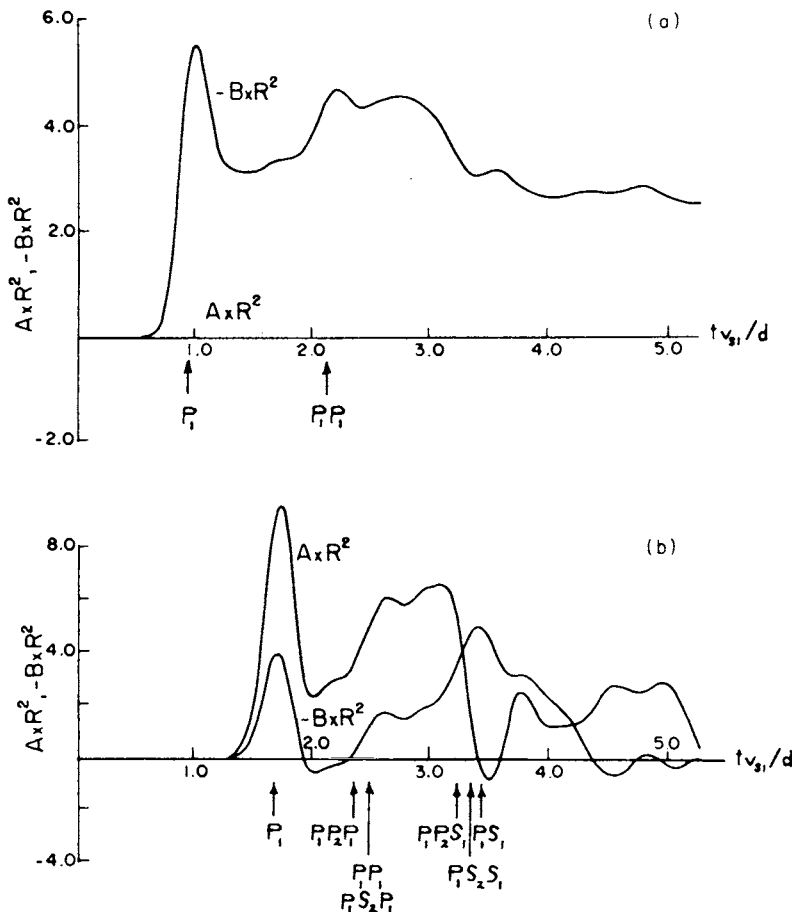


FIG. 52. Horizontal and vertical displacements on the surface of a layered half-space. A compressional point source of pulse width 0.8 is located midway between the surface and interface. The shear and compressional speeds in the lower medium are much larger than in the layer ( $\rho_2 = 1.5\rho_1$ ,  $v_{p2} = 3v_{p1}$ ,  $v_{s2} = 3v_{s1}$ ). The curves are for observation points located at the epicenter (a) and at a distance of one layer thickness (b) from the epicenter.

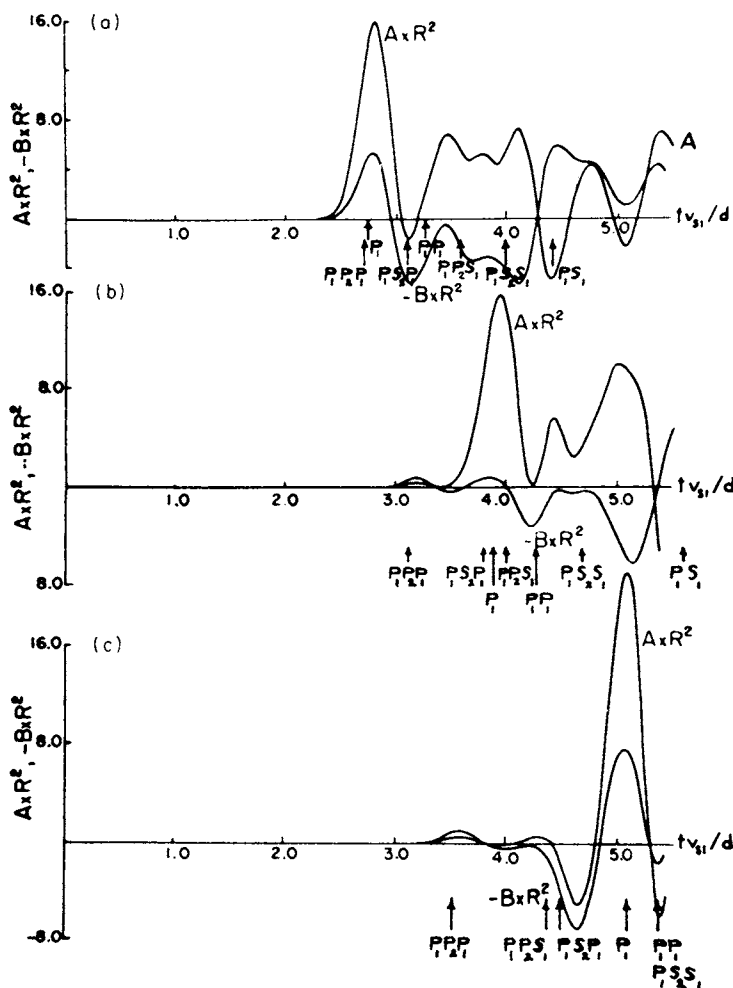


FIG. 53. Horizontal and vertical displacements on the surface of a layered half-space (continuation of Fig. 52). The three curves are for observation points located at distances of (a) two, (b) three, and (c) four layer thicknesses from the epicenter.

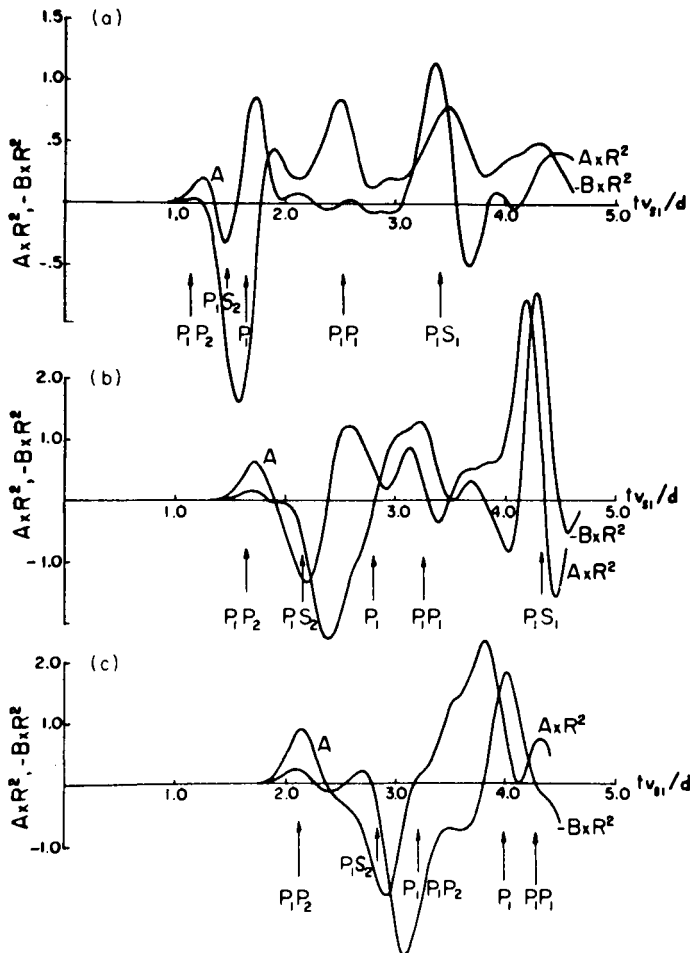


FIG. 54. Horizontal and vertical displacements on the interface of a layered half-space. A compressional point source of pulse width 0.8 is located midway between the surface and interface. The shear and compressional speeds in the lower medium are much larger than in the layer ( $\rho_2 = 1/5\rho_1$ ,  $v_{p2} = 3v_{p1}$ ,  $v_{s2} = 3v_{s1}$ ). The three curves are for observation points located on the interface at distances of (a) one, (b) two, and (c) three layer thicknesses away from the point directly below the source.

FIG. 55. Horizontal and vertical displacements on the interface separating two semi-infinite elastic media. A compressional point source of pulse width 0.8 is located in the upper medium [ $v_{p2} = (1.05v_{p1})^{1/2}$ ,  $v_{s2} = (1.05v_{s1})^{1/2}$ ]. The observation point is located on the interface at a distance of four times the height of the source above the interface measured from a point directly below the source. The four curves are for density contrasts  $\rho_2/\rho_1$  given by 0, 0.2, 0.4, and 1.0.

FIG. 56. Horizontal and vertical displacements on the interface separating two semi-infinite elastic media (continuation of Fig. 55). The four curves are for density contrasts  $\rho_1/\rho_2$  given by 1.4, 2.0, 3.0, and 5.0.

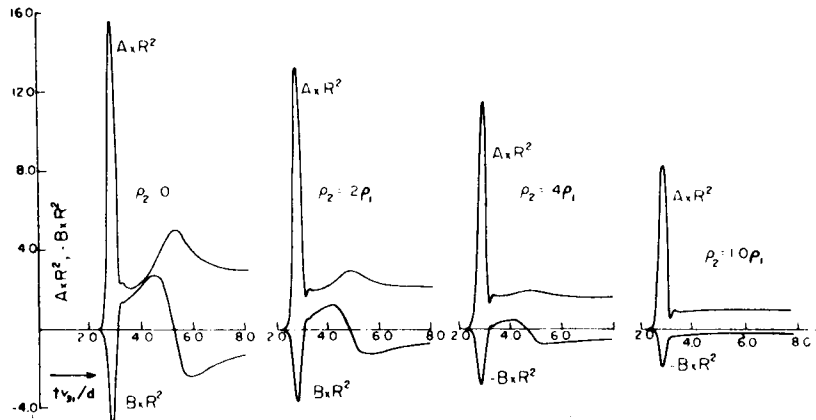


FIG. 55

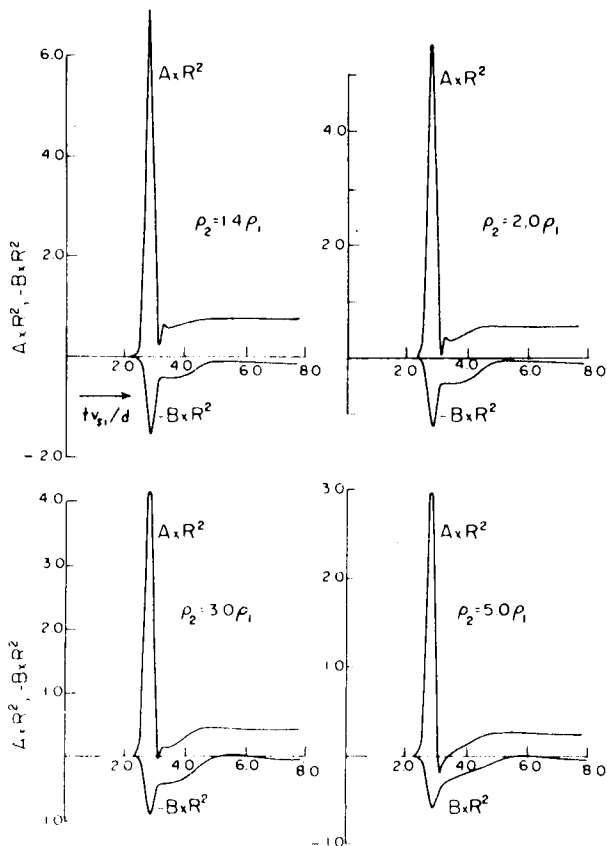


FIG. 56

## D. SEISMOGRAMS FOR THE LAYERED SPHERE

### 1. Group Velocity

The radial displacement at the surface of a homogeneous sphere given in Section II, B, 2, a, Eq. (178), and of a layered sphere given in the Appendix, Eqs. (254) and (257), were evaluated on the computer summing over such a number of normal modes as to assure the accuracy of each wavelet occurring in the graphs. In a specific case the following material constants were chosen as averages for a real earth model. In the solid mantle  $\rho_1 = 4.46 \text{ g/cm}^3$ ,  $v_{p1} = 11.39 \text{ km/sec}$ ,  $v_{s1} = 6.24 \text{ km/sec}$ , and in the core  $\rho_2 = 11.02 \text{ g/cm}^3$  and  $v_{p2} = 9.28 \text{ km/sec}$ .

Group velocity dispersion curves (Fig. 57)<sup>5</sup> show the group velocity  $U$  against period  $T$ , where

$$\frac{v_s y_{jn}}{2\pi a} = \frac{1}{T}, \quad U = \frac{d}{dn} \left( \frac{v_s y_{jn}}{a} \right), \quad (229)$$

and where  $y_{jn}$  are defined by Eq. (254) of the Appendix.

$U$  is obtained numerically from Eq. (229) and the  $y_{jn}$ . The curve for  $j = 1$  tends to  $v_R/v_s$  for  $T \rightarrow 0$ , similar to the case of a homogeneous sphere solved by Alterman and Abramovici (1965). Here  $v_R$  is the velocity of Rayleigh waves in a half-space. The curve  $j = 2$  for the layered sphere differs from all curves for a homogeneous sphere and from the curves  $j \geq 3$  for the layered sphere. It tends to  $U/v_s = 1.1$  for  $T \rightarrow 0$ , whereas the curves  $j \geq 3$  have the limit  $U/v_s = 1.0$ . The curve for  $j = 2$  is connected with Stoneley waves and does not appear among the dispersion curves for a homogeneous sphere. The curves for  $j \geq 3$  have several maximum values in addition to those of the homogeneous sphere (e.g., at  $U/v_s = 1.15$  and 1.18). The maxima are connected with higher mode guided surface waves.

The group velocities are determined by the constants of the sphere alone and are independent of assumptions about depth, geometry, and time functions of the source. The depth of the source, its geometry, and time function are expressed by the common spectrum  $(2n + 1)B_{jn}$  and  $(2n + 1)nC_{jn}$  in the Appendix, Eqs. (255) and (258). Details of the common spectrum of the explosive point source in the layered sphere have been given by Alterman and Aboudi (1968). The complete theoretical seismograms involve a combination of the common spectra, the location of observer, and the time of observation. They show several modes of surface waves which are discussed in the following sections.

<sup>5</sup> Figures 57-82 appear on pages 138-152.

## 2. Rayleigh Waves

The group velocity dispersion curve for  $j = 1$  tends to the value  $v_R/v_s$  for high frequency. Here  $v_R$  is the Rayleigh wave velocity in a homogeneous half-space. For the ratio of shear wave velocity to compressional wave velocity,  $v_s/v_p = 6.24/11.39$ , which is the same as the value in the spherical layer, the value of  $v_R$  is  $0.9251 v_s$ . For finite frequency the dispersion curve is above this value, and the computed seismograms indeed show dispersion of the Rayleigh waves to higher velocity. The arrival time of Rayleigh waves is indicated in the computed seismograms by an arrow and the letter R. By taking in Eqs. (254) and (257) in the Appendix for  $u_R$  and  $u_\theta$  the terms in  $j = 1$  only, the Rayleigh wave contribution to the motion of the sphere is singled out of the total displacement. Figure 58 shows the Rayleigh terms for  $u_R$  and  $u_\theta$  at  $45^\circ$  distance from a source at depth  $a - b = a/32$ . The direct Rayleigh wave entering in a clockwise direction is denoted by  $R_{11}$ , the first wave coming in an anticlockwise direction is denoted by  $R_{12}$ , and waves arriving after a complete circuit in clockwise or anticlockwise directions are denoted by  $R_{13}$  and  $R_{14}$ , respectively. The arrows indicate the arrival time corresponding to velocity  $v_R$ . The Rayleigh waves are found to arrive before and up to that time. Figure 58 shows the dispersion to higher velocity mainly in the low-frequency components. Whereas the source emits a pulse of duration  $0.03a/v_s$  the Rayleigh wave  $R_{12}$  in Fig. 58 extends over more than  $1.5a/v_s$ . The dispersion is larger than the dispersion in a homogeneous sphere which is shown by the dotted line in Fig. 58. The decrease in amplitude of the Rayleigh wave with increasing depth of source (down to a source at  $b = \frac{7}{8}a$ ) is similar to the findings for a homogeneous sphere. Also, the variation in amplitude with distance from the source is similar to the homogeneous case. The amplitudes of the radial and angular components  $A_R$  and  $A_\theta$  of  $R_{11}$  are largest at  $0^\circ$  and at  $180^\circ$  and have a minimum at  $90^\circ$  from the source. The ratio  $A_\theta/A_R$  changes with distance from the source; at  $90^\circ$  it is nearest its value in a half-space.

Although previous work indicated a quite constant phase of the Rayleigh wave from  $0^\circ$  to  $180^\circ$  and a phase shift in the antipodal region, possibly for large  $n$  (Brune *et al.*, 1961), the complete seismograms show a gradual shift in phase of the Rayleigh waves, which involves a wide range of frequencies with varying distance for  $0^\circ \leq \theta \leq 180^\circ$  (see Figs. 62 and 63). The Rayleigh waves indicated  $R_{11}$  and  $R_{12}$  in Fig. 59 show the gradual phase shift in the range  $172^\circ \leq \theta \leq 180^\circ$ . The same has also been established experimentally by Shimamura and Satô (1965).

## 3. Stoneley Waves

Stoneley waves occur at the interface between solid and fluid half-spaces for all values of the elastic constants and densities. The phase velocity of

Stoneley waves at the plane interface between a solid and a fluid half-space of the same constants as assumed for the sphere is  $v_{st} = 0.601 v_s$ . When a Stoneley wave propagates along the core boundary from a point below the source at an angular distance  $\theta$ , the distance from the epicenter to  $\theta$  on the surface is larger by a factor of  $a/d$  and the apparent velocity on the surface is larger by the same factor or  $0.601 v_s a/d = 1.102 v_s$ . This value is the high-frequency limit of the phase velocity in the layered sphere as well as of the group velocity for  $j = 2$  (Fig. 57). For lower frequencies the curve  $j = 2$  assumes slightly different values, which indicate the deviation of the interface wave velocity in the sphere from its value in plane half-spaces.

As the Stoneley waves decrease exponentially in amplitude with distance from the core boundary, they are not found in the seismograms computed for sources at depths of  $a - b = a/8$  and less. Stoneley waves are found, however, in the seismogram for a source at the interface. Figure 60 shows the Stoneley waves due to a source at  $b = d$ . In this case the Stoneley wave has a larger amplitude than any other wave.

#### 4. Higher Modes

The connection between multiply-reflected pulses and higher-mode surface waves has been demonstrated for P- and S-waves in a homogeneous sphere (Altermann and Abramovici, 1966) and for SH reflections in a layered sphere (Altermann and Kornfeld, 1966). An analysis of the relation between normal mode and ray representations of body waves has been given by Brune (1966). A similar interpretation has also been given for the layered sphere (Altermann and Aboudi, 1969). Several modes of guided waves in the layered sphere due to a P-wave source are connected with pulses of the form  $P_\alpha k(S_c S)$ , which are reflected  $\alpha$  times as P at the surface of the sphere and  $k$  times as S at the core. For fixed  $k$  let us consider the pulses obtained in the limit as  $\alpha \rightarrow \infty$ , when the segments of reflected P approximate an arc on the spherical surface. The arrival time is given by

$$\lim_{\alpha \rightarrow \infty} \tau[P_\alpha k(S_c S)] = \frac{v_s}{a} \cdot \left\{ \frac{l - 2k[a\bar{\gamma} - d\omega]}{v_{p1}} + 2k \frac{a \sin \bar{\gamma} - d \sin \bar{\omega}}{v_s} \right\}, \quad (230)$$

where

$$\begin{aligned} \tau &= v_s t/a, \\ \bar{\gamma} &= \text{arc cos}(v_s/v_p), \\ \bar{\omega} &= \text{arc cos}[(a/d)(v_s/v_p)], \\ l &= \begin{cases} (2\pi m + \theta)a, \\ (2\pi(m + 1) - \theta)a. \end{cases} \end{aligned} \quad (231)$$

The group velocity of the surface wave represented by these pulses is

$$U/v_s = l/a/\lim_{\alpha \rightarrow \infty} \tau [P_\alpha k(S_c S)]. \quad (232)$$

Values of  $U/v_s$  calculated according to Eq. (232) for several values of  $k$  are

$$U/v_s = 1.15, 1.18, 1.25, 1.30, \dots \quad (233)$$

These values are related to the group velocities in the dispersion curves in the following manner.

The Fourier components of the initial pulse of duration  $3\delta = 0.03$  are mainly in the range of periods  $0.003 < v_s T / 2\pi a < 0.008$ . Figure 61 shows group velocity dispersion curves in this range. The lowest maximum values of each of the dispersion curves are almost independent of  $k$  and are in the range of  $1.15 < U/v_s < 1.18$ . This range coincides with the lowest values of  $U/v_s$  calculated according to Eq. (232). The next higher maximum in Fig. 61 occurs at  $U/v_s = 1.25$ , and the following one is near  $U/v_s = 1.30$ , again in agreement with the group velocities obtained from Eq. (232). Reflected pulses that have other ray paths are connected with different group velocities. They can be found in other ranges of periods for sources having a different frequency spectrum.

The theoretical seismograms in Figs. 62 and 63 show higher mode surface waves having the group velocities given in Eq. (233). They are indicated by horizontal lines. The guided waves with velocities of  $1.15 v_s - 1.18 v_s$  are denoted by  $T_{2i}$ . The index  $i$  has here the same meaning as for the Rayleigh waves. The waves of velocity  $1.25 v_s$  are denoted  $T_{3i}$ .  $T_{4i}$  denotes waves with a velocity of  $1.30 v_s$ . Table IV shows the reflected pulses representing the waves  $T_{ki}$  in various ranges of distance  $\theta$  from the source.

The waves  $T_{ki}$  are indicated on the computed seismograms in Figs. 62 and 63. The  $T_{2i}$  waves have larger angular than radial components; the angular component is even larger than the Rayleigh wave. This is similar to the amplitude distribution in the second-mode surface wave in a homogeneous sphere (Alterman and Abramovici, 1966).  $T_{3i}$  has a larger radial component than an angular component. This again is similar to the third-mode surface wave in a homogeneous sphere. The values of  $T_{4i}$  are found also in the theoretical seismograms; they have smaller amplitudes than the  $T_{3i}$ .

TABLE IV

GUIDED WAVES  $T_{ik}$  AND THE REFLECTED PULSES THAT CONTRIBUTE TO EACH GUIDED WAVE IN THE INDICATED RANGE OF DISTANCE  $\theta$

Guided wave	Pulse	Range of $\theta$
$T_{21}$	$P_sS_cS$	$90^\circ$
$T_{22}$	$P_s3S_cS$	$10^\circ-90^\circ$
	$P_s2S_cS$	$135^\circ-170^\circ$
$T_{23}$	$P_s4S_cS$	$10^\circ-90^\circ$
	$P_s5S_cS$	$135^\circ-170^\circ$
$T_{24}$	$P_s5S_cS$	$170^\circ$
	$P_s6S_cS$	$45^\circ-135^\circ$
	$P_s7S_cS$	$10^\circ$
$T_{25}$	$P_s7S_cS$	$10^\circ-90^\circ$
$T_{31}$	$P_oS_cS$	$135^\circ$
$T_{32}$	$P_o2S_cS$	$90^\circ$
$T_{33}$	$P_o3S_cS$	$10^\circ-60^\circ$
	$P_o4S_cS$	$135^\circ-170^\circ$
$T_{34}$	$P_o5S_cS$	$10^\circ-135^\circ$
	$P_o4S_cS$	$170^\circ$
$T_{35}$	$P_o6S_cS$	$10^\circ-135^\circ$

### 5. Diffracted Pulses

Diffraction effects of the spherical surface occur as a continuation of reflected pulses through the caustic, where real reflected rays cannot occur. Their arrival time is determined by the complex angle of reflection in Snell's law. Diffraction at the core-mantle interface occurs in a similar way at points that cannot be reached by real reflected rays passing partly through the core. As an example, let us consider the PKP pulse. At distances  $\theta$  in the range  $149.1^\circ < \theta \leq 180^\circ$  two different PKP rays arrive at the surface. They coincide at  $\theta_0 = 149.1^\circ$ . At  $\theta_0$  the caustic intersects the surface of the sphere, and at  $\theta < \theta_0$  there is no real solution according to ray theory. Owing to diffraction, however, a PKP pulse is found at  $\theta < \theta_0$ . It is denoted PKP(D). Its amplitude decreases with distance from  $\theta_0$ . The arrival times of several diffracted pulses (diffraction at the surface or at the interface) are indicated in the theoretical seismograms by arrows. The notation is the same as for the corresponding ray with D added [e.g., PKP(D), PKKS(D) for diffraction at the interface and PP(D), P<sub>3</sub>(D) for diffraction at the surface].

Another form of diffraction is the well-known phenomenon of diffraction into the shadow zone of the core. It is described by the following ray path. The initial P pulse arrives from the source along a tangent to the surface of the

core, continues along the surface of the core through an angular distance  $\phi$ , and then leaves the core in tangential direction. Following Knopoff and Gilbert (1961), this pulse is denoted P(P)P. Figure 64 shows the path of P(P)P and of a similar diffracted pulse P(P)S, which leaves the core as a shear wave. Any number of reflections at the surface or interface or transmission through the core may occur before or after this core diffraction. The arrival time of such a pulse is given by

$$\begin{aligned}\tau = \alpha \frac{v_s}{v_{p1}} \sin \gamma + (2k - \alpha) \left( \sin \bar{\gamma} - \frac{d}{a} \sin \bar{\omega} \right) + 2r \frac{v_s d}{v_p a} \sin \varepsilon \\ + \frac{v_s d}{v_p a} \phi \pm \left( \frac{v_s}{v_{p1}} \sin \gamma - \frac{v_s b}{v_{p1} a} \sin \delta \right),\end{aligned}\quad (234)$$

where  $k$ ,  $\alpha$ , and  $r$  are determined by the number of chords between the source, the points of reflection, and the receiver.

$\gamma$ ,  $\bar{\gamma}$ ,  $\delta$ ,  $k$ , and  $\alpha$  have been defined in Section II, B.  $\bar{\omega}$  and  $\varepsilon$  denote the complementary angles of incidence at the core boundary for S incident from the mantle and for P in the core, respectively.  $r$  denotes the number of chords in the core which a ray has passed up to arrival at the point of observation. For P(P)P the parameters take the value  $\alpha = 2$ ,  $k = 1$ ,  $r = 0$ .

In the following sections, we discuss the properties of some of the reflected and diffracted pulses. If not otherwise stated, the source is located at  $b/a = 7/8$ .

## 6. Direct Pulse and First Core Diffraction

The boundary of the shadow zone,  $\theta_1$ , is determined by the depth of the source and by the radius of the core through  $\theta_1 = \arccos(d/a) + \arccos(d/b)$ . For rays from a source at  $b = 7a/8$  the shadow zone of the core starts at  $\theta_1 = 108.4^\circ$ . The amplitude of the direct pulse up to the shadow zone is drawn in Fig. 65. The curve extends continuously into the shadow zone showing the amplitude of the diffracted pulse P(P)P.

The continuous variation of the amplitude is expected according to observations (Lehmann, 1953) and seismic models (Gutenberg, 1960). This continuous variation in amplitude explains the difficulty in defining the exact shadow boundary of the earth's core from observation.

The amplitude of the direct P pulse, according to ray theory, is represented as a dashed curve in Fig. 65. The complete result differs from the result of ray theory. Whereas the result from ray theory takes into account the curvature of the surface and of the wave front, it is correct for infinite frequency only. The complete result for the amplitude depends on the duration of the initial pulse or on its frequency content. The ratio between the exact amplitude

$A(\delta)$  read from the theoretical seismograms and those given by steepest descents,  $A_{sd}$ , show the deviations due to finite frequency. Comparing this ratio for pulses of duration  $3\delta = 0.03$  and  $3\delta = 0.15$  shows variations due to the different frequency content of the two pulses. A similar frequency dependence has been investigated by Červený (1967) in the case of half-spaces.

The diffracted pulse can be followed deep into the shadow zone. The same has been found in analytic approximations by Scholte (1956) and in seismic models described by Gutenberg (1960). Figures 67–74 show enlarged portions of theoretical seismograms at several distances from a source at  $b = 7a/8$ . These figures include the direct P pulse and the diffracted P(P)P, and show the diffracted pulse up to an angular distance  $\theta = 160^\circ$  from the source. This distance is similar to the distances up to which the diffracted P has been found in observation (Gutenberg and Richter, 1934; Jeffreys, 1959; Alexander and Phinney, 1966). Gutenberg and Richter (1935), and Alexander and Phinney point out that the diffracted waves are best found in vertical instruments, or in our notation  $u_R$  is appreciably larger than  $u_\theta$ . The theoretical seismograms in Fig. 72 show indeed that the radial component  $u_R$  of P(P)P is larger than  $u_\theta$ .

As expected according to theory (Duwalo and Jacobs, 1959; Scholte, 1956), and as found in seismic models (Knopoff and Gilbert, 1961) and in observed results (Ry kunov, 1959; Alexander and Phinney, 1966), the diffracted P(P)P decreases exponentially with distance from the shadow boundary. This is found again in the theoretical seismograms.

The amplitude of P(P)P as read from the theoretical seismograms is drawn in Fig. 66 and is indeed linear on the logarithmic scale of the figure.

### 7. Pulses $P_cP$ and $pP_cP$

The pulse  $P_cP$ , which is reflected once at the core, arrives at distances up to the limit  $\theta_1$  of the shadow zone, where it coincides with the direct P pulse and then goes over into the diffracted P(P)P. Figure 75 shows the arrival time as a function of distance from the source together with the arrival of P and P(P)P. Although we consider here a simple model, the arrival-time curves are similar to the ones given by Jeffreys and Bullen (1940).

The radial component of  $P_cP$  is larger than the angular component at all distances shown. The same is found in recorded seismograms (Ergin, 1952; Richter, 1958). For  $\theta < 50^\circ$  the amplitude of the radial component is more than twice as large as the amplitude of the angular component. The  $P_cP$  has the same properties in the theoretical seismograms (Figs. 69, 70).

In seismograms observed at small distance from the source,  $P_cP$  was not determined definitely as it arrives shortly after the Rayleigh waves. It was finally identified satisfactorily in seismograms from deep sources (Jeffreys, 1959). The theoretical seismograms at  $\theta = 10^\circ$  (Fig. 67) show  $P_cP$  clearly superimposed on the earlier arriving low-frequency Rayleigh wave.

In Fig. 69 at  $\theta = 30^\circ$  the Rayleigh wave  $R_{11}$  arrives simultaneously with  $P_cP$ . Owing to the small amplitude of  $R_{11}$  for this deep source and owing to its low frequencies, the  $P_cP$  is clearly distinguishable.

The pulse  $pP_cP$  is reflected once at the surface before the reflection at the core. It occurs in the range  $0^\circ \leq \theta \leq 119^\circ$ . As found before for  $P_cP$  the radial component of  $pP_cP$  is larger than the angular component. At  $\theta = 119^\circ$  it coincides with the  $pP$  wave and is continued by the diffracted  $pP(P)P$  for  $\theta > 119^\circ$ . The arrival-time curves for  $pP_cP$ ,  $pP$  and  $pP(P)P$ , given in Fig. 75 are similar to the observed values given by Richter (1958). Figures 69 and 70 show clearly the phase change in  $pP_cP$  as opposed to the direct  $P$ . It is similar to the phase change in  $pP$  versus  $P$ .

#### 8. Pulses $P_cS$ , $pP_cS$ , $PS_cS$ , and $P(P)S$

The  $P_cS$  pulse occurs in the model under discussion in the range of angular distances  $0^\circ \leq \theta \leq 67^\circ$ . This is similar to the range of distances  $0^\circ \leq \theta \leq 65^\circ$  given by Dana (1945) and Danes (1962) and to the range  $0^\circ \leq \theta \leq 72$  given by Scholte (1956). In the Jeffreys-Bullen (1940) tables of arrival times of  $P_cS$  are listed up to  $\theta = 70^\circ$ .

Table V shows the amplitudes  $A_R$  and  $A_\theta$  of the radial and angular components of  $P_cS$  as they appear on the computed seismograms. With the exception of the epicenter,  $A_\theta$  is from three to nine times larger than  $A_R$  and indeed mainly the angular component has been observed (Ergin, 1952). In Table V,  $A_\theta$  is largest in the range  $20^\circ < \theta < 30^\circ$ , in agreement with observations by Gutenberg and Richter (1935) and with results obtained by Danes (1962) (see Fig. 76).

In the layered sphere the diffracted  $P(P)S$  occurs at  $\theta > 67^\circ$  and is found to be strongly damped with increasing  $\theta$ . The theoretical seismogram at  $\theta = 90^\circ$  (Fig. 77) still shows the angular component of this pulse. At larger  $\theta$  it is too small to be found. Figure 75 shows the arrival times of  $P_cS$  and of  $P(P)S$ .

The  $pP_cS$  pulse arrives at the surface in the range of distances  $0^\circ \leq \theta \leq 78^\circ$  from the source. For small values of  $\theta$  (near  $10^\circ$ ) the ratio of  $A_\theta$  to  $A_R$  is similar to that for  $P_cS$ , namely, the angular component of  $pP_cS$  is larger than the radial component. For larger  $\theta$ , however, the amplitude  $A_R$  of  $pP_cS$  is larger than  $A_\theta$ . The diffracted  $pP(P)S$  occurs at larger distances than  $78^\circ$  (see Fig. 77). Its radial component is again found to be larger than the angular component.

The  $P_cS$  and  $pP_cS$  pulses have opposite phases. Whereas the angular component of  $P_cS$  is in phase with the direct pulse and its radial component has opposite sign, the angular component of  $pP_cS$  differs in phase from the direct pulse and its radial component has the same phase as the direct pulse (see Figs. 68–70).

TABLE V

AMPLITUDES OF RADIAL AND ANGULAR COMPONENTS OF  $P_cS$ 

$\theta$ (deg)	$\tau$	$A_R$	$A_\theta$
0	0.65	0.05	0
10	0.66	0.05	0.45
20	0.68	0.1	0.7
30	0.71	0.15	0.65
40	0.75	0.1	0.55
45	0.77	0.1	0.45
50	0.8	0.1	0.3
60	0.85	0.075	0.2

9. Pulses  $P_2$ ,  $P_2(D)$ 

In a homogeneous sphere three once-reflected pulses arrive at any distance  $\theta > \theta_0$  from the source. Here  $\theta_0$  is the angular distance of the intersection of the caustic with the surface of the sphere. At  $\theta = \theta_0$  two of the pulses ( $pP$  and  $PP$ ) coincide and, according to ray theory, do not appear at  $\theta < \theta_0$ . Instead, a diffracted pulse  $P_2(D)$  is found. At  $\theta_0$  the arrival-time curves of  $pP$  and  $PP$  form a cusp (Fig. 75). Another cusp is formed by the arrival-time curves of two different  $PP$  pulses at  $\theta = 180^\circ$ .

For a source at  $b = 7a/8$  the intersection of the caustic with the sphere is at  $\theta_0 = 82^\circ$ , so that in a homogeneous sphere  $pP$ , together with two additional  $PP$  pulses, occur at all distances in the range  $82^\circ \leq \theta \leq 180^\circ$ . In the layered sphere, however,  $pP$  arrives in the range  $82^\circ \leq \theta \leq 119^\circ$  only. For  $\theta > 119^\circ$  the pulse is diffracted by the core as is  $pP_cP$  and both are continued to  $0 > 119^\circ$  by  $pP(P)P$ .

The second  $PP$  pulse occurs in the layered sphere in the same range as in the homogeneous sphere, namely,  $82^\circ \leq \theta \leq 180^\circ$ . The latest arriving  $PP$  pulse occurs in the layered sphere in the range  $138^\circ \leq \theta \leq 180^\circ$  only.

As the steepest descent approximation breaks down near the caustic, it is of interest to study the behavior of  $PP$  and  $P_2(D)$  in the complete seismograms near  $\theta_0$ . Figure 78 shows sections of the computed seismograms at  $1^\circ$  intervals in the range  $82^\circ \leq \theta \leq 86^\circ$ . The arrival times of  $pP$  and  $PP$  are so close that the two pulses appear superposed. Their amplitudes increase with increasing  $\theta$  and they do not have a maximum at the caustic  $\theta_0 = 82^\circ$ . This is in contrast to the steepest descent result which not only has a maximum at  $\theta = \theta_0$  but also has infinite amplitude at  $\theta = \theta_0$ .

The large variation in amplitude of the  $PP$  pulses near  $\theta = 180^\circ$  is depicted in Fig. 79. As expected according to the steepest descent approximation, the

amplitude of the radial component increases with increasing  $\theta$  and has a maximum at  $\theta = 180^\circ$ . The same has been reported by Gutenberg and Richter (1935).

Finally, we consider the shape of the once-reflected pulses. The pP pulse is similar to the direct P; however, it has opposite sign. The PP pulse which travels in the same direction as pP shows a phase shift, as for example in Fig. 72 at  $\theta = 110^\circ$ .

According to the analysis by Jeffreys and Lapwood (1957), the form of the PP pulse in a fluid sphere is determined by the function allied to the function describing the pP pulse. When pP has the form of a step function, PP has a logarithmic infinity, rising from a gradual beginning slightly before the actual arrival time. The phase shift in pP and its gradual beginning have been established in the complete theoretical seismograms for a fluid sphere by Alterman and Kornfeld (1963) and for a homogeneous solid elastic sphere by Alterman and Abramovici (1965). Shimamura and Satô (1965) obtained similar pulse forms for pP and PP from an experimental model.

Owing to diffraction at the spherical surface, the reflected pP and PP pulses which exist for  $\theta > 82$  are continued to  $\theta < 82^\circ$  by diffracted PP(D) pulses, the diffracted pulses decrease in amplitude with decreasing  $\theta$ . The angular component of PP(D) is larger than its radial component and is found down to  $\theta = 40^\circ$  (see Fig. 69). The PP(D) pulse has been found near the caustic in the experimental model by Shimamura and Satô.

Diffraction of pP at the core occurs at distances  $\theta > 119^\circ$ . The decrease in amplitude of pP(P)P is shown in Figs. 72 and 73. Here the radial component is larger than the angular component, and pP(P)P can be found up to  $\theta = 165^\circ$ . The arrival of pP(P)P is similar to results given by Richter (1958) for the same wave from an earthquake at 600 km depth.

#### 10. *Transmission Through the Core*

Two different PKP pulses arrive at the surface at distances  $149.1^\circ < \theta < 180^\circ$ . According to Richter (1958), these pulses are denoted  $\text{PKP}_1$  and  $\text{PKP}_2$  so that  $\text{PKP}_1$  arrives earlier and has the smaller angle of incidence;  $\text{PKP}_2$  arrives later and has the larger angle of incidence. The arrival-time curve in Fig. 75 shows the two branches for  $\text{PKP}_1$  and  $\text{PKP}_2$  having a cusp at the caustic point  $\theta_0 = 149.1$ . Figure 74 shows that the form of  $\text{PKP}_1$  is similar to the form of the direct  $P_1$  whereas  $\text{PKP}_2$  has the same "logarithmic form" connected with diffuse onset and phase shift as PP. The same properties of  $\text{PKP}_2$  in observed seismograms were pointed out by Jeffreys (1939).

In the theoretical seismogram at  $\theta = 150^\circ$  (in Fig. 73) the pulses  $\text{PKP}_1$  and  $\text{PKP}_2$  arrive almost simultaneously. The radial component of the combined pulse is larger than all other arrivals. This large amplitude has been found, and attempts have been made to determine the caustic from observation of

large amplitude PKP (Denson, 1952). However, this procedure may be misleading as a further analysis of Figs. 73 and 74 shows that a maximum in PKP occurs at  $\theta = 155^\circ$ , and not at the caustic  $\theta_0 = 149.1$ . A similar deviation of the location of the maximum amplitude from the caustic, due to the finite frequency of the pulses, has been pointed out by Ergin (1967).

Figures 73 and 74 show that at all distances the radial component of PKP is larger than the angular component, in agreement with observation (Jeffreys, 1959).

As indicated by Lehmann (1954), the horizontal or angular component of PKP<sub>2</sub> at  $160.9^\circ$  is much larger than that of PKP<sub>1</sub>. The theoretical seismograms in Figs. 73 and 74 show indeed that throughout the range  $160^\circ \leq \theta \leq 175^\circ$  the angular component of PKP<sub>2</sub> is larger than that of PKP<sub>1</sub>. They also show that in this range the radial component of PKP<sub>2</sub> is smaller than that of PKP<sub>1</sub>, a result that a plane-wave analysis failed to show. At  $\theta = 180^\circ$  the amplitude of PKP<sub>2</sub> is 1.6 times as large as the amplitude of PKP<sub>1</sub>. Similar observed results have been mentioned by Gutenberg (1958) and Ergin (1967).

The diffracted PKP(D) occurs when  $\theta < 149.1^\circ$ . Figure 75 shows the arrival-time curve, and the pulse is found at distances from  $\theta = 149^\circ$  down to  $\theta = 135^\circ$ . This indicates a far more rapid decrease of PKP(D) with distance from the caustic than the decrease of P(P)P into the shadow zone of the core. The same difference in observed seismograms has been pointed out by Gutenberg (1960). Gutenberg and Richter (1935) found PKP(D) mainly in vertical instruments. The theoretical seismograms show that the radial component of PKP(D) is always larger than the angular component.

There are three different pPKP pulses in the range  $170^\circ \leq \theta \leq 180^\circ$ . One of the pulses is continued to  $\theta < 170^\circ$  by diffraction at the core pPKP(P)P. Two reflected pPKP occur in the range  $170^\circ \geq \theta \geq 158^\circ$ , and at  $\theta < 158^\circ$  a diffracted pPKP(D) pulse occurs. Its amplitude decreases rapidly with decreasing  $\theta$  but it is still visible at  $\theta = 140^\circ$  (Figs. 73 and 74).

Considering the form of the pulses, it is seen that PKP<sub>1</sub> is similar to the direct pulse and pPKP<sub>1</sub> has opposite sign. PKP<sub>2</sub> shows a phase change similar to PP, while pPKP<sub>2</sub> shows the same phase change as PKP<sub>2</sub> with an additional change in sign.

Let us consider now the pulses PKS<sub>1</sub>, PKS<sub>2</sub>, PKS(D), pPKS; their properties are similar to the previously considered pulses. Figure 75 shows the arrival times in their ranges of existence. The caustic point for PKS is at  $\theta = 129^\circ$ , near values quoted by Forester (1955) and Gutenberg and Richter (1935). In Figs. 72 and 73 the maximum amplitude of PKS occurs as for PKP, not at the caustic but at  $\theta = 135^\circ$ . The figures show that the angular component of PKS is larger than the radial component, and the same is found in observation (Forester, 1955; Lehmann, 1954).

As for the pulse form of PKS, the radial component is similar to the direct pulse but its angular component has opposite sign. For pPKS the situation is reversed: the radial component differs in sign from the direct pulse, and the angular component has the same sign as the direct pulse.

Diffracted PKS(D) are indicated in Figs. 72 and 73. They decrease rapidly with distance from  $\theta_0$ .

The PKKP and PKKS pulses and associated diffracted pulses are found in Fig. 77 and depicted in detail in Figs. 80 and 81.

At distances  $\theta < 90^\circ$ , PKKP has only small amplitude, the angular component being even smaller than the radial component. Figure 80 shows that for  $\theta > 100^\circ$  the amplitude increases up to a maximum at  $120^\circ$ . At the caustic,  $\theta_0 = 126^\circ$ , the amplitude is again smaller. Similar observed results have been pointed out by Gutenberg (1951) and by Gutenberg and Richter (1935).

PKKP is very small at distances  $\theta < 90^\circ$ . Figure 81 shows PKKS in the range  $120^\circ \leq \theta \leq 155^\circ$  where it has a large amplitude, mainly in the angular component. Similar results in observed seismograms have been pointed out by Gutenberg (1959). The diffracted PKKS(D) occurs for  $\theta > 155^\circ$  and is shown in Fig. 81 at  $160^\circ$ . According to Gutenberg (1959), however, in observation "there is no indication of appreciable diffraction."

An analysis of pulses that are once reflected at the core and once transmitted through the core shows the following main properties:  $P_c$ PPKP arrives at distances  $67^\circ \leq \theta \leq 180^\circ$ . In this entire range the radial component is larger than the angular component. For  $\theta < 90^\circ$  the amplitude is small. Near  $\theta = 180^\circ$ , however, the amplitude becomes quite large (Fig. 82). Large amplitudes in observed seismograms have been pointed out by Gutenberg and Richter (1934, 1935). Figure 82 shows also the  $pP_c$ PPKP pulse, which has a large radial component and a small angular component near  $\theta = 180^\circ$ . With decreasing  $\theta$  the amplitude decreases. The form of  $P_c$ PPKP and of  $pP_c$ PPKP is similar to the form of the initial P pulse. However, the angular component of the first and the radial component of the second have opposite sign.

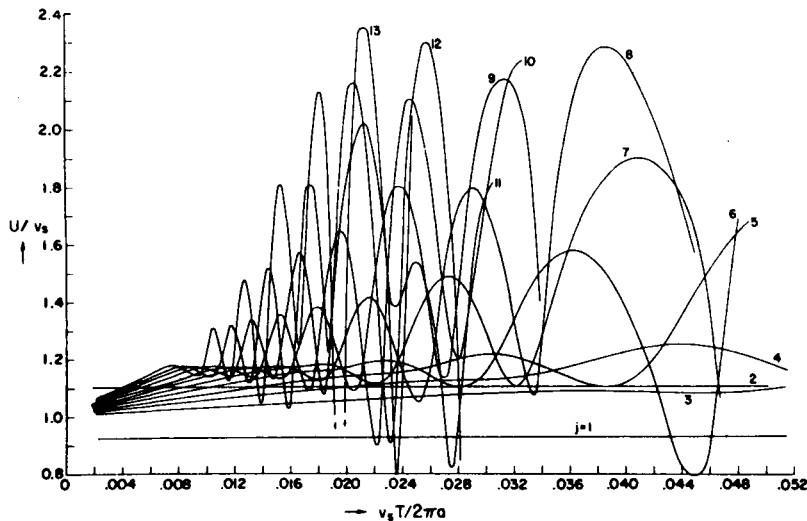


FIG. 57. The group velocity  $U$  in a layered sphere as function of  $T$ .  $0.004 \leq v_s T / 2\pi a \leq 0.052$ ,  $1 \leq j \leq 13$ .

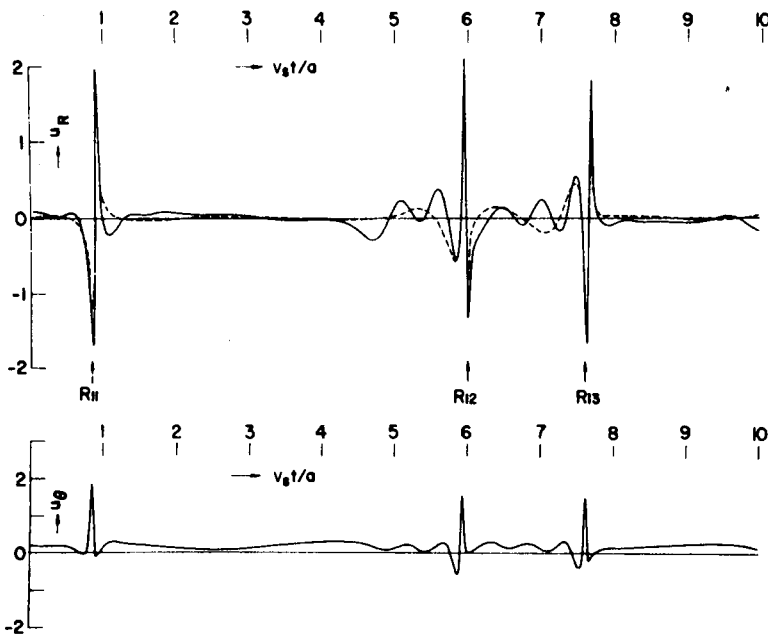


FIG. 58. The radial components of the Rayleigh wave in the layered sphere (solid line) and in the homogeneous sphere (dotted line) at distance  $\theta = 45^\circ$  ( $\delta = 0.01$ ) from a point source located at depth  $a - b = a/32$ . Arrows indicate arrival times of Rayleigh waves  $R_{1i}$  in a half-space. The lower curve shows the angular component of Rayleigh waves.

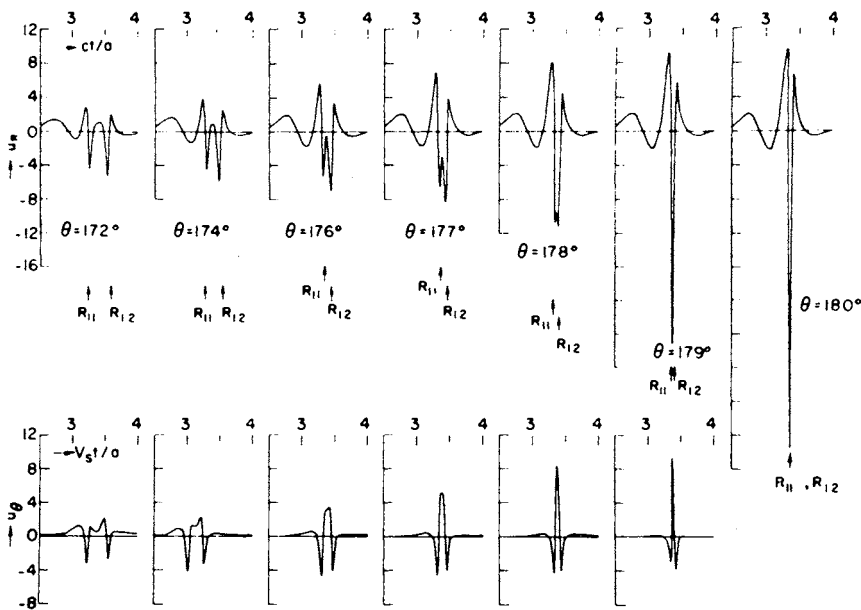


FIG. 59. The radial and the angular components of the Rayleigh waves  $R_{11}$  at distances  $172^\circ \leq \theta \leq 180^\circ$  from a point source located at depth  $a - b = a/32$ ,  $\delta = 0.01$ . Arrows indicate arrival times of Rayleigh waves  $R_{11}$  in a half-space.

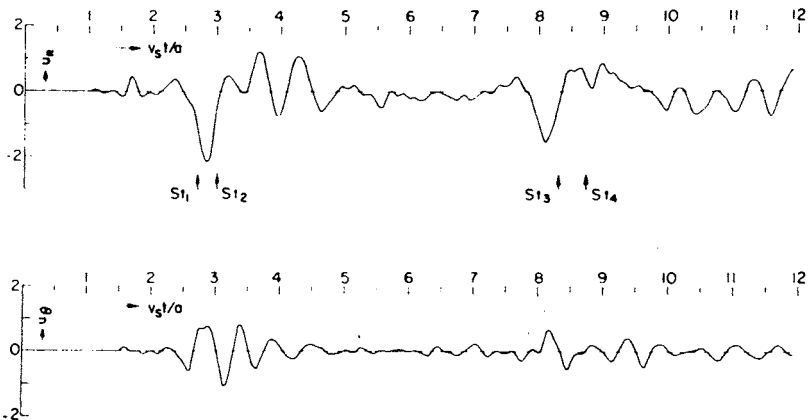


FIG. 60. The radial and the angular components of the displacement at distance  $\theta = 170^\circ$  from a point-source located at the core boundary,  $\delta = 0.1$ . Arrows indicate arrival times of Stoneley waves in a half-space.

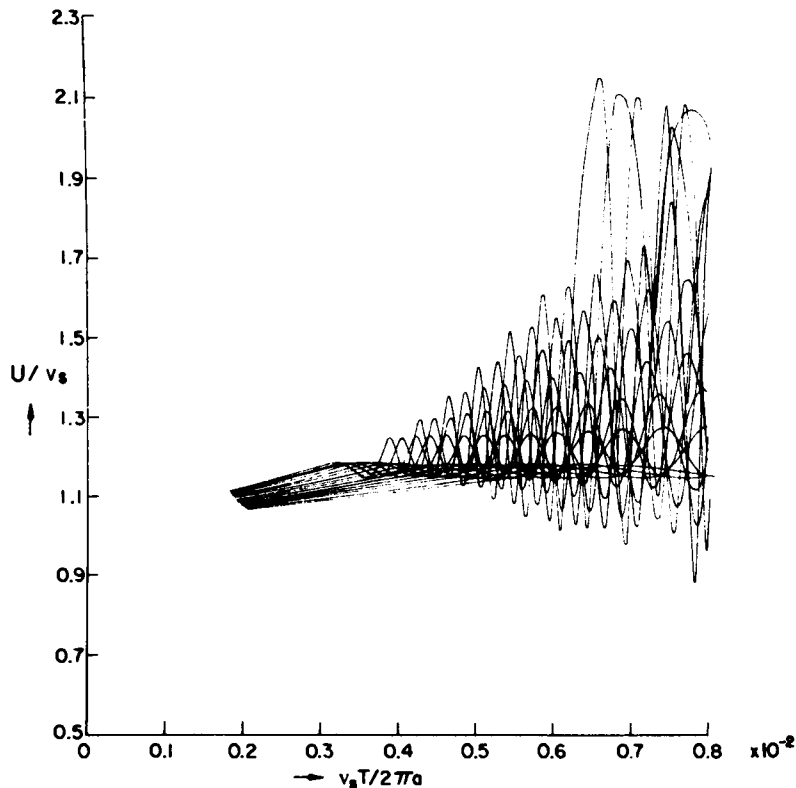


FIG. 61. The group velocity  $U$  in a layered sphere as function of  $T$  in the range of periods  $0.003 \leq v_s T / 2\pi a \leq 0.008$ ,  $15 \leq j \leq 30$ .

FIG. 62. The radial and the angular components of displacement at distance  $\theta = 90^\circ$  from a point source located at depth  $a - b = a/32$ ,  $\delta = 0.01$ . Horizontal lines indicate arrival times of higher mode surface waves  $T_{lk}$ . Arrows indicate arrival times of Rayleigh waves  $R_{1l}$ .

FIG. 63. The radial and the angular components of displacement at distance  $\theta = 170^\circ$  from a point source located at depth  $a - b = a/32$ ,  $\delta = 0.01$ . Horizontal lines indicate arrival times of higher mode surface waves  $T_{lk}$ . Arrows indicate arrival times of Rayleigh waves  $R_{1l}$ .

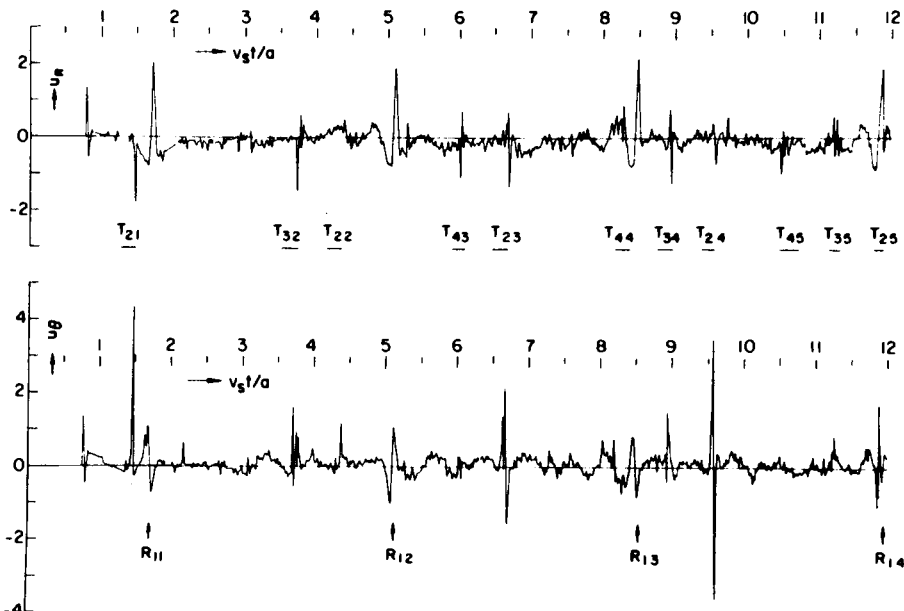


FIG. 62.

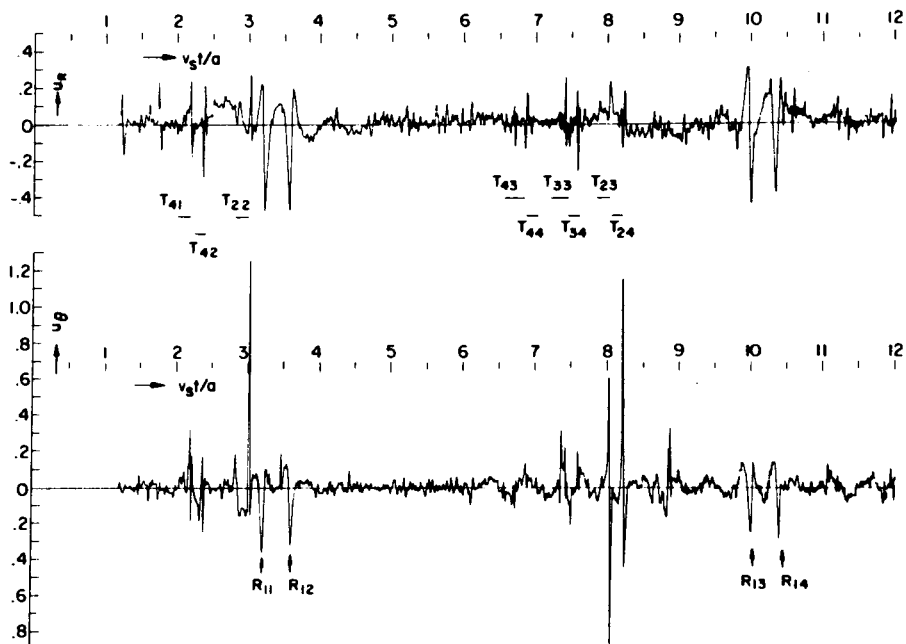


FIG. 63.

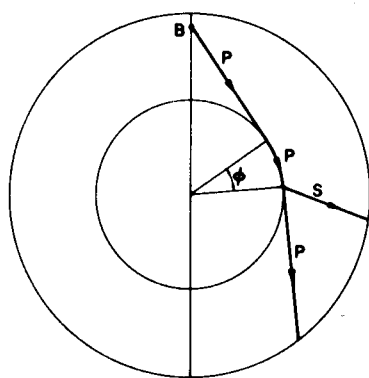
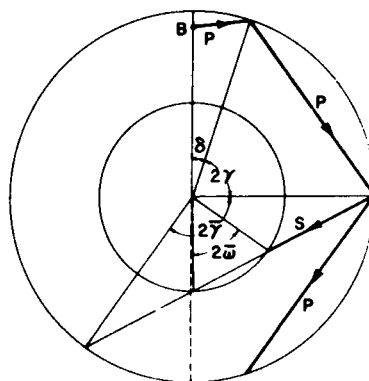
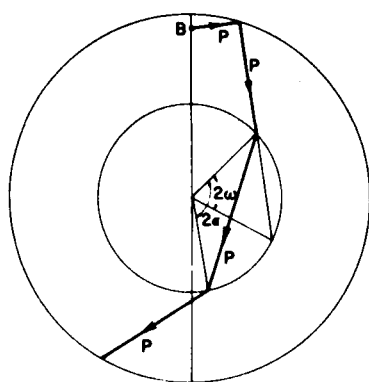


FIG. 64. Reflected rays in the layered sphere and diffraction at the core.  $\phi$  denotes the angle of diffraction.

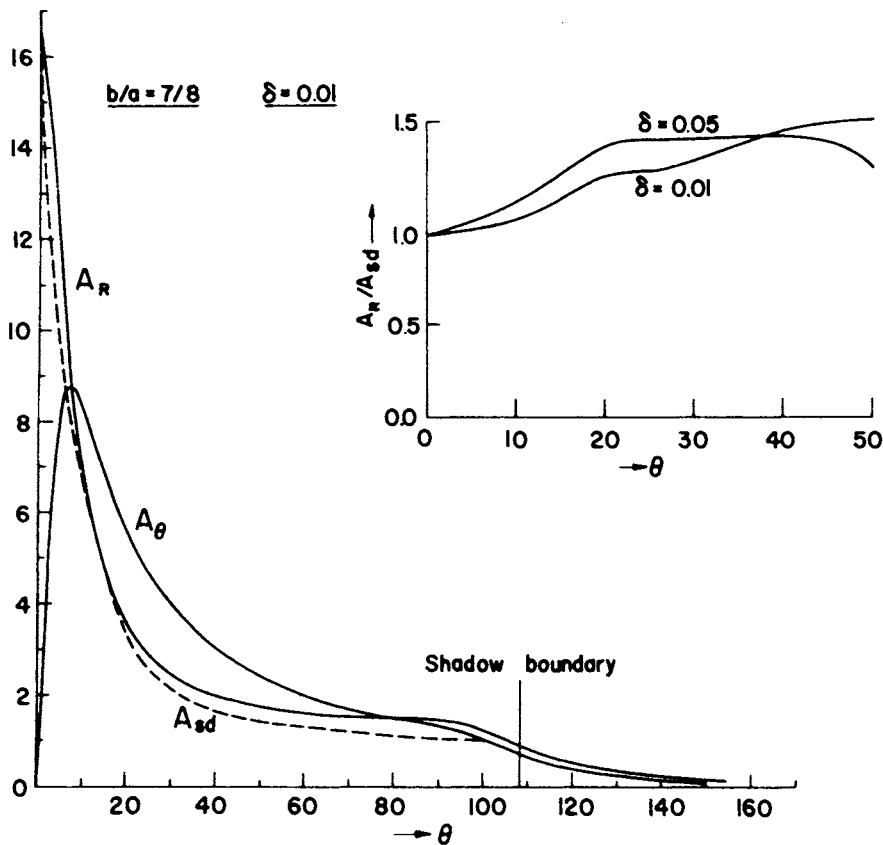


FIG. 65. The amplitude of the radial  $A_R$  and angular  $A_\theta$  components of the direct pulse and of the first core diffraction as a function of the angular distance  $\theta$ .  $A_R$  and  $A_\theta$  are results of the complete solution.  $A_{sd}$  is the amplitude of the radial component in a steepest descent approximation. The insert curves show  $A_R/A_{sd}$  for pulse widths determined by  $\delta = 0.01$  and  $\delta = 0.05$ .

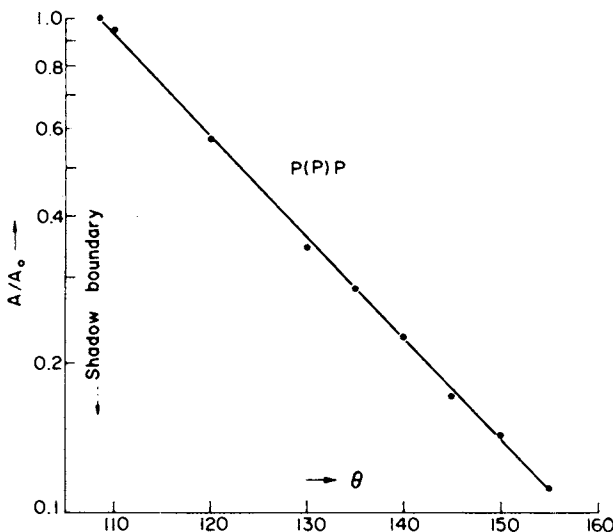


FIG. 66. The amplitude  $A$  of  $P(P)P$  as a function of the angular distance  $\theta$ , in units of the amplitude at the shadow boundary.  $a - b = a/8$ .

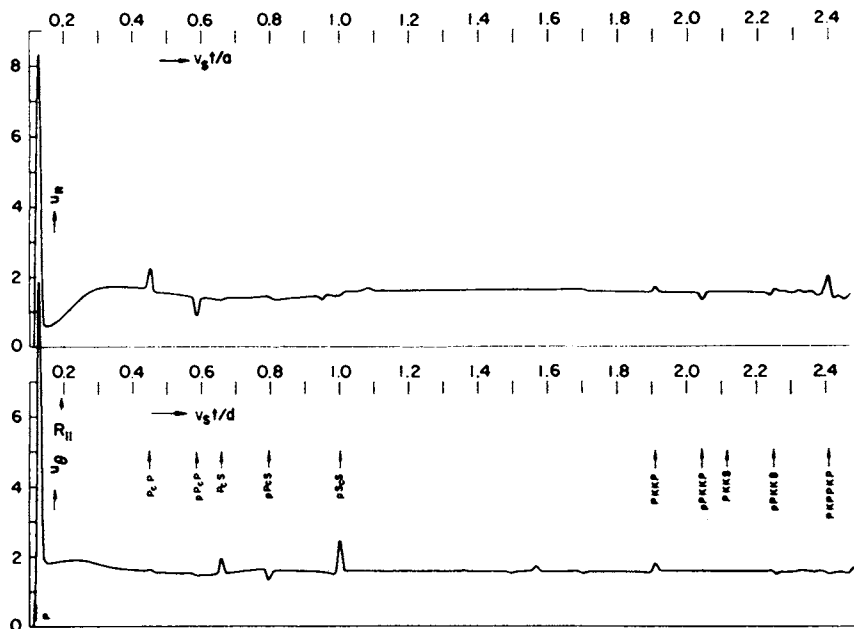


FIG. 67. The radial  $u_R$  and the angular  $u_\theta$  components of displacement at an angular distance  $\theta = 10^\circ$  from a point source located at depth  $a - b = a/8$ ,  $\delta = 0.01$ .

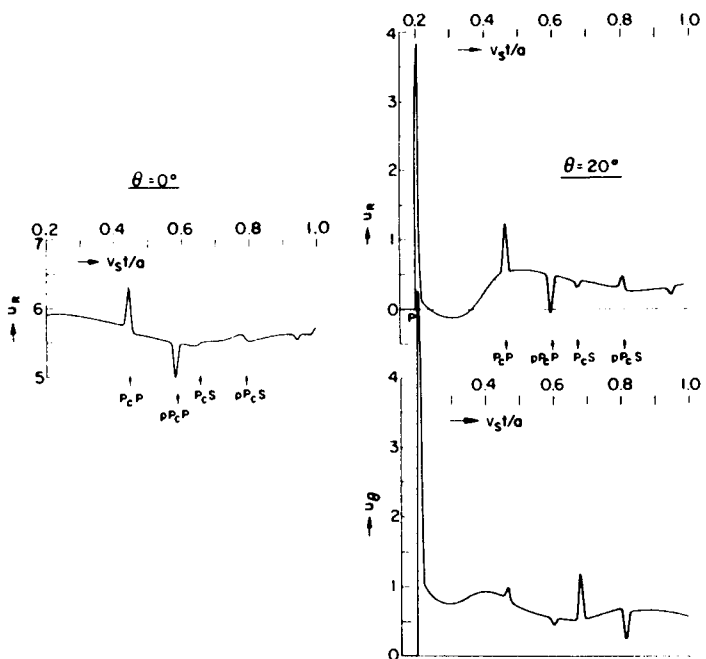


FIG. 68. The radial  $u_R$  and the angular  $u_\theta$  components of displacement at angular distances  $\theta = 0^\circ$  and  $20^\circ$  from a point source located at depth  $a - b = a/8$ .

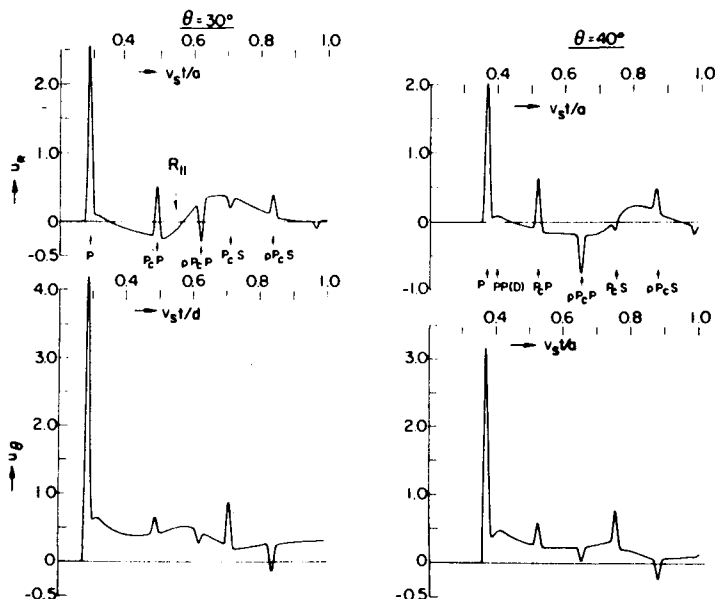


FIG. 69. The radial  $u_R$  and the angular  $u_\theta$  components of displacement at angular distances  $\theta = 30^\circ$  and  $40^\circ$  from a point source located at depth  $a - b = a/8$ .

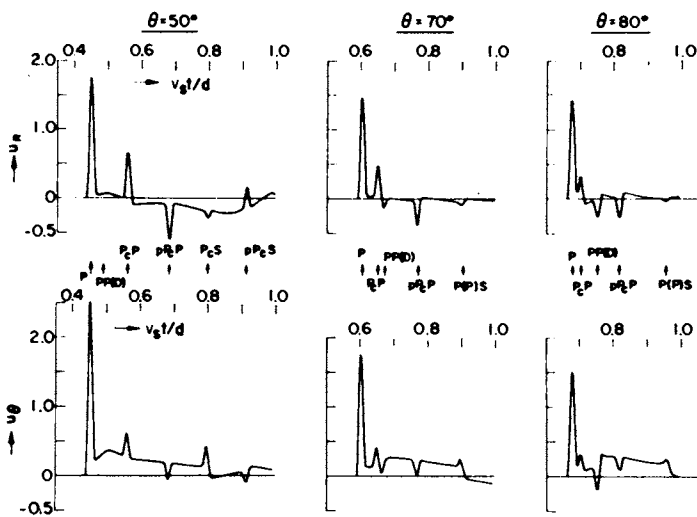


FIG. 70. The radial  $u_R$  and the angular  $u_\theta$  components of displacement at angular distances  $\theta = 50^\circ$ ,  $70^\circ$ , and  $80^\circ$  from a point source located at depth  $a - b = a/8$ .

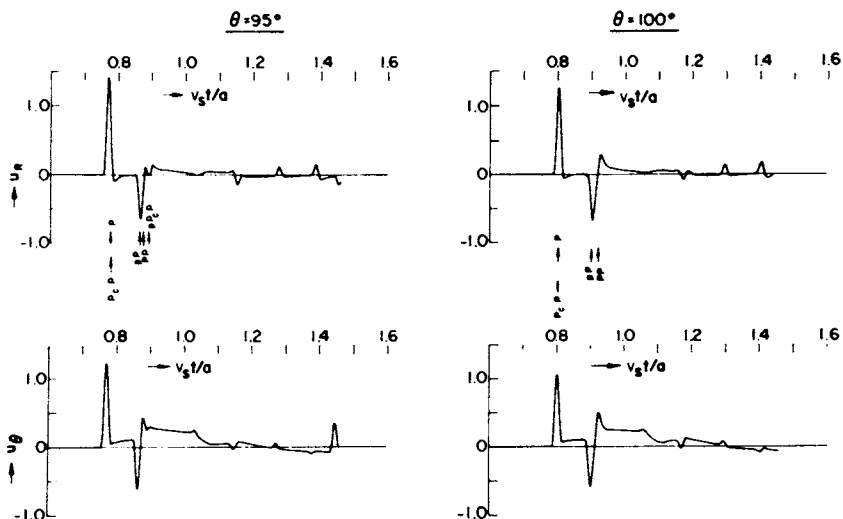


FIG. 71. The radial  $u_R$  and the angular  $u_\theta$  components of displacement at angular distances  $\theta = 95^\circ$  and  $100^\circ$  from a point source at depth  $a - b = a/8$ .

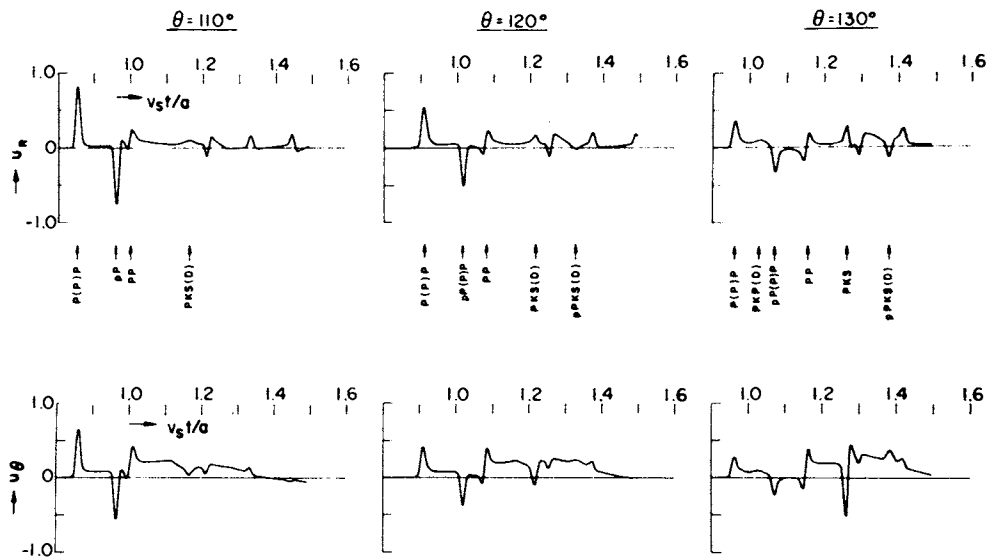


FIG. 72. The radial  $u_r$  and the angular  $u_\theta$  components of displacement at angular distances  $\theta = 110^\circ, 120^\circ$ , and  $130^\circ$  from a point source located at depth  $a - b = a/8$ .

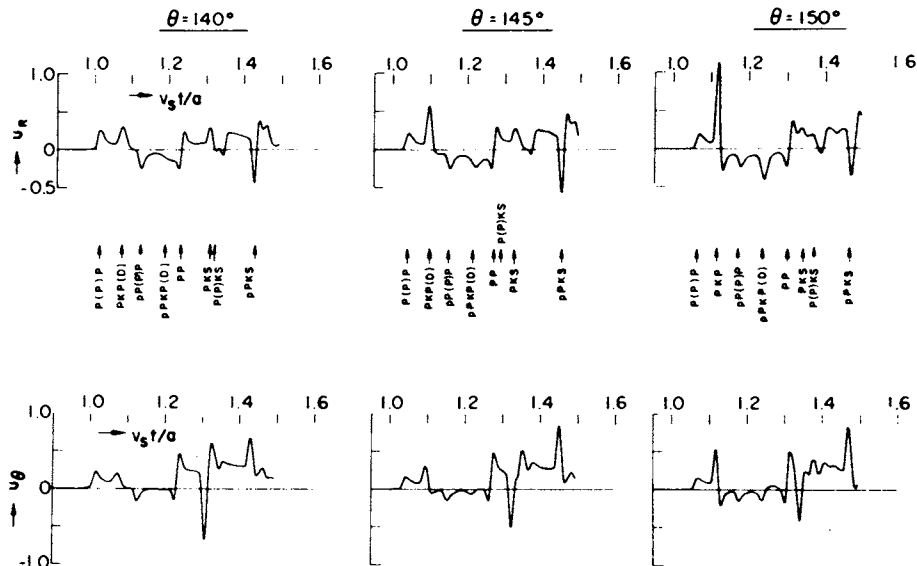


FIG. 73. The radial  $u_r$  and the angular components of displacement at angular distance  $\theta = 140^\circ, 145^\circ$ , and  $150^\circ$  from a point source located at depth  $a - b = a/8$ .

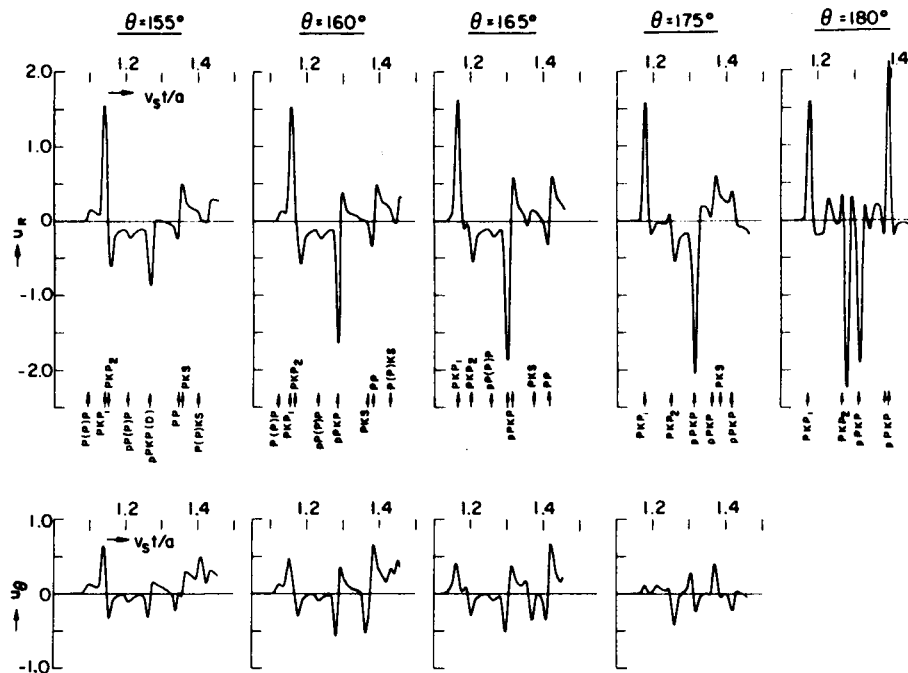


FIG. 74. The radial  $u_R$  and the angular  $u_\theta$  components of displacement at angular distances  $\theta = 155^\circ$ ,  $160^\circ$ ,  $165^\circ$ ,  $175^\circ$ , and  $180^\circ$  from a point source located at depth  $a - b = a/8$ .

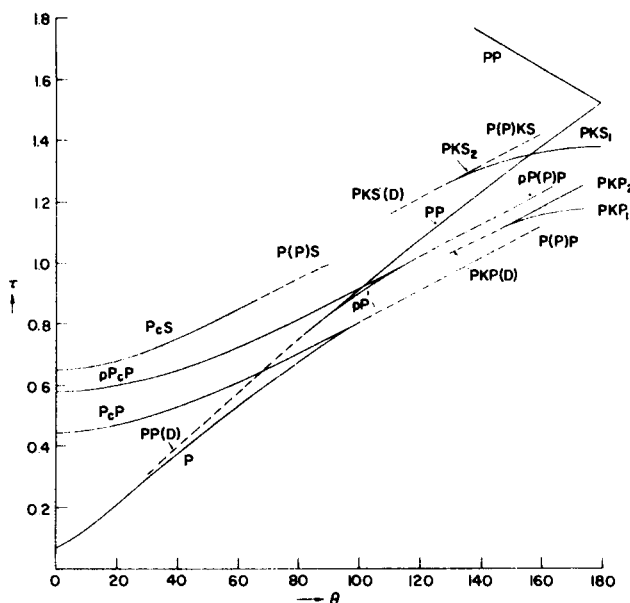


FIG. 75. Arrival times of pulses at angular distance  $\theta$  from a source at depth  $a - b = a/8$  in the layered sphere.

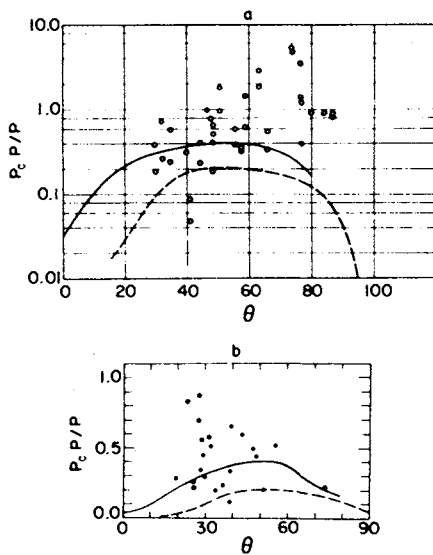


FIG. 76. Amplitude ratio of  $P_e P$  to  $P$ . Circles denote observed values. The solid curves show the complete theoretical solution; the dashed curves show the calculation for plane waves. (a) Observed values from various sources. (b) Observed values from explosive sources.

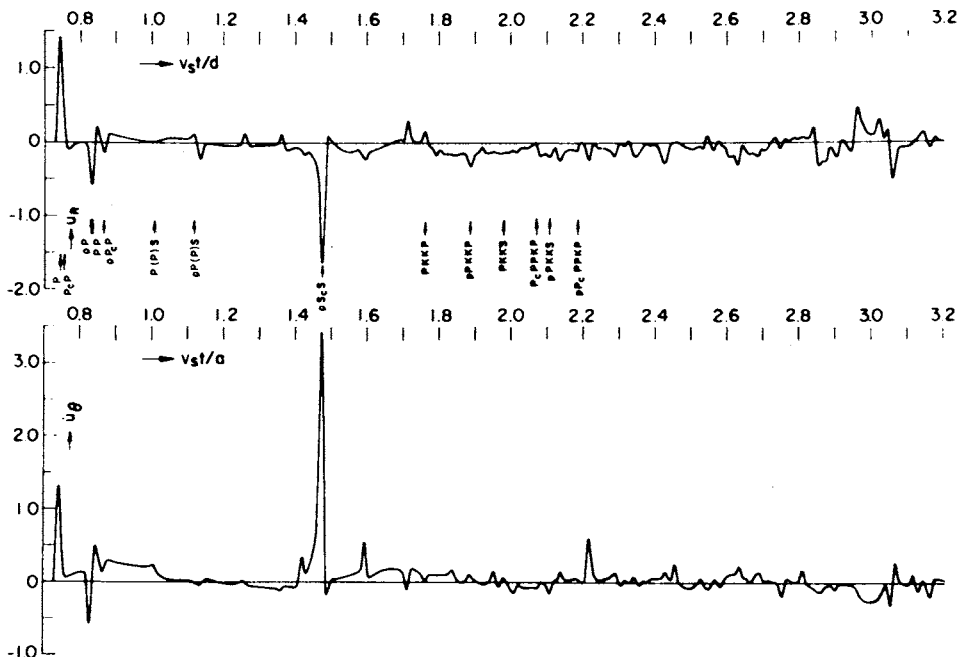


FIG. 77. The radial  $u_R$  and the angular  $u_\theta$  components of displacement at angular distance  $\theta = 90^\circ$  from a point source located at depth  $a - b \approx a/8$ .

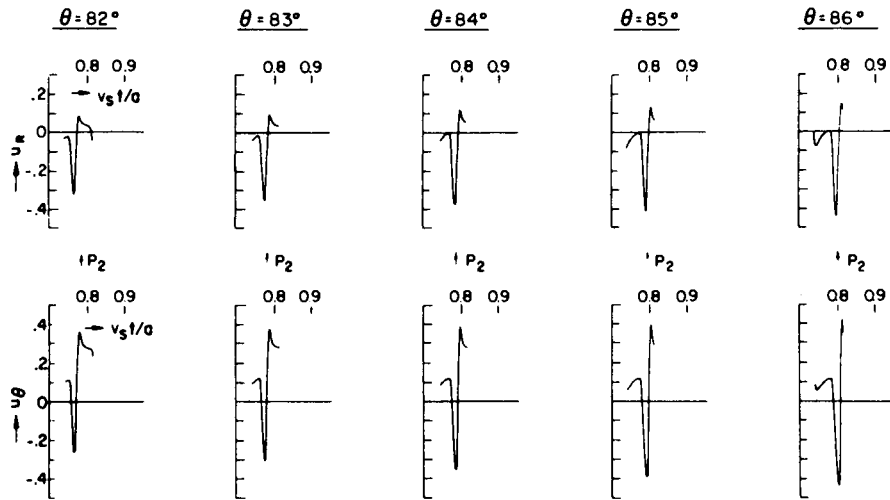


FIG. 78. The radial  $u_R$  and the angular  $u_\theta$  components of the  $P_2$  pulse at  $82^\circ \leq \theta \leq 86^\circ$ . The source is located at depth  $a - b = a/8$ . The caustic point is at  $\theta = 82^\circ$ .

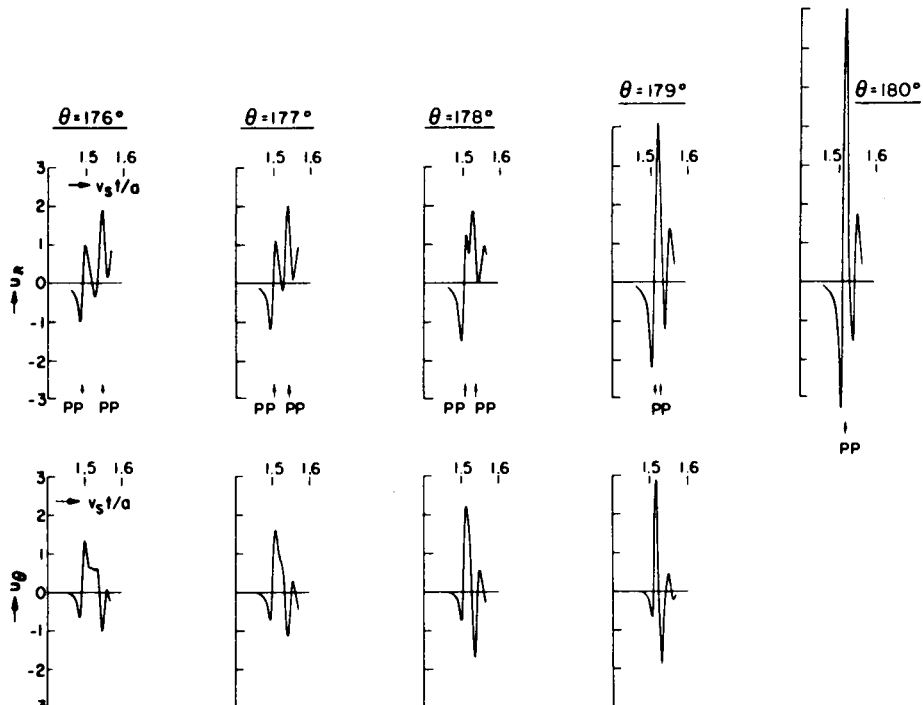


FIG. 79. The radial  $u_R$  and the angular  $u_\theta$  components of the  $P_2$  pulse traced at distances near  $\theta = 180^\circ$ , for a source located at depth  $a - b = a/8$ .

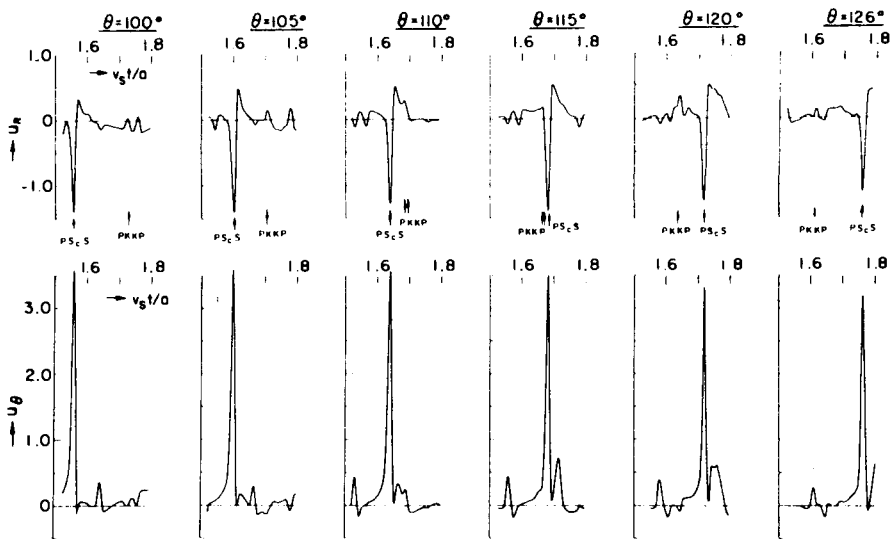


FIG. 80. The radial  $u_R$  and the angular  $u_\theta$  components of displacement at distances  $\theta = 100^\circ, 105^\circ, 110^\circ, 115^\circ, 120^\circ$ , and  $126^\circ$  from a point source located at depth  $a - b = a/8$ , in the time interval  $1.5 \leq v_s t/a \leq 1.8$ .

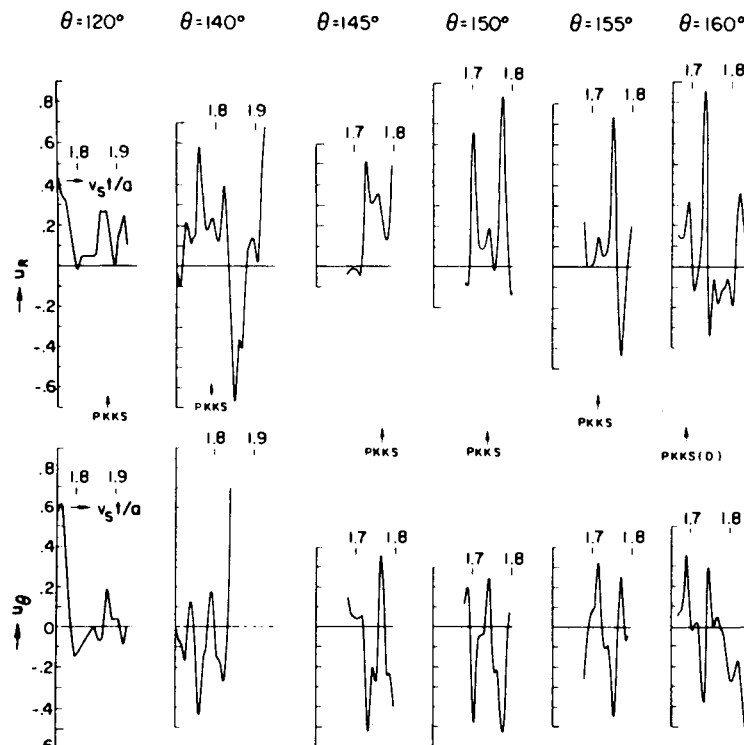


FIG. 81. The radial  $u_R$  and the angular  $u_\theta$  components of displacement at distances  $\theta = 120^\circ, 140^\circ, 145^\circ, 150^\circ, 155^\circ$ , and  $160^\circ$  from a point source located at depth  $a - b = a/8$ , in the time interval  $1.6 \leq v_s t/a \leq 1.9$ .

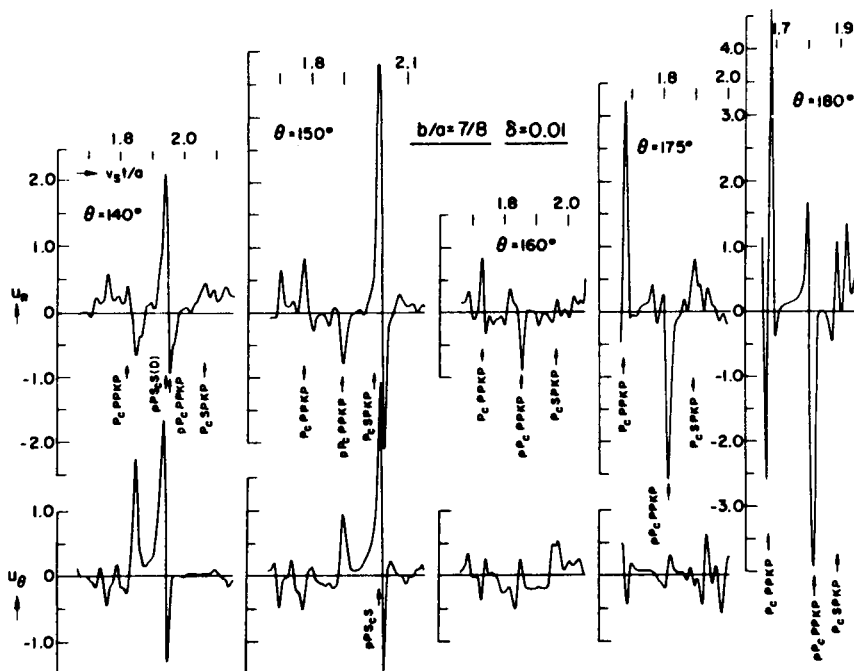


FIG. 82. The radial  $u_R$  and the angular  $u_\theta$  components of displacement at distances  $\theta = 140^\circ, 150^\circ, 160^\circ, 170^\circ$ , and  $180^\circ$  from a point source located at depth  $a - b = a/8$ , in the time interval  $1.6 \leq v_s t/a \leq 2.1$ .

### E. RESULTS FOR THE LATERALLY HETEROGENEOUS SPHERE

The occurrence of lateral heterogeneity in the earth's upper mantle has recently been discussed by several authors (Toksoz *et al.*, 1967, 1969; Greenfield and Sheppard, 1969.) The finite difference scheme of Section II, A has been applied not only to spherically symmetric models, for which the equations of motion are separable, but also to such a laterally heterogeneous sphere.

As a simple example of lateral heterogeneity, Alterman *et al.* (1970) considered the configuration depicted in Fig. 83. A conical wedge is defined by  $d \leq R \leq a$  and  $0 \leq \theta \leq \theta_1$ .

The elastic material inside the wedge has parameters  $v_{s1}, v_{p1}, \rho_1$  while in the remaining part of the sphere the parameters are  $v_{s2}, v_{p2}, \rho_2$ . Instead of imposing boundary conditions on the surfaces of the wedge and on its edges, the complete equations (54)–(58) of Section II,A.4,b are applied. They allow for variation of the elastic parameters both in radial and in angular direction.

The transition at the boundary of the wedge is performed over two grid points near the boundaries of the wedge. The wedge causes reflection and diffraction which is exhibited in the computed results. Let us consider the specific values of parameters  $d = 0.7a$  and  $\theta_1 = 36^\circ$ . A comparison is made between:

- (a) a high density, high velocity wedge in which  $\rho_1 = 2\rho_2$ ,  $v_{s1} = 1.1 v_{s2}$ ,
  - (b) a high velocity wedge in which  $\rho_1 = \rho_2$ ,  $v_{s1} = 1.1 v_{s2}$ ,
  - (c) a high density wedge in which  $\rho_1 = 2\rho_2$ ,  $v_{s1} = v_{s2}$ ,
  - (d) a low velocity low density wedge in which  $\rho_1 = 0.5\rho_2$ ,  $v_{s1} = v_{s2}/1.1$ ,
- and

- (e) an empty wedge  $\rho_1 = 0$ ,  $v_{s1} = 0$ .

In all cases  $v_p = \sqrt{3} v_s$ .

The motion of the sphere due to a source at  $b = 0$  in these five cases is compared with results for homogeneous sphere. Figures 84-86 show  $u_R$  at the points  $\theta = 60^\circ$ ,  $R = 0.4a$ ;  $\theta = 10^\circ$ ,  $R = 0.8a$ ; and  $\theta = 180^\circ$ ,  $R = 0.6a$ , respectively. The point  $R = 0.8a$ ,  $\theta = 10^\circ$  in Fig. 85 is inside the wedge. The first arriving pulse is the transmitted  $PP_1$ . The index 1 indicates a ray path inside the wedge. The next arriving pulse is  $P_cP_1$ . Here "c" indicates that the pulse arrives at an edge of the wedge and diffraction takes place. An index "i" indicates reflection at a boundary surface of the wedge. Examples of ray paths of pulses  $P_cP$  and  $P_iP$  are indicated in Fig. 83. As another example  $PP_1P_{1i}P_1$  is transmitted into the wedge, reflected at the surface, and then reflected back into the wedge from the interface at  $R = d$ . Figure 85 shows that the amplitude of reflected pulses in the high density wedge are smaller than in the homogeneous sphere while in the low density wedge they are larger. The amplitude of pulses which are reflected at the interface are smaller in cases (a) and (c) for a high density wedge than in (d) for a low density wedge. Curve (b) differs only slightly from the homogeneous case. Two diffracted pulses are indicated:  $P_cP_1$  and  $PP_{1c}P$ . Their amplitudes are small at the given location.

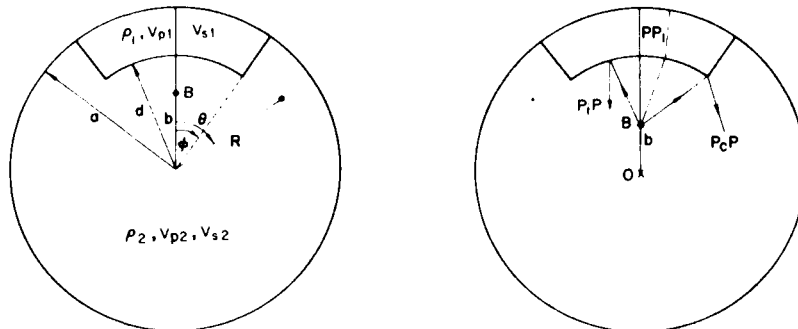


FIG. 83. Point source located at **B** in the sphere of radius  $a$ . The sphere has density  $\rho_2$  and elastic velocities  $v_{p2}$ ,  $v_{s2}$ . It contains a conical wedge of density  $\rho_1$  and velocities  $v_{p1}$ ,  $v_{s1}$ .

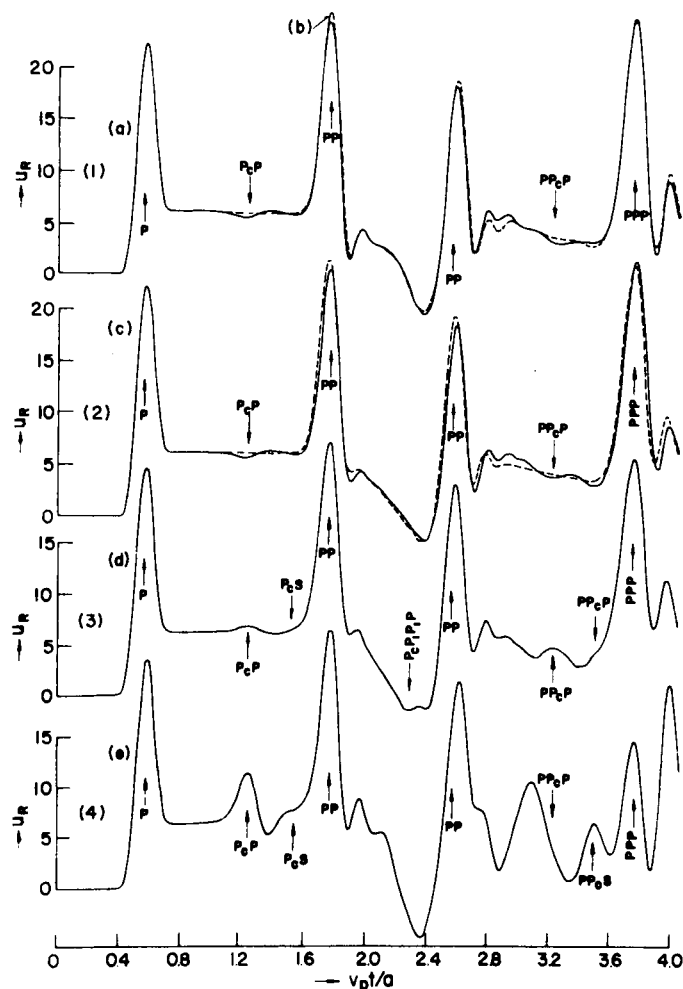


FIG. 84. Radial displacement at  $\theta = 60^\circ$  and distance  $R = 0.4a$  from the center of the heterogeneous sphere. The curves (1) show the solution for (a)  $v_{p1} = 1.1v_{p2}$ ,  $v_{s1} = 1.1v_{s2}$ ,  $\rho_1 = 2\rho_2$  (solid curve) and (b) for the above velocities and  $\rho_1 = \rho_2$  (dashed curve). The curves (2) show the solution for (c)  $v_{p1} = v_{p2}$ ,  $v_{s1} = v_{s2}$ ,  $\rho_1 = 2\rho_2$  (solid curve), and  $\rho_1 = 2\rho_2$  (dashed curve). The curve (3) shows the solution for (d)  $v_{p1} = v_{p2}/1.1$ ,  $v_{s1} = 1.1v_{s2}$ ,  $\rho_1 = 0.5\rho_1$ . The curve (4) is the solution for (e)  $v_{p1} = 0$ ,  $v_{s1} = 0$ ,  $\rho_1 = 0$ .

Figure 84 shows the variation in time of  $u_R$  at  $\theta = 60^\circ$ ,  $R = 0.4a$  outside the wedge. Some well separated diffracted pulses as  $P_cP$ ,  $P_S$ ,  $PP_cP$ ,  $PP_S$  are clearly exhibited. The direction of the diffracted pulses changes with changing density. The amplitude of the diffracted pulses is largest in case (e) for the empty wedge.

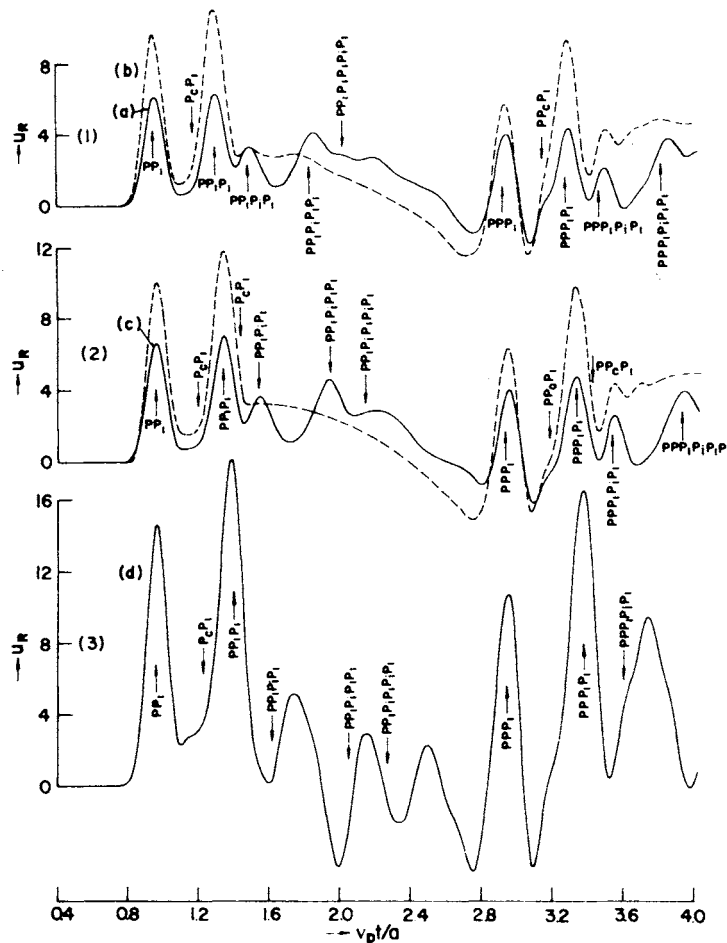


FIG. 85. Radial displacement at  $\theta = 10^\circ$  and distance  $R/a = 0.8$  from the center of the heterogeneous sphere. The curves (1) show the solution for (a)  $v_{p1} = 1.1v_{p2}$ ,  $v_{s1} = 1.1v_{s2}$ ,  $\rho_1 = 2\rho_2$  (solid curve) and (b) for the above velocities and  $\rho_1 = \rho_2$  (dashed curve). The curves (2) show the solution for (c)  $v_{p1} = v_{p2}$ ,  $v_{s1} = v_{s2}$ ,  $\rho_1 = 2\rho_2$  (solid curve) and  $\rho_1 = \rho_2$  (dashed curve). The curve (3) shows the solution for (d)  $v_{p1} = v_{p2}/1.1$ ,  $v_{s1} = 1.1v_{s2}$ ,  $\rho_1 = 0.5\rho_2$ .

Figure 86 shows the influence of the wedge at a distant point  $\theta = 180^\circ$ ,  $R = 0.6a$ . As expected, the direct pulse  $P$  and the first once-reflected  $PP$  are the same in all cases, unchanged by the wedge. The  $P_cP$  and  $P_1P$  change sign with changing density. The  $PPP_1P_1P$  pulse has the largest amplitude for the high velocity wedges and is small for the sphere with the low velocity wedge. Several other pulses are indicated in the figure.

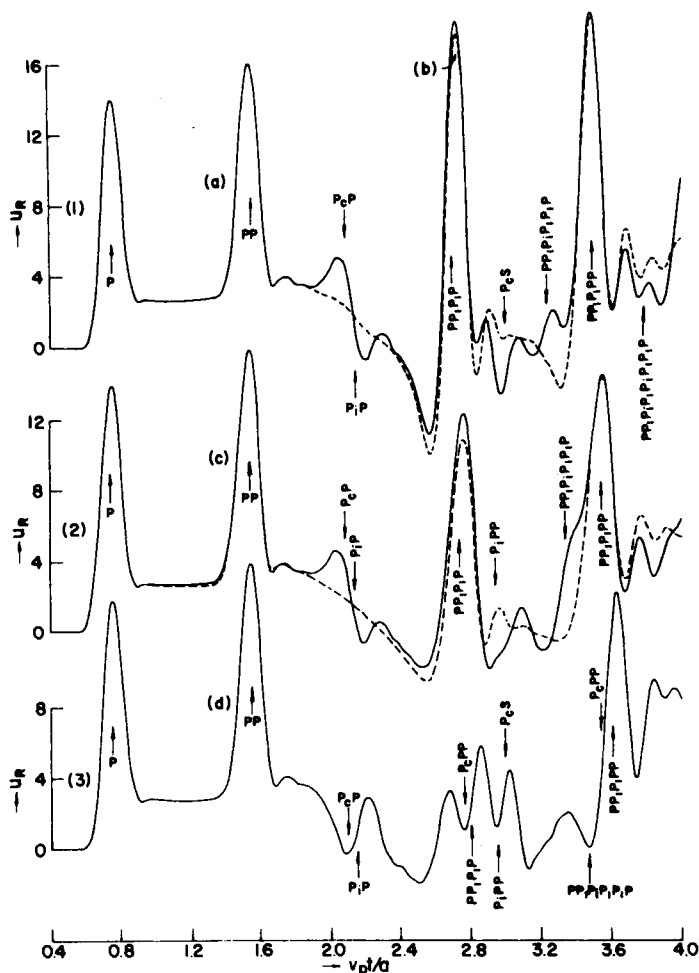


FIG. 86. Radial displacement at  $\theta \approx 180^\circ$  at distance  $R/a = 0.6$  from the center of the heterogeneous sphere. The curves (1) show the solution for (a)  $v_{p1} = 1.1v_{p2}$ ,  $v_{s1} = 1.1v_{s2}$ ,  $\rho_1 = 2\rho_2$  (solid curve) and (b) for the above velocities and  $\rho_1 = \rho_2$  (dashed curve). The curves (2) show the solution for (c)  $v_{p1} = v_{p2}$ ,  $v_{s1} = v_{s2}$ ,  $\rho_1 = 2\rho_2$  (solid curve) and  $\rho_1 = \rho_2$  (dashed curve). The curve (3) shows the solution for (d)  $v_{p1} = v_{p2}/1.1$ ,  $v_{s2} = 1.1v_{s1}$ ,  $\rho_1 = 0.5\rho_2$ .

These examples show that the motion of a heterogeneous sphere can be easily derived and analyzed. Further models of a heterogeneous sphere where  $\rho$ ,  $\lambda$ ,  $\mu$  are arbitrary functions of the coordinates  $R$  and  $\theta$  can be treated by the same method.

#### IV. Appendix: Equations for the Layered Sphere

The propagation of a pulse from a point source in a layered sphere is obtained by a similar analysis as in Section II, B, 1.

The formal solution and operational interpretation are as follows:

##### A. FORMAL SOLUTION

Consider a sphere of radius  $a$  with a fluid core of radius  $d$  ( $d < a$ ). The core is a homogeneous compressible fluid of density  $\rho_2$ . The mantle consists of a homogeneous isotropic elastic solid having Lamé elastic constants  $\lambda_1$  and  $\mu_1$  and density  $\rho_1$ .

A point source located at a distance  $b$  from the center of the sphere ( $d < b < a$ ) starts to emit at time  $t = 0$  (Fig. 87). The subsequent displacements in the sphere have cylindrical symmetry.

For a seismic source of finite energy, we consider a source that causes a variation in stresses only during a finite time interval and leads to a constant displacement for each particle for  $t \rightarrow \infty$ . To avoid discontinuities of displacement as functions of time, the potential is defined as the third finite difference of a third-order polynomial in time.

The displacement potential of the source is defined in Section II,A,6 by Eq. (86) for  $n = 3$ .

A solution of the wave equations (94) and (95) is sought that satisfies the boundary conditions of zero normal and tangential stresses on the surface of the sphere,  $R = a$ :

$$\begin{aligned} \tau_{RR} &= \gamma \operatorname{div} v + 2\mu \frac{\partial v_R}{\partial R} = 0 \\ \tau_{R\theta} &= \mu \left( \frac{\partial v_\theta}{\partial R} - \frac{v_\theta}{R} - \frac{\partial v_R}{\partial \theta} \right) = 0 \quad \text{at } R = a. \end{aligned} \quad (235)$$

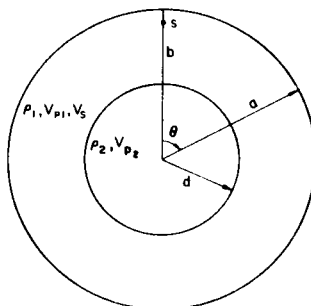


FIG. 87. Point sources located at distance  $b$  from the center of the layered sphere.

On the interface the normal and tangential stresses are continuous

$$\tau_{RR1} = \tau_{RR2}, \quad \tau_{R\theta1} = \tau_{R\theta2} = 0 \quad \text{at } R = d, \quad (236)$$

and the radial component of displacement is continuous

$$v_{R1} = v_{R2} \quad \text{at } R = d. \quad (237)$$

Here the subscript 1 refers to the mantle and the subscript 2 refers to the core. When a Laplace transform multiplied by the transform parameter  $p$  is performed,

$$f(R, \theta, p) = p \int_0^{\infty} (R, \theta, t) e^{-pt} dt, \quad (238)$$

the expansion of the initial potential  $f_0$  in Eq. (87) and the solution of the reduced wave equations are given in the form

$$\bar{\Phi} = h_1^{1/2} \frac{\pi A^3}{p^3 b^{1/2}} \sum_{n=0}^{\infty} (n + \frac{1}{2}) P_n(\cos \theta) \{ A_n i_n(h_1 R) + B_n k h_n(h_1 R) \} + f_0 \\ d < R < a, \quad (239)$$

$$f_0 = -(h_1)^{1/2} \frac{\pi A^3}{p^3 b^{1/2}} \sum_{n=0}^{\infty} (n + \frac{1}{2}) k h_n(h_1 R) i_n(h_1 b) (h_1 b)^{1/2} P_n(\cos \theta) \\ b < R < a \quad (240)$$

$$f_0 = -(h_1)^{1/2} \frac{\pi A^3}{p^3 b^{1/2}} \sum_{n=0}^{\infty} (n + \frac{1}{2}) i_n(h_1 R) k h_n(h_1 b) (h_1 b)^{1/2} P_n(\cos \theta) \\ d < R < b$$

$$\bar{M} = h_1^{1/2} \frac{\pi A^3}{p^3 b^{1/2}} \sum_{n=0}^{\infty} (n + \frac{1}{2}) P_n(\cos \theta) \{ C_n i_n(k R) + E_n k h_n(k R) \} \\ d < R < a. \quad (241)$$

In the core

$$\bar{\Phi} = h_2^{1/2} \frac{\pi A^3}{p^3 b^{1/2}} \sum_{n=0}^{\infty} (n + \frac{1}{2}) P_n(\cos \theta) F_n i_n(h_2 R), \quad \bar{M} = 0, \quad R < d. \quad (242)$$

Here  $i_n$  and  $kh_n$  are modified spherical Bessel functions of the first and second kind, respectively.  $P_n$  is the Legendre polynomial of order  $n$ . Also

$$k = p/v_s, \quad h_1 = p/v_{p1}, \quad h_2 = p/v_{p2}. \quad (243)$$

$v_s$ ,  $v_{p1}$  are the shear and compressional wave velocities in the mantle, and  $v_{p2}$  is the P-wave velocity in the core. The solution for the complete source  $\phi_s$  is later obtained by finite-differencing.

The coefficients  $A_n$ ,  $B_n$ ,  $C_n$ ,  $E_n$ , and  $F_n$  are determined by inserting (239), (241), and (242) in the boundary conditions, leading to a set of five equations:

$$\begin{aligned} A_n g(i_n; h_1 a) + B_n g(kh_n; h_1 a) + C_n n(n+1) f(i_n; ka) + E_n n(n+1) f(kh_n; ka) \\ = (h_1 b)^{1/2} i_n(h_1 b) g(kh_n; h_1 a), \end{aligned} \quad (244)$$

$$\begin{aligned} A_n f(i_n; h_1 a) + B_n f(kh_n; h_1 a) + C_n \{g(i_n; ka) + f(i_n; ka)\} \\ + E_n \{g(kh_n; ka) + f(kh_n; ka)\} \\ = (h_1 b)^{1/2} i_n(h_1 b) f(kh_n; h_1 a), \end{aligned} \quad (245)$$

$$\begin{aligned} A_n h_1 d i_n'(h_1 d) + B_n h_1 d k h_n'(h_1 d) + C_n n(n+1) i_n(kd) + E_n n(n+1) k h_n(kd) \\ - F_n h_2 d i_n'(h_2 d) = h_2 d i_n'(h_1 d) k h_n(h_1 b) (h_1 b)^{1/2}, \end{aligned} \quad (246)$$

$$\begin{aligned} \rho_1 A_n g(i_n; h_1 d) + \rho_1 B_n g(kh_n; h_1 d) + \rho_1 C_n n(n+1) f(i_n; kd) \\ + \rho_1 E_n n(n+1) f(kh_n; kd) - F_n \rho_2 k^2 d^2 i_n(h_2 d) \\ = (h_1 b)^{1/2} k h_n(h_1 b) \rho_1 g(i_n; h_1 d), \end{aligned} \quad (247)$$

$$\begin{aligned} A_n f(i_n; h_1 d) + B_n f(kh_n; h_1 d) + C_n \{g(i_n; kd) + f(i_n; kd)\} \\ + E_n \{g(kh_n; kd) + f(kh_n; kd)\} = (h_1 b)^{1/2} k h_n(h_1 b) f(i_n; h_1 d). \end{aligned} \quad (248)$$

Here

$$\begin{aligned} f(i_n; ay) &= 2ayi_n'(ay) - 2i_n(ay). \\ g(i_n; ay) &= i_n(ay)\{a^2 k^2 + 2n(n+1)\} - 4ayi_n'(ay). \end{aligned} \quad (249)$$

Similar definitions apply when  $i_n$  is replaced by the function  $kh_n$ .

The period equations for the layered sphere is given by the vanishing of the determinant of coefficients  $D_n$  of Eqs. (244)-(248).

$D_n$ 

$$\begin{vmatrix} g(i_n; h_1 a) & g(kh_n; h_1 a) & n(n+1)f(i_n; ka) & n(n+1)f(kh_n; ka) & 0 \\ f(i_n; h_1 a) & f(kh_n; h_1 a) & g(i_n; ka) + f(i_n; ka) & g(kh_n; ka) + f(kh_n; ka) & 0 \\ h_1 d i_n'(h_1 d) & h_1 d k h_n'(h_1 d) & n(n+1)i_n(kd) & n(n+1)k h_n(kd) & -h_2 d i_n'(h_2 d) \\ g(i_n; h_1 d) & g(kh_n; h_1 d) & n(n+1)f(i_n; kd) & n(n+1)f(kh_n; kd) & -(\rho_2/\rho_1)k^2 d^2 i_n(h_2 d) \\ f(i_n; h_1 d) & f(kh_n; h_1 d) & g(i_n; kd) + f(i_n; kd) & g(kh_n; kd) + f(kh_n; kd) & 0 \end{vmatrix} = 0. \quad (250)$$

The coefficients  $A_n$ ,  $B_n$ ,  $C_n$ ,  $E_n$ , and  $F_n$  are expressed according to Eqs. (244)–(249) with

$$\begin{aligned} A_n &= \hat{A}_n/D_n, & B_n &= \hat{B}_n/D_n, & C_n &= \hat{C}_n/D_n, \\ E_n &= \hat{E}_n/D_n, & F_n &= \hat{F}_n/D_n, \end{aligned}$$

as quotients of determinants.  $\hat{A}_n$ ,  $\hat{B}_n$ ,  $\hat{C}_n$ ,  $\hat{E}_n$ , and  $\hat{F}_n$  are determinants of the same order as  $D_n$  constructed according to Cramer's rule.

The operational form of displacements at the surface  $R = a$ , denoted  $\bar{u}_R$  and  $\bar{u}_\theta$  for the partial potential  $f_0$ , is

$$\begin{aligned} \hat{u}_R &= h_1^{1/2} \frac{\pi A^3}{p^3 b^{1/2}} \sum_{n=0}^{\infty} (n + \frac{1}{2}) P_n(\cos \theta) \frac{1}{a D_n} \\ &\times \{h_1 a i_n'(h_1 a) \hat{A}_n + h_1 a k h_n'(h_1 a) \hat{B}_n - h_1 a k h_n'(h_1 a) i_n(h_1 b) (h_1 b)^{1/2} D_n \\ &+ n(n+1) i_n(ka) \hat{C}_n + n(n+1) k h_n(ka) \hat{E}_n\}, \end{aligned} \quad (251)$$

and

$$\begin{aligned} \hat{u}_\theta &= h_1^{1/2} \frac{\pi A^3}{p^3 b^{1/2}} \sum_{n=0}^{\infty} (n + \frac{1}{2}) \frac{d}{d\theta} P_n(\cos \theta) \frac{1}{a D_n} \\ &\times \{i_n(h_1 a) \hat{A}_n + k h_n(h_1 a) \hat{B}_n - (h_1 b)^{1/2} i_n(h_1 b) k h_n(h_1 a) D_n \\ &+ [i_n(ka) + k a i_n'(ka)] \hat{C}_n + [k h_n(ka) + k a k h_n'(ka)] \hat{E}_n\}. \end{aligned} \quad (252)$$

## B. TIME-DEPENDENT SOLUTION

The operational inverse of Eq. (252) is obtained by evaluating

$$u_R(\theta, \tau) = \frac{1}{2\pi i} \int_{\gamma-i\infty}^{\gamma+i\infty} \bar{u}_R(\theta, z) e^{\tau z} \frac{dz}{z}, \quad (253)$$

where

$$r = v_s t/a, \quad z = ap/v_s = ka.$$

The integral in (253) is expressed as a sum of residues at the poles of the integrand. All the poles are on the imaginary axis. The nonzero poles are simple poles, whereas at  $z = 0$  there is a third-order pole. The result, after taking third finite differences, and going over from the partial potential  $f_0$  to  $\phi_0$  in Eq. (86), is

$$u_R(\theta, r) = \sum_{n=0}^{\infty} (2n+1) P_n(\cos \theta) \left\{ \sum_{j=1}^r B_{jn} \cos(r - 1.5\delta) + \text{res}_{n0} \right\}, \quad (254)$$

where  $z = \pm iy_{jn}$  are the zeros of  $D_n = 0$  in Eq. (250) and  $\delta = v_s \Delta / a$ . The term  $\text{res}_{n0}$  denotes the residue at  $z = 0$ , and

$$B_{jn} = 2i U_{jn} \delta^{-3} \sin^3(\delta y_{jn}/2), \quad (255)$$

$$\begin{aligned} U_{jn} = & \left\{ \frac{1}{z^4 D_n'} \left( \frac{v_s z}{v_{p1}} \frac{b}{a} \right)^{1/2} \left[ \frac{v_s z}{v_{p1}} i_n' \left( \frac{v_s z}{v_{p1}} \right) \hat{A}_n + \frac{v_s z}{v_{p1}} k h_n' \left( \frac{v_s z}{v_{p1}} \right) \hat{B}_n - \frac{v_s z}{v_{p1}} \right. \right. \\ & \times k h_n' \left( \frac{v_s z}{v_{p1}} \right) i_n \left( \frac{v_s z}{v_{p1}} \frac{b}{a} \right) \left( \frac{v_s z}{v_{p1}} \frac{b}{a} \right)^{1/2} \\ & \left. \left. \times D_n + n(n+1)i_n(z)\hat{C}_n + n(n+1)k h_n(z)\hat{E}_n \right] \right\} \\ & z = iy_{jn}. \end{aligned} \quad (256)$$

$D_n'$  is the derivative of  $D_n$  in Eq. (250) with respect to  $z$ .

The angular component of displacement is found in a similar manner by starting from (253):

$$u_\theta(\theta, r) = \sum_{n=1}^{\infty} (2n+1) \frac{d}{d\theta} P_n(\cos \theta) \left\{ \sum_{j=1}^r C_{jn} \cos(r - 1.5\delta) y_{jn} + \text{res}_{n0}' \right\}, \quad (257)$$

$$C_{jn} = 2i V_{jn} \delta^{-3} \sin^3(\delta y_{jn}/2), \quad (258)$$

$$\begin{aligned} V_{jn} = & \left\{ \frac{1}{z^4 D_n'} \left( \frac{v_s z}{v_{p1}} \frac{b}{a} \right)^{1/2} \left( i_n \left( \frac{v_s z}{v_{p1}} \right) \hat{A}_n + k h_n \left( \frac{v_s z}{v_{p1}} \right) \hat{B}_n - \frac{v_s z}{v_{p1}} \frac{b}{a} i_n \left( \frac{v_s z}{v_{p1}} \frac{b}{a} \right) \right. \right. \\ & \times k h_n \left( \frac{v_s z}{v_{p1}} \right) D_n + (i_n(z) + z i_n'(z)) \\ & \left. \left. \times \hat{C}_n + (k h_n(z) + z k h_n'(z)) \hat{E}_n \right) \right\} \quad z = iy_{jn}. \end{aligned} \quad (259)$$

The components of displacement  $u_R$  and  $u_\theta$  in eqs. (254) and (257) were calculated for model  $\alpha$  (Alterman *et al.*, 1959) which consists of a homogeneous solid mantle enclosing a homogeneous fluid core, with properties equal to the averages in the respective regions of Bullen's model  $B$ :

$$\begin{aligned}\rho_1 &= 4.46 \text{ g/cm}^3, & \rho_2 &= 11.02 \text{ g/cm}^3, \\ v_{p1} &= 11.39 \text{ km/sec}, & v_{p2} &= 9.28 \text{ km/sec}, \\ v_s &= 6.24 \text{ km/sec}, & d/a &= 3473/6371.\end{aligned}$$

The summations in Eqs. (254) and (257) were taken up to values of  $j$  and  $n$  determined by the absolute value of the common spectrum in Eqs. (256) and (258).

#### ACKNOWLEDGMENT

Special thanks are extended to Mr. T. Meyer for help in using the computational facilities of the Computation Center of Tel-Aviv University.

We wish to thank Mrs. Hanna Fibach for her help in preparing the manuscript and Mrs. Rodi Wiener for her work in drafting the many figures.

#### REFERENCES

- ABRAMOVICI, F. (1965). Doctoral Dissertation, Hebrew University, Jerusalem.
- ABRAMOVICI, F., and ALTERMAN, Z. (1965). *Meth. Computat. Phys.* **4**, 349.
- ALEXANDER S. S., and PHINNEY, R. A. (1966). *J. Geophys. Res.* **71**, 5943.
- ALTERMAN, Z., and ABOUDI, J. (1968). *Isr. J. Technol.* **6**, 187.
- ALTERMAN, Z., and ABOUDI, J. (1969). *J. Geophys. Res.* **74**, 2618.
- ALTERMAN, Z. S., and ABOUDI, J. (1970). *Geophys. J. Roy. Astron. Soc.* **21**, 47.
- ALTERMAN, Z., and ABRAMOVICI, F. (1965). *Bull. Seismol. Soc. Amer.* **55**, 821.
- ALTERMAN, Z., and ABRAMOVICI, F. (1966). *Geophys. J. Roy. Astron. Soc.* **11**, 189.
- ALTERMAN, Z., and ABRAMOVICI, F. (1967). *Geophys. J.* **13**, 117.
- ALTERMAN, Z., and KARAL, F. C. (1968). *Bull. Seismol. Soc. Amer.* **58**, 367.
- ALTERMAN, Z., and KORNFIELD, P. (1963). *J. Acoust. Soc. Amer.* **35**, 1649.
- ALTERMAN, Z., and KORNFIELD, P. (1965). *Rev. Geophys.* **3**, 55.
- ALTERMAN, Z., and KORNFIELD, P. (1966). *Geophysics* **31**, 741.
- ALTERMAN, Z. S., and LOEWENTHAL, D. (1969). *Isr. J. Technol.* **7**, 495.
- ALTERMAN, Z. S., and LOEWENTHAL, D. (1970). *Geophys. J. Roy. Astron. Soc.* **20**, 101.
- ALTERMAN, Z. S., and ROTENBERG, A. (1969). *Bull. Seismol. Soc. Amer.* **59**, 347.
- ALTERMAN, Z., JAROSCH, H., and PEKERIS, C. L. (1959). *Proc. Roy. Soc. Ser. A* **252**, 80.
- ALTERMAN, Z. S., ABOUDI, J., and KARAL, F. C. (1970). *Geophys. J. Roy. Astron. Soc.* **11**, 189.
- ALTERMAN, Z., BURRIDGE, R., and LOEWENTHAL, D. (1971). *Geophys. J. Roy. Astron. Soc.* **26**, 641.
- ARCHAMBEAU, C. B. (1968). *Rev. Geophys.* **6**, 241.

- BOORE, D. M. (1970). Ph.D. Thesis, Massachusetts Institute of Technology, Cambridge.
- BREMNER, H. (1949). "Terrestrial Radio Waves." American Elsevier, New York.
- BRUNE, J. N. (1966). *J. Geophys. Res.* **71**, 2952.
- BRUNE, J. N., NAFE, J. E., and ALSOP, L. E. (1961). *Bull. Seismol. Soc. Amer.* **51**, 247.
- BUCHBINDER, G. (1965). *Bull. Seismol. Soc. Amer.* **55**, 441.
- BURRIDGE, R. (1969). *Phil. Trans. Roy. Soc. London, Ser. A* **265**, 353.
- CAGNIARD, L. (1939). "Réflexion et réfraction des ondes séismiques progressives." Gauthier-Villars, Paris.
- CAGNIARD, L. (1962). "Reflection and Refraction of Progressive Seismic Waves" (translated and revised by E. A. Flinn and C. H. Dix). McGraw-Hill, New York.
- Červený, V. (1967). *Geophys. J.* **13**, 187.
- DANA, S. W. (1945). *Bull. Seismol. Soc. Amer.* **35**, 27.
- DANES, Z. F. (1962). *Geofis. Pura Appl.* **53**, 13.
- DE BREMAECKER, J. C. (1958). *Geophysics* **23**, 253.
- DENSON, M. E. (1952). *Bull. Seismol. Soc. Amer.* **42**, 119.
- DUWALO, G., and JACOBS, J. A. (1959). *Can. J. Phys.* **37**, 109.
- ERGIN, K. (1952). *Bull. Seismol. Soc. Amer.* **42**, 263.
- ERGIN, K. (1967). *J. Geophys. Res.* **72**, 2669.
- EWING, W. M., JARDETZKY, W. S., and PRESS, F. (1957). "Elastic Waves in Layered Media." McGraw-Hill, New York.
- FORESTER, R. D. (1955). *Bull. Seismol. Soc. Amer.* **45**, 187.
- FUCHS, K. (1965). *Z. Geophys.* **31**, 51.
- GARVIN, W. W. (1956). *Proc. Roy. Soc., Ser. A* **234**, 528.
- GILBERT, F., and LASTER, S. J. (1962). *Bull. Seismol. Soc. Amer.* **52**, 299.
- GREENFIELD, R. J., and SHEPPARD, R. M. (1969). *Bull. Seismol. Soc. Amer.* **59**, 409.
- GUTENBERG, B. (1951). *Trans. Amer. Geophys. Un.* **32**, 373.
- GUTENBERG, B. (1958). *Geophys. J.* **1**, 238.
- GUTENBERG, B. (1959). *J. Geophys. Res.* **64**, 1503.
- GUTENBERG, B. (1960). *J. Geophys. Res.* **65**, 1013.
- GUTENBERG, B., and RICHTER, C. (1934). *Gerlands Beitr. Geophys.* **43**, 56.
- GUTENBERG, B., and RICHTER, C. (1935). *Gerlands Beitr. Geophys.* **45**, 280.
- JEFFREYS, H. (1939). *Mon. Notic. Roy. Astron. Soc., Geophys. Suppl.* **4**, 548.
- JEFFREYS, H. (1959). "The Earth." Cambridge Univ. Press, London and New York.
- JEFFREYS, H., and BULLEN, K. E. (1940). "Seismological Tables." Brit. Ass. Advan. Sci., London.
- JEFFREYS, H., and JEFFREYS, B. S. (1956). "Methods of Mathematical Physics," Cambridge Univ. Press, London and New York.
- JEFFREYS, H., and LAPWOOD, E. R. (1957). *Proc. Roy. Soc., Ser. A* **241**, 455.
- KANAMORI, H. (1967). *J. Geophys. Res.* **72**, 559.
- KNOPOFF, L., and GILBERT, F. (1961). *Bull. Seismol. Soc. Amer.* **51**, 35.
- LAPWOOD, E. R. (1961). *Geophys. J.* **4**, 174.
- LEHMANN, I. (1953). *Bull. Seismol. Soc. Amer.* **43**, 291.
- LEHMANN, I. (1954). *Mem. Inst. Geod. Dan.* [3] **18**, 1.
- LOEWENTHAL, D. (1970). Ph.D. Thesis, Weizmann Institute, Rehovot, Israel.
- LOEWENTHAL, D., and ALTERMAN, Z. S. (1972). *Bull. Seismol. Soc. Amer.* **61**, 163.
- MARTINER, S. T. (1950). *Bull. Seismol. Soc. Amer.* **40**, 95.
- MCGARR, A., and ALSOP, L. F. (1967). *J. Geophys. Res.* **72**, 2169.
- MÜLLER, G. (1967). Ph.D. Thesis, Technischen Hochschule, Clausthal.
- MÜLLER, G. (1970). *Geophys. J. Roy. Astron. Soc.* **21**, 261.
- NAKANO, H. (1925). *Jap. J. Astron. Geophys.* **2**, 1.

- OLIVER, J., PRESS, F., and EWING, W. M. (1954). *Geophysics* **19**, 202.
- RICHTER, C. (1958). "Elementary Seismology." Freeman, San Francisco, California.
- ROEVER, W. L., Vining, T. F., and STRICK, E. (1959). *Phil. Trans. Roy. Soc. London, Ser A* **251**, 455.
- RYKUNOV, L. N. (1959). *Bull. Acad. Sci., USSR, Geophys. Ser.* **7**, 678.
- SATÔ, Y., and USAMI, T. (1964). *Bull. Earthq. Res. Inst. Tokyo* **42**, 407.
- SATÔ, Y., USAMI, T., and EWING, M. (1962). *Geophys. Mag.* **31**, 237.
- SATÔ, Y., USAMI, T., LANDISMAN, M., and EWING, M. (1963). *Geophys. J. Roy. Astron. Soc.* **8**, 44.
- SATÔ, Y., USAMI, T., and LANDISMAN, M. (1967). *Bull. Earthq. Res. Inst. Tokyo* **45**, 601.
- SCHOLTE, J. G. J. (1956). *Ned. Meteorol. Inst. Meded. Verh.* **65**, 1.
- SHIMAMURA, H., and SATÔ, R. (1965). *J. Phys. Earth* **13**, 10.
- STARR, A. T. (1928). *Cambridge Phil. Soc.* p. 489.
- STONELEY, R. (1924). *Proc. Roy. Soc., Ser A* **106**, 416.
- TOKSÖZ, M. N., CHINNERY, M. A., and ANDERSON, D. L. (1967). *Geophys. J. Roy. Astron. Soc.* **13**, 31.
- TOKSÖZ, M. N., ARKANI-HAMED, J., and KNIGHT, C. A. (1969). *J. Geophys. Res.* **74**, 3751.
- USAMI, T., and SATÔ, Y. (1964). *Bull. Earthq. Res. Inst. Tokyo* **42**, 273.
- USAMI, T., and SATÔ, Y. (1970). *Bull. Earthq. Res. Inst. Tokyo* **48**, 351.

# Diffracted Seismic Signals and Their Numerical Solution

C. H. CHAPMAN

INSTITUTE OF EARTH AND PLANETARY PHYSICS

DEPARTMENT OF PHYSICS

UNIVERSITY OF ALBERTA, EDMONTON, ALBERTA, CANADA

and

R. A. PHINNEY

DEPARTMENT OF GEOLOGICAL AND GEOPHYSICAL SCIENCES

PRINCETON UNIVERSITY, PRINCETON, NEW JERSEY

I. Introduction . . . . .	166
II. Outline of Basic Theory . . . . .	167
A. The Wave Equations . . . . .	167
B. The Coordinate Transformations . . . . .	169
C. A Point Source . . . . .	171
D. The Watson Transformation . . . . .	173
E. The Complete Solution and the Rainbow Expansion . . . . .	175
III. The Reflection Coefficient . . . . .	179
A. The Haskell Matrix Method . . . . .	179
B. The WKBJ and Wave Solution Method . . . . .	187
IV. The Asymptotic Behavior of the Wave Solutions . . . . .	191
A. The Stokes Phenomena . . . . .	191
B. The Spherical Hankel Functions and Legendre Function . . . . .	193
C. The WKBJ Solution . . . . .	196
V. Numerical Solution of the Wave Equation . . . . .	198
A. The Runge-Kutta and Hamming's Modified Predictor-Corrector Methods . . . . .	198
B. Boundary Conditions for Reflection Coefficients . . . . .	203
C. Analytic Independence-Numerical Dependence of Solutions . . . . .	205
VI. The Response Integral . . . . .	208
A. The Saddle Points . . . . .	208
B. The Diffraction Poles . . . . .	211
C. Numerical Evaluation of the Contour Integral . . . . .	213
VII. Numerical Results . . . . .	215
References . . . . .	229

## I. Introduction

GEOMETRICAL RAY THEORY (BULLEN, 1963) has been very adequate for the interpretation of many seismic signals. The differences in the classic models of Jeffreys and Bullen (1940) and Gutenberg (1958) are small except in regions where nongeometrical effects occur. It is only with the improved coverage by standardized stations of the USCGS worldwide network and the LRSM stations that departures from geometrical ray theory are clearly evident and can be interpreted. The diffraction of P waves into the geometrical shadow of the Earth's core and the more general problem of amplitude studies near singularities of travel time curves is now of significant theoretical and experimental interest to seismologists.

The mathematical techniques which describe ray propagation in a sphere were developed by Watson (1918) and Van der Pol and Bremmer (1937) who studied the diffraction of radio waves by the Earth. Scholte (1956) and Duwalo and Jacobs (1959) applied the same method to a fluid core surrounded by an elastic mantle and obtained asymptotic solutions valid in the illuminated and shadow regions. The subsequent development of the method has been limited by computing power and lack of amplitude data. Nussenzveig (1965) treated the acoustic diffraction problem of an impenetrable sphere in great detail giving asymptotic solutions for all regions and Teng and Richards (1968, 1969) have studied elastic diffraction by a cylindrical cavity. In a very complete study Nussenzveig (1969a,b) has treated the scattering of acoustic waves by a transparent sphere. Spectral amplitudes of diffracted P waves, valid for all receiver ranges, have been computed by Phinney and Cathles (1969) for a homogeneous mantle and core. Chapman (1969) and Richards (1970) have both extended these results to cover other diffracted waves. Ansell (1970) has made a more detailed study of the mathematical aspects of the elastic scattering problem. The high-frequency diffracted signals in the core shadow can be interpreted as rays traveling along the core-mantle interface (Gutenberg and Richter, 1934, p. 89). Knopoff and Gilbert (1961) studied the diffraction problem in the time domain but their method cannot easily be extended to long-period arrivals.

To model the core-mantle interface with a homogeneous mantle and core is inadequate to explain the experimental data (Alexander and Phinney, 1966; Phinney and Cathles, 1969). Phinney and Alexander (1966) made the first attempt to extend the theory by modeling the Earth with homogeneous layers. Although this method could have been extended to model realistic Earth models, Chapman and Phinney (1970) developed an alternative technique which is applicable to any body wave in the Earth. Many of the results used here can be found in Phinney and Alexander (1966), Chapman (1969).

and Chapman and Phinney (1970). The evaluation of the response integral makes heavy demands on numerical computations and only by understanding the details of the theoretical results in these papers can this be performed efficiently.

In this chapter we will concentrate on the signals diffracted by the Earth's core. These are particularly important in a study of the Bullen region D" (Bullen, 1963) at the base of the mantle. Shimamura (1969) gave a review of the theoretical and experimental studies on the core-mantle interface. A glance at the recent literature on this problem shows that the nature of the structure here is still unresolved (Phinney and Alexander, 1969; Bolt, 1970) so the problem is still relevant. With minor changes, however, the method is applicable to any body wave in the Earth. In particular it could be used to study in more detail the PKP caustic (Jeffreys, 1939) and the other end points in the core phases caused by the inner core and structure at its boundary (Bolt, 1962). Diffracted signals will also exist at other discontinuities in the travel-time curves such as the "20° discontinuity" caused by a low velocity zone, and triplications caused by high velocity gradients in the upper mantle (Johnson, 1967).

In Section II a brief outline of the theory and method of solution is given. In particular the response integral, the differential equations, and boundary conditions needed are indicated. Section III contains two different methods of finding the reflected wave and in Section IV the analytic and numerical complications of these solutions are discussed. Section V deals with the method of finding numerically the reflection coefficient in an inhomogeneous model. Finally in Section VI the methods of evaluating the response integral are discussed and in Section VII numerical examples are given.

## II. Outline of Basic Theory

### A. THE WAVE EQUATIONS

The model for the Earth will be taken as spherically symmetric, isotropic, and loss-free. In addition the effects of gravity, rotation, and body forces other than the source will be neglected. These assumptions are certainly not an exact reflection of reality. A simple energy consideration shows that for a wave of amplitude  $A$  and wavenumber  $k$  (hence strain  $\sim kA$ ; stress  $\sim \mu kA$ ) Eq. (1):

- (a) strain energy/unit area  $\sim \mu k A^2 = E$ , say
- (b) gravitational energy/unit area (Gilbert, 1967)

$$\sim \rho g A^2 = (g/\beta^2 k)E = v_g E, \text{ say}$$

(c) rotational energy/unit area

$$\sim \rho A^2 R \Omega^2 = (R \Omega^2 / \beta^2 k) E = \varepsilon_r E, \text{ say} \quad (1)$$

(d) Coriolis energy/unit area (Backus and Gilbert, 1961)

$$\sim \rho A^2 \beta \Omega = (\Omega / \omega) E = \varepsilon_c E, \text{ say}$$

where the variables all have their standard meaning. Clearly at body-wave frequencies with  $g \simeq 10^3 \text{ cm sec}^{-2}$ ,  $\beta > 4 \text{ km sec}^{-1}$ , period  $< 50 \text{ sec}$ ,  $R < 6371 \text{ km}$ , and  $\Omega \simeq 7.4 \times 10^{-5} \text{ sec}^{-1}$  (the frequency of rotation of the Earth)

$$\varepsilon_r \ll \varepsilon_g \ll \varepsilon_c \ll 1. \quad (2)$$

The source and solution are assumed to be axially symmetric. While this restriction and the spherical symmetry of the Earth could be removed there would be little practical value. With the short wavelengths of body waves (up to a maximum of a few hundred kilometers) local inhomogeneities would have to be known in detail for a complete theoretical solution to be worthwhile. To a good approximation, body waves traveling along different paths through an asymmetric Earth can be studied separately using different symmetrical models. Naturally, the position is different for the long-period normal modes when large scale departures from symmetry, e.g., the equatorial bulge, crustal and upper-mantle structure, rotation, etc., will produce significant effects (Dahlen, 1968).

The other restrictions of isotropy and perfect elasticity can also be partially removed. A radially oriented, transversely anisotropic material can be introduced by minor changes to the differential equations (Anderson, 1961) and the effects of attenuation introduced using complex wave velocities (Ewing *et al.*, 1957, p. 272; Phinney and Alexander, 1966; and Section IV, C below).

The general representation of stress, displacement, and potential fields in spherical coordinates in terms of scalar functions has been given by Backus (1967). Only a very restricted form of these equations will be needed. If spherical coordinates  $(r, \theta, \phi)$  are set up with the origin  $r = 0$  at the center of the sphere and the axis  $\theta = 0$  through the source, the axial symmetry of the solution implies  $\partial/\partial\phi \equiv 0$ .

Under the above assumptions, the Navier elastodynamic equation of motion is

$$\rho \partial^2 \mathbf{u} / \partial t^2 = (\lambda + \mu) \nabla (\nabla \cdot \mathbf{u}) + \mu \nabla^2 \mathbf{u} + \mathbf{f}, \quad (3)$$

where  $\mathbf{u}$  is the infinitesimal elastic displacement,  $\lambda$  and  $\mu$  are the Lamé elastic parameters, and  $\rho$  the density. The stress tensor  $\mathbf{p}$  is related to the strain tensor  $\mathbf{e}$  by the usual constitutive relationship

$$p_{ij} = \lambda \operatorname{div} \mathbf{u} \delta_{ij} + 2\mu e_{ij}. \quad (4)$$

In a homogeneous region the wave equation (3) can be separated into Helmholtz equations using the usual scalar potentials

$$\mathbf{u} = \nabla\phi + \nabla \times \nabla \times (\mathbf{e}_r r\psi) + \nabla \times (\mathbf{e}_r r\chi). \quad (5)$$

The homogeneous form of these is then

$$\nabla^2\phi - \frac{1}{\alpha^2} \frac{\partial^2\phi}{\partial t^2} = 0, \quad (6a)$$

$$\nabla^2\psi - \frac{1}{\beta^2} \frac{\partial^2\psi}{\partial t^2} = 0, \quad (6b)$$

$$\nabla^2\chi - \frac{1}{\beta^2} \frac{\partial^2\chi}{\partial t^2} = 0, \quad (6c)$$

where  $\alpha = [(\lambda + 2\mu)/\rho]^{1/2}$ , the P wave velocity, and  $\beta = (\mu/\rho)^{1/2}$ , the S wave velocity. Richards (1971) has shown how the potentials may be generalized to a spherically symmetric inhomogeneous medium, but we will defer a discussion of this until Section III. B.

## B. THE COORDINATE TRANSFORMATIONS

The equation of motion (3) consists of three coupled second-order differential equations. In order to solve this we must either separate the variables in the equations or equivalently transform them. The equations of motion (3) and the constitutive equation (4) are Fourier transformed with respect to time, i.e.,

$$\begin{aligned} f(t) &= \frac{1}{2\pi} \int_{-\infty}^{\infty} e^{-i\omega t} \int_{-\infty}^{\infty} f(t') e^{i\omega t'} dt' d\omega \\ &= \frac{1}{2\pi} \int_{-\infty}^{\infty} \tilde{f}(\omega) e^{-i\omega t} d\omega. \end{aligned} \quad (7)$$

The Fourier transform of any variable is represented by the same tilde. This sign of the exponent is used as the definition of the physical Riemann sheet for the wavenumber is more natural (Section IV, C) and it has been used in much of the literature on diffraction theory. The equations are also Legendre transformed with respect to angle, i.e.

$$\begin{aligned}\tilde{f}(\theta) &= \sum_{n=0}^{\infty} (n + \frac{1}{2}) P_n(\cos \theta) \int_0^{\pi} \tilde{f}(\theta') P_n(\cos \theta') \sin \theta' d\theta' \\ &= \sum_{n=0}^{\infty} (n + \frac{1}{2}) P_n(\cos \theta) \bar{f}_n\end{aligned}\quad (8)$$

(Morse and Feshbach, 1953, Section 6.3). Again the Legendre transform of any variable is represented by the same tilde. Use is made of the Legendre equation

$$d^2y/d\theta^2 + \cot \theta dy/d\theta + n(n+1)y = 0, \quad (9)$$

a solution of which is  $P_n(\cos \theta)$ , to reduce the second-order differential equations. In addition we note that some variables, e.g.,  $u_\theta$ ,  $p_{r\theta}$ ,  $u_\phi$ , and  $p_{r\phi}$ , occur in the equations as first derivatives with respect to  $\theta$ . They are replaced by other differentiated variables, e.g.

$$u_\theta = du_\theta'/d\theta, \text{ etc.} \quad (10)$$

(except for the derivative of the Hankel functions  $h_n'(z)$  and Eqs. 98 and 135–139 a prime does not denote a derivative in this chapter). The resultant differential equations are for the variables  $\bar{u}_\theta'$ ,  $\bar{p}_{r\theta}'$ , etc. and the inverse transformation gives

$$u_\theta = \sum_{n=0}^{\infty} (n + \frac{1}{2}) \frac{\partial P_n(\cos \theta)}{\partial \theta} \bar{u}_\theta' \quad (11)$$

etc., a form commonly assumed initially (Alterman *et al.*, 1959). We define the displacement-stress vector

$$\mathbf{u}(t, r, \theta) = (u_r, u_\theta', p_{rr}, p_{r\theta}')^\top \quad (12)$$

where each component is dependent on time and position. Similarly, we define another displacement-stress vector

$$\mathbf{v}(t, r, \theta) = (u_\phi', p_{r\phi}')^\top. \quad (13)$$

As is well known, the equation of motion (3) separates and can be written as a fourth-order differential system for the transformed variables:

$$\partial \bar{\mathbf{u}} / \partial r = \mathbf{M} \bar{\mathbf{u}} \quad (14)$$

for the P-SV motion, and a second-order differential system:

$$\partial \bar{\mathbf{v}} / \partial r = \mathbf{N} \bar{\mathbf{v}} \quad (15)$$

for the SH motion. The matrices  $\mathbf{M}$  and  $\mathbf{N}$  are given by

$$\mathbf{M} = \begin{pmatrix} -\frac{2\lambda}{(\lambda + 2\mu)r} & \frac{\lambda n(n+1)}{(\lambda + 2\mu)r} & \frac{1}{\lambda + 2\mu} & 0 \\ -\frac{1}{r} & \frac{1}{r} & 0 & \frac{1}{\mu} \\ \left[ \frac{4\mu(3\lambda + 2\mu)}{(\lambda + 2\mu)r^2} - \rho\omega^2 \right] & -\frac{n(n+1)2\mu(3\lambda + 2\mu)}{(\lambda + 2\mu)r^2} & -\frac{4\mu}{(\lambda + 2\mu)r} & \frac{n(n+1)}{r} \\ -\frac{2\mu(3\lambda + 2\mu)}{(\lambda + 2\mu)r^2} & \left[ \frac{2\mu}{\lambda + 2\mu} \left\{ \lambda(2n^2 + 2n - 1) + 2\mu(n^2 + n - 1) \right\} - \rho\omega^2 \right] & -\frac{\lambda}{(\lambda + 2\mu)r} & -\frac{3}{r} \end{pmatrix} \quad (16)$$

and

$$\mathbf{N} = \begin{pmatrix} \frac{1}{r} & \frac{1}{\mu} \\ \left[ \frac{\mu(n-1)(n+2)}{r^2} - \rho\omega^2 \right] - \frac{3}{r} & \frac{3}{r} \end{pmatrix} \quad (17)$$

(Alterman *et al.*, 1959, with the gravitational terms omitted). The components of the vectors now depend on the frequency  $\omega$ , the radius  $r$ , and the order number  $n$ .

### C. A POINT SOURCE

Let us consider a pressure point source at  $r = b$ ,  $\theta = 0$  in a homogeneous region of the Earth model. The homogeneous potential equation (6a) is replaced by the inhomogeneous equation

$$\nabla^2 \phi - \frac{1}{\alpha^2} \frac{\partial^2 \phi}{\partial t^2} = -\frac{2i}{k^2} \frac{\phi_0(t) \delta(r - b) \delta(\theta)}{r^2 \sin \theta}. \quad (18)$$

Transformation of this equation according to (7) and (8) leads to

$$\frac{\partial^2 \bar{\phi}}{\partial r^2} + \frac{2}{r} \frac{\partial \bar{\phi}}{\partial r} + \left[ k^2 - \frac{n(n+1)}{r^2} \right] \bar{\phi} = -\frac{2i}{k^2} \frac{\tilde{\phi}_0(\omega) \delta(r-b)}{r^2} \quad (19)$$

(using  $P_n(1) = 1$  in the Legendre transform of  $\delta(\theta)$  and  $k = \omega/\alpha$ . Later we use  $k' = \omega/\beta$ ). The homogeneous form of the differential equation (19) is the modified Bessel equation. Solutions are the spherical Bessel or Hankel functions. Taking solutions of the homogeneous equation as the spherical Hankel functions

$$\bar{\phi}_1 = h_n^{(1)}(kr), \quad \bar{\phi}_2 = h_n^{(2)}(kr), \quad (20)$$

and using the result from Morse and Feshbach (1953, p. 530) the solution of (19) can be written as

$$\begin{aligned} \bar{\phi} &= \bar{\phi}_1 \left[ \tilde{\phi}_0(\omega) h_n^{(1)}(kb) + \int_r^\infty \left( -\frac{2i\tilde{\phi}_0(\omega) \delta(r-b)}{k^2 r^2} \right) \frac{\bar{\phi}_2}{W\{\bar{\phi}_1, \bar{\phi}_2\}} dr \right] \\ &\quad + \bar{\phi}_2 \int_r^\infty \left( -\frac{2i\tilde{\phi}_0(\omega) \delta(r-b)}{k^2 r^2} \right) \frac{\bar{\phi}_1}{W\{\bar{\phi}_1, \bar{\phi}_2\}} dr, \\ &= 2\tilde{\phi}_0(\omega) h_n^{(1)}(kb) j_n(kr) \quad r \leq b, \\ &= 2\tilde{\phi}_0(\omega) h_n^{(1)}(kr) j_n(kb) \quad r > b, \end{aligned} \quad (21)$$

where  $j_n(kr)$  is the spherical Bessel function. We have used the Wronskian

$$W\{h_n^{(1)}(kr), h_n^{(2)}(kr)\} = -2i/k^2 r^2 \quad (22)$$

(Abramowitz and Stegun, 1965, Eq. 10.1.7) and introduced a constant of integration to satisfy the boundary conditions. The radiation solution of Eq. (18) is

$$\begin{aligned} \tilde{\phi}(\omega, r, \theta) &= \tilde{\phi}_0(\omega) e^{ikR}/ikR, \\ R^2 &= r^2 + b^2 - 2br \cos \theta, \end{aligned} \quad (23)$$

and Eq. (21) is its Legendre transformation (Clebsch, 1863). The solution in terms of the transformed wave functions (21) is often called the partial-wave expansion and has been used extensively in scattering theory. We have derived the results for the transformed potential (21) by transforming the differential equation (18) as this method is applicable in an inhomogeneous medium.

Richards (1970, p. 178) has shown that a result equivalent to (21) can be obtained using the WKBJ solutions instead of the spherical Hankel functions. This result will be used in Section III, B. Any other source containing shear terms can be similarly set up for the potentials  $\bar{\psi}$  and  $\bar{\chi}$ .

#### D. THE WATSON TRANSFORMATION

The inverse transformation of (21) is a very slowly converging series unless  $kr \ll 1$ . The terms only become small for  $n \gg kr$  and for body waves  $kr$  may be of the order of a thousand. Although similar series have been summed successfully numerically (Alterman and Aboudi, 1969a,b; Sato 1969a,b; Landisman *et al.*, 1970) the most powerful method to derive the body-wave and high frequency asymptotic results is based on the Watson transformation (Watson, 1918). Ben-Menahem (1964) has discussed the connection between the summation of normal modes and the wavenumber integral ray method.

We consider a general inverse Legendre transform of the form (8) where the function  $\tilde{f}_n$  has been determined by applying some physical boundary conditions (see Section II, E and Section III). Then the Watson transformation allows the summation to be converted into a complex integral, i.e.

$$\begin{aligned}\tilde{f}(\omega) &= \sum_{n=0}^{\infty} (n + \frac{1}{2}) P_n(\cos \theta) \tilde{f}_n, \\ &= \frac{1}{2i} \int_C \frac{v dv}{\cos(v\pi)} P_{v-1/2}[\cos(\pi - \theta)] \tilde{f}(v),\end{aligned}\quad (24)$$

where the contour C is shown in Fig. 1. The formula can be checked by taking the residues of the integrand at the half-integral values of v on the positive real axis. The function  $\tilde{f}(v)$  must be such that

$$\tilde{f}(v) = \tilde{f}_n \quad \text{where} \quad v = n + \frac{1}{2}. \quad (25)$$

Provided  $\tilde{f}(v)$  is an even function the lower part of the contour can be reflected in the origin so that the contour runs along the real axis. When  $\text{Im}(v) > 0$ ,  $\sec(v\pi)$  can be expanded as

$$\sec(v\pi) = 2e^{iv\pi} \sum_{m=0}^{\infty} (-1)^m e^{2ivm\pi}. \quad (26)$$

Using this result, the integral (24) is easily seen to be equivalent to the Poisson sum formula

$$\sum_{n=-\infty}^{\infty} \tilde{f}_n = \sum_{m=-\infty}^{\infty} \left( \int_{-\infty}^{\infty} \tilde{f}(v) e^{2ivm\pi} dv \right) \quad (27)$$

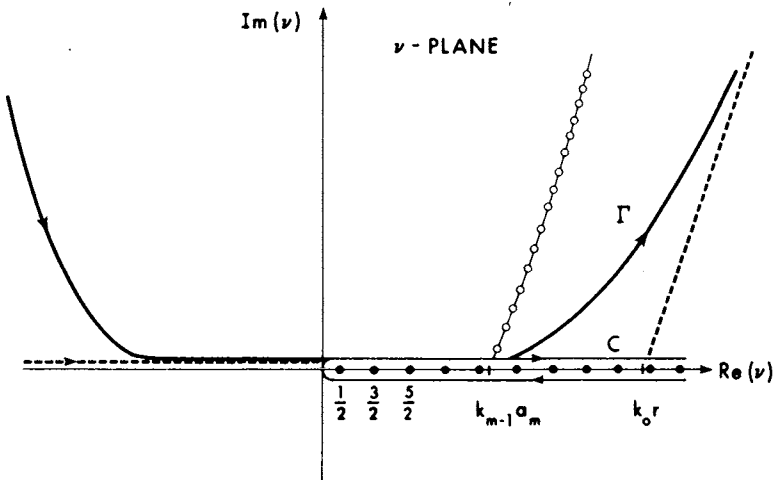


FIG. 1. The contours of integration  $C$  and  $\Gamma$  in the complex  $\nu$ -plane. The poles of the Watson transformation and typical diffraction poles of the response integrand are shown diagrammatically.

(Morse and Feshbach, 1953, p. 466). Similarly if the contour is taken below the real axis,  $\text{Im}(\nu) < 0$  and the relevant expansion is

$$\sec(\nu\pi) = 2e^{-i\nu\pi} \sum_{m=0}^{\infty} (-1)^m e^{-2\pi\nu m i}. \quad (28)$$

The Legendre function can also be expanded as

$$P_{\nu-1/2}[\cos(\pi - \theta)] = -ie^{i\nu\pi} Q_{\nu-1/2}^{(1)}(\cos \theta) + ie^{-i\nu\pi} Q_{\nu-1/2}^{(2)}(\cos \theta), \quad (29)$$

where the Legendre functions  $Q_{\nu-1/2}^{(1)}(\cos \theta)$  and  $Q_{\nu-1/2}^{(2)}(\cos \theta)$  were defined by Nussenzveig (1965).

The physical interpretation of the terms in the expansions is important. Terms in the series (26) together with the Legendre function of the second kind represent waves traveling  $m$  times around the origin in the positive  $\theta$  direction. Similarly terms in the series (28) and the Legendre function of the first kind have traveled  $m$  times around the origin in the negative  $\theta$  direction.

Provided certain conditions are satisfied, the contour integrals along the real axis can be distorted and closed in the upper or lower half  $\nu$ -plane. The mathematical details of this have been given elsewhere and we shall restrict ourselves to some general comments. First, we note that the choice of functions  $\tilde{f}(\nu)$  and  $\sec(\nu\pi)$  in the Watson transformation is to some degree arbitrary. All that is required is that  $\tilde{f}(\nu)$  should be analytic near the positive real

axis and the contour C, and that the singularities of  $\sec(v\pi)$  should give the correct residues. The choice of  $\tilde{f}(v)$  is determined by the requirement of the appropriate behavior at infinity in the  $v$ -plane so that the contour can be distorted away from the real axis.

In the problem of acoustic scattering by an impenetrable sphere (Nussenzveig, 1965) and the equivalent elastic SH problem (Ansell, 1970), the only singularities of the integrand lie in the upper half  $v$ -plane. The response integral can be closed in the upper half  $v$ -plane to enclose these poles. Typically the response integral is evaluated along a contour  $\Gamma$  (Fig. 1) distorted into the upper half  $v$ -plane.

In the elastic P-SV case, the situation is more complicated. Poles can exist in the lower half  $v$ -plane due to "interface waves" and diffraction at critical points. These waves travel in the opposite direction to the normal interface waves. Nussenzveig (1969a,b) has discussed the waves due to the critical transmission of acoustic waves through a transparent sphere and Ansell (1970) has treated the elastic case. The residues of the diffraction poles would be important at the critical point of the SKS ray but make negligible contribution to other signals. The interface waves are only important near the interface and can be neglected in the normal seismology problem.

For all cases we will consider here, the contour of the Watson transformation can be distorted into a contour  $\Gamma$  in the upper half  $v$ -plane.

## E. THE COMPLETE SOLUTION AND THE RAINBOW EXPANSION

The simplest realistic problem which has received much attention is that of a point source in an infinite homogeneous medium with a spherical fluid core included (Scholte, 1956; Duwalo and Jacobs, 1959) or the equivalent problem in electromagnetic or quantum theory (Van der Pol and Bremmer, 1937; Nussenzveig, 1965, 1969a,b). For the Earth this amounts to ignoring reflections from the free surface. Further expansion of the solution is necessary in order to study the various core rays. This has been called the *rainbow expansion* or the Debye expansion (Debye, 1908).

In a realistic inhomogeneous Earth model the application of the rainbow expansion is less obvious and can only be applied in a restricted fashion. The normal mode solution for a spherical Earth (Alterman and Aboudi 1969a,b) is the most complete formulation and satisfies the following conditions:

- (a) The Earth's surface is stress free, i.e.  $\bar{p}_{rr} = \bar{p}'_{r\theta} = \bar{p}'_{r\phi} = 0$ .
- (b) The solution is finite everywhere except at the source and in particular must behave as  $\bar{\phi} = j_n(kr)$ , etc., near  $r = 0$ .
- (c) The transformed components of displacement and stress must satisfy the differential equations (14) and (15) everywhere.

(d) The transformed components of displacement and stress are continuous at discontinuities in the model except at solid-fluid interfaces where the tangential displacement may be discontinuous and the shear stress must be zero.

(e) The solution must contain the singular source solution such as Eq. (23).

We have ignored the extra conditions concerning the gravitational potential field and the replacement of the differential equation (14) by a sixth-order system (Alterman *et al.*, 1959). They do not influence the arguments concerning the rainbow expansion but, of course, would be included in a detailed solution. If the normal modes are added together the resultant theoretical seismogram contains all rays, surface waves, etc. (Alterman and Aboudi 1969a,b; Landisman *et al.*, 1970). However, a very large number of terms would be necessary to study details of body waves. It should be noted that, provided attenuation is ignored, the normal mode solution would consist of poles on the real axis in the  $v$ -plane and the Watson transformation cannot be applied. This solution is represented diagrammatically in Fig. 2a.

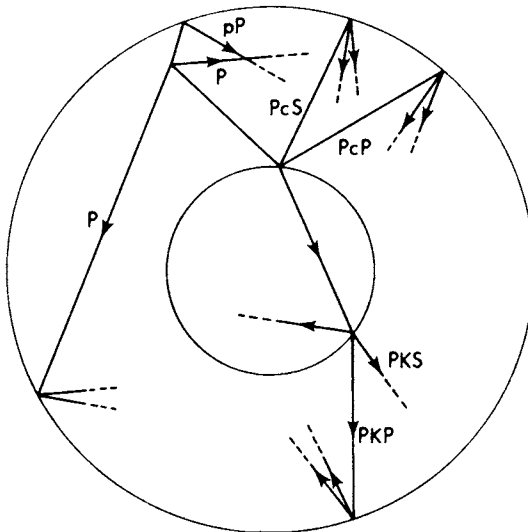


FIG. 2a. The normal mode solution contains all the rays generated by the point source, including all orders of reflection in all interfaces.

If we now relax the first condition and assume that above the source the Earth model is homogeneous, the mathematical and physical picture changes significantly. The stress free boundary condition is replaced by a radiation condition: at large radius the wave solution must represent energy flux in an outward direction, e.g.,  $\bar{\phi} = h_n^{(1)}(kr)$  as  $r \rightarrow \infty$ , etc.

This condition and the condition (b) have been used in setting up the source solution (21). Physically all the reflections from interfaces and the free surface above the source have been eliminated. Mathematically, the real poles have been replaced by a new set of poles in the upper half plane. This situation is represented in Fig. 2b. Physically, these new poles represent resonances of

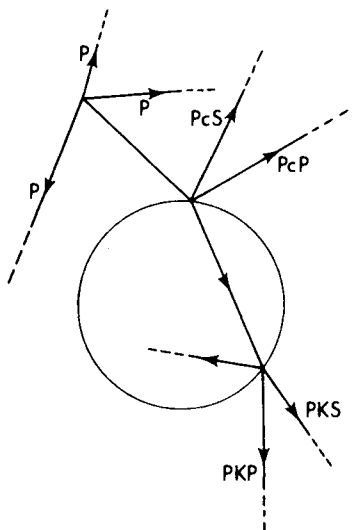


FIG. 2b. The complete core solution contains all the rays generated by the core-mantle interface but no reflections from the Earth's free surface.

the interior of the Earth model which are attenuated due to radiation outward. Thus they lie just above the real  $v$  axis and are for wavenumbers less than the source value  $v = kb$ . They resemble the Regge poles of quantum scattering theory. Other poles which are new are due to interfaces in the model and physically are connected with diffracted waves. They lie near the critical wavenumbers for the interfaces, e.g.,  $v = ka$ , and are off the real axis. These two classes of poles were studied by Nussenzveig (1969a) for the acoustic scattering problem and were discussed briefly by Chapman (1969) for the seismic case.

Although the Watson transformation is applicable to this problem the resultant integral is not easily evaluated. Sato (1969a,b) has summed the Legendre series (8) directly for this problem for a limited range of frequency. The response can be reduced to a series of residues from the two classes of poles. This series only converges rapidly for the diffraction poles. The residues from the resonance poles will all be of the same order of magnitude and not decay rapidly.

Now suppose that we relax the other conditions. Principally, we will be concerned with the second and fourth conditions. Removing the stress-free surface above the source was equivalent to making the Earth model unbounded. However, implicitly it amounted to taking the first term in a rainbow expansion in the free surface. The rainbow expansion for the interfaces below the source cannot be attained by a change in the Earth model (except by introducing some form of energy sink) but represents an equivalent expansion. The boundary conditions are set up to describe the ray we wish to study. Thus in order to study a ray reflected from the core, the boundary condition is not that the solution must remain finite at  $r = 0$  but that energy must be transmitted into the core, e.g.,  $\bar{\phi} = h_n^{(2)}(kr)$  below the core-mantle interface. The rainbow expansion in a single spherical interface has been used extensively by Van der Pol and Bremmer (1937), Scholte (1956), and Duwalo and Jacobs (1959). The equivalence of the physical ray expansion and the mathematical expansion of the complete solution is then easily demonstrated. However, in a more complicated layered or inhomogeneous model the expansion is less direct. If two interfaces exist then we may wish to study a ray which is a term in a rainbow expansion in both interfaces, e.g. PKIKP, or if the interfaces are close together a wave which is a term in a rainbow expansion in the combined interfaces but includes all multiple reflections between the interfaces, e.g., PcP in Phinney and Alexander's (1966) study. A condition equivalent to this second condition will frequently apply to an inhomogeneous region, e.g., PcP in Chapman and Phinney (1970). In the next sections we will see that mathematically the rainbow expansion is implicit in our method of evaluation of the response. The WKBJ solution is used in regions where reflections from velocity gradients are not wanted whereas a solution of the exact wave equation is used in regions where no expansion is required.

In our inhomogeneous or many-layered model it is very difficult to write the rainbow expansion explicitly. Physically, however, the expansion is still obvious (the very fact that we can study body waves and identify signals as PcP, PKP, PKIKP, etc., implies the usefulness of the rainbow expansion). The validity of the rainbow expansion depends on the separation of signals in the time domain. This implies separation of the contributing features in the complex wavenumber plane. If the signals from two terms of the rainbow expansion arrive less than the pulse duration apart the rainbow expansion should not have been used. Mathematically, of course, the signals could be evaluated separately and later combined. When the rainbow expansion is used properly the important features of the complex  $v$ -plane will all be localized and the response integral readily evaluated asymptotically or numerically. Thus for the first term of the rainbow expansion in the core-mantle interface, e.g. P and PcP, two saddle points exist and one set of diffraction poles is important. This result is represented in Fig. 2c. The resonance poles do not

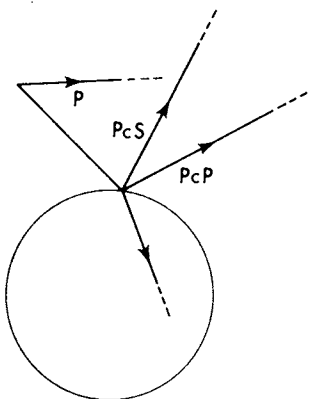


FIG. 2c. The first term in the rainbow expansion contains the direct ray and reflection from the core only.

in general exist for a ray term. Poles due to interface waves, such as the pseudo-Rayleigh and Stonely waves, may still exist and be modified by the rainbow expansion but except near the interface will not generally be important (Ansell, 1970).

### III. The Reflection Coefficient

#### A. THE HASKELL MATRIX METHOD

If the Earth is modeled using homogeneous spherical layers a modified version of the Haskell matrix method (Haskell, 1953) can be used to determine the response function. This technique has been used by Phinney and Alexander (1966) and the special case of a single interface by Scholte (1956) and Duwalo and Jacobs (1959). The method was reformulated by Chapman (1969) to allow numerical solutions for S-waves to be performed. This extension is very instructive physically and indicates why numerical difficulties arise. It also makes the extension to the solution for a realistic inhomogeneous Earth model dealt with in Section III, B more obvious.

In a homogeneous layer, the Helmholtz wave equations (6) for the elastic potentials are valid. The transformed solutions of these are

$$\bar{\phi}_n = h_n(kr), \quad \bar{\psi}_n = h_n(k'r), \quad \bar{\chi}_n = h_n(k'r), \quad (30)$$

corresponding to traveling P-, SV-, and SH-waves, respectively. An index (1) or (2) is understood to refer to outward or inward traveling waves, respectively, and each potential solution can, in general, be written as a linear combination of the two solutions. Substituting in the displacement equation we obtain for the vector (12)

$$\bar{\mathbf{u}}_p = \frac{1}{\alpha(\rho k \omega)^{1/2}} \begin{pmatrix} kh_n'(kr) \\ \frac{h_n(kr)}{r} \\ k^2 \left( -\lambda + 2\mu \left( \frac{n(n+1)}{(kr)^2} - 1 \right) \right) h_n(kr) - 4\mu \frac{h_n'(kr)}{kr} \\ \frac{2\mu}{r^2} \{ krh_n'(kr) - h_n(kr) \} \end{pmatrix} \quad (31)$$

for the P potentials (a constant of normalization has been introduced). Similarly for the SV potentials we obtain

$$\bar{\mathbf{u}}_s = \frac{1}{\beta} \left( \frac{k'}{\rho \omega n(n+1)} \right)^{1/2} \begin{pmatrix} \frac{n(n+1)h_n(k'r)}{k'r} \\ \frac{h_n(k'r)}{k'r} + h_n'(k'r) \\ \frac{2\mu n(n+1)}{r} \left\{ h_n'(k'r) - \frac{h_n(k'r)}{k'r} \right\} \\ \mu k' \left\{ \left( \frac{2n(n+1)-2}{(k'r)^2} - 1 \right) h_n(k'r) - \frac{2}{k'r} h_n'(k'r) \right\} \end{pmatrix}. \quad (32)$$

These wave solutions were used by Phinney and Alexander (1966) in forming the Haskell matrices. For the SH potentials the displacement-stress vector (13) becomes

$$\bar{\mathbf{v}} = \frac{1}{\beta} \left( \frac{k'}{\rho \omega n(n+1)} \right)^{1/2} \begin{pmatrix} h_n(k'r) \\ \mu k' \left\{ h_n'(k'r) - \frac{h_n(k'r)}{k'r} \right\} \end{pmatrix}. \quad (33)$$

The vectors (31) and (32) are solutions of the differential system (14) when the elastic parameters are constants, and the vector (33) is a solution of (15). They are often called the eigenvectors of the differential system although in the usual sense they are not eigenvectors of the matrices M and N. The external factors have been introduced to normalize each vector with respect to its radial energy flux. This is physically and algebraically convenient. For

cartesian components of displacement and stress given in a complex transform form, Biot (1957) has shown that the net energy flux per unit area in the  $x_i$  direction is

$$\frac{1}{4}i\omega \sum_j (\bar{u}_j \bar{p}_{ij}^* - \bar{u}_j^* \bar{p}_{ij}). \quad (34)$$

In spherical coordinates the corresponding form for the radial energy flux is

$$\begin{aligned} \frac{1}{4}i\omega [(\bar{u}_r \bar{p}_{rr}^* - \bar{u}_r^* \bar{p}_{rr}) + n(n+1)(\bar{u}_\theta' \bar{p}_{r\theta}^{*\prime} - \bar{u}_\theta'^* \bar{p}_{r\theta}') \\ + n(n+1)(\bar{u}_\phi' \bar{p}_{r\phi}^{*\prime} - \bar{u}_\phi'^* \bar{p}_{r\phi}')]. \end{aligned} \quad (35)$$

Using the Wronskian (22) and the identities

$$h_n^{(1)*}(z) = h_n^{(2)}(z^*), \quad h_n^{(2)*}(z) = h_n^{(1)}(z^*), \quad (36)$$

the energy flux per unit area (35) reduces to  $\pm 1/2r^2$  for any of the vectors (31), (32), or (33). Thus their net flux through any spherical coordinate surface is constant for any frequency  $\omega$  or mode number  $n$ .

In any homogeneous layer the displacement and stress can be written as a sum of the vectors (31), (32), and (33) times their amplitudes. Restricting ourselves to the P-SV case, we define a matrix

$$\mathbf{U} = [\bar{\mathbf{u}}_p^{(2)}, \bar{\mathbf{u}}_s^{(2)}, \bar{\mathbf{u}}_p^{(1)}, \bar{\mathbf{u}}_s^{(1)}] \quad (37)$$

with the vectors as columns, and a vector

$$\Phi = (\phi^{(2)}, \psi^{(2)}, \phi^{(1)}, \psi^{(1)})^T, \quad (38)$$

where  $\phi^{(2)}$  and  $\psi^{(2)}$  are the amplitudes of the P-and SV-waves, respectively, traveling inwards in the layer and  $\phi^{(1)}$  and  $\psi^{(1)}$  are amplitudes traveling outwards. Thus the general solution is

$$\bar{\mathbf{u}}_i(r) = \mathbf{U}_i(r)\Phi_i, \quad (39)$$

where subscripts  $i$  have been added to denote the variables in the  $i$ th layer between  $a_i$  and  $a_{i+1}$ . This is shown diagrammatically in Fig. 3. Using the condition of continuity of the components of stress and displacement at the interfaces, i.e.,

$$\bar{\mathbf{u}}_{i-1}(a_i) = \bar{\mathbf{u}}_i(a_i) \quad (40)$$

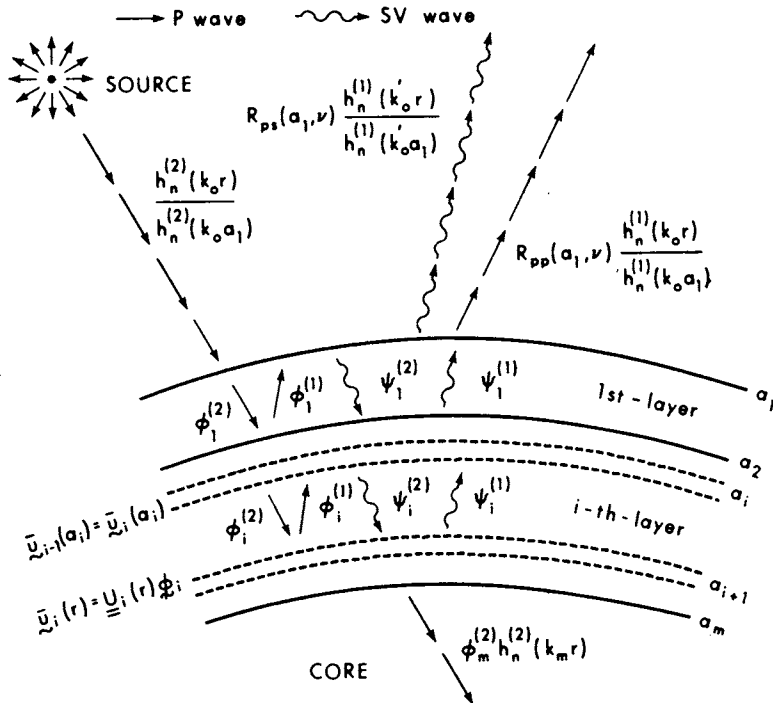


FIG. 3. A diagrammatic representation of the Haskell matrix method. All notation is as in text.

and Eq. (39) to obtain the displacement and stress at the two boundaries of the layer, we can connect the wave amplitudes at the limits of the layers by

$$U_m(a_m)\phi_m = Q_{m-1}Q_{m-2}\cdots Q_1U_0(a_1)\phi_0. \quad (41)$$

where

$$Q_i = U_i(a_i)U_i^{-1}(a_{i+1}). \quad (42)$$

Boundary conditions can be applied in the core, i.e., to  $\phi_m$ , and the matrix equation solved for the reflected waves, i.e.,  $\phi_0$ . This formulation corresponds to that of Phinney and Alexander (1966), and was used for the P-PcP-rays. It must be modified, however, to allow numerical solutions for other rays such as S-ScS.

For the P-PcP signal, terms of the matrices must be evaluated near the wavenumber for a core-grazing P-ray, i.e.,  $v = k_{m-1}a_m$ . In this region the spherical Hankel functions  $h_n(kr)$  and  $h_n(k'r)$  are not large and the matrices

can be numerically inverted and manipulated without loss in accuracy. To study the ScS diffracted signal the Hankel functions must be evaluated near  $v = k'_{m-1}a_m$ . In this region both  $h_n^{(1)}(kr)$  and  $h_n^{(2)}(kr)$  are exponentially large and the matrices cannot be handled numerically.

First we note that the inverse of the matrix  $\mathbf{U}$  needed in the expression (42) is easily obtained analytically. It is given by

$$\mathbf{U}^{-1} = -\frac{ir^2\omega}{2} \begin{pmatrix} U_{33} & n(n+1)U_{43} & -U_{13} & -n(n+1)U_{23} \\ U_{34} & n(n+1)U_{44} & -U_{14} & -n(n+1)U_{24} \\ -U_{31} & -n(n+1)U_{41} & U_{11} & n(n+1)U_{21} \\ -U_{32} & -n(n+1)U_{42} & U_{12} & n(n+1)U_{22} \end{pmatrix}. \quad (43)$$

This result has been used by Chapman (1969) and has also been derived by Teng (1970). It is very useful numerically but is also useful in indicating an *orthogonality* condition between the P- and SV-wave types. Defining a product between two displacement-stress vectors  $\bar{\mathbf{u}}_1$  and  $\bar{\mathbf{u}}_2$  as

$$\bar{\mathbf{u}}_1 * \bar{\mathbf{u}}_2 = (\bar{u}_{r_1}\bar{p}_{rr_2}^* - \bar{u}_{r_2}^*\bar{p}_{rr_1}) + n(n+1)(\bar{u}'_{\theta_1}\bar{p}'_{r\theta_2}^* - \bar{u}'_{\theta_2}\bar{p}'_{r\theta_1}) \quad (44)$$

we see that the eigenvectors (31) and (32) are orthogonal, e.g.,

$$\begin{aligned} \bar{u}_p^{(2)} * \bar{u}_p^{(2)} &= 2i/r^2\omega, & \bar{u}_p^{(1)} * \bar{u}_p^{(1)} &= -2i/r^2\omega, \\ \bar{u}_p^{(2)} * \bar{u}_s^{(1)} &= 0, & \bar{u}_p^{(2)} * \bar{u}_p^{(1)} &= 0, \text{ etc.} \end{aligned} \quad (45)$$

This result is a modification to spherical coordinates of the orthonormality condition used by Herrera (1964) and extended to body waves by Alsop (1968). The connection of the vector product (44) with the energy flux (35) is immediately obvious and the inverse matrix (43) follows directly from the orthogonality condition (45). These results are very useful in allowing reflection coefficients to be calculated and similar results hold for the plane wave-plane interface problem.

The eigenvectors used in forming the matrix (37) contain the traveling wave solutions. The matrices are therefore complex. In the traditional Haskell matrix formulation (Haskell, 1953) the standing wave solutions are taken and the matrices consist of purely real or imaginary terms. This can be attained in the spherical Haskell matrix formulation, by using the spherical Bessel functions rather than the spherical Hankel functions. If in the eigenvectors we replace  $h_n^{(1)}(z)$  by  $i j_n(z)$  and  $h_n^{(2)}(z)$  by  $2 j_n(z)$ , the matrices contain only real or imaginary terms for real wavenumbers. The response integral has to be evaluated for complex wavenumber  $v$ , however, and then this advantage is not generally

useful. The factors  $i$  and 2 have been introduced so that the Wronskian of the two types of solutions remains the same, i.e.,

$$W\{ij_n(z), 2j_n(z)\} = -2i/z^2 \quad (46)$$

(Abramowitz and Stegun, 1965, Eq. 10.1.6) compared with (22). The inverse matrix still has the form (43) with Bessel functions replacing the Hankel functions. The Bessel functions have the advantage that they are exponentially large and small in the evanescent region while the Hankel functions are both exponentially large and numerically will not be independent.

The matrix  $\mathbf{Q}_i$  (42) can be rewritten as

$$\mathbf{Q}_i = \mathbf{U}'_i(a_i) \mathbf{F}_i \mathbf{U}'_{i+1}^{-1}(a_{i+1}), \quad (47)$$

where the normalization and factors of the Hankel function have been removed from each column of  $\mathbf{U}_i(r)$ , i.e.,

$$\mathbf{U}'_i(r) = [\bar{\mathbf{u}}_p^{(2)\prime}, \bar{\mathbf{u}}_s^{(2)\prime}, \bar{\mathbf{u}}_p^{(1)\prime}, \bar{\mathbf{u}}_s^{(1)\prime}] \quad (48)$$

with

$$\bar{\mathbf{u}}_p' = [\alpha(\rho k \omega)^{1/2}/h_n(kr)] \bar{\mathbf{u}}_p, \text{ etc.}, \quad (49)$$

and the matrix  $\mathbf{F}_i$  is given by

$$\begin{pmatrix} \frac{h_n^{(2)}(k_i a_i)}{h_n^{(2)}(k_i a_{i+1})} & 0 & 0 & 0 \\ 0 & \frac{h_n^{(2)}(k_i' a_i)}{h_n^{(2)}(k_i' a_{i+1})} & 0 & 0 \\ 0 & 0 & \frac{h_n^{(1)}(k_i a_i)}{h_n^{(1)}(k_i a_{i+1})} & 0 \\ 0 & 0 & 0 & \frac{h_n^{(1)}(k_i' a_i)}{h_n^{(1)}(k_i' a_{i+1})} \end{pmatrix}. \quad (50)$$

The diagonal terms represent the potential change across the layer. It should be noted that in this form  $\bar{\mathbf{u}}_s'$  remains determined in a fluid layer, i.e.,

$$\bar{\mathbf{u}}_s' = \frac{\beta}{h_n(k'r)} \left( \frac{\rho \omega n(n+1)}{k'} \right)^{1/2} \bar{\mathbf{u}}_s \rightarrow (0, \pm i, 0, 0)^T \quad (51)$$

as  $\mu \rightarrow 0$ , the sign depending on the index (1) or (2).

With these modifications it is possible to solve the matrix equation (41) in all the required regions. Equation (41) is rewritten as

$$\begin{aligned}\Phi_0' &= U_0'^{-1}(a_1) Q_1^{-1} \cdots Q_{m-1}^{-1} U_m'(a_m) \Phi_m' \\ &= R \Phi_m', \quad \text{say.}\end{aligned}\quad (52)$$

The boundary conditions to describe the required solution are introduced in the component vectors  $\Phi_0'$  and  $\Phi_m'$ . For instance, for the first term in the rainbow expansion an acoustic wave is transmitted into the core. Thus the component vector in the core must be of the form

$$\Phi_m' = (\phi^{(2)'}, \psi^{(2)'}, 0, 0)^T, \quad (53)$$

where the outward traveling components are zero.  $\phi^{(2)'}$  is the amplitude of the acoustic wave transmitted into the core, which would be used in higher order terms in the rainbow expansion such as PKP, while  $\psi^{(2)'}$  is a measure of the discontinuity in tangential displacement at the solid–fluid core interface. Two source conditions are possible. For a compressional source, the mantle wave components are given by

$$\Phi_0' = (1, 0, R_{pp}(a_1, v), \left(\frac{k_0'^3}{k_0 n(n+1)}\right)^{1/2} R_{ps}(a_1, v))^T, \quad (54)$$

and for a shear source

$$\Phi_0' = (0, 1, \left(\frac{k_0 n(n+1)}{k_0'^3}\right)^{1/2} R_{sp}(a_1, v), R_{ss}(a_1, v))^T. \quad (55)$$

The incident downgoing wave of unit amplitude is given by one of the first two components, the reflected P-wave by the third component, and the reflected SV by the fourth. The reflection coefficients are normalized with respect to the energy flux and are the potential amplitudes at the radius  $r = a_1$ . It is easily shown that with this normalization the reflection coefficients for a single interface are symmetric, i.e.,

$$R_{ps}(a_1, v) h_n^{(1)}(k_0 a_1) h_n^{(2)}(k_0 a_1) = R_{sp}(a_1, v) h_n^{(1)}(k_0' a_1) h_n^{(2)}(k_0' a_1) \quad (56)$$

Using (54) or (55) together with (53) in the four equations (52) the unknowns are easily found. For instance,

$$R_{pp}(a_1, v) = -R_{12}^{23}/R_{12}^{12}. \quad (57)$$

a ratio of second-order minors of the matrix  $R$ .

In passing it is worth noting that the complete solution discussed in Section II, E would be obtained by solving the equations (52) with

$$\Phi_m' = \frac{1}{2}(\phi^{(2)\prime} h_n^{(2)}(k_m a_m), \quad \psi^{(2)\prime}, \quad \phi^{(2)\prime} h_n^{(1)}(k_m a_m), \quad -\psi^{(2)\prime})^T \quad (58)$$

so that the core solution behaves as  $\tilde{\phi}_n = j_n(k_m a_m)$ . The additional resonance poles mentioned in Section II, E arise from the function  $j_n'(k_m a_m)/j_n(k_m a_m)$  in the denominator of the response integral.

In the Haskell matrix formulation a rainbow expansion of the rays has only been assumed at the extreme interfaces, i.e.  $r = a_1$  and  $r = a_m$ . Otherwise all multiple reflections and the resultant resonances have been included. The method could be generalized to include other interfaces, such as in the crust or upper mantle, at which only the transmitted ray is included. A system of equations such as

$$U_i(a_i)\Phi_i = U_{i-1}(a_i)\Phi_{i-1} \quad (59)$$

would be solved for the appropriate transmission coefficient. Modeling the Earth with homogeneous layers is very restrictive, however, and this case is considered only as a special part of the more general solution in the next section.

The Haskell matrix method can also be applied to the SH case. As the matrix equation is only  $2 \times 2$  and the waves are always totally reflected by the core, the solution is considerably simpler and no details will be given here.

The source function (21) contains an outward traveling wave function  $h_n^{(1)}(kr)$  for  $r > b$  and the nonsingular wave function  $j_n(kr)$  for  $r < b$ . Physically this wave solution contains the inward traveling wave from the source  $h_n^{(2)}(kr)$  plus the same wave after it has passed through the origin  $r = 0$  and become the outward traveling wave  $h_n^{(1)}(kr)$ , e.g.,

$$2j_n(kr) = h_n^{(1)}(kr) + h_n^{(2)}(kr). \quad (60)$$

Phinney and Alexander (1966) have shown that in the rainbow expansion the outward traveling source rays cancel and the direct ray is contained in the reflection coefficient (57). We will therefore assume the following simple physical picture of the source and reflection holds: the source causes an inward traveling wave  $h_n^{(2)}(kr)$  whose amplitude at the source is

$$\tilde{\phi}_0(\omega)h_n^{(1)}(kb)h_n^{(2)}(kb). \quad (61)$$

This wave propagates inwards, is reflected by the core or has a turning point, and then propagates outwards to the receiver. Thus the transformed potential response for the P signal at the receiver is

$$\begin{aligned}\tilde{\phi}(\omega, r, \theta) = \tilde{\phi}_0(\omega) \int_{\Gamma} \{h_{v-1/2}^{(1)}(k_0 b) h_{v-1/2}^{(2)}(k_0 b)\} & \left\{ \frac{h_{v-1/2}^{(2)}(k_0 a_1)}{h_{v-1/2}^{(2)}(k_0 b)} \right\} R_{pp}(a_1, v) \\ & \times \left\{ \frac{h_{v-1/2}^{(1)}(k_0 r)}{h_{v-1/2}^{(1)}(k_0 a_1)} \right\} Q_{v-1/2}^{(2)}(\cos \theta) v dv. \quad (62)\end{aligned}$$

The first pair of curly brackets in the integrand contains the source strength taken from (61); the second contains the change in the source ray  $h_n^{(2)}(k_0 r)$  in traveling inwards from the source at  $r = b$  to the first interface at  $r = a_1$ ; the third term is the reflection coefficient for the required ray of the rainbow expansion, e.g., P and Pcp from result (57); the next pair of curly brackets contains the change in the wave propagating outwards from the interface at  $r = a_1$  to the receiver. Only the term  $m = 0$  and the Legendre function of the second kind are included as we are only interested in the wave traveling in the positive  $\theta$  direction which has not passed around the origin.

An integral such as (62) can be evaluated either asymptotically for the ray solution (Scholte, 1956) or numerically (Phinney and Cathles, 1969). The integral has been written in more detail here in order to illustrate the physical significance of the various terms. The response integral for any other signal is then easy to formulate. For instance, the Ps potential solution will be

$$\begin{aligned}\tilde{\psi}(\omega, r, \theta) = \tilde{\phi}_0(\omega) \int_{\Gamma} \{h_{v-1/2}^{(1)}(k_0 b) h_{v-1/2}^{(2)}(k_0 b)\} & \left\{ \frac{h_{v-1/2}^{(2)}(k_0 a_1)}{h_{v-1/2}^{(2)}(k_0 b)} \right\} R_{ps}(a_1, v) \\ & \times \left\{ \frac{h_{v-1/2}^{(1)}(k_0' r)}{h_{v-1/2}^{(1)}(k_0' a_1)} \right\} Q_{v-1/2}^{(2)}(\cos \theta) v dv. \quad (63)\end{aligned}$$

## B. THE WKBJ AND WAVE SOLUTION METHOD

In the previous section the response integral has been established for an Earth model of homogeneous layers. Under these conditions the exact solutions of the wave equations (3) are known analytically and the required solutions are easily obtained. In an inhomogeneous Earth model, solutions of the wave equations (3) can only be obtained numerically or by an approximate analytic method. Inhomogeneities in the Earth have two different effects on body waves. The velocity structure causes the ray paths to bend according to

Snell's law. This is the purely geometrical effect which changes the range and amplitudes of rays. A more complicated effect is the nongeometrical interactions of the wave with inhomogeneities in the Earth.

From observations it is well known that different rays exist in the Earth—the P- and S-rays—and that for a wide range of frequency these are clearly distinguishable. Geometrical ray results apply to a very good degree of approximation and only at the longer periods of normal modes is the distinction between P and S rays irrelevant. The geometrical ray results are contained mathematically in the WKBJ solutions. Richards (1971) has shown that if the potential representation (5) is replaced by the more general form

$$\mathbf{u} = \frac{1}{g} \left\{ \nabla \left( \frac{g\phi}{\rho^{1/2}} \right) + \nabla \times \nabla \times \left( \frac{rg\psi}{\rho^{1/2}} \mathbf{e}_r \right) \right\} + \nabla \times \left( \frac{r\chi}{\mu^{1/2}} \mathbf{e}_r \right), \quad (64)$$

the potentials  $\phi$ ,  $\psi$ , and  $\chi$  can be considered as representing the P-, SV-, and SH-waves in the high-frequency limit. The arbitrary function  $g(r)$  need not concern us here. When (64) is substituted in the wave equation (3), with the body force  $\mathbf{f}$  similarly represented, a second-order differential equation for  $\chi$  plus two coupled second-order differential equations for  $\phi$  and  $\psi$  are obtained. These equations are equivalent to the Helmholtz equations (6) with extra coupling terms included. By comparison these terms are small either when the medium is nearly homogeneous or when the frequency is high. Thus in the high-frequency limit the equations decouple and the  $\phi$  and  $\psi$  potentials can be associated with the P- and SV-waves, respectively. If the coupling terms can be neglected, solutions of the Helmholtz wave equations can be used as approximate solutions. The geometrical ray results are obtained from these solutions and, as mentioned above, neglecting the coupling terms is implicit in the use of the rainbow expansion. Thus in regions of the inhomogeneous Earth model where the geometrically transmitted ray is required, the decoupled form of the potential equation will be assumed. Physically this amounts to neglecting any nongeometrical conversions and reflections of the ray. Transforming the decoupled Helmholtz potential equation we obtain for the P potential

$$\frac{\partial^2 \bar{\phi}}{\partial r^2} + \frac{2}{r} \frac{\partial \bar{\phi}}{\partial r} + \left\{ k^2(r) - \frac{n(n+1)}{r^2} \right\} \bar{\phi} = 0. \quad (65)$$

This equation has the approximate WKBJ solutions

$$\bar{\phi}(v) \propto \frac{1}{r(q_\alpha)^{1/2}} \exp\left\{ \pm i \int^r q_\alpha(\zeta) d\zeta \right\} \quad (66)$$

except in regions of high velocity gradient, where  $q_\alpha$  varies rapidly, or near the ray's turning point, where  $q_\alpha(r_0) = 0$ . The radial wavenumber is given by

$$q_\alpha^2 = k^2 - (v^2/r^2), \quad (67)$$

where the factor  $n(n + 1)$  in (65) is replaced by  $v^2 = (n + \frac{1}{2})^2$  (Morse and Feshbach, 1953, p. 1101). The transformed displacement can be found by substituting the solutions (66) in Eq. (64). The factor  $[r(\rho q_\alpha)^{1/2}]^{-1}$  is such that the energy flux for each solution is conserved as it propagates radially.

In obtaining the approximate analytic WKBJ solution (66), we have assumed that the P ray propagates independently through an inhomogeneous medium and that the turning point  $r_0$  is not approached. The former condition is physically required in the rainbow expansion, and the WKBJ solution must be used in those regions of the Earth where the expansion is needed. In the next section we discuss the range of validity of the WKBJ approximation for complex wavenumbers. In regions of the Earth where the nongeometrical wave interactions are important, such as near the turning point of the ray grazing the core, the WKBJ solutions cannot be used. Then a solution of the exact wave equation (14) must be employed. In Section V we discuss how this is obtained numerically and the reflection coefficient calculated. Suppose, for instance, that the WKBJ solution is valid for  $r \geq r^*$  and by solving the wave equation (14) for  $r \leq r^*$  we have found the reflection coefficient for this region, e.g.,  $R_{pp}(r^*, v)$ . This reflection coefficient is comparable with the reflection coefficient (57). The radius  $r^*$  does not correspond to an interface now but the limit of an inhomogeneous region from which we wish to study reflections.

Combining these results a response integral equivalent to (62) can be formed for an inhomogeneous Earth model:

$$\begin{aligned} \tilde{\phi}(\omega, r, \theta) = & \tilde{\phi}_0(\omega) \int_{\Gamma} \left\{ \frac{1}{k_s q_\alpha(b) b^2} \right\} \left\{ \frac{b[\rho(b)q_\alpha(b)]^{1/2}}{r^*[\rho(r^*)q_\alpha(r^*)]^{1/2}} \exp - i \int_b^{r^*} q_\alpha(\zeta) d\zeta T_D(v) \right\} \\ & \times R_{pp}(r^*, v) \left\{ \frac{r^*[\rho(r^*)q_\alpha(r^*)]^{1/2}}{r[\rho(r)q_\alpha(r)]^{1/2}} \exp i \int_{r^*}^r q_\alpha(\zeta) d\zeta T_U(v) \right\} \\ & \times Q_{v-1/2}^{(2)}(\cos \theta) v dv. \end{aligned} \quad (68)$$

The potential  $\tilde{\phi}$  corresponds to the potential in (5) not (64); hence the factors  $\rho^{1/2}$ . The parentheses contain terms which are equivalent to those in the integral (62). The source strength is obtained from matching the WKBJ solutions at the source (Richards, 1970) and can also be obtained from the Hankel asymptotic expansions for the spherical Hankel functions in (61)

(Abramowitz and Stegun, 1965, Section 9.2). The second pair of curly brackets contains the inward traveling wave from  $r = b$  to  $r = r^*$  given by the WKBJ solution (66). The factor  $T_D(v)$  contains the product of any interface transmission coefficients in this range, found by solving Eq. (59). The reflection coefficient for the turning point of the ray is given by  $R_{pp}(r^*, v)$ , the outgoing traveling wave and transmission coefficients by the next pair of curly brackets, and finally the Legendre function and  $v$  are identical to the previous result. The form of the solution is indicated diagrammatically in Fig. 4 and has been used by Chapman and Phinney (1970). It is easy to construct the response integral for another term in the rainbow expansion such as  $\text{PcS}$ :

$$\begin{aligned} \tilde{\psi}(\omega, r, \theta) &= \tilde{\phi}_0(\omega) \int_{\Gamma} \left\{ \frac{1}{k_s q_a(b) b^2} \right\} \left\{ \frac{b[\rho(b)q_a(b)]^{1/2}}{(r^*[\rho(r^*)q_a(r^*)]^{1/2})} \exp -i \int_b^{r^*} q_a(\zeta) d\zeta T_D(v) \right\} \\ &\quad \times R_{ps}(r^*, v) \left( \frac{r^*[\rho(r^*)q_\beta(r^*)]^{1/2}}{r[\rho(r)q_\beta(r)]^{1/2}} \exp i \int_{r^*}^r q_\beta(\zeta) d\zeta T_U(v) \right) \\ &\quad \times Q_{v-1/2}^{(2)}(\cos \theta) v dv \end{aligned} \quad (69)$$

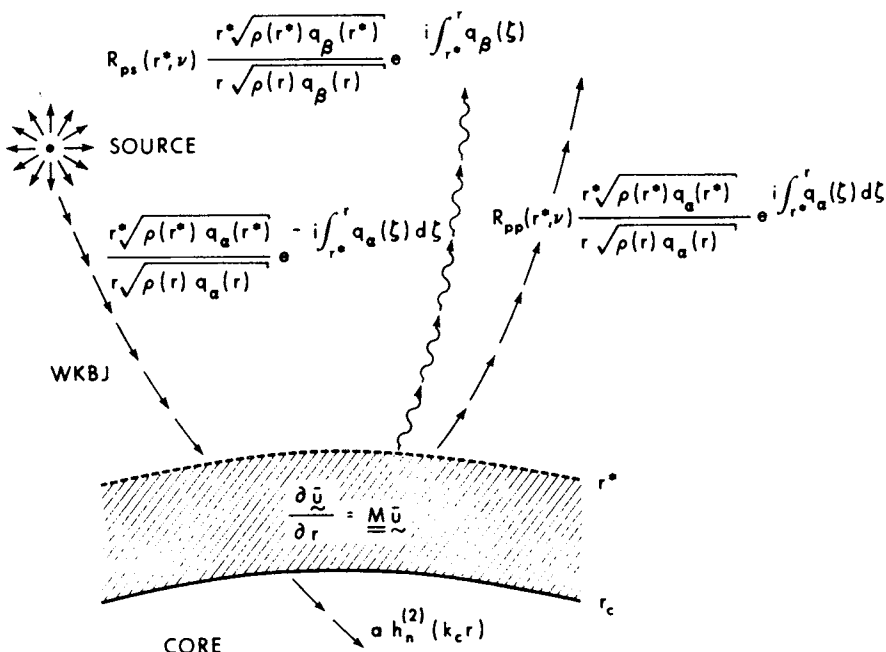


FIG. 4. A diagrammatic representation of the WKBJ and wave solution method. All notation is as in text.

where

$$q_\beta^2 = k^{12} - (v^2/r^2). \quad (70)$$

The product of transmission coefficients  $T_U(v)$  will, of course, be for SV-waves rather than P-waves.

#### IV. The Asymptotic Behavior of the Wave Solutions

##### A. THE STOKES PHENOMENA

The asymptotic behavior of the analytic functions used in Section III, A and the properties of the WKBJ solutions in Section III, B are closely connected. The asymptotic approximations to the solutions of second-order wave equations always exhibit the Stokes phenomena. This was first noted by Stokes (1858) in studying the Airy integral but is equally important in asymptotic approximations to the spherical Hankel functions or the WKBJ solutions. Excellent discussions on the Stokes phenomena can be found in Budden (1966, Ch. 15) and Heading (1962), who deals in more detail with the WKBJ solutions or *phase-integral method*. Only the details necessary to understand our solutions will be given here.

Two concepts are essential to understanding the Stokes phenomena: the existence of *Stokes* and *anti-Stokes* lines in the complex plane, and the distinction between the *dominant* and *subdominant* asymptotic solutions. These are best illustrated by studying the Airy function and its Stokes diagram. The Stokes equation

$$d^2y/dt^2 - ty = 0 \quad (71)$$

has a solution  $\text{Ai}(t)$ , the Airy function, which is defined as real and bounded on the positive real  $t$  axis. The asymptotic form for  $t \gg 1$  is the WKBJ solution

$$\text{Ai}(t) \simeq \frac{1}{2}\pi^{-1/2}t^{-1/4}e^{-2/3t^{3/2}}. \quad (72)$$

If we let  $\text{Arg}(t)$  increase from 0 to  $\pi$  this becomes

$$y(t) \simeq \frac{1}{2}\pi^{-1/2}e^{-i\pi/4}|t|^{-1/4}e^{2/3i|t|^{3/2}}, \quad (73a)$$

and if we let  $\text{Arg}(t)$  decrease from 0 to  $-\pi$

$$y(t) \simeq \frac{1}{2}\pi^{-1/2}e^{i\pi/4}|t|^{-1/4}e^{-2/3i|t|^{3/2}}. \quad (73b)$$

Thus the WKBJ solutions are multivalued and cannot correspond in all regions to the real solution of (71). The actual asymptotic solution for  $t \ll -1$  is

$$\text{Ai}(t) \simeq \pi^{-1/2} |t|^{-1/4} \sin(\frac{1}{3}\pi + \frac{2}{3}|t|^{3/2}), \quad (74)$$

a linear combination of (73a) and (73b).

The Airy integral

$$\frac{1}{2\pi i} \int_C \exp(-\frac{1}{3}z^3 + zt) dz \quad (75)$$

is a solution of the Stokes equation (71). The integrand has two saddle points at  $z = \pm t^{1/2}$  which give second-order saddle point contributions of

$$\frac{1}{2} \pi^{-1/2} t^{-1/4} e^{-2/3 t^{3/2}} \quad (76a)$$

and

$$\frac{i}{2} \pi^{-1/2} t^{-1/4} e^{2/3 t^{3/2}}, \quad (76b)$$

corresponding to the WKBJ solutions. On the lines  $\text{Arg}(t) = 0, 2\pi/3$ , and  $4\pi/3$  the exponents are purely real and the solutions exponential—these are called the *Stokes* lines. On the lines  $\text{Arg}(t) = \pi/3, \pi$ , and  $5\pi/3$  the exponents are purely imaginary and the solutions oscillatory—these are called the *anti-Stokes* lines. The sector between two anti-Stokes lines is called a Stokes region and, as the solutions are exponential, one solution is *dominant* and the other *subdominant*. On the positive real  $t$  axis, by definition the function  $\text{Ai}(t)$  is bounded and must be obtained from just the subdominant term, i.e., Eq. (72). For  $|\text{Arg}(t)| < 2\pi/3$ , the contour  $C$  for the solution of the integral (75) corresponding to the function  $\text{Ai}(t)$  passes over the first saddle point (76a) only. At  $|\text{Arg}(t)| = 2\pi/3$  the second saddle point contribution (76b) enters discontinuously and the contour  $C$  passes over both saddles. This is the *Stokes phenomenon*. The second saddle's contribution (76b) is subdominant on the Stokes line  $\text{Arg}(t) = \pm 2\pi/3$ . The dominant term (76a) is exponentially large and the error inherent in the asymptotic series from the saddle point integration is greater than the subdominant term. As  $|\text{Arg}(t)|$  approaches  $\pi$ , the two terms (76) become equal in magnitude and on the anti-Stokes line  $\text{Arg}(t) = \pi$  both terms contribute equally to the asymptotic series. Thus near a Stokes line one WKBJ solution can be used as an approximation, whereas near an anti-Stokes line, it may be necessary to use a combination of both solutions. This is shown diagrammatically in Fig. 5. We will

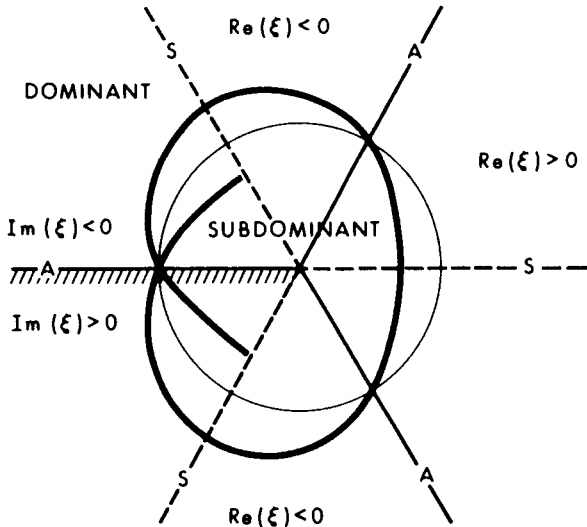


FIG. 5. Stokes diagram of  $Ai(t)$ .  $A = \pi^{-1/2} t^{-1/4}$ ,  $\xi = \frac{2}{3}t^{3/2}$  and  $Ai(t) = \frac{1}{2}Ae^{-\xi}$  in all Stokes regions. Diagram represents  $\text{Arg}(t)$  but not  $|t|$ . Stokes lines (S)  $Im(\xi) = 0$ , and anti-Stokes lines (A)  $Re(\xi) = 0$  are indicated. The heavy line represents the terms present in the asymptotic series for  $Ai(t)$ . When inside the circle, the term is subdominant and when outside dominant.

only be interested in the solution which is subdominant in one Stokes region and so have restricted discussion to the solution  $Ai(t)$ . Details of the other solution  $Bi(t)$  can be found in Budden (1966, Ch. 15). The same behavior applies to the spherical Hankel function and to the WKBJ solutions. Only by studying the Stokes and anti-Stokes lines for these solutions can the valid regions of approximation be established.

## B. THE SPHERICAL HANKEL FUNCTIONS AND LEGENDRE FUNCTION

The spherical Hankel functions which are used in the wave solution in homogeneous regions are related to the cylindrical Hankel functions by

$$h_n^{(k)}(z) = (\pi/2z)^{1/2} H_v^{(k)}(z) \quad v = n + \frac{1}{2}. \quad (77)$$

These are solutions of the normal Bessel equation

$$z \frac{d}{dz} \left( z \frac{dy}{dz} \right) + (z^2 - v^2)y = 0. \quad (78)$$

Letting  $z = e^x$ , we obtain

$$\frac{d^2y}{dx^2} - (v^2 - e^{2x})y = 0 \quad (79)$$

which has the same form as the Stokes equation (71). The WKBJ solutions of this are obtained using the phase integral result

$$\begin{aligned}\xi &= \int_v^z (v^2 - z^2)^{1/2} \frac{dz}{z}, \\ &= (v^2 - z^2)^{1/2} - v \log \left[ \frac{v}{z} + \frac{(v^2 - z^2)^{1/2}}{z} \right].\end{aligned} \quad (80)$$

Stokes lines are again defined by  $\text{Im}(\xi) = 0$  and anti-Stokes lines by  $\text{Re}(\xi) = 0$ , which are curves starting at  $v = z$  initially at  $\pi/3$  to one another in the complex  $v$ -plane. The Stokes regions and the corresponding dominant term of the asymptotic series are shown in Fig. 6. More detail of this behavior can be found in Nussenzveig (1965). In the Stokes region near the real axis with  $v \gg z$  we obtain the Debye asymptotic expansion (Abramowitz and Stegun, 1965, Section 9.3)

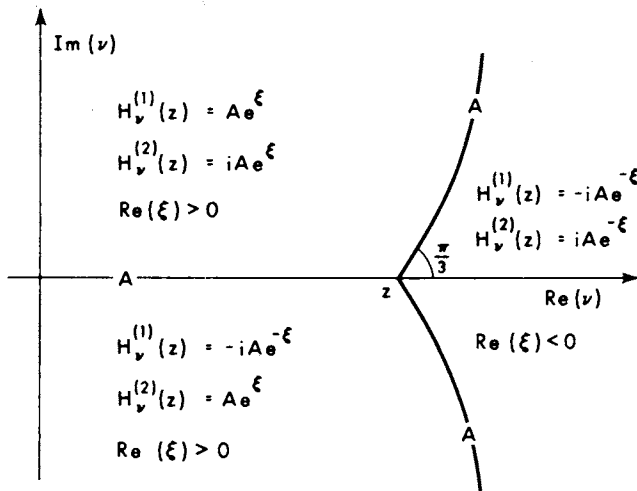


FIG. 6. Stokes regions for the Hankel functions.

$$A = (2/\pi)^{1/2}/(v^2 - z^2)^{1/4} \text{ and } \xi = (v^2 - z^2)^{1/2} - v \log[v/z + (v^2 - z^2)^{1/2}/z].$$

$$\begin{aligned} h_n^{(1)}(z) &\simeq -iz^{-1/2}(v^2 - z^2)^{-1/4}e^{-\xi}, \\ h_n^{(2)}(z) &\simeq iz^{-1/2}(v^2 - z^2)^{-1/4}e^{-\xi}, \end{aligned} \quad (81)$$

while the subdominant term is

$$j_n(z) \simeq \frac{1}{2}z^{-1/2}(v^2 - z^2)^{-1/4}e^{\xi}. \quad (82)$$

Near the anti-Stokes lines combinations of both terms must be used. In particular, on the real axis for  $v < z$  the Hankel asymptotic forms can be used (Abramowitz and Stegun, 1965, Section 9.2)

$$\begin{aligned} h_n^{(1)}(z) &\simeq z^{-1/2}(z^2 - v^2)^{-1/4} \exp\{i[(z^2 - v^2)^{1/2} - v \cos^{-1}(v/z) - \frac{1}{4}\pi]\}, \\ h_n^{(2)}(z) &\simeq z^{-1/2}(z^2 - v^2)^{-1/4} \exp\{-i[(z^2 - v^2)^{1/2} - v \cos^{-1}(v/z) - \frac{1}{4}\pi]\}. \end{aligned} \quad (83)$$

In order to calculate the spherical Hankel functions needed in the response integrals numerically, the HANKEL package was used (Share No. 3157 NBS HNKL). This is suitable for cylindrical Hankel functions with large complex arguments and orders. In the Stokes regions the dominant term of the asymptotic solutions is used and near an anti-Stokes line, a linear combination of both solutions. Near the critical point  $v = z$  the Langer approximation

$$H_v^{(k)}(z) \simeq \exp[(-1)^{k-1}\frac{1}{6}i\pi] \sqrt{1 - \eta} \coth \eta H_{1/3}^{(k)}(-i\xi), \quad (84)$$

where  $\xi = v(\tanh \eta - \eta)$  and  $\eta = \cosh^{-1}(v/z)$ , is used.

The Legendre functions are solutions of Eq. (9) and again we can find approximate solutions using the WKBJ method. Letting  $y = \sin^{-1/2}\theta w$ , the differential equation becomes

$$\frac{\partial^2 w}{\partial \theta^2} + \left(v^2 + \frac{\text{cosec}^2 \theta}{4}\right)w = 0. \quad (85)$$

The solution we require is obtained if  $\theta \neq 0$  or  $\pi$  and  $v \gg 1$  as

$$Q_{v-1/2}^{(2)}(\cos \theta) \simeq e^{i(v\theta - \pi/4)} / (2\pi v \sin \theta)^{1/2}, \quad (86)$$

where the constants have been introduced to satisfy the Legendre series normalization. The second kind of Legendre function is defined as

$$Q_n^{(2)}(\cos \theta) = \frac{1}{2}[P_n(\cos \theta) - (2i/\pi)Q_n(\cos \theta)]. \quad (87)$$

and the full asymptotic expansion for this is (Erdélyi, 1953, p. 162)

$$Q_{v-1/2}^{(2)}(\cos \theta) = \frac{e^{iv\theta}}{(2\pi \sin \theta)^{1/2}} \sum_{l=0}^{\infty} \frac{\Gamma(v + \frac{1}{2}) \exp\{i[l(\theta - \frac{1}{2}\pi) - \frac{1}{4}\pi]\}}{\Gamma(v + l + 1)l!(2 \sin \theta)^l} \left( \frac{\Gamma(l + \frac{1}{2})}{\Gamma(\frac{1}{2})} \right)^2 \quad (88)$$

which is convergent for  $\pi/6 < \theta < 5\pi/6$  and is valid asymptotically provided  $\theta \neq 0$  or  $\pi$ . The first-order term can be found using

$$\Gamma(v + \frac{1}{2})/\Gamma(v) \simeq v^{1/2} + O(1/v) \quad (89)$$

giving the result (86). The Legendre function was evaluated numerically using (88) and an asymptotic series for (89) (Erdélyi, 1953, p. 5).

### C. THE WKBJ SOLUTION

The WKBJ solutions are normally only considered for purely real or imaginary wavenumbers, i.e. the solutions are oscillatory or exponential. They remain valid subject to the limitations of the Stokes phenomena for complex wavenumbers (Budden, 1966, Chapter 20). In Section V, B we will discuss how the limits of the range of validity are determined. Here we discuss the properties of the WKBJ solution when the wavenumber is complex.

Clearly the wavenumber (67) cannot have a zero for real  $r$  if the wavenumber  $v$  is complex. We can consider the  $P$  velocity  $\alpha$  as a function of a complex variable  $r$  and analytically continue the velocity into the complex  $r$ -plane. Then a zero  $q_\alpha(r_0)$  usually exists. Defining the phase integral as

$$\xi = \int_{r_0}^r q_\alpha(\zeta) d\zeta, \quad (90)$$

Stokes [ $\text{Re}(\xi) = 0$ ] and anti-Stokes [ $\text{Im}(\xi) = 0$ ] lines exist in the complex  $r$ -plane starting at the point  $r_0$ . We define the top Riemann sheet such that  $\text{Re}(q_\alpha) > 0$  so the branch cut lies near the Stokes line. If  $\text{Im}(v) > 0$  then using the Cauchy-Riemann relations we can see that  $\text{Im}(r_0) > 0$ . The WKBJ solution on the top Riemann sheet

$$\bar{\phi} = [1/r(\rho q_\alpha)^{1/2}] e^{i\xi} \quad (91)$$

is exponentially growing in the direction of propagation outwards. Similarly the inward traveling solution

$$\bar{\phi} = [1/r(\rho q_\alpha)^{1/2}] e^{-i\xi} \quad (92)$$

grows in the direction of propagation. These solutions will only be valid at radii well above the point  $r_0$ . In the region near  $r_0$  they must be connected by a numerical solution of the exact wave equation (see Section V). Figure 7a shows details of features in the complex  $r$ -plane.

If  $\text{Im}(\nu) < 0$  then the zero is below the real axis. Solutions (91) and (92) both decay in their direction of propagation. Figure 7b shows the complex  $r$ -plane for this case. Both these cases will arise in evaluating the complex

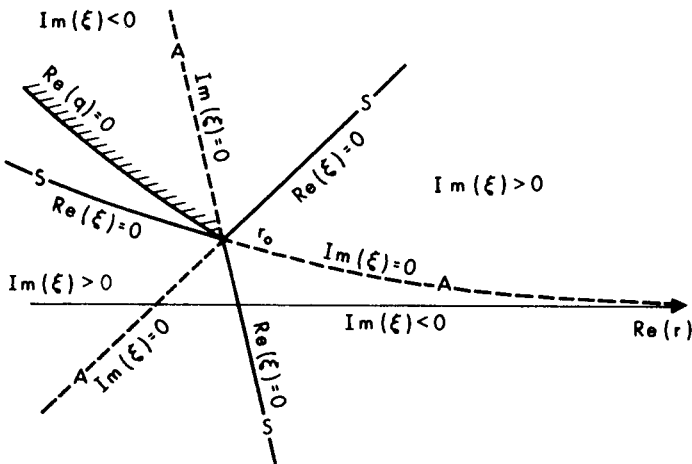


FIG. 7a. The complex  $r$ -plane when  $\text{Im}(\nu) > 0$ . Stokes and anti-Stokes lines defined by  $\text{Re}(\xi) = 0$  and  $\text{Im}(\xi) = 0$ , respectively, and the branch cut defined by  $\text{Re}(q_a) = 0$  are indicated.

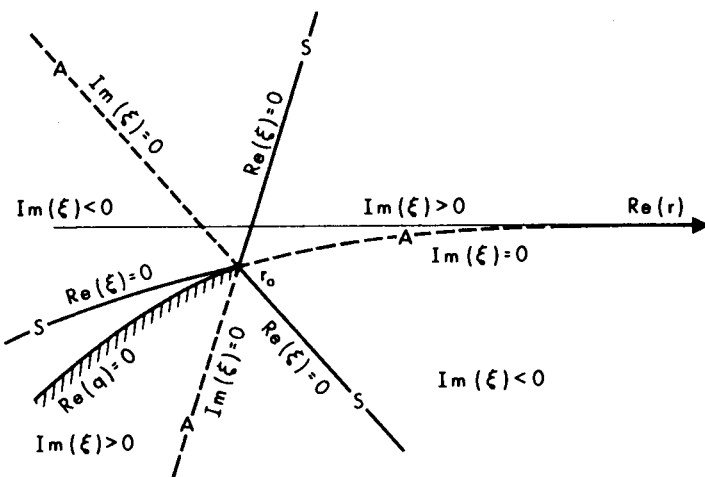


FIG. 7b. Same as Fig. 7a except  $\text{Im}(\nu) < 0$ .

response integral. The WKBJ solution is used on the real  $r$  axis in its range of validity and connected to a solution of the wave equation at  $r = r^*$ . Well below the zero  $r_0$  the wave solution must decay exponentially and correspond to the subdominant WKBJ solution. This is used as the starting condition in the Stokes region on the real axis.

Figure 7b would also apply for a real wavenumber  $v$  if attenuation were added to the model. It has been shown (Ewing *et al.*, 1957, p. 272) that attenuation can be approximated theoretically using complex wave velocities. Thus for a dilatational loss-free medium

$$\begin{aligned}\alpha' &= \alpha[1 - \frac{4}{3}iQ^{-1}(\beta/\alpha)^2]^{1/2}, \\ \beta' &= \beta[1 - iQ^{-1}]^{1/2},\end{aligned}\quad (93)$$

as used by Phinney and Alexander (1966). Introducing attenuation has the effect of reducing  $\text{Im}(r_0)$  and increases the decay or reduces the growth of the WKBJ solution taken on the real  $r$  axis.

## V. Numerical Solution of the Wave Equation

### A. THE RUNGE-KUTTA AND HAMMING'S MODIFIED PREDICTOR-CORRECTOR METHODS

Many methods exist for solving a system of coupled, linear, first-order differential equations such as (14) and (15). Replacing the differential equation by a finite difference equation, a step method can be used to integrate the equations. The Runge-Kutta interpolation methods are the easiest to use for solving an initial-value problem. The methods are self-starting and so require no special treatment initially or at discontinuities. Extrapolation methods, such as the Adams or Milne method, are more efficient for the same step size but may be unstable (e.g., the Milne method—Scheid, 1968, p. 195). Typically several hundred solutions of the differential system (14) will be required for each evaluation of the response integral (68). Thus it is important that we use the most efficient method which will give the required accuracy.

In a similar problem, Gilbert and Backus (1969) have automatically chosen the step size and order of the Runge-Kutta method to obtain the required accuracy. The truncation error in using an  $m$ th-order method is

$$\delta \leq \gamma \frac{h_m^{m+1}}{(m+1)!} y^{(m+1)}(\zeta), \quad (94)$$

where  $y(r)$  is the solution and  $\zeta$  lies within the step. For extrapolation methods the numerical constant  $\gamma$  is often known, but this is rarely so for Runge-Kutta

methods. However,  $\gamma$  is often of order unity and is ignored in (94). Thus the relative truncation error is

$$\varepsilon \lesssim (\lambda h_m)^{m+1} e^{\lambda h_m} / (m+1)! \quad (95)$$

Provided  $\varepsilon \ll 1$  this can be solved iteratively for  $\lambda h_m$  (Gilbert and Backus, 1969) and, if  $\lambda$  is known or can be estimated, provides a conservative estimate for  $h_m$ . Table I contains solutions to (95) for  $m = 1, \dots, 8$  and three values of  $\varepsilon$  ( $10^{-5}$ ,  $10^{-10}$ , and  $10^{-15}$ ).

In general, an  $m$ th-order Runge-Kutta method can be written as

$$\begin{aligned} x_{j-1} &= x_0 + a_j h_m & j = 1, \dots, l & (a_1 = 0, a_l = 1), \\ k_j &= h_m f(x_{j-1}, y_{j-1}) & j = 1, \dots, l, \\ y_j &= y_0 + \sum_{n=0}^j b_{jn} k_n & j = 1, \dots, l-1, \end{aligned} \quad (96)$$

and finally

$$y_l = y_0 + \sum_{j=1}^l c_j k_j,$$

where  $y_0 = y(x_0)$  and  $y_l = y(x_{l-1}) = y(x_0 + lh)$ . The number of intermediate steps  $l$  is dependent on  $m$  ( $l \geq m$ ) and can be found in Table I for  $m \leq 8$ . Details of the constant  $a_j$ ,  $b_{jn}$ ,  $c_j$  can be found in Isaacson and Keller (1966, p. 402) (orders 1, 2, 3, and 4), Sarafyan (1966) (order 5), Huta (1957) (order 6), and Shanks (1966) (orders 7 and 8). The fourth-order method has been commonly used as it is relatively simple and requires little intermediate storage ( $l = 4$ ,  $a_2 = a_3 = b_{11} = b_{22} = \frac{1}{2}$ ,  $b_{33} = 1$ ,  $c_1 = c_4 = \frac{1}{6}$ ,  $c_2 = c_3 = \frac{1}{3}$ , and all other constants are zero). With modern digital computers, however, any order method is easy to program. Using the definition (95) for the step size it is clear that  $h_1 < h_2 < \dots < h_8$ . However, the relative step size for methods of different order is dependent on the relative truncation error  $\varepsilon$ . For very small truncation error  $\varepsilon$ , Gilbert and Backus' (1969) assumption that "the computing time using the  $m$ th one-step method increases with  $m$  less rapidly than does the step-size" holds. However, for  $\varepsilon$  larger little advantage is to be gained by using higher order methods as the extra computations per step outweigh the extra step size. Let us estimate how many computations (a multiplication and addition) per step are needed in a Runge-Kutta method. If the matrix  $M$  is  $n \times n$  we might expect about  $n^2$  computations for each determination of  $M$  and  $n^2$  computations for each determination of the derivative. In addition, intermediate solutions have to be multiplied by the

TABLE I  
STEP SIZE PARAMETERS FOR INTEGRATING USING DIFFERENT METHODS<sup>a</sup>

$m$	$l$	$N$	$\varepsilon = 10^{-5}$			$\varepsilon = 10^{-10}$			$\varepsilon = 10^{-15}$		
			$\lambda h$	$N_t$	$\lambda h$	$N_t$	$\lambda h$	$N_t$	$\lambda h$	$N_t$	$\lambda h$
1	1	56	$0.4462 \times 10^{-2}$	$1255 \times 10$	$0.1414 \times 10^{-4}$	$3960 \times 10^3$	$0.4472 \times 10^{-7}$	$1252 \times 10^6$			
2	2	120	$0.3865 \times 10^{-1}$	$3105$	$0.8432 \times 10^{-3}$	$1413 \times 10^2$	$0.1817 \times 10^{-4}$	$6604 \times 10^3$			
3	3	192	$0.1208$	$1589$	$0.6987 \times 10^{-2}$	$2748 \times 10$	$0.3936 \times 10^{-3}$	$4878 \times 10^2$			
4	4	272	$0.2479$	$1097$	$0.2592 \times 10^{-1}$	$1049 \times 10$	$0.2604 \times 10^{-2}$	$1044 \times 10^2$			
5	6	456	$0.4104$	$1111$	$0.6382 \times 10^{-1}$	$7145$	$0.9452 \times 10^{-2}$	$4824 \times 10$			
6	8	672	$0.5991$	$1122$	$0.1238$	$5428$	$0.2424 \times 10^{-1}$	$2772 \times 10$			
7	9	792	$0.8070$	$981$	$0.2063$	$3839$	$0.4989 \times 10^{-1}$	$1587 \times 10$			
8	12	1200	$1.029$	$1166$	$0.3102$	$3868$	$0.8847 \times 10^{-1}$	$1357 \times 10$			
4*	4	232	$0.2479$	$936$	$0.2592 \times 10^{-1}$	$8951$	$0.2604 \times 10^{-2}$	$8909 \times 10$			
4+	2	176	$0.2479$	$710$	$0.2592 \times 10^{-1}$	$6790$	$0.2604 \times 10^{-2}$	$6759 \times 10$			

<sup>a</sup>  $m$  is the order of the Runge-Kutta method,  $l$  the number of intermediate steps (see references in text). The number of computations per step is approximately  $N = (1 + k)n^2 l + \frac{1}{2} kn(l+1)$  with  $n = 4$  and  $k = 2$  for  $m = 1$  to 8,  $m = 4^*$  is the reduced Runge-Kutta program and  $m = 4^+$  is the Hamming's modified predictor-corrector method. Note for  $m = 4$ ,  $N = 4(1 + k)n^2 + 10 kn$  whereas for  $m = 4^*$ ,  $N = 3(1 + 4k)n^2 + 7kn$ , and for  $m = 4^+$ ,  $N = (1 + 2k)n^2 + 12 kn$ . The step size  $\lambda h_m$  for the three values of  $\varepsilon$  is given using Eq. (95).  $N_t$  is an approximation to the number of computations for a distance  $\lambda^{-1}$ .

constants  $b_{jn}$  and  $c_j$ . There are  $\frac{1}{2}l(l+1)$  of these additions and for a vector of  $n$  components this gives  $\frac{1}{2}nl(l+1)$ . Suppose that  $k$  solutions of (14) are performed simultaneously, so an estimate of the number of computations per step is

$$N = (1 + k)n^2l + \frac{1}{2}knl(l+1). \quad (97)$$

This number is included in Table I for  $n = 4$  and  $k = 2$ . Finally, in Table I an estimate of the number of computations necessary to integrate a distance  $\lambda^{-1}$  is listed. From this table it is clear that at the highest accuracy tabulated ( $\epsilon = 10^{-15}$ ) the use of the higher order methods is advantageous, whereas at the lowest accuracy ( $\epsilon = 10^{-5}$ ), there is no advantage in using methods above the fourth-order method. If we restrict ourselves to the fourth-order method, we can take advantage of the fact that two of the  $a_j$ 's are equal [and the function is linear in  $y$ , i.e.,  $f(x, y) = M(x)y'(x)$ ], to reduce the number of matrix calculations to 3 (rather than  $l = 4$ ), and that many of the  $b_{jn}$ 's are zero to reduce the number of multiplications and additions of solutions to 7 (rather than  $\frac{1}{2}l(l+1) = 10$ ). The reduced figure is also included in Table I ( $m = 4^*$ ) for comparison. Although the number of computations differs somewhat the same conclusion would be drawn if  $n = 6$  and only one solution were needed ( $k = 1$ ). We shall see later that it is advantageous to replace the fourth-order differential system by a sixth-order system (117) but only one solution will then be needed. Similarly for an SH solution  $n = 2$  and  $k = 1$  but the same methods are used.

In studying the Earth's normal modes, Gilbert and Backus (1969) obtained several advantages using Runge-Kutta methods of orders 1 to 8. High accuracy was necessary [see, for instance, Derr (1967) for a discussion of root finding] and high order methods could be used to advantage. As the Runge-Kutta methods are self-starting the step size could be reset at each step. Typically in evaluating the response integral (68) the frequency and wave-number are larger than in normal mode calculations. Thus the step size will be smaller. The integral will be over a smaller range and a larger relative truncation error  $\epsilon$  can be tolerated at each step. Using single-precision arithmetic on an IBM 360 computer a relative truncation error  $\epsilon = 10^{-5}$  or  $10^{-6}$  comparable with the rounding error is realistic. Thus we see that it is most efficient, and simplest, to restrict the integration scheme to the fourth-order Runge-Kutta method.

As was mentioned above, extrapolation integration methods are more efficient than the equivalent Runge-Kutta method but may be unstable. Stable low order extrapolation methods exist but higher order methods are often unstable (Mitchell and Craggs, 1953). The Hamming's modified predictor-corrector method is a stabilized version of Milne's classical fourth-order predictor-corrector method (Ralston, 1965, p. 189):

$$\begin{aligned}
 p_{j+1} &= y_{j-3} + \frac{4}{3}h(2y_j' - y_{j-1}' + 2y_{j-2}') && \text{predictor.} \\
 m_{j+1} &= p_{j+1} - \frac{1}{2}\gamma^2(p_j - c_j) && \text{modifier,} \\
 m_{j+1}' &= f(x_{j+1}, m_{j+1}), \\
 c_{j+1} &= \frac{1}{8}[9y_j - y_{j-2} + 3h(m_{j+1}' + 2y_j' - y_{j-1}')] && \text{corrector.} \\
 y_{j+1} &= c_{j+1} + \frac{9}{2}\gamma(p_{j+1} - c_{j+1}),
 \end{aligned} \tag{98}$$

where  $x_j = x_0 + jh$  and  $y_j = y(x_j)$ . The subscript has a different meaning from Eq. (96) and  $h = h_4$ . The truncation error is given by

$$\varepsilon = -\frac{1}{40}h^5\gamma^{(5)}(\zeta), \tag{99}$$

i.e.,  $\gamma = -3$  in expression (94), where  $\zeta \in (x_{j-2}, x_{j+1})$ . Only two derivative calculations are now necessary per step. The reduced number of computations per step and per distance  $\lambda^{-1}$  are included in the final line of Table I. Clearly the method is more efficient than the fourth-order Runge-Kutta method. The step size must be kept constant, however.

Usually, the Earth model is specified by velocities at approximately 50 km intervals. In each interval the step size is chosen using the result (95) with  $m = 4$ . The integration is started using the fourth-order Runge-Kutta method for four steps and continued using the Hamming's modified predictor-corrector method for the remainder of the interval. The integration in the next interval is started again using the Runge-Kutta method and a new step size.

In order to estimate the step size we assume that the wave equation separates, e.g. Eq. (65). The local wavenumber of the WKBJ solution is

$$\lambda = |q_x| \quad \text{or} \quad |q_\beta| \tag{100}$$

but this solution breaks down for small  $r$ . Suppose we assume that  $y \sim e^{2r}$  then Eq. (65) becomes

$$\lambda^2 r^2 + 2r\lambda + [k^2 r^2 - n(n+1)] = 0 \tag{101}$$

and the maximum solution for  $\lambda$  is

$$\begin{aligned}
 |\lambda| &= \left| \frac{1}{r} + \left( \frac{n^2 + n + 1}{r^2} - k^2 \right)^{1/2} \right|, \\
 &\leqq \frac{1}{r} + \left| \left( \frac{n^2 + n + 1}{r^2} - k^2 \right)^{1/2} \right|.
 \end{aligned} \tag{102}$$

The wavenumber which maximizes (100) or (102) for either of the two velocities is chosen to define the step size.

### B. BOUNDARY CONDITIONS FOR REFLECTION COEFFICIENTS

In Section IV we showed that the WKBJ solution could be used except near Stokes lines. We must define a band on either side of the Stokes lines outside which the WKBJ solutions are valid. The most obvious choice is to require

$$r \operatorname{Re}(q(r)) > C_1 \quad (103)$$

outside the band.  $C_1$  is a dimensionless constant large compared with unity such that  $C_1^{-1}$  is an approximate measure of the fractional error in the WKBJ solution. Experience has shown that  $C_1 \approx 50$  is suitable. The error in the dominant solution is less than the subdominant term at the Stokes line. Thus an alternative condition would be

$$2\operatorname{Re}\left(\int_{r_0}^r q(\zeta) d\zeta\right) > C_2 \quad (104)$$

assuming the solutions have comparable magnitude at  $r_0$ . This is a condition on the exponential growth and decay of the solutions, i.e., they differ in magnitude by  $e^{C_2}$ . Assuming  $q(r)$  is linear in the neighborhood of  $r_0$  this reduces to the condition

$$\operatorname{Re}((r - r_0)q(r)) > C_2. \quad (105)$$

In practise it is simpler to use the first condition (103). The second would be more satisfactory if  $r_0$  changed greatly: different values of  $C_1$  would be appropriate for studying Pcp and PKP whereas the same value of  $C_2$  could be used.

Two conditions may apply to the wave solution for  $r < r^*$  where  $r = r^*$  is the radius at which the WKBJ solution breaks down. If  $v$  is real, then for  $r < r_0$  the solutions will be evanescent. If  $v$  is complex, then for  $r < r^*$  an anti-Stokes line will be crossed and below this, a region in which the evanescent WKBJ solutions are valid will be entered (Fig. 7). Similar conditions to (103) and (104) will apply to the imaginary part of the wavenumber. Thus we can try to find a radius  $r_D$  such that

$$-\operatorname{Im} \int_{r_D}^{r_0} q(\zeta) d\zeta < \log_e S, \quad (106)$$

where  $S$  is a small number (say  $10^{-4}$ ). At this radius  $r = r_D$  the solution will have decayed by a factor  $S^{-1}$ . A similar condition has been used by Wiggins

(1968) to find the starting point for normal mode solutions. Note that as  $\text{Im}(v)$  is generally small, we have assumed that  $r_D$  is below the radius at which the anti-Stokes lines crosses the real  $r$  axis and have ignored the possibility of a region near  $r_0$  between the Stokes and anti-Stokes lines in which WKBJ solutions are again valid.

If a radius  $r_D$  exists which satisfies (106) such that  $r_D > r_c$ , then the wave solution has decayed by a factor  $S^{-1}$  at  $r_D$  and the numerical solution is started at this radius. The interaction of the wavefunction with the core is ignored since the incident P-wavefunction has negligible amplitude at  $r_c$ , i.e., less than a factor  $S$  of the incident wave. The only waves which may exist at  $r_D$  are an evanescent P-wave, i.e.

$$\bar{\mathbf{u}}_1(r_D) = \bar{\mathbf{u}}_p^{(1)}(r_D) + \bar{\mathbf{u}}_p^{(2)}(r_D) \quad (107)$$

and a downward traveling SV wave, i.e.,

$$\bar{\mathbf{u}}_2(r_D) = \bar{\mathbf{u}}_s^{(2)}(r_D) \quad (108)$$

caused by interaction of the P-wave with the velocity gradient near its turning point. The upward traveling SV wave reflected by the core does not exist at  $r = r_0$  in the solution we require as it is part of another term in the rainbow expansion. The starting solutions (107) and (108) apply for the direct P ray when the turning point  $r_0$  is well above the core-mantle interface. In the diffraction problem, however, such a radius often cannot be found and the starting radius is taken as the core boundary, i.e.,  $r_D = r_c$ .

Using the rainbow expansion at the core-mantle interface, we know that energy must be transmitted into the core wave. This wave, the degenerate case ( $\mu_c = 0$ ) of (32) is taken as the solution in the fluid core, i.e.,

$$\bar{\mathbf{u}}_1(r_D) = \bar{\mathbf{u}}_p^{(2)}(r_c) = \frac{1}{\alpha(\rho k \omega)^{1/2}} \begin{pmatrix} k_c h_{v-1/2}^{(2)}(k_c r_c) \\ \frac{h_{v-1/2}^{(2)}(k_c r_c)}{r_c} \\ -\lambda_c k_c^2 h_{v-1/2}^{(2)}(k_c r_c) \\ 0 \end{pmatrix}. \quad (109)$$

In addition, the tangential displacement may be discontinuous at the solid-fluid boundary so another starting solution is

$$\bar{\mathbf{u}}_2(r_D) = (0, 1, 0, 0)^T. \quad (110)$$

Under either condition for the starting radius  $r_D$ , two independent displacement-stress vectors,  $\bar{\mathbf{u}}_1$  and  $\bar{\mathbf{u}}_2$ , have been specified. These two solutions can be integrated through increasing radius  $r$  to give  $\bar{\mathbf{u}}_1(r^*)$  and  $\bar{\mathbf{u}}_2(r^*)$  at  $r^*$  using the methods outlined in Section V, A.

At  $r^*$  each solution will contain components of all four wave types, P- and SV-waves traveling in both directions. A linear combination can be chosen in which the only incident wave is the P-wave and the downgoing SV-waves cancel. Algebraically this can be written as

$$\mathbf{U}_0'(r^*)\phi_0' = c\bar{\mathbf{u}}_1(r^*) + d\bar{\mathbf{u}}_2(r^*). \quad (111)$$

where the right-hand side is the linear combination of solutions and the left-hand side contains the incident and reflected waves.  $\phi_0'$  is defined by (54) with  $r^*$  replacing  $a_1$ , and  $\mathbf{U}_0'(r^*)$  by (48). A subscript 0 refers to the values at  $r^*$  in both  $\phi_0'$  and  $\mathbf{U}_0'(r^*)$ . This can be solved for the reflection coefficients. The required solution is

$$R_{pp}(r^*, v) = -\frac{\bar{w}_1 a_6 - \bar{w}_2 a_5 + \bar{w}_3 a_4 + \bar{w}_4 a_3 - \bar{w}_5 a_2 + \bar{w}_6 a_1}{\bar{w}_1 b_6 - \bar{w}_2 b_5 + \bar{w}_3 b_4 + \bar{w}_4 b_3 - \bar{w}_5 b_2 + \bar{w}_6 b_1}, \quad (112)$$

where  $\bar{w}_i$ ,  $a_i$ , and  $b_i$  are the second-order minors formed from the pairs of vectors  $\bar{\mathbf{u}}_1(r^*)$  and  $\bar{\mathbf{u}}_2(r^*)$ ,  $\bar{\mathbf{u}}_p^{(2)}(r^*)$  and  $\bar{\mathbf{u}}_p^{(1)}(r^*)$ , and  $\bar{\mathbf{u}}_p^{(1)}(r^*)$  and  $\bar{\mathbf{u}}_p^{(1)}(r^*)$ , respectively (Gantmacher, 1959, p. 2). For instance

$$\bar{\mathbf{w}} = \bar{\mathbf{u}}_1 \otimes \bar{\mathbf{u}}_2 = \begin{pmatrix} \bar{u}_{11}\bar{u}_{22} - \bar{u}_{12}\bar{u}_{21} \\ \bar{u}_{11}\bar{u}_{23} - \bar{u}_{13}\bar{u}_{21} \\ \bar{u}_{11}\bar{u}_{24} - \bar{u}_{14}\bar{u}_{21} \\ \bar{u}_{12}\bar{u}_{23} - \bar{u}_{13}\bar{u}_{22} \\ \bar{u}_{12}\bar{u}_{24} - \bar{u}_{14}\bar{u}_{22} \\ \bar{u}_{13}\bar{u}_{24} - \bar{u}_{14}\bar{u}_{23} \end{pmatrix} \quad (113)$$

### C. ANALYTIC INDEPENDENCE—NUMERICAL DEPENDENCE OF SOLUTIONS

The Runge-Kutta and Hamming's modified predictor-corrector methods are stable methods and so, provided the step size is chosen small enough, we might expect the solution for  $R_{pp}(r^*, v)$  to be accurate. Unfortunately this is not necessarily so.

Some of the numerical difficulties in integrating the differential system (14) can be removed by transformations of the variables  $\bar{\mathbf{u}}$  and  $r$ . The most important difficulty can only be avoided, however, by a more significant change. From the Jacobi identity

$$|\mathbf{F}(r)| = |\mathbf{F}(r_D)| \exp\left\{\int_{r_D}^r \text{tr } \mathbf{M}(\zeta) d\zeta\right\} \quad (114)$$

where  $\mathbf{F}(r)$  is a fundamental matrix of the differential system (Gilbert and Backus, 1966), we can deduce the well-known result that if the solutions in the matrix  $\mathbf{F}$  are initially independent at  $r = r_D$ , then they remain so (Gantmacher, 1959, Vol. II, p. 114). In addition it will be an advantage in a numerical integration scheme if

$$\text{tr } \mathbf{M}(\zeta) = 0. \quad (115)$$

Wiggins (1968) has indicated how, using the Lyapunov transformations, the modified differential matrix will satisfy condition (115). In addition, none of the terms of the matrix will become very large for large  $n$  or small  $r$ , and its eigenvalues are well behaved for all values of  $n$  and  $r$ . While this transformation minimizes some of the numerical difficulties in integrating the differential system, it does not influence the fundamental difficulty.

Lyapunov's stability criterion states that the solution of a differential system such as (14) is stable if all the eigenvalues of the differential matrix  $\mathbf{M}$  have negative real parts (Gantmacher, 1959, Vol. I, p. 129). This stability condition will not be altered by a Lyapunov transformation (Gantmacher, 1959, Vol. II, p. 117). These conditions as given in Gantmacher (1959) apply to a mechanical system being integrated through increasing time. They apply equally to our system being integrated through increasing radius. If integrated in the decreasing radius direction, then the eigenvalues must have a positive real part for stability. A good discussion of this problem is contained in Lanczos (1961, Section 9.13).

Two types of instability can occur in integrating a differential system numerically. Instabilities may be introduced by the finite difference scheme used (Todd, 1950). This can be avoided, however, by a choice of stable methods. The other type of instability is a property of the differential system being integrated. Locally, the rates of growth of the independent solutions of the differential system (14) are controlled by the eigenvalues of the matrix  $\mathbf{M}$ . If one eigenvalue has a positive real value  $\text{Re}(\lambda)$  then a solution will grow as  $e^{\text{Re}(\lambda)r}$ . Suppose that we are integrating two independent solutions of (14) corresponding to the P- and SV-waves below the turning point of the P ray but in the traveling wave region of the SV ray. This is typical of the solutions set up in Section V, B. Assuming  $v$  is real, the P solution will locally behave as  $\exp[|\text{Im}(q_s)|r]$  whereas the SV solution will only vary slowly. Numerically the solution will be unstable. Any error in the SV solution will contain a component of the P solution and this will grow exponentially. Eventually this exponential growth of the error will predominate the SV solution and both

solutions will be equivalent to the P-wave function. Although we know that initially the solutions were independent and according to (114) must remain so, numerically they have become dependent. In general, all the numerical solutions will be dominated by the solution with the greatest rate of growth, i.e. the eigenvalue with the maximum real part. This difficulty is not avoided by any Lyapunov transformation of the differential system.

This difficulty was encountered and solved by Pitteway (1965) in a similar problem of integrating the wave equations in the ionosphere. Essentially, the independence of the numerical solutions is maintained throughout the integration so that the error in the unstable solution is never allowed to grow significantly. Only a linear combination of the solutions is required, so at some points during the integration a certain fraction of the dominant solution can be subtracted from the other solution. This subtraction must be done before the error has grown significantly and must remove the component of the dominant solution present. Thus if  $\bar{u}_1(r)$  is the dominant solution, the other solution  $\bar{u}_2(r)$  is modified to

$$\bar{u}_2'(r) = \bar{u}_2(r) - \frac{\bar{u}_1(r)*\bar{u}_2(r)}{\bar{u}_1(r)*\bar{u}_1(r)} \bar{u}_1(r). \quad (116)$$

The product used in the orthogonalization has already been defined in (44). Note that the dominant solution  $\bar{u}_1$  is obtained without difficulty.

A more elegant method to overcome the instability is to replace the fourth-order differential system by the equivalent sixth-order differential system for the second-order minors (Gilbert and Backus, 1966, 1969). The system (14) is replaced by

$$\partial \bar{w} / \partial r = .// \bar{w} \quad (117)$$

where the  $6 \times 6$  matrix  $.//$  has been given by Gilbert and Backus (1966, 1969):

$$\mathcal{M} = \begin{pmatrix} M_{11} + M_{22} & M_{23} & M_{24} & -M_{13} & -M_{14} & 0 \\ M_{32} & M_{11} + M_{33} & M_{34} & M_{12} & 0 & -M_{14} \\ M_{42} & M_{43} & M_{11} + M_{44} & 0 & M_{12} & M_{13} \\ -M_{31} & M_{21} & 0 & M_{22} + M_{33} & M_{34} & -M_{24} \\ -M_{41} & 0 & M_{21} & M_{43} & M_{22} + M_{44} & M_{23} \\ 0 & -M_{41} & M_{31} & -M_{42} & M_{32} & M_{33} + M_{44} \end{pmatrix} \quad (118)$$

From Kronecker's theorem (Gantmacher, 1959, Vol. 1, p. 75) it follows that the six eigenvalues of  $.//$  are equal to the sums of the four eigenvalues of  $M$  taken in pairs. Thus they will be approximately given by zero and  $\pm iq_a \pm iq_b$ .

The system is still unstable according to the Lyapunov criterion, and the maximum rate of growth is approximately given by

$$\exp\{| \operatorname{Im}(q_\alpha)| + | \operatorname{Im}(q_\beta)| \}r. \quad (119)$$

Fortunately, however, the solution we require corresponds to this eigenvalue. Any of the five other solutions would be dominated by this solution. For a similar reason no numerical difficulties will be encountered integrating the SH system directly. Below the turning point the system is unstable but the solution we require is the dominant solution which grows exponentially with radius. Difficulties would occur if the decaying solution were required.

In order to underestimate the step size, we can take

$$\lambda = | q_\alpha | + | q_\beta | + (2/r) \quad (120)$$

instead of expression (102). The starting solution for the one solution required is

$$\bar{\mathbf{w}}(r_D) = \bar{\mathbf{u}}_1(r_D) \otimes \bar{\mathbf{u}}_2(r_D), \quad (121)$$

and the second-order minors needed for the reflection coefficient (112) are obtained directly. The numerical difficulty encountered calculating minors by subtracting large and nearly equal terms is thus avoided. Similar difficulties arising in computations using Haskell matrices are also overcome using second-order minors (Dunkin, 1965), and such a scheme would be used to implement the results in Section III, A.

Although the step size used with expression (120) in Eq. (95) is naturally smaller than for the system (14) the loss in efficiency is not great. The numerical integration only occurs near the turning point  $r_0$  when one of the wave-numbers is zero, i.e.  $q_\alpha(r_0) = 0$ . The  $4 \times 4$  matrix has been replaced by a  $6 \times 6$  matrix but only one solution is needed. Again the loss of efficiency is small. An estimate of the number of operations per step of the Runge-Kutta method is 294 compared with 232 for the equivalent solution using the differential equation (14).

## VI. The Response Integral

### A. THE SADDLE POINTS

The response integrals for the homogeneous layered model (62) or the inhomogeneous model (68) can both be approximately evaluated in some regions. In order to perform the integration numerically it is essential to study the approximate analytic behavior. We shall restrict ourselves to the response

integral for an inhomogeneous model (68) but the results are identical for the layered model (62) if the spherical Hankel functions are approximated by the Hankel asymptotic expansion (83).

If  $v = k_\alpha r_c$  where

$$k_\alpha = \omega/\alpha(r_c) \quad (122)$$

then the turning point of the P ray will be at the core-mantle boundary, i.e.,  $r_0 = r_c$  and  $q_\alpha(r_c) = 0$ . Three separate cases can be considered: (1)  $v \gg k_\alpha r_c$ , (2)  $v \ll k_\alpha r_c$ , and (3)  $v \approx k_\alpha r_c$ . In this section we shall discuss the second-order saddle point approximations for the first two cases and in Section VI, B the diffraction pole approximation to the third case. Using these results we will indicate in Section VI, C how the integral can be evaluated numerically for all regions.

### 1. The Direct Ray

Suppose  $v \gg k_\alpha r_c$  so that the turning point is well above the core-mantle boundary, i.e.,  $r_0 \gg r_c$ . Then normally we can approximate  $q_\alpha^2(r)$  by a linear function near  $r_0$  and the potential equation (65) reduces to the Stokes equation (71). The WKBJ solutions for the incident and reflected waves can be connected using the Airy solution (72) of the Stokes equation in the standard fashion (Budden, 1966, p. 325):

$$R_{pp}(r^*, v) = -i \exp\left(2i \int_{r_0}^{r^*} q_\alpha(\zeta) d\zeta\right). \quad (123)$$

This result would be incorrect if  $q_\alpha^2(r)$  was significantly nonlinear near  $r_0$ . The most important cases when this occur are if  $r_0$  is near  $r_c$  [where  $q_\alpha^2(r)$  is discontinuous] or when  $r_0$  is near a velocity reversal [when  $q_\alpha^2(r)$  will be approximately parabolic and contain two neighboring zeros]. Both these possibilities will be covered in Section VI, B. Assuming (123) holds, and approximating the Legendre function by (86), we obtain for the phase of the integrand

$$\xi = - \int_b^{r_0} q_\alpha(\zeta) d\zeta + \int_{r_0}^r q_\alpha(\zeta) d\zeta + v\theta \quad (124)$$

plus some constant terms. A saddle point exists when

$$\frac{d\xi}{dv} = v \int_b^{r_0} \frac{d\zeta}{\zeta^2 q_\alpha(\zeta)} - v \int_{r_0}^r \frac{d\zeta}{\zeta^2 q_\alpha(\zeta)} + \theta = 0. \quad (125)$$

If  $\theta < \theta_c$ , the shadow angle, this is satisfied for  $v > k_x r_c$ . By comparison with the classical ray result (Bullen, 1963, p. 111)

$$\Delta(p) = p \int_{r_0}^b \frac{dr}{r(\eta^2 - p^2)^{1/2}} + p \int_{r_0}^r \frac{dr}{r(\eta^2 - p^2)^{1/2}}, \quad (126)$$

we can identify  $v = \omega p$  [where  $p = (r \sin i)/\alpha$ , with the same notation as Bullen, 1963]. Evaluating the second-order saddle point contribution we find

$$\begin{aligned} \tilde{\phi}_p(\omega, r, \theta) = & \frac{\tilde{\phi}_0(\omega)}{ik_s br} \cdot \frac{T_D(\omega p) T_U(\omega p) \omega p^{1/2}}{(q_x(b) q_x(r) \sin \Delta)^{1/2}} \left( \frac{\rho(b)}{\rho(r)} \right)^{1/2} \left| \frac{d\Delta}{dp} \right|^{-1/2} \\ & \times \exp \left\{ i\omega \left[ p\Delta + \int_{r_0}^b r^{-1}(\eta^2 - p^2)^{1/2} dr + \int_{r_0}^r r^{-1}(\eta^2 - p^2)^{1/2} dr \right] \right\}, \end{aligned} \quad (127)$$

where we have used

$$\frac{d^2 \xi}{dv^2} = -\frac{1}{\omega} \frac{d\Delta}{dp} \quad (128)$$

and

$$q_x(r) = \omega r^{-1}(\eta^2 - p^2)^{1/2}. \quad (129)$$

The steepest descent path for which the integral is evaluated is at  $\pi/4$  to the real  $v$  axis as (128) is positive. The exponent in (127) gives the ray arrival time

$$T = p\Delta + \int_{r_0}^b r^{-1}(\eta^2 - p^2)^{1/2} dr + \int_{r_0}^r r^{-1}(\eta^2 - p^2)^{1/2} dr \quad (130)$$

(Bullen, 1963, p. 112). With minor notational changes the magnitude of (127) can be identified with the geometrical ray amplitude (Bullen, 1963, p. 126).

## 2. The Reflected Ray

If  $v \ll k_x r_c$  then the turning point  $r_0$  will not exist above the core-mantle interface. Under these conditions the WKBJ solutions will be valid up to the core-mantle interface, i.e.,  $r^* = r_c$ . Thus no integration will be required

( $r_D = r^*$ ) and substituting the starting conditions (109) and (110) into (112) will amount to finding the reflection coefficient from the interface alone, i.e.,  $R_{pp}(r_c, v)$ . The phase of the integrand is

$$\xi = - \int_b^{r_c} q_x(\zeta) d\zeta + \int_{r_c}^r q_x(\zeta) d\zeta + v\theta, \quad (131)$$

and the saddle point condition (125), range (126), and arrival time (130) will still hold provided  $r_c$  is substituted for  $r_0$ . The saddle point will now be at  $-\pi/4$  to the real axis as (128) is negative. The second-order saddle point approximation for the reflected ray is

$$\begin{aligned} \tilde{\phi}_{Pcp}(\omega, r, \theta) &= \frac{-\tilde{\phi}_0(\omega)}{k_s br} \frac{T_D(\omega p)T_U(\omega p)R_{pp}(r_c, \omega p)\omega p^{1/2}}{(q_x(b)q_x(r)\sin\Delta)^{1/2}} \left( \frac{\rho(b)}{\rho(r)} \right)^{1/2} \left| \frac{d\Delta}{dp} \right|^{-1/2} \\ &\times \exp \left\{ i\omega \left[ p\Delta + \int_{r_c}^b r^{-1}(\eta^2 - p^2)^{1/2} dr + \int_{r_c}^b r^{-1}(\eta^2 - p^2)^{1/2} dr \right] \right\}. \end{aligned} \quad (132)$$

Solutions to the saddle point equation (124) exist for the direct and reflected rays provided

$$\theta < \theta_c = \Delta[r_c/\alpha(r_c)], \quad (133)$$

i.e., the range of the core-grazing ray. The saddles lie on the real  $v$  axis on either side of the critical value  $v = k_s r_c$  and the steepest descent path passes over both (see Phinney and Cathles, 1969; Chapman and Phinney, 1970).

## B. THE DIFFRACTION POLES

Near the critical point  $v = k_s r_c$ , poles of the reflection coefficient exist. Beyond the core shadow  $\theta_c$ , the integral can be approximated by the residues of these poles and in the deep shadow the first pole gives the asymptotic decay rate of the signal. Thus if the first pole lies at  $v_1$ , the decay rate is given by the factor  $e^{-\text{Im}(v_1)\theta}$  in the Legendre function. The slowness or ray parameter of the diffracted signal is given by  $p = dT/d\Delta = \text{Re}(v_1)/\omega$ . For a homogeneous model, the poles lie near the anti-Stokes line of the spherical Hankel function  $h_n^{(1)}(k_s r_c)$  and Duvalo and Jacobs (1959) found the approximate positions of the low order poles are

$$v_p = k_s r_c \left[ 1 + \frac{1}{2}(4p + c)^{2/3} \left( \frac{3\pi}{4k_s r_c} \right)^{2/3} e^{i\pi/3} \right]. \quad (134)$$

The most important feature of this result is that the decay constant is proportional to  $\omega^{1/3}$ . The constant  $c$  is difficult to find analytically and depends on the boundary conditions. In this and the following results we know  $c$  is small, i.e.,  $-1 \leq c \leq 1$ . Phinney and Alexander (1966) found similar poles for a homogeneous layered model but the poles were modified slightly due to resonances within the layers. Using the phase-integral method, i.e., connecting WKBJ solutions to Airy functions near the turning point and interface, the equivalent approximate result for an inhomogeneous model is

$$v_p = k_a r_c \left[ 1 + \frac{1}{2}(4p + c)^{2/3} \left( 1 - \frac{r_c \alpha'(r_c)}{\alpha(r_c)} \right)^{2/3} \left( \frac{3\pi}{4k_a r_c} \right)^{2/3} e^{i\pi/3} \right]. \quad (135)$$

Eckersley (1932) first used a similar phase-integral result without proof to confirm Watson's (1918) results for radiowave diffraction and the method was later justified by Heading (1953) and used recently by Phinney and Alexander (1969). For the direct ray's reflection coefficient (123), the WKBJ solutions had to be connected to the Airy function  $Ai(t)$  so that the solution was evanescent below the ray's turning point. When the turning point is near the core-mantle interface, however, the solution need not be evanescent and the dominant Airy function  $Bi(t)$  can also be included in order to satisfy the boundary condition. It is still assumed that  $q_a^2(r)$  is linear near the turning point but the discontinuity at  $r_c$  is allowed for. This result is only valid provided

$$\zeta(r_c) = r_c \alpha'(r_c)/\alpha(r_c) < 1, \quad (136)$$

the usual condition for a ray turning point at  $r_c$  (Bullen, 1963, p. 112). If this inequality is invalid, then  $q_a^2(r)$  may be parabolic. The potential equation can no longer be approximated by the Stokes equation, and the Airy functions are no longer applicable as approximate solutions. The appropriate functions to connect with the WKBJ solutions are the parabolic cylindrical functions (Abramowitz and Stegun, 1965, Chapter 19). An example of this can be found in Phinney (1969) for the acoustic wave reflection from a velocity reversal with no interface present. The reflection coefficient has poles whose imaginary part is independent of frequency, which lie at

$$v_p = k_* r_* + i \left| \frac{r_*^2 \alpha''(r_*)}{\alpha(r_*)} \right|^{1/2} (p + c), \quad (137)$$

where the subscript \* denotes the values at the reversal (derived using Abramowitz and Stegun, 1965, Eq. 19.18.3). If an interface exists near the velocity reversal then, as with the Airy functions, both types of parabolic

cylindrical functions can exist below the reversal. The diffraction poles are now determined by zeros of the parabolic cylindrical functions. For the special case of an interface at the reversal, i.e.,

$$\zeta(r_c) = r_c \alpha'(r_c)/\alpha(r_c) = 1 \quad \text{and} \quad r_c = r_* \quad (138)$$

the poles lie at

$$v_p = k_\alpha r_c + 2i \left| \frac{r_c^2 \alpha''(r_c)}{\alpha(r_c)} \right|^{1/2} (p + c) \quad (139)$$

(derived using Abramowitz and Stegun, 1965, Eq. 19.9.1), i.e., the even asymmetric poles of the series (137), a result that might have been anticipated as we now have half the complete parabolic barrier. This result was confirmed by Chapman and Phinney (1970) and more details were given in Chapman (1969). Friedman's (1951) result for an equivalent problem, that  $\text{Im}(v_1) \propto \omega^{1/4}$ , appears to be in error as the approximations used are incompatible.

Physically, the poles  $v_p$  represent diffracted signals which propagate along the interface or the velocity reversal. None of the formulas given here are useful for exact numerical work as the constant  $c$  is complicated. However, poles of the integrands (62) or (68), or rather zeros of the denominator of (57) or (112), can be found numerically. The approximate expressions (135) and (139) are then useful to indicate the behavior and frequency dependence expected.

### C. NUMERICAL EVALUATION OF THE CONTOUR INTEGRAL

The approximate results of the previous two sections for the geometrical rays in the illuminated region and the diffracted signal in the deep shadow are useful indications of the behavior of the response integrals (62) and (68) but are insufficient to study the signals near the shadow boundary. For this region the response integral must be evaluated numerically.

The contour  $\Gamma$  (Fig. 1) can be distorted in the complex  $v$ -plane provided no poles are crossed. In the illuminated zone,  $\theta < \theta_c$ , the contour most readily evaluated passes over the two saddle points on the real  $v$  axis (Section VI, A). At the shadow edge,  $\theta = \theta_c$ , the saddles coalesce at the critical point  $v = k_\alpha r_c$  and beyond this the contour is best closed around the diffraction poles (Section VI, B). Thus theoretically the optimum contour  $\Gamma$  varies with position. In practice, however, it is a great advantage to use the same contour for a range of distances. This method was used by Phinney and Cathles (1969) to evaluate

the P-PcP signal across the shadow boundary of a homogeneous model and has since been used by Chapman (1969), Richards (1970), and Chapman and Phinney (1970) for other signals and the response of an inhomogeneous model.

If the contour  $\Gamma$  is kept fixed, and the response integral evaluated at various ranges, advantage can be taken of the independence of the majority of the integrand on  $\theta$ . In particular, the reflection coefficient (57) or (112), and the term (89) of the Legendre functions only depend on  $v$  and need only be evaluated once at each point on the contour  $\Gamma$ . In the numerical calculations, the contour  $\Gamma$  is composed of straight segments approximating the steepest descent path in the upper half  $v$ -plane and joining the two saddles on the real axis. Because of the constant phase along the steepest descent path, the Simpson's method of integration is sufficiently accurate. The variable phase between the two saddle points on the real axis is only troublesome at high frequency and/or ranges well into the illuminated zone [an exact condition depending on the phase differences of the geometrical results (127) and (132)]. The two saddles are then well separated [the distance apart of the saddles is proportional to frequency  $\omega$  whereas the width is proportional to  $\omega^{1/2}$  from (128)] and correspondingly the direct and reflected signals are separated in the time domain. The two signals interfere and the spectral amplitudes oscillate with distance or frequency. It is then advantageous to distort the contour into the lower half  $v$ -plane and evaluate the two saddle points separately but with the same end point so that the combined results correspond to the contour  $\Gamma$ . This method is essential in interpolating the spectral amplitudes to synthesize a theoretical seismogram (Section VII).

The contour  $\Gamma$  is chosen so as to be optimum at about the midpoint of the range required. The step size for each segment of the contour  $\Gamma$  is estimated from the gradient of the response integrand. The maximum gradient at either end of the segment and either end of the range is used. If the same contour  $\Gamma$  is used over too large a range, the rapid phase changes on the contour cause the step size to be unreasonably small. In addition, to compensate for the finite length of the contour  $\Gamma$  in numerical calculations, an end correction is included. It is assumed that the integrand decays uniformly from the end of the contour.

The zeros of the denominators of (57) and (112) are found using the Newton-Raphson method. The residue of the pole can then be calculated using the derivative of the denominator.

The numerical contour integration was checked by using different contours, contours around poles, and closed contours, etc. The fractional error appears to be about 0.1% of the amplitude computed for the response integral (62). For the response integral (68) for an inhomogeneous model the fractional error is usually larger due to the various approximations involved, but is always less than 1%.

## VII. Numerical Results

In Section VI we have indicated how the response integral may be evaluated numerically or asymptotically. In this section a selection of typical numerical results is presented.

Calculations were performed for two models: a homogeneous mantle-core model U and an inhomogeneous model A. The inhomogeneous model A is shown in Fig. 8 and is the same as used by Wiggins (1968) based on Birch (1964). The homogeneous model U has the same values at the core-mantle interface, i.e.,

$$\begin{aligned} \alpha_0 &= 13.64 \text{ km sec}^{-1}, & \beta_0 &= 7.3 \text{ km sec}^{-1}, & \rho_0 &= 5.43 \text{ g cm}^{-3}, \\ \alpha_1 &= 8.10 \text{ km sec}^{-1}, & \rho_1 &= 9.95 \text{ g cm}^{-3}, & a_1 &= 3473 \text{ km}. \end{aligned}$$

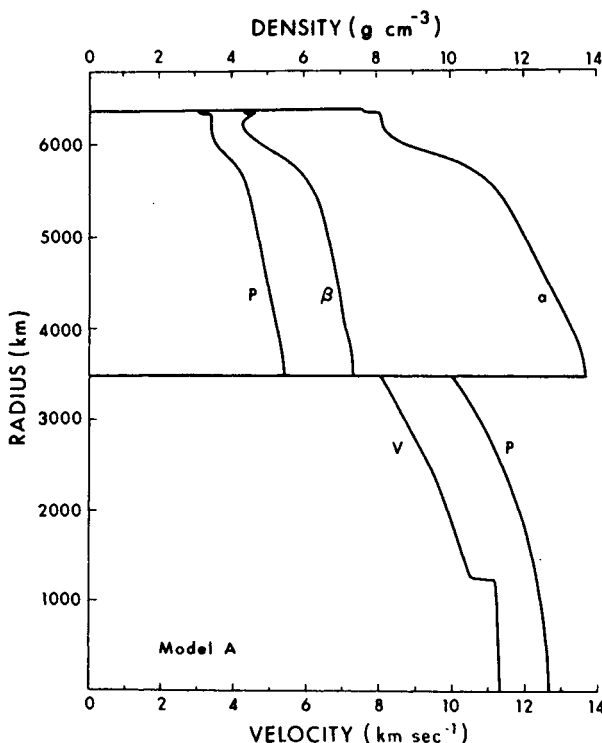


FIG. 8. Earth Model A from Wiggins (1968) based on Birch (1964).

First the diffraction poles of the reflection coefficients were found. For the P wave these correspond to zeros of the denominator of (57),  $R_{12}^{12}$ , near the point  $v = k_0 a_1$  and for the SV signal, zeros of the same function near  $v = k_0' a_1$ . These are plotted in Fig. 9 normalized with respect to the cube root frequency

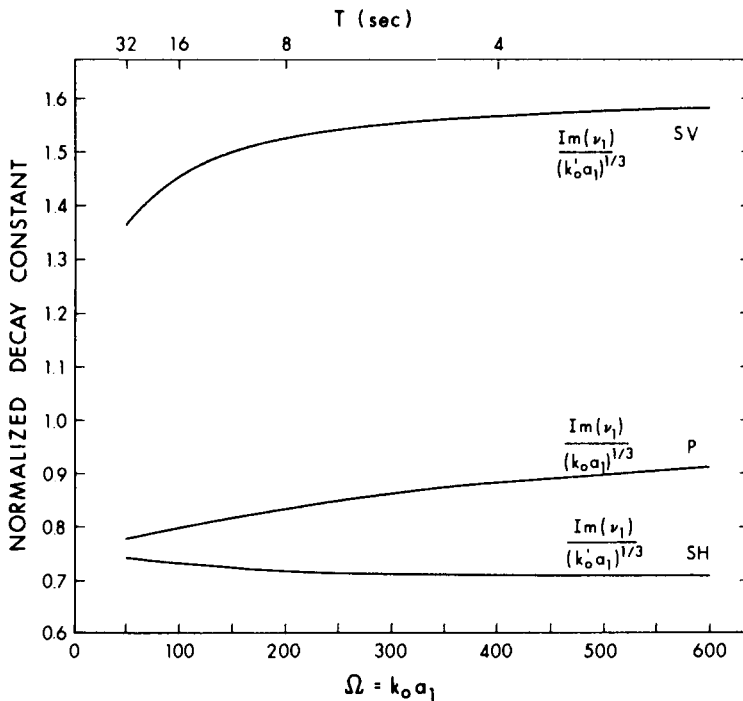


FIG. 9. The normalized decay constant for the homogeneous Earth model U.  $\Omega = k_0 a_1$  is a dimensionless frequency parameter. The first diffraction poles for P, SV, and SH signals are plotted.

dependence of the asymptotic results (134). The first diffraction pole for the SH signal is also plotted. Similar results for the P diffraction pole were given in Phinney and Alexander (1966). We immediately notice that while the P and SH decay constants are very similar, the SV decay rate is considerably greater. This is confirmed by the evaluation of the spectral amplitudes using the method of contour integration described in Section VI, C. Figure 10 contains a plot of the P, SV, and SH spectral amplitudes across the core shadow for a range of frequencies. Similar results for the P signal were calculated by Phinney and Cathles (1969). Also included in the figure are the residue from the first diffraction pole, the geometrical amplitude of the direct ray in the illuminated zone, and the shadow boundary defined as the point

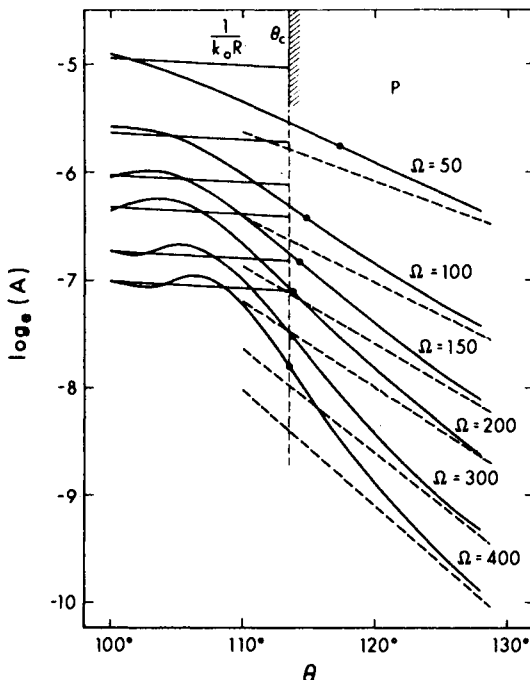


FIG. 10a. The natural logarithm of the spectral amplitude of the P signal across the shadow for the homogeneous model U. The geometrical shadow,  $\theta_c$ , and the direct ray amplitude,  $1/k_0 R$ , are indicated. The shadow boundary is marked on each curve and the residue of the first diffraction pole is plotted.  $\Omega = k_0 a_1$  and  $r = b = 6338$  km.

where the diffracted signal drops to half the geometrical value. The curves are asymptotic to the residue contribution deep in the shadow, and oscillate about the direct ray amplitude due to interference with the reflected wave. The shift of the shadow boundary is similar to Teng and Richards' (1968, 1969) result for a cylindrical cavity. The SV shadow boundary shifts into the illuminated region while the SH and P shadow boundaries shift into the shadow region. As Teng and Richards (1968) suggested, this is a possible explanation for the observations made by Cleary *et al.* (1967) of diffracted S-waves. The particle motion for the core-grazing longitudinal P ray and transverse SH ray is parallel to the core-mantle boundary while for the transverse SV ray it is perpendicular to the boundary. Thus it would appear that although part of the P-wave can be transmitted into the core ray, PKP, etc., the diffracted P and SH signals are similar because the particle motion is parallel to the interface. As the tangential motion can be discontinuous at the interface the wave is relatively unrestricted compared with the SV wave whose motion perpendicular to the interface must be continuous. This is

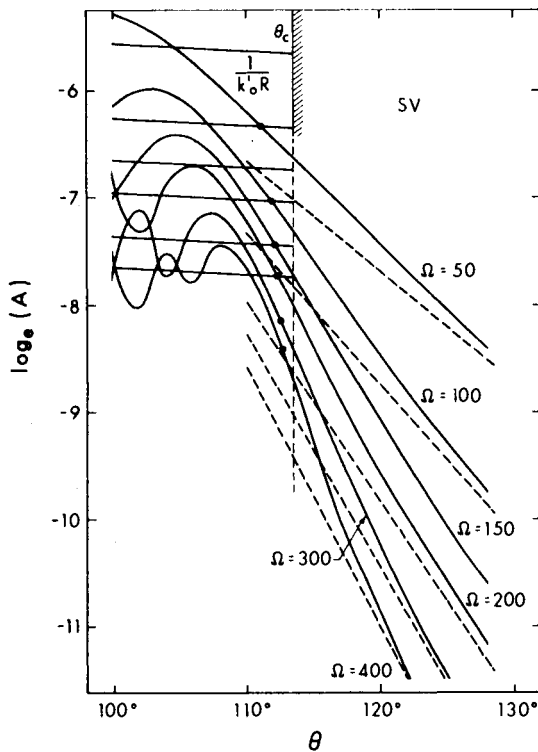


FIG. 10b. Same as Fig. 10a  
but for the SV signal.

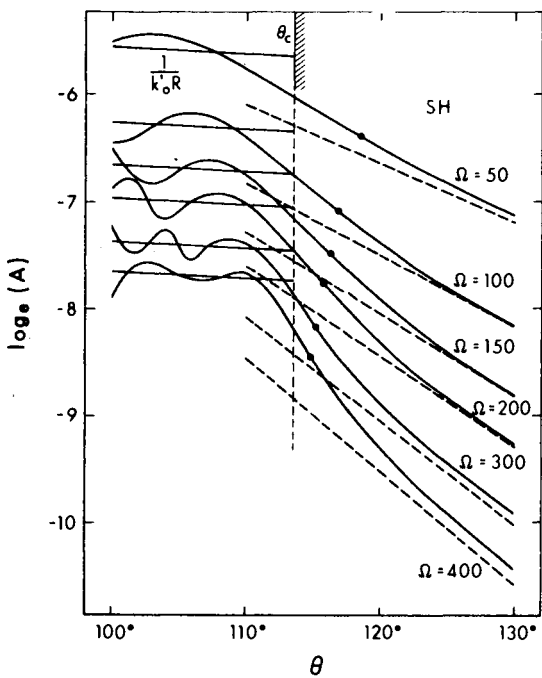


FIG. 10c. Same as Fig. 10a  
but for the SH signal.

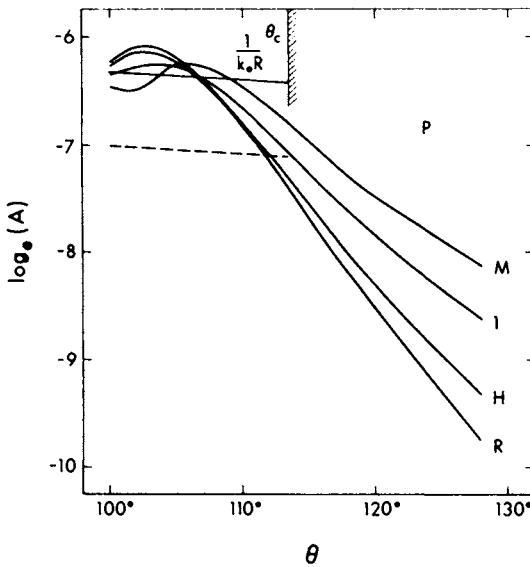


FIG. 11a. The natural logarithm of the spectral amplitude of the P signal across the shadow. All curves are for  $\Omega = 200$  (period  $\sim 8$  sec). Curve I corresponds to the usual boundary conditions, curve H to hollow core boundary conditions ( $p_{rr} = p_{r\theta} = 0$ ), curve R to rigid boundary conditions ( $u_r = u_\theta = 0$ ), and curve M to mixed boundary conditions ( $u_r = p_{r\theta} = 0$ ).

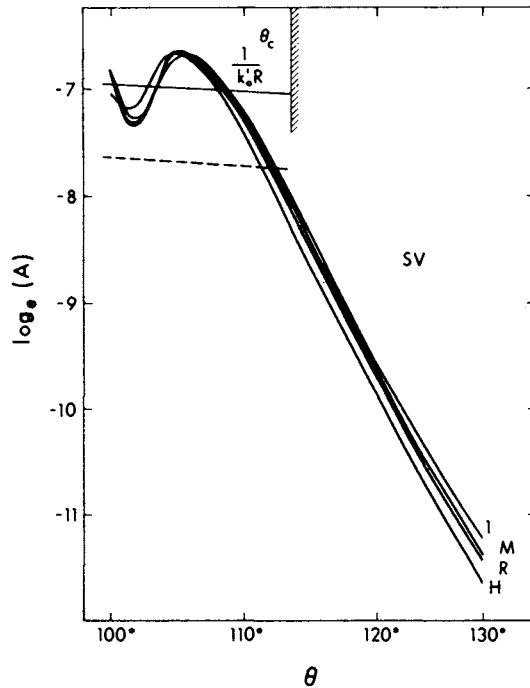


FIG. 11b. As Fig. 11a but for the SV signal.

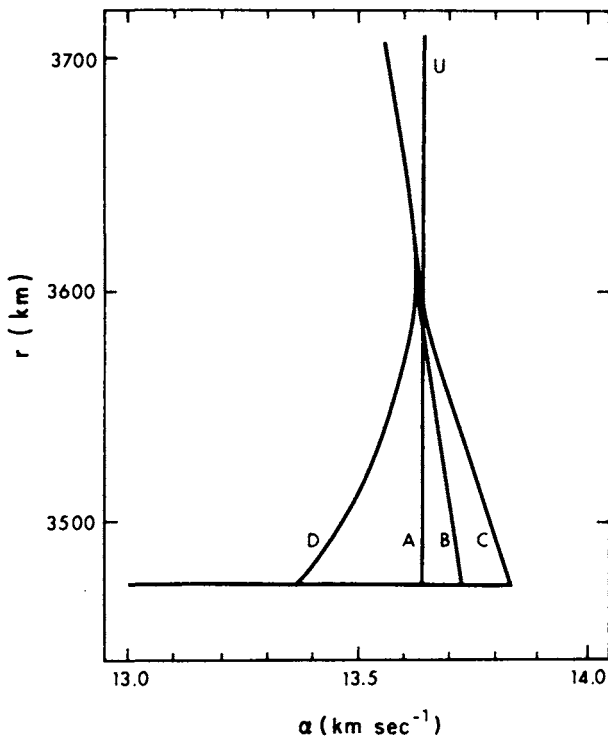


FIG. 12. Detail of the model A in Fig. 8 with three different models B, C, and D indicated. The homogeneous model used for Figs. 9 and 10 is marked U.

confirmed by changing the boundary conditions at the core-mantle interface. Following Phinney and Cathles (1969) we have computed the diffracted amplitudes for a hollow core ( $H$ ,  $p_{rr} = p_{r\theta} = 0$ ), a rigid core ( $R$ ,  $u_r = u_\theta = 0$ ), and a mixed core ( $M$ ,  $u_r = p_{r\theta} = 0$ ). This is shown in Fig. 11. The results for P are similar to those given by Phinney and Cathles (1969). Compared with the P results the change in the SV curves is slight. Making the core rigid, i.e. restricting the tangential motion, shifts the shadow boundary of the P wave into the illuminated zone and increases the decay rate. The increased value of the decay constant was also obtained by Phinney and Alexander (1966).

Using the methods described in Section III, B and Section V, we can confirm the asymptotic results (135) and (139). The model used is shown in Fig. 8 and in Fig. 12 small variations to the structure in the Bullen Region  $D'$  (Bullen, 1963) are indicated. Models like B or C, with a negative velocity gradient similar to the Bullen region  $D'$ , were suggested by Phinney and Alexander (1969). The model D, with a positive velocity gradient near the interface, is similar to that suggested by Bolt (1970). The normalized decay constant for these models is plotted in Fig. 13 (Chapman and Phinney, 1970).

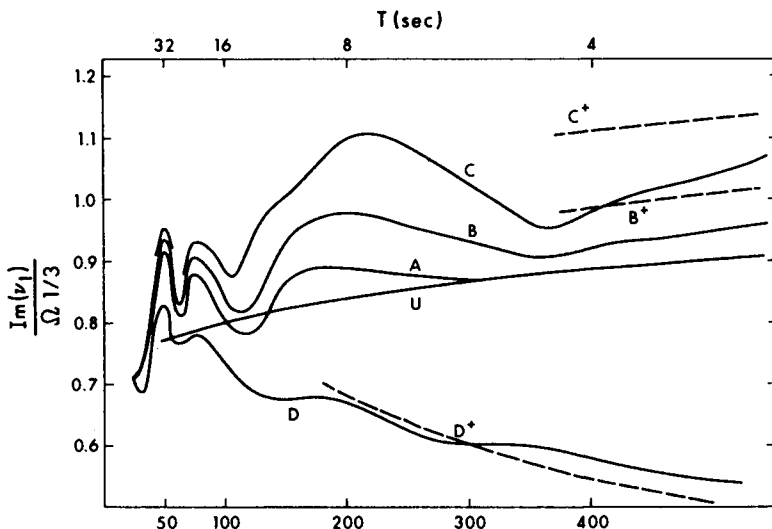


FIG. 13a. The normalized decay constant for the models A, B, C, and D (as Fig. 9). Curves  $B^+$ ,  $C^+$ , and  $D^+$  are asymptotic results explained in text.

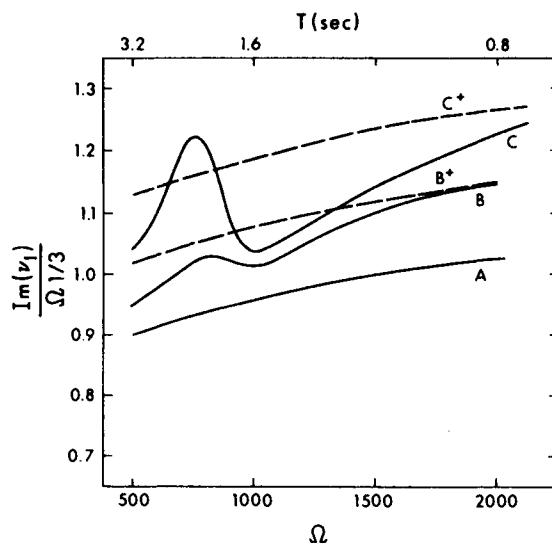


FIG. 13b. As Fig. 13a at higher frequency.

The decay constant has a similar low frequency behavior for all four models. A slight shift occurs between the curves but the basic oscillatory nature is identical for all the models and significantly different from the smooth curve of the homogeneous model. This behavior is due to the velocity gradient in the Bullen region D'. The radius  $r^*$  lies in this region. For a sharp interface above the core-mantle boundary, Phinney and Alexander (1966) found similar resonance peaks given by a simple phase condition in the layer. In the inhomogeneous case, no sharp interface exists but the velocity gradient effectively forms a layer. Reflection occurs at  $r_0$  and using the phase-integral method (Heading, 1953), a resonance condition can be obtained. The peaks are no longer spaced evenly in frequency as the radius  $r_0$  is frequency dependent. The variations of the decay constant from the uniform curve U have been observed at low frequencies (Alexander and Phinney, 1966; Phinney and Cathles, 1969) and are probably caused by the velocity gradient in the lower mantle and not a special structure near the core-mantle interface. At higher frequencies, the decay constant for the model A is the same as for the homogeneous model U because the two models are equivalent for the lowest 100 km of the mantle. The decay constant for the models B and C are greater due to the gradient and are asymptotic to the curves  $B^+$  and  $C^+$ . These are obtained from the curve U by including the gradient factor of (135). Increased decay constants for short period data have been observed by Phinney and Alexander (1969). The decay constant for the model D is considerably reduced. The condition (138) is almost exactly satisfied for this model. The curve  $\text{Im}(v_i) = 4$ , which corresponds to  $c \approx -0.65$  in expression (139), has been plotted. The agreement between the numerical calculation and the approximate result (139) is good.

The response integral (68) has also been evaluated for the models A and D. The spectral amplitudes are plotted in Figs. 14 and 15. Superimposed on Fig. 14 are the equivalent results for the homogeneous model U in such a way that the shadow angles,  $\theta_c$ , coincide and the geometrical ray amplitudes in the illuminated zone are approximately the same. The shadow boundary for the model A is shifted into the illuminated zone due to the defocusing effect of the gradient decrease in the region D''. This is more noticeable at the higher frequencies. Perturbations to the wavefronts caused by the inhomogeneity of the lower mantle will be more significant at shorter wavelengths. The amplitude curves for the model A show significant variations from the smooth curves of the model U at higher frequencies. At the longer periods the amplitude curves are smooth but show different decay rates. In Fig. 15 the spectral amplitudes and the residue of the first diffraction pole are plotted for the model D. The shadow angle,  $\theta_c$ , is now very much greater ( $135^\circ$ ) and only very small changes in the model are necessary to make it indeterminate.

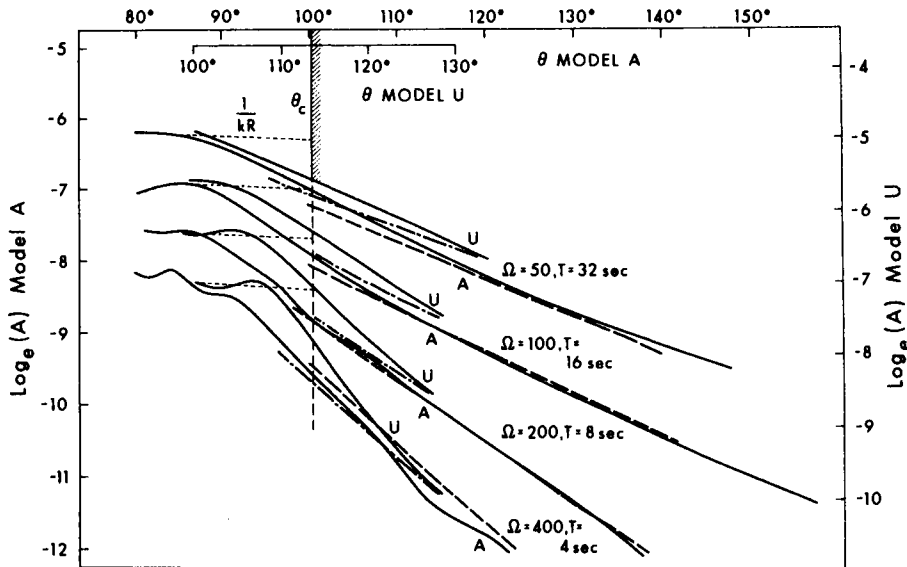


FIG. 14. The natural logarithm of the spectral amplitudes for the models U and A. The range scales agree at the geometrical shadow,  $\theta_c$ . The residue contribution from the first pole and the geometrical amplitudes for the model U are shown.

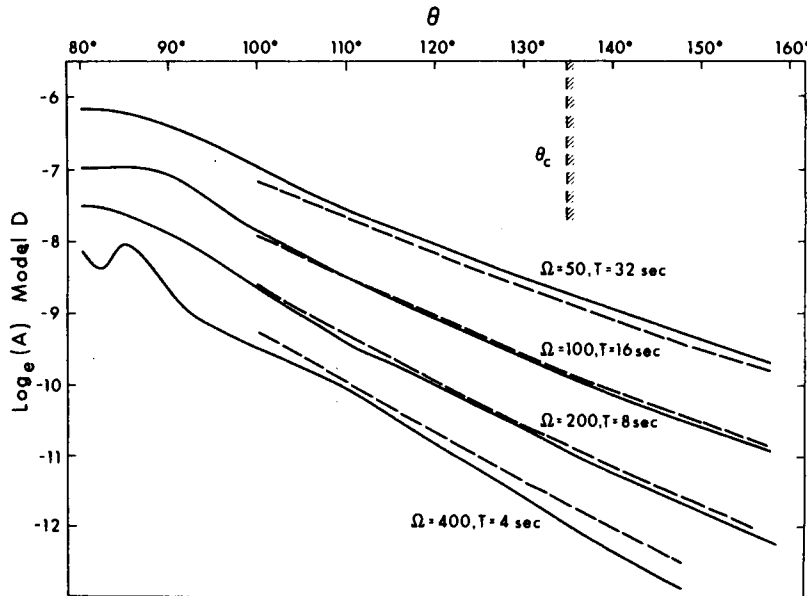


FIG. 15. As Fig. 14 for the model D. The geometrical shadow position is only approximate.

The signal decays exponentially in the illuminate zone and the residue of the first diffraction pole is a good approximation beyond 100°. The decay rate at all frequencies is seen to be approximately the same.

Finally, we have synthesized theoretical seismograms for the homogeneous model U. A long period seismometer (30 sec) and galvanometer (100 sec) with critical damping are assumed. The transfer function is taken as

$$\frac{\omega^2}{(\Omega_0^2 - \omega^2 - i\omega\Delta)(\omega_0^2 - \omega^2 - i\omega\delta)}, \quad (140)$$

where  $\omega_0$  and  $\Omega_0$  are the natural frequencies of the seismometer and galvanometer, and  $\delta = 2\omega_0$  and  $\Delta = 2\Omega_0$  for critical damping. In Fig. 16 the transfer function (140) is plotted and the resultant seismogram for an impulse source shown. Due to the source function assumed, the geometrical ray results (127) and (132) have a frequency dependence  $\omega^{-1}\tilde{\phi}_0(\omega)$ . Thus if we take  $\tilde{\phi}_0(\omega) \propto \omega$ , the synthetic seismogram obtained combining (127) with (140) will have the same spectrum as Fig. 16. In addition a factor  $i$  is included so that the direct pulse has the same form as Fig. 16. In order to evaluate the inverse Fourier transform (7), a finite Fourier sum is used. Spectral amplitudes calculated from (62) for a range of frequencies must be interpolated for the Fourier sum. The response function (62) is a complex function and the amplitude and phase must be interpolated separately. As calculated the phase is a discontinuous function in the range  $-\pi$  to  $\pi$ . The  $2\pi$  ambiguity between the various frequencies and ranges can be removed using the geometrical ray results. If the correct continuous phase function is  $\xi(\theta, \omega)$ , we can see from the results (127), (130), and (132) that in the high frequency limit, i.e., geometrical ray theory,

$$\partial\xi/\partial\Delta = \omega p = \omega dT/d\Delta. \quad (141)$$

In addition, the arrival time is given by

$$T = \partial\xi/\partial\omega. \quad (142)$$

Provided these equalities are replaced by approximate equalities at finite frequencies, they can be used to form the continuous phase function needed for interpolation. In the illuminated zone when the phase difference of the direct (127) and reflected (132) rays is large (greater than  $2\pi$ , say) the contour integral must be evaluated in two parts and the two signals interpolated

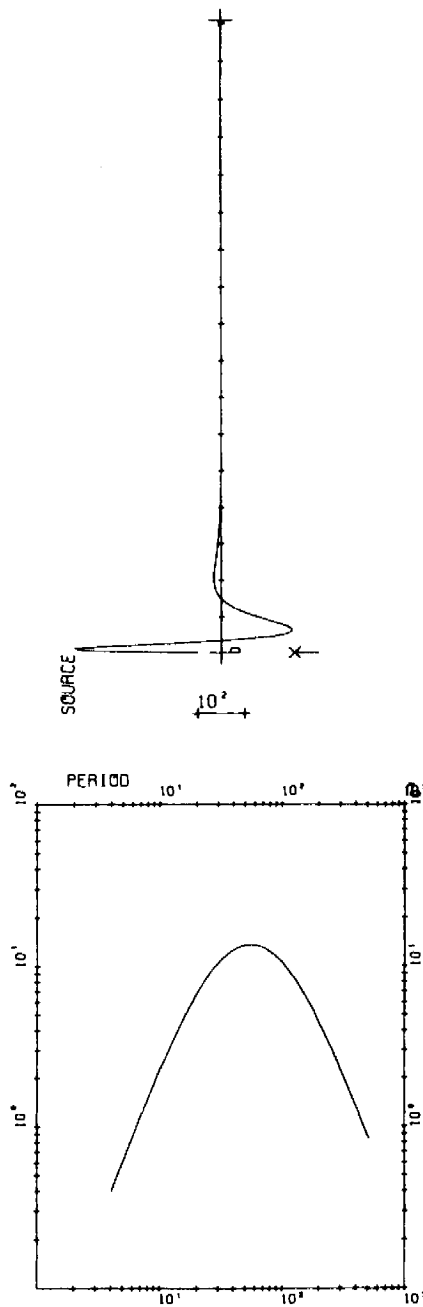


FIG. 16. The transfer spectrum of the critically damped seismometer and galvanometer (periods 30 sec and 100 sec, respectively) with the impulse response. The marks on the time scale are every 30 sec.

separately. In the shadow zone, the ray parameter in (141) is that of a core-grazing ray and the arrival time (142) is that of a ray which travels along the interface.

In Fig. 17 the theoretical seismograms for a P, SV, and SH source are plotted normalized with respect to direct ray amplitude in the illuminated zone. No correction has been made for a free surface at the receiver nor have the results been converted into components of displacement. In this example, calculation of the response integral was done at 16 frequencies ranging from 0.015625 Hz ( $\Omega = 25$ ) to 0.25 Hz ( $\Omega = 400$ ). Interpolation of the frequency spectrum was 16-fold, giving 256 spectral values as input to the Fourier synthesis, and a  $\Delta f$  of about 0.001 Hz.

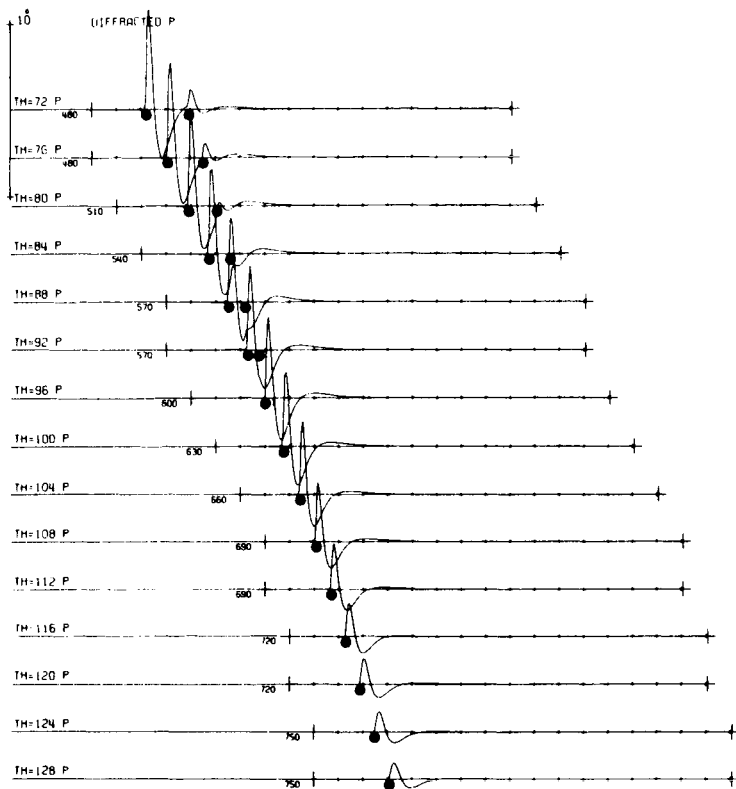


FIG. 17a. The theoretical seismograms for the P potential at ranges across the core shadow. The marks on the time scale are every 30 sec. The geometrical arrival times for P and P<sub>c</sub>P are indicated by black dots.

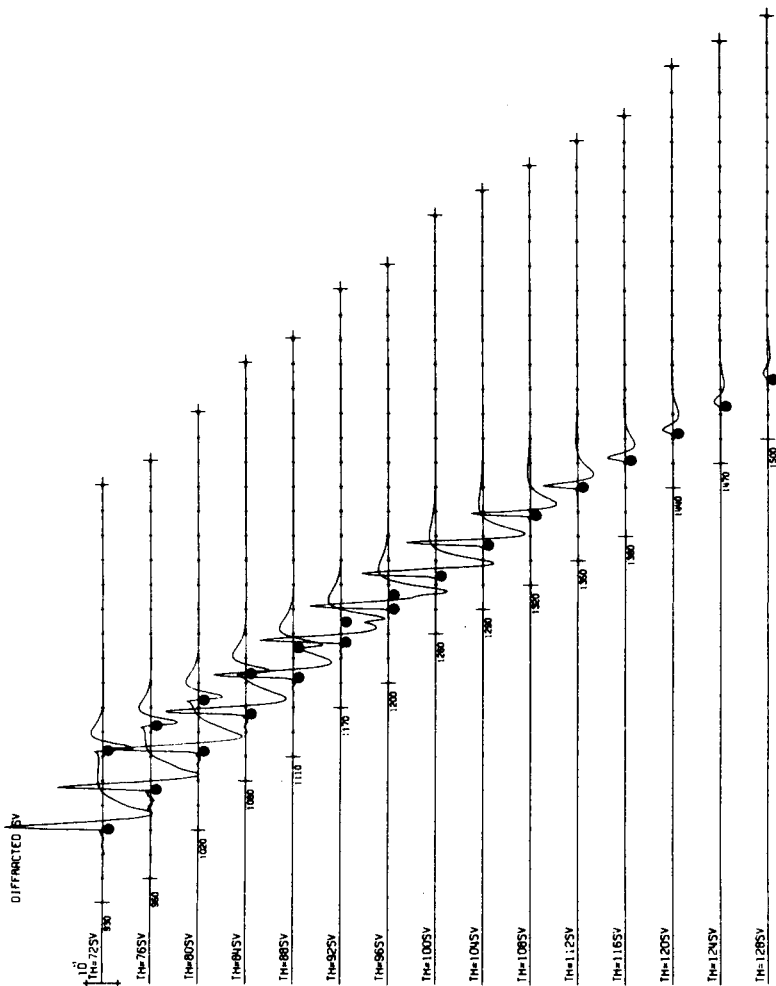


FIG. 17b. As Fig. 17a for the SV potential, showing S and Scs.

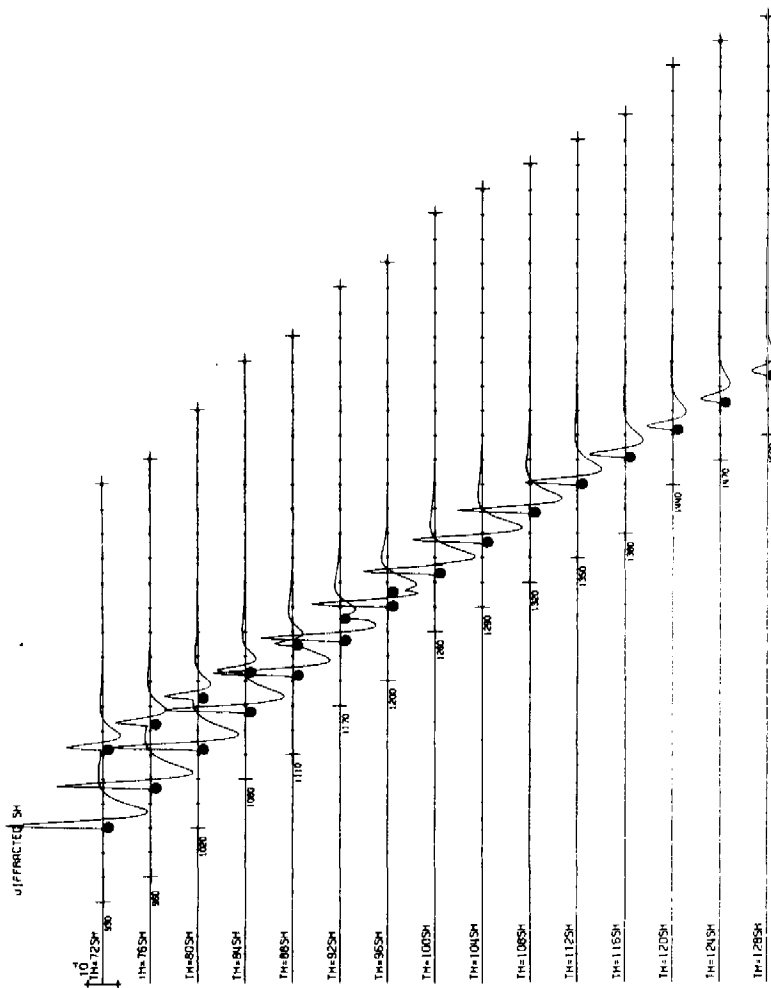


FIG. 17c. As Fig. 17a for the SH potential, showing S and Scs.

## ACKNOWLEDGMENTS

Computations in this chapter were performed at the Princeton University Computer Center, the Institute of Theoretical Astronomy, Cambridge, and the Computing Center of the University of Alberta. The work at Princeton was supported by the Air Force Office of Scientific Research under contract AF49(638)-1243 and the computer facilities were partly supported by a National Science Foundation grant GP 579. The work at Cambridge was supported by the Natural Environment Research Council and at Edmonton by a National Research Council operating and computing grant.

## REFERENCES

- ABRAMOWITZ, M., and STEGUN, I. A. (1965). "Handbook of Mathematical Functions." Dover, New York.
- ALEXANDER, S. S., and PHINNEY, R. A. (1966). *J. Geophys. Res.* **71**, 5943-5958.
- ALSOP, L. E. (1968). *Bull. Seismol. Soc. Amer.* **58**, 1949-1954.
- ALTERMAN, Z. S., and ABOUDI, J. (1969a). *J. Geophys. Res.* **74**, 2618-2636.
- ALTERMAN, Z. S., and ABOUDI, J. (1969b). *J. Geophys. Res.* **74**, 5903-5922.
- ALTERMAN, Z., JAROSCH, H., and PEKERIS, C. L. (1959). *Proc. Roy. Soc., Ser. A* **252**, 80-95.
- ANDERSON, D. L. (1961). *J. Geophys. Res.* **66**, 2953-2963.
- ANSELL, J. H. (1970). Ph.D. Thesis, University of Cambridge.
- BACKUS, G. E. (1967). *Geophys. J. Roy. Astron. Soc.* **13**, 71-101.
- BACKUS, G. E., and GILBERT, F. (1961). *Proc. Nat. Acad. Sci. U.S.* **47**, 362-371.
- BEN-MENAHEM, A. (1964). *Bull. Seismol. Soc. Amer.* **54**, 1315-1321.
- BIOT, M. A. (1957). *Phys. Rev.* **105**, 1129-1137.
- BIRCH, F. (1964). *J. Geophys. Res.* **69**, 4377-4388.
- BOLT, B. A. (1962). *Nature (London)* **196**, 122-124.
- BOLT, B. A. (1970). *Geophys. J. Roy. Astron. Soc.* **20**, 367-382.
- BUDDEN, K. G. (1966). "Radio Waves in the Ionosphere." Cambridge Univ. Press, London and New York.
- BULLEN, K. E. (1963). "An Introduction to the Theory of Seismology." Cambridge Univ. Press, London and New York.
- CHAPMAN, C. H. (1969). Ph.D. Thesis, University of Cambridge.
- CHAPMAN, C. H., and PHINNEY, R. A. (1970). *Geophys. J. Roy. Astron. Soc.* **21**, 185-205.
- CLEARY, J., PORRA, K., and READ, L. (1967). *Nature (London)* **216**, 905-906.
- CLEBSCH, A. (1863). *J. Math. (Crelle)* **61**, 195-262.
- DAHLEN, F. A. (1968). *Geophys. J. Roy. Astron. Soc.* **16**, 329-367.
- DEBYE, P. J. (1908). *Phys. Z.* **9**, 775-778.
- DERR, J. S. (1967). *Bull. Seismol. Soc. Amer.* **57**, 1047-1061.
- DUNKIN, J. W. (1965). *Bull. Seismol. Soc. Amer.* **55**, 335-358.
- DUWALO, G., and JACOBS, J. A. (1959). *Can. J. Phys.* **37**, 109-128.
- ECKERSLEY, T. L. (1932). *Proc. Roy. Soc. Ser. A* **136**, 499-527.
- ERDÉLYI, A., ed. (1953). "Higher Transcendental Functions," Vol. I. McGraw-Hill, New York.
- EWING, W. M., JARDETZKY, W. S., and PRESS, F. (1957). "Elastic Waves in Layered Media." McGraw-Hill, New York.
- FRIEDMAN, B. (1951). *Commun. Pure Appl. Math.* **4**, 317-350.
- GANTMACHER, F. R. (1959). "The Theory of Matrices." Chelsea Publ., New York.
- GILBERT, F. (1967). *Bull. Seismol. Soc. Amer.* **57**, 783-794.
- GILBERT, F., and BACKUS, G. E. (1966). *Geophysics* **31**, 326-332.

- GILBERT, F., and BACKUS, G. E. (1969). *AFIPS Conf. Proc.* **33**, 1273-1277.
- GUTENBERG, B. (1958). *Trans. Amer. Geophys. Un.* **39**, 486-489.
- GUTENBERG, B., and RICHTER, C. F. (1934). *Gelands Beitr. Geophys.* **43**.
- HASKELL, N. A. (1953). *Bull. Seismol. Soc. Amer.* **43**, 17-34.
- HEADING, J. (1953). Ph.D. Thesis, University of Cambridge.
- HEADING, J. (1962). "An Introduction to Phase-Integral Methods," Methuen's Monographs on Physical Subjects. Wiley, New York.
- HERRERA, I. (1964). *Bull. Seismol. Soc. Amer.* **54**, 1087-1096.
- HUTA, A. (1957). *Acta Fac. Rerum Natur. Univ. Comenianae, Math.* **2**, 21-23.
- ISAACSON, E. and KELLER, H. B. (1966). "Analysis of Numerical Methods." Wiley, New York.
- JEFFREYS, H. (1939). *Mon. Not. Roy. Astron. Soc., Geophys. Suppl.* **4**, 548-561.
- JEFFREYS, H., and BULLEN, K. E. (1940). "Seismological Tables." Brit. Ass. Advan. Sci., London.
- JOHNSON, L. R. (1967). *J. Geophys. Res.* **72**, 6309-6325.
- KNOPOFF, L., and GILBERT, F. (1961). *Bull. Seismol. Soc. Amer.* **51**, 35-49.
- LANCZOS, C. (1961). "Linear Differential Operators." Van Nostrand-Reinhold.
- LANDISMAN, M., USAMI, T., SATO, Y., and MASSE, R. (1970). *Rev. Geophys.* **8**, 533-589.
- MITCHELL, A. R., and CRAGGS, J. W. (1953). *Math. Tables, Wash.* **7**, 127-129.
- MORSE, P. M., and FESHBACH, H. (1953). "Methods of Theoretical Physics," McGraw-Hill, New York.
- NUSSENZVEIG, H. M. (1965). *Ann. Phys. (New York)* **34**, 23-95.
- NUSSENZVEIG, H. M. (1969a). *J. Math. Phys.* **10**, 82-124.
- NUSSENZVEIG, H. M. (1969b). *J. Math. Phys.* **10**, 125-176.
- PHINNEY, R. A. (1969). *Rev. Geophys.* **8**, 517-532.
- PHINNEY, R. A., and ALEXANDER, S. S. (1966). *J. Geophys. Res.* **71**, 5959-5975.
- PHINNEY, R. A., and ALEXANDER, S. S. (1969). *J. Geophys. Res.* **74**, 4967-4971.
- PHINNEY, R. A., and CATHLES, L. M. (1969). *J. Geophys. Res.* **74**, 1556-1574.
- PITTEWAY, M. L. V. (1965). *Phil. Trans. Roy. Soc. London Ser. A* **257**, 219-241.
- RALSTON, A. (1965). "A First Course in Numerical Analysis." McGraw-Hill, New York.
- RICHARDS, P. G. (1970). Ph.D. Thesis, California Institute of Technology.
- RICHARDS, P. G. (1971). *J. Acoust. Soc. Amer.* **50**, 188-197.
- SARAFYAN, D. (1966). "Composite and Multi-Step Runge-Kutta Formulas," Tech. Rep. No. 18, p. 2, Dept. Mathematics, Louisiana State Univ., New Orleans.
- SATO, R. (1969a). *Geophys. J. Roy. Astron. Soc.* **17**, 527-544.
- SATO, R. (1969b). *J. Phys. Earth* **17**, 1-12.
- SCHEID, F. (1968). "Theory and Problems of Numerical Analysis," Schaum's Outline Series. McGraw-Hill, New York.
- SCHOLTE, J. G. J. (1956). *Kon. Ned. Meterol. Inst. Publ.* **65**.
- SHANKS, E. B. (1966). *Math. Comp.* **20**, 21-38.
- SHIMAMURA, H. (1969). *J. Phys. Earth* **17**, 133-168.
- STOKES, Sir G. G. (1858). *Trans. Cambridge Phil. Soc.* **10**, 106-128.
- TENG, T. (1970). *Bull. Seismol. Soc. Amer.* **60**, 317-320.
- TENG, T., and RICHARDS, P. G. (1968). *Nature (London)* **218**, 1154-1155.
- TENG, T., and RICHARDS, P. G. (1969). *J. Geophys. Res.* **74**, 1537-1555.
- TODD, J. (1950). *Math. Tables, Wash.* **4**, 39-44.
- VAN DER POL, B., and BREMMER, H. (1937). *Phil. Mag. [7]* **24**, Parts I and II, 141-176 and 825-864.
- WATSON, G. N. (1918). *Proc. Roy. Soc. Ser. A* **95**, 83-99.
- WIGGINS, R. A. (1968). *Phys. Earth Planet. Interiors* **1**, 201-266.

# Inversion and Inference for Teleseismic Ray Data

LEONARD E. JOHNSON\*

and

FREEMAN GILBERT

INSTITUTE OF GEOPHYSICS AND PLANETARY PHYSICS  
UNIVERSITY OF CALIFORNIA, SAN DIEGO  
LA JOLLA, CALIFORNIA

I.	Introduction . . . . .	231
A.	Traditional Methods . . . . .	232
B.	The Backus-Gilbert Method . . . . .	235
II.	Theory . . . . .	236
A.	Inversion Theory . . . . .	236
B.	Resolving Power Theory . . . . .	240
III.	Data . . . . .	248
A.	Traditional Data . . . . .	248
B.	A New Datum: $(T - p\Delta)$ . . . . .	248
C.	The Teleseismic Data Set . . . . .	250
IV.	Numerical Methods . . . . .	253
A.	Representation of Model . . . . .	253
B.	Inversion . . . . .	254
C.	Resolving Power . . . . .	254
V.	Results . . . . .	254
A.	Inversion . . . . .	254
B.	Resolving Power . . . . .	257
	References . . . . .	266

## I. Introduction

ONE OF THE CLASSICAL inverse problems of geophysics is the seismic body-wave travel time problem. Given a set of data consisting of measured travel times for various seismic phases from a particular source to a number of surface locations, what can we infer about the seismic velocity as a function of depth?

During the first two decades of this century, an approximate seismic velocity distribution was derived based on the work of Oldham (1900, 1906),

\* Present address: Cooperative Institute for Research in Environmental Sciences, University of Colorado, Boulder, Colorado.

Zöppritz (1907), Mohorovičić (1909), Gutenberg (1915), and others. By 1939, the velocity models of Gutenberg and Jeffreys (1939) had been established and have been changed relatively little, below a depth of 900 km, by more modern studies.

A knowledge of the distribution of seismic velocity with depth plays a central role in our inference of the distribution of other physical properties of the earth such as density, elastic constants, and chemical composition. Thus, any improvements that we can make in our knowledge of their values or in a quantification of the degree to which our knowledge of them is uncertain is very important.

This paper describes a method for finding seismic velocity distributions which fit a given set of data and having found such distributions how to quantitatively assess their degree of uncertainty, i.e., their uniqueness.

#### A. TRADITIONAL METHODS

The traditional method of inverting body-wave travel time data is due to Herglotz (1907) and Wiechert (1910). If, in a spherically symmetric earth, the seismic velocity  $v$  is a function of the radius  $r$  alone, and  $v(r)/r$  increases with depth, the inversion amounts to solving a form of Abel's integral equation. An elementary solution is given by Jeffreys (1962)

$$\int_0^{\Delta_1} \cosh^{-1}(p/p_1) d\Delta = \pi \ln(R_e/r_1), \quad (1)$$

where (see Fig. 1):  $\Delta$  is the angular distance separating the source and receiver, both on the surface of the Earth,  $p$  is the ray parameter; it can be shown that  $p = dT/d\Delta$ , the derivative of the travel time curve,  $p_1$  is the value of  $p$  at  $\Delta = \Delta_1$  and is also equal to  $r_1/v_1$  for the seismic ray which has its deepest point

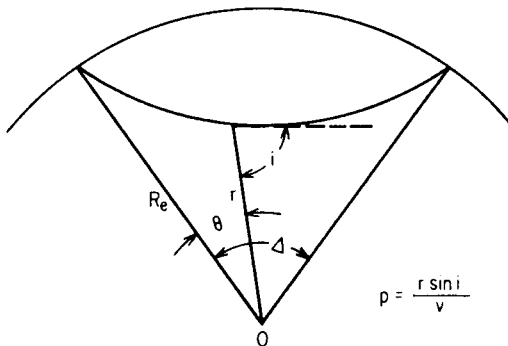


FIG. 1. Seismic ray geometry.

of penetration at  $r_1$ , and  $R_e$  is the radius of the Earth. Now,  $p$  is a known function of  $\Delta$  and Eq. (1) thus determines  $r_1$  corresponding to  $\Delta_1$  and therefore to  $r_1/v_1$  and so determines  $r$  as a function of  $r$ . Although Eq. (1) is an exact solution of the Abel integral equation, the Herglotz-Wiechert method of inverting travel time data suffers from several limitations.

First, the method requires that the ray parameter  $p$  be known for all values of  $\Delta$  between 0 and  $\Delta_1$ . This requirement cannot be met when there is a shadow zone in the interval 0 to  $\Delta_1$  in which there are no arrivals of the particular seismic phase being considered. Shadow zones are caused by regions in the earth where the velocity decreases with depth at a rate such that  $dv/dr > v/r$ . Figure 2b shows a typical time-distance curve in the presence of such a region. The shadow zone for P caused by the core is the most obvious example. This shadow zone prevents the simultaneous inversion of P and PKP data by the Herglotz-Wiechert method. Dorman *et al.* (1960) claim to have made a convincing case for a shadow zone for S in the upper mantle from a study of mantle Rayleigh wave dispersion data.

A practical difficulty of the requirement that the ray parameter be known for all  $\Delta$  in the range of interest is that there may be loops or triplications in the travel time curve. These loops are caused by regions in the earth where the velocity increases with depth at a rate such that seismic rays penetrating to different depths are refracted to the same location on the surface. Figure 2a shows a typical time-distance curve caused by such a region. Provided that all the later arrivals at any given distance are taken into account, there is no problem. In practice, however, the time intervals between successive arrivals

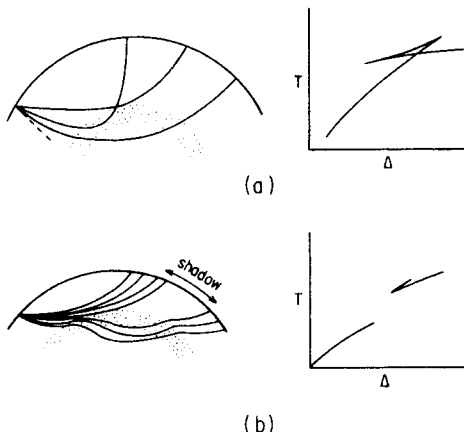


FIG. 2. (a) The effect on seismic rays of a layer in which the velocity increases rapidly with depth and the corresponding travel time curve. (b) The effect of a low velocity zone and the corresponding travel time curve.

at a given distance in the presence of a loop in the travel time curve may be very short and the arrivals may not be satisfactorily resolved on the seismogram.

Second, since the slope of the travel time curve is required, the data are usually smoothed and fitted with a curve which is then differentiated. This process requires a large amount of data closely spaced with respect to epicentral distance for accurate slope information.

Third, the method is based on classical ray theory which is known to be inadequate in regions of high velocity gradients and in the neighborhood of the geometrical boundaries of shadows due to discontinuities in velocity (see for example, Richards, 1970). This limitation usually manifests itself again as a gap in the observed range of ray parameters and prevents the simultaneous inversion of P and PcP or S and ScS data for example. In this case, as P or S near grazing incidence for the core, P and PcP or S and ScS begin to interfere and cannot be separated in the time domain. This leads to a dispersion in the measured values of  $dT/d\Delta$  and Johnson (1969) and Richards (1970) have discussed the frequency dependent correction that needs to be made to the measured values to approximate the infinite frequency (or ray theory) value of the ray parameter. In practice, the measured  $dT/d\Delta$  vs.  $\Delta$  curve begins to flatten beyond 90° and the Herglotz-Wiechert method cannot determine the velocity below the point at which the corresponding values of  $dT/d\Delta$  are constant. Usually, the velocity is only determined to within about 100 km of the accepted value of the core radius (somewhat closer when the  $dT/d\Delta$  data are corrected for the dispersion mentioned above, Johnson, 1969). The procedure then is to try several extrapolations of the velocity profile downwards and to try several values of the core radius in an attempt to find a combination of extrapolated profile and core radius which best fits the PcP or ScS data. Note that in the procedure just outlined it is necessary to have a velocity model for the whole mantle in order to determine the core radius and the value obtained will depend on the accuracy of the velocity model in the mantle. Thus, the core radius is not a free parameter in the inversion and it is not surprising that substantially different core radii are found from the inversion of P and PcP and S and ScS data (Taggart and Engdahl, 1968; Hales and Roberts, 1970). The dispersion of  $dT/d\Delta$  data mentioned above will also affect the inversion of PKP and SKS data near grazing incidence for the core.

Fourth, the Herglotz-Wiechert method has no provision for taking into account observational errors in the data and the effect that these errors may have on the solution.

In spite of the limitations mentioned above, the Herglotz-Wiechert method is valuable in the sense that, in the absence of low velocity zones, it establishes the existence of a solution to the seismic velocity inverse problem.

Moreover, Gerver and Markushevich (1966, 1967) have proved that if we are given an infinite amount of perfectly accurate travel time data at all distances from sources above and below all the low velocity zones, a solution exists and is unique except in the low velocity zones themselves. It is always comforting to know that a solution to an idealized version of one's problem exists and is unique.

### B. THE BACKUS-GILBERT METHOD

Given a finite amount of data, Backus and Gilbert (1967) prove that the collection of Earth models (velocity profiles) which fit the measured data is either empty or infinite dimensional. We know that provided very general conditions are satisfied by a given set of travel time data (Gerver and Markushevich, 1967), conditions almost always satisfied for the real Earth, we can construct a velocity profile by the Herglotz-Wiechert method and so we know that the collection of profiles which satisfy the data is infinite dimensional. The Backus-Gilbert method of inverting travel time data provides a way of selecting velocity profiles from this infinite dimensional manifold of solutions that is not subject to many of the limitations of the Herglotz-Wiechert method mentioned above.

First, there is no need for a complete travel time curve, i.e., the ray parameter need not be known for all values of  $\Delta$  in the range of interest.

Second, there is no need to fit the data with a smooth curve in order to differentiate it before inverting.

Third, the Backus-Gilbert method can simultaneously invert data on any number of seismic phases such as P, PKP, PcP, S, SKS, and ScS. The core radius is a free parameter in the inversion and the resulting value will thus be consistent with both P, PcP and S, ScS data. When applied to body-wave travel time data, the method is still subject to the errors inherent in a ray theoretical interpretation, but the effects of these errors do not restrict the application of the Backus-Gilbert method in certain regions of the earth as they do the Herglotz-Wiechert method.

Fourth, the Backus-Gilbert method takes observational errors in the data into account and makes a quantitative estimate of their effect on the solution.

It is worthwhile emphasizing at this point that once we have found a model that fits our observational data to within the desired degree of accuracy (to within one standard error in the data, say), whether we have found the model using the Herglotz-Wiechert, Backus-Gilbert or some other method, the most important next step is to describe the uniqueness of the model. The Backus-Gilbert method actually exploits the nonuniqueness of the problem to generate solutions which fit the data and then allows us to make a quantitative statement about the degree of nonuniqueness of any solution.

## II. Theory

### A. INVERSION THEORY

For our purposes, we consider spherically symmetric Earth models in which the velocity is only a function of the radius  $r$ . To apply the Backus-Gilbert method we must find, to first order, the change in the travel times  $\delta T$  produced by a small change in the velocity  $\delta v(r)$ . Following Backus and Gilbert (1969), the travel time of a group of nondispersive body waves from a source  $P_1$  to a receiver  $P_2$  is given by

$$T = \int_{P_1}^{P_2} v^{-1} ds, \quad (2)$$

where  $ds$  is the element of path length. According to Fermat's principle, to first order in  $\delta v$ , we have

$$\delta T = - \int_{P_1}^{P_2} v^{-2} \delta v ds. \quad (3)$$

If we introduce spherical polar coordinates, radius  $r$ , colatitude  $\theta$ , and longitude  $\lambda$ , choose units so that the radius of the Earth is at  $r = 1$ , and consider the ray path from  $r = 1, \theta = 0$  to  $r = 1, \theta = \Delta, \lambda = 0$ , we have (Bullen, 1963)

$$\delta T = -2 \int_{r_p}^1 \eta(r) r(r)^{-2} [\eta(r)^2 - p^2]^{-1/2} \delta r(r) dr, \quad (4)$$

where  $r_p$  is the minimum radius reached by the ray,  $\eta(r) = rr(r)^{-1}$ , and  $p = r^{-1}r \sin i$  is called the ray parameter which, according to Snell's law, is constant along the ray. The angle  $i$  is the angle between the ray and the local radius vector (see Fig. 1). At  $r = r_p$ ,  $i = 90^\circ$  and  $p = r_p/v_p$  where  $v_p = v(r_p)$ .

We can regard  $T_i$ , the travel time calculated from a given model  $v(r)$  at epicentral distance  $\Delta_i$ ,  $i = 1, \dots, N$ , as a nonlinear functional of that model. To linearize the problem, we appeal to Fréchet differentiability of the functional  $T_i$  (Dunford and Schwartz, 1958). Then, correct to first order in the small quantity  $\delta r(r)$ ,  $\delta T_i$  is a well-defined linear functional and we write (4) as

$$\delta T_i = \int_0^1 K_i(r) \delta r(r) dr. \quad (5)$$

where  $K_i(r)$  is the  $i$ th data kernel or so called "Fréchet kernel" and is defined as

$$\begin{aligned} K_i(r) &= -2\eta(r)v(r)^{-2}[\eta(r)^2 - p^2]^{-1/2}, \quad r_p^i < r \leq 1 \\ &= 0, \quad 0 \leq r \leq r_p^i. \end{aligned} \quad (6)$$

In the nonlinear case, the data kernels are different for different Earth models  $v(r)$ .

It is often preferable to consider a relative perturbation to the model rather than an absolute one. If we define  $G_i(r) = v(r)K_i(r)$  and  $m(r) = \delta v(r)/v(r)$  we can write (5) as

$$\delta T_i = \int_0^1 G_i(r)m(r) dr, \quad (7)$$

and  $G_i(r)$  is now our data kernel for the model  $\mathcal{V}(r) = \ln v(r)$ , i.e.  $m(r) = \delta \mathcal{V}(r) = \delta v(r)/v(r)$ .

Associated with each travel time  $T_i$  is an observational error which we assume has zero mean and variance  $\sigma_i^2$ . If we let  $\delta T_i$  be the difference between the observed travel time for the real Earth,  $T_i^E$ , and the travel time calculated from a particular model,  $T_i$ , and define  $\gamma_i \equiv T_i^E - T_i$  we can write (7) as

$$\gamma_i - \sigma_i \leq \int_0^1 G_i(r)m(r) dr \leq \gamma_i + \sigma_i. \quad (8)$$

Our objective is now to determine  $m(r)$  from (8) given a finite number of known  $\gamma_i \pm \sigma_i$ ,  $i = 1, \dots, N$ . Formulated in this way, the problem is ill-posed in the sense that we are trying to determine a continuous function  $m(r)$  from a finite number of its moments. The solution is thus nonunique; in fact, there is an infinite number of solutions. We can take advantage of this nonuniqueness if we are willing to accept any  $m(r)$  which is a solution to (8). A method proposed by Backus and Gilbert (1967) for choosing a solution is to find that model which satisfies (8) and is closest in the least squares sense to a given starting model. However, their method requires the data kernels  $G_i(r) = v(r)K_i(r)$  to be square integrable and it is obvious from (6) that this is not the case.

We can remedy this situation by integrating (7) by parts. In particular, we choose to integrate by parts twice so that, as is shown below, we will be trying to find the smoothest perturbation  $m(r)$  to our given starting model. If we integrate (7) by parts twice we have

$$\begin{aligned} \delta T_i &= \mathcal{G}_i(1)m(1) + \mathcal{G}_i(r_c^-)[m(r_c^-) - m(r_c^+)] - \mathcal{H}_i(1)m'(1) \\ &\quad - \mathcal{H}_i(r_c^-)[m'(r_c^-) - m'(r_c^+)] + \int_0^1 \mathcal{H}_i(r)m''(r) dr, \end{aligned}$$

where the primes denote differentiation with respect to  $r$  and

$$\mathcal{G}_i(r) = \int_0^r G_i(s) ds$$

and

$$\mathcal{H}_i(r) = \int_0^r \mathcal{H}_i(s) ds.$$

The terms  $\mathcal{G}_i(r_c^-)m(r_c^\pm)$  and  $\mathcal{H}_i(r_c^-)m'(r_c^\pm)$  are due to the discontinuity in velocity at the core-mantle boundary which when approached from below is designated by  $r_c^-$  and when approached from above by  $r_c^+$ .

Now, let us define  $x_0 \equiv [m(r_c^-) - m(r_c^+)]$  and  $x_1 \equiv [m'(r_c^-) - m'(r_c^+)]$ ; then we can write (8) as

$$\begin{aligned} \gamma_i - \sigma_i &\leq \mathcal{G}_i(1)m(1) + \mathcal{G}_i(r_c^-)x_0 - \mathcal{H}_i(1)m'(1) - \mathcal{H}_i(r_c^-)x_1 \\ &\quad + \int_0^1 \mathcal{H}_i(r)m''(r) dr \leq \gamma_i + \sigma_i. \end{aligned} \quad (9)$$

The problem is now to determine  $m''(r)$  from (9) and as before we use a least squares criterion to select one of the infinite number of solutions to (9). In particular, we seek to minimize

$$\frac{1}{2} \int_0^1 m''(r)^2 dr + \frac{1}{2} [m(1)^2 + m'(1)^2 + x_0^2 + x_1^2] \quad (10)$$

subject to the constraints (9). As mentioned above, the criterion (10) amounts to finding the smoothest perturbation to our given starting model. Minimizing (10) subject to the constraints (9) is a classic problem in the calculus of variations, and if we introduce Lagrange multipliers  $v_j$  and carry out the minimization we have the solution

$$\begin{aligned} m''(r) &= \sum_j v_j \mathcal{H}_j(r), \\ m'(1) &= - \sum_j v_j \mathcal{H}_j(1), \\ m(1) &= \sum_j v_j \mathcal{G}_j(1), \\ x_0 &= \sum_j v_j \mathcal{G}_j(r_c^-), \\ x_1 &= - \sum_j v_j \mathcal{H}_j(r_c^-). \end{aligned} \quad (11)$$

To determine the  $v_j$ , we substitute (11) into (9) to obtain

$$\gamma_i - \sigma_i \leq \sum_j \left[ \int_0^1 \mathcal{H}_i(r) \mathcal{H}_j(r) dr + \mathcal{H}_i(1) \mathcal{H}_j(1) + \mathcal{H}_i(r_c^-) \mathcal{H}_j(r_c^-) + \mathcal{G}_i(1) \mathcal{G}_j(1) + \mathcal{G}_i(r_c^-) \mathcal{G}_j(r_c^-) \right] v_j \leq \gamma_i + \sigma_i. \quad (12)$$

If we define the symmetric inner product matrix

$$A_{ij} = \int_0^1 \mathcal{H}_i(r) \mathcal{H}_j(r) dr + \mathcal{H}_i(1) \mathcal{H}_j(1) + \mathcal{H}_i(r_c^-) \mathcal{H}_j(r_c^-) + \mathcal{G}_i(1) \mathcal{G}_j(1) + \mathcal{G}_i(r_c^-) \mathcal{G}_j(r_c^-), \quad (13)$$

we can write (12) in matrix form as

$$\gamma - \sigma \leq \mathbf{A} \cdot \mathbf{v} \leq \gamma + \sigma. \quad (14)$$

The system of equations (12) or (14) would be much simpler to solve if the  $\mathcal{H}_i(r)$  and  $\mathcal{G}_i(r)$  were orthogonal. Then, the matrix  $\mathbf{A}$  would be diagonal and (14) would be a system of linear algebraic equations, one for each  $v_i$ . Since  $\mathbf{A}$  is symmetric and positive definite there is a linear transformation which diagonalizes  $\mathbf{A}$  and simultaneously diagonalizes the covariance matrix  $E_{ij}$  of the observed data (Gilbert, 1971). Usually we assume the data have independent standard errors  $\sigma_i$  so that  $E_{ij}$  is already diagonal, but this need not be the case. Following Gilbert (1971) we let  $\mathbf{T}$  be the matrix of the diagonalizing transformation and the transformed version of (14) becomes

$$(\mathbf{T} \cdot \gamma - \Lambda^{-1/2}) \leq \mathbf{T} \cdot \mathbf{v} \leq (\mathbf{T} \cdot \gamma + \Lambda^{-1/2}), \quad (15)$$

where  $\Lambda^{-1}$  is the transformed diagonal covariance matrix. Now, the transformed data kernels are orthogonal so we have from (10) and (11)

$$\int_0^1 m''(r)^2 dr + m(1)^2 + m'(1)^2 + x_0^2 + x_1^2 = \sum_j (\mathbf{T} \cdot \mathbf{v})_j^2. \quad (16)$$

Thus, the minimum in (16) occurs when each  $(\mathbf{T} \cdot \mathbf{v})_i$  in (15) is as small as possible. We write

$$\mathbf{l} = (\mathbf{T} \cdot \gamma - \Lambda^{-1/2}), \quad \mathbf{u} = (\mathbf{T} \cdot \gamma + \Lambda^{-1/2}), \quad \mathbf{c} = \mathbf{T} \cdot \mathbf{v},$$

and we have

$$l_i \leq c_i \leq u_i, \quad i = 1, \dots, N. \quad (17)$$

When  $l_i > 0$  we take  $c_i = l_i$ ; when  $u_i < 0$  we take  $c_i = u_i$  and  $c_i = 0$  otherwise. Gilbert (1971) shows that the elements of the transformed diagonal covariance matrix  $\Lambda^{-1}$  are the reciprocals of the eigenvalues of the matrix

$$\mathcal{A}_{ij} = \sigma_i^{-1} A_{ij} \sigma_j^{-1}$$

in the case where the original covariance matrix  $E_{ij}$  is already diagonal. Thus, the transformed data can be ranked according to standard error, i.e., large eigenvalues of  $\mathcal{A}$  correspond to transformed data with small standard error. This permits us to monitor the growth of the perturbation to the model in (16) and to reject those transformed data which have standard errors larger than we wish to consider.

Once we have found the  $v_i$ 's from (17) we calculate  $m''(r)$  from (11) and integrate twice to get  $m(r) = \delta r(r)/r(r)$ . The two integrations provide a further smoothing of the perturbation  $\delta r(r)$  we make to the starting model. We now increment the starting model to give a new model  $r(r) + \delta r(r)$  from which we can calculate new travel times to compare with the observed travel times. Because we have linearized the problem, the new calculated travel times may not agree with the observed travel times to within one standard error. So, we use the model  $r(r) + \delta r(r)$  as a new starting model and repeat the process outlined above. This iterative scheme should converge provided the initial values of  $\gamma_i = T_i^E - T_i$  are not too large.

## B. RESOLVING POWER THEORY

Now that we have a method for generating models which fit the observed data, what can we say about their uniqueness? There are two approaches to the question of uniqueness which have recently been developed. We will briefly outline both of them and how they apply to the travel time problem. The first approach was developed by Backus and Gilbert (1968, 1970) and we shall refer to it as the "objective" approach. The second approach was developed by Backus (1970a,b,c) and we shall refer to it as the "subjective" approach.

### 1. *Objective Approach*

We refer to the method about to be described as "objective" because we only use the observed data to derive a quantitative statement about the uniqueness of our model, i.e., we use no *a priori* judgments about the model in describing its degree of uniqueness.

When we have only a finite amount of data we cannot expect to resolve details of arbitrarily small scale. The best we can hope for is that our data

provide us with an estimate of the true value of the model at any particular radius that is in some sense a smoothed or averaged version of the structure around that radius.

Neglecting errors in the data for the moment we have

$$\gamma_i = \int_0^1 G_i(r) m(r) dr. \quad (18)$$

If we wish to consider linear averages of  $m(r)$ , we have

$$\sum_i a_i \gamma_i = \int_0^1 \left[ \sum_i a_i G_i(r) \right] m(r) dr. \quad (19)$$

We would like to choose the constants  $a_i$  in (19) so that the function in square brackets is localized around some value of the radius, say  $r_0$ . In other words, if we define

$$A(r, r_0) \equiv \sum_i a_i(r_0) G_i(r), \quad (20)$$

we would like  $A(r, r_0)$  to resemble a Dirac delta function centered on  $r_0$ ; if this were possible, (19) would simply give  $m(r_0)$ , the exact value of  $m(r)$  at  $r_0$ . As mentioned above, it is impossible to construct a perfect delta function with only a finite amount of data, but by choosing the  $a_i$  carefully we may be able to do a good job of approximating a delta function at  $r_0$ . Then (19) would give us

$$\sum_i a_i \gamma_i = \int_0^1 A(r, r_0) m(r) dr \equiv \langle m, A \rangle, \quad (21)$$

where  $\langle m, A \rangle$  is a smoothed or averaged version of  $m(r)$  around  $r_0$ . The averaging length would correspond to the width of  $A(r, r_0)$  at  $r_0$ .

How can we choose the  $a_i$  so that  $A(r, r_0)$  is an approximation to a delta function? Backus and Gilbert have investigated several so called “ $\delta$ -ness criteria” which are numerical measures of the difference between  $A(r, r_0)$  and a delta function. One such measure is

$$d = \int_0^1 [\delta(r - r_0) - A(r, r_0)]^2 dr \quad (22)$$

with the condition that

$$\int_0^1 A(r, r_0) dr = 1. \quad (23)$$

The  $a_i$  are found by minimizing (22) subject to the condition (23).

The criterion (22) is not the most appropriate one to use in the travel time problem because the data kernels  $G_i(r)$  in (20) are not square integrable. However, the  $\mathcal{G}_i(r) = \int_0^r G_i(r') dr'$  are square integrable and so an obvious extension of (22) is

$$s = 12 \int_0^1 \left[ H(r - r_0) - \int_0^r A(r, r_0) dr \right]^2 dr, \quad (24)$$

where  $H(r - r_0)$  is the unit step function. Suppose  $A(r, r_0)$  were the "box car" function, i.e.,

$$\begin{aligned} A(r, r_0) &= 1/l, & |r - r_0| < l/2, \\ &= 0, & |r - r_0| > l/2. \end{aligned}$$

then  $s = l$ . Thus, we see that  $s$  is a measure of the width of our averaging function  $A(r, r_0)$ , which we will call the "spread." Once we have found the constants  $a_i$  from the minimization of (24) subject to the condition (23) we can calculate the smoothed or averaged version of  $m(r)$  from (21). If  $m(r)$  has any fine scale structural detail with wavelengths smaller than our measure  $s$  of the spread of the averaging function  $A(r, r_0)$  we will not be able to resolve it. This is an inevitable consequence of the finite amount of data we have available and the spread  $s$  is a quantitative measure of the uniqueness of our inversion.

So far, in discussing resolving power, we have assumed perfectly accurate data. What effect do the observational errors in the data have on the resolving power? If the data have observational errors  $\Delta T_i$ , then it is easy to see from (21) that these errors produce an error  $\Delta \langle m, A \rangle$  in our averaged value of  $m(r)$  at  $r_0$ , given by

$$\Delta \langle m, A \rangle = \sum_i a_i \Delta T_i. \quad (25)$$

It is clear that a highly localized average of  $m(r)$  at  $r_0$  is not very useful if the associated error in the average (25) is large. We would be willing to accept an average with a slightly larger spread if we could reduce the error (25) appreciably.

Now we do not know the  $\Delta T_i$  exactly, but we assume we know something about their statistics. In particular, we assume they have zero mean and finite variance, i.e., we assume that the covariance matrix

$$E_{ij} = \mathcal{E}\{\Delta T_i \Delta T_j\}$$

exists, where  $\mathcal{E}\{\cdot\}$  means expected value. We take the square root of the variance of  $\Delta \langle m, A \rangle$  as an estimate of the error we make in calculating  $\langle m, A \rangle$  with erroneous data; call it  $\rho$ . We have

$$\rho^2 = \sum_i \sum_j a_i a_j E_{ij} \quad (26)$$

or, in matrix notation,

$$\rho^2 = \mathbf{a} \cdot \mathbf{E} \cdot \mathbf{a}. \quad (27)$$

Similarly, after some algebraic manipulation, we can write (24) as

$$s = \mathbf{a} \cdot \mathbf{S} \cdot \mathbf{a} - 2\Gamma \cdot \mathbf{a} + k, \quad (28)$$

where

$$\begin{aligned} S_{ij} &= \int_0^1 G_i(r) G_j(r) dr, \\ \Gamma_j &= \int_0^1 H(r - r_0) G_j(r) dr, \\ k &= 1 - r_0, \end{aligned} \quad (29)$$

and the condition (23) as

$$\mathbf{a} \cdot \mathbf{g} = 1, \quad (30)$$

where  $g_i = \int_0^1 G_i(r) dr$ .

Our object is now to find the  $\mathbf{a}$ 's which minimize both the spread given by (28) and the error in the average of  $m(r)$  given by (27) while satisfying the condition (30). Clearly, we cannot minimize (28) and (30) with the same set of  $\mathbf{a}$ 's, but Backus and Gilbert (1970) show that we can minimize a linear combination of the two. Consider the combination

$$q = s \cos \theta + \rho^2 \sin \theta \quad (31)$$

where  $\theta$  is a parameter which runs from 0 to  $\pi/2$ . When  $\theta = 0$  we are minimizing spread and when  $\theta = \pi/2$  we are minimizing the error in the average of  $m(r)$ . Backus and Gilbert (1970) prove that as  $\theta$  goes from 0 to  $\pi/2$  the curve  $\rho^2(s)$ , called the tradeoff curve of error vs spread, is a monotonically decreasing function of  $s$ , i.e., we can lower the error in the estimate of  $\langle m, A \rangle$  by willingness to accept a larger spread.

Minimizing (31) leads to a system of equations for the  $\mathbf{a}$ 's of the form

$$\mathbf{Q} \cdot \mathbf{a} = 12\Gamma \cos \theta, \quad (32)$$

where

$$Q_{ij} = 12S_{ij} \cos \theta + E_{ij} \sin \theta. \quad (33)$$

There will be a different set of  $\mathbf{a}$ 's for each value of  $\theta$  on the tradeoff curve. Once again, the system (32) would be much simpler to solve if  $\mathbf{Q}$  were a diagonal matrix; and once again we can use the diagonalizing transformation developed by Gilbert (1971) to simultaneously diagonalize  $\mathbf{S}$  and  $\mathbf{E}$ .

To summarize briefly, at each radius  $r_0$  where we wish to calculate  $\langle m, A \rangle$  we minimize (31) subject to the condition (30) to determine the  $\mathbf{a}$ 's at each point on the tradeoff curve. At each point on the tradeoff curve at  $r_0$  we calculate the spread  $s$  by (28) and the error in  $\langle m, A \rangle$  by (27).

## 2. Subjective Approach

We use the term "subjective" in describing this method because it allows us to incorporate *a priori* subjective judgments in our estimate of the error we make when we try to predict the value of a particular datum for the real Earth, e.g., the seismic velocity at a given depth.

Following Backus (1970a) we can characterize the method, as applied to the travel time problem, as follows: we are given  $N$  measured travel times for the real Earth along with their associated experimental errors. From these data we wish to predict the value of the seismic velocity at a given depth and to estimate the error of our prediction.

Let us say that we wish to predict the value of the seismic velocity at  $r_0$  for the real Earth, call it  $v_E(r_0)$ . Because the travel time problem is nonlinear in the velocity, we linearize the problem as described previously so that instead of predicting  $v_E(r_0)$  we wish to predict  $v(r_0) - v_E(r_0)$ , where  $v(r_0)$  is the velocity at  $r_0$  of a model which fits the travel time data for the real Earth. If we are interested in relative prediction errors we again may take as our model  $m(r) = \ln[v(r)/v_E(r)]$ .

Now, from the discussion of the objective approach, we saw that an inevitable consequence of a finite amount of data is that the data will only provide us with a smoothed or averaged version of  $m(r)$  around  $r_0$ . In (21) we defined this average as  $\langle m, A \rangle = \sum a_i \gamma_i$ , where  $\gamma_i = T_i^E - T_i$ , the difference between the  $i$ th travel time for the real Earth and the  $i$ th travel time for a model which fits the measured travel time data,  $T_i^M$ ,  $i = 1, \dots, N$ , for the real Earth, and

$A(r, r_0)$  as defined in (20) is our averaging function. We also saw that the observational errors  $\Delta T_i$  in  $T_i^M$  led to an error in our average given by

$$\Delta \langle m, A \rangle = \sum_i a_i \Delta T_i.$$

If  $A(r, r_0)$  were a delta function centered on  $r_0$ , i.e., if  $A(r, r_0) = \delta(r - r_0)$  and we had perfectly accurate data, we could predict  $m(r_0)$  exactly with no error. However, when we try to predict  $m(r_0)$  using a finite amount of inaccurate data  $\gamma_i^M = T_i^M - T_i$ , we commit an error

$$\sum_i a_i \gamma_i^M - \langle m, \delta \rangle = \langle m, A \rangle - \langle m, \delta \rangle + \sum_i a_i \Delta T_i. \quad (34)$$

We define  $\varepsilon^2$  as the expected value of the square of this error (the variance) and we have

$$\varepsilon^2 = \mathcal{E} \left\{ \left( \langle m, (A - \delta) \rangle + \sum_i a_i \Delta T_i \right)^2 \right\}. \quad (35)$$

We assume that  $\mathcal{E}\{\Delta T_i\} = 0$  so we have

$$\varepsilon^2 = |\langle m, (A - \delta) \rangle|^2 + \sum_i \sum_j a_i a_j E_{ij}, \quad (36)$$

where, as before,  $E_{ij}$  is the covariance matrix of the data.

Now, suppose that by some *a priori* knowledge we have reason to believe that we can prescribe an upper bound, say  $M$ , for  $\|m\|$ , i.e., we are willing to say that

$$\|m\| \leq M. \quad (37)$$

We admit that  $\|m\|$  may be greater than  $M$  but we consider it unlikely until we find new data that force us to change our opinion.

If we are willing to grant (37), then by Schwartz's inequality we have an *upper bound* for the error we make in estimating  $\langle m, \delta \rangle$  as  $\sum a_i \gamma_i^M$ , i.e.,

$$\varepsilon^2(\mathbf{a}) = M^2 \|A - \delta\|^2 + \sum_i \sum_j a_i a_j E_{ij}, \quad (38)$$

where we have written  $\varepsilon^2(\mathbf{a})$  to show the dependence on the  $N$  vector  $\mathbf{a} = (a_1, \dots, a_N)$ . However, if we recall that  $A(r, r_0) = \sum a_i(r_0) G_i(r)$  we see that we are again faced with the problem of the nonsquare integrability of the  $G_i(r)$  in (38), i.e., the norms  $\|(A - \delta)\|$  and  $\|m\|$  are not well defined. This is an

example of the more general problem of discontinuous linear functionals on our linear space of models  $\mathcal{M}$  which we now regard as an arbitrary real linear space and not a Hilbert space in which the norms in (38) are well defined. However, as Backus (1970b) shows, we can reduce the problem to one in a Hilbert space with a well-defined norm by a transformation which he refers to as a "quelling."

Basically, a "quelling" consists of four objects:

- (i) a real linear space  $\mathbf{R}^*$ , the space of linear functionals on  $\mathcal{M}$ ;
- (ii) a Hilbert space  $\mathbf{H}$ . If  $\mathbf{h}_1$  and  $\mathbf{h}_2$  are vectors in  $\mathbf{H}$  then  $(\mathbf{h}_1, \mathbf{h}_2) = \int_0^1 h_1(r)h_2(r) dr$  defines their inner product and  $\|\mathbf{h}_1\|^2 = (\mathbf{h}_1, \mathbf{h}_1)$  defines a norm;
- (iii) a linear mapping  $Q : \mathbf{R}^* \rightarrow \mathbf{H}$ ;
- (iv) a linear mapping  $Q^{-1} : \mathcal{M} \rightarrow \mathbf{H}$ .

The connection between these four objects which make them a "quelling" as defined by Backus (1970b) is that for any functional  $g$  in  $\mathbf{R}^*$  and any  $m$  in  $\mathcal{M}$  we have

$$[m, g] = (Q^{-1}m, Qg) \leq \|Q^{-1}m\|^2 \|Qg\|^2, \quad (39)$$

where  $[m, g]$  is the real number  $g(m)$  which the functional  $g$  assigns to the member  $m$  of  $\mathcal{M}$ . Thus, by means of the mappings  $Q$  and  $Q^{-1}$  we can reduce the problem of prediction on arbitrary linear spaces to one of prediction on a Hilbert space where a norm is well defined. Quelling will usually be needed when some of the functionals in  $\mathbf{R}^*$  are discontinuous; thus, we can think of  $Q$  in (39) as a smoothing operator and the action of  $Q^{-1}$  will then be one of "roughening"  $m$ . Equation (39) can then be viewed as a demand on the smoothness and the overall size of  $m$ .

The question now is, what are the mappings  $Q$  and  $Q^{-1}$  appropriate to the travel time problem? The difficulty, we have seen, is the inverse square root singularity of the  $G_i(r)$  in  $A(r, r_0) = \sum a_i(r_0)G_i(r)$  so that  $A$  is a discontinuous linear functional on  $\mathcal{M}$ . Thus, in (36) we wish to find the mappings  $Q, Q^{-1}$  such that

$$\langle m, (A - \delta) \rangle = (Q^{-1}m, Q(A - \delta)). \quad (40)$$

We have already seen that a remedy for the nonsquare integrability of the  $G_i(r)$  is a simple integration by parts. This is an example of what Backus (1970b) refers to as quelling by integration. In this case we have

$$\langle m, (A - \delta) \rangle = \left( -dm/dr, \int_0^r (A(r, r_0) - \delta(r - r_0)) dr \right). \quad (41)$$

where we require  $\int_0^1 A(r, r_0) dr = 1$ . Now,

$$\int_0^r (A(r, r_0) - \delta(r - r_0)) dr = \int_0^r A(r, r_0) dr - H(r - r_0)$$

and by Schwartz's inequality we have

$$\begin{aligned} & \left( -dm/dr, \int_0^r (A(r, r_0) - \delta(r - r_0)) dr \right) \\ & \leq \| dm/dr \| ^2 \left\| H(r - r_0) - \int_0^r A(r, r_0) dr \right\|^2. \end{aligned} \quad (42)$$

Equation (36) for our prediction error now becomes

$$\varepsilon^2(\mathbf{a}) \leq \| dm/dr \| ^2 \left\| H(r - r_0) - \int_0^r A(r, r_0) dr \right\|^2 + \sum_i \sum_j a_i a_j E_{ij}. \quad (43)$$

If we are willing to prescribe an upper bound for  $\| dm/dr \|$  where  $m(r) = \ln[v(r)/v_E(r)]$ , say  $M$ , (43) again gives us an *upper bound* on the error we make in estimating  $m(r_0)$ , i.e.,

$$\varepsilon^2(\mathbf{a}) = M^2 \left\| H(r - r_0) - \int_0^r A(r, r_0) dr \right\|^2 + \sum_i \sum_j a_i a_j E_{ij}. \quad (44)$$

Having prescribed the *a priori* bound  $M$  on  $\| dm/dr \|$ , the best strategy to use in estimating  $m(r_0)$  is to choose  $\mathbf{a}(M)$  and thus  $A(r, r_0)$  so as to minimize the error in (44). As in the discussion of the objective approach, the numerical problem is to minimize the inhomogeneous quadratic polynomial (44) in  $a_1, \dots, a_N$  subject to the condition  $\int_0^1 A(r, r_0) dr = 1$ . We note that the minimization of Eq. (44) is formally equivalent to the minimization of Eq. (31) where from (24) we see that

$$s = 12 \left\| H(r - r_0) - \int_0^1 A(r, r_0) dr \right\|^2$$

and we make the identification  $M^2 = \cos \theta / \sin \theta$ .

When we have found the  $\mathbf{a}$  which minimizes (44) we estimate  $m(r_0)$  as  $\sum a_i(r_0) \gamma_i^M$  and the variance of the error committed in this estimate is  $\varepsilon^2(\mathbf{a}(M))$ . Clearly, this error is a function of our *a priori* value of  $M$ . In a real problem, we would be wise to examine  $\varepsilon^2(\mathbf{a}(M))$  as a function of  $M$ . Some results of such an examination using the travel time data will be shown in section V.

### III. Data

#### A. TRADITIONAL DATA

The traditional data inverted to find a velocity profile are values of  $p(\Delta) = dT/d\Delta$ . When there is a triplication in the travel time curve, such as the one in Fig. 2a,  $p(\Delta)$  is a multivalued function of  $\Delta$ . This can cause some computational difficulty in any inversion scheme which requires us to solve the direct problem for some model, i.e., given a  $\Delta_i$  calculate the corresponding  $T_i(\Delta_i)$  to compare with the measured  $T_i(\Delta_i)$  for the real Earth. As mentioned in Section I, the time intervals between successive arrivals at  $\Delta_i$ , in the presence of a triplication, may be very short and we may have a difficult time deciding which branch of the travel time curve, i.e., which value of  $p(\Delta_i)$ , is the appropriate one.

To overcome this difficulty, we would like data that is a single valued function of some independent variable. Such data would have the effect of "unfolding" any multiplicities in the travel time curve.

#### B. A NEW DATUM: $(T - p\Delta)$

We notice that  $T(p)$  and  $\Delta(p)$  are single valued functions of  $p$ , and both can be determined from a measured  $T(\Delta)$  curve. However, when we attempt to calculate  $\delta(T)_p$  and  $\delta(\Delta)_p$  due to a small change  $\delta r(r)$ , we encounter singularities that cannot be removed by a simple integration by parts as was the case with  $\delta(T)_\Delta$ . The subscripts  $p$  or  $\Delta$  indicate which one of them is being held fixed. We note that the singularities are of the same order, so perhaps if we could find a suitable combination of  $T(p)$  and  $\Delta(p)$  we could overcome this difficulty. In short, the proper combination is  $[T - p\Delta](p)$ , as we shall see.

We define

$$\tau(p) = [T - p\Delta](p)$$

and note the following properties of this function.

First, we have experimentally measured values of  $T(\Delta)$  from which we can obtain  $p$  or we can measure  $p$  directly with large seismic arrays. Thus, we have measured values of  $T(p)$ ,  $p$ , and  $\Delta(p)$  at our disposal to construct the function  $\tau(p)$ . We are using the same data as that used in the Herglotz-Wiechert inversion method, but we are combining it in a different way. We can look at this as a mapping of one data set into another.

Second,

$$d\tau(p)/dp = -\Delta(p),$$

so  $\tau(p)$  is a monotonically decreasing, single valued function of  $p$ . The data  $\tau(p)$  thus fulfill our objective of "unfolding" the multiplicities in the travel time curve. The curve  $\tau$  vs  $p$  may have discontinuities in  $\tau$  due to low velocity zones, but since the value of  $p$  is the same for the rays which bottom just above and just below a low velocity zone, there will be no discontinuity in  $p$  (Gerver and Markushevich, 1967, and see Fig. 3).

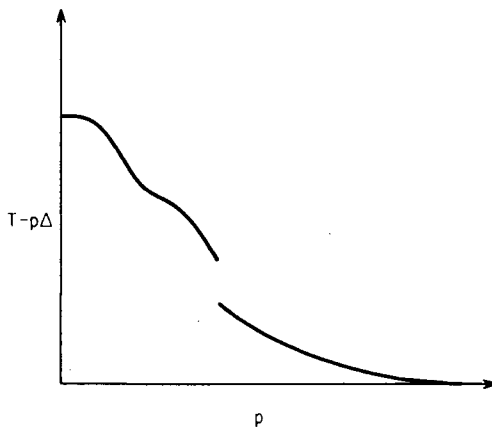


FIG. 3. A typical  $\tau(p) = T - p\Delta$  vs  $p$  curve. The discontinuity in  $\tau(p)$  is due to a low velocity zone. Note that  $d\tau/dp = -\Delta$ .

Third, we see from Eq. (4) and the relation (Bullen, 1963)

$$T - p\Delta = 2 \int_0^1 r^{-1} (\eta^2(r) - p^2)^{1/2} dr$$

that due to a small change  $\delta r(r)$  we have (Julian and Anderson, 1968)

$$\delta(T)_\Delta = \delta(T - p\Delta)_p. \quad (45)$$

As a result of Eq. (45), the data kernels or "Fréchet kernels" derived in Section II for the inversion of  $T(\Delta)$  data are the same as the kernels needed for the inversion of  $\tau(p)$  data. Thus, all the theory of Section II can be used verbatim when we replace  $T(\Delta)$  by  $\tau(p)$  as the data.

Fourth, since the ray parameter  $p$  is the independent variable, errors in  $\tau(p)$  due to errors  $\delta p$  in  $p$  are of second order in  $\delta p$ . For example, suppose we

are trying to construct a  $\tau(p)$  curve and we are at the point corresponding to  $p_0$  on the curve. The value of  $\tau(p)$  at a point  $p_1 = p_0 + \delta p$  may be written as

$$\tau(p_1) = \tau(p_0) - \Delta(p_0) \delta p + \text{terms of order } (\delta p)^2, \quad (46)$$

where we have used  $d\tau/dp = -\Delta$ . Using the fact that  $\tau(p_0) = T(p_0) - p_0 \Delta(p_0)$  and  $\delta p = p_1 - p_0$  we can write (46) as

$$\tau(p_1) = T(p_0) - p_1 \Delta(p_0) + \text{terms of order } (\delta p)^2.$$

Thus, if we approximate  $\tau(p_1) = T(p_1) - p_1 \Delta(p_1)$  by  $\hat{\tau}(p_1) = T(p_0) - p_1 \Delta(p_0)$  we make an error  $\tau(p_1) - \hat{\tau}(p_1)$  which is of second order in  $\delta p$  (Brune, 1964). The major source of error in the datum  $\tau(p)$  is then due to errors in the travel time  $T$  and errors in  $\Delta$ . However, if we have an experimentally determined  $\Delta(p)$  curve, measured with a large seismic array for example, we can construct a  $\tau(p)$  curve by simply integrating  $d\tau/dp = -\Delta(p)$ . Then, the errors in  $\tau$  will be primarily due to errors in  $\Delta$  and, as we have seen, to errors in  $p$  to second order. We shall see, in the discussion of the real data used in this study, that errors in  $\Delta$  are relatively small, at least for the P and PcP data.

### C. THE TELESEISMIC DATA SET

The data used in this study are values of  $\tau(p)$  for P, PcP, PKP and S, ScS, SKS derived from several sources described below.

#### 1. P Data

The P data were taken from the array measurements of  $dT/d\Delta$  for the lower mantle by Johnson (1969). A  $\Delta(p)$  curve was obtained from the data given in Table 1 of his paper, excluding data from the mid-Atlantic ridge, as follows: The values of  $\Delta(p)$  were grouped into 0.1 sec/deg cells from  $p = 4.5$  sec/deg to  $p = 9.0$  sec/deg. The average value of  $\Delta(p)$  was found for each cell, and these average values were then smoothed using a five point cubic approximation.

Starting with a known  $\tau = T - p\Delta$  at  $30^\circ$  [the value of  $T$  at  $30^\circ$  was taken as the average of  $T$  at  $30^\circ$  given by Herrin *et al.* (1968) and Carder *et al.* (1966)], the  $\Delta(p)$  curve was integrated to obtain  $\tau(p)$  at 0.1 sec/deg intervals in  $p$  from  $p = 9.0$  sec/deg to  $p = 4.7$  sec/deg (see Fig. 4). The travel time at  $90^\circ$  calculated from the value of  $\tau(p)$  obtained by integrating the  $\Delta(p)$  curve as just described

agrees with the Carder *et al.* (1966) travel time at  $90^\circ$  to within 0.5 sec. Since the Carder *et al.* travel times are derived from nuclear explosions for which the epicenters are known precisely and since we believe 0.5 sec to be a reasonable standard error in travel times for P, we conclude that whatever errors existed in  $\Delta(p)$  have been effectively averaged out by the integration and that the major source of error in  $\tau(p)$  is the error in travel times. Accordingly, we have taken a relative standard error of 0.2% in  $\tau(p)$  for P which is equivalent to a 0.5 sec error in travel time at teleseismic distances of  $80^\circ$  to  $90^\circ$ .

## 2. PcP Data

The PcP data were taken from Taggart and Engdahl (1968). The surface focus travel times were smoothed, again using a five-point cubic approximation, and the resulting  $T(\Delta)$  values were differentiated with a five-point differentiation formula with weights  $(1, -8, 8, -1)$  to get  $p = dT/d\Delta$  at  $5^\circ$  intervals from  $15^\circ$  to  $80^\circ$ . Relative standard errors of 0.2% were assigned to the corresponding values of  $\tau(p)$  which are plotted in Fig. 4.

## 3. PKP Data

The PKP data were taken from Bolt (1968). The same smoothing and differentiating procedures that were used for the PcP data were used for the various branches of the  $T$  vs.  $\Delta$  curve for PKP, except for the values on the GH branch. For this branch, Bolt's polynomial representation of the  $T(\Delta)$  data was differentiated directly to obtain  $p$  at  $2^\circ$  intervals from  $126^\circ$  to  $144^\circ$ . The corresponding values of  $\tau(p)$  were assigned relative standard errors of 0.3%.

Six values of  $\tau(p)$  from  $151^\circ$  to  $174^\circ$  were used for the AB branch ( $\text{PKP}_2$ ). These data were assigned a relative standard error of 0.4% because of the greater uncertainty in arrival times relative to the other branches.

Only one value of  $\tau(p)$  was needed for the DE part of the DF branch ( $\text{PKIKP}$ ). This is because the DE part of the branch is essentially linear and whenever the  $T(\Delta)$  curve is linear,  $\tau(p)$  is the same for all values of  $\Delta$ . A relative standard error of 0.2% was assigned to this value of  $\tau(p)$ .

Values of  $\tau(p)$  were calculated at  $1^\circ$  intervals between  $151^\circ$  and  $180^\circ$  for the EF portion of the DF branch. These values of  $\tau(p)$  were assigned relative standard errors of 0.1%. Typical  $\tau(p)$  values on this branch are on the order of 1000 sec, so a relative standard error of 0.1% is equivalent to a 1 sec error in travel time.

The  $\tau(p)$  values for PKP are shown in Fig. 4.

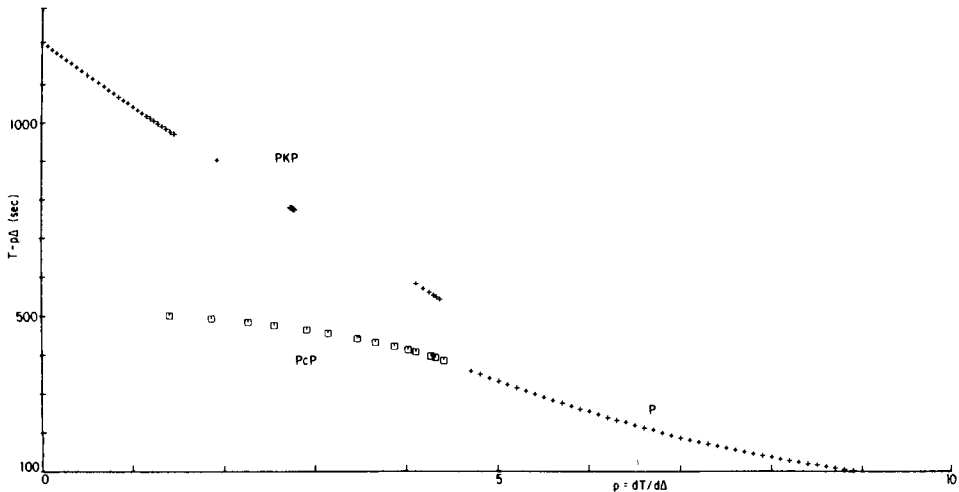


FIG. 4.  $\tau(p)$  for the teleseismic data P, PCP, PKP,  $p$  in sec/deg.

#### 4. S Data

The S data were taken from Randall (1971). The  $T(\Delta)$  values were smoothed and differentiated as described above and 34  $\tau(p)$  values calculated from  $26^\circ$  to  $78^\circ$  (see Fig. 5). Relative standard errors of 0.3% were assigned to the  $\tau(p)$  values. This corresponds to an error in travel time of about 1.3 sec at  $80^\circ$  which is  $2\frac{1}{2}$  times the error in P at the same distance. This is a consequence of the greater uncertainty involved in picking S arrival times from a seismogram.

#### 5. ScS Data

The ScS data were taken from the Jeffreys-Bullen Tables (1958). The  $T(\Delta)$  values were again smoothed and differentiated as above and  $\tau(p)$  values calculated at  $5^\circ$  intervals from  $15^\circ$  to  $80^\circ$  (see Fig. 5). The same relative standard errors assigned to the S data, 0.3%, were assigned to the  $\tau(p)$  values for ScS.

#### 6. SKS Data

The SKS data were taken from Hales and Roberts (1970). The usual smoothing and differentiation of the  $T(\Delta)$  values were performed to obtain 36 values of  $\tau(p)$  between  $83^\circ$  and  $120^\circ$  (see Fig. 5). These values of  $\tau(p)$  were also assigned 0.3% relative standard errors.

The total data set described above consists of 188 values of  $\tau(p)$  for teleseismic distances ( $20^\circ$  to  $180^\circ$ ). In Section V we describe the results of the

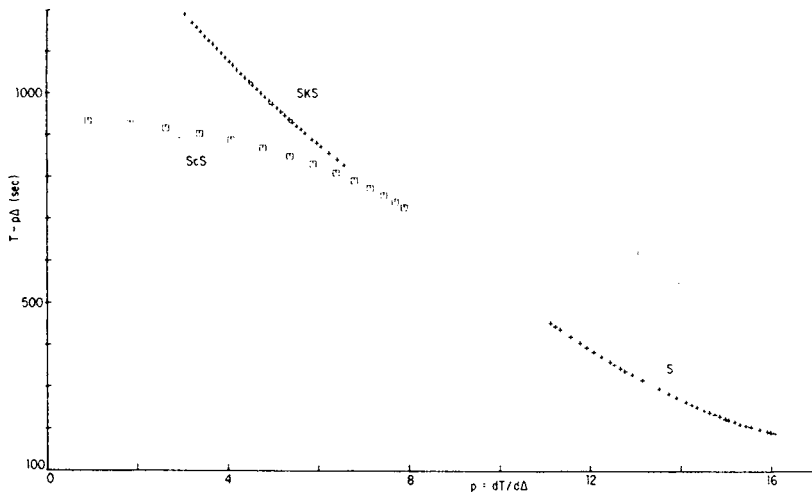


FIG. 5.  $\tau(p)$  for the teleseismic data S, ScS, SKS,  $p$  in sec/deg.

simultaneous inversion of the complete set of data and the application of the resolving power theory described in Section II,B to the final P and S velocity profiles.

#### IV. Numerical Methods

When dealing with a large data set, especially one that is highly redundant as are closely spaced travel time data when observational errors are included, it is important to have fast, efficient, and stable numerical techniques for determining the most linearly independent subset of the data to use in the inversion and resolving power calculations. This section briefly describes some of the numerical methods used in these calculations.

##### A. REPRESENTATION OF MODEL

The velocity profiles were represented by 167 spherical shells in each of which the velocity was assumed to vary as  $v(r) = ar^b$  where  $a$  and  $b$  are determined in the  $i$ th layer, for example, by the pair of equations

$$v(r_i) = a_i r_i^{b_i},$$

$$v(r_{i+1}) = a_i r_{i+1}^{b_i}.$$

In this case, the expressions for travel time  $T$  and angular distance  $\Delta$  for a particular seismic ray are then just sums over the number of layers traversed by the ray (see, for example, Julian and Anderson, 1968).

## B. INVERSION

Determining the diagonalizing transformation  $T$  of Section II,A is a standard problem in numerical analysis (Wilkinson, 1965). The matrix  $\mathcal{A}_{ij} = \sigma_i^{-1} A_{ij} \sigma_j^{-1}$  is first tridiagonalized by Householder's method. The eigenvalues of  $\mathcal{A}$  are equal to the eigenvalues of the tridiagonal matrix and are found by Sturm's bisection method. Wilkinson's method of iterative improvement is used to find the eigenvectors of the tridiagonal matrix and are transformed into the eigenvectors of  $\mathcal{A}$  by the tridiagonalization transformation.

The diagonalization process is very stable numerically and as pointed out in Section II,A it allows us to rank the transformed data according to standard error and to reject, if we wish, those transformed data with excessively large errors. Thus, instead of working with the full set of highly redundant data at each stage of the iterative inversion scheme, we only work with a subset of linear combinations of the original data which have acceptable errors. This results in a considerable saving of computer time.

## C. RESOLVING POWER

When we solve an  $N \times N$  system of equations such as (32), where the matrix  $\mathbf{Q}$  is symmetric, approximately  $\frac{1}{6}N^3$  operations are required (Forsythe and Moler, 1967). If we consider  $Z$  values of  $\theta$  on the tradeoff curve approximately  $\frac{1}{6}N^3Z$  operations will be required. In the diagonalization method just described, about  $\frac{4}{3}N^3$  operations are required. The ratio of these two is  $\frac{1}{8}Z$ . Thus, for  $Z > 8$ , the diagonalization method is more efficient.

We note that the matrix  $\mathbf{Q}$  in (32) does not depend on  $r_0$ , so that the diagonalization need be done only once for the whole resolving power calculation. This leads to an increase in efficiency of computing equal to the number of radii used in preparing the contoured inference maps discussed in Section V. The increase in efficiency is about 100-fold for the mantle teleseismic ray data.

## V. Results

### A. INVERSION

The starting model for the inversion of the data set, consisting of 188 values of  $\tau(p)$  described in Section III, is shown in Fig. 6. This model fits the Carder *et al.* (1966) P travel times to within 0.01 sec. Three applications of the

iterative procedure outlined in Section II,A produced the model shown in Fig. 7. The maximum absolute relative deviations and mean absolute relative deviations from the observed  $\tau(p)$  values are, respectively:

- (i) 0.6%, 0.15% for P,
- (ii) 0.12%, 0.03% for PcP,
- (iii) 0.29%, 0.26% for AB branch of PKP,
- (iv) 0.38%, 0.35% for GH branch of PKP,
- (v) 0.03%, 0.02% for DEF branch of PKP,
- (vi) 0.28%, 0.11% for S,
- (vii) 0.32%, 0.20% for ScS,
- (viii) 0.15%, 0.10% for SKS.

We see that most of the average deviations are well within the relative standard errors assigned to the data in Section III, the one exception being the GH branch of PKP.

The most significant differences between the initial and final models are the additional structure in the final model near  $r/R_e = 0.75$ , the higher P velocity in the core for the final model, and the higher S velocity in the deep mantle for the final model.

In Fig. 8 we show plots of the dimensionless quantity  $(-r/v) dv/dr$  for both the P and S velocity profiles of the final model. These were calculated by fitting the velocity profiles with a cubic spline function and then differentiating the spline fit. In particular, we will refer later to the regions of rapidly

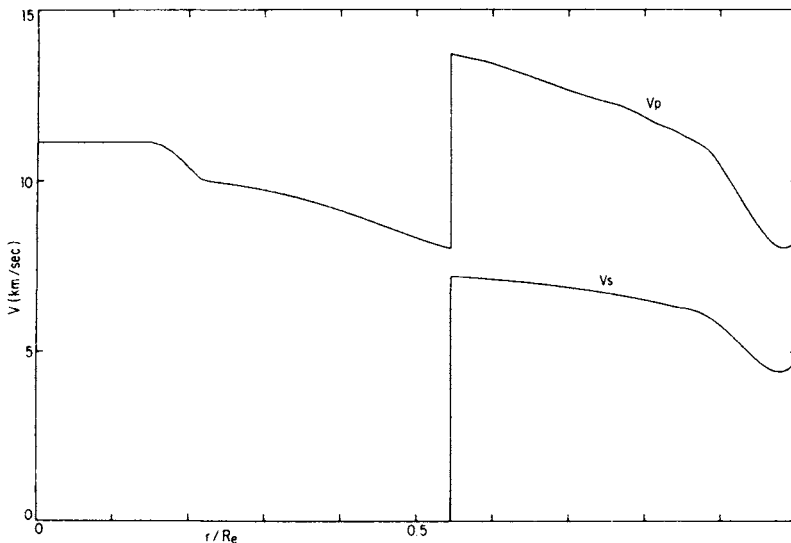


FIG. 6. The starting model for the inversion of the teleseismic data set.  $R_e$  = radius of the Earth.

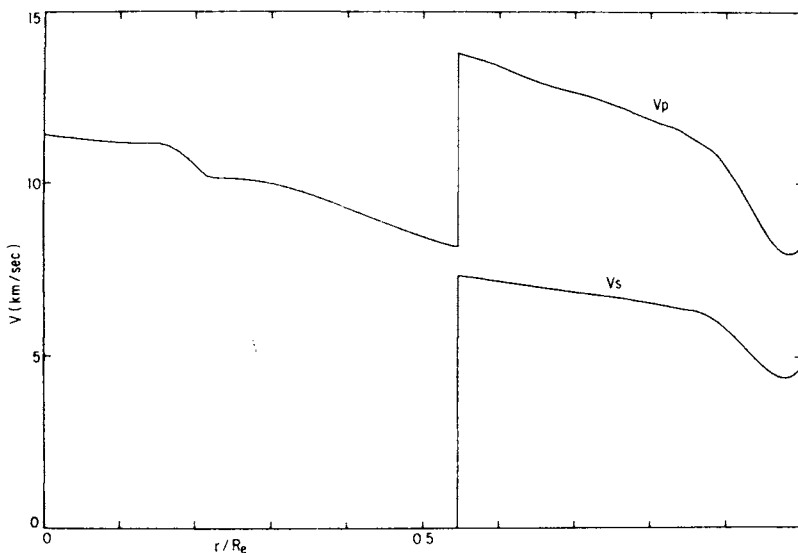


FIG. 7. The third iterate obtained from Fig. 6.  $R_e$  = radius of the Earth.

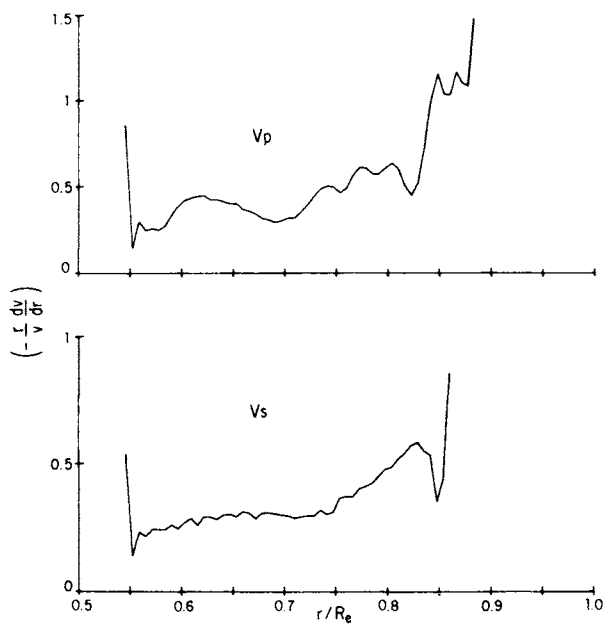


FIG. 8. Gradients of P and S velocities in the mantle.

changing velocity gradient near  $r/R_e = 0.64, 0.72, 0.76, 0.81, 0.85$ , and  $0.87$  for P corresponding to depths of 2293, 1784, 1529, 1210, 955, and 828 km, respectively; and near  $0.74, 0.79$ , plus the range 0.55 to 0.67 for S corresponding to depths of 1656, 1338, and 2867 to 2102 km.

The final model has a core radius of 3477.3 km which, as pointed out in Section I, is compatible with both the P, PcP and S, ScS data used in the inversion.

## B. RESOLVING POWER

We have done the resolving power calculations for the mantle and the core separately. In the calculations for the mantle we used only the P, PcP and S, ScS data, and in the calculations for the core we used only the PKP and SKS data. We feel this procedure is justified because the range of ray parameters covered by PKP and PcP overlaps to a great extent and so the PKP data is largely redundant for determining mantle P velocity structure. The same is true of the SKS and ScS ray parameters, so SKS is very redundant in determining mantle S velocity structure.

### 1. Mantle P Velocity (*Objective*)

Figure 9 shows the resolving power map for the mantle P velocity structure of the final model shown in Fig. 7. This shows the contours of spread or distance over which we have to average the model to achieve a desired level of relative error in velocity at any given radius. The contours of spread are given in fractions of an Earth radius. For example, the structural detail in the P velocity profile in the mantle between the core-mantle boundary and  $r/R_e = 0.9$  consists of 2% to 3% variations in velocity over distances of 100 to 200 km or greater. We wish to know whether these details are resolvable.

In order to resolve 2% to 3% detail we follow a horizontal line across Fig. 9 at the 1% level to see over how much distance we must average the velocity to achieve a 1% relative error in the value of the velocity at any given radius. As we see from the figure, between the core-mantle boundary and  $r/R_e = 0.9$ , the spreads range from 20 km near  $r/R_e = 0.78$  to 640 km near  $r/R_e = 0.9$ . The spread is large near  $r/R_e = 0.9$  because we only used P data from epicentral distances of  $30^\circ$  and larger, and these rays only begin to bottom at about 650 km for this model. The spreads are large immediately above the core-mantle boundary because only P data out to  $90^\circ$  were used and these rays bottom slightly above the core-mantle boundary at 3477 km.

In the rest of the mantle the spreads seem quite localized, alternating between regions of small and relatively larger spread. Upon closer examination we see that the regions of relatively large spread are closely correlated with

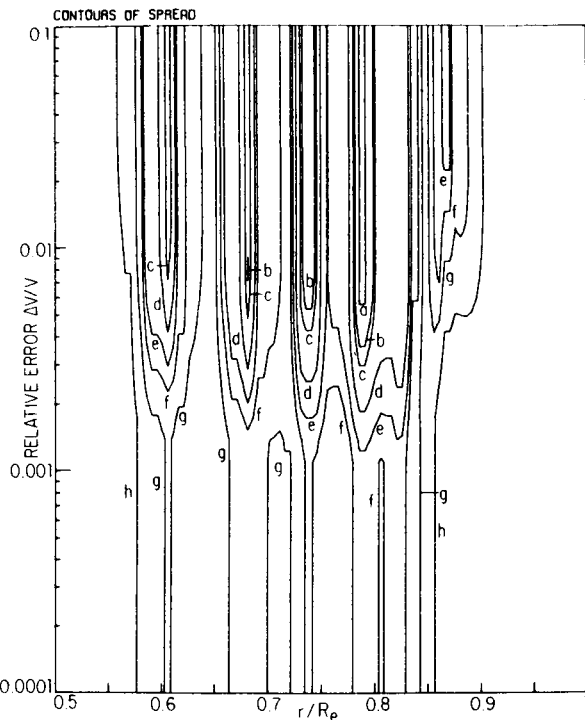


FIG. 9. Resolving power map for P velocity in the mantle. The contour levels of spread are in fractions of an Earth radius ( $R_e$ ) and are:  $a = 0.003$ ,  $b = 0.007$ ,  $c = 0.01$ ,  $d = 0.02$ ,  $e = 0.03$ ,  $f = 0.04$ ,  $g = 0.06$ ,  $h = 0.1$ .

the regions of rapidly changing velocity gradient mentioned above and that the regions of relatively small spread are correlated with regions in the model where the velocity gradient is not changing very rapidly.

Now, if we average our model with the spreads we obtain from Fig. 9 we see that in the regions of relatively small spread, i.e., spreads on the order of 20 to 100 km, we will not smear out the detail in the model, we say that it is resolvable, but in the regions of relatively large spread, i.e., spreads on the order of 180 to 360 km, we are likely to lose some detail in the final averaged model. Thus, our knowledge of the velocity is less precise in regions where the velocity gradient is changing rapidly and more precise in regions where the gradient is not changing very much.

## 2. Mantle P Velocity (Subjective)

Figure 10 is a contour map of prediction error for P velocity in the mantle. In Section II,B,2 we saw that this is the error we make in trying to predict the

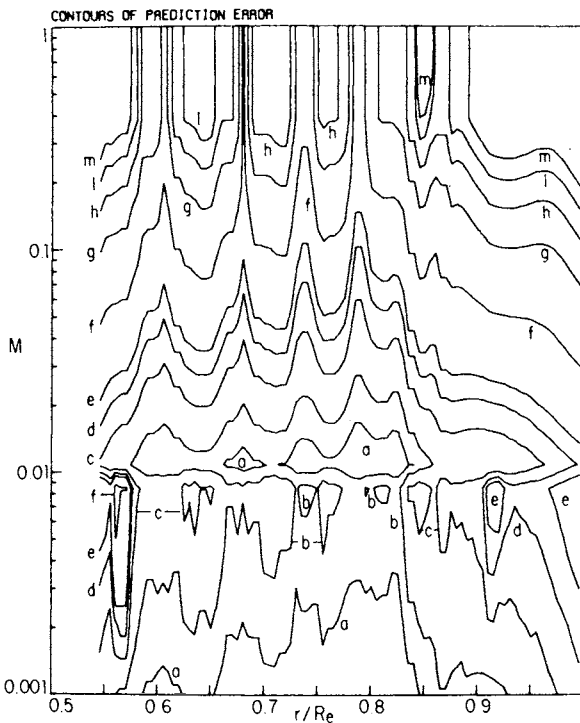


FIG. 10. Contours of relative prediction error for P velocity in the mantle as a function of the bound,  $M$ , on  $\|dm/dr\|$  and the radius,  $r_e$  = radius of the Earth and the contour levels are:  $a = 0.003$ ,  $b = 0.004$ ,  $c = 0.006$ ,  $d = 0.008$ ,  $e = 0.01$ ,  $f = 0.02$ ,  $g = 0.04$ ,  $h = 0.06$ ,  $i = 0.08$ ,  $m = 0.10$ .

value of the velocity for the real Earth  $v_E(r_0)$  at a particular  $r_0$ , given a particular set of measured data for the real Earth. The contours in Fig. 10 are contours of relative prediction error  $\varepsilon = \delta v(r)/v(r)$ .

As we saw in Section II,B,2, the prediction error is a function of our *a priori* bound,  $M$ , on  $\|dm/dr\|$  where  $m(r) = \ln[v(r)/v_E(r)]$ . Figure 10 thus presents an examination of the prediction error  $\varepsilon(M)$  for a range of values of  $M$ . Now, we must subjectively determine what we think is a geophysically reasonable value for  $M$ , and by following a horizontal line across Fig. 10 at this or any other value of  $M$  we can determine the relative prediction error in velocity as a function of radius.

We have, for the mantle only,

$$\frac{1}{12} \|dm/dr\|^2 = \frac{1}{12} \int_{r_e}^{R_e} \{d/dr \ln[v(r)/v_E(r)]\}^2 dr \quad (47)$$

(we include the factor  $\frac{1}{12}$  because we have included a factor of 12 in the numerical calculation of

$$\left\| H(r - r_0) - \int_0^r A(r - r_0) dr \right\|^2$$

in Eq. 44). As we mentioned in Section I, various models of the seismic velocity in the lower mantle, below 900 km, are very similar, i.e., they all agree to within a few percent. If we are willing to quantify this observation and hypothesize that the real Earth is also similar to these various models we can obtain an estimate for (47). Thus, if we hypothesize that a reasonable value for  $\ln[v(r)/v_E(r)] = 0.02$ , that such changes in velocity can occur over distances as small as 60 km, and normalize all length scales by  $R_e$  we have for (47)

$$\frac{1}{12} \|dm/dr\|^2 \leq (0.41)^2. \quad (48)$$

We believe that  $M = 0.41$  is a conservative value. If we are willing to be slightly less conservative, say  $\ln[v(r)/v_E(r)] = 0.01$  and let changes occur over distances of 100 km, we have

$$\frac{1}{12} \|dm/dr\|^2 \leq (0.12)^2, \quad (49)$$

i.e.,  $M = 0.12$ . As we saw in Section II,B,2, Eqs. (48) and (49) can be viewed as demands on the smoothness and overall size of  $m(r)$ . Thus, being less conservative in our value of  $M$  is equivalent to demanding a smoother  $m(r) = \ln[v(r)/v_E(r)]$ .

If we follow a horizontal line across Fig. 10 at  $M = 0.41$  we find relative prediction errors as a function of radius ranging from 2% to 10%. If we follow a horizontal line across at  $M = 0.12$  we have relative prediction errors between 0.9% and 4%, the average being about 2%. We see that we do a better job of prediction when we make more stringent *a priori* demands on the smoothness of what we are trying to predict. This is what we would intuitively expect. Note that we are free to consider any value of  $M$  in the range  $0 \leq M \leq \infty$ . However, extremely small values of  $M$  will be geophysically implausible and extremely large values of  $M$  will be too conservative resulting in large prediction errors and geophysically uninteresting results.

We also see that regions of relatively small and large prediction error are quite localized as a function of radius at a given value of  $M$ . In fact, the regions of relatively large prediction error, along a line of constant  $M$ , are precisely correlated with the regions of rapidly changing gradient in velocity mentioned above. Similarly, the areas of relatively small prediction error, along a line of constant  $M$ , are correlated with the regions where the velocity gradient is not changing very much. Again, this is an intuitively reasonable

result; that we should be able to predict the velocity better in regions where it is not changing rapidly.

Figures 9 and 10 present two different but compatible ways of examining how well we know the P velocity profile in the mantle given a particular set of data. We say compatible because a comparison of the two figures shows that the regions of small spread are exactly correlated with the regions of small prediction error and vice versa. This is obvious from Eq. (44) if we examine prediction error vs spread for a constant value of  $M$ .

### 3. Mantle S Velocity (Objective)

We see from Fig. 7 or from Fig. 8 that the S velocity profile in the mantle is much smoother with smaller scale structural detail than the P velocity profile. What detail there is consists of about 1% variations in velocity over distances of 300 km or greater. Figure 11 shows the resolving power map for the mantle S velocity profile. The spreads are large near the core-mantle boundary because we only used data out to epicentral distances of  $78^\circ$  and these rays do not bottom near the core-mantle boundary (see Fig. 5). Again, the spread

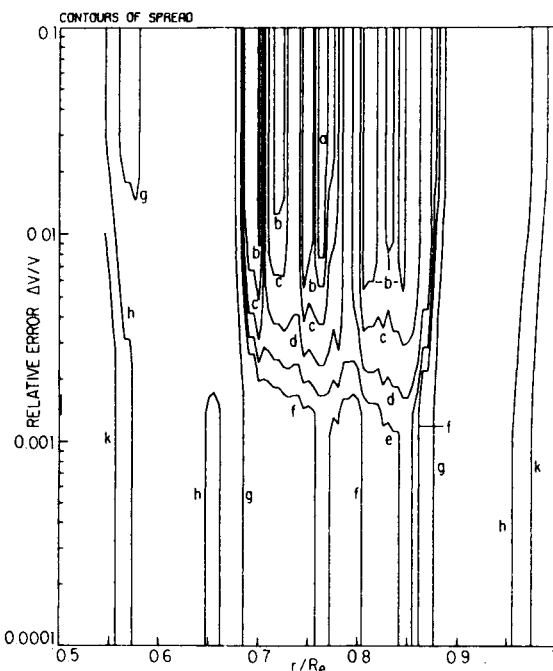


FIG. 11. The resolving power map for S velocity in the mantle. The contour levels of spread are in fractions of an Earth radius ( $R_e$ ) and are:  $a = 0.002$ ,  $b = 0.004$ ,  $c = 0.01$ ,  $d = 0.02$ ,  $e = 0.03$ ,  $f = 0.04$ ,  $g = 0.1$ ,  $h = 0.2$ ,  $k = 0.3$ .

is large near the surface because our data start at  $26^\circ$ . However, the S velocity in the mantle between  $r/R_e = 0.69$  and 0.87 is well determined at the 0.5% level, i.e., if we follow a horizontal line across Fig. 11 at a relative error level of 0.5% we see that the spreads, except near the core-mantle boundary, near the surface, and near  $r/R_e = 0.79$  are on the order of 50 to 130 km. Thus, if we average the S velocity profile with these spreads the detail mentioned above will not be lost.

We see, again, that the regions of relatively large and small spread are quite localized as a function of radius. The regions of relatively large spread are correlated with the regions of rapidly changing S velocity gradients mentioned above, while regions of relatively small spread are correlated with S velocity gradients which are not changing very much.

#### 4. Mantle S Velocity (Subjective)

Figure 12 is a contour map of prediction error for S velocity in the mantle. If we consider  $M = 0.12$ , a more reasonable value for the S velocity profile

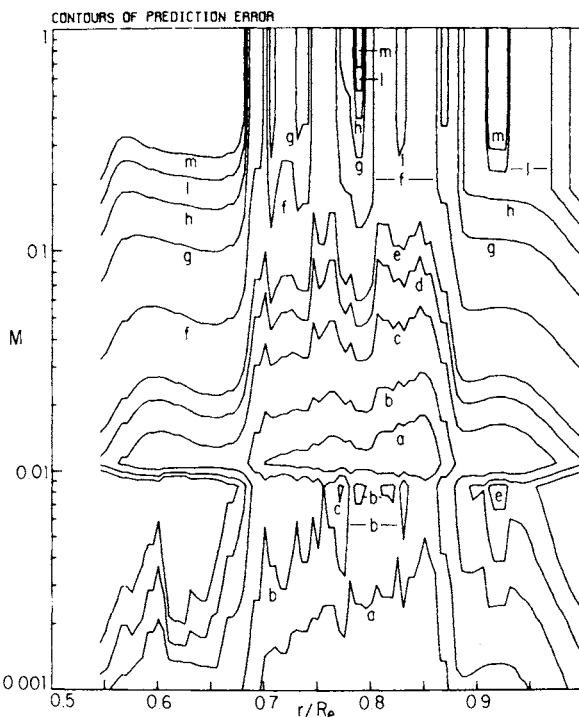


FIG. 12. Contours of relative prediction error for S velocity in the mantle as a function of the bound,  $M$ , on  $|dm/dr|$  and the radius. The contour levels are:  $a = 0.003$ ,  $b = 0.004$ ,  $c = 0.006$ ,  $d = 0.008$ ,  $e = 0.01$ ,  $f = 0.02$ ,  $g = 0.04$ ,  $h = 0.06$ ,  $l = 0.08$ ,  $m = 0.10$ .

than  $M = 0.41$ , we see that we have relative prediction errors as a function of radius from 1% to 5%, the average in the region where the S velocity is well determined being about 2%.

Regions of relatively poor prediction error are again correlated with the regions of rapidly changing S velocity gradient and with regions of relatively large spreads in the resolving power map for S. The correlations mentioned above are not quite as pronounced as was the case for P. This is because the structural detail in the S velocity profile is smaller and smoother than the detail in the P velocity profile.

Note that both the spread and prediction error contours for S are shifted up relative to the similar contours for P at the same values for relative error in velocity and  $M$ . This is due to the larger standard errors assigned to the S data.

### 5. Core (*Objective*)

We see from the plot of the final model (Fig. 7) that the P velocity in the core is very smooth, the main feature being the jump in velocity at the inner core boundary. Figure 13 shows a plot of  $(-r/v)dv/dr$  for the P velocity profile in the core. Other than the region around the inner core boundary, the only other regions of rapidly changing velocity gradient are in the vicinity of  $r/R_c = 0.27$  and  $0.53$ .

Figure 14 shows the resolving power map for the P velocity in the core. The contour levels are given in fractions of the core radius (3477 km). We see that the main features of the map are two broad regions of relatively small spread (above the 0.5% relative error level) on either side of a region of relatively large spread centered on the inner core boundary at  $r/R_c = 0.2$ . There is also a narrow region of relatively large spread centered on  $r/R_c = 0.27$ . The spreads are large near the core mantle boundary because the PKP and

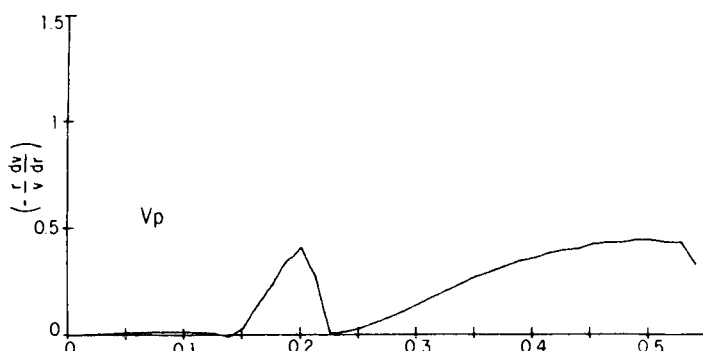


FIG. 13. Gradient of P velocity in the core.

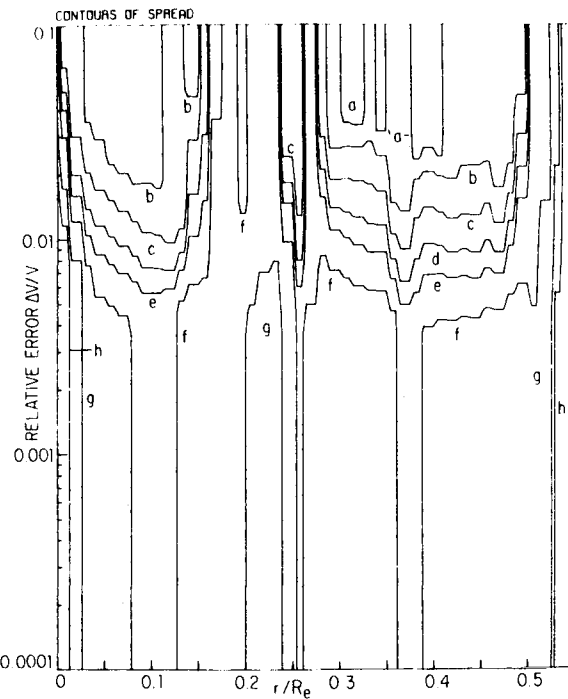


FIG. 14. The resolving power map for P velocity in the core. The contour levels of spread are in fractions of the core radius (3477 km) and are:  $a = 0.002$ ,  $b = 0.006$ ,  $c = 0.02$ ,  $d = 0.04$ ,  $e = 0.06$ ,  $f = 0.10$ ,  $g = 0.20$ ,  $h = 0.30$ .

SKS data do not have turning points in this region of the core. Again, we see that the regions of rapidly changing velocity gradient, i.e.,  $r/R_e = 0.20, 0.27$ , and  $0.53$  are associated with the regions of relatively large spread, while the two broad regions of relatively small spread correlate with regions where the velocity gradient is not changing very rapidly.

#### 6. Core (*Subjective*)

Figure 15 shows the contour map of prediction error for P velocity in the core. As usual, the regions of relatively large prediction error are localized in the regions of rapidly changing velocity gradient.

The values of  $M$  for the core, corresponding to  $\ln[v(r)/v_E(r)] = 0.02$  with velocity changes occurring over distances on the order of 60 km, and to  $\ln[v(r)/v_E(r)] = 0.01$  with velocity changes occurring over distances on the

order of 100 km, are 0.33 and 0.10, respectively. If we follow horizontal lines across Fig. 15 at these values of  $M$  we see that for  $M = 0.33$  we have an average prediction error of about 3% in the broad regions of relatively small prediction error and an average prediction error of about 10% in the localized regions of relatively large prediction error. For  $M = 0.1$  the figures are about 2% in the regions of small prediction error and about 4% in the localized regions of large prediction error.

The values of radii at which the velocity was specified were more coarsely spaced in the core than in the mantle. This accounts for the more "steplike" appearance of the contours in the figures for the core compared to the figures for the mantle.

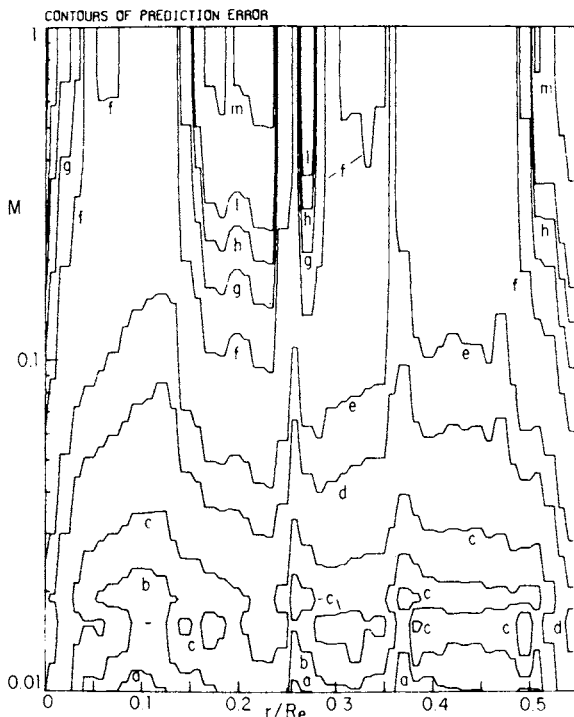


FIG. 15. Contours of relative prediction error for P velocity in the core as a function of the bound,  $M$ , on  $\|dm/dr\|$  and the radius. The contour levels are:  $a = 0.007$ ,  $b = 0.008$ ,  $c = 0.01$ ,  $d = 0.015$ ,  $e = 0.02$ ,  $f = 0.04$ ,  $g = 0.06$ ,  $h = 0.08$ ,  $i = 0.10$ ,  $m = 0.20$ .

Finally, we emphasize that all the inversion and resolving power calculations are pertinent to the real Earth *only* if the real Earth is linearly close, in the sense in which we have linearized the problem, to our final model. This is an assumption that we must make in order to make the nonlinear travel

time problem tractable. However, if this assumption is correct, then Backus and Gilbert (1968, 1970) prove that the real Earth will have the same linear averages as the averages of our final model. It is these average properties that are of interest to the geophysicist.

## REFERENCES

- BACKUS, G. (1970a). *Proc. Nat. Acad. Sci.* **65**, 1.
- BACKUS, G. (1970b). *Proc. Nat. Acad. Sci. U.S.* **65**, 281.
- BACKUS, G. (1970c). *Proc. Nat. Acad. Sci. U.S.* **67**, 282.
- BACKUS, G., and GILBERT, F. (1967). *Geophys. J. Roy. Astron. Soc.* **13**, 247.
- BACKUS, G., and GILBERT, F. (1968). *Geophys. J. Roy. Astron. Soc.* **16**, 169.
- BACKUS, G., and GILBERT, F. (1969). *Bull. Seismol. Soc. Amer.* **59**, 1407.
- BACKUS, G., and GILBERT, F. (1970). *Phil. Trans. Roy. Soc. London, Ser. A* **266**, 123.
- BOLT, B. (1968). *Bull. Seismol. Soc. Amer.* **58**, 1305.
- BRUNE, J. N. (1964). *Bull. Seismol. Soc. Amer.* **54**, 2099.
- BULLEN, K. E. (1963). "Introduction to the Theory of Seismology." Cambridge Univ. Press, London and New York.
- CARDER, D. S., GORDON, D. W., and JORDAN, J. N. (1966). *Bull. Seismol. Soc. Amer.* **56**, 815.
- DORMAN, J., EWING, M., and OLIVER, J. (1960). *Bull. Seismol. Soc. Amer.* **50**, 87.
- DUNFORD, N., and SCHWARTZ, J. T. (1958). "Linear Operators," Part I. Wiley (Interscience), New York.
- FORSYTHE, G., and MOLER, C. (1967). "Computer Solution of Linear Algebraic Systems." Prentice-Hall, Englewood Cliffs, New Jersey.
- GERVER, M. L., and MARKUSHEVICH, V. M. (1966). *Geophys. J. Roy. Astron. Soc.* **11**, 165.
- GERVER, M. L., and MARKUSHEVICH, V. M. (1967). *Geophys. J. Roy. Astron. Soc.* **13**, 241.
- GILBERT, F. (1971). *Geophys. J. Roy. Astron. Soc.* **23**, 125.
- GUTENBERG, B. (1915). *Veroeff. Zentral. Bur. Int. Seismol. Ass.*, Strassburg.
- HALES, A. L., and ROBERTS, J. L. (1970). *Bull. Seismol. Soc. Amer.* **60**, 461.
- HERGLOTZ, G. (1907). *Phys. Z.* **8**, 145.
- HERRIN, E., TUCKER, W., TAGGART, J. N., GORDON, D. W., and LOBDELL, J. L. (1968). *Bull. Seismol. Soc. Amer.* **58**, 1273.
- JEFFREYS, H. (1939). *Mon. Not. Roy. Astron. Soc., Geophys. Suppl.* **4**, 498.
- JEFFREYS, H. (1962). "The Earth," 4th ed. Cambridge Univ. Press, London and New York.
- JEFFREYS, H., and BULLEN, K. E. (1958). "Seismological Tables." Brit. Ass. Advan. Sci., London.
- JOHNSON, L. R. (1969). *Bull. Seismol. Soc. Amer.* **59**, 973.
- JULIAN, B. R., and ANDERSON, D. L. (1968). *Bull. Seismol. Soc. Amer.* **58**, 339.
- MOHOROVICIĆ, A. (1909). *Jahrb. Meteorol. Obs. Zagreb* **9**, 1.
- OLDHAM, R. D. (1900). *Phil. Trans. Roy. Soc. London, Ser. A* **194**, 135.
- OLDHAM, R. D. (1906). *Quart. J. Geol. Soc. London* **62**, 456.
- RANDALL, M. J. (1971). *Geophys. J. Roy. Astron. Soc.* **22**, 229.
- RICHARDS, P. G. (1970). Ph.D. Thesis, California Institute of Technology, Pasadena.
- TAGGART, J. N., and ENGAHL, E. R. (1968). *Bull. Seismol. Soc. Amer.* **58**, 1293.
- WIECHERT, E. (1910). *Phys. Z.* **11**, 294.
- WILKINSON, J. H. (1965). "The Algebraic Eigenvalue Problem." Oxford Univ. Press, London and New York.
- ZÖPPRITZ, K. (1907). *Nachr. Kgl. Ges. Wiss. Goettingen, Math.-Phys. Kl.* p. 529.

# Multipolar Analysis of the Mechanisms of Deep-Focus Earthquakes

M. J. RANDALL

GEOPHYSICS DIVISION

DEPARTMENT OF SCIENTIFIC AND INDUSTRIAL RESEARCH  
WELLINGTON, NEW ZEALAND

I. Introduction . . . . .	267
II. Integral Theory for Seismic Sources . . . . .	269
A. Potentials of Waves from an Initial Displacement . . . . .	269
B. Static Multipole Theory . . . . .	273
C. A General Dislocation Source . . . . .	276
D. Sources with Volume Change . . . . .	278
III. The Measurement of Displacement Impulse . . . . .	280
A. Effects of the Instrument and of Attenuation . . . . .	280
B. Effects of Crustal Structure and Wave Spreading . . . . .	283
IV. Estimation of Multipolar Coefficients . . . . .	285
A. Least-Squares Estimations . . . . .	285
B. Statistical Model of the Smoothing . . . . .	287
V. Multipolar Analysis in Practice . . . . .	288
A. Reduction to Values on the Focal Sphere . . . . .	288
B. Applications of the Method . . . . .	292
References . . . . .	298

## I. Introduction

THIS CHAPTER WILL DEAL with the theory of an observational technique for studying earthquake mechanism. The technique, which makes use of amplitude information rather than just the direction of initial motion, grew from a need to discriminate between two possible source mechanisms: the classical dislocation source on the one hand, and a phase transition model that has featured in recent speculations on the other.

The prevailing hypothesis is that tectonic earthquakes are caused by elastic rebound of the earth when movement suddenly becomes possible on a geologic fault which is subject to a regional shear stress. This view gained prominence when put forward by Reid (1910) to explain the large shallow earthquake of San Francisco in 1906. When deep earthquakes occurred and no obvious dissimilarity in seismograms was found, which might indicate a difference in mechanism, Reid's hypothesis came to be accepted for deep

earthquakes also. More recently, the tacit assumption of the fault hypothesis that sudden movement is possible on faults at significant depths began to be questioned. Orowan (1960) argued that frictional stresses would preclude sudden faulting, at least as usually conceived, at depths of more than a few kilometers. Griggs and Handin (1960), in considering forms of instability which could occur at high pressures and temperatures, called attention to Bridgman's (1937) "snapping" phenomenon and suggested that it could well have a mechanism related to that of deep-focus earthquakes. An explanation in terms of shear melting instabilities was attempted, and has since been refined (Griggs and Baker, 1969).

Evison (1963), after reviewing the known relationships between earthquakes and faults, made the controversial suggestion that faulting is but a gross form of earthquake damage restricted to the vicinity of the earth's surface, which is, as he pointed out, a geometrically singular part of the earth. He further suggested that the cause of earthquakes lies rather in the phenomenon of metastable phase transition. The importance of solid-solid phase transitions in geophysics was first recognized by Bridgman (1945); precise applications had to await the development of higher pressure techniques. Ringwood, in a series of papers since 1956 (see Ringwood, 1966, for a complete review), advanced a mineralogical model of the upper mantle in which solid-solid phase transitions play an integral role in both the steady state structure and tectonic activity. Ringwood (1967) has speculated that the occurrence of a pyroxene-garnet transformation in a sinking block of eclogite, which he argues might possibly proceed very quickly through a large volume, could provide a mechanism for some deep-focus earthquakes. Also suggested as a possible mechanism for deep and intermediate shocks is the inversion of rhombic to monoclinic enstatite; Riecker and Rooney (1966) found that this transition, while ordinarily quite slow, is very much accelerated in the presence of shear stress. Theoretical investigations (Randall, 1964a,b, 1966) have shown that sudden phase transition can provide a source with higher energy density than faulting, and even of quadrantal radiation patterns if the transformation involves a change of shape.

There are several excellent reviews of earthquake mechanism studies, among them those of Kawasumi (1937), Honda (1962), and Stauder (1962). Kawasumi's paper is particularly germane to the present work, drawing an illuminating picture of the breadth of early Japanese work, especially the lively era of the thirties when the relative merits of quadrantal and conical radiation patterns were contested. Kawasumi himself was a pioneer in the use of amplitude data to augment the observations of the direction of first motion (Kawasumi, 1933). He also made an early contribution to the concept of seismic waves arising from the potential energy of initial strain from a position of final equilibrium (Kawasumi and Yosiyama, 1935). Honda and Stauder, in their contemporary reviews, view the subject from different

standpoints and their papers, exhibiting complementary insights, together form as complete a study as could be desired. It would therefore be gratuitous to attempt here to go over any of the same ground.

Perhaps because the fault hypothesis has gone so long unchallenged, studies of focal mechanism have occupied themselves in the main with the determination from the seismological data of the parameters of an assumed fault source—its orientation and extent, and the magnitude and speed of propagation of its dislocation. Although such studies have amassed a formidable array of evidence which is consistent with a fault hypothesis, they do not entirely dispel the doubt that other theories may fit the data as well. Without an observational criterion, however, the phase transition hypothesis remains scarcely more than idle speculation; the development of a numerical criterion which might discriminate between these hypotheses has been the underlying aim of the work to be discussed. In addition, measures of the source of seismic radiation which are as free as possible of assumptions as to the mechanical nature of the source have been sought.

The method of multipolar analysis of earthquake mechanisms has developed around three separate nuclei, the three aspects combining to yield a powerful technique in its area of application. The first point of nucleation is a set of theoretical relationships between certain characteristics of seismic sources and the *impulse* (or time integral) of ground displacement. The foundation for this work is the theoretical study of Randall (1964a, 1971b). Second, there are certain properties of the typical long-period seismograph and the medium of propagation of seismic waves which allow the estimation of the impulse of ground displacement from the amplitudes of body-wave pulses recorded from deep earthquakes. Third, there are the techniques of estimation of the multipolar nature of the seismic radiation using the estimates of displacement impulse at various directions about the focus.

The method, when compared with the classical first motion analysis, has both advantages and drawbacks. The principal advantage (apart from its not assuming a quadrantal radiation pattern *a priori*) lies in its use of amplitude information, which allows more precise location of nodal surfaces. The main drawback is caused by shortcomings of dynamic range, which restrict the applicability of the method. Earthquakes that are too large overload the closer instruments, while the smaller earthquakes have their more distant signals lost in noise.

## II. Integral Theory for Seismic Sources

### A. POTENTIALS OF WAVES FROM AN INITIAL DISPLACEMENT

A basic assumption implicit in most studies of earthquake mechanism is that (apart from the distortion due to the radial inhomogeneity of the mantle)

the pattern of radiation from a source is the same as if it were situated in an infinite uniform elastic solid. Associated with this assumption is the concept of the *focal sphere*, on which one visualizes the far-field radiation pattern from the source in the infinite medium, while simultaneously thinking of it as shrunk about the source in the real earth, with observations being traced back to it along the ray paths and corrected for the effects of propagation. In this way it becomes possible to make comparisons on the focal sphere between theoretical radiation patterns and estimates derived from observations. The validity of this approach weakens as the earthquakes concerned become shallower. In practice, once the direct pulse and that reflected from the earth's surface cannot be resolved, one should incorporate the surface into the theoretical model and make comparisons on a focal *hemisphere*.

Figure 1 defines some of the parameters to be used to describe the geometry of the problem. A wave pulse from the source  $H$  is observed at  $O$ , a

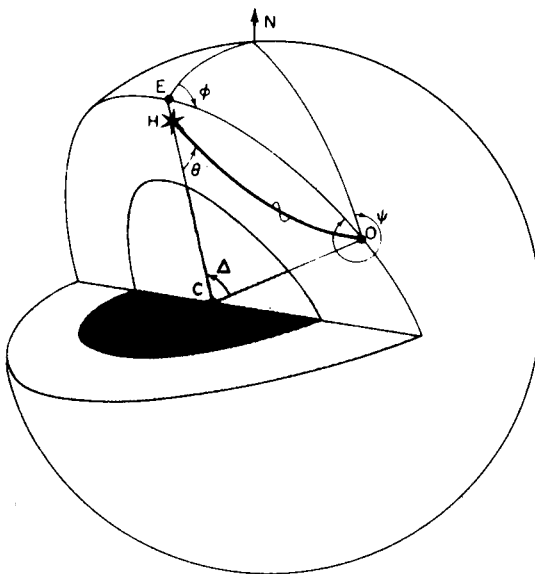


FIG. 1. Geometry of the radiation angles.

point whose position relative to the epicenter  $E$  is described by the geocentric distance  $\Delta$  and the azimuth  $\phi$ . The wave at  $O$  arrives from the direction  $\psi$ . It left the source in a direction described by the polar coordinates  $\theta$  and  $\phi$ . Figure 2 shows the corresponding point  $P$  on the focal sphere. To observations variously scattered over the earth's surface there corresponds a set of corresponding points such as  $P$  on the focal sphere.

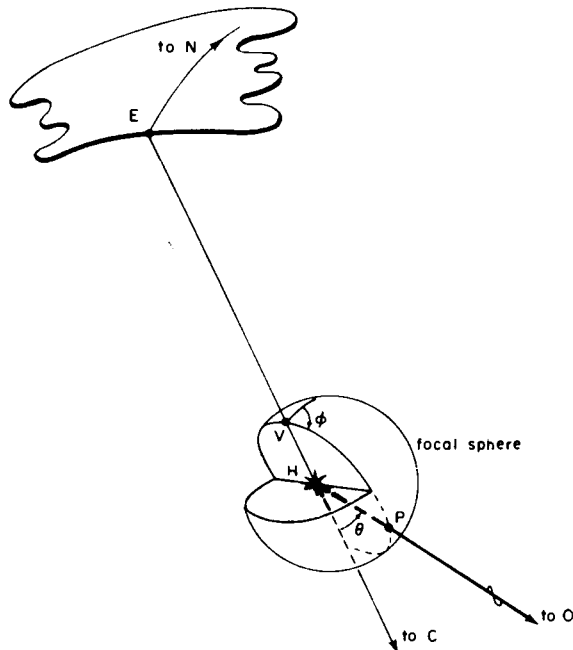


FIG. 2. The focal sphere.

In the following discussion it will be assumed that the source has been removed from the real earth to an infinite uniform elastic solid. In this situation the motions are governed by the elastic wave equation:

$$\alpha^2 \nabla \nabla \cdot \mathbf{u} - \beta^2 \nabla \times \nabla \times \mathbf{u} - \partial^2 \mathbf{u} / \partial t^2 = 0, \quad (1)$$

where  $\alpha$ ,  $\beta$  are the P- and S-wave velocities and  $\mathbf{u}$  is the displacement field measured from the final equilibrium.  $\mathbf{u}$  may be taken to be continuous, except possibly on a finite fault surface  $f$ , across which it has a discontinuity  $[\mathbf{u}]$ . In these circumstances one can express the displacement field  $\mathbf{u}$  in terms of scalar and vector potentials  $V$  and  $\mathbf{A}$ :

$$\mathbf{u} = \nabla V + \nabla \times \mathbf{A} \quad (\nabla \cdot \mathbf{A} = 0), \quad (2)$$

where

$$4\pi V = - \int_{\infty} r^{-1} \nabla \cdot \mathbf{u} d\tau - \int_f r^{-1} \mathbf{n} \cdot [\mathbf{u}] dS, \quad (3)$$

$$4\pi\mathbf{A} = \int_{\infty} r^{-1} \nabla \times \mathbf{u} d\tau + \int_f r^{-1} \mathbf{n} \times [\mathbf{u}] dS. \quad (4)$$

Here  $V$  and  $\mathbf{A}$  take on the form of potentials whose volume densities are  $\nabla \cdot \mathbf{u}$  and  $\nabla \times \mathbf{u}$  respectively. At the surface of discontinuity these derivatives degenerate to  $\mathbf{n} \cdot [\mathbf{u}]$  and  $\mathbf{n} \times [\mathbf{u}]$ , where  $\mathbf{n}$  is the unit normal to  $f$ .

The potentials are governed by classical wave equations

$$\alpha^2 \nabla^2 V - \partial^2 V / \partial t^2 = 0 \quad (5)$$

and

$$\beta^2 \nabla^2 \mathbf{A} - \partial^2 \mathbf{A} / \partial t^2 = 0. \quad (6)$$

In solving these equations, most writers take a Kirchoff approach in terms of delayed functions in which  $V(t)$  is replaced by  $V(t - r/\alpha)$  and  $\mathbf{A}(t)$  by  $\mathbf{A}(t - r/\beta)$ . For the present purpose it is better to take the Poisson approach, which uses the properties of spherical means. Details of the argument were given by Randall (1964a); it is sufficient here to note the solutions:

$$4\pi V(P, t) = - \int_{B_1} r^{-1} \nabla \cdot \mathbf{u}_0 d\tau - \int_{f_1} r^{-1} \mathbf{n} \cdot [\mathbf{u}_0] dS, \quad (7)$$

$$4\pi \mathbf{A}(P, t) = \int_{B_2} r^{-1} \nabla \times \mathbf{u}_0 d\tau + \int_{f_2} r^{-1} \mathbf{n} \times [\mathbf{u}_0] dS, \quad (8)$$

where  $B_1$  is the exterior of the sphere of radius  $\alpha t$  centered on  $P$ ;  $B_2$  is the exterior of the sphere of radius  $\beta t$  centered on  $P$ ;  $f_1$  is that part of  $f$  included in the region  $B_1$ ;  $f_2$  is that part of  $f$  included in the region  $B_2$ ; and  $\mathbf{u}_0$  is the initial displacement field. It is of some interest to compare this solution of the initial value problem with the instantaneous potential representations (3) and (4). For the P-wave potential  $V$ ,  $B_1$  is the exterior of the "sphere of influence." Sources which at zero time influenced the potential at  $P$ , and which lie within  $B_1$  and hence beyond the "sphere of influence," still contribute to the potential at time  $t$ . It is clear from the comparison that the potentials are, at  $t = 0$ , those of  $\mathbf{u}_0$ , and that they eventually vanish. More than this, however, may be deduced. Because  $\nabla \cdot \mathbf{u}_0$  and  $\nabla \times \mathbf{u}_0$  are harmonic functions outside some source region, it is possible to show (Randall, 1964a) that until  $t = R_1/\alpha$  (where  $R_1$  is the distance from the observer to the closest point of the source)

$$V(t) = \frac{1}{2} \alpha^2 t^2 \nabla \cdot \mathbf{u}_0 + V(0), \quad (9)$$

and until  $t = R_1/\beta$

$$\mathbf{A}(t) = -\frac{1}{2}\beta^2 t^2 \nabla \times \mathbf{u}_0 + \mathbf{A}(0). \quad (10)$$

Hence, until the first wave arrives,

$$\begin{aligned} \mathbf{u}(t) &= \mathbf{u}_0 + \frac{1}{2}t^2[\alpha^2 \nabla \nabla \cdot \mathbf{u}_0 - \beta^2 \nabla \times \nabla \times \mathbf{u}_0], \\ &= \mathbf{u}_0. \end{aligned}$$

Furthermore, if  $R_2$  is the distance of the observer to the farthest part of the source, it can be demonstrated, again because of the harmonicity of  $\nabla \cdot \mathbf{u}_0$  and  $\nabla \times \mathbf{u}_0$  outside the source, that after  $t = R_2/\alpha$ ,  $V(t)$  is zero, and after  $t = R_2/\beta$ ,  $\mathbf{A}(t)$  is zero. Thus, the displacement wave is confined to the interval between the times of arrival of the P-wave from the closest point of the source and the S-wave from the farthest point. In this interval a permanent displacement occurs which corresponds to the difference in equilibrium configurations associated with the mechanism.

While the displacement field falls from  $\mathbf{u}_0$  to zero, the change in potentials is more involved. Just as the first P-wave is arriving

$$V = V(0) + \frac{1}{2}r^2 \nabla \cdot \mathbf{u}_0, \quad (11)$$

and as the first S-wave is arriving

$$\mathbf{A} = \mathbf{A}(0) - \frac{1}{2}r^2 \nabla \times \mathbf{u}_0. \quad (12)$$

Later it will be shown that certain relationships exist for static displacement fields, and that for the case of most interest

$$V(0) = -\frac{1}{6}r^2 \nabla \cdot \mathbf{u}_0, \quad (13)$$

$$\mathbf{A}(0) = \frac{1}{6}r^2 \nabla \times \mathbf{u}_0. \quad (14)$$

Thus, in the interval between the arrival of the first and last P-waves the scalar potential drops from  $\frac{1}{2}r^2 \nabla \cdot \mathbf{u}_0$  to zero. For S-waves the vector potential changes from  $-\frac{1}{2}r^2 \nabla \times \mathbf{u}_0$  to zero in the corresponding interval.

## B. STATIC MULTPOLE THEORY

Outside the source region, the initial displacement field in an infinite, perfectly elastic, homogeneous solid obeys the elastostatic equation

$$\alpha^2 \nabla \nabla \cdot \mathbf{u}_0 - \beta^2 \nabla \times \nabla \times \mathbf{u}_0 = 0, \quad (15)$$

where  $\alpha$  and  $\beta$  are the P and S-wave velocities. Taking the divergence and curl, we find that  $\nabla \cdot \mathbf{u}_0$  and  $\nabla \times \mathbf{u}_0$  are scalar and vector harmonic functions, respectively. An expansion of these functions in terms of scalar and vector spherical harmonics is therefore possible. Corresponding to the scalar harmonic

$$X_{nm} = e^{im\phi} P_n^m (\cos \theta),$$

there are three forms of vector harmonic (Morse and Feshbach, 1953),

$$\mathbf{P}_{nm} = \mathbf{a}_r X_{nm},$$

( $\mathbf{a}_r$  being a radial unit vector),

$$\mathbf{B}_{nm} = r \nabla X_{nm},$$

and

$$\mathbf{C}_{nm} = \nabla \times (r \mathbf{a}_r X_{nm}).$$

$\mathbf{P}_{nm}$  is a radial vector and  $\mathbf{B}_{nm}$  and  $\mathbf{C}_{nm}$  are transverse and mutually orthogonal, and satisfy the relations

$$\mathbf{B}_{nm} = \mathbf{a}_r \times \mathbf{C}_{nm}, \quad (16)$$

$$\mathbf{C}_{nm} = -\mathbf{a}_r \times \mathbf{B}_{nm}. \quad (17)$$

Relationships among the derivatives of the vector functions which will be found useful include:

$$\begin{aligned} \nabla(r^p X_{nm}) &= r^{p-1}(p \mathbf{P}_{nm} + \mathbf{B}_{nm}), \\ \nabla \cdot (r^p \mathbf{P}_{nm}) &= (p+2)r^{p-1} X_{nm}, \\ \nabla \cdot (r^p \mathbf{B}_{nm}) &= -n(n+1)r^{p-1} X_{nm}, \\ \nabla \cdot (r^p \mathbf{C}_{nm}) &= 0, \\ \nabla \times (r^p \mathbf{P}_{nm}) &= r^{p-1} \mathbf{C}_{nm}, \\ \nabla \times (r^p \mathbf{B}_{nm}) &= -(p+1)r^{p-1} \mathbf{C}_{nm}, \\ \nabla \times (r^p \mathbf{C}_{nm}) &= n(n+1)r^{p-1} \mathbf{P}_{nm} + (p+1)r^{p-1} \mathbf{B}_{nm}, \\ \nabla^2(r^p X_{nm}) &= [p(p+1) - n(n+1)]r^{p-2} X_{nm}, \end{aligned} \quad (18)$$

where  $p$  is an arbitrary integer.

Consider an individual multipole field in which

$$\nabla \cdot \mathbf{u}_0 = Kr^{-n-1} X_{nm}. \quad (19)$$

Then, since  $\nabla V \cdot \mathbf{u}_0$  (and hence  $\nabla \times \nabla \times \mathbf{u}_0$ ) involves the vector harmonic of type **B**,  $\nabla \times \mathbf{u}_0$  involves that of type **C**:

$$\nabla \times \mathbf{u}_0 = Lr^{-n-1} \mathbf{C}_{nm}. \quad (20)$$

The elastostatic equation (15) requires that the ratio  $K:L$  be  $-n\beta^2/\alpha^2$ . Moreover, the potentials  $V_0$  and  $\mathbf{A}_0$  of the initial displacement field, where

$$\mathbf{u}_0 = \nabla V_0 + \nabla \times \mathbf{A}_0,$$

are

$$V_0 = -\frac{K}{2(2n-1)} r^{-n+1} X_{nm}, \quad (21)$$

$$\mathbf{A}_0 = \frac{L}{2(2n-1)} r^{-n+1} \mathbf{C}_{nm}. \quad (22)$$

Once an expansion for  $\nabla \cdot \mathbf{u}_0$  is determined, the expansions for  $\nabla \times \mathbf{u}_0$ ,  $V_0$ , and  $\mathbf{A}_0$  may be written by inspection using these relationships.

The multipoles of degree zero correspond to a permanent change of volume in the source region; those of the first degree correspond to net forces or torques at the source (which are therefore absent in the radiation from equilibrium sources), and those of the second degree to strain at the source. We shall therefore be concerned mostly with the zero- and second-degree multipoles. The multipole of degree zero requires separate treatment because both  $\nabla \cdot \mathbf{u}_0$  and  $\nabla \times \mathbf{u}_0$  are zero outside the source (Randall, 1964b). For present purposes the second-degree multipole is of most interest; in this case Eqs. (19) and (21) and (20) and (22) yield the expressions (13) and (14) quoted above.

Anticipate, for the moment, the result that the *impulse*,  $I$ , of ground displacement,  $I = \int u dt$ , can be measured in terms of the amplitude of the pulse usually observed on long-period instruments. Now  $I$  is related to the change in potential, as follows. In the case of the P-wave, the potential has the form

$$V = r^{-1} f(r - \alpha t),$$

where  $f$  is a steplike function, slowly varying except in the interval  $t_1$  to  $t_2$  when it changes by  $\Delta V$ , say. Then the (longitudinal) P-wave displacement is of the form

$$u_p = r^{-1}f'(r - \alpha t) + O(r^{-2})$$

so that

$$\begin{aligned} I &= \int_{t_1}^{t_2} u_p dt \\ &= -(1/\alpha)r^{-1}[f(r - \alpha t)]_{t_1}^{t_2} + O(r^{-2}), \end{aligned}$$

i.e.,

$$I = -\Delta V/\alpha + O(r^{-2}). \quad (23)$$

For second-degree multipolar sources  $\Delta V = -\frac{1}{2}r^2\nabla \cdot \mathbf{u}_0$ , so that

$$I = \frac{1}{2}r^2\nabla \cdot \mathbf{u}_0/\alpha. \quad (24)$$

Thus we have a relationship between the observable  $I$  and an easily derived parameter of any proposed mechanism—the divergence of the static displacement field.

### C. A GENERAL DISLOCATION SOURCE

As an example, consider a general dislocation that involves a varying discontinuity in displacement  $[\mathbf{u}]$  across the surface  $f$  with normal  $\mathbf{n}$ .

Randall (1966) derives the static field for such a dislocation in the form

$$4\pi\mathbf{u}_0(P) = \int_f [\mathbf{u}(Q)] \cdot \mathbf{T}\{\mathcal{L}(P, Q)\} dS_Q, \quad (25)$$

where  $\mathcal{L}$  is the Somigliana tensor defined in Cartesian notion by

$$\mathcal{L}_{ij} = r^{-1} \delta_{ij} - \frac{\alpha^2 - \beta^2}{2\alpha^2} r_{,ij} \quad (26)$$

( $r$  is the distance  $|PQ|$ ,  $\delta_{ij}$  is the Kronecker delta, subscripts following the comma denote Cartesian derivatives with respect to the point Q).

The operator  $\mathbf{T}$  is related to the traction across the surface divided by the modulus of rigidity, and is defined by

$$\mathbf{T}\{\mathbf{u}\} = \mathbf{n} \frac{\alpha^2 - 2\beta^2}{\beta^2} \nabla \cdot \mathbf{u} + 2(\mathbf{n} \cdot \nabla)\mathbf{u} + \mathbf{n} \times \nabla \times \mathbf{u}. \quad (27)$$

Then, in Cartesian notation,

$$4\pi u_{0i} = \int_f \left\{ \frac{\alpha^2 - 2\beta^2}{\alpha^2} n_j[u_j] r_{,1}^{-1} + n_i r_{,j}^{-1}[u_j] + [u_i] n_k r_{,k}^{-1} - \frac{\alpha^2 - \beta^2}{\alpha^2} n_k r_{,ijk}[u_j] \right\} dS.$$

Therefore,

$$4\pi \nabla \cdot \mathbf{u}_0 = -2 \int_f \frac{\beta^2}{\alpha^2} r_{,jk}^{-1} n_k[u_j] dS.$$

Thus, in the far field, at a point whose direction cosines are  $(l_1, l_2, l_3)$ ,

$$4\pi \nabla \cdot \mathbf{u}_0 = \frac{\beta^2}{\alpha^2} r^{-3} l_j l_k A_{jk}, \quad (28)$$

where  $A_{jk}$  is a symmetric tensor with zero trace:

$$A_{jk} = \int_f \left\{ \frac{1}{2} n_j[u_k] + \frac{1}{2} n_k[u_j] - \frac{1}{3} n_i[u_i] \right\} dS. \quad (29)$$

This corresponds to a second-degree multipole, and application of the previous result (24) yields

$$I = \frac{1}{4\pi} \frac{\beta^2}{\alpha^3} r^{-1} 2l_j l_k A_{jk}. \quad (30)$$

In the case of a plane fault perpendicular to the  $x_3$  axis with dislocation parallel to the  $x_2$  axis,  $A$  reduces to

$$A = Mo/\mu \begin{bmatrix} 0 & 0 & 0 \\ 0 & 0 & \frac{1}{2} \\ 0 & \frac{1}{2} & 0 \end{bmatrix},$$

and

$$I = \frac{1}{4\pi} \frac{\beta^2}{\alpha^3} \frac{Mo}{\mu} r^{-1} \sin 2\theta \sin \phi. \quad (31)$$

Generalizing the expression for the impulse, to allow for any kind of second-degree source, yields the form

$$I = \frac{1}{4\pi} \frac{\beta^2}{\alpha^3} r^{-1} L \left( \frac{16\pi}{15} \right)^{1/2} Y(\theta, \phi), \quad (32)$$

where  $Y(\theta, \phi)$  is a second-degree surface harmonic, normalized so that the integral of its square over the spherical surface is unity.  $L$  is then a general measure of shear distortion at the source. It reduces, in the case of the dislocation source, to the invariant of the tensor  $A$  (Eq. 29). An appropriate name for it is therefore the "shear invariant" (Randall, 1971a); for plane shear it reduces to the seismic moment divided by the shear modulus,  $Mo/\mu$ .

#### D. SOURCES WITH VOLUME CHANGE

In the notation of Randall (1966) the effect of a sudden change in a volume  $B$  is the same as introducing a stress discontinuity  $[T]$  on its boundary  $S$ . If the fractional change of volume is  $k$ , then

$$[T] = T\{\mathbf{u}_3\}; \quad \mathbf{u}_3 = \frac{1}{3}kr\mathbf{a}_r.$$

Here  $\mathbf{u}_3$  describes the deformation as it would be in the volume where the transition occurs if the constraint of the surrounding medium were not present. Then

$$\begin{aligned} T\{\mathbf{u}_3\} &= \frac{\alpha^2 - 2\beta^2}{\beta^2} k\mathbf{n} + \frac{2}{3}k\mathbf{n} \\ &= \frac{\alpha^2 - \frac{4}{3}\beta^2}{\beta^2} k\mathbf{n}. \end{aligned}$$

Now it has been demonstrated (Randall, 1966) that for the static field corresponding to such a source,

$$4\pi \nabla \cdot \mathbf{u}_0 = \frac{\beta^2}{\alpha^2} \int_s [T] \cdot \nabla r^{-1} dS. \quad (33)$$

Thus inside the source the divergence of  $\mathbf{u}_0$  is constant,

$$\nabla \cdot \mathbf{u}_0 = -\frac{\alpha^2 - \frac{4}{3}\beta^2}{\alpha^2} k,$$

while outside

$$\nabla \cdot \mathbf{u}_0 = 0.$$

The initial potential in the far field is therefore

$$V_0 = \frac{1}{4\pi} \frac{\alpha^2 - \frac{4}{3}\beta^2}{\alpha^2} kvr^{-1}, \quad (34)$$

where  $v$  is the source volume. In the time that a P-wave traverses the source, the dynamic potential drops from this value to zero, and hence

$$I = \frac{1}{4\pi} \frac{\alpha^2 - \frac{4}{3}\beta^2}{\alpha^3} kvr^{-1}. \quad (35)$$

The special case in which the source volume is spherical has been considered from a different standpoint (Randall, 1964b).

An analogous argument, making use of the way in which the divergence degenerates at a surface of discontinuity, yields for the case of normal dislocation (say, caused by fluid injection at a fault), a contribution

$$I = \frac{1}{4\pi} \frac{1}{\alpha} r^{-1} \int_f \mathbf{n} \cdot [\mathbf{u}] dS. \quad (36)$$

Both of these results may be expressed in terms of the permanent change of volume at the source,  $\Delta v$ :

$$I = \frac{1}{4\pi} \frac{1}{\alpha} r^{-1} \Delta v. \quad (37)$$

In addition to this zero-degree multipole there will be the second-degree contribution of Eq. (32).

### III. The Measurement of Displacement Impulse

#### A. EFFECTS OF THE INSTRUMENT AND OF ATTENUATION

The pulses from deep-focus earthquakes on long-period instruments of the type used by WWSSN often have the characteristic appearance of the examples in Fig. 3. The principal features are a half cycle in one direction, of duration about 4–5 sec, followed by a smaller and longer movement in the opposite direction. The shape is essentially that of the impulse response of the instrument with some loss of high frequency components. The following short theoretical discussion will show the relationship of the amplitude of such an observed pulse to the impulse (or time integral) of displacement.

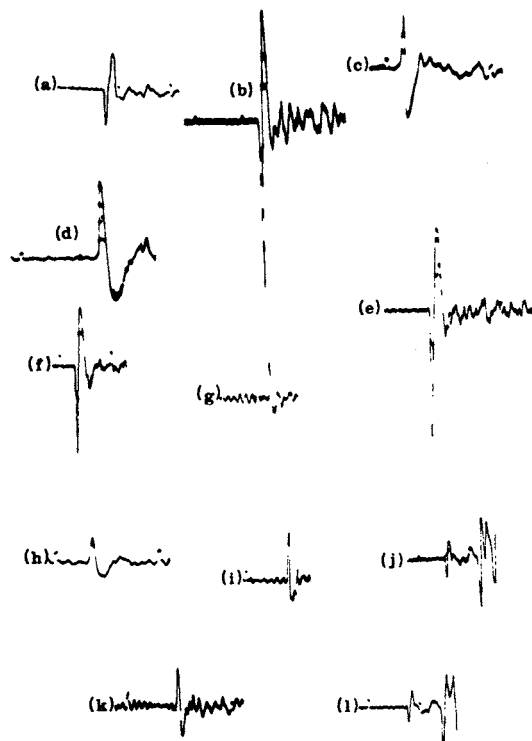


FIG. 3. Typical pulses from deep-focus earthquakes recorded on long-period WWSSN instruments. Event 5: (a) MUN; (b) ANP; (c) SDB; (d) WEL; (e) COL; (f) TUC; (g) TAU. Event 6: (h) WEL; (i) RIV; (j) CHG; (k) AFI; (l) SHL.

Consider a system whose complex transfer function is  $S(\omega)$  and whose impulse response is  $s(t)$  where

$$s(t) = (1/2\pi) \int_{-\infty}^{\infty} S(\omega) e^{i\omega t} d\omega.$$

Such a system will respond to an input pulse  $f(t)$  (which is assumed to be zero outside a time interval from zero to  $\tau$ ) with an output pulse  $F(t)$  where

$$F(t) = \frac{1}{2\pi} \int_{-\infty}^{\infty} S(\omega) e^{i\omega t} \int_0^{\tau} f(t') e^{-i\omega t'} dt' d\omega. \quad (38)$$

Expanding the time integral as a power series in  $\omega$ :

$$I_0 - i\omega I_1 - \omega^2 I_2 + \cdots + (i\omega)^n I_n + \cdots,$$

where

$$I_n = \frac{1}{n!} \int_0^{\tau} f(t) t^n dt,$$

yields, after performing the frequency integration,

$$F(t) = I_0 s(t) - I_1 s'(t) + I_2 s''(t) + \cdots. \quad (39)$$

For a given pulse shape,  $I_k/I_0 = c_k \tau^k$ , where  $c_k$  is a numerical parameter, so that Eq. (39) is a power series expansion in  $\tau$ . For  $\tau$  sufficiently small, therefore,  $F(t)$  may be approximated by

$$F(t) \doteq I_0 s(t). \quad (40)$$

In particular, to an even better degree of approximation, the maximum of  $F(t)$  is  $I_0$  multiplied by the maximum of  $s(t)$ :

$$F_{\max} \doteq I_0 s_{\max}. \quad (41)$$

A sufficient indicator of the validity of the approximation is that the output pulse  $F(t)$  has nearly the same shape as the impulse response  $s(t)$ .

It is possible to include in the "system" not only the seismograph but also other frequency dependent effects; special advantage is gained by including

the attenuation suffered during transmission along the ray path. If the attenuation parameter  $\tau_Q$  is introduced, where

$$\tau_Q = \int dt/2Q,$$

with integration along the ray path, then the effect of attenuation on the pulse shape may be represented by a transfer function

$$G(\omega) = \exp(-\omega\tau_Q\{1 - i[0.6366 \ln(\omega/0.03) - 4.672]\}). \quad (42)$$

This is an approximation sufficient for numerical studies relevant to the spectral window of the long-period WWSSN instruments. Multiplying  $G(\omega)$  by the instrument transfer function, and numerically performing the Fourier transform to the time domain yields a series of impulse response functions such as those depicted in Fig. 4. As  $\tau_Q$  is typically in the neighborhood of 0.3

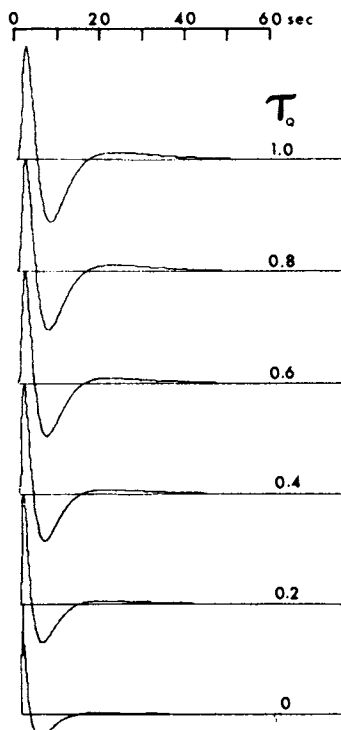


FIG. 4. Synthetic pulses for various values of the attenuation-constant  $\tau_Q$ ; 15–100 sec critically damped instrument.

to 0.5 sec for the paths traversed by the observed P-wave pulses, which are fairly well modeled by the theoretical impulse responses, the approximation of Eq. (41) may be safely made.

To an adequate degree of approximation

$$s_{\max} \doteq 0.531 k e^{-\omega_0 \tau_Q},$$

where  $k$  is a seismometer constant of dimension  $T^{-1}$  and  $\omega_0$  is a slowly varying function of  $\tau_Q$ . For a seismograph system of the WWSSN type, critically damped with pendulum period 15 sec and galvanometer period 100 sec and maximum magnification  $M$ , the approximation may be rewritten as

$$s_{\max} \doteq M K e^{-\omega_0 \tau_Q}, \quad (43)$$

where

$$K \doteq 0.46 \text{ sec}^{-1},$$

and  $\omega_0(\tau_Q)$  is as depicted in Fig. 5.

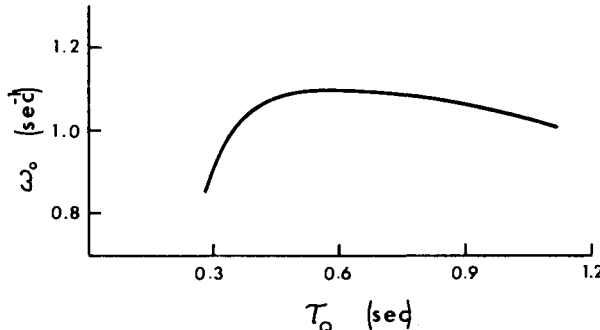


FIG. 5. Variation of the frequency constant  $\omega_0$  with the attenuation constant  $\tau_Q$ .

## B. EFFECTS OF CRUSTAL STRUCTURE AND WAVE SPREADING

If, in addition, the complex transfer function that represents the response of a horizontally layered crustal model is incorporated into the system response  $S(\omega)$ , Randall and Knopoff (1970) have shown that only the tail of the pulse depends significantly on the crustal structure (Fig. 6); the main swing is essentially the same as if the structure were simplified to a free surface. A multiplicative factor equal to the free surface effect must be applied:

$$C_T = \frac{6 \sin e \sec^2 e (1 + 3 \tan^2 e)}{4 \tan e \tan f + (1 + 3 \tan^2 e)^2}, \quad (44)$$

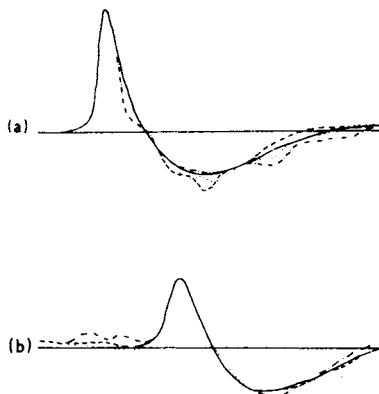


FIG. 6. Effect of variations of crustal structure on the pulses, (a) for P, (b) for pP. —, No crust; - - -, subcontinental; ····, continental shield; - - - - , Colorado. After Randall and Knopoff (1970). Reproduced with permission of A.G.U.

where  $e$  is the angle of emergence at the base of the crust and  $\cos f = (\beta/\alpha) \cos e$ . A similar investigation of the effect of crustal structure on the reflection of the pulse showed that, again, only the free surface effect is significant to the measured impulse and the appropriate reflection coefficient

$$C_R = \frac{4 \tan e \tan f - (1 + 3 \tan^2 e)^2}{4 \tan e \tan f + (1 + 3 \tan^2 e)^2} \quad (45)$$

may be used to allow for the reflection when using  $pP$  pulses.

The geometric spreading factor  $1/r$  for waves in a uniform medium must, in a realistic earth model, be replaced by

$$F(\Delta) = R^{-1} \left[ \frac{180}{\pi} \frac{\rho_h \alpha_h}{\rho_0 \alpha_0} \frac{\eta_0}{\eta_h} p \left| \frac{d^2 t}{d\Delta^2} \right| \right]^{1/2} [(\eta_0^2 - p^2)(\eta_h^2 - p^2)]^{-1/4}, \quad (46)$$

where  $R$  is the earth's radius,  $\rho$  the density,  $\alpha$  the P-wave velocity,  $\eta$  a parameter of the velocity profile ( $= 180r/\pi\alpha$  at radius  $r$ ), and  $p$  is the seismic ray parameter. The subscripts 0 and  $h$  refer to the earth's surface and the earthquake focus, respectively.  $\Delta$  is measured here in degrees and the unit of  $p$  and  $\eta$  is sec/deg. At a point on the focal sphere corresponding to a point on the earth's surface where the observed pulse amplitude is  $A$ , the displacement impulse  $I$  is

$$I = A/[Mf] \times R/K, \quad (47)$$

where, for the P pulse,

$$f = e^{-\omega_0 t_0} C_T R F(\Delta), \quad (48)$$

and for the  $pP$  pulse,

$$f = e^{-\omega_0 t_0} C_T C_R RF(\Delta). \quad (49)$$

#### IV. Estimation of Multipolar Coefficients

##### A. LEAST-SQUARES ESTIMATION

Let it be assumed that, having allowed for the effects of the geometrical attenuation, intrinsic absorption, the crustal transfer function (and reflection for observations of  $pP$ ), and the response of the seismograph, we have at our disposal estimates of the displacement impulse at a number of points on the focal sphere. We seek the best estimates of the six coefficients  $c_i$ ,  $i = 0, \dots, 5$  of an expansion

$$\hat{y} = \sum_{i=0}^5 c_i f_i(\mathbf{x}) \quad (50)$$

to fit the  $n$  corrected observations  $y_\gamma(\mathbf{x}_\gamma)$ ,  $\gamma = 1, \dots, n$  made at the  $n$  points  $\mathbf{x}_\gamma$ . Subscripts  $\gamma$  are associated with observations, whereas subscripts  $(i, j)$  refer to the various coefficients and orthonormal functions:

$$\begin{aligned} f_0 &= Y_0 = (1/4\pi)^{1/2}, \\ f_1 &= Y_2^0 = (5/16\pi)^{1/2}(3 \cos^2 \theta - 1), \\ f_2 &= Y_2^{1c} = (15/16\pi)^{1/2} \sin 2\theta \cos \phi, \\ f_3 &= Y_2^{1s} = (15/16\pi)^{1/2} \sin 2\theta \sin \phi, \\ f_4 &= Y_2^{2c} = (15/16\pi)^{1/2} \sin^2 \theta \cos 2\phi, \\ f_5 &= Y_2^{2s} = (15/16\pi)^{1/2} \sin^2 \theta \sin 2\phi. \end{aligned} \quad (51)$$

We consider first a nonweighted least-squares criterion of best fit, choosing the  $c_i$  so as to minimize

$$S = \sum_{\gamma} \left[ y_{\gamma} - \sum_i c_i f_i(\mathbf{x}_{\gamma}) \right]^2.$$

The conditions  $\partial S / \partial c_j = 0$ ,  $j = 0, \dots, 5$  yield the normal equations which, expressed in matrix form, are

$$\mathcal{M}c = b, \quad (52)$$

where the normal matrix  $\mathcal{M}$  is defined by

$$\mathcal{M}_{ij} = \mathcal{M}_{ji} = \sum_{\gamma} f_i(\mathbf{x}_{\gamma}) f_j(\mathbf{x}_{\gamma}), \quad (53)$$

and the vector  $b$  is defined by

$$b_i = \sum_{\gamma} y_{\gamma} f_i(\mathbf{x}_{\gamma}). \quad (54)$$

Thus if  $\mathcal{N} = \mathcal{M}^{-1}$  is the inverse of the normal matrix, the best estimates, in this least-squares sense, of the coefficients are

$$c_i = \sum_{j=0}^5 \mathcal{N}_{ij} \sum_{\gamma} y_{\gamma} f_j(\mathbf{x}_{\gamma}). \quad (55)$$

Since  $\mathcal{M}$ , and hence  $\mathcal{N}$ , depends only on the distribution of the points of observation on the focal sphere,  $c_i$  is a linear combination of the observed values  $y_{\gamma}$ . Thus, provided that the error in the estimates are normally distributed with variance  $\sigma_y^2$ , then the variances of the coefficients are given by

$$\sigma_{c_i}^2 = \mathcal{N}_{ii} \sigma_y^2, \quad (56)$$

(Scheffé, 1959, p. 12), where  $\mathcal{N}_{ii}$  is the  $i$ th diagonal element of the inverse matrix  $\mathcal{N}$ .

The best estimate of  $\sigma_y^2$  is

$$\begin{aligned} \sigma_y^2 &= \frac{1}{n-6} \sum_{\gamma} [y_{\gamma} - \hat{y}]^2 \\ &= \frac{1}{n-6} \left( \sum_{\gamma} y_{\gamma}^2 - \sum_i c_i b_i \right). \end{aligned} \quad (57)$$

Thus the variances of the coefficients are best estimated by

$$\sigma_{c_i}^2 = \frac{\mathcal{N}_{ii}}{n-6} \left( \sum_{\gamma} y_{\gamma}^2 - \sum_i c_i b_i \right). \quad (58)$$

In this derivation it has been assumed that the errors in the corrected observations are normally distributed. Because the  $c_i$  are linear estimates, this restriction is not necessary, and deviation from normality of the error distribution of the observations has little effect on the normality of the distribution of coefficients. It is therefore to be expected that the estimates of the standard errors of the coefficients made by applying Eq. (58) will usefully indicate the reliability of the solution. A numerical experiment to verify this conclusion is described below.

It is not immediately clear that this method of smoothing is invariant with respect to changes in the coordinate system or in the particular set of orthogonal functions, but this fact is readily proved. The smoothed values  $\hat{y}_e$ ,  $e = 1, \dots, n$ , are linearly related to the observed values  $y_{\gamma}$

$$\hat{y}_e = \sum_{\gamma} T_{e\gamma} y_{\gamma}, \quad (59)$$

where the matrix elements  $T_{\epsilon\gamma}$  depend only on the positions of the points of observation on the focal sphere:

$$T_{\epsilon\gamma} = \sum_i \sum_j f_j(\mathbf{x}_\gamma) f_i(\mathbf{x}_\epsilon) \mathcal{N}_{ij} \quad \text{or} \quad \mathbf{f}^T(\mathbf{x}_\epsilon) \mathcal{N} \mathbf{f}(\mathbf{x}_\gamma). \quad (60)$$

Although in appearance these matrix elements depend on the choice of coordinate system and the orthogonal functions, they are in fact invariant. If either the coordinate system or the orthogonal set or both are changed, the new set will be related to the old by a linear transformation of the form

$$f'_i(\mathbf{x}'_\gamma) = \sum_j m_{ij} f_j(\mathbf{x}_\gamma) \quad \text{or} \quad \mathbf{f}' = \mathbf{m} \mathbf{f}, \quad (61)$$

where the elements of the transformation matrix  $\mathbf{m}$  do not depend on the positions of the points of observation. In the new system the elements of the smoothing matrix are

$$T'_{\epsilon\gamma} = \mathbf{f}'^T(\mathbf{x}'_\epsilon) \mathcal{N}' \mathbf{f}'(\mathbf{x}'_\gamma). \quad (62)$$

Now

$$\begin{aligned} \mathcal{M}' &= \sum_\gamma \mathbf{f}'(\mathbf{x}'_\gamma) \mathbf{f}'^T(\mathbf{x}'_\gamma) \\ &= \sum_\gamma \mathbf{m} \mathbf{f}(\mathbf{x}_\gamma) \mathbf{f}^T(\mathbf{x}_\gamma) \mathbf{m}^T \\ &= \mathbf{m} \mathcal{M} \mathbf{m}^T. \end{aligned} \quad (63)$$

Inverting,

$$\mathcal{N}' = (\mathbf{m}^T)^{-1} \mathcal{N} \mathbf{m}^{-1}, \quad (64)$$

Thus

$$\begin{aligned} T'_{\epsilon\gamma} &= \mathbf{f}'^T(\mathbf{x}'_\epsilon) \mathbf{m}^T (\mathbf{m}^T)^{-1} \mathcal{N} \mathbf{m}^{-1} \mathbf{m} \mathbf{f}(\mathbf{x}_\gamma) \\ &= T_{\epsilon\gamma}, \end{aligned} \quad (65)$$

proving the invariance of the smoothing matrix. In practice this means that, in smoothing by fitting to six orthogonal zero- and second-degree functions on the focal sphere, we avoid the biasing problems that arise when a plane projection is used and model fitting is attempted on this plane, with its inevitable distortion.

## B. STATISTICAL MODEL OF THE SMOOTHING

While the method of smoothing yields results that are independent of the choice of representation on the focal sphere, there remains a problem that is difficult to resolve theoretically. Is it possible that a limited coverage of the

focal sphere might result in a tendency to bias in the radiation pattern? This essentially statistical question may be rephrased as follows. Assuming that there is some "true" radiation pattern, which can be described in terms of a set of coefficients  $c_i^1$ ,  $i = 0, \dots, 5$ , and that the observed amplitudes  $y_y$  differ from the "true" amplitudes  $y_y^1$  because of observation errors, what are the relationships between the distribution of errors in the  $y_y$  and the distributions of the estimates  $c_i$  and  $\sigma_{c_i}$ ; and are the  $c_i$  biased estimates of the  $c_i^1$ ?

In an attempt to answer this question, numerical experiments of a Monte Carlo type have been performed. Starting from a particular set of coefficients  $c_i^1$  and a distribution on the focal sphere of points of observation  $x_y$ , a set of "true" amplitudes  $y_y^1$  was calculated. A random number generator was used to perturb these amplitudes on the hypothesis that the error in amplitude is due to an unknown amplification factor. The perturbations were made in the form

$$y_y = y_y^1 K^p \quad (66)$$

where  $K$  is a constant parameter (greater than 1) and  $p$  is a random number between -1 and 1.  $K$  may be regarded as an index of the degree of scatter of the data;  $K = 1$  corresponds to no scatter, and the scatter increases with  $K$ . Applying the smoothing technique to these values of  $y_y$  yields a set of estimates of the coefficients  $c_i$  and their standard errors  $\sigma_i$ . By repeating this process many times, while keeping  $K$  constant, one can form a statistical ensemble  $S(K)$  and investigate the distribution of the  $c_i$  and the  $\sigma_i$  within the ensemble. Further, by varying  $K$ , it is possible to compare the statistics of the  $c_i$  and the  $\sigma_i$  from ensemble to ensemble. Broadly, the results were as follows. Firstly, the distributions of the  $\sigma_i$  were very narrow, the magnitude of each mean increasing with  $K$ , while the relative values between standard errors remained fixed. It was possible to choose  $K$  so that the values of  $\sigma_i$  found in practice were correctly modeled ( $K \approx 1.5$ ). Secondly, the distributions of the  $c_i$  were normal and were centered on the  $c_i^1$ . This statistical model is successful and indicates that there is no biasing of the radiation patterns due to a non-uniform distribution of observation points, that the estimated standard errors may be usefully employed to indicate the significance of the estimates of the coefficients, and that scatter is typified by a factor of about 1.5.

## V. Multipolar Analysis in Practice

### A. REDUCTION TO VALUES ON THE FOCAL SPHERE

To perform a multipolar analysis on observations at points such as O in Fig. 1, with its corresponding point P on the focal sphere (Fig. 2), it is necessary to know the relationship between  $\Delta$  and  $\theta$  for a given depth of focus  $h$ ,

as well as the amplitude factor  $f$  (Eqs. 48 and 49) associated with propagation along the ray path HO. The seismic ray theory of Bullen (1961) is the appropriate tool. In a sphere with seismic velocity a function of radius only,  $\alpha(r)$ , a ray leaving a surface source at an angle  $\theta$  reaches the surface at a geocentric angle  $\Delta$ ,

$$\Delta = 2p \int_{r^*}^R r^{-1} (\eta^2 - p^2)^{-1/2} dr, \quad (67)$$

where  $\eta = r/\alpha(r)$ ,  $p = \eta_0 \sin \theta$ ,  $\eta_0 = R/\alpha(R)$ ,  $R$  being the earth's radius. The integral is a convergent improper integral, in that the lower limit  $r^*$  is defined by the singularity of the integrand,  $\eta(r^*) = p$ . For practical purposes it is useful to transform the integral to the form

$$\Delta = \int_0^{\pi/2 - \theta} \zeta d(\cos^{-1} p/\eta), \quad (68)$$

where the parameter

$$\zeta = 2/[1 - d(\log \alpha)/d(\log r)]. \quad (69)$$

Thus if an earth model is approximated by a series of layers in which  $\zeta$  is constant (i.e., in which the velocity variation can be described by a power law in the radius) then

$$\Delta = \sum_{i=1}^{m-1} \zeta_i \left( \cos^{-1} \frac{p}{\eta_i} - \cos^{-1} \frac{p}{\eta_{i+1}} \right) + \zeta_m \cos^{-1} \frac{p}{\eta_m}. \quad (70)$$

Such an expression is easily programmed for a digital computer to yield a table of  $\Delta$  as a function of  $p$ . In addition, the parameter  $\tau_Q$  for such a model can be calculated from the formula

$$\tau_Q = \sum_{i=1}^{m-1} \frac{\zeta_i}{2Q_i} [(\eta_i^2 - p^2)^{1/2} - (\eta_{i+1}^2 - p^2)^{1/2}] + \frac{\zeta_m}{2Q_m} (\eta_m^2 - p^2)^{1/2} \quad (71)$$

For deep sources, corrections to both  $\Delta$  and  $\tau_Q$  must be applied to allow for the upper layers which are not traversed. The corrections

$$\Delta_h = \frac{1}{2} \sum_{i=1}^{m_h} \zeta_i \left( \cos^{-1} \frac{p}{\eta_i} - \cos^{-1} \frac{p}{\eta_{i+1}} \right) \quad (72)$$

$$\tau_{Q_h} = \frac{1}{2} \sum_{i=1}^{m_h} \frac{\zeta_i}{2Q_i} [(\eta_i^2 - p^2)^{1/2} - (\eta_{i+1}^2 - p^2)^{1/2}] \quad (73)$$

are subtracted for the P pulse and added for pP. Tables of  $\theta(P)$ ,  $f(P)$ ,  $\theta(pP)$ , and  $f(pP)$  have been calculated for  $h = 100(50)650$  km at intervals of  $\Delta$ . Table I is a sample page from these tables. The velocity distribution used was that of Herrin *et al.* (1968), the distribution of the attenuation parameter  $Q$  for P-waves was obtained by multiplying by  $\frac{9}{4}$  the  $Q$  values (model H) of Anderson and Archambeau (1964).

The magnification  $M$  of the WWSSN instruments can be obtained from the amplitude  $D$  of the calibration pulse (Espinosa *et al.*, 1965). For a seismometer of free period 15 sec and galvanometer of free period 100 sec, both critically damped,

$$M = 0.407 D/GI, \quad (74)$$

where  $D$  is the amplitude of the calibration pulse in mm,  $G$  is the seismometer constant in N/A, and  $I$  is the calibration current in mA.

Observed amplitudes  $A$  are referred to the focal sphere by the formula

$$y = A/Mf \quad (75)$$

and the multipolar analysis performed on the values of  $y$ , to yield coefficients  $c_i$ ,  $i = 0, \dots, 5$  and their standard errors. In terms of the second-degree variance,

$$\sigma_2^2 = c_0^2 + c_1^2 + c_2^2 + c_3^2 + c_4^2 + c_5^2; \quad (76)$$

therefore, the shear variant  $L$  [Eqs. (32), (47)] is given by the formula

$$L = (15\pi)^{1/2}(\alpha^3/\beta^2)(R/K)\sigma^2 \quad (77)$$

( $K \doteq 0.46 \text{ sec}^{-1}$ ). The ratio of volume change to the shear invariant expressed in terms of the multipolar coefficients is

$$\Delta v/L = (4/15)^{1/2}(\beta^2/\alpha^2)(c_0/\sigma_2). \quad (78)$$

The principal axes and ratio of eigenvalues for a radiation pattern are those of the quadratic form obtained when the orthogonal functions of the expansion are expressed in terms of the direction cosines ( $l_1, l_2, l_3$ ). With the zero-degree term removed, the eigenvalues and eigenvectors of shear at the source are therefore those of the matrix

$$\begin{bmatrix} -c_1 + c_5 & \sqrt{3}c_4 & \sqrt{3}c_3 \\ \sqrt{3}c_4 & -c_1 - c_5 & \sqrt{3}c_2 \\ \sqrt{3}c_3 & \sqrt{3}c_2 & 2c_1 \end{bmatrix},$$

and are readily evaluated.

TABLE I  
SAMPLE PAGE FROM TABLES OF TAKE-OFF ANGLE AND  
AMPLITUDE FACTOR (DEPTH = 150 km)

Distance	$\theta(P)$	$f(P)$	$\theta(pP)$	$f(pP)$
8	88.5	6.21		
9	85.4	5.09		
10	82.8	4.30		
11	80.5	3.72		
12	78.4	3.28		
13	75.0	3.47		
14	72.5	2.99		
15	69.0	3.03		
16	65.6	3.04		
17	62.2	2.97		
18	59.0	2.94		
19	55.8	2.96		
20	52.9	2.74		
21	50.4	2.40		
22	48.1	2.05		
23	46.1	2.09	126.7	-1.39
24	44.7	2.02	130.1	-1.34
25	43.8	1.23	132.7	-1.28
26	42.9	1.55	134.6	-1.09
27	42.5	1.02	136.0	-0.68
28	42.3	0.56	136.9	-0.88
29	42.1	0.62	137.5	-0.70
30	41.8	0.76	137.6	-0.36
31	41.5	0.76	137.8	-0.34
32	41.3	0.68	138.1	-0.44
33	41.0	0.75	138.4	-0.45
34	40.7	0.76	138.7	-0.41
35	40.3	0.76	139.0	-0.45
36	40.0	0.79	139.3	-0.46
37	39.6	0.77	139.6	-0.46
38	39.2	0.80	140.0	-0.49
39	38.8	0.71	140.4	-0.48
40	38.5	0.76	140.8	-0.51
41	38.1	0.71	141.2	-0.45
42	37.7	0.75	141.6	-0.49
43	37.3	0.71	141.9	-0.45
44	37.0	0.75	142.3	-0.49
45	36.6	0.72	142.7	-0.46
46	36.2	0.74	143.1	-0.49
47	35.8	0.73	143.5	-0.48
48	35.4	0.70	143.9	-0.49
49	35.0	0.72	144.3	-0.50
50	34.6	0.66	144.7	-0.47

## B. APPLICATIONS OF THE METHOD

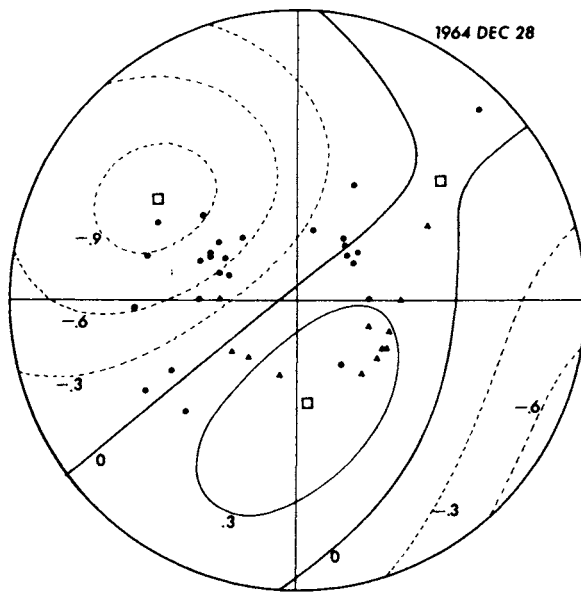
Table II lists a selection of earthquakes which have been analyzed by this technique. Events 1–4 were discussed in detail by Randall and Knopoff (1970). A summary of the solutions for these earthquakes is given in Table III; their radiation patterns are reproduced in Figs. 7–10. The data for event 6 is given in Table IV. The last column contains the ratio of the corrected amplitude on the focal sphere to the smoothed amplitude  $\hat{y}$ . This gives some indication of the magnitude of the residual scatter. The station codes in the first column are the standard three-letter codes of USNOS, with an "R" added to denote an observation derived from  $pP$ . Details of the solutions for events 5 and 6 are given in Table V; the corresponding radiation patterns are shown in Figs. 11 and 12.

TABLE II  
EARTHQUAKES ANALYZED

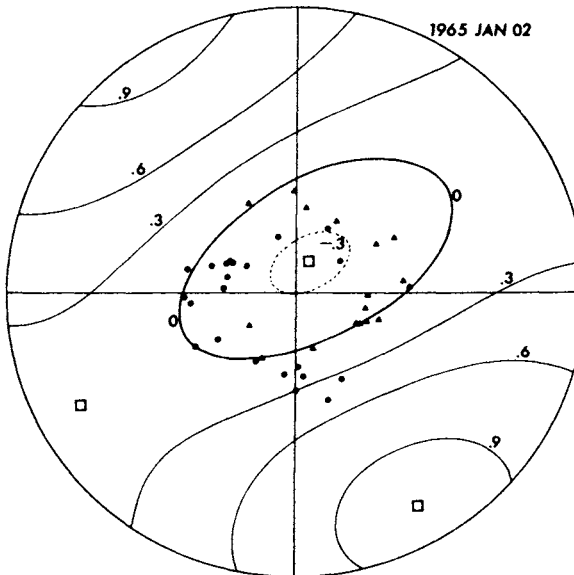
Event	Date	Coordinates	Depth (km)	Magnification ( $M_B$ )	Location
1	1964 Dec. 28	22.1°S 179.6°W	611	6.2	South of Fiji
2	1965 Jan. 2	19.1°N 145.4°E	142	6.1	Mariana Islands
3	1965 Jul. 6	4.4°S 155.1°E	510	6.5	Solomon Islands
4	1965 Nov. 3	9.1°S 71.4°W	593	6.2	Peru–Brazil Border
5	1967 Oct. 9	21.1°S 179.4°W	654	6.3	Fiji Islands
6	1969 Aug. 8	6.1°S 129.7°E	196	5.9	Banda Sea

TABLE III  
SUMMARY OF SOLUTIONS FOR EVENTS 1–4

	1964 Dec. 28	1965 Jan. 2	1965 Jul. 6	1965 Nov. 3
Location	S. Fiji	Mariana Is.	Solomon Is.	Peru–Brazil
Depth	611	142	510	593
$\Delta v/L$	-0.063	0.149	-0.080	0.008
$L(\text{km}^3)$	0.129	0.043	0.021	0.116
$M_o (10^{26} \text{ dyn cm})$	1.71	0.30	0.23	1.53
$\lambda_{\min}/\lambda_{\max}$	0.195	0.138	0.091	0.089
$\varepsilon_{\text{rms}}/\sigma_2$	0.103	0.230	0.240	0.089



**FIG. 7.** Radiation pattern for event 1. Stereographic projection of lower focal hemisphere. Circles correspond to observations of P, triangles to antipodes of observations of  $pP$ . Principal axes are denoted by squares. The contours are labeled in units of the amplitude at the major axis. After Randall and Knopoff (1970). Reproduced with permission of A.G.U.



**FIG. 8.** Radiation pattern for event 2. After Randall and Knopoff (1970). Reproduced with permission of A.G.U.

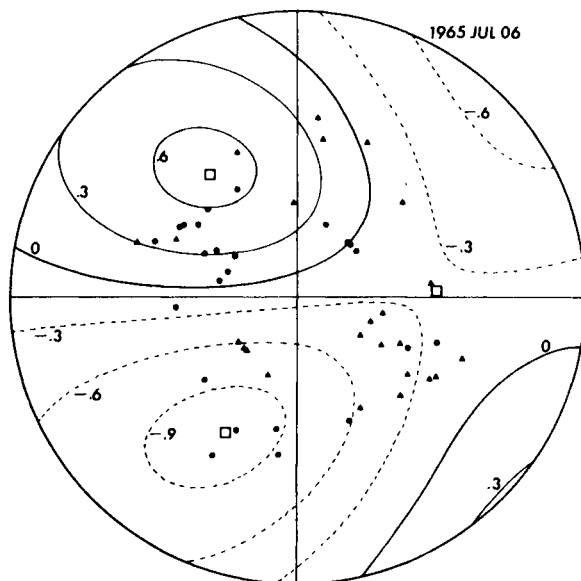


FIG. 9. Radiation pattern for event 3. After Randall and Knopoff (1970). Reproduced with permission of A.G.U.

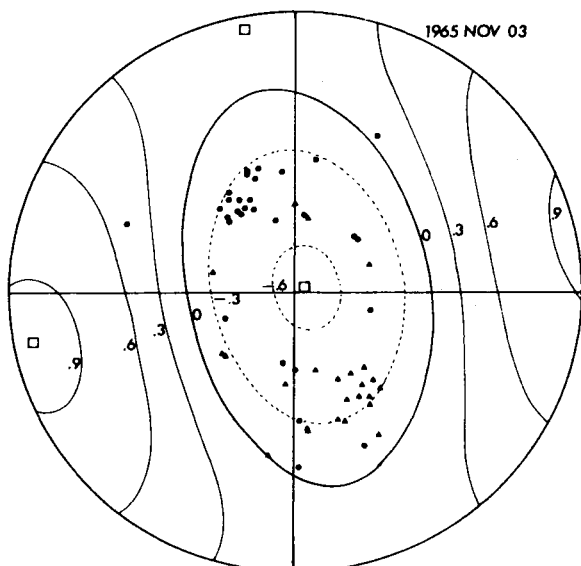


FIG. 10. Radiation pattern for event 4. After Randall and Knopoff (1970). Reproduced with permission of A.G.U.

TABLE IV  
DATA FOR THE EARTHQUAKE OF 1969 AUG. 8

Station	$\theta$	$\phi$	$y$	$y/\dot{y}$
AFI	32.5	102.5	22.8	1.33
ANP	42.3	346.0	-9.2	0.84
BAG	45.5	338.1	-10.1	0.97
CHG	39.8	309.9	-2.8	1.23
CHGR	139.2	309.9	11.9	0.69
GUA	45.0	33.7	-14.1	1.85
HKC	42.3	332.2	-9.5	1.17
HKCR	136.8	332.2	8.9	0.85
HNR	43.0	98.2	35.3	1.91
HNRR	136.3	98.2	0.0	0.00
KIP	26.0	66.2	11.6	1.30
KOD	33.7	287.1	1.8	1.34
KODR	145.5	287.1	13.0	0.73
LAH	30.0	309.0	-2.9	2.78
LAHR	149.2	309.0	13.7	0.84
LEM	48.5	266.9	3.5	1.30
LEMR	113.0	266.9	14.6	0.95
MUN	43.3	204.4	-5.9	1.85
NDI	31.3	307.3	-1.6	1.61
NDIR	148.0	307.3	9.8	0.59
POO	31.5	295.3	0.0	0.00
POOR	147.7	295.3	13.0	0.74
QUE	28.3	305.0	1.5	-5.56
QUER	151.0	305.0	8.1	0.50
RAB	47.5	86.2	15.2	0.96
RAR	28.3	110.3	22.6	1.37
RIV	41.7	147.0	25.4	2.03
RIVR	137.5	147.0	-9.1	1.33
SBA	26.5	172.4	14.9	1.75
SEO	38.0	356.8	-5.5	0.55
SHI	23.7	301.2	2.1	2.43
SHIR	155.7	301.2	12.3	0.80
SHL	36.0	312.2	-2.4	1.00
SHLR	143.0	312.2	9.2	0.56
SNG	42.5	294.0	2.0	2.33
SNGR	136.7	294.0	16.2	0.83
SPA	22.8	180.0	9.2	1.15
TAB	21.5	308.3	1.6	2.16
TABR	158.3	308.3	12.5	0.88
TAU	39.5	159.7	10.9	1.24
WEL	34.2	138.2	18.3	1.21

TABLE V  
SOLUTIONS FOR EVENTS 5 AND 6

	1967 Oct. 9	1969 Aug. 6
Location	Fiji Is.	Banda Sea
Depth (km)	654	196
Coefficients ( $10^{-6}$ m)		
$c_0$	$-12.3 \pm 14.3$	$-1.5 \pm 7.8$
$c_1$	$-26.1 \pm 14.0$	$12.3 \pm 6.3$
$c_2$	$41.8 \pm 6.6$	$13.1 \pm 2.7$
$c_3$	$-95.6 \pm 7.5$	$-12.6 \pm 3.1$
$c_4$	$-7.1 \pm 11.7$	$-16.8 \pm 7.8$
$c_5$	$7.1 \pm 17.5$	$-30.1 \pm 5.7$
$\sigma_2$	108.0	40.8
$\Delta v/L$	-0.020	-0.007
$L(\text{km}^3)$	0.35	0.11
$M_0 (10^{26} \text{ dyn cm})$	4.9	0.83
Eigenvalues	0.955 : -1 : 0.045	0.89 : -1 : 0.11
Eigenvectors		
$\theta$ (deg)	52.4 : 37.6 : 0.2	55.6 : 80.6 : 36.0
$\phi$ (deg)	156.6 : 336.2 : 66.5	109.0 : 12.5 : 269.3
$\varepsilon_{\text{rms}}/\sigma_2$	0.116	0.144

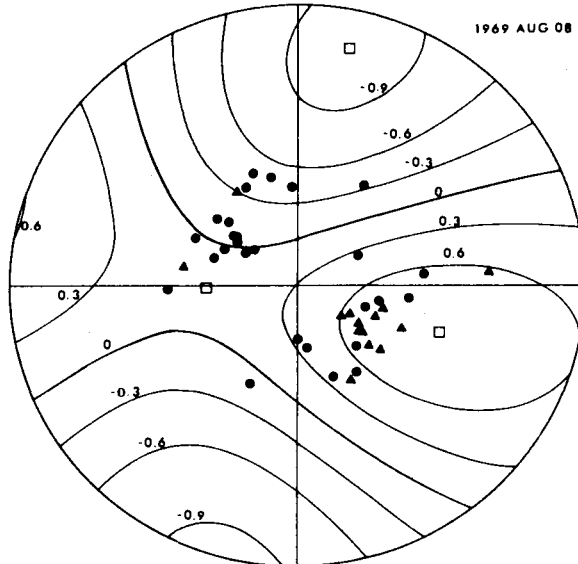


FIG. 11. Radiation pattern for event 5.

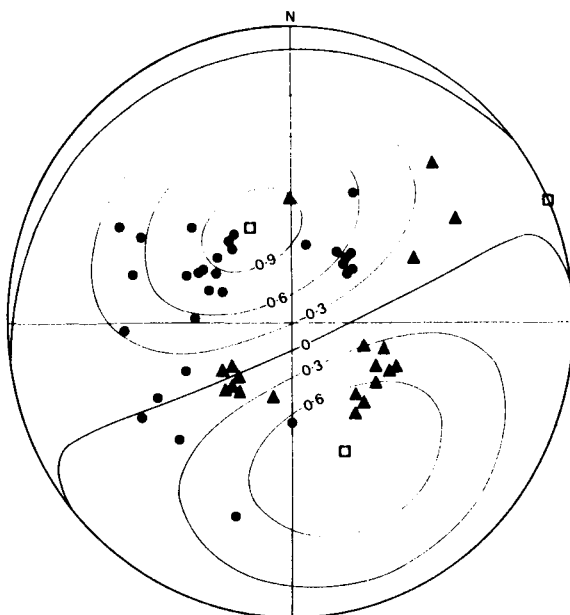


FIG. 12. Radiation pattern for event 6.

As an aid to evaluating the significance of such parameters as the ratio of volume change to the shear invariant,  $\Delta v/L$ , and the ratio of minimum and maximum eigenvalues  $\lambda_{\min}/\lambda_{\max}$  (which measures the departure of the shear at the source from pure plane shear), the rms error of coefficients  $\varepsilon_{\text{rms}}$  has been expressed as a fraction of the second-degree variance,  $\sigma_2$ . Comparison of  $\Delta v/L$  and  $\lambda_{\min}/\lambda_{\max}$  with  $\varepsilon_{\text{rms}}/\sigma_2$  does indeed indicate that in no case is there either significant volume change or departure from plane shear. Many more earthquakes would need to be analyzed, however, before this result could be accepted as general. In spite of the well-defined *adequacy* of the double-couple model (Isacks and Molnar, 1971), its *necessity* is far from justified on the evidence of first-motion solutions alone. (An interesting exercise would be to test what proportion of the "204 reliable focal-mechanism solutions" of Isacks and Molnar could be adequately modeled by, say, the CLVD source of Knopoff and Randall (1970), which represents an extreme departure from the double couple.) Nevertheless, limited though the number of cases might be, there is room for cautious optimism on behalf of the double couple. It is perhaps with some poetic justice that this work, which had its beginnings in the speculative phase transition theory, should in the end contribute to its refutation.

## REFERENCES

- ANDERSON, D., and ARCHAMBEAU, C. (1964). *J. Geophys. Res.* **69**, 2071.
- BRIDGMAN, P. W. (1937). *Proc. Amer. Acad. Arts Sci.* **71**, 387.
- BRIDGMAN, P. W. (1945). *Amer. J. Sci.* **243**, A, 90.
- BULLEN, K. E. (1961). *Geophys. J.* **4**, 93.
- ESPINOSA, A. F., SUTTON, G. H., and MILLER, H. J. (1965). VESIAC Spec. Rep. 4410-106-X. University of Michigan, Ann Arbor.
- EIVISON, F. F. (1963). *Bull. Seismol. Soc. Amer.* **53**, 873.
- GRIGGS, D. T., and BAKER, D. W. (1969). In "Properties of Matter under Unusual Conditions" (H. Mark and S. Fernbach, eds.), p. 23. Wiley, New York.
- GRIGGS, D. T., and HANDIN, J. (1960). *Geol. Soc. Amer., Mem.* **79**, 347.
- HERRIN, E., ARNOLD, E. P., BOLT, B. A., CLAWSON, G. E., ENGDAHL, E. R., FREEDMAN, H. W., GORDON, D. W., HALES, A. L., LOBDELL, J. L., NUTTLI, O., ROMNEY, C., TAGGART, J., and TUCKER, W. (1968). *Bull. Seismol. Soc. Amer.* **58**, 1193.
- HONDA, H. (1962). *J. Phys. Earth.* **10**, 1.
- ISACKS, B., and MOLNAR, P. (1971). *Rev. Geophys.* **9**, 103.
- KAWASUMI, H. (1933). *Bull. Earthq. Res. Inst. Tokyo* **11**, 403.
- KAWASUMI, H. (1937). *Publ. Bur. Cent. Sismol. Int., Ser. A, Trav. Sci.* **15**, 258.
- KAWASUMI, H., and YOSIYAMA, R. (1935). *Bull. Earthq. Res. Inst. Tokyo* **13**, 496.
- KNOPOFF, L., and RANDALL, M. J. (1970). *J. Geophys. Res.* **75**, 4957.
- MORSE, P. M., and FESHBACH, H. (1953). "Methods of Mathematical Physics." McGraw-Hill, New York.
- OROWAN, E. (1960). *Geol. Soc. Amer., Mem.* **79**, 323.
- RANDALL, M. J. (1964a). *Bull. Seismol. Soc. Amer.* **54**, 1283.
- RANDALL, M. J. (1964b). *Bull. Seismol. Soc. Amer.* **54**, 1291.
- RANDALL, M. J. (1966). *J. Geophys. Res.* **71**, 5297.
- RANDALL, M. J. (1971a). *J. Geophys. Res.* **76**, 4991.
- RANDALL, M. J. (1971b). *Bull. Seismol. Soc. Amer.* **61**, 1321.
- RANDALL, M. J., and KNOPOFF, L. (1970). *J. Geophys. Res.* **75**, 4965.
- REID, H. F. (1910). "Report of the State Earthquake Investigation Commission on the California Earthquake of 1906." Carnegie Institute, Washington, D.C.
- RIECKER, R. E., and ROONEY, T. P. (1966). *AFCRL Environ. Res. Pap.* **216**.
- RINGWOOD, A. E. (1966). *Advan. Earth Sci., Contrib. Int. Conf.*, 1964, pp. 357-399.
- RINGWOOD, A. E. (1967). *Earth Planet. Sci. Lett.* **2**, 255.
- SCHEFFÉ, H. (1959). "The Analysis of Variance." Wiley, New York.
- STAUDER, W. (1962). *Advan. Geophys.* **9**, 1-76.

# Computation of Models of Elastic Dislocations in the Earth

ARI BEN-MENAHEM and SARVA JIT SINGH<sup>1</sup>

DEPARTMENT OF APPLIED MATHEMATICS  
THE WEIZMANN INSTITUTE OF SCIENCE  
REHOVOT, ISRAEL

I. Introduction . . . . .	300
II. Mathematical Theory of Seismic Fields . . . . .	301
A. The Volterra Relation for Dislocations . . . . .	301
B. Multipolar Expansions of Green's Tensors . . . . .	303
C. Ray-Theoretical Spectral Displacements in Unbounded Media . . . . .	305
D. Normal Mode Solution for a Real Earth Model . . . . .	309
E. Surface-Wave Theory . . . . .	320
F. Effects of Anelasticity . . . . .	333
G. Seismic "Doppler-Effect" . . . . .	336
III. Calculation of Body-Wave Amplitudes . . . . .	340
A. Divergence Coefficient . . . . .	340
B. Physical Attenuation . . . . .	342
C. Effect of the Earth's Crust . . . . .	344
D. Influence of the Source . . . . .	347
E. Methods for Source Studies . . . . .	349
IV. Calculation of Amplitudes and Phases of Surface Waves . . . . .	352
A. Preliminary Remarks . . . . .	352
B. Evaluation of Theoretical Spectra . . . . .	352
C. Applications to Source Studies: The Method of Spectral Equalization . . . . .	354
V. Calculation of Terrestrial Line-Spectra . . . . .	364
A. General Description . . . . .	364
B. Details of Computations . . . . .	364
C. Application to Source Studies . . . . .	366
VI. List of Symbols . . . . .	370
References . . . . .	372

<sup>1</sup> On leave from the Department of Mathematics, Kurukshetra University, Kurukshetra, India.

## I. Introduction

THIS REVIEW IS INTENDED to acquaint physicists and geoscientists with the current state of research in the field of earthquake source mechanism. It will be assumed that the reader is familiar with the fundamentals of linear elasticity and that he also has a fair knowledge of the basic techniques of mathematical physics, such as integral transforms, differential equations, special functions, complex variable theory, tensor analysis, and matrix theory.

We shall begin with a brief historical survey of seismology. We could, quite arbitrarily, divide its history into three intervals:

- I. 1821–1891      The pre-seismograph era.
- II. 1892–1950      The pre-computer era.
- III. 1951–?      The pre-prediction era.

The first period is distinguished for the intensive theoretical work done by mathematicians and physicists that laid the foundations to the mathematical theory of infinitesimal elasticity. Louis Navier derived in 1821 the differential equations of static and dynamic elasticity. In 1829, Simeon-Denis Poisson established the existence of longitudinal and transverse elastic waves. George Gebriel Stokes (1849) conceived the first mathematical model of an earthquake point-source. Somigliana (1885) produced a formal solution to Navier's equations for a wide class of sources and boundary conditions. In the same year Rayleigh (1885) predicted the existence of elastic surface waves. Voigt (1892) derived the stress-strain relations for a viscoelastic medium. Other important contributions in this period were by Kelvin (1848), Lorentz (1861), and Betti (1872).

In 1892 the first seismograph for worldwide use was invented by John Milne and seismological observatories were set up on a global basis to record ground movements.

The second era is characterized by the availability of seismic data which motivated theoretical research. Simple models for Earth structure were established and tested against the data. Knott (1899) derived general equations for reflection and refraction of plane seismic waves at plane boundaries. A. E. H. Love (1903, 1911) developed the fundamental theory of point sources in an infinite elastic space and also gave a theoretical explanation to a new type of horizontally polarized surface waves which now bear his name. Horace Lamb (1904) laid the theoretical foundation for propagation of seismic waves in layered media. Soon after, Vito Volterra (1907) published his theory of dislocations based on Somigliana's work.

Concurrently, mathematicians and theoretical physicists in Europe were striving to discover new methods for tackling problems of radio-wave propagation. Among these were the method of steepest descent (Debye, 1909),

integral relations among plane, spherical, and cylindrical waves (Sommerfeld, 1909; Weyl, 1919), the Watson transformation (Poincaré, 1910; Watson, 1918), and operational methods (Bromwich, 1916). Later, the quest for analytic solutions to problems of quantum mechanics gave birth to new asymptotic solutions of differential equations (Jeffreys, 1923; Langer, 1937), perturbation methods, and variational techniques. All these methods were soon used by seismologists to solve problems of wave propagation in the earth.

Jeans (1923) was first to treat propagation of seismic waves in a spherical earth model. His work was continued by Sezawa (1927) and others. On the other hand, Jeffreys (1931), Smirnov and Sobolev (1932), Cagniard (1939), Lapwood (1949), Pekeris (1955), and Garvin (1956) used operational methods to solve problems of wave propagation from point and line sources in half-space configurations.

The third era is marked with two outstanding features: The development of sensitive long-period seismographs and the increasing influence of the computer both on the choice of the problems and the methods of attack. In anticipation of the increasing role of computers in seismological theory, new methods were introduced to calculate dispersion, spectral amplitudes, and theoretical seismograms for realistic source models in realistic Earth structures.

This article is divided into two parts. In the first part (Section II) we portray a summary of current theories of seismology. The second part (Sections III-V) include important computational techniques together with some of their applications to seismic-source studies.

## II. Mathematical Theory of Seismic Fields

### A. THE VOLterra RELATION FOR DISLOCATIONS

Seismologists believe that earthquake sources can be represented by a displacement discontinuity over an internal surface  $S$ . Such a source is known as a displacement dislocation and is characterized by two vector distributions. Let  $Q(\mathbf{r}_0)$  be a variable point of  $S$  and let  $\mathbf{n}(\mathbf{r}_0)$  and  $\mathbf{u}_0(\mathbf{r}_0)$  be the unit normal to  $S$  at  $Q$  and the dislocation vector at  $Q$ , respectively. It has then been shown by Volterra (1907), de Hoop (1958), Steketee (1958), Knopoff and Gilbert (1960), Maruyama (1964), and Burridge *et al.* (1964) that the displacement field at  $P(\mathbf{r})$  due to a displacement dislocation at  $Q(\mathbf{r}_0)$  is expressible in the compact form (Ben-Menahem and Singh, 1968a)

$$\mathbf{u}(\mathbf{r}; t) = \int_S \{\mathbf{n}\mathbf{u}_0 : \mathbf{T}_0[\mathbf{G}(\mathbf{r}/\mathbf{r}_0; t)]\} dS, \quad (1)$$

where  $\mathbf{m}\mathbf{u}_0$  is a dyad, the symbol  $(\cdot)$  stands for the double-dot product and  $\mathbf{T}_0$  is a tensorial differential operator in source coordinates which is explained later.

The symbol  $\mathfrak{G} \equiv G_i^j$  is the symmetric Green's tensor for the elastic medium. For an infinite homogeneous isotropic substance it has the spectral closed form

$$\mathfrak{G}_x(\mathbf{r}/\mathbf{r}_0; \omega) = \frac{1}{4\pi\mu} \left\{ \frac{e^{-ik_\beta R}}{R} \mathfrak{J} + \text{grad div} \left[ \frac{e^{-ik_\beta R} - e^{-ik_x R}}{k_\beta^2 R} \mathfrak{J} \right] \right\} \quad (2)$$

with  $\mathfrak{J} \equiv \delta_{ij}$ ,  $R = |\mathbf{r} - \mathbf{r}_0|$ ,  $k_x = \omega \alpha$ ,  $k_\beta = \omega \beta$ , and the factor  $e^{i\omega t}$  is understood.

It is easy to show that for an arbitrary source-time function  $f(t)$ , the time-dependent Green's tensor assumes the form

$$\begin{aligned} \mathfrak{G}_x(\mathbf{r}/\mathbf{r}_0; t) = & \frac{1}{4\pi\mu} \left\{ \frac{f(t - R/\beta)}{R} \mathfrak{J} + \left[ \frac{\beta^2}{\alpha^2} f\left(t - \frac{R}{\alpha}\right) - f\left(t - \frac{R}{\beta}\right) \right] \frac{\mathbf{e}_R \mathbf{e}_R}{R} \right. \\ & \left. - \frac{(\mathfrak{J} - 3\mathbf{e}_R \mathbf{e}_R)}{R^3} \beta^2 \int_{R/\alpha}^{R/\beta} \tau f(t - \tau) d\tau \right\}, \end{aligned} \quad (3)$$

where  $\mathbf{e}_R$  is a unit vector in the  $\mathbf{R} = \mathbf{r} - \mathbf{r}_0$  direction.

A special case of interest arises for  $f(t) = H(t)$  and  $t \rightarrow \infty$ . One then derives from Eq. (3) the Green's tensor for the static case, namely, the Somigliana tensor

$$\mathfrak{G}_x(\mathbf{r}/\mathbf{r}_0; t \rightarrow \infty) = \frac{1}{4\pi\mu} \left[ \frac{\mathfrak{J}}{R} - \frac{1}{4(1-\sigma)} \frac{(\mathfrak{J} - \mathbf{e}_R \mathbf{e}_R)}{R} \right]. \quad (4)$$

Finally, we explain the meaning of the symbol

$$\mathbf{T}(\mathfrak{G}) \equiv T_{ij}^l = \lambda \delta_{jl} G_i^{k,k} + \mu (G_i^{j,l} + G_i^{l,j}), \quad (5)$$

in which, for example,  $G_i^{j,l} = \hat{c} G_i^j \hat{c} x_l$  and the summation convention is used.

One may notice from Eq. (15) that  $[\mathbf{T}(\mathfrak{G})]_{ijk} = [\mathbf{T}(\mathfrak{G})]_{jik}$ . Hence we deduce from Eq. (1)

$$\mathbf{u}(\mathbf{n}, \mathbf{u}_0) = \mathbf{u}(\mathbf{u}_0, \mathbf{n}) \quad (6)$$

which means that the displacement field at  $P(r)$  is invariant with respect to the interchange of  $\mathbf{n}$  and  $\mathbf{u}_0$  at the source. We shall, henceforth, restrict our analysis to cases in which  $S$  is a plane surface and  $\mathbf{n}$  is everywhere perpendicular to  $\mathbf{u}_0$ . The dislocation for which  $\mathbf{n} \cdot \mathbf{u}_0 = 0$  is known as a tangential or shear dislocation.

## B. MULTIPOLAR EXPANSIONS OF GREEN'S TENSORS

In order to simplify the classification of seismic sources and enhance the unification of seismic field theories, Ben-Menahem (1964) and Ben-Menahem and Singh (1968a,b) have adopted the electromagnetic eigenvector method of Hansen (1935), Stratton (1941), and Morse and Feshbach (1953) and adapted it to elastic media.

Consider first homogeneous isotropic media. Let  $\Psi^\pm$  be the eigenfunction solutions of the scalar Helmholtz equation  $\nabla^2\Psi + k_0^2\Psi = 0$  where (+) indicates a solution that is finite at the origin (interior) and (-) stands for a solution that is finite at infinity and singular at the origin (exterior). It may be shown that the vector solutions  $\mathbf{M}^\pm$ ,  $\mathbf{N}^\pm$ , and  $\mathbf{L}^\pm$  of the corresponding vector Helmholtz equation  $\nabla^2\mathbf{A} + k_0^2\mathbf{A} = 0$  can be derived from the scalar eigenfunctions. Table I includes the explicit form of these vector solutions for two common coordinate systems. In this table  $\bar{v} = (k^2 - k_0^2)^{1/2}$ ;  $l, m$  are separation indices and  $k \geq 0$  is a separation parameter. The general solution is obtained by integrating over all permissible values of  $k$  and summing over  $l$  and  $m$ . The vectors  $\mathbf{P}_{m,l}$ ,  $\mathbf{B}_{m,l}$ , and  $\mathbf{C}_{m,l}$  are complex vector functions on the unit sphere.  $\mathbf{P}_{m,l}$  is normal pointwise to  $\mathbf{B}_{m,l}$  and  $\mathbf{C}_{m,l}$  but these vectors themselves are orthogonal only "distributionwise." We have

$$\int_{\theta} \int_{\phi} (\mathbf{B}_{m,l} \cdot \mathbf{C}_{m',l'}^*) d\Omega = 0, \quad (7a)$$

$$\begin{aligned} \int_{\theta} \int_{\phi} (\mathbf{P}_{m,l} \cdot \mathbf{P}_{m',l'}^*) d\Omega &= \int_{\theta} \int_{\phi} (\mathbf{B}_{m,l} \cdot \mathbf{B}_{m',l'}^*) d\Omega \\ &= \int_{\theta} \int_{\phi} (\mathbf{C}_{m,l} \cdot \mathbf{C}_{m',l'}^*) d\Omega \\ &= \Omega_{m,l} \delta_{ll'} \delta_{mm'}, \end{aligned} \quad (7b)$$

where

$$d\Omega = \sin \theta d\theta d\phi, \quad \Omega_{m,l} = \frac{4\pi}{2l+1} \frac{(l+m)!}{(l-m)!}. \quad (8)$$

TABLE I: EIGENFUNCTIONS AND EIGENVECTORS FOR THE HELMHOLTZ EQUATION

Spherical ( $r, \theta, \phi$ )		Cylindrical ( $\rho, \phi, z$ )	
Equation	Interior	Exterior	Interior
$\nabla^2 \Psi + k_0^2 \Psi = 0$	$\Psi_{m,t}^+ = j_l(k_0 r) Y_{m,l}(\theta, \phi)$	$\Psi_{m,t}^- = h_l^{(2)}(k_0 r) Y_{m,l}(\theta, \phi)$	$\Psi_m^+ = e^{iz} Y_m(k\rho, \phi)$
$\nabla^2 \mathbf{A} + k_0^2 \mathbf{A} = 0$	$\mathbf{M}_{m,t}^+ = \text{rot}(\mathbf{r} \Psi_{m,t}^+)$ $= j_l(k_0 r)[l(l+1)]^{1/2} \mathbf{C}_{m,l}$	$\mathbf{M}_{m,t}^- = \text{rot}(\mathbf{r} \Psi_{m,t}^-)$ $= h_l^{(2)}(k_0 r)[l(l+1)]^{1/2} \mathbf{C}_{m,l}$	$\mathbf{M}_m^+ = \frac{1}{k} \text{rot}(\mathbf{e}_z \Psi_m^+)$ $= e^{iz} \mathbf{C}_m$
$\nabla^2 \mathbf{A} + k_0^2 \mathbf{A} = 0$	$\mathbf{N}_{m,t}^+ = \frac{1}{k_0} \text{rot rot}(\mathbf{r} \Psi_{m,t}^+)$ $= \frac{l+1}{2l+1} j_{l-1}(k_0 r) \mathbf{A}_{m,l}^1$	$\mathbf{N}_{m,t}^- = \frac{1}{k_0} \text{rot rot}(\mathbf{r} \Psi_{m,t}^-)$ $= \frac{l+1}{2l+1} h_{l-1}^{(2)}(k_0 r) \mathbf{A}_{m,l}^1$	$\mathbf{N}_m^+ = \frac{1}{kk_0} \text{rot rot}(\mathbf{e}_z \Psi_m^+)$ $= \frac{1}{k_0} e^{iz} [k \mathbf{P}_m + \bar{v} \mathbf{B}_m]$
$\nabla^2 \mathbf{A} + k_0^2 \mathbf{A} = 0$	$\mathbf{L}_{m,t}^+ = \frac{1}{k_0} \text{grad} \Psi_{m,t}^+$ $= \frac{1}{2l+1} j_{l+1}(k_0 r) \mathbf{A}_{m,l}^2$	$\mathbf{L}_{m,t}^- = \frac{1}{k_0} \text{grad} \Psi_{m,t}^-$ $= \frac{1}{2l+1} h_{l+1}^{(2)}(k_0 r) \mathbf{A}_{m,l}^2$	$\mathbf{L}_m^+ = \frac{1}{k_0} \text{grad} \Psi_m^+$ $= \frac{1}{k_0} e^{iz} [\bar{v} \mathbf{P}_m + k \mathbf{B}_m]$
$\nabla^2 \mathbf{A} + k_0^2 \mathbf{A} = 0$	$\mathbf{B}_{m,t}^+ = \frac{i}{k_0} \mathbf{e}_\phi Y_{m,l}(\theta, \phi)$ $= \frac{1}{2l+1} [j_{l-1}(k_0 r) \mathbf{A}_{m,l}^1$	$\mathbf{B}_{m,t}^- = -\frac{i}{k_0} \mathbf{e}_\phi Y_{m,l}(\theta, \phi)$ $= \frac{1}{2l+1} [h_{l-1}^{(2)}(k_0 r) \mathbf{A}_{m,l}^1$	$\mathbf{B}_m^+ = \left[ \mathbf{e}_\theta \frac{i}{ck\rho} + \mathbf{e}_\phi \frac{1}{k\rho} \frac{\partial}{\partial \phi} \right] Y_m$ $= -\frac{1}{k_0} e^{-iz} [-\bar{v} \mathbf{P}_m + k \mathbf{B}_m]$
$\nabla^2 \mathbf{A} + k_0^2 \mathbf{A} = 0$	$\mathbf{C}_{m,t}^+ = \frac{1}{k_0} \frac{\partial}{\sin \theta} \frac{\partial}{i\phi} - \mathbf{e}_\phi \frac{\partial}{i\theta}$ $= [h_{l+1}^{(2)}(k_0 r) \mathbf{A}_{m,l}^2]$	$\mathbf{C}_{m,t}^- = \left[ \mathbf{e}_\theta \frac{1}{\sin \theta} \frac{\partial}{i\phi} - \mathbf{e}_\phi \frac{\partial}{i\theta} \right] Y_{m,l}$	$\mathbf{C}_m^+ = \left[ \mathbf{e}_\theta \frac{1}{k\rho} \frac{\partial}{ck\rho} - \mathbf{e}_\phi \frac{\partial}{ck\rho} \right] Y_m$
$\nabla^2 \mathbf{A} + k_0^2 \mathbf{A} = 0$	$\mathbf{Y}_{m,l}(\theta, \phi) := P_m^l(\cos \theta) e^{im\phi}$ , $\mathbf{A}_{m,l}^1 := l \mathbf{P}_{m,l} + [l(l+1)]^{1/2} \mathbf{B}_{m,l}$	$\mathbf{Y}_m(k\rho, \phi) := J_m(k\rho) e^{im\phi}$	
Surface harmonics	$\mathbf{Y}_{m,l}(\theta, \phi) := \mathbf{e}_z Y_{m,l}(\theta, \phi)$ , $\mathbf{A}_{m,l}^2 := -(l+1) \mathbf{P}_{m,l} + [l(l+1)]^{1/2} \mathbf{B}_{m,l}$	$\mathbf{P}_m := \mathbf{e}_z Y_m(k\rho, \phi)$	
	$[l(l+1)]^{1/2} \mathbf{B}_{m,l} := \left[ \mathbf{e}_\theta \frac{i}{\sqrt{\theta}} + \mathbf{e}_\phi \frac{1}{\sin \theta} \frac{\partial}{\partial \phi} \right] Y_{m,l}$	$\mathbf{B}_m := \left[ \mathbf{e}_\theta \frac{i}{ck\rho} + \mathbf{e}_\phi \frac{1}{k\rho} \frac{\partial}{\partial \phi} \right] Y_m$	
	$[l(l+1)]^{1/2} \mathbf{C}_{m,l} := \left[ \mathbf{e}_\theta \frac{1}{\sin \theta} \frac{\partial}{i\phi} - \mathbf{e}_\phi \frac{\partial}{i\theta} \right] Y_{m,l}$	$\mathbf{C}_m := \left[ \mathbf{e}_\theta \frac{1}{k\rho} \frac{\partial}{ck\rho} - \mathbf{e}_\phi \frac{\partial}{ck\rho} \right] Y_m$	

Small deformations in homogeneous isotropic elastic media are governed by the well-known Navier equation

$$\alpha^2 \operatorname{grad} \operatorname{div} \mathbf{u} - \beta^2 \operatorname{rot} \operatorname{rot} \mathbf{u} + \omega^2 \mathbf{u} = 0. \quad (9)$$

It is easy to prove that the vectors

$$\mathbf{L}^\pm = \frac{1}{k_\alpha} \operatorname{grad} \Psi_\alpha^\pm, \quad \mathbf{M}^\pm = \operatorname{rot}(\mathbf{r} \Psi_\beta^\pm), \quad \mathbf{N}^\pm = \frac{1}{k_\beta} \operatorname{rot} \operatorname{rot}(\mathbf{r} \Psi_\beta^\pm)$$

are independent solutions of Eq. (9) provided that  $\Psi_{\alpha,\beta}^\pm$  obey the scalar Helmholtz equations

$$\nabla^2 \Psi_\alpha + k_\alpha^2 \Psi_\alpha = 0, \quad \nabla^2 \Psi_\beta + k_\beta^2 \Psi_\beta = 0.$$

Starting from this point, Ben-Menahem and Singh (1968b) showed that the spectral Green's tensor (Eq. 2) is expandable in terms of the spherical eigenvector solutions of Eq. (9). Thus

$$\begin{aligned} & \mathfrak{G}_\infty(\mathbf{r}/\mathbf{r}_0; \omega) \\ &= -\frac{i k_\beta}{\mu} \sum_{l=1, 1, 0}^{\infty} \frac{1}{l(l+1)} \sum_{m=-l}^l \frac{1}{\Omega_{m,l}} \\ & \times \left[ \overset{*}{\mathbf{M}_{m,l}^{\varepsilon}(\mathbf{r}_0)} \overset{*}{\mathbf{M}_{m,l}^{-\varepsilon}(\mathbf{r})} + \overset{*}{\mathbf{N}_{m,l}^{\varepsilon}(\mathbf{r}_0)} \overset{*}{\mathbf{N}_{m,l}^{-\varepsilon}(\mathbf{r})} + l(l+1) \left( \frac{\beta}{\alpha} \right)^3 \overset{3*}{\mathbf{L}_{m,l}^{\varepsilon}(\mathbf{r}_0)} \overset{3*}{\mathbf{L}_{m,l}^{-\varepsilon}(\mathbf{r})} \right], \quad (10) \end{aligned}$$

where  $\varepsilon = \operatorname{sgn}(r - r_0)$ . The summation over  $l$  for the first two dyads starts from  $l = 1$ , while for the third dyad it starts from  $l = 0$ . The symbol (\*) denotes complex conjugate.

### C. RAY-THEORETICAL SPECTRAL DISPLACEMENTS IN UNBOUNDED MEDIA

We shall develop approximate expressions for the displacements in a medium with weak radial heterogeneity. Let us first consider a *canonical* problem in which the medium is homogeneous. Let a dislocation source be placed at the point  $Q$  whose coordinates are  $(r_h, 0, 0)$  in a spherical coordinate system with origin at the center of the Earth, O. Let the observer be at the point  $P(r, \theta, \phi)$  with respect to the same system (Fig. 1a). It is convenient to introduce another coordinate system  $x_i$  at the source with unit vectors  $\mathbf{e}_i$ . It is common to choose  $x_3$  through the source while  $x_1$  is drawn in the plane of the dislocation parallel to the equatorial plane. The direction of  $x_1$  is known

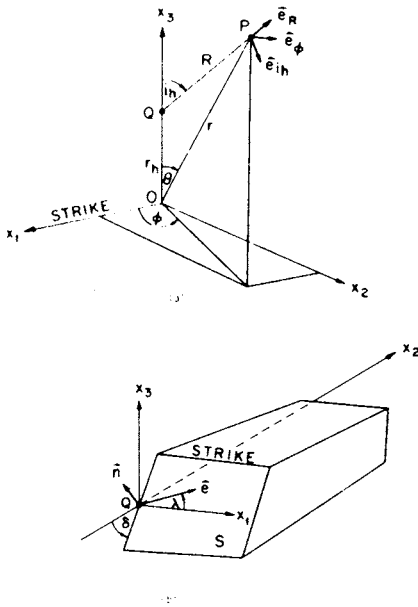


FIG. 1. Coordinate systems and source geometry.

as the strike of the fault. The third axis,  $x_3$ , is chosen in such a way that  $x_1, x_2, x_3$  form a right-hand system. Let  $\mathbf{e}$  be a unit vector along  $\mathbf{u}_0$  and let  $\delta$  (dip) and  $\lambda$  (slip) be the two angles that determine the orientation of  $\mathbf{n}$  and  $\mathbf{e}$  in the source's system. From Fig. 1, we find

$$\begin{aligned}\mathbf{e} &= \cos \lambda \mathbf{e}_1 + \sin \lambda \cos \delta \mathbf{e}_2 + \sin \lambda \sin \delta \mathbf{e}_3, \\ \mathbf{n} &= -\sin \delta \mathbf{e}_2 + \cos \delta \mathbf{e}_3, \\ \mathbf{e}_R &= \sin i_h \cos \phi \mathbf{e}_1 + \sin i_h \sin \phi \mathbf{e}_2 + \cos i_h \mathbf{e}_3, \\ \mathbf{e}_\phi &= -\sin \phi \mathbf{e}_1 + \cos \phi \mathbf{e}_2, \\ \mathbf{e}_{i_h} &= \cos i_h \cos \phi \mathbf{e}_1 + \cos i_h \sin \phi \mathbf{e}_2 - \sin i_h \mathbf{e}_3,\end{aligned}\quad (11)$$

where  $\phi$  is the azimuth of the observer with respect to the strike of the fault.

We wish to derive the field, at large distances, of a localized dislocation of elementary area  $dS$ . We substitute the explicit expression for the Green's tensor from Eq. (2) in Eq. (1) and perform the operations indicated in Eq. (5). Neglecting terms that decay faster than  $1/R$ , we obtain the following expressions for the far-field displacements in the source coordinates:

$$u_R = i\omega g(\omega) \frac{U_0}{2\pi} \frac{dS}{x^3} \left( \frac{\beta^2}{x^3} \right) (\mathbf{n} \cdot \mathbf{e}_R)(\mathbf{e} \cdot \mathbf{e}_R) \frac{e^{i(\omega t - k_x R)}}{R}, \quad (12)$$

$$u_{i_h} = i\omega g(\omega) \frac{U_0 dS}{4\pi\beta} [(\mathbf{e} \cdot \mathbf{e}_{i_h})(\mathbf{n} \cdot \mathbf{e}_R) + (\mathbf{n} \cdot \mathbf{e}_{i_h})(\mathbf{e} \cdot \mathbf{e}_R)] \frac{e^{i(\omega t - k_\beta R)}}{R}, \quad (13)$$

$$u_\phi = i\omega g(\omega) \frac{U_0 dS}{4\pi\beta} [(\mathbf{e} \cdot \mathbf{e}_\phi)(\mathbf{n} \cdot \mathbf{e}_R) + (\mathbf{n} \cdot \mathbf{e}_\phi)(\mathbf{e} \cdot \mathbf{e}_R)] \frac{e^{i(\omega t - k_\beta R)}}{R}, \quad (14)$$

where  $g(\omega)$  is the Fourier transform of the source time function. Equations (12), (13), and (14) represent the seismic fields of P, SV, and SH waves, respectively.

If we replace the unit vectors  $\mathbf{n}$ ,  $\mathbf{e}$ ,  $\mathbf{e}_R$ ,  $\mathbf{e}_{i_h}$ , and  $\mathbf{e}_\phi$  by their equivalent expressions in terms of the unit vectors  $\mathbf{e}_1$ ,  $\mathbf{e}_2$ , and  $\mathbf{e}_3$  from Eqs. (11), we obtain for a step function time-dependence [ $g(\omega) = 1/(i\omega)$ ]

$$(\mathbf{n} \cdot \mathbf{e}_R)(\mathbf{e} \cdot \mathbf{e}_R) = \frac{1}{6}F(\delta, \lambda, i_h, \phi), \quad (15)$$

$$(\mathbf{e} \cdot \mathbf{e}_{i_h})(\mathbf{n} \cdot \mathbf{e}_R) + (\mathbf{n} \cdot \mathbf{e}_{i_h})(\mathbf{e} \cdot \mathbf{e}_R) = \frac{1}{6}\partial F/\partial i_h, \quad (16)$$

$$(\mathbf{e} \cdot \mathbf{e}_\phi)(\mathbf{n} \cdot \mathbf{e}_R) + (\mathbf{n} \cdot \mathbf{e}_\phi)(\mathbf{e} \cdot \mathbf{e}_R) = \frac{1}{6}(1/\sin i_h)\partial F/\partial \phi, \quad (17)$$

where

$$F(\lambda, \delta; i_h, \phi) = \cos \lambda [\sin \delta A_1 + \cos \delta A_2^{**}] + \sin \lambda [\sin 2\delta A_3 - \cos 2\delta A_2], \quad (18)$$

$$\begin{aligned} A_1 &= -\sin 2\phi P_2^2(\cos i_h), \\ A_2 &= -2 \sin \phi P_2^1(\cos i_h), \\ A_3 &= 3P_2(\cos i_h) + \frac{1}{2} \cos 2\phi P_2^2(\cos i_h), \\ A_2^{**} &= A_2(\phi - \frac{1}{2}\pi) = 2 \cos \phi P_2^1(\cos i_h). \end{aligned} \quad (19)$$

Thus, the new form of the displacements is

$$\begin{aligned} u_P &= \frac{U_0 dS}{12\pi\alpha(r_h)} \left(\frac{\beta}{\alpha}\right)^2 r_h F \left[ \frac{e^{i(\omega t - k_\alpha R)}}{R} \right] + O\left(\frac{1}{R^2}\right), \\ u_{SV} &= \frac{U_0 dS}{24\pi\beta(r_h)} \frac{\partial F}{\partial i_h} \left[ \frac{e^{i(\omega t - k_\beta R)}}{R} \right] + O\left(\frac{1}{R^2}\right), \\ u_{SH} &= \frac{U_0 dS}{24\pi\beta(r_h)} \frac{1}{\sin i_h} \frac{\partial F}{\partial \phi} \left[ \frac{e^{i(\omega t - k_\beta R)}}{R} \right] + O\left(\frac{1}{R^2}\right). \end{aligned} \quad (20)$$

Note that in Eq. (19),  $A_1$  is obtained from  $F$  by taking  $\lambda = 0$ ,  $\delta = 90^\circ$ ,  $A_2$  corresponds to  $\lambda = 90^\circ$ ,  $\delta = 90^\circ$ , and  $A_3$  to  $\lambda = 90^\circ$ ,  $\delta = 45^\circ$ . We will refer to these three dislocations as Case I, Case II, and Case III, respectively. It is clear from Eqs. (1) and (11) that a dislocation of arbitrary orientation ( $\lambda, \delta$ ) is expressible as a linear combination of these three cases. Of these, Case I is termed by geologists as a "strike-slip" fault and Case II as a "dip-slip" fault.

Equations (20) constitute the solution to our canonical problem. We now go on to consider a radially heterogeneous Earth model in which the structural parameters depend on the radial coordinate  $r$  alone. In such a medium the ray path from  $Q$  to  $P$  (Fig. 1a) is no longer along  $R$  but, instead, is a curved path according to the well-known law of Snell (Fig. 2). Singh and Ben-Menahem (1969c,d) have shown that if the variation in the constitutive parameters over a wavelength is small, Eq. (20) will still hold provided we make the change

$$\begin{aligned} \frac{e^{i\omega(t-R/v)}}{R} &\rightarrow \frac{e^{i\omega(t-T)}}{r_0} \left[ \frac{v(r_h)\rho(r_h)}{v(r_0)\rho(r_0)} \frac{\sin i_h}{\sin \theta \cos i_0} \left( \frac{\partial i_h}{\partial \theta} \right)_{r_0} \right]^{1/2} \\ &= Ge^{i\omega(t-T)}. \end{aligned} \quad (21)$$

The angles  $i_h$  and  $i_0$  are shown in Fig. 2. The derivative is taken at constant value of the coordinate  $r$ ,  $\rho$  is the density,  $v$  is  $\alpha$  or  $\beta$ , and  $T$  is the travel time along the ray. The factor  $G$  in Eq. (21) is known as the Gutenberg *divergence coefficient* (Zoeppritz *et al.*, 1912) and is due to the geometrical spreading of the ray tube in the medium. From elementary ray theory, we have the Benndorf relation (Benndorf, 1905)

$$p = \frac{dT}{d\theta} = \frac{r_h \sin i_h}{v_h} = \frac{r_0 \sin i_0}{v_0}, \quad (22)$$

where  $p$  is the ray parameter.

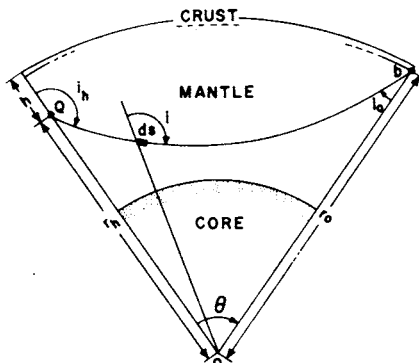


FIG. 2. Ray path and ray parameters.

## D. NORMAL MODE SOLUTION FOR A REAL EARTH MODEL

### 1. Equations of Motion

In the previous section we have derived explicit asymptotic expressions for displacements valid at large distances and high frequencies. We shall next derive a representation for the total elastodynamic field in a radially heterogeneous and self-gravitating spherical Earth model of radius  $a$  excited by a point dislocation at depth  $h = a - r_0$ . Our plan consists of deriving first the equations of motion and their Green's dyadic. This will be followed by the expressions for the ensuing motion and deformation in and on the sphere for a given profile of the structural parameters  $\lambda$ ,  $\mu$ ,  $\rho$ , and  $g$ . We start from the Fourier-transformed Navier equation

$$\operatorname{div} \mathbf{T} + \rho \mathbf{F}_e + \rho \omega^2 \mathbf{u} = 0, \quad (23)$$

where  $\mathbf{F}_e$  denotes the external body force per unit mass,  $\mathbf{T}$  the stress tensor, and  $\rho$  the density.

The application of this equation to the Earth calls for the following assumptions:

1. The stress tensor  $\mathbf{T}$  is composed of two parts; an initial equilibrium stress that is assumed to be hydrostatic plus an elastic stress measured from this fiducial level (Rayleigh, 1906). Thus

$$\mathbf{T} = \mathbf{T}_e - p_0 \mathbf{J}, \quad \mathbf{T}_e = \lambda \mathbf{J} \operatorname{div} \mathbf{u} + \mu (\nabla \mathbf{u} + \mathbf{u} \nabla), \quad (24)$$

where  $p_0$  denotes the hydrostatic pressure.

2. Body forces are derived from a potential,  $\mathbf{F}_e = \operatorname{grad} \Phi'$ .  
 3. The values of  $\rho$  and  $\Phi'$  in the strained state are assumed to be equal to their equilibrium values  $\rho_0$  and  $\Phi_0$  plus a small perturbation caused by the motion (Pekeris and Jarosch, 1958).

4. The initial stress at a point  $(x, y, z)$  is taken equal to the value of the initial stress at the point where the particle, now at  $(x, y, z)$ , originated (Love, 1911, p. 89).

With these assumptions, the first-order vibration equations become

$$\begin{aligned} \nabla^2 \mathbf{u} + \operatorname{grad} \operatorname{div} \mathbf{u} + \frac{\dot{\mu}}{\mu} \left( 2 \frac{\partial \mathbf{u}}{\partial r} + \mathbf{e}_r \times \operatorname{rot} \mathbf{u} \right) + \frac{1}{\mu} \operatorname{grad} (\lambda \operatorname{div} \mathbf{u}) \\ + \frac{1}{\beta^2} \mathbf{W} + k_\beta^2 \mathbf{u} = 0, \quad (25) \end{aligned}$$

where

$$\mathbf{W} = \text{grad}(\Phi - g_0 u_r) + g_0 \mathbf{e}_r \cdot \text{div } \mathbf{u}, \quad x^2 = (\lambda + 2\mu) \rho_0, \quad \beta^2 = \mu \rho_0$$

and the dot signifies differentiation with respect to  $r$ .

The perturbation in the gravitational potential  $\Phi$  satisfies the equation

$$\nabla^2 \Phi = 4\pi G(\rho_0 \text{div } \mathbf{u} + \dot{\rho}_0 u_r), \quad (26)$$

where  $G$  denotes the constant of gravitation.

The boundary conditions are (Pekeris and Jarosch, 1958):

1. Regularity of the solution at the origin.
2. Vanishing of the stresses on the deformed surface of the Earth.
3. Equality at the deformed surface of the Earth, of the values of the internal and external gravitational potentials and of their respective derivatives.

## 2. Derivation of the Green's Tensor

To derive the Green's tensor for this problem we must solve the inhomogeneous vector equation

$$K(\mathbf{u}) = -(\mathbf{f}_0 / \mu)g(\omega)\delta(\mathbf{r} - \mathbf{r}_0), \quad (27)$$

where

$$K(\mathbf{u}) = L(\mathbf{u}) + \frac{1}{\mu} \text{grad}(\lambda \text{div } \mathbf{u}) + \text{grad div } \mathbf{u} + \frac{1}{\beta^2} \mathbf{W}, \quad (28)$$

$$L(\mathbf{u}) = \nabla^2 \mathbf{u} + \frac{\dot{\mu}}{\mu} \left( 2 \frac{\partial \mathbf{u}}{\partial r} + \mathbf{e}_r \times \text{rot } \mathbf{u} \right) + k_\beta^{-2} \mathbf{u}, \quad (29)$$

and  $\mathbf{f}_0$  is a localized force at  $\mathbf{r} = \mathbf{r}_0$  with spectrum  $g(\omega)$ . Let us split the total displacement field into two parts

$$\mathbf{u} = \mathbf{u}^s + \mathbf{u}^l$$

and require that

$$\mathbf{u}^l = \sum_{l=1}^{\infty} \sum_{m=-l}^l y_l(r) [l(l+1)]^{1/2} \mathbf{C}_{m,l}(\theta, \phi), \quad (30)$$

$$\mathbf{u}^s = \sum_{l=0,1}^{\infty} \sum_{m=-l}^l \{y_1(r)\mathbf{P}_{m,l} + y_3(r)[l(l+1)]^{1/2}\mathbf{B}_{m,l}(\theta, \phi)\}, \quad (31)$$

$$\Phi = \sum_{l=0}^{\infty} \sum_{m=-l}^l y_5(r)Y_{m,l}(\theta, \phi). \quad (32)$$

The corresponding stress vectors at level  $r$  can be calculated through Eq. (24). We find

$$(\mathbf{T} \cdot \mathbf{e}_r)_s = \sum_{l=1,0}^{\infty} \sum_{m=-l}^l \{y_2(r)\mathbf{P}_{m,l}(\theta, \phi) + y_4(r)[l(l+1)]^{1/2}\mathbf{B}_{m,l}(\theta, \phi)\}, \quad (33)$$

$$(\mathbf{T} \cdot \mathbf{e}_r)_t = \sum_{l=1}^{\infty} \sum_{m=-l}^l y_2^t(r)[l(l+1)]^{1/2}\mathbf{C}_{m,l}(\theta, \phi), \quad (34)$$

where

$$y_2 = (\lambda + 2\mu)\dot{y}_1 + (\lambda/r)[2y_1 - l(l+1)y_3], \quad (35)$$

$$y_4 = (\mu/r)[y_1 - y_3 + r\dot{y}_3], \quad (36)$$

$$y_2^t = [\dot{y}_1^t - (1/r)y_1^t]. \quad (37)$$

Clearly,  $\operatorname{div} \mathbf{u}_t = 0$  and  $(\mathbf{u}_t)_r = 0$ . Hence  $\mathbf{u}_t$  represents a tangential motion unaffected by gravity. Moreover, from Eq. (27)

$$L(\mathbf{u}^t) = -(\mathbf{f}_0/\mu)g(\omega)\delta(\mathbf{r} - \mathbf{r}_0), \quad (38)$$

$$K(\mathbf{u}^s) = -(\mathbf{f}_0/\mu)g(\omega)\delta(\mathbf{r} - \mathbf{r}_0), \quad (39)$$

which shows that the toroidal motion ( $\mathbf{u}_t$ ) is completely decoupled from the spheroidal motion ( $\mathbf{u}_s$ ). We shall, therefore, treat these cases separately keeping in mind that the total Green's tensor is the sum of  $\mathbf{G}^t$  and  $\mathbf{G}^s$ .

a. *Toroidal Field.* Singh and Ben-Menahem (1969a) obtained an explicit form of the toroidal Green's tensor at the free surface

$$\mathbf{G}^t(\mathbf{a}/\mathbf{r}_0; \omega) = \frac{g(\omega)}{a^2} \sum_{l=1}^{\infty} \sum_{m=-l}^l \frac{1}{\Omega_{m,l}} \frac{y_1(r_0)}{y_2(a)} \mathbf{C}_{m,l}^*(\theta_0, \phi_0) \mathbf{C}_{m,l}(\theta, \phi). \quad (40)$$

The superscript  $t$  (for toroidal) of  $y_1$  and  $y_2$  is understood.

Choosing the Heaviside step function as the time variation of the source, we find the inverse Fourier transform of the above expression and obtain the time-dependent Green's tensor. The integral over  $\omega$  can be evaluated as a sum of residues at the poles of the integrand, yielding

$$\mathbf{G}^t(\mathbf{a}/\mathbf{r}_0; t) = \mathbf{G}_{(0)}^t + 2 \sum_{l, m, n} \frac{1}{\Omega_{m, l}} \mathbf{C}_{m, l}^*(\theta_0, \phi_0) \mathbf{C}_{m, l}(\theta, \phi) \left\{ \frac{y_1(r_0)}{a^2 \omega \partial y_2 / \partial \omega} \right\} \cos(\omega t), \quad (41)$$

where  $\omega = {}_n\omega_l$  and use has been made of the fact that  $[y_1(r_0), y_2(a)]$  is even in  $\omega$ . By using a method of Sommerfeld (1949), it can be shown that, for  $\omega = {}_n\omega_l$ ,

$$a^2 \omega \frac{\partial y_2(a)}{\partial \omega} = - \frac{2\omega^2}{y_1(a)} \int_b^a \rho_0 r^2 y_1^2 dr, \quad (42)$$

where  $b$  is the lowest level which partakes in the toroidal motion.  $\mathbf{G}_{(0)}^t$  in Eq. (41) corresponds to the pole at the origin and represents the static response of the sphere.

Using Eq. (42), we have

$$\mathbf{G}^t(\mathbf{r}/\mathbf{r}_0; t) = \mathbf{G}_{(0)}^t - \sum_{l, m, n} \left\{ \frac{1}{l(l+1)\Omega_{m, l}} \frac{\mathbf{M}_{m, l}^+(\mathbf{r}_0) \mathbf{M}_{m, l}^+(\mathbf{r})}{\omega^2 \int_b^a \rho_0 r^2 y_1^2(r) dr} \right\} \cos(\omega t), \quad (43)$$

where  $\mathbf{M} = y_1(r)[l(l+1)]^{1/2} \mathbf{C}_{m, l}(\theta, \phi)$  is a generalization of the Hansen eigenvector for the homogeneous case (Table I). We next invoke the Volterra relation of Eq. (1) for a dislocation source at  $(r_0, 0, 0)$  and obtain the desired toroidal dynamic displacements in the form of a sum of infinite normal modes

$$\mathbf{u}_I(\mathbf{r}; t) = - \frac{\mu_0}{r_0} \Omega \sum_{l=2}^{\infty} \sum_n \left\{ \frac{2l+1}{l(l+1)} [l(l+1)]^{1/2} \mathbf{C}_{2, l}^c y_1(r_0) y_1(r) \right\} \frac{\cos \omega t}{\omega^2 I_1}, \quad (44)$$

$$\mathbf{u}_{II}(\mathbf{r}; t) = - \Omega \sum_{l=1}^{\infty} \sum_n \left\{ \frac{2l+1}{l(l+1)} [l(l+1)]^{1/2} \mathbf{C}_{1, l}^c y_2(r_0) y_1(r) \right\} \frac{\cos \omega t}{\omega^2 I_1}, \quad (45)$$

$$\mathbf{u}_{III}(\mathbf{r}; t) = - \frac{\mu_0}{r_0} \Omega \sum_{l=2}^{\infty} \sum_n \left\{ \frac{2l+1}{l(l+1)} [l(l+1)]^{1/2} \mathbf{C}_{2, l}^c \left( \phi - \frac{\pi}{4} \right) y_1(r_0) y_1(r) \right\} \frac{\cos \omega t}{\omega^2 I_1}, \quad (46)$$

where

$$\Omega = \frac{U_0 dS}{4\pi a^2}, \quad I_1 = \frac{1}{a^2} \int_b^a \rho_0 r^2 y_1^2 dr, \quad (47)$$

$$[l(l+1)]^{1/2} \mathbf{C}_{m,l}^c(\theta, \phi) = -m \sin m\phi \frac{P_l^m}{\sin \theta} \mathbf{e}_\theta - \cos m\phi \frac{\partial P_l^m}{\partial \theta} \mathbf{e}_\phi.$$

It may be noted that  $\mathbf{C}_{m,l}^c$  is obtained from  $\mathbf{C}_{m,l}$  of Table I by replacing  $e^{im\phi}$  by  $\cos m\phi$ . The subscripts I, II, and III in Eqs. (44)–(46) refer to Cases I, II, and III of Section II, C.

b. *Spheroidal Field.* The discussion of the spheroidal case is similar. Singh and Ben-Menahem (1969b) have shown that the normal mode spheroidal Green's tensor has the form

$$\mathbf{G}^s(\mathbf{r}/\mathbf{r}_0; t) = \mathbf{G}_{(0)}^s - \sum_{l,m,n} \frac{1}{\Omega_{m,l}} \left\{ \frac{\cos \omega t}{a^2 \omega^2 I_2} \overset{*}{\mathbf{Q}}_{m,l}(\mathbf{r}_0) \mathbf{Q}_{m,l}(\mathbf{r}) \right\}_{\omega=n\omega_l}, \quad (48)$$

where

$$\mathbf{Q}_{m,l}(\mathbf{r}) = y_1(r) \mathbf{P}_{m,l}(\theta, \phi) + y_3(r) [l(l+1)]^{1/2} \mathbf{B}_{m,l}(\theta, \phi). \quad (49)$$

$$I_2 = \frac{1}{a^2} \int_0^a \rho_0 r^2 [y_1^2 + l(l+1)y_3^2] dr. \quad (50)$$

As before, the Volterra relation is used to obtain the explicit form of the displacement field everywhere in the sphere. We find, for a point dislocation with step function time-dependence

$$\mathbf{u}_I = \frac{\Omega}{2} \sum_{l=2}^{\infty} \sum_n (2l+1) y_8(r_0) \frac{\cos \omega t}{\omega^2 I_2} \{ y_1(r) \mathbf{P}_{2,l}^s + y_3(r) [l(l+1)]^{1/2} \mathbf{B}_{2,l}^s \}, \quad (51)$$

$$\mathbf{u}_{II} = \Omega \sum_{l=1}^{\infty} \sum_n (2l+1) y_4(r_0) \frac{\cos \omega t}{\omega^2 I_2} \{ y_1(r) \mathbf{P}_{1,l}^s + y_3(r) [l(l+1)]^{1/2} \mathbf{B}_{1,l}^s \}, \quad (52)$$

$$\begin{aligned}
 \mathbf{u}_{\text{III}} = & -\frac{\Omega}{4} \sum_{l=0}^{\infty} \sum_n (2l+1) y_9(r_0) \frac{\cos \omega t}{\omega^2 I_2} \\
 & \times \left[ y_1(r) P_l(\cos \theta) \mathbf{e}_r + y_3(r) \frac{\partial}{\partial \theta} P_l(\cos \theta) \mathbf{e}_\theta \right] \\
 & + \frac{\Omega}{4} \sum_{l=2}^{\infty} \sum_n (2l+1) y_8(r_0) \frac{\cos \omega t}{\omega^2 I_2} \\
 & \times \left[ y_1(r) \mathbf{P}_{2,l}^s \left( \phi - \frac{\pi}{4} \right) + y_3(r) [l(l+1)]^{1/2} \mathbf{B}_{2,l}^s \left( \phi - \frac{\pi}{4} \right) \right], \quad (53)
 \end{aligned}$$

with

$$\mathbf{P}_{m,l}^s(\theta, \phi) = \sin m\phi P_l^m(\cos \theta) \mathbf{e}_r,$$

$$[l(l+1)]^{1/2} \mathbf{B}_{m,l}^s(\theta, \phi) = \sin m\phi \frac{\partial P_l^m}{\partial \theta} \mathbf{e}_\theta + m \cos m\phi \frac{P_l^m}{\sin \theta} \mathbf{e}_\phi, \quad (54)$$

$$y_8(r_0) = 2\mu_0 y_3(r_0) r_0, \quad (55)$$

$$y_9(r_0) = 2\mu_0 \left[ 2 \left( \frac{d}{dr_0} - \frac{1}{r_0} \right) y_1(r_0) + l(l+1) \frac{1}{r_0} y_3(r_0) \right]. \quad (56)$$

Here,  $\mathbf{P}_{m,l}^s$  and  $\mathbf{B}_{m,l}^s$  can be obtained from  $\mathbf{P}_{m,l}$  and  $\mathbf{B}_{m,l}$  respectively of Table I, by changing  $e^{im\phi}$  to  $\sin m\phi$ .

### 3. Transformation of the Equations of Motion

It has been shown by Alterman *et al.* (1959) that the four scalar equations (25) and (26) can be transformed to the following set of simultaneous, linear, first-order differential equations:

$$\dot{y}_i = \sum_{j=1}^6 c_{ij}(r) y_j, \quad i = 1, 2, \dots, 6, \quad (57)$$

$$\dot{y}_i^t = \sum_{j=1}^2 c_{ij}^t(r) y_j^t, \quad i = 1, 2, \quad (58)$$

where

$$y_6 = \dot{y}_5 - 4\pi G\rho_0 y_1, \quad (59)$$

and the nonzero elements of the matrices  $c_{ij}$  and  $c_{ij}^t$  are:

$$\begin{aligned}
 c_{11} &= -\frac{2\lambda}{(\lambda + 2\mu)r}, & c_{12} &= \frac{1}{\lambda + 2\mu}, \\
 c_{13} &= \frac{l(l+1)\lambda}{(\lambda + 2\mu)r}, & c_{21} &= -\omega^2\rho_0 + \frac{4\mu(3\lambda + 2\mu)}{(\lambda + 2\mu)r^2} - \frac{4\rho_0 g_0}{r}, \\
 c_{22} &= -\frac{4\mu}{(\lambda + 2\mu)r}, & c_{23} &= -l(l+1) \left[ \frac{2\mu(3\lambda + 2\mu)}{(\lambda + 2\mu)r^2} - \frac{\rho_0 g_0}{r} \right], \\
 c_{24} &= l(l+1)/r, & c_{26} &= -\rho_0, \\
 c_{31} &= -1/r, & c_{33} &= 1/r, \\
 c_{34} &= \frac{1}{\mu}, & c_{41} &= -\frac{2\mu(3\lambda + 2\mu)}{(\lambda + 2\mu)r^2} + \frac{\rho_0 g_0}{r}, \quad (60)
 \end{aligned}$$

$$\begin{aligned}
 c_{42} &= -\frac{\lambda}{(\lambda + 2\mu)r}, & c_{43} &= -\omega^2\rho_0 + \frac{4l(l+1)\mu(\lambda + \mu)}{(\lambda + 2\mu)r^2} - \frac{2\mu}{r^2}, \\
 c_{44} &= -3/r, & c_{45} &= -\rho_0/r, \\
 c_{51} &= 4\pi G\rho_0, & c_{56} &= 1, \\
 c_{63} &= -4\pi Gl(l+1)\rho_0/r, & c_{65} &= l(l+1)/r^2, & c_{66} &= -2/r; \\
 c_{11}^t &= 1/r, & c_{12}^t &= 1/\mu, \\
 c_{21}^t &= [l(l+1) - 2](\mu/r^2) - \omega^2\rho_0, & c_{22}^t &= -3/r. \quad (61)
 \end{aligned}$$

It may be noted that Eqs. (25) and (26) are not suitable for numerical solution, since one needs to evaluate the derivative of the empirically determined quantities  $\mu(r)$ ,  $\lambda(r)$ , and  $\rho_0(r)$ . The derived Eqs. (57) and (58) are free from this defect.

In terms of the  $y$ 's, the boundary conditions at the Earth's surface are

$$y_2 = y_4 = y_6 + [(l+1)/r]y_5 = 0, \quad \text{at } r = a; \quad (62)$$

$$y_2^t = 0, \quad \text{at } r = a. \quad (63)$$

Equations (57) and (58) are to be used for the mantle. In the liquid core,  $\mu = 0$  and so  $y_4 = 0$ . Therefore, Eq. (57) is replaced by

$$\dot{y}_i = \sum_{j=1, 2, 3, 5, 6} c_{ij}(r)y_j, \quad i = 1, 2, 5, 6, \quad (64)$$

$$y_3 = \frac{1}{r\omega^2} \left( g_0 y_1 - \frac{y_2}{\rho_0} - y_5 \right), \quad (65)$$

where  $c_{ij}$  are given by Eq. (60) with  $\mu = 0$ . Moreover, there is no toroidal motion in the liquid core, so that Eq. (58) is no more required.

#### 4. Dimensionless Form

a. *Toroidal*. We introduce the dimensionless variables and parameters

$$\begin{aligned} \bar{t} &= r_0/a, & \bar{r} &= r/a, & \bar{\tau} &= b/a, & \bar{\mu} &= \mu/\mu_r, \\ \bar{\rho}_0 &= \rho_0/\rho_r, & \bar{\omega} &= \omega/\omega_r, & \bar{\Omega} &= \Omega/a, & \omega_r &= (1/a)(\mu_r/\rho_r)^{1/2} \end{aligned} \quad (66)$$

(in which  $\mu_r$ ,  $\rho_r$  are reference values for rigidity and density, respectively) together with the radial functions

$$\begin{aligned} \bar{I}_1 &= \int_{\bar{r}}^1 \bar{\rho}_0 \bar{r}^2 \left[ \frac{y_1(\bar{r})}{y_1(1)} \right]^2 d\bar{r}, \\ \hat{y}_2(\bar{r}) &= \frac{a}{\mu_r} y_2 = \bar{\mu} \left[ \frac{dy_1}{d\bar{r}} - \frac{y_1}{\bar{r}} \right], \\ G_1(\bar{t}) &= \frac{\bar{\mu}_0}{\bar{t}} \frac{2l+1}{l(l+1)} \frac{1}{\bar{I}_1 \bar{\omega}^2} \left[ \frac{y_1(\bar{t})}{y_1(1)} \right], \\ G_2(\bar{t}) &= \frac{2l+1}{l(l+1)} \frac{1}{\bar{I}_1 \bar{\omega}^2} \left[ \frac{\hat{y}_2(\bar{t})}{y_1(1)} \right]. \end{aligned} \quad (67)$$

We then rewrite Eqs. (44)–(46) in the dimensionless form:

$$\begin{aligned} \mathbf{u}_1 &= \Omega \sum_{l=2}^{\infty} \sum_n G_1 [H_1 \sin 2\phi \mathbf{e}_\theta + H_2 \cos 2\phi \mathbf{e}_\phi] \cos(\omega t), \\ \mathbf{u}_2 &= \Omega \sum_{l=1}^{\infty} \sum_n G_2 [H_3 \sin \phi \mathbf{e}_\theta + H_4 \cos \phi \mathbf{e}_\phi] \cos(\omega t), \\ \mathbf{u}_3 &= \frac{1}{2} \Omega \sum_{l=2}^{\infty} \sum_n G_1 [-H_1 \cos 2\phi \mathbf{e}_\theta + H_2 \sin 2\phi \mathbf{e}_\phi] \cos(\omega t), \end{aligned} \quad (68)$$

where  $\omega$  stands for  $\omega_l$  and

$$\begin{aligned} H_1 &= 2P_l^2(\cos \theta) \sin \theta, & H_2 &= (\partial/\partial \theta) P_l^2(\cos \theta), \\ H_3 &= P_l^1(\cos \theta)/\sin \theta, & H_4 &= (\partial/\partial \theta) P_l^1(\cos \theta), \\ H_5 &= [2H_2 - H_1 \cos \theta] \sin \theta, \\ H_6 &= \{[8 - l(l+1) \sin^2 \theta]H_1 - 4H_2 \cos \theta\}/(2 \sin \theta). \end{aligned} \quad (69)$$

Thus, we obtain a compact set of equations for the toroidal displacements and strains for the three fundamental shear dislocations. We write them below in the component form.

Case I ( $\lambda = 0, \delta = 90^\circ$ ) ( $l \geq 2$ )

$$\begin{aligned} u_\theta &= \Omega G_1 H_1 \sin 2\phi \cos(\omega t), \\ u_\phi &= \Omega G_1 H_2 \cos 2\phi \cos(\omega t), \\ \varepsilon_{\theta\theta} &= -\varepsilon_{\phi\phi} = \bar{\Omega} G_1 H_5 \sin 2\phi \cos(\omega t), \\ \varepsilon_{\theta\phi} &= \bar{\Omega} G_1 H_6 \cos 2\phi \cos(\omega t). \end{aligned} \quad (70)$$

Case II ( $\lambda = 90^\circ, \delta = 90^\circ$ ) ( $l \geq 1$ )

$$\begin{aligned} u_\theta &= \Omega G_2 H_3 \sin \phi \cos(\omega t), \\ u_\phi &= \Omega G_2 H_4 \cos \phi \cos(\omega t), \\ \varepsilon_{\phi\phi} &= -\varepsilon_{\theta\theta} = \frac{1}{2} \bar{\Omega} G_2 H_1 \sin \phi \cos(\omega t), \\ \varepsilon_{\theta\phi} &= -\bar{\Omega} G_2 H_2 \cos \phi \cos(\omega t). \end{aligned} \quad (71)$$

Case III ( $\lambda = 90^\circ, \delta = 45^\circ$ ) ( $l \geq 2$ )

$$\begin{aligned} u_\theta &= -\frac{1}{2} \Omega G_1 H_1 \cos 2\phi \cos(\omega t), \\ u_\phi &= \frac{1}{2} \Omega G_1 H_2 \sin 2\phi \cos(\omega t), \\ \varepsilon_{\theta\theta} &= -\varepsilon_{\phi\phi} = -\frac{1}{2} \bar{\Omega} G_1 H_5 \cos 2\phi \cos(\omega t), \\ \varepsilon_{\theta\phi} &= \frac{1}{2} \bar{\Omega} G_1 H_6 \sin 2\phi \cos(\omega t). \end{aligned} \quad (72)$$

Summation over all permissible  $l$  and  $n$  values is understood. The functions  $\varepsilon_{\theta\theta}$ ,  $\varepsilon_{\phi\phi}$ , and  $\varepsilon_{\theta\phi}$  are the colatitudinal, azimuthal, and shear strains, respectively.

b. *Spheroidal*. We introduce the following dimensionless variables and parameters in addition to those already introduced in Eq. (66)

$$\begin{aligned} \ell &= \lambda \mu_r, & \tilde{g}_0 &= g_0 g_r, & \bar{G} &= G/G_r, & g_r &= \mu_r a \rho_r, & G_r &= \mu_r (a^2 \rho_r^2), \end{aligned} \quad (73)$$

and define

$$\begin{aligned}\hat{y}_2(\bar{r}) &= \frac{a}{\mu_r} y_2 = \frac{\lambda}{\bar{r}} [2y_1(\bar{r}) - l(l+1)y_3(\bar{r})] + (\lambda + 2\bar{\mu}) \frac{dy_1(\bar{r})}{d\bar{r}}, \\ \hat{y}_4(\bar{r}) &= \frac{a}{\mu_r} y_4 = \bar{\mu} \left[ \frac{dy_3(\bar{r})}{d\bar{r}} - \frac{y_3(\bar{r})}{\bar{r}} + \frac{y_1(\bar{r})}{\bar{r}} \right], \\ \hat{y}_8(\bar{t}) &= 2\bar{\mu}_0 y_3(\bar{t})/\bar{t}, \\ \hat{y}_9(\bar{t}) &= \frac{2\bar{\mu}_0}{\bar{t}} \left( \frac{3\lambda_0 + 2\bar{\mu}_0}{\lambda_0 + 2\bar{\mu}_0} \right) [l(l+1)y_3(\bar{t}) - 2y_1(\bar{t})] + \frac{4\bar{\mu}_0}{(\lambda_0 + 2\bar{\mu}_0)} \hat{y}_2(\bar{t}).\end{aligned}\quad (74)$$

We next define the dimensionless functions

$$\begin{aligned}F_1 &= \frac{1}{2} \frac{2l+1}{\bar{\omega}^2 \bar{I}_2} \frac{\hat{y}_8(\bar{t})}{y_1(1)}, & F_2 &= F_1 \frac{y_3(\bar{t})}{y_1(1)}, \\ F_3 &= \frac{2l+1}{\bar{\omega}^2 \bar{I}_2} \frac{\hat{y}_4(\bar{t})}{y_1(1)}, & F_4 &= F_3 \frac{y_3(\bar{t})}{y_1(1)}, \\ F_5 &= -\frac{1}{4} \frac{2l+1}{\bar{\omega}^2 \bar{I}_2} \frac{\hat{y}_9(\bar{t})}{y_1(1)}, & F_6 &= F_5 \frac{y_3(\bar{t})}{y_1(1)}, \\ \bar{I}_2 &= \int_0^1 \bar{\rho}_0 \bar{r}^2 \left\{ \left[ \frac{y_1(\bar{r})}{y_1(1)} \right]^2 + l(l+1) \left[ \frac{y_3(\bar{r})}{y_1(1)} \right]^2 \right\} d\bar{r},\end{aligned}\quad (75)$$

and the colatitude functions

$$\begin{aligned}H_7 &= P_l^2(\cos \theta), & H_8 &= P_l^1(\cos \theta), & H_9 &= P_l(\cos \theta), \\ H_{10} &= \frac{[4 - l(l+1) \sin^2 \theta] H_1 - 2H_2 \cos \theta}{2 \sin \theta} = \frac{\partial^2 P_l^2}{\partial \theta^2}, \\ H_{11} &= \frac{[1 - l(l+1) \sin^2 \theta] H_3 - H_4 \cos \theta}{\sin \theta} = \frac{\partial^2 P_l^1}{\partial \theta^2}, \\ H_{12} &= H_4 \cot \theta - H_3 / \sin \theta.\end{aligned}\quad (76)$$

The resulting displacements and strains in terms of the radial functions  $F_i$  and the angle functions  $H_i$  are given by Eqs. (77) to (79).

## Case I

$$\begin{aligned}
 u_r &= \Omega F_1 H_7 \sin 2\phi \cos(\omega t), \\
 u_\theta &= \Omega F_2 H_2 \sin 2\phi \cos(\omega t), \\
 u_\phi &= \Omega F_2 H_1 \cos 2\phi \cos(\omega t), \\
 \varepsilon_{\theta\theta} &= \bar{\Omega} \sin 2\phi [F_1 H_7 + F_2 H_{10}] \cos(\omega t), \\
 \varepsilon_{\phi\phi} &= \bar{\Omega} \sin 2\phi [F_1 H_7 + F_2 (H_{10} - H_6)] \cos(\omega t), \\
 \varepsilon_{\theta\phi} &= 2\bar{\Omega} \cos 2\phi [F_2 H_5] \cos(\omega t), \\
 \varepsilon_{rr} &= \bar{\Omega} [\sigma/(1 - \sigma)] \sin 2\phi H_7 \{l(l+1)F_2 - 2F_1\} \cos(\omega t).
 \end{aligned} \tag{77}$$

## Case II

$$\begin{aligned}
 u_r &= \Omega F_3 H_8 \sin \phi \cos(\omega t), \\
 u_\theta &= \Omega F_4 H_4 \sin \phi \cos(\omega t), \\
 u_\phi &= \Omega F_4 H_3 \cos \phi \cos(\omega t), \\
 \varepsilon_{\theta\theta} &= \bar{\Omega} \sin \phi [F_3 H_8 + F_4 H_{11}] \cos(\omega t), \\
 \varepsilon_{\theta\phi} &= -\bar{\Omega} \cos \phi [F_4 H_1] \cos(\omega t), \\
 \varepsilon_{\phi\phi} &= \bar{\Omega} \sin \phi [F_3 H_8 + F_4 H_{12}] \cos(\omega t), \\
 \varepsilon_{rr} &= [\sigma/(1 - \sigma)] \bar{\Omega} \sin \phi H_8 \{l(l+1)F_4 - 2F_3\} \cos(\omega t).
 \end{aligned} \tag{78}$$

## Case III

$$\begin{aligned}
 u_r &= \frac{1}{2}\Omega [2F_5 H_9 - F_1 H_7 \cos 2\phi] \cos(\omega t), \\
 u_\theta &= -\frac{1}{2}\Omega [2F_6 H_8 + F_2 H_2 \cos 2\phi] \cos(\omega t), \\
 u_\phi &= \frac{1}{2}\Omega F_2 H_1 \sin 2\phi \cos(\omega t), \\
 \varepsilon_{\theta\theta} &= \frac{1}{2}\bar{\Omega} [2(F_5 H_9 - F_6 H_4) - \cos 2\phi (F_1 H_7 + F_2 H_{10})] \cos(\omega t), \\
 \varepsilon_{\phi\phi} &= \frac{1}{2}\bar{\Omega} [-2(H_7 + H_4)F_6 + 2F_5 H_9 \\
 &\quad - \{F_1 H_7 + F_2 (H_{10} - H_6)\} \cos 2\phi] \cos(\omega t), \\
 \varepsilon_{\theta\phi} &= \bar{\Omega} \sin 2\phi (F_2 H_5) \cos(\omega t), \\
 \varepsilon_{rr} &= -[\sigma/(1 - \sigma)] \frac{1}{2}\bar{\Omega} \{2[2F_5 - l(l+1)F_6]H_9 \\
 &\quad - \cos 2\phi H_7 [2F_1 - l(l+1)F_2]\} \cos(\omega t).
 \end{aligned} \tag{79}$$

## E. SURFACE-WAVE THEORY

### 1. Watson's Transformation of the Spectral Field

A partial field of the normal mode solution can be interpreted as waves, known as surface waves, whose energy flux is parallel to the surface of the earth. To achieve this objective we must return to Eqs. (1), (40), and (43), and derive through it the displacements for the spectral excitation  $g(\omega)e^{i\omega t}$ . Let us demonstrate this for a particular case, say, the toroidal displacements for Case I. The response of the sphere for this case is found to be equal to

$$\mathbf{u}_l^t(a; \omega) = g(\omega)\Omega \frac{\mu_0}{r_0} e^{i\omega t} \sum_{l=2}^{\infty} \frac{(2l+1)}{l(l+1)} \left[ \frac{y_1(r_0, \omega; l)}{y_2(a, \omega; l)} \right] [l(l+1)]^{1/2} C_{2,l}^c(\theta, \phi). \quad (80)$$

Note that Eq. (44) is obtained from Eq. (80) by taking its inverse Fourier transform and calculating the residues at the poles. Let  $v_j$  be a real zero of  $y_2(a, \omega; l) = 0$ , for a fixed value of  $\omega \neq {}_n\omega_l$  ( ${}_n\omega_l$  is a root of the same equation for fixed value of  $l$ ). Applying to the right-hand side of Eq. (80) the transformation of Watson (1918), we find

$$\begin{aligned} \mathbf{u}_l^t(a; \omega) = & -\Omega \frac{\mu_0}{r_0} g(\omega) e^{i\omega t} \sum_{v=0}^{\infty} \left\{ \pi \frac{2v+1}{v(v+1)} \frac{1}{\cos \pi(v+\frac{1}{2})} \left[ \frac{y_1(r_0, \omega; v)}{(\partial/\partial v) y_2(a, \omega; v)} \right] \right. \\ & \times \left. \left[ 2 \sin 2\phi \frac{P_v^2(-\cos \theta)}{\sin \theta} \mathbf{e}_\theta + \cos 2\phi \frac{\partial P_v^2(-\cos \theta)}{\partial \theta} \mathbf{e}_\phi \right] \right\}_{v=v_j} \\ & + \text{a line integral}. \end{aligned} \quad (81)$$

Approximate evaluation of the line integral leads eventually to body waves (rays) which are not relevant to the present discussion. Furthermore, we shall confine ourselves only to the displacements which are associated with large roots. Thus, for  $v_j \gg 1$  and for values of  $\theta$  which are sufficiently removed from the pole and the antipode, we use the expansions

$$\begin{aligned} \frac{1}{\cos \pi(v+\frac{1}{2})} &= 2 \sum_{n=0}^{\infty} (-)^n \exp[-(2n+1)(v+\frac{1}{2})\pi i], \\ P_v^2[\cos(\pi-\theta)] &= \frac{-v^2}{(2\pi v \sin \theta)^{1/2}} (\exp\{i[(v+\frac{1}{2})(\pi-\theta)-\frac{1}{4}\pi]\}) \\ &+ \exp\{-i[(v+\frac{1}{2})(\pi-\theta)-\frac{1}{4}\pi]\} + O(v^{-1}). \end{aligned} \quad (82)$$

Let  $\Delta = a\theta$  and define a parameter  $k_L$  through the relation  $v + \frac{1}{2} = k_L a$ . One then obtains from Eq. (82)

$$\begin{aligned} & \left( -\frac{2\pi}{v} \right) \frac{e^{i\omega t}}{\cos \pi(v + \frac{1}{2})} \cdot \frac{\partial P_v^2[\cos(\pi - \theta)]}{\partial \theta} \\ &= v^{3/2} \left[ \frac{8\pi}{\sin(\Delta/a)} \right]^{1/2} e^{-3\pi i/4} \left[ \left( \sum_{n=0}^{\infty} e^{is_1} + \sum_{n=0}^{\infty} e^{is_2} \right) + O(v^{-1}) \right], \quad (83) \end{aligned}$$

where

$$s_1 = \omega t - k_L \Delta - k_L (2\pi n a) + n\pi, \quad (84)$$

$$s_2 = \omega t - k_L (2\pi a - \Delta) - k_L (2\pi n a) + (n + \frac{1}{2})\pi + \pi.$$

Note that  $s_1$  is the phase of a wave that traveled on the spherical surface along the minor arc ( $n = 0$ ) and continued on its way to complete one revolution ( $n = 1$ ), two revolutions ( $n = 2$ ), etc. The corresponding waves are known in seismology as  $G_1$ ,  $G_3$ ,  $G_5$ , etc. On the other hand,  $s_2$  is the phase of a wave that left the source in the opposite direction and reached the observer via the major arc ( $n = 0$ ). These waves are known in seismology as  $G_2$ ,  $G_4$ ,  $G_6$ , etc. Thus, for large values of  $l = v_j$  the eigen vibrations are decomposed into two systems of waves that travel in opposite directions. The parameter  $k_L$  plays the role of the wavenumber and is equal to  $\omega C_L$  where  $C_L$  is the phase velocity. Equation (84) reveals another interesting phenomenon. First, we note that waves of type  $s_2$  have advanced their phase by  $\pi$  with respect to waves of type  $s_1$  due to a change of polarity. When this difference is equalized, there still is a phase shift of  $n\pi$  for  $s_1$  and  $(n + \frac{1}{2})\pi$  for  $s_2$ . This is the phenomenon of "polar phase-shift" caused by sphericity (Brune, 1961) according to which each polar or antipodal crossing advances the phase by  $\pi/2$ .

Substituting Eq. (83) into Eq. (81) and keeping only the first arrival ( $n = 0$ ) along the minor arc for a step function source excitation [ $g(\omega) = 1(i\omega)$ ], we have

$$\begin{aligned} \mathbf{u}_L^t(\omega) &= \mathbf{e}_\phi \frac{\Omega}{\omega} \frac{\cos 2\phi}{[\sin(\Delta/a)]^{1/2}} \left( \frac{y_1(r_0; v)/r_0}{\partial y_2(a; v)/\mu_0 \partial v} \right)_{v=k_L a} \\ &\times [(k_L a)^{3/2} (8\pi)^{1/2}] \exp[i(\omega t - k_L \Delta + \frac{3}{4}\pi)]. \quad (85) \end{aligned}$$

Expressions similar to Eq. (85) can be obtained for Love and Rayleigh waves due to the three fundamental sources.

Amplitude calculations of surface waves in spherical Earth models have not yet been attempted for reasons which depend on the form and content of the amplitude term in Eq. (85) and the similar equations for the other cases. If, however, we restrict ourselves to source studies from spectra of surface waves in the period range 350–50 sec ( $l = 20\text{--}150$ ), we may do away with the sphericity altogether and solve, instead, the problem of surface wave propagation in a multilayered half-space. Indeed, Biswas and Knopoff (1970) have shown that the correction in the group velocity in neglecting the sphericity is not higher than one percent for Love waves in the above period range.

It can be shown that as we increase the radius of the sphere to infinity while keeping  $a - r_0 = h$  constant, the right-hand side of Eq. (85) becomes identical with the corresponding expression for Love waves in a vertically heterogeneous half-space.

We shall present next the method by which the spectral amplitudes of Love and Rayleigh waves are evaluated for a multilayered half-space.

## 2. Spectral Response of a Multilayered Half-Space

In the usual treatment of the dispersion of Rayleigh waves in a multilayered half-space consisting of  $p$  layers, the dependence of phase velocity on wavelength is expressed by the vanishing of a certain determinant of order  $4p - 2$ . Similarly, in the case of Love waves, the dispersion equation is obtained by equating to zero a certain determinant of order  $2p - 1$ . The computational labor involved in determining the roots of these determinants is formidable for values of  $p$  greater than 2 in the case of Rayleigh waves and for larger values of  $p$  for Love waves.

To overcome this difficulty, Haskell (1953) formulated the problem of the dispersion of surface waves in terms of matrices following a method of Thomson (1950). This formulation proved very useful when high speed computers were introduced in the early fifties. Dorman *et al.* (1960) utilized this scheme in the calculation of surface wave dispersion in multilayered elastic media. Since then many papers on the subject have appeared in the literature suggesting various modifications and improvements in the method.

The dispersion of surface waves is independent of the source depth. But in order to study the effect of source location on the amplitudes of surface waves, it is necessary to include a source at depth in the multilayered formulation of Haskell (1953). Haskell (1964) and Harkrider (1964) derived integral solutions for some point sources in a multilayered semi-infinite medium. From the residue contribution of the integral solutions, they obtained the Rayleigh and Love wave spectral displacements. Ben-Menahem and Harkrider (1964) computed radiation patterns of surface waves from buried dipolar sources in a flat stratified Earth. They demonstrated that the radiation pattern

may depend strongly on the depth of the source. Ben-Menahem *et al.* (1970) and Harkrider (1970) produced extensive tables for spectral displacements of seismic surface waves from shear dislocations in a flat stratified Earth for various modes, periods, source depths, and Earth models.

The present method of finding the spectral amplitudes of Rayleigh and Love waves due to a point dislocation in a multilayered half-space is similar to the treatment of Haskell (1964). Explicit expressions for the far-field spectral surface displacements for an arbitrary shear dislocation are obtained.

a. *Basic Equations.* Consider a semi-infinite elastic medium consisting of  $p - 1$  parallel, homogeneous, isotropic layers lying over a half-space. The layers are numbered serially, the layer at the top being layer 1 and the half-space layer  $p$ . We place the origin of a cylindrical coordinate system  $(\rho, \phi, z)$  at the free surface and the  $z$  axis is drawn into the medium. The  $n$ th layer is of thickness  $d_n$  and is bounded by the planes  $z = z_{n-1}, z_n$ . Other parameters for this layer are

$$\lambda_n, \mu_n = \text{Lamé parameters,}$$

$$\alpha_n, \beta_n = \text{wave velocities,}$$

$$\begin{aligned} k_{\alpha_n} &= \omega/\alpha_n, & k_{\beta_n} &= \omega/\beta_n, \\ v_n &= (k^2 - k_{\alpha_n}^2)^{1/2}, & k > k_{\alpha_n}, \\ &= i(k_{\alpha_n}^2 - k^2)^{1/2}, & k < k_{\alpha_n}, \\ v_n' &= (k^2 - k_{\beta_n}^2)^{1/2}, & k > k_{\beta_n}, \\ &= i(k_{\beta_n}^2 - k^2)^{1/2}, & k < k_{\beta_n}, \\ \Omega_n &= k^2 - \frac{1}{2}k_{\beta_n}^2. \end{aligned} \quad (86)$$

Let  $\mathbf{u}_n$  denote the displacement at any point in the  $n$ th layer and  $(\mathbf{T}_n \cdot \mathbf{e}_z)$  the corresponding stress vector across a plane  $z = \text{const.}$  in that layer. Assume

$$\mathbf{u}_n = \sum_m \int_0^\infty \mathbf{u}_{nm}(k) k dk, \quad (87)$$

$$\mathbf{T}_n \cdot \mathbf{e}_z = \sum_m \int_0^\infty \mathbf{T}_{nm}(k) k dk. \quad (88)$$

It may be shown that  $\mathbf{u}_{nm}$  and  $\mathbf{T}_{nm}$  are of the form

$$\mathbf{u}_{nm} = \mathbf{u}_{nm}^R + \mathbf{u}_{nm}^L, \quad (89)$$

$$\mathbf{T}_{nm} = \mathbf{T}_{nm}^R + \mathbf{T}_{nm}^L, \quad (90)$$

where

$$\mathbf{u}_{nm}^R = x_{nm} \mathbf{P}_m + y_{nm} \mathbf{B}_m, \quad (91)$$

$$\mathbf{T}_{nm}^R = X_{nm} \mathbf{P}_m + Y_{nm} \mathbf{B}_m, \quad (92)$$

$$\mathbf{u}_{nm}^L = z_{nm} \mathbf{C}_m, \quad (93)$$

$$\mathbf{T}_{nm}^L = Z_{nm} \mathbf{C}_m. \quad (94)$$

The vector cylindrical harmonics  $\mathbf{P}_m$ ,  $\mathbf{B}_m$ , and  $\mathbf{C}_m$  are defined in Table I and

$$x_{nm} = v_n [-A'_{nm} e^{-v_n z} + A''_{nm} e^{v_n z}] + k[B'_{nm} e^{-v_n' z} + B''_{nm} e^{v_n' z}], \quad (95)$$

$$y_{nm} = k[A'_{nm} e^{-v_n z} + A''_{nm} e^{v_n z}] + v_n' [-B'_{nm} e^{-v_n' z} + B''_{nm} e^{v_n' z}], \quad (96)$$

$$X_{nm} = 2\mu_n [\Omega_n \{A'_{nm} e^{-v_n z} + A''_{nm} e^{v_n z}\} - kv_n' \{B'_{nm} e^{-v_n' z} - B''_{nm} e^{v_n' z}\}], \quad (97)$$

$$Y_{nm} = 2\mu_n [-kv_n \{A'_{nm} e^{-v_n z} - A''_{nm} e^{v_n z}\} + \Omega_n \{B'_{nm} e^{-v_n' z} + B''_{nm} e^{v_n' z}\}], \quad (98)$$

$$z_{nm} = [C'_{nm} e^{-v_n' z} + C''_{nm} e^{v_n' z}], \quad (99)$$

$$Z_{nm} = -\mu_n v_n' [C'_{nm} e^{-v_n' z} - C''_{nm} e^{v_n' z}]. \quad (100)$$

In the above equations  $A'_{nm}$ , etc., are arbitrary constants.

Equations (91) and (92) correspond to the problem of Rayleigh waves and Eqs. (93) and (94) to that of Love waves. We shall distinguish the quantities related to the Love wave problem by attaching the superscript L to them.

b. *Rayleigh Waves.* Let

$$\begin{aligned} a'_{nm} &= A'_{nm} e^{-v_n z_{n-1}} + A''_{nm} e^{v_n z_{n-1}}, \\ a''_{nm} &= -A'_{nm} e^{-v_n z_{n-1}} + A''_{nm} e^{v_n z_{n-1}}, \end{aligned} \quad (101)$$

and similar expressions for  $b'_{nm}$ ,  $b''_{nm}$ . We define column vectors

$$\begin{aligned} [A_{nm}] &= [x_{nm}, y_{nm}, X_{nm}, Y_{nm}], \\ [K_{nm}] &= [a'_{nm}, a''_{nm}, b'_{nm}, b''_{nm}]. \end{aligned} \quad (102)$$

It may be shown that

$$[A_{nm}(z_{n-1})] = [Z_n(z_{n-1})][K_{nm}], \quad (103)$$

$$[A_{nm}(z_n)] = [A_n][A_{n-1,m}(z_{n-1})], \quad (104)$$

where

$$[Z_n(z_{n-1})] = \begin{bmatrix} 0 & v_n & 1 & 0 \\ k & 0 & 0 & v'_n \\ 2\mu_n \Omega_n & 0 & 0 & 2k\mu_n v_n' \\ 0 & 2k\mu_n v_n & 2\mu_n \Omega_n & 0 \end{bmatrix}, \quad (105)$$

$$[A_n] = (1/k\beta_n^2)[B_n], \quad (106)$$

and the elements of the matrix  $[B_n]$  are given below

$$(11) = -2\Omega_n C_{\alpha_n} + 2k^2 C_{\beta_n},$$

$$(12) = 2kv_n S_{\alpha_n} - \frac{2k\Omega_n}{v_n'} S_{\beta_n},$$

$$(13) = -\frac{v_n}{\mu_n} S_{\alpha_n} + \frac{k^2}{\mu_n v_n'} S_{\beta_n},$$

$$(14) = \frac{k}{\mu_n} [C_{\alpha_n} - C_{\beta_n}],$$

$$(21) = -\frac{2k\Omega_n}{v_n} S_{\alpha_n} + 2kv_n' S_{\beta_n},$$

$$(22) = 2k^2 C_{\alpha_n} - 2\Omega_n C_{\beta_n}, \quad (107)$$

$$(23) = -(14),$$

$$(24) = \frac{k^2}{\mu_n v_n} S_{\alpha_n} - \frac{v_n'}{\mu_n} S_{\beta_n},$$

$$(31) = -\frac{4\mu_n \Omega_n^2}{v_n} S_{\alpha_n} + 4k^2 \mu_n v_n' S_{\beta_n},$$

$$(32) = 4k\mu_n \Omega_n (C_{\alpha_n} - C_{\beta_n}),$$

$$(33) = (11),$$

$$(34) = -(21),$$

$$(41) = -(32),$$

$$(42) = 4k^2 \mu_n v_n S_{\alpha_n} - \frac{4\mu_n \Omega_n^2}{v_n'} S_{\beta_n},$$

$$(43) = -(12),$$

$$(44) = (22),$$

in which

$$\begin{aligned} C_{\alpha_n} &= \cosh v_n d_n, & S_{\alpha_n} &= \sinh v_n d_n, \\ C_{\beta_n} &= \cosh v_n' d_n, & S_{\beta_n} &= \sinh v_n' d_n. \end{aligned} \quad (108)$$

Let a point source be placed on the  $z$  axis at a depth  $h$  below the free surface. Let the source layer be designated as layer  $s$ . We divide the source layer into two sublayers;  $s_1(z_{s-1} \leq z \leq z_{s_1})$  and  $s_2(z_{s_1} \leq z \leq z_{s_2})$ .

We use the following representation of the point source

$$[A_{s_2m}(z_{s_1})] - [A_{s_1m}(z_{s_1})] = [D_m]. \quad (109)$$

For a given source,  $[D_m]$  is known. The relation

$$[A_{n-1,m}(z_{n-1})] = [A_{n,m}(z_{n-1})], \quad (110)$$

expresses the fact that the displacements and stresses are continuous across the interface  $z = z_{n-1}$ . Equation (104) then gives

$$[A_{pm}(z_{p-1})] = [A_{p-1}][A_{p-2}] \cdots [A_{s+1}][A_{s_2}][A_{s_2m}(z_{s_1})], \quad (111)$$

$$[A_{s_1m}(z_{s_1})] = [A_{s_1}][A_{s-1}] \cdots [A_2][A_1][A_{1m}(0)]. \quad (112)$$

Next, Eqs. (109)–(112) yield

$$[A_{pm}(z_{p-1})] = [U][A_{1m}(0)] + [V][D_m], \quad (113)$$

where

$$\begin{aligned} [U] &= [A_{p-1}][A_{p-2}] \cdots [A_1], \\ [V] &= [A_{p-1}][A_{p-2}] \cdots [A_{s+1}][A_{s_2}]. \end{aligned} \quad (114)$$

If the free surface is regarded as stress free, we have

$$[A_{1m}(0)] = [x_{1m}(0), y_{1m}(0), 0, 0]. \quad (115)$$

The radiation condition requires that in the half-space (layer  $p$ )  $A''_{pm} = B''_{pm} = 0$ . Hence, from Eqs. (101)–(103), (113), and (115), we get

$$[Z_p(z_{p-1})](a'_{pm}, -a'_{pm}, b'_{pm}, -b'_{pm}) = [U][x_{1m}(0), y_{1m}(0), 0, 0] + [F_m], \quad (116)$$

where

$$[F_m] = [V][D_m]. \quad (117)$$

Equation (116) may be written as

$$[a'_{pm}, -a'_{pm}, b'_{pm}, -b'_{pm}] = [J][x_{1m}(0), y_{1m}(0), 0, 0] + [S_m], \quad (118)$$

where

$$\begin{aligned} [J] &= [Z_p(z_{p-1})]^{-1}[U], \\ [S_m] &= [Z_p(z_{p-1})]^{-1}[F_m]. \end{aligned} \quad (119)$$

Eliminating  $a'_{pm}$ ,  $b'_{pm}$  from Eq. (118), we obtain

$$x_{1m}(0) = -[\Delta_1(G_m)_1 - \Delta_2(G_m)_2]/\Delta^R, \quad (120)$$

$$y_{1m}(0) = [\Delta_3(G_m)_1 - \Delta_4(G_m)_2]/\Delta^R, \quad (121)$$

where

$$\begin{aligned} \Delta^R &= \Delta_1\Delta_4 - \Delta_2\Delta_3, \\ \Delta_1 &= J_{32} + J_{42}, \quad \Delta_2 = J_{12} + J_{22}, \\ \Delta_3 &= J_{31} + J_{41}, \quad \Delta_4 = J_{11} + J_{21}, \\ (G_m)_1 &= (S_m)_1 + (S_m)_2, \quad (G_m)_2 = (S_m)_3 + (S_m)_4. \end{aligned} \quad (122)$$

Using the definitions of the vectors  $\mathbf{P}_m$  and  $\mathbf{B}_m$  (Table I), we get the following expressions for the cylindrical components of the displacement at the free surface:

$$\begin{aligned} u_\rho(0) &= \sum_m \int_0^\infty \frac{1}{\Delta^R} [\Delta_3(G_m)_1 - \Delta_4(G_m)_2] \left[ J_{m-1}(k\rho) - \frac{m}{k\rho} J_m(k\rho) \right] k dk e^{im\phi}, \\ u_\phi(0) &= \sum_m \int_0^\infty \frac{1}{\Delta^R} [\Delta_3(G_m)_1 - \Delta_4(G_m)_2] \frac{im}{\rho} J_m(k\rho) dk e^{im\phi}, \\ u_z(0) &= - \sum_m \int_0^\infty \frac{1}{\Delta^R} [\Delta_1(G_m)_1 - \Delta_2(G_m)_2] J_m(k\rho) k dk e^{im\phi}. \end{aligned} \quad (123)$$

We denote the roots of the Rayleigh wave dispersion equation  $\Delta^R = 0$  by  $k_R$ . Finding the contribution of the pole  $k_R$  in the complex  $k$ -plane, we get

$$u_\rho = \sum_m \pi i \left\{ \left( \frac{\partial \Delta^R}{\partial k} \right)^{-1} [\Delta_3(G_m)_1 - \Delta_4(G_m)_2] \times \left[ \frac{m}{\rho} H_m^{(2)}(k\rho) - k H_m^{(2)\prime}(k\rho) \right] \right\}_{k=k_R} e^{im\phi}, \quad (124a)$$

$$u_\phi = \sum_m \pi \left\{ \left( \frac{\partial \Delta^R}{\partial k} \right)^{-1} [\Delta_3(G_m)_1 - \Delta_4(G_m)_2] H_m^{(2)}(k\rho) \right\}_{k=k_R} \frac{m}{\rho} e^{im\phi}, \quad (124b)$$

$$u_z = \sum_m \pi i \left\{ \left( \frac{\partial \Delta^R}{\partial k} \right)^{-1} [\Delta_3(G_m)_1 - \Delta_4(G_m)_2] \frac{\Delta_2}{\Delta_4} k H_m^{(2)}(k\rho) \right\}_{k=k_R} e^{im\phi}. \quad (124c)$$

While obtaining Eq. (124c), use has been made of the fact that at  $k = k_R$ ,  $\Delta_1/\Delta_2 = \Delta_3/\Delta_4$ . Equations (105), (119), and (122) yield

$$\begin{aligned} \Delta_1 &= \frac{1}{k_{\beta_p}^2} \left[ 2kU_{21} - \frac{2\Omega_p}{v_p'} U_{22} + \frac{k}{\mu_p v_p'} U_{23} - \frac{1}{\mu_p} U_{24} \right], \\ \Delta_2 &= \frac{1}{k_{\beta_p}^2} \left[ -\frac{2\Omega_p}{v_p} U_{21} + 2kU_{22} - \frac{1}{\mu_p} U_{23} + \frac{k}{\mu_p v_p} U_{24} \right], \\ \Delta_3 &= \frac{1}{k_{\beta_p}^2} \left[ 2kU_{11} - \frac{2\Omega_p}{v_p'} U_{12} + \frac{k}{\mu_p v_p'} U_{13} - \frac{1}{\mu_p} U_{14} \right], \\ \Delta_4 &= \frac{1}{k_{\beta_p}^2} \left[ -\frac{2\Omega_p}{v_p} U_{11} + 2kU_{12} - \frac{1}{\mu_p} U_{13} + \frac{k}{\mu_p v_p} U_{14} \right], \\ (G_m)_1 &= \frac{1}{k_{\beta_p}^2} \left[ -\frac{2\Omega_p}{v_p} (F_m)_1 + 2k(F_m)_2 - \frac{1}{\mu_p} (F_m)_3 + \frac{k}{\mu_p v_p} (F_m)_4 \right], \\ (G_m)_2 &= \frac{1}{k_{\beta_p}^2} \left[ 2k(F_m)_1 - \frac{2\Omega_p}{v_p'} (F_m)_2 + \frac{k}{\mu_p v_p'} (F_m)_3 - \frac{1}{\mu_p} (F_m)_4 \right]. \end{aligned} \quad (125)$$

c. *Love Waves.* Treatment of Love waves is exactly similar to that of Rayleigh waves and, of course, much simpler. Therefore, we give below only important results without going into the details of their derivation. Previous notation is retained except that the superscript L is attached to the quantities related to Love waves.

We now have

$$\begin{aligned} [A_{nm}^L] &= [z_{nm}, Z_{nm}], \\ [A_{nm}^L(z_n)] &= [A_n^L][A_{nm}^L(z_{n-1})] = [A_n^L][A_{n-1,m}^L(z_{n-1})], \quad (126) \\ [A_n^L] &= \begin{bmatrix} C_{\beta_n} & (1/\mu_n v'_n) S_{\beta_n} \\ \mu_n v'_n S_{\beta_n} & C_{\beta_n} \end{bmatrix}. \end{aligned}$$

The source is represented as follows:

$$[A_{s_2m}^L(z_{s_1})] - [A_{s_1m}^L(z_{s_1})] = [D_m^L]. \quad (127)$$

The boundary condition at the free surface and the radiation condition yield

$$[C'_{pm} e^{-v_p' z_{p-1}}, -C'_{pm} e^{-v_p' z_{p-1}}] = [J^L][z_{1m}(0), 0] + [S_m^L], \quad (128)$$

where  $[J^L]$  and  $[S_m^L]$  are matrices for Love waves corresponding to the matrices  $[J]$  and  $[S_m]$  for Rayleigh waves (Eq. 119). Equation (128) gives

$$z_{1m}(0) = -G_m^L / \Delta^L, \quad (129)$$

where

$$\begin{aligned} G_m^L &= (F_m^L)_1 + \frac{1}{\mu_p v_p} (F_m^L)_2, \\ \Delta^L &= U_{11}^L + \frac{1}{\mu_p v_p} U_{22}^L, \quad (130) \\ [F_m^L] &= [V^L][D_m^L], \\ [U^L] &= [A_{p-1}^L][A_{p-2}^L] \cdots [A_2^L][A_1^L], \\ [V^L] &= [A_{p-1}^L][A_{p-2}^L] \cdots [A_{s+1}^L][A_{s_2}^L]. \end{aligned}$$

Using Eq. (129), one can find the surface displacement from Eqs. (87) and (93) in the form of an integral over  $k$ . Evaluating the residue contribution at the poles  $k_L$  given by  $\Delta_L = 0$ , we get the following expressions for the cylindrical components of the displacement at the free surface for the case of Love waves:

$$\begin{aligned} u_\rho &= -\sum_m \pi \left[ \left( \frac{\partial \Delta^L}{\partial k} \right)^{-1} G_m^L H_m^{(2)}(k\rho) \right]_{k=k_L} \frac{m}{\rho} e^{im\phi}, \\ u_\phi &= -\sum_m \pi i \left[ \left( \frac{\partial \Delta^L}{\partial k} \right)^{-1} G_m^L \left\{ k H_{m-1}^{(2)}(k\rho) - \frac{m}{\rho} H_m^{(2)}(k\rho) \right\} \right]_{k=k_L} e^{im\phi}. \end{aligned} \quad (131)$$

d. *Specification of the Source.* Equations (124) are general expressions for the surface displacements for Rayleigh waves excited by an arbitrary point source placed at the point  $r = 0, z = h$  of a multilayered half-space. The corresponding expressions for Love waves are given by Eq. (131). Knowing the source matrices  $[D_m]$  and  $[D_m^L]$  for any source, the above mentioned equations immediately give the spectral displacements.

Singh (1970) has given the source matrices  $[D_m]$  and  $[D_m^L]$  for the six displacement dislocations defined by Steketee (1958). The corresponding source matrices for Cases I, II, and III can be derived from these results. We give below the nonzero elements of  $[D_m]$  and  $[D_m^L]$  for all  $m$  values and for a delta function time dependence.

Case I ( $m = 2$ )

$$(D_2)_4 = -2ik\Gamma\mu_s, \quad (D_2^L)_2 = -2k\Gamma\mu_s, \quad (132)$$

where

$$\Gamma = \frac{1}{4\pi} U_0 dS.$$

Case II ( $m = 1$ )

$$(D_1)_2 = 2i\Gamma, \quad (D_1^L)_1 = 2\Gamma. \quad (133)$$

Case III ( $m = 0, 2$ )

$$\begin{aligned} (D_0)_1 &= 2\Gamma \frac{\mu_s}{\lambda_s + 2\mu_s}, & (D_0)_4 &= -k\Gamma\mu_s \frac{3\lambda_s + 2\mu_s}{\lambda_s + 2\mu_s}, \\ (D_2)_4 &= -k\Gamma\mu_s, & (D_2^L)_2 &= ik\Gamma\mu_s. \end{aligned} \quad (134)$$

We now make the following observations:

- (i) For a step source, the elements of the matrices  $[D_m]$ ,  $[D_m^L]$  as given by Eqs. (132)–(134) must be multiplied by  $1/(i\omega)$ .
- (ii) The elements of the matrices  $[A_n]$ ,  $[U]$ ,  $[V]$ ,  $[A_n^L]$ ,  $[U^L]$ , and  $[V^L]$  are real. Moreover,  $v_p$  and  $v_p'$  are real. Therefore  $[Z_p(z_{p-1})]$ ,  $[J]$ ,  $[J^L]$  have real elements and  $\Delta^{R,L}$ ,  $\Delta_1$  to  $\Delta_4$  are real.

(iii) With regard to the dependence on the azimuthal angle, one may go from the exponential form to the trigonometric equivalent by using the convention  $\exp(im\phi) \rightarrow \cos m\phi$ ,  $i \exp(im\phi) \rightarrow -\sin m\phi$ . This convention had been used in deriving Eqs. (132)–(134).

(iv) For  $|k\rho| \gg 1$ ,

$$H_m^{(2)}(k\rho) = (2/\pi k\rho)^{1/2} e^{i[-k\rho + \pi(m/2 + 1/4)]}. \quad (135)$$

e. *Spectral Displacements.* Using the values of  $(D_m)_i$  and  $(D_m^L)_i$  from Eqs. (132)–(134) and the asymptotic expansion of the Hankel functions, we obtain the following expressions for the far-field spectral surface displacements for a step time-dependence. Here we have not included the radial component of the displacement for Rayleigh waves because it can be calculated from the vertical component by using the relation

$$u_\rho/u_z = i(\Delta_4/\Delta_2)_{k_R} = -i\varepsilon_0, \quad (136)$$

where  $\varepsilon_0$  denotes the Rayleigh wave surface ellipticity.

Since the azimuthal component of the displacement for Rayleigh waves and the radial component for Love waves vary as  $(k\rho)^{-3/2}$ , these have not been included. We have, therefore,

$$\begin{aligned} u_z^R &= i D_1^R W_1 k_R \sin 2\phi, && \text{Case I,} \\ &= -D_1^R W_2 k_R \sin \phi, && \text{Case II,} \\ &= i D_1^R k_R [W_3 - \frac{1}{2} W_1 \cos 2\phi], && \text{Case III,} \end{aligned} \quad (137)$$

$$\begin{aligned} u_\phi^L &= D_1^L B_3 k_L \cos 2\phi, && \text{Case I,} \\ &= -i D_1^L B_6 k_L \cos \phi, && \text{Case II,} \\ &= \frac{1}{2} D_1^L B_3 k_L \sin 2\phi, && \text{Case III.} \end{aligned} \quad (138)$$

The various functions appearing in the above equations are defined as follows:

$$D_1^R = \frac{\Gamma}{\omega} \left( \frac{\partial \Delta^R}{\partial k_R} \right)^{-1} \left( \frac{2\pi}{k_R \rho} \right)^{1/2} e^{-i(k_R \rho + \pi/4)} \left[ 1 + O\left(\frac{1}{k_R \rho}\right) \right],$$

$$D_1^L = \frac{\Gamma}{\omega} \left( \frac{\partial \Delta^L}{\partial k_L} \right)^{-1} \left( \frac{2\pi}{k_L \rho} \right)^{1/2} e^{-i(k_L \rho + \pi/4)} \left[ 1 + O\left(\frac{1}{k_L \rho}\right) \right],$$

$$W_1 = (B_1 \Delta_1 - B_2 \Delta_2),$$

$$W_2 = (B_4 \Delta_1 - B_5 \Delta_2),$$

$$W_3 = (B_7 \Delta_1 - B_8 \Delta_2).$$

$$\begin{aligned}
B_1 &= \frac{2k_R \mu_s}{k_{\beta_p}^2} \left[ \frac{2\Omega_p}{v_p} V_{14} - 2k_R V_{24} + \frac{1}{\mu_p} V_{34} - \frac{k_R}{\mu_p v_p} V_{44} \right], \\
B_2 &= -\frac{2k_R \mu_s}{k_{\beta_p}^2} \left[ 2k_R V_{14} - \frac{2\Omega_p}{v_p'} V_{24} + \frac{k_R}{\mu_p v_p'} V_{34} - \frac{1}{\mu_p} V_{44} \right], \\
B_3 &= -2k_L \mu_s \left[ V_{12}^L + \frac{1}{\mu_p v_p'} V_{22}^L \right], \\
B_4 &= \frac{2}{k_{\beta_p}^2} \left[ -\frac{2\Omega_p}{v_p} V_{12} + 2k_R V_{22} - \frac{1}{\mu_p} V_{32} + \frac{k_R}{\mu_p v_p} V_{42} \right], \\
B_5 &= \frac{2}{k_{\beta_p}^2} \left[ 2k_R V_{12} - \frac{2\Omega_p}{v_p'} V_{22} + \frac{k_R}{\mu_p v_p'} V_{32} - \frac{1}{\mu_p} V_{42} \right], \\
B_6 &= 2 \left[ V_{11}^L + \frac{1}{\mu_p v_p} V_{21}^L \right], \\
B_7 &= \frac{2}{k_{\beta_p}^2} \frac{\mu_s}{\lambda_s + 2\mu_s} \left[ -\frac{2\Omega_p}{v_p} V_{11} + 2k_R V_{21} - \frac{1}{\mu_p} V_{31} + \frac{k_R}{\mu_p v_p} V_{41} \right] \\
&\quad + \frac{1}{2} \frac{3\lambda_s + 2\mu_s}{\lambda_s + 2\mu_s} B_1, \\
B_8 &= \frac{2}{k_{\beta_p}^2} \frac{\mu_s}{\lambda_s + 2\mu_s} \left[ 2k_R V_{11} - \frac{2\Omega_p}{v_p'} V_{21} + \frac{k_R}{\mu_p v_p'} V_{31} - \frac{1}{\mu_p} V_{41} \right] \\
&\quad + \frac{1}{2} \frac{3\lambda_s + 2\mu_s}{\lambda_s + 2\mu_s} B_2.
\end{aligned} \tag{139}$$

It is now possible to write down explicit expressions for the far-field spectral surface displacements due to an arbitrary shear dislocation with dip  $\delta$  and slip  $\lambda$  having a step function time variation. The source is placed on the z axis at a depth  $h$  below the free surface of a multilayered semi-infinite medium. From Eq. (18)

$$u(\lambda, \delta) = \cos \lambda [\sin \delta u_I + \cos \delta u_{II}^{**}] + \sin \lambda [\sin 2\delta u_{III} - \cos 2\delta u_{II}], \tag{140}$$

where  $u_I, u_{II}, u_{III}$  correspond to Cases I, II, III respectively, and  $u_{II}^{**}$  is obtained from  $u_{II}$  by changing  $\phi$  to  $(\phi - \pi/2)$ . Thus, for the present problem

$$u_z^R = \frac{U_0 dS}{\omega} \left( \frac{a}{\rho} \right)^{1/2} e^{-i(k_R \rho + 3\pi/4)} [s_R S_R + p_R P_R + i q_R Q_R], \tag{141a}$$

$$u_\phi^L = \frac{U_0 dS}{\omega} \left( \frac{a}{\rho} \right)^{1/2} e^{-i(k_L \rho - 3\pi/4)} [p_L P_L + i q_L Q_L], \tag{141b}$$

where

$$\begin{aligned}
 p_R &= (\cos \lambda \sin \delta) \sin 2\phi - (\tfrac{1}{2} \sin \lambda \sin 2\delta) \cos 2\phi, \\
 q_R &= (\sin \lambda \cos 2\delta) \sin \phi + (\cos \lambda \cos \delta) \cos \phi, \\
 s_R &= \tfrac{1}{2} \sin \lambda \sin 2\delta, \\
 p_L &= (\tfrac{1}{2} \sin \lambda \sin 2\delta) \sin 2\phi + (\cos \lambda \sin \delta) \cos 2\phi, \\
 q_L &= -(\cos \lambda \cos \delta) \sin \phi + (\sin \lambda \cos 2\delta) \cos \phi, \\
 P_R &= \frac{1}{4\pi a^2} [(k_R a)^{3/2} (8\pi)^{1/2}] \left[ \frac{-W_1}{2k_R \partial \Delta^R / \partial k_R} \right], \\
 Q_R &= -(W_2/W_1)P_R, \\
 S_R &= 2(W_3/W_1)P_R, \\
 P_L &= \frac{1}{4\pi a^2} [(k_L a)^{3/2} (8\pi)^{1/2}] \left[ -\frac{B_3}{2k_L \partial \Delta^L / \partial k_L} \right], \\
 Q_L &= (B_6/B_3)P_L.
 \end{aligned} \tag{142}$$

It may be noted here that  $D_1^R$  and  $D_1^L$  are functions of frequency, mode number, and the properties of the medium but are independent of source type or source depth. Functions  $P_R$ ,  $P_L$ , etc., depend upon the properties of the medium and source depth but do not depend upon source type. Lastly,  $p_R$ ,  $p_L$ , etc., are independent of the properties of the medium, of source depth, but are functions of the source orientation and give the azimuthal radiation pattern of surface waves.

#### F. EFFECTS OF ANELASTICITY

The study of seismic sources from analysis of signals requires a knowledge of the anelastic properties of the medium through which these signals travel. A model based upon a superposition of linear elasticity and Stokes' viscosity is commonly used (Voigt, 1892; Sezawa, 1927; Jeffreys, 1931, 1970). This model of anelasticity presupposes that the stress is proportional to the strain and its time derivative, namely

$$\mathfrak{T}(\mathbf{r}, t) = \left( \lambda + \lambda' \frac{\partial}{\partial t} \right) \mathfrak{J} \operatorname{div} \mathbf{D}(\mathbf{r}, t) + 2 \left( \mu + \mu' \frac{\partial}{\partial t} \right) \mathfrak{E}(\mathbf{r}, t), \tag{143}$$

where  $\lambda'$  and  $\mu'$  are Stokes' constants of viscosity of the material and are independent of the conditions of excitation. In Eq. (143),  $\mathfrak{T}$  and  $\mathfrak{E}$  are,

respectively, the stress and strain tensors. Let us consider first nondispersive waves in a homogeneous isotropic medium of density  $\rho$ . Choosing a harmonic time-dependence  $\mathbf{D}(\mathbf{r}, t) = \mathbf{u}(r)e^{i\omega t}$ , and using Eqs. (23) and (143), the new equation of motion in the absence of body forces assumes the form

$$(\lambda + 2\mu)\left(1 + \frac{i}{Q_p}\right) \operatorname{grad} \operatorname{div} \mathbf{u} - \mu\left(1 + \frac{i}{Q_s}\right) \operatorname{rot} \operatorname{rot} \mathbf{u} + \rho\omega^2 \mathbf{u} = 0, \quad (144)$$

where

$$1/Q_p = \omega(\lambda' + 2\mu')/(\lambda + 2\mu), \quad 1/Q_s = \omega\mu'/\mu. \quad (145)$$

Introducing the representation

$$\mathbf{u} = \operatorname{grad} \chi + \operatorname{rot} \mathbf{A},$$

Eq. (144) is satisfied if

$$\nabla^2 \chi + (\omega^2/\alpha^2)\chi = 0, \quad \nabla^2 \mathbf{A} + (\omega^2/\beta^2)\mathbf{A} = 0, \quad (146a,b)$$

with

$$\alpha^2 = \alpha^2[1 + (i/Q_p)], \quad \beta^2 = \beta^2[1 + (i/Q_s)]. \quad (147)$$

Assuming  $Q_p \gg 1$ ,  $Q_s \gg 1$ , the lossless wavenumbers  $k_\alpha = \omega/\alpha$  and  $k_\beta = \omega/\beta$  transform into

$$\begin{aligned} \hat{k}_\alpha &= k_\alpha[1 - (i/2Q_p)] + O(1/Q_p^2), \\ \hat{k}_\beta &= k_\beta[1 - (i/2Q_s)] + O(1/Q_s^2). \end{aligned} \quad (148)$$

Hence, a plane-wave solution of Eq. (146a) will become

$$\chi = e^{-ik_\alpha \Delta} e^{-\gamma \Delta}, \quad (149)$$

where the attenuation coefficient  $\gamma$  is given by

$$\gamma_p = \omega/(2Q_p \alpha). \quad (150)$$

In the earth  $Q_p$  is of the order 100–1000. It depends weakly on the frequency, but strongly on the depth (Anderson and Archambeau, 1964). The

total dissipation at a given frequency along a given ray is governed by the factor  $\exp[-\int \gamma(\omega, s) ds]$  where  $s$  is the arc length parameter along the ray. But from ray theory (Jeffreys, 1970)

$$ds = \eta dr / (\eta^2 - p^2)^{1/2},$$

where  $p$  is the ray parameter and  $\eta = r/v(r)$  ( $v = \alpha$  or  $\beta$ ). This yields an overall dissipation

$$\exp \left[ -\frac{\omega}{2} \int_{\text{ray}} \frac{\eta^2}{(\eta^2 - p^2)^{1/2}} \frac{dr}{r Q(r)} \right]. \quad (151)$$

Dispersive surface waves decay according to Eq. (149). But  $\gamma = \omega/(2Q U_g)$ ,  $U_g$  being the frequency dependent group velocity (Brune, 1961). The attenuation of surface waves is demonstrated in Fig. 3. It shows a wave ( $G_2$ ) which

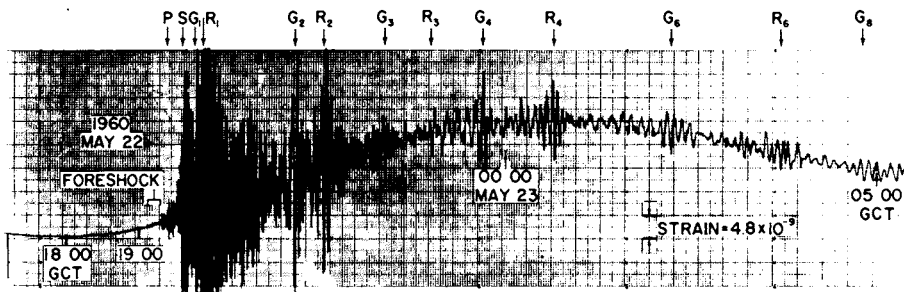


FIG. 3. Unfiltered strain record of the Chilean earthquake of May 22, 1960.

arrived from the source to the station via the major arc. The same wave circled the globe once and arrived later as  $G_4$ . Since the attenuation coefficient  $\gamma$  increases with the frequency, the shorter periods were filtered out. Hence the smoothed shape of  $G_4$ .

The attenuation of the normal modes of the Earth excited by large earthquakes were discussed by Ness *et al.* (1961). Let the amplitude  $A(t)$  of a free mode  $\omega_n$  decrease with time according to the law

$$A(t) \equiv \xi = \xi_0 e^{-t/\tau}, \quad \tau = 2Q/\omega_n, \quad Q \gg 1, \quad (152)$$

where  $\xi_0$  is the amplitude at the source. An average estimate of  $\xi$  over any time interval  $t_2 - t_1$  ( $t_2 > t_1$ ) can be made

$$\begin{aligned}\xi_{12} &= \frac{1}{t_2 - t_1} \int_{t_1}^{t_2} \xi(t) dt \\ &= \xi_0 \left[ \frac{\tau}{t_2 - t_1} \right] [e^{-t_1/\tau} - e^{-t_2/\tau}],\end{aligned}\quad (153)$$

which may be written as

$$\xi_{12} = \xi_0 e^{-t_1/\tau} [(1 - e^{-y})/y], \quad y = (t_2 - t_1)/\tau. \quad (154)$$

Thus, we get a correction factor  $y/(1 - e^{-y})$  which compensates for the dissipation of the normal mode  ${}_n\omega_l$  over a given time interval.

#### G. SEISMIC "DOPPLER-EFFECT"

So far we have used the Volterra relation in its differential form. This is permitted as long as the linear dimensions of the dislocation are small with respect to both the wavelength of the radiation and the distance to the observer. Ben-Menahem (1961a, 1962) presented a basic theory that accounts for the finiteness of the source and the propagating rupture. Consider first the influence on the spectrum of surface waves. There is no loss of generality in applying the theory to a particular field component. Let us choose, as an example, the azimuthal component of the ground motion for Love waves due to a point dislocation of type I with a step function time-dependence. We find from Eqs. (141b) and (142) the spectral representation

$$\begin{aligned}u_\phi^L &= \left[ \frac{U_0 dS}{4\pi a^2} \right] \frac{e^{3\pi i/4}}{\omega(k_L \rho)^{1/2}} \cos 2\phi [(k_L a)^2 (8\pi)^{1/2}] \left[ -\frac{B_3}{2k_L \partial \Delta^L / \partial k_L} \right] \\ &\quad \times e^{i(\omega t - k_L \rho)} [1 + O(k_L \rho)^{-1}].\end{aligned}\quad (155)$$

The source is assumed to have the following additional specifications:

1. Horizontal rupture is in the strike direction (Fig. 4b) over a finite distance  $b$ . The source has a finite vertical extent  $D = \Delta h$  (Fig. 4b).
2. The velocity of rupture  $v_f$  is constant and the magnitude of the dislocation is independent of the coordinates.
3.  $(b/\rho_0) \ll 1$ ,  $(D/\rho_0) \ll 1$ ,  $(k_L \rho_0) \gg 1$ . Here  $(\rho_0, \phi_0)$  are the observer's coordinates with respect to an origin that coincides with the point of rupture initiation.

Under these conditions

$$\rho = \rho_0 [1 - (\xi/\rho_0) \cos \phi_0 + O(\xi^2/\rho_0^2)]. \quad (156)$$

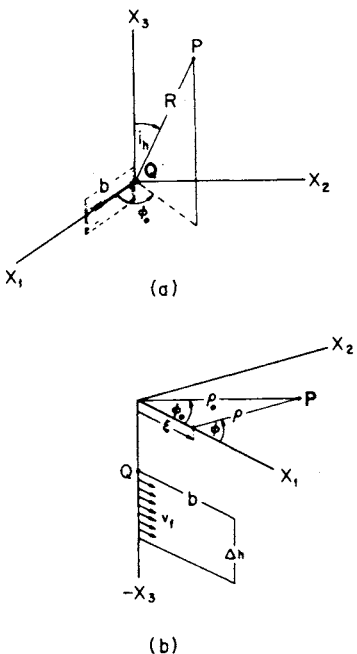


FIG. 4. Geometry of finite source. (a) Spherical coordinates. (b) Cylindrical coordinates.

In Eq. (155), we replace  $\exp(-ik_L \rho)$  by

$$\exp\{-ik_L \rho_0 [1 - (\xi/\rho_0) \cos \phi]\},$$

and replace  $\rho; \phi$  by  $\rho_0, \phi_0$  in the amplitude. We then integrate the resulting expression over  $\xi$  and  $h$  within the limits  $0 \leq \xi \leq b, h_1 \leq h \leq h_2$ . The  $\xi$ -integral is

$$\int_0^b \frac{\cos 2\phi}{(k_L \rho)^{1/2}} \exp[-ik_L \rho + i\omega(t - \xi/v_f)] d\xi = \frac{b \cos 2\phi_0}{(k_L \rho_0)^{1/2}} e^{i(\omega t - k_L \rho_0)} \times \left[ \frac{\sin X_L}{X_L} e^{-iX_L} \right] \left[ 1 + O\left(\frac{b}{\rho_0}\right) \right], \quad (157)$$

where

$$X_L = \frac{1}{2}(b/v_f)\omega', \quad \omega' = \omega[1 - (v_f/C_L) \cos \phi_0], \quad (158)$$

in which  $C_L(\omega)$  is the phase velocity for Love waves.

The total displacement field at  $(\rho_0, \phi_0)$  will therefore be

$$\begin{aligned} u_{\phi}^{(1)} = & \left[ \frac{U_0 b}{4\pi a^2} \right] \left[ \frac{\cos 2\phi_0}{\omega(k_L \rho_0)^{1/2}} \right] e^{(3\pi i/4) - iX_L} [(k_L a)^2 (8\pi)^{1/2}] \frac{\sin X_L}{X_L} \\ & \times \left[ - \frac{1}{2k_L \partial \Delta^L / \partial k_L} \int_{h_1}^{h_2} B_A(h) dh \right] e^{i(\omega t - k_L \rho_0)} \left\{ 1 + O\left[\frac{b}{\rho_0}, (k_L \rho_0)^{-1}\right] \right\}, \end{aligned} \quad (159)$$

where  $\Delta h = h_2 - h_1 = D$ .

Similar expressions are obtained for the Rayleigh waves for which  $X_L$  is replaced by  $X_R$

$$\begin{aligned} X_R = & \frac{1}{2}(b/r_f)\omega', \quad \omega' = \omega[1 - \omega(r_f/C_R) \cos \phi_0], \\ C_R = & C_R(\omega). \end{aligned} \quad (160)$$

The factor  $[(\sin X)/X]e^{-iX}$  is a first-order correction for the source finiteness and motion. The Doppler-like shift affects both amplitudes and phases and an observer at the receiving end will notice a phase retardation and a modulated amplitude pattern with minima at various frequencies that depend on the azimuth  $\phi_0$ , the rupture duration  $b/r_f$ , and the velocity ratio  $r_f/C_L$  (or  $r_f/C_R$ ). These minima or "holes" as they are sometimes called, are determined by the equation

$$(b/r_f)C_L - b \cos \phi_0 = N \quad (\text{wavelengths}) \quad (161)$$

which is the condition for destructive interference at the point of observation.

The treatment of the finiteness effect on the body waves is analogous. Let us take, for example, the expression for the P-wave displacement in a lossless radially heterogeneous unbounded medium excited by source of type I [Eqs. (20), (21)]

$$u_p(\omega) = - \frac{U_0 dS}{4\pi \alpha(r_h)} \left( \frac{\beta}{\alpha} \right)_{r_h}^2 G_p \sin 2\phi \sin^2 i_h e^{i(\omega t - T_p)}, \quad (162)$$

where  $G_p$  is the divergence coefficient and  $T_p$  the travel time of P waves for the distance  $\Delta = r_0 \theta$ . For a point  $(\xi, 0, 0)$  on the  $x_1$  axis (Fig. 4a), the corresponding travel time is approximately equal to

$$\hat{T}_p = T_p - (\xi/x_h) \cos \phi_0 \sin i_h, \quad \xi/r_0 \ll 1. \quad (163)$$

For a source at the point  $(\xi, 0, 0)$ , Eq. (162) becomes

$$u_p(\omega) = -\frac{U_0 dS}{4\pi\alpha(r_h)} \left(\frac{\beta}{\alpha}\right)^2_{r_h} G_p \sin 2\phi \sin^2 i_h \times \exp[i\omega(t - \hat{T}_p)]. \quad (164)$$

Replacing  $dS$  by  $Dd\xi$  and integrating over  $\xi$  from 0 to  $b$  we find, on taking into account the effect of the propagating rupture as well,

$$\begin{aligned} u_p(\omega) = & -\frac{U_0 b D}{4\pi\alpha(r_h)} \left(\frac{\beta}{\alpha}\right)^2_{r_h} G_p \sin 2\phi_0 \sin^2 i_h \\ & \times \left\{ e^{i\omega(t - T_p)} \left[ \frac{\sin X}{X} e^{-iX} \right] \right\} \left[ 1 + O\left(\frac{b}{r_0}, \frac{D}{r_0}\right) \right], \end{aligned} \quad (165)$$

where

$$X = (b/2v_f)\omega', \quad \omega' = \omega[1 - (v_f/v_a) \cos \phi_0], \quad (166)$$

and  $v_a$  is the apparent velocity  $\alpha_h/\sin i_h$ .

The dependence of  $u_p$  on the frequency is limited to the factors inside the curly brackets. Using the Fourier integral

$$\frac{1}{2\pi} \int_{-\infty}^{\infty} \frac{\sin \omega x}{\omega x} e^{i\omega y} d\omega = \frac{1}{2x} [H(y+x) - H(y-x)], \quad (167)$$

we can obtain the functional dependence of the displacements on time at the base of the crust. The final results for P waves for the three fundamental faults (Eqs. 19, 20) are

$$u_p(t) = -\frac{U_0 b D}{4\pi\alpha(r_h)} \left(\frac{\beta}{\alpha}\right)^2_{r_h} \frac{G_p}{\tau} S(\phi_0, i_h) [H(t - T_p) - H(t - T_p - \tau)], \quad (168)$$

where

$$\tau = \frac{b}{v_f} \left[ 1 - \frac{v_f}{\alpha(r_h)} \cos \phi_0 \sin i_h \right],$$

$$\begin{aligned} S(\phi_0, i_h) &= \sin 2\phi_0 \sin^2 i_h, & \text{Case I,} \\ &= \sin \phi_0 \sin 2i_h, & \text{Case II,} \\ &= -1 + \frac{1}{2} \sin^2 i_h (3 - \cos 2\phi_0), & \text{Case III.} \end{aligned} \quad (169)$$

It may be noted that  $\tau$  is the *duration* of the pulse caused by the finiteness and rupture of the source (Savage, 1965; Hirasawa, 1965; Berckhemer and Jacob, 1968).

### III. Calculation of Body-Wave Amplitudes

Equation (20) renders the ray-theoretical spectral displacements of P, SV, and SH waves induced by a shear dislocation localized at the point ( $r = r_h$ ,  $\theta = 0$ ) in an unbounded, radially heterogeneous, isotropic, elastic medium. In the presence of boundaries we have to multiply these expressions with appropriate reflection and refraction coefficients. The source time-dependence is a step function. We now describe how to compute the various factors occurring in these expressions.

#### A. DIVERGENCE COEFFICIENT

Of all the factors that constitute the spectral amplitudes of body waves, the divergence coefficient is the most difficult to compute since it depends on the first and second derivatives of a tabulated function. Using Eq. (22), we can recast our previous expression for  $G$  [Eq. (21)] into a more useful form

$$G = \frac{1}{r_0} \left| \frac{r_h \rho_h}{r_0 \rho_0} \left( \frac{\eta_0}{\eta_h} \right)^2 \frac{1}{\sin \theta} p \frac{d^2 T}{d\theta^2} \frac{1}{(\eta_0^2 - p^2)^{1/2}} \frac{1}{(\eta_h^2 - p^2)^{1/2}} \right|^{1/2}, \quad (170)$$

where  $r$  is the distance from the center,  $p = dT/d\theta$  is the ray parameter,  $\eta = r/v(r)$ , and  $T$  is the travel time along the ray. The suffix  $h$  is always assigned to the focus and the suffix 0 indicates the level of the recording station (with or without stripping the crust). This is shown in Fig. 2. The above form of  $G$  underlines the difficulty of evaluating the divergence coefficient from travel time tables as it necessitates two numerical differentiations, with all the problems that ensue. If the Earth had full spherical symmetry, and all its parameters were exactly known, amplitude factors to any desired accuracy could be obtained. In reality there is no such symmetry, and the parameters are only known up to a certain error (in the best case). Our results will therefore be only approximately correct.

In the calculations we use as input data the Jeffreys-Bullen travel times (1967) for surface foci, which constitute a discrete set of information. As we need the first two derivatives of the times we have to use some form of interpolation. Lagrangian interpolation, or divided differences (which is another name for the same method) fits polynomials between two neighboring points, causing discontinuities in the derivatives at every tabulated point. Curtis and

Shimshoni (1970) have recently used cubic splines successfully in the somewhat related problem of smoothing observational seismic travel times. Shimshoni and Ben-Menahem (1970) computed divergence coefficients of seismic phases using cubic splines. Their method will be described in some detail.

Cubic splines get their name from a tool used by draftsmen to draw a continuous curve between points, using a flexible thin strip of wood (the spline). With this tool the draftsmen have a flexible French curve. The strip is anchored in place by weights and made to pass through or near specified points. The resulting line has continuous curvature, with jumps in the rate of change of the curvature at the points of the weights (the joints or the knots). Mathematically, the line is continuous and also has continuous first and second derivatives. At the joints, jumps of the third derivative are permitted, but between them the line is described by a cubic polynomial. A curve of  $n$  joints is determined by  $n + 2$  parameters.

The computational program finds the required number and location of the joints. Then one minimizes the squares of the deviations at the original tabulated points, while attempting to minimize the jumps of the third derivatives at the joints. One tries to use the smallest possible number of joints while still keeping the deviations within the uncertainties of the travel times. One also pays attention to the sign of the deviations. If it is noticed that between two joints all the deviations or almost all of them have the same sign, another joint is added in the middle.

Shimshoni and Ben-Menahem (1970) used cubic splines on the surface foci times of Jeffreys and Bullen (1967) for P, and then computed the amplitude factor  $G_p$  from the reconstructed travel time function.

As the travel time curve of P is made up of two branches, one up to about  $19^\circ$  and the other from there onwards, it has a discontinuous first derivative near  $19^\circ$ . Thus travel times up to  $19^\circ$  are fitted by one cubic spline and from  $19^\circ$  up to the end by another cubic spline. Formula (170) is invalid at the discontinuity. It is claimed that the results are as good an approximation to the amplitude factor as can be obtained from the available data.

In general, for phases with discontinuous derivatives, one can still use cubic splines as long as one remains on a single branch and treats the other branches separately.

At the final stage, while computing the cubic spline values for the times of P and S phases (surface foci), the range of interest was split into the two branches caused by the  $20^\circ$  discontinuity of the Jeffreys-Bullen times. It was found that the two branches meet at a distance of about  $9.6^\circ$  for P and about  $20.3^\circ$  for S. At these points the travel times are still continuous but the first derivatives are discontinuous. Because of this discontinuity, special care must be taken when dealing with P and S times. Shimshoni and Ben-Menahem

(1970) have also computed the splines for P and S, for each depth given in the J-B tables starting with the distance 0° (where  $dT/d\theta = 0$ ) and stopping at the point where the ray leaves the focus horizontally. At this distance,  $dT/d\theta$  reaches its maximal value which equals  $\eta = r/v$  for that depth.

Figure 5 shows the divergence coefficients for P and S waves for a focus at a depth of about 400 km ( $h = 0.06a$ ). The recording station is on the top of the mantle ( $r_0 = 6338$  km). The unit in this figure is  $8.233 \times 10^{-11} \text{ cm}^{-1}$ . We left out distances near the end of the range if values of  $dT/d\theta$  and  $d^2T/d\theta^2$  were unreliable, because they were tied to the tables from one side only.

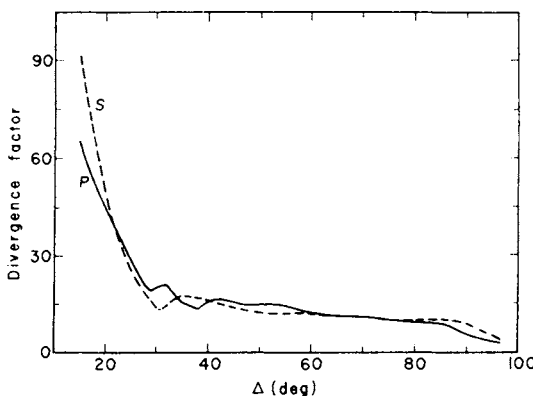


FIG. 5. Dependence of the divergence coefficient on the epicentral distance.

In Table II, we give results for the phases P and S. No claim for high accuracy is made. An uncertainty of about 5% can be expected. Coefficients with smaller uncertainties are unobtainable, not only because of our limited knowledge of the structure of the Earth, but also because the deviations in this structure from spherical symmetry make higher accuracy meaningless.

## B. PHYSICAL ATTENUATION

From Eq. (151), the attenuation is given by  $\exp[-\omega g(\theta, h)]$  with

$$g(\theta, h) = \frac{1}{2} \int_{\text{ray}} \frac{\eta^2 dr}{(\eta^2 - p^2)^{1/2} r Q(r)}, \quad (171)$$

where  $Q(r)$  is the radial profile of the intrinsic dimensionless dissipation factor in the earth. Integration is done along the radius from the source level to the bottom of the ray and from there to the surface. Observed values

TABLE II

DIVERGENCE COEFFICIENTS ( $G$ ) FOR P AND S WAVES FOR DEEP FOCUS  
( $h = 380$  km) EVENTS<sup>a</sup>

$G \times 10^{10}$ (cm $^{-1}$ )								
$\Delta$	$G_p$	$G_s$	$\Delta$	$G_p$	$G_s$	$\Delta$	$G_p$	$G_s$
15	53.70	75.53	45	12.71	11.41	75	8.36	8.05
16	49.55	67.56	46	12.46	11.11	76	8.26	8.11
17	45.80	60.20	47	12.22	10.82	77	8.15	8.15
18	42.42	53.40	48	12.09	10.54	78	8.04	8.19
19	39.30	46.99	49	12.12	10.34	79	7.94	8.23
20	36.37	40.75	50	12.14	10.19	80	7.82	8.27
21	33.68	34.32	51	12.14	10.04	81	7.71	8.30
22	31.29	30.21	52	12.14	9.90	82	7.60	8.32
23	28.56	27.23	53	12.14	9.84	83	7.49	8.34
24	25.85	24.25	54	12.10	9.95	84	7.39	8.33
25	23.17	21.20	55	11.76	10.05	85	7.29	8.27
26	20.81	17.98	56	11.45	10.14	86	6.90	8.19
27	18.75	16.26	57	11.14	10.22	87	6.39	8.12
28	16.68	14.61	58	10.84	10.08	88	5.86	8.05
29	15.54	12.90	59	10.55	9.90	89	5.30	7.60
30	16.36	11.09	60	10.27	9.73	90	4.69	7.05
31	17.03	10.87	61	10.09	9.57	91	4.00	6.47
32	17.26	12.08	62	9.94	9.44	92	3.52	5.86
33	15.70	13.06	63	9.78	9.34	93	3.24	5.27
34	14.10	13.86	64	9.64	9.25	94	2.94	4.70
35	12.45	14.47	65	9.49	9.15			
36	11.90	14.23	66	9.35	9.06			
37	11.39	14.00	67	9.23	9.10			
38	10.91	13.78	68	9.12	9.14			
39	11.81	13.57	69	9.02	9.16			
40	12.76	13.24	70	8.91	9.20			
41	13.54	12.84	71	8.80	9.06			
42	13.53	12.45	72	8.70	8.78			
43	13.24	12.08	73	8.60	8.53			
44	12.97	11.72	74	8.48	8.27			

<sup>a</sup> The recording station is on the top of the mantle. The epicentral distance ( $\Delta$ ) is given in degrees.

of  $Q_p(r)$  and  $Q_s(r)$  were given by Anderson and Archambeau (1964) and Anderson *et al.* (1965). These results were used by Ben-Menahem *et al.* (1965) to derive the approximate expression

$$g(\theta, h) \approx \frac{r_0}{v(r_0)} \left| \frac{\sin(i_h - i_0)}{\sin i_h} \right| \times 10^{-3} \text{ sec}, \quad (172)$$

where  $i_h$ ,  $i_0$ , and  $r_0$  are shown in Fig. 2. Using Eq. (172) for periods above 10 sec, it can be shown that the attenuation factor decreases from unity down to approximately 0.8 at  $\theta = 100^\circ$ . The data which led to the derivation of Eq. (172) yields an average  $Q_p$  of 1000 for the upper mantle.

### C. EFFECT OF THE EARTH'S CRUST

The crust of the Earth which extends to some 10 km under the oceans and about 35 km under the continents, plays a dominant role in shaping the form of the seismic pulse as it travels along the ray on the way from the source to the receiving instrument. The influence of the crust on the spectrum of body waves must therefore be calculated if we wish to use body-wave signals for source studies.

Haskell (1960, 1962) carried out calculations for the response of an arbitrary layered elastic medium to incident plane harmonic waves of P, SV, and SH types, using a special matrix technique.

In the present section we shall obtain expressions in terms of layer matrices for the amplitudes of the free surface displacements due to plane P, SV, or SH waves incident at any angle at the base of a multilayered crust by using Haskell's method in the notation described in Section II,E,2.

#### 1. Incident P Wave

To find the crustal transfer functions, we return to Eq. (113). For an incident P wave at the base of the crust, we take  $B_{pm}'' = 0$ . Further, since there is no source,  $[D_m] = 0$  and the subscript  $m$  is superfluous. Equation (118) now becomes

$$\begin{aligned} & [A_p' e^{-v_p z_p - i} + A_p'' e^{v_p z_p - i}, -A_p' e^{-v_p z_p - i} + A_p'' e^{v_p z_p - i}, \\ & \quad B_p' e^{-v_p' z_p - i}, -B_p' e^{-v_p' z_p - i}] \\ & \quad = [J][x_1(0), y_1(0), 0, 0], \quad (173) \end{aligned}$$

in which  $A_p''$  is known. Equation (173) is a set of four equations in four unknowns;  $A_p'$ ,  $B_p'$ ,  $x_1(0)$ ,  $y_1(0)$ . Solving it, we get

$$\begin{aligned} x_1(0) &= (2\Delta_1/\Delta^R)A_p'' e^{v_p z_p - i}, \quad y_1(0) = -(2\Delta_3/\Delta^R)A_p'' e^{v_p z_p - i}, \\ A_p' &= (1/\Delta^R)[(J_{11} - J_{21})\Delta_1 - (J_{12} - J_{22})\Delta_3]A_p'' e^{2v_p z_p - i}, \quad (174) \\ B_p' &= (2/\Delta^R)[J_{31}J_{42} - J_{32}J_{41}]A_p'' e^{(v_p + v_p')z_p - i}. \end{aligned}$$

In order to exhibit the combined effect of the free surface and the crustal layering on the motion at the free surface, we may find the ratio of the surface motion with the corresponding components of the motion in the half-space ( $p$ th layer) due to the incident wave alone. From Eqs. (95) and (96), the parts corresponding to an incident P wave (IP) in the half-space are

$$\begin{aligned} x_p^{\text{IP}}(z_{p-1}) &= v_p A_p'' e^{v_p z_{p-1}}, \\ y_p^{\text{IP}}(z_{p-1}) &= k A_p'' e^{v_p z_{p-1}}. \end{aligned} \quad (175)$$

From Eqs. (174) and (175), we deduce the following expressions for the crustal transfer functions

$$\frac{x_1(0)}{x_p^{\text{IP}}(z_{p-1})} = \frac{2\Delta_1}{v_p \Delta^R}, \quad \frac{y_1(0)}{y_p^{\text{IP}}(z_{p-1})} = -\frac{2\Delta_3}{k \Delta^R}. \quad (176)$$

Equation (174) also gives the crustal reflection coefficients

$$\begin{aligned} x_p^{\text{RP}}(z_{p-1})/x_p^{\text{IP}}(z_{p-1}) &= -(A_p'/A_p'') e^{-2v_p z_{p-1}} \\ &= -(1/\Delta^R)[(J_{11} - J_{21})\Delta_1 - (J_{12} - J_{22})\Delta_3] \\ &= -y_p^{\text{RP}}(z_{p-1})/y_p^{\text{IP}}(z_{p-1}), \end{aligned} \quad (177)$$

$$\begin{aligned} x_p^{\text{RS}}(z_{p-1})/x_p^{\text{IP}}(z_{p-1}) &= (k/v_p)(B_p'/A_p'') e^{-(v_p + v_p')z_{p-1}} \\ &= (2k/v_p \Delta^R)[J_{31}J_{42} - J_{32}J_{41}] \\ &= -(k^2/v_p v_p') y_p^{\text{RS}}(z_{p-1})/y_p^{\text{IP}}(z_{p-1}). \end{aligned} \quad (178)$$

## 2. Incident SV Wave

For the case of an incident SV wave (IS), we take  $A_p'' = 0$ . Proceeding as in the case of a P wave, we obtain

$$\begin{aligned} x_1(0)/x_p^{\text{IS}}(z_{p-1}) &= -2\Delta_2/k\Delta^R, \\ y_1(0)/y_p^{\text{IS}}(z_{p-1}) &= 2\Delta_4/v_p'\Delta^R, \\ x_p^{\text{RP}}(z_{p-1})/x_p^{\text{IS}}(z_{p-1}) &= -(v_p v_p'/k^2) y_p^{\text{RP}}(z_{p-1})/y_p^{\text{IS}}(z_{p-1}) \\ &= (2v_p/k\Delta^R)[J_{11}J_{22} - J_{12}J_{21}], \\ x_p^{\text{RS}}(z_{p-1})/x_p^{\text{IS}}(z_{p-1}) &= -y_p^{\text{RS}}(z_{p-1})/y_p^{\text{IS}}(z_{p-1}) \\ &= (1/\Delta^R)[-(J_{31} - J_{41})\Delta_2 + (J_{32} - J_{42})\Delta_4]. \end{aligned} \quad (179)$$

### 3. Incident SH Wave

The crustal transfer function and the reflection coefficient can be derived in a straightforward manner. For an incident SH wave (IS) at the base of the crust,  $C_p''$  is a known quantity. Proceeding as in the case of P and SV waves,  $C_p'$  and  $z_1(0)$  can be obtained in terms of  $C_p''$ . Thus, from Eqs. (99) and (128), we find

$$\begin{aligned} z_1(0)/z_p^{\text{IS}}(z_{p-1}) &= 2/\Delta^L, \\ z_p^{\text{RS}}(z_{p-1})/z_p^{\text{IS}}(z_{p-1}) &= (J_{11}^L - J_{21}^L)/\Delta^L. \end{aligned} \quad (180)$$

### 4. Applications

Ben-Menahem *et al.* (1965) calculated amplitudes of horizontal and vertical components of surface motions due to a plane wave incident at the base of the crust. The incoming ray was considered to be a plane wave and its curvature neglected. The calculations were made for a number of well documented crustal models (Gutenberg, 1952; Aki, 1961; Aki and Press, 1961; Healy, 1963; Jackson *et al.*, 1963; Roller and Healy, 1963). The corresponding amplitude response curves for these models are shown in Fig. 6. These results

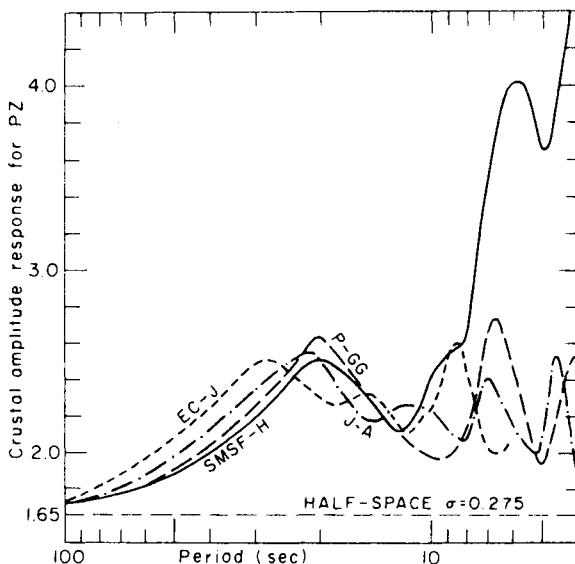


FIG. 6. Amplitude response of six crustal models. SMSF-H Santa Monica-San Francisco (Healy, 1963); EC-J Eastern Colorado (Jackson *et al.*, 1963); J-A Japan 6EJ (Aki, 1961); P-GG Pacific 6EGH (Gutenberg, 1952).

are for a compressional body wave of unit amplitude and an apparent velocity of 15 km/sec. It is clear from these curves that the different geological provinces are significant even for periods as long as 10 sec. However, beyond this period the variations in the response do not exceed 20% of their average value. The object of displaying these curves is to show the kind of distortion that can be expected from a nonhomogeneous structure. In order to estimate the length of the time interval that should be considered when doing numerical analysis of real seismograms, Ben-Menahem *et al.* (1965) performed a Fourier synthesis for the incident plane wave taking into account the response of a recording instrument together with a proper time function for the source.

Using a synthesis technique described by Aki (1960), a plane wave with a delta function time-dependence [equivalent to a step function time-dependence from a shear dislocation (Section II)] was simulated at the base of a stack of layers and the resulting transient pulse was calculated at the free surface. Prior to the synthesis, the frequency dependent transmission coefficients for the layered model were multiplied by the frequency response of a critically damped long-period seismograph of the type used by the USCGS World Wide Standard Stations (30 sec pendulum, 100 sec galvanometer). As a check on the quality of the frequency synthesis, a model was used in which all the layers had identical parameters; thus there should be no change in the pulse form due to the layered medium. The resulting surface motion was rectilinearly polarized and closely approximated the impulse response of the seismograph system. Synthesized seismograms are shown in Fig. 7 for a P wave incident at the base of the crust with an apparent velocity of 25 km/sec. In Fig. 7 the first arrival in all cases is the direct P wave. From this figure it is also clear that a typical time window which includes most of the converted waves and multiple reverberations will be about 60 sec. It is important that no other rays interfere during this time interval. The analysis must therefore be restricted to seismic events that occur at depths greater than about 350 km (Jeffreys and Bullen, 1967, p. 19).

#### D. INFLUENCE OF THE SOURCE

Ample evidence has been documented in the past decade which supports the conjecture that earthquake foci release their energy through a moving rupture over a finite area (Ben-Menahem, 1961a,b, 1962). Indeed, data analysis of body waves from many seismic events proved this to be the case (Teng and Ben-Menahem, 1965; Berckhemer and Jacob, 1968; Bollinger, 1968; Davies and Smith, 1968; Chandra, 1970).

The source parameters enter the wave amplitude spectrum in three ways: through the "radiation-pattern" function  $F(\lambda, \delta; i_h, \phi)$  (Eq. 18) which incorporates a dependence on the orientation angles  $(\lambda, \delta)$  of the dislocation

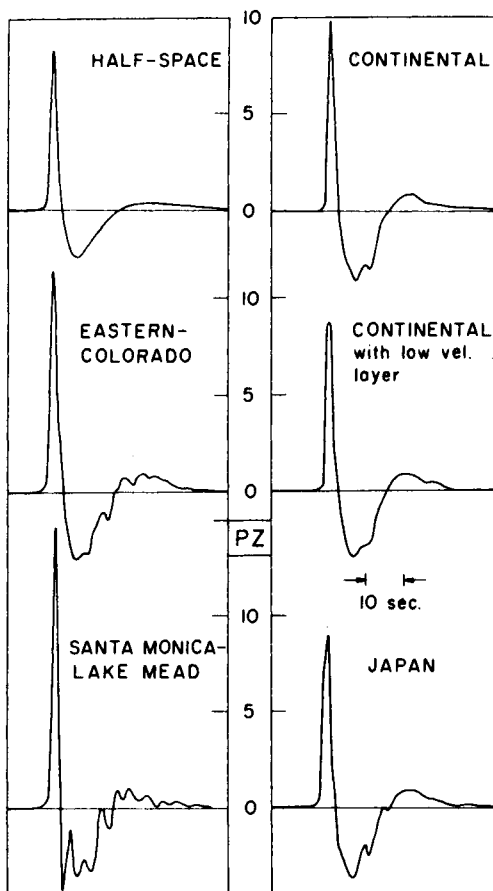


FIG. 7. Synthesized P wave-forms.

through the source potency ( $U_0 dS$ ) and, finally, through the finiteness factor  $(\sin X)/X$  where  $X$  [Eqs. (158), (160), (166)] depends on  $(i_h, v_f, b, h, \phi_0)$  for a uniform rupture that propagates horizontally.

In cases where the resolution of the observed body-wave spectra is insufficient to determine the source parameters, the analysis can be carried out directly on the seismograph traces (Ben-Menahem and Toksöz, 1963a,b; Hirasawa and Stauder, 1965; Berckhemer and Jacob, 1968; Bollinger, 1970). Use is made of the result [Eq. (168)] that the total duration of the body-wave pulse which hits the base of the crust is modulated azimuthally through the factor  $1 - [v_f/v(r_h)] \sin i_h \cos \phi_0$ .

### E. METHODS FOR SOURCE STUDIES

There are today two fundamental methods for the derivation of the source parameters from observations of body-wave signals. They are: (1) polarity of initial motions, and (2) spectral equalization.

The first method is older than the second, easier to use, and less accurate. The underlying idea came in 1917 from Shida and the theory from Nakano (1923). Byerly (1926) and later Hodgson (1957) turned it into a working tool.

We have already shown (Eq. 15) that the "radiation-pattern" function is expressible as a product of two factors

$$F = F(i_h, \phi) = F(\mathbf{e}, \mathbf{n}) = F(\mathbf{n}, \mathbf{e}) = 6(\mathbf{e} \cdot \mathbf{e}_R)(\mathbf{n} \cdot \mathbf{e}_R). \quad (181)$$

Let us imagine a hypothetical unit sphere surrounding a localized dislocation. We could consider  $F(i_h, \phi)$  to be the amplitude distribution of the source over this sphere, with nodal lines given by the equations  $(\mathbf{e} \cdot \mathbf{e}_R) = 0$  and  $(\mathbf{n} \cdot \mathbf{e}_R) = 0$ .

Karal and Keller (1959) and Singh and Ben-Menahem (1969c,d) have shown that seismic rays in media with weak heterogeneity conserve the polarity of the first motion together with the angle between the SV and SH vectors (polarization angle). Thus, rays leaving the focal sphere in a given direction  $(i_h, \phi)$  will pick the corresponding polarity  $\text{sgn}[F(i_h, \phi)]$  and carry it unchanged to the surface of the Earth. The nodal lines on the focal sphere will therefore be "transplanted" by the rays as new nodal lines on the Earth's surface. The deduction of the orientation of the dislocation at the source from the observed distribution of polarities is the objective of this method.

From Eq. (11) we find that the condition  $(\mathbf{n} \cdot \mathbf{e}_R) = 0$  is equivalent to  $(\cot i_h - \sin \phi \tan \delta = 0)$  and the condition  $(\mathbf{e} \cdot \mathbf{e}_R) = 0$  is equivalent to  $(\cot i_h \sin \delta + \cos \delta \sin \phi + \cot \lambda \cos \phi = 0)$ . Define a vector  $(x, y)$  on an equatorial plane with respect to the source such that its polar representation is given by  $(\hat{R}, \phi)$  where  $\hat{R} = \cot i_h$ . The equations of the nodal lines on this plane then become  $x^2 + y^2 - y \tan \delta = 0$  and  $x^2 + y^2 + x(\cot \lambda / \sin \delta) + y \cot \delta = 0$ , respectively. The first one is a circle centered at  $(0, \frac{1}{2} \tan \delta)$  with diameter  $\tan \delta$ . The second nodal line is another circle centered at  $[-\cot \lambda / (2 \sin \delta), -\cot \delta / 2]$  with diameter  $\tan \delta'$  where  $\cos \delta' = \sin \lambda \sin \delta$ .

These results are utilized in Byerly's method in the following way: The observed polarity of the P wave first motion at a given station may be either a compression (+) or a dilatation (-). This is marked on the equatorial plane with the proper azimuth of the station, but at a distance which is obtained by a stereographic image of the extended position of the station on that plane ( $= \cot i_h$ ). The procedure is repeated for each station of the network. The resulting nodal lines are the above mentioned circles that separate regions of compression from regions of dilatation.

By a comparison of the observational results with the above theory one is able, in principle, to deduce the orientation of two planes, one of which is the plane of motion and the other is the plane normal to it, known as the auxiliary plane. This unavoidable ambiguity arises from the symmetry of  $F$  in  $\mathbf{e}$  and  $\mathbf{n}$ . It can be shown (e.g., Jarosch and Aboodi, 1970) that if  $(\lambda, \delta, \phi)$  define the orientation of the plane of motion and  $(\lambda', \delta', \phi')$  define the orientation of the auxiliary plane, the following reciprocal relations hold:

$$\begin{aligned}\cos \delta &= \sin \lambda' \sin \delta', & \cos \lambda &= \sin \delta' \sin (\phi - \phi'), \\ \cos \delta' &= \sin \lambda \sin \delta, & \cos \lambda' &= \sin \delta \sin (\phi' - \phi).\end{aligned}\quad (182)$$

Also, the orthogonality of the two planes provides the constraint

$$\tan \delta \tan \delta' \cos (\phi - \phi') + 1 = 0.$$

Wickens and Hodgson (1967) wrote a computer program which takes any set of P-wave polarity observations from a predetermined epicenter and determines the best solution of the nodal planes together with the corresponding orientation parameters. Their program has been applied to data of 618 earthquakes that occurred during the interval 1922–1962. Isacks and Molnar (1971) have found 179 solutions for deep and intermediate-depth earthquakes in the interval 1962–1968.

The effect of the free surface on the initial motion was studied by Burridge *et al.* (1964). They found that initial motion patterns for earthquakes with surface foci may be modified by the proximity of the free surface.

Teng and Ben-Menahem (1965), Alsop and Brune (1965), Berckhemer and Jacob (1968), Ben-Menahem *et al.* (1968), and Chandra (1970) have shown that first-motion solutions from deep earthquakes generally agree with solutions obtained by spectral methods. The same result holds for shallow earthquakes with magnitudes less than  $7\frac{1}{2}$  (Wu and Ben-Menahem, 1965; Ben-Menahem and Aboodi, 1971). This is not always the case with major shallow seismic events. Here, the departure from the point source model in time and space is so pronounced that polarity alone is insufficient to characterize the entire source.

The method of spectral amplitude equalization of body waves was introduced in 1965 by Ben-Menahem, Smith, and Teng in order to set up a routine procedure for extracting source parameters from spectral analyses of isolated body-wave signals recorded at a network of stations around a deep source. The method consists of compensating the observed spectrums for instrumental and propagational effects. A combined study of the resulting radiation patterns and the residual amplitudes supply information on the spatial and temporal characteristics of the source as seen through a spectral window of 10–100 sec. Shorter periods interact strongly with the crust below the recording station (Fig. 6) and longer periods can hardly be considered as rays.

Let  $f(t)[H(t - t_1) - H(t - t_0)]$  denote the analyzed seismograph trace. Let its spectrum be denoted by

$$s(\omega) = \int_{t_0}^{t_1} f(t) e^{-i\omega t} dt = |s(\omega)| e^{i\zeta(\omega)}.$$

The equalization procedure is conceptually analogous to an inverse filtering process through a series of three linear filters: the recording instrument, the Earth's crust, and the Earth's interior. If the transfer function of each of these is known in the said frequency range one may, in principle, remove their effects upon  $s(\omega)$  and plot the resulting equalized spectrum as a function of the azimuth angle. The observed P-wave radiation pattern from a deep shock in the Banda Sea recorded on a network of seismic stations equipped with similar instruments is shown in Fig. 8. Close to it we see a calculated pattern that was obtained through a best-fit search. By means of this comparison one is able to find the orientation parameters of the source  $\delta$ ,  $\lambda$ , and  $\phi_s$  (geographical azimuth of the strike). Once these parameters are known, Eqs. (12)–(14) are used to estimate the entity  $[U_0 dS g(\omega)]$ .

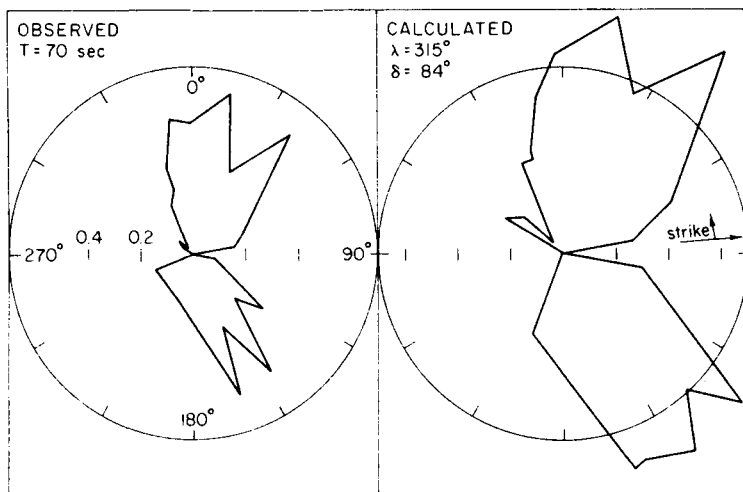


FIG. 8. Radiation patterns of P waves for the Banda Sea earthquake of March 21, 1964.

Ben-Menaem (1961a) and Ben-Menaem *et al.* (1965) conjectured that the fault length and the rupture velocity can, in principle, be derived from spectrums of body waves of deep shocks. Data analysis by Hirasawa (1965), Berckhemer and Jacob (1968), Bollinger (1968, 1970), Davies and Smith (1968), Khattri (1969a,b), and Chandra (1970) have verified this conjecture and lend support to a deep-shock source model in which seismic energy is

being released through a progressive rupture along a shear dislocation. These investigators agree that earthquake foci at depths of 350–600 km in the magnitude range  $6\frac{1}{4}$ – $7\frac{1}{4}$  have a linear dimension of 20–50 km, a rupture speed of 3–5 km/sec, and hence an overall duration of the order of 10 sec. Bollinger (1968, 1970) claimed that these results hold also for some shallow shocks in the magnitude range  $6\frac{1}{4}$ – $6\frac{1}{2}$ .

#### IV. Calculation of Amplitudes and Phases of Surface Waves

##### A. PRELIMINARY REMARKS

Considerable progress has been made during the last decade in the understanding of the kinematic processes at the focal region. It was achieved mainly due to the recognition that long-period surface waves are particularly useful for the study of earthquakes in the magnitude range  $6\frac{1}{2}$ – $8\frac{1}{2}$  since the wavelengths of these waves (200–1800 km) commensurate with the linear dimensions of intermediate and large earthquake sources.

The earliest observations of long-period surface waves were made by Ewing and Press (1954). The method of phase equalization was used by Aki (1960), Brune (1961), and Ben-Menahem and Toksöz (1963a,b). Toksöz *et al.* (1964) used the method of amplitude equalization for the determination of the source time function of underground nuclear explosions. Chander and Brune (1965), Filson and McEvilly (1967), and Ben-Menahem and Aboodi (1971) have shown that source mechanism studies by means of spectral analysis of surface waves are highly rewarding.

Chinnery (1963) introduced the concept of "stress drop" that accompanies earthquakes during faulting. Aki (1966) and Wyss and Brune (1968) used surface waves, among other data, to study the source mechanism of earthquakes in Japan and California.

##### B. EVALUATION OF THEORETICAL SPECTRA

Using Eqs. (141), (142), (149), and (159), one may write the far-field spectral patterns for the vertical Rayleigh displacement ( $u_z^R$ ) and the azimuthal Love displacement ( $u_\phi^L$ ) in the form:

$$u_z^R = \left[ \frac{U_0 dS}{\omega} \right] \frac{\exp(-\gamma_R \Delta - \frac{3}{4}\pi i - iX_R)}{[\sin(\Delta/a)]^{1/2}} [s_R S_R + p_R P_R + iq_R Q_R] \frac{\sin X_R}{X_R}, \quad (183a)$$

$$u_\phi^L = \left[ \frac{U_0 dS}{\omega} \right] \frac{\exp(-\gamma_L \Delta + \frac{3}{4}\pi i - iX_L)}{[\sin(\Delta/a)]^{1/2}} [p_L P_L + iq_L Q_L] \frac{\sin X_L}{X_L}, \quad (183b)$$

where the phase term  $e^{-ik\Delta}$  is omitted and  $(a/\Delta)^{1/2}$  is replaced by  $1/[\sin(\Delta/a)]^{1/2}$  [Eq. (85)]. The effects of anelasticity and finiteness were also taken into account [Eqs. (149), (159)]. The quantities  $\gamma_R$  and  $X_R$  are defined by Eqs. (150) and (160), respectively.

In the notation of Ben-Menahem *et al.* (1970), the functions  $S_R$ , etc., have the form:

$$\begin{aligned} S_R &= P_R \left( \frac{1 + \sigma_s}{1 - \sigma_s} + \frac{\sigma_{R_s}^*(h)}{\mu_s} \frac{C_R}{\dot{u}_s^*} \frac{1 - 2\sigma_s}{1 - \sigma_s} \right), \\ Q_R &= -P_R [\tau_{R_s}(h)/\mu_s] (C_R/\dot{u}_s^*), \\ P_R &= \frac{1}{4\pi a^2} [(k_R a)^{3/2} (8\pi)^{1/2}] \left[ \frac{\mu_s A_R}{k_R} \right] \left[ \frac{\dot{u}_s^*}{\dot{w}_0} \right], \\ Q_L &= P_L [\tau_{L_s}^*(h)/\mu_s] (C_L/\dot{v}_s), \\ P_L &= (1/4\pi a^2) [(k_L a)^{3/2} (8\pi)^{1/2}] (\mu_s A_L/k_L) (\dot{v}_s/\dot{v}_0). \end{aligned} \quad (184)$$

The symbols that appear in these expressions may be grouped as follows:

I. *Geometrical parameters*: Earth's radius ( $a$ ), epicentral distance ( $\Delta$ ), source depth ( $h$ ), station azimuth with respect to fault's strike ( $\phi$ ).

II. *Source parameters*: Spectral displacement ( $U_0$ ), fault area ( $dS$ ), slip angle ( $\lambda$ ), dip angle ( $\delta$ ), azimuth of the strike ( $\phi_s$ ).

III. *Wave parameters*: Wavenumbers ( $k_R, k_L$ ), phase velocities ( $C_R, C_L$ ), attenuation coefficients ( $\gamma_R, \gamma_L$ ), angular frequency ( $\omega$ ).

IV. *Plane-wave functions*: Surface particle velocities ( $\dot{u}_0, \dot{v}_0, \dot{w}_0$ ), particle velocities at source's depth ( $\dot{u}_s, \dot{v}_s, \dot{w}_s$ ), depth-dependent factors of the stresses [ $\tau_{R_s}(h), \sigma_{R_s}(h), \tau_{L_s}(h)$ ].

V. *Medium parameters*: Poisson's ratio at source level ( $\sigma_s$ ), rigidity at source level ( $\mu_s$ ).

VI. *Medium amplitude functions*:  $A_R, A_L$ , independent of source type and depth (Harkrider, 1964).

VII. *Rupture parameters*:  $b, r_f$ . A horizontal rupture with uniform velocity is assumed throughout.

Clearly, the spectral displacements are composite functions of the wave period and mode, the source depth and orientation, the station azimuth, and the structural and dissipation parameters of the layered medium. The dependence of the displacements on the angle  $\phi$  is known as the *radiation pattern* of the wave. Since both  $u_z^R(\phi)$  and  $u_\phi^L(\phi)$  are complex there exist both amplitude and phase patterns. It can be shown that the radiation pattern for surface waves is invariant under the transformation in which the fault plane and the auxiliary plane are interchanged (Jarosch and Aboodi, 1970).

Surface waves fall off with distance like  $e^{-\gamma\Delta}/(\sin \Delta)^{1/2}$ , where  $\gamma(\omega)$  is the frequency-dependent attenuation coefficient. The inverse of this factor is known as the diminution factor. The derivatives  $\partial\Delta^L/\partial k_L$  and  $\partial\Delta^R/\partial k_R$  can be expressed in terms of depth integrals similar to  $I_1$ , and  $I_2$  for the case of the free oscillations (Eqs. 47, 50).

The variation of the functions  $P_R$  and  $Q_R$  with depth is shown in Figs. 9 and 10. Depth in these figures refers to the source depth. These functions were computed from the defining equation (142) for three basic half-space models of the Earth.

The influence of the finiteness factor  $\sin X/X$  on the radiation pattern is demonstrated in Fig. 11 for a source with rupture parameters similar to that of the great Alaskan earthquake of March 28, 1964. It is obvious that the modulation of the pattern due to the finiteness factor is dominating.

### C. APPLICATIONS TO SOURCE STUDIES: THE METHOD OF SPECTRAL EQUALIZATION

Surface waves, as their name suggests, can be effectively regarded as propagating along great circles on the surface of the Earth. A convenient point of reference for them is the epicenter. As a surface wave signal spreads out from the epicenter on its way to the recording station, its spectrum is modified by several factors: (1) attenuation caused by the anelasticity of the upper mantle, (2) dispersion, geometrical spreading, and polar phase-shift over a spherical Earth, and (3) filtering and directional effects of the recording instrument.

Before we can compare recorded spectral amplitudes and phases with theoretical ones, we must compensate the spectrum for these distorting agents. This compensation is known as the amplitude and phase equalization of the signal's spectrum.

The basic assumption in the equalization procedure is that the trace spectrum  $F(\omega)$  of the signal can be considered to be the final output of a series of linear filters, each of which represents one of the agents acting to distort the spectrum of the signal on its way from the source to the station. Each such filter can be characterized by its transfer function, the amplitude, and phase characteristics. One can then recover the original spectrum by carrying out a careful "bookkeeping" of the amplitude and phase history of the signal. For the phases, the rule is that one must *subtract* from the Fourier analysis phases all phase *advances* due to propagation, sphericity, source-to-station geometry, and instrumental distortion. Similarly one must *add* to the Fourier phases all phase *retardations*.

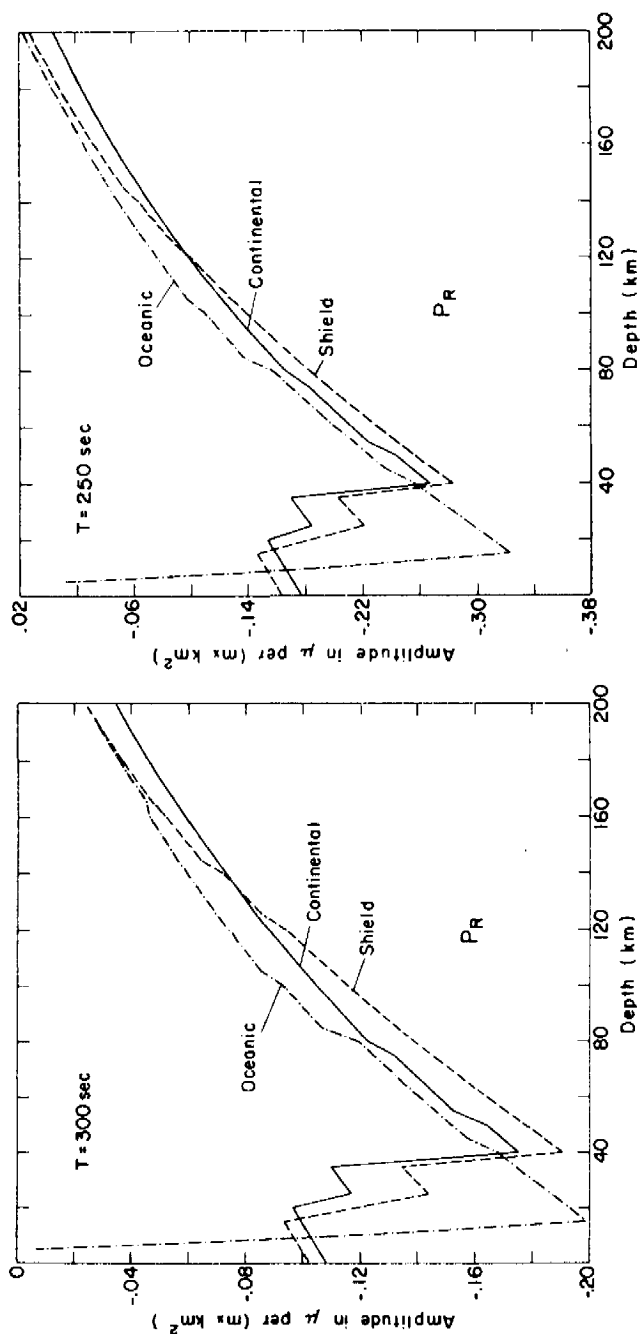


FIG. 9. Amplitude response functions  $P_R$  for Rayleigh waves in flat Earth models.

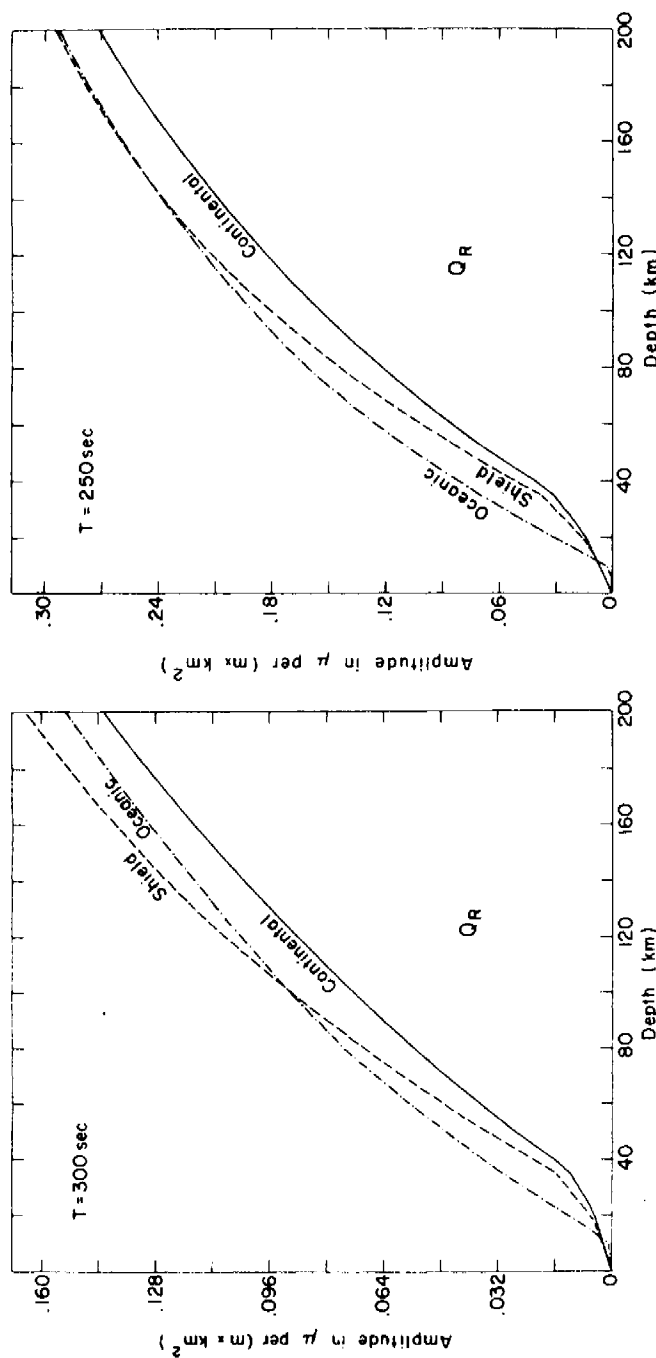


FIG. 10. Amplitude response function  $Q_R$  for Rayleigh waves in flat Earth models.

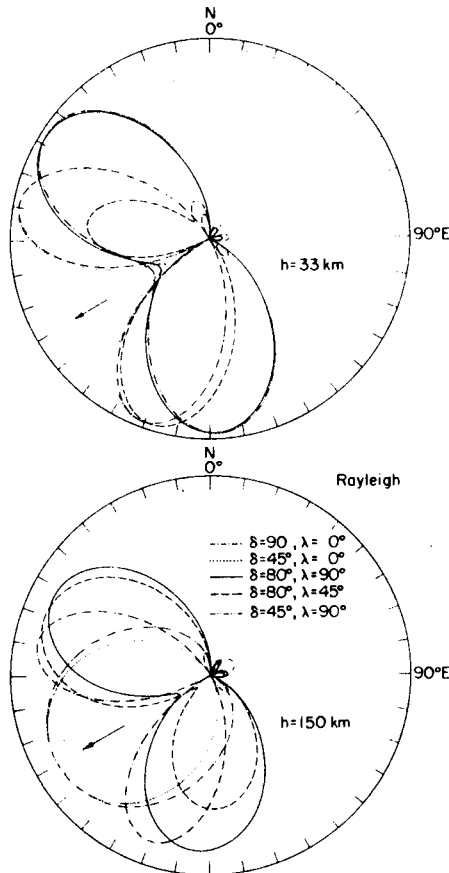


FIG. 11. The influence of finiteness and propagating rupture on the patterns of surface waves.  $b = 600$  km;  $v_f = 3.5$  km/sec;  $T = 250$  sec.

The analyzed data consists of recordings of surface wave signals at a network of stations that is distributed around the source. Any station may record multiple arrivals of both Love and Rayleigh waves. Figure 3 shows an example of such arrivals. In this figure,  $G_1$  is a direct Love wave. This wave continued to travel on the surface of the Earth and arrived again as  $G_3$ . On the other hand,  $G_2$  is a Love wave that left the source in the *opposite* direction and arrived by the major arc. The same wave circled the Earth and arrived again as  $G_4$ , and so on. The same applies to the Rayleigh wave arrivals  $R_1, R_2, R_3, \dots$ , etc.

The set of all such signals that were generated at the source of the same seismic event are separated from the records and subjected to a Fourier analysis. A numerical search procedure is then set up to derive from this data

the unknown source parameters which constitute the theoretical model given by Eq. (245). The "best solution" is that point in the eight-dimensional parameter space ( $\lambda, \delta, \phi_s, b, r_f, h, U_0, D$ ) which produces the best fit between the theoretical and the observed spectra, with respect to the largest possible assembly of signals employed.

Instead of trying to solve for all the unknown quantities in one swoop, we break up the search process into several stages. The first step is to estimate values for  $\phi_s$ ,  $b$ , and  $r_f$ . To this end, we use records from stations which show multiple surface wave arrivals of both even and odd orders. We compute the ratio of the spectral amplitudes of even and odd arrivals over a frequency band having a width of at least several millihertz in the low frequency range, and we correct for possible differences in attenuation. We then search over a three-dimensional grid in the  $(b, r_f, \phi_s)$  space to find the combination which produces the best fit, in a least squares sense, of the "directivity function" (Ben-Menahem, 1961a) given by [cf. Eq. (159)]

$$D(b, r_f, \phi_0, T) = \frac{1 + (v_f/C) \cos \phi_0}{1 - (v_f/C) \cos \phi_0} \times \frac{\sin[(\pi b/v_f T)(1 - (v_f/C) \cos \phi_0)]}{\sin[(\pi b/v_f T)(1 + (v_f/C) \cos \phi_0)]}, \quad (185)$$

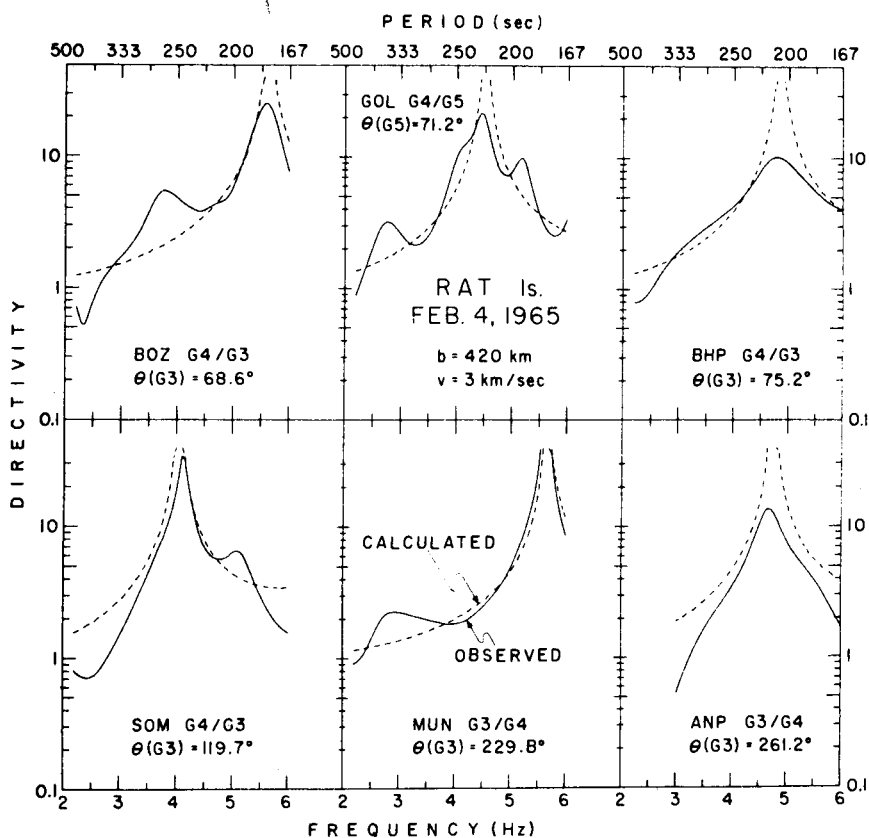
where  $\phi_0 + \phi_s$  is the geographical azimuth of the observer.

Referring to Eqs. (158) and (160), we notice that the directivity function is the ratio of the amplitude finiteness correction factors for waves going in the forward and backward directions, respectively. The directivity function possesses poles or zeroes at those points where the quantity  $b[C/v_f \pm \cos \phi_0]$  is an integral multiple of the wavelength of the Fourier component propagating with phase velocity  $C$ .

Thus, the spectral ratio of the forward to the backward fields of  $G_n/G_{n+1}$  or  $R_n/R_{n+1}$  (e.g., Fig. 3) is diagnostic of the length and velocity of the radiating source.

The location of the nodal lines on the patterns enables us to make a first guess as to the azimuth of the fault strike (which is often parallel or perpendicular to a nodal line). Having chosen a strike direction  $\phi_s$ , one can obtain some idea of the possible range of values of  $b$  and  $r_f$  by checking the degree of asymmetry which the pattern exhibits with respect to the forward and backward directions as defined by  $\phi_s$ . Examples of this "terrestrial interferometry" are shown in Fig. 12 in which the fit of the theoretical with the observed curves is apparent.

Having obtained fairly reliable estimates of  $b$ ,  $r_f$ , and  $\phi_s$ , we proceed to the next stage of the search procedure, namely, the use of the amplitude radiation patterns to determine the source orientation and the average depth.

FIG. 12. Observed vs. calculated directivities of  $G$  waves.

Let  $|u_z|_{\text{obs}}$  denote the spectral amplitude of the vertical component of Rayleigh waves at a given station, after the corrections pertaining to the recording process have been performed, and let  $|u_\phi|_{\text{obs}}$  denote the corresponding spectral amplitude of Love waves. Then, omitting the pure phase factors and using Eq. (183), we may write the following equations relating the observed and theoretical amplitudes,

$$[e^{iR\Delta} \sqrt{\sin(\Delta/a)}] |u_z|_{\text{obs}} = (U_0 dS/\omega) |(p_R P_R + s_R S_R + iq_R Q_R)| |(\sin X_R)/X_R|, \quad (186a)$$

$$[e^{iL\Delta} \sqrt{\sin(\Delta/a)}] |u_\phi|_{\text{obs}} = (U_0 dS/\omega) |[p_L P_L + iq_L Q_L]| |(\sin X_L)/X_L|, \quad (186b)$$

where the factor  $1/\omega$  on the right-hand side arises from an assumed step-function dependence on time. For each station the quantities on the left-hand sides of Eqs. (186a,b) represent "corrected observed amplitudes." The right-hand sides are the "calculated amplitudes," which depend on  $\lambda$ ,  $\delta$ ,  $\phi_s$ ,  $b$ , and  $v_f$ , and also on  $h$ , the source depth. For a given period, the term  $U_0 dS/\omega$  on the right-hand sides of Eqs. (186a,b) is treated as a constant for the purpose of the research in this section.

For each signal analyzed, we store a set of corrected observed amplitudes, for different periods, on magnetic tape together with the appropriate geodetic azimuth and an index indicating which of the three common Earth structures (continental, shield, or oceanic) is most appropriate for the path over which the wave traveled. On another tape we store the values of the spectral amplitude functions  $P_R$ ,  $Q_R$ ,  $S_R$ ,  $P_L$ , and  $Q_L$  for the fundamental mode for each of the three structural models, for periods of 10 (2) 400 sec and for source depths 0 (2) 50, 50 (5) 650 km.

The search program then operates in the following manner: Over each of the several periods which are read in as input data, a search is made for each of the angular orientation parameters  $\lambda$ ,  $\delta$ , and  $\phi_s$ . The assumed source depth (as a first approximation, we take the value proposed by the USCGS) is also read in, with an option of integrating over a depth interval to approximate a fault of finite vertical extent. There is an additional option to read in the limits for ranges of values of  $b$  and  $v_f$  which are needed to calculate the finiteness factors.

The program then makes a search over a grid in the five-dimensional space ( $\lambda$ ,  $\delta$ ,  $\phi_s$ ,  $b$ ,  $v_f$ ) according to the following criterion. Let  $X = (x_i)$  be the vector (for a given period) of corrected observed amplitudes, such that each signal (with its azimuth  $\phi_0$ ) contributes one component of this vector. For any fixed point in the five-dimensional parameter space, we can calculate the vector  $Y = (y_i)$  of theoretical amplitudes at each station under consideration. Assuming  $y_i = A + Bx_i$ , we calculate  $A$  and  $B$  according to the least squares criterion. The normal equations yield the solution

$$A = \frac{(\sum y_i)(\sum x_i^2) - (\sum x_i)(\sum x_i y_i)}{M \sum x_i^2 - (\sum x_i)^2}, \quad B = \frac{M \sum x_i y_i - (\sum x_i)(\sum y_i)}{M \sum x_i^2 - (\sum x_i)^2}, \quad (187)$$

where  $M$  is the number of stations and each sum is taken over all the stations employed in the computation. With these values of  $A$  and  $B$ , we can calculate  $C^2$ , the square of the correlation coefficient,

$$C^2 = \frac{M(A \sum y_i + B \sum x_i y_i) - (\sum y_i)^2}{M \sum y_i^2 - (\sum y_i)^2}. \quad (188)$$

Rejecting, as devoid of any physical significance, all cases where  $B < 0$ , we calculate  $C^2$  for each of the remaining points of our grid in the five-dimensional parameter space and check which combination of parameters leads to the highest  $C$ -value. This is considered our "best" solution in the region where the search has been performed.

We remark that, in practice, since  $b$ ,  $r_f$ , and  $\phi_s$  are reasonably well determined as a result of the directivity search described earlier, the major portion of the search using the amplitude radiation patterns is done with respect to  $\lambda$  and  $\delta$ .

For a given source depth (assuming for the moment infinitesimal vertical extent), the search is repeated for each of the input periods. If no solution is found which is acceptable with respect to all the input periods, then the assumed source depth is increased by 5 km and the entire search procedure is repeated over all input periods to try to obtain an acceptable solution for the new source depth. This method thus constitutes an indirect search over the source depth  $h$  as well; since if we obtain a consistent solution over all the periods for one depth whereas we fail to find a consistent solution for a shallower depth, we would prefer the larger depth as the more correct value of this parameter.

Even if we should obtain a consistent solution for a particular depth, we can always perform a search over depth indirectly in several steps, by rerunning the program with an initial depth input which is larger than that for which an acceptable solution was previously obtained. We can then choose between the possible allowed values of  $h$  by comparing the values of  $C^2$  obtained in the search procedure over the individual input periods. We also impose the requirement that the values of  $\lambda$ ,  $\delta$ ,  $\phi_s$ ,  $b$ ,  $r_f$ , and  $h$  be consistent with both Rayleigh and Love wave observations. A fit of calculated and observed patterns thus obtained for Rayleigh waves for two earthquakes is shown in Fig. 13.

Similarly, one can search for a best solution using the initial spatial phases. The corrected observed initial spatial phases are given by

$$[\psi_0]_{\text{obs}} = \omega[(\Delta_i/C) - t_i] - \psi_F - \psi_{\text{inst}} - \psi_{\text{polar}} + N - \psi_{\text{step}} - \psi_{\text{fin}}, \quad (189)$$

where  $N$  is an integer,  $\psi_{\text{inst}}$  is the instrumental phase advance plus the instrumental polarity correction,  $\psi_{\text{polar}}$  is the phase advance of  $\pi/2$  for each polar and antipodal passage (Section II, E, 1; Brune, 1961),  $\psi_F$  is the phase of the Fourier integral,  $\Delta_i$  is the distance traveled by a surface wave of order  $i$  (thus  $\Delta_1$  is the direct wave,  $\Delta_2$  is the wave that reached the station via the major arc, etc.),  $t_i$  is the fiducial time at the beginning of the window,  $\psi_{\text{step}} = -\pi/2$ , the phase of the Fourier transform of the Heaviside unit step function, and  $\psi_{\text{fin}}$  is  $-X$  radians, the phase advance due to the source finiteness and rupture velocity.

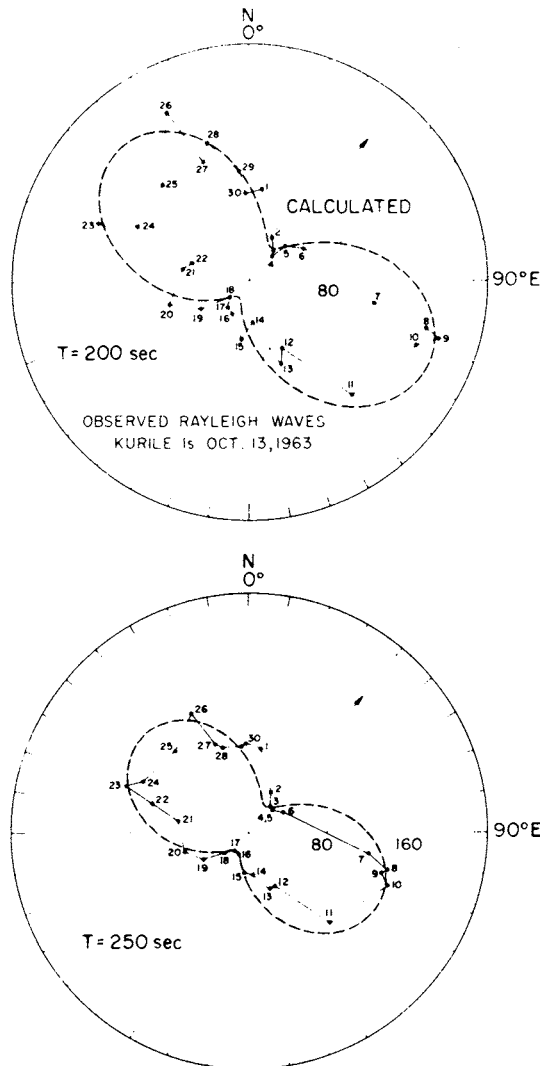


FIG. 13. Observed vs. calculated radiation patterns of Rayleigh waves.  $\delta = 41^\circ$ ;  $\lambda = 99$ ;  $h = 35$  km;  $b = 250$  km;  $v_f = 3.5$  km/sec.

The search over the initial phases is in general similar to the search over the amplitudes.

The third stage of the search is the computation of  $U_0$ , the amount of the dislocation at the source. In the search for the best solution, we neglected the vertical extent of the source and sought the virtual equivalent seismic

source located at depth  $h$ . In order to compute the source displacement, however, we make the assumption that the fault extends from the surface to a depth  $D$ . Taking  $dS = b dh$ , we integrate over the depth and recast Eq. (186a,b) in the form

$$\{e^{i\kappa\Delta}[\sin(\Delta/a)]^{1/2}\}|u_z|_{\text{obs}} = U_0(b/\omega)(\sin X_R/X_R) \times \left| \int_0^D [p_R P_R(h) + s_R S_R(h) + iq_R Q_R(h)] dh \right|, \quad (190a)$$

$$\{e^{i\kappa\Delta}[\sin(\Delta/a)]^{1/2}\}|u_\phi|_{\text{obs}} = U_0(b/\omega)(\sin X_L/X_L) \times \left| \int_0^D [p_L P_L(h) + iq_L Q_L(h)] dh \right|. \quad (190b)$$

The problem posed by Eqs. (190a,b) may be stated as follows: Given the corrected observed spectral amplitudes, it is required to find scalars  $D$  and  $U_0$  such that both equations are satisfied for a given set of source parameters ( $\lambda, \delta, \phi_s, b, v_f$ ) at each station over a preassigned frequency band. For the calculations of this section the depth dependence of the basic amplitude functions  $P_R(h)$ ,  $Q_R(h)$ ,  $S_R(h)$ ,  $P_L(h)$ , and  $Q_L(h)$  was chosen to be that of an average Earth model composed of oceanic, continental, and shield paths in the ratio 4 : 1 : 1.

If we assume a value for  $D$ , the integrals on the right-hand sides of Eqs. (190a,b) may be evaluated numerically. For each station used in the radiation pattern solution, the corrected observed amplitudes for a given period, which constitute the left-hand sides of Eqs. (190a,b), are divided by all the calculated amplitude factors multiplying  $U_0$  on the right-hand sides. These factors depend on the acceptable values of  $\lambda, \delta, \phi_s, b$ , and  $v_f$  which are presumably known as a result of the search procedure. Thus one can evaluate  $U_0$  for each period at each station.

Ideally,  $U_0$  should prove to be a constant for a particular source. In practice, however, because of the imperfect fit of the calculated "best fit" solution to the observed values, there are likely to be variations in the calculated values of  $U_0$ . For lack of any particular indication to the contrary, we assume that the values of  $U_0$  are roughly normally distributed about some mean value, which is assumed to be independent of the period and the station azimuths.

For large magnitude earthquakes, the most reliable portion of the spectrum is considered to lie in the period range 200–250 sec. Thus for each station an average value of  $U_0$  is computed by averaging over the six values

obtained by taking for the period,  $T$ , the values 200 (10) 250 sec. Then for a particular solution, the average  $U_0$  is computed by taking the average over the average station values.

These calculations are carried out for different values of  $D$ , taking for an initial trial value  $D \approx 2h$ , where  $h$  is the mean source depth found earlier from radiation pattern observation.

## V. Calculation of Terrestrial Line-Spectra

### A. GENERAL DESCRIPTION

Alterman *et al.* (1959) and Gilbert and MacDonald (1960) studied the relative excitation of various free modes by compressional and torque-like point sources situated at various depths. Ben-Menahem (1964), Saito (1967), and Singh and Ben-Menahem (1969a,b) have formulated a theory for spectral line amplitudes of toroidal and spheroidal motions for various sources.

Ben-Menahem *et al.* (1972b) have prepared tables of spectral line amplitudes of surface displacements and strains for a radially heterogeneous gravitating earth. Given a structural model and a dislocation source of arbitrary orientation and depth, spheroidal and toroidal line amplitudes are calculable for  $l \leq 100$ ,  $n \leq 4$  everywhere on the Earth's surface. These authors have shown that:

- (i) The combination of a realistic Earth model with a dislocation source model produces theoretical displacements and strains that match the observations.
- (ii) The theoretical calculations of the spectral line amplitudes can be used as an additional tool for the investigation of the earthquake source mechanism and the infrastructure of the interior of the Earth.

To demonstrate the use of the program for the inversion of source data, Ben-Menahem *et al.* (1972a,b) derived the force system at the source of the Alaskan earthquake of 1964.

### B. DETAILS OF COMPUTATIONS

The numerical evaluation of the toroidal eigenfunctions  $y_1(\bar{r})$  and  $\hat{y}_2(\bar{r})$  for a radially heterogeneous Earth model is done by the Runge-Kutta integration routine. Equation (58) may be written in terms of the dimensionless variables introduced earlier [Eqs. (66), (67)]. We find

$$\begin{aligned} \frac{dy_1(\bar{r})}{d\bar{r}} &= \frac{y_1(\bar{r})}{\bar{r}} + \frac{\hat{y}_2(\bar{r})}{\bar{\mu}}, \\ -\frac{d\hat{y}_2(\bar{r})}{d\bar{r}} &= \left[ \bar{\omega}^2 \bar{\rho}_0 - \frac{\bar{\mu}(l-1)(l+2)}{\bar{r}^2} \right] y_1(\bar{r}) + \frac{3}{\bar{r}} \hat{y}_2(\bar{r}). \end{aligned} \quad (191)$$

These equations are solved with the boundary conditions  $\hat{y}_2(1) = \hat{y}_2(\bar{\tau}) = 0$ . The eigenfrequencies are obtained from these equations by applying a fourth-order Runge-Kutta iteration procedure. At  $\bar{r} = \bar{\tau}$ ,  $\dot{y}_2 = 0$  and  $y_1$  is arbitrarily chosen as unity.

The values obtained for the eigenfrequencies were first compared with the solutions of the closed-form frequency equation for a homogeneous sphere. Eigenfrequencies were then calculated for two realistic earth models: Jeffreys-Bullen A' and Gutenberg-Bullard I.

The resulting periods are then used in the calculation of the amplitude factors  $\bar{I}_1$ ,  $G_1$ , and  $G_2$ . These amplitudes can be checked by calculating them for a homogeneous sphere and comparing the results with those calculated from closed-form analytic expressions. A second check can be made against the case of a uniform elastic shell  $b \leq r \leq a$  overlying a liquid core. The analytic expressions for this case also are known.

The method of deriving the eigenvalues and eigenfunctions for the spheroidal oscillations under the proper boundary conditions has been described in detail by Jarosch (1962) and will not be repeated here. The functions  $F_i$  of Eq. (75) are evaluated from the calculated eigenvalues and eigenfunctions. The integral  $\bar{I}_2$  defined in Eq. (75) is evaluated by the extended Simpson rule for each of the layers defined by the model.

In computing the associated Legendre polynomials, use is made of the following recursion formula for the Legendre polynomials

$$lP_l(\cos \theta) = (2l - 1) \cos \theta P_{l-1}(\cos \theta) - (l - 1)P_{l-2}(\cos \theta). \quad (192)$$

However, to control round-off errors that may occur by the excessive use of this formula, its use is limited to ten successive values of  $l$ . For the next two  $l$  values, one uses the trigonometric series representation of the Legendre polynomials

$$\begin{aligned} P_l(\cos \theta) &= \frac{(2l)!}{2^{2l}(l!)^2} \left[ \cos l\theta + \frac{1}{1} \frac{l}{2l-1} \cos(l-2)\theta \right. \\ &\quad \left. + \frac{1 \cdot 3}{1 \cdot 2} \frac{l(l-1)}{(2l-1)(2l-3)} \cos(l-4)\theta + \cdots + \cos(-l)\theta \right]. \end{aligned} \quad (193)$$

Thus, a proper computation of the Legendre polynomials for all values of  $l$  and  $\theta$  is assured. To compute higher order polynomials and their derivatives the following relations were used:

$$\begin{aligned}
 P_l^1(\cos \theta) &= \frac{-l}{\sin \theta} [\cos \theta P_l(\cos \theta) - P_{l-1}(\cos \theta)], \\
 P_l^2(\cos \theta) &= \left[ -2l \frac{1 + \cos 2\theta}{1 - \cos 2\theta} - l(l+1) \right] P_l(\cos \theta) \\
 &\quad + 4l \frac{\cos \theta}{1 - \cos 2\theta} P_{l-1}(\cos \theta), \\
 (\hat{c}/\partial \theta) P_l''(\cos \theta) &= -(1/\sin \theta)[(l+n)P_{l-1}''(\cos \theta) - l \cos \theta P_l''(\cos \theta)].
 \end{aligned} \tag{194}$$

These equations do not entail the compounding of round-off errors since they are given directly in terms of previously computed Legendre polynomials. The resulting values have been checked with tables and were found to agree up to eight significant places.

Using the above scheme for the evaluation of the Legendre functions and their derivatives, the colatitude functions  $H_1$  to  $H_{12}$  are calculated.

The four radial functions  $G_1$ ,  $G_2$ ,  $F_1$ ,  $F_2$  for the fundamental mode are shown in Figs. 14 and 15 for the Jeffreys-Bullen A' Earth model. The effect of the source depth is demonstrated by obtaining these functions for four values of  $h$  (550 km, 250 km, 100 km, 30 km).

An example of the variation of the displacement and strain fields can be seen in Fig. 16. In this figure, we have plotted the strain component  $\varepsilon_{\theta\theta}$  for a source of the strike-slip type placed at a depth of 250 km. The oscillations are of the toroidal type and their order  $l = 2$ . In our mapping of the surface of the sphere on the plane of the paper, the sphere is mapped onto a tangent plane at the epicenter. Each point is moved in such a way that the epicentral distance and the azimuth are preserved. The angle  $\phi$  runs in a counterclockwise direction from the strike of the fault. Lines of equal magnitude are drawn either as solid thin lines (for positive values) or broken lines (for negative values). The nodal lines are exhibited as heavy solid lines. The source constant ( $= U_0 dS / 4\pi a^2$ ) is assigned a magnitude of  $3000 \mu$ . This represents, for example, an earthquake fault of 700 km with a vertical extent of some 100 km and a source dislocation of 20 m.

### C. APPLICATION TO SOURCE STUDIES

A comparison of the calculated values for the amplitudes of the toroidal and spheroidal oscillations of the Earth with the observed values gives useful information about the force system of the corresponding event. If some of the parameters of the source are known from other studies, the rest may be calculated with the help of a search program which gives one or more solutions that fit the observed amplitude data of the free oscillations.

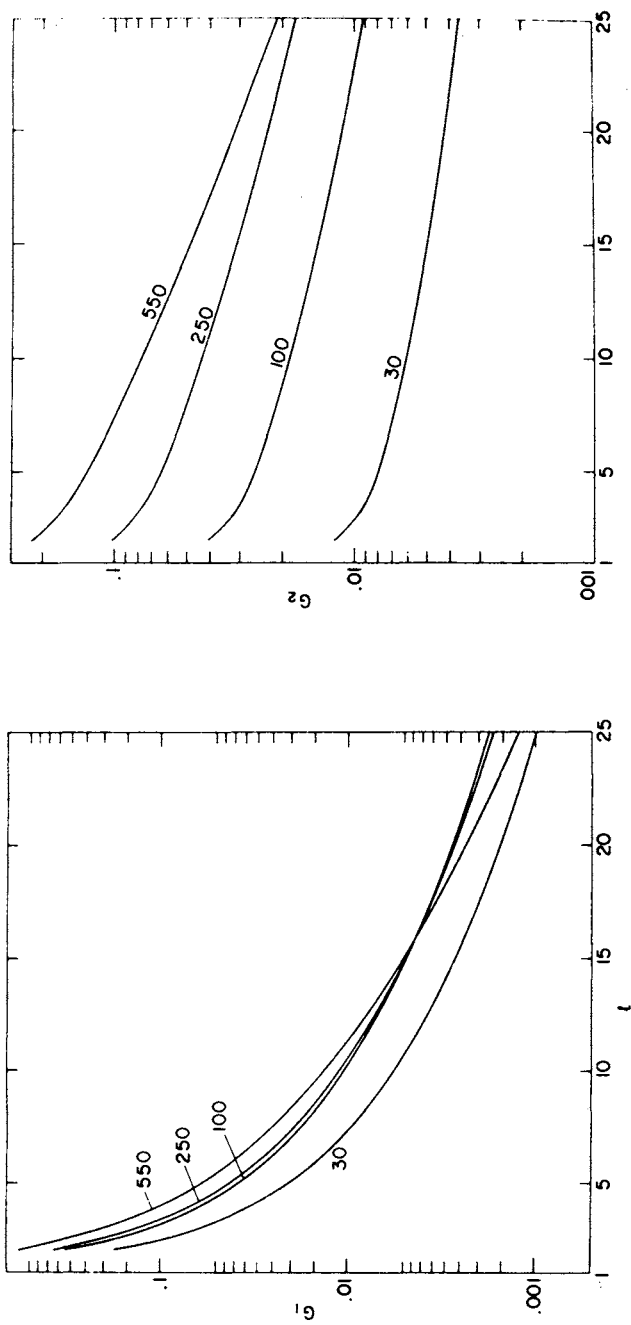


FIG. 14. The dependence of the toroidal radial function on the mode number  $l$ . Numerals on curves represent source' depth in kilometers.

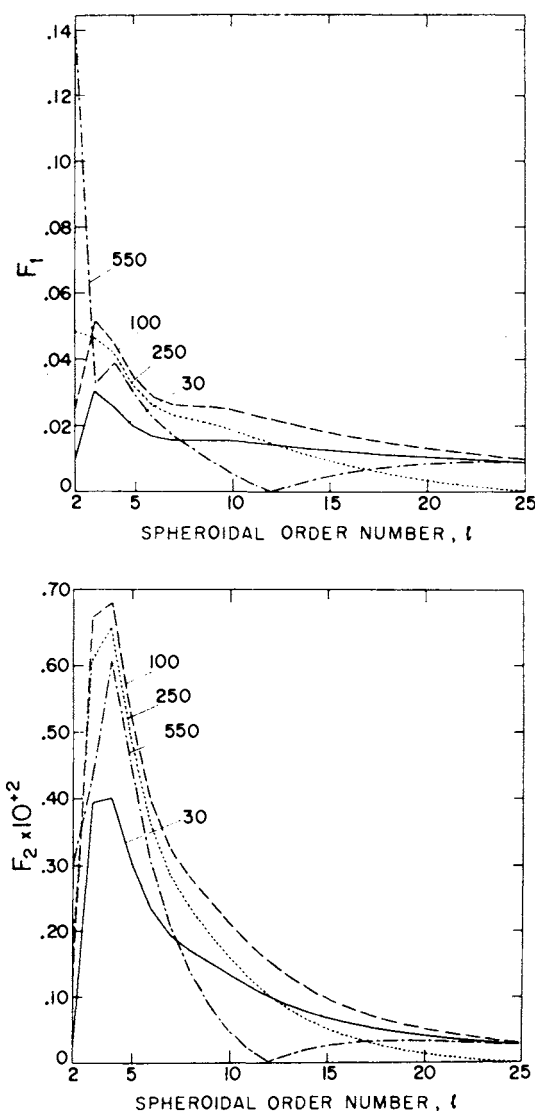


FIG. 15. The dependence of two of the spheroidal radial functions on the mode number  $l$ . Numerals on curves represent source' depth in kilometers.

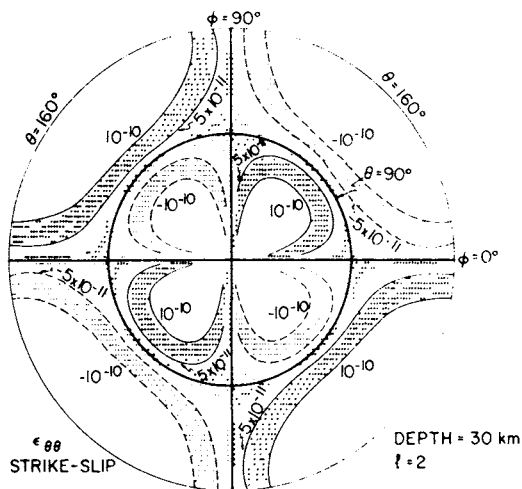


FIG. 16. Distribution of a toroidal strain component on the Earth's surface for a pointsource with  $\Omega = 3000 \mu$ , for the Jeffreys-Bullen 'A' Earth model.

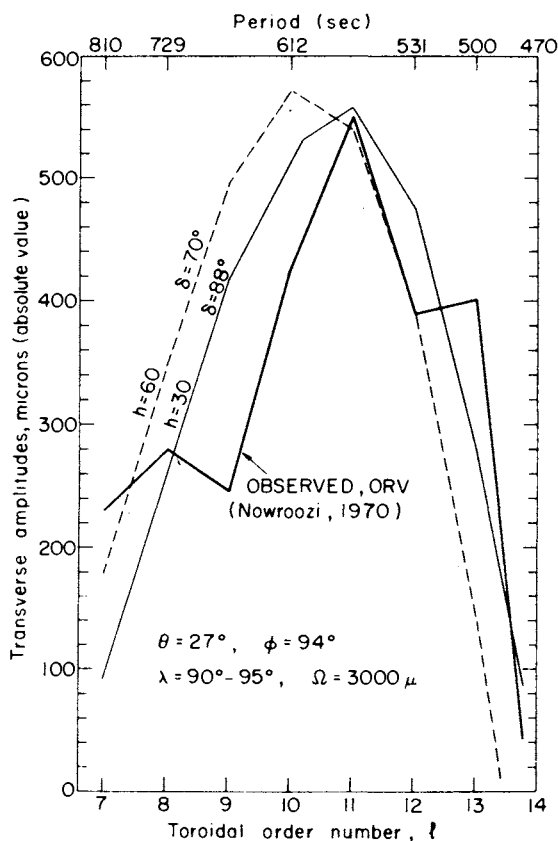


FIG. 17. Observed vs. calculated toroidal amplitudes for the Alaskan earthquake of March 28, 1964.

In order to test the dependence of the results on the choice of the earth's structural model, one may run the program for various Earth models. The dimensionless functions  $G_1, G_2, F_1$  to  $F_6$  depend on the structural parameters of a chosen Earth model, source depth, and the mode numbers  $l$  and  $n$ .

For a source with a given orientation ( $\delta, \lambda$ ), the spectral amplitudes can be calculated from Eqs. (70)–(72), (77)–(79), and (140).

Given the basic source parameters ( $\delta, \lambda, \Omega, h, \phi_s$ ), together with a certain structural Earth model, the amplitudes of the terrestrial line spectra can be obtained from Eq. (140).

To search for the best calculated fit, Eq. (140) can be programmed for a possible range of values of  $\delta, \lambda$ , and  $h$ . All the corresponding solutions are inspected. Those solutions which fit both the toroidal and spheroidal data are chosen.

Figure 17 shows the values of the amplitudes of the toroidal vibrations of the Earth observed at Oroville during the Alaskan earthquake of March 28, 1964 (Nowroozi, 1970) and the corresponding values calculated for the Jeffreys–Bullen A' model of the Earth.

## VI. List of Symbols

$a$	Mean radius of the Earth
$b$	Fault length. Also radius of the core
$\mathbf{B}_m, \mathbf{C}_m, \mathbf{P}_m$	Vector cylindrical harmonics (Table I)
$\mathbf{B}_{m,l}, \mathbf{C}_{m,l}, \mathbf{P}_{m,l}$	Vector spherical harmonics (Table I)
$C_R, C_L$	Phase velocities
$dS$	Area element of the fault. Implies integration over the dislocation surface for finite faults
$D$	Vertical extent of the fault
$\mathbf{e} = \mathbf{u}_0/U_0$	Unit vector along the dislocation
$\mathbf{e}_r, \mathbf{e}_\theta, \mathbf{e}_\phi$	Unit vectors along $r, \theta, \phi$ , respectively
$\mathbf{e}_\rho, \mathbf{e}_\phi, \mathbf{e}_z$	Unit vectors along $\rho, \phi, z$ , respectively
$\mathbf{e}_1, \mathbf{e}_2, \mathbf{e}_3$	Unit vectors along $x_1, x_2, x_3$ , respectively
$\mathbf{e}_R, \mathbf{e}_{i_h}, \mathbf{e}_\phi$	Unit vectors along $R, i_h, \phi$ , respectively
$\mathfrak{E}$	Strain tensor
$g_0$	Gravity
$g(\omega)$	Spectrum of the source
$G$	Constant of gravitation
$G_p, G_\varsigma$	Divergence coefficients
$\mathfrak{G}(\mathbf{r} \mathbf{r}_0)$	Green's tensor
$h$	Source depth
$h_m^{(2)}(z)$	Spherical Hankel function of the second kind

$H(t)$	Heaviside's step function
$i$	Angle between the ray and the radius vector (Fig. 2)
$i_0, i_h$	$i(r_0), i(r_h)$
$\mathfrak{I}$	Idemfactor or unit tensor
$j_m(z)$	Spherical Bessel function of the first kind
$J_m(z)$	Bessel function of the first kind
$k$	Separation variable
$k_R, k_L$	Wavenumbers
$k_\alpha, k_\beta$	$\omega/\alpha, \omega/\beta$
$\mathbf{n}$	Unit vector along the normal to $dS$
$p$	Ray parameter
$P_l^m(\cos \theta)$	Associated Legendre function of the first kind
$Q_p, Q_s$	Dimensionless dissipation parameter
$r, \theta, \phi$	Spherical coordinates
$r_0, \theta_0, \phi_0$	Coordinates of the source. In Fig. 2 the coordinates of the observer at the base of the crust are $(r_0, \theta, \phi)$ and for the focus $r = r_h, \theta = 0$
$\mathbf{r}$	$r\mathbf{e}_r$
$R, i_n, \phi$	Intrinsic coordinates (Fig. 2)
$R$	$ \mathbf{r} - \mathbf{r}_0 $
$t$	Time
$\bar{t}$	$r_0/a$
$T$	Travel time. Also period $2\pi/\omega$
$\mathfrak{T}$	Stress tensor
$\mathbf{u}(u_r, u_\theta, u_\phi)$	Displacement vector in spherical coordinates
$\mathbf{u}(u_\rho, u_\phi, u_z)$	Displacement vector in cylindrical coordinates
$U_0$	Magnitude of dislocation
$v$	Velocity ( $\alpha$ or $\beta$ )
$v_0, v_h$	$v(r_0), v(r_h)$
$v_a$	Apparent velocity
$v_f$	Rupture velocity
$Y_m(k\rho, \phi)$	$J_m(k\rho)e^{im\phi}$
$Y_{m,l}(\theta, \phi)$	$P_l^m(\cos \theta)e^{im\phi}$
$\alpha, \beta$	Wave velocities
$\gamma_p, \gamma_s$	Attenuation coefficients
$\Gamma$	$U_0 dS/4\pi$
$\delta, \lambda$	Dip and slip angles
$\delta_{kl}$	Kronecker delta
$\delta(r - r_0)$	Dirac delta function
$\Delta$	Epicentral distance
$\varepsilon$	$\operatorname{sgn}(r - r_0)$
$\varepsilon_0$	Rayleigh wave ellipticity

$\eta$	$r/v$
$\eta_0, \eta_h$	$\eta(r_0), \eta(r_h)$
$\lambda, \mu$	Lamé parameters. $\mu$ also denotes micron
$\lambda_0, \mu_0$	$\lambda(r_0), \mu(r_0)$
$v$	$(k^2 - k_\alpha^2)^{1/2}$
$v'$	$(k^2 - k_\beta^2)^{1/2}$
$\bar{v}$	$(k^2 - k_0^2)^{1/2}$
$\rho_0$	Density
$\rho, \phi, z$	Cylindrical coordinates
$\sigma$	Poisson ratio
$\bar{\tau}$	$b/a$
$\phi_s$	Geographical azimuth of the source. The geographical azimuth of the observer is $\phi_0 + \phi_s$
$\omega$	Circular frequency
$n\omega_l$	Eigenfrequency
$\Omega$	$U_0 dS / 4\pi a^2$
$\bar{\Omega}$	$\Omega/a$
$\Omega_{m,l}$	$\frac{4\pi}{2l+1} \frac{(l+m)!}{(l-m)!}$
$\Omega_n$	$k^2 - \frac{1}{2}k_{\beta_n}^2$

#### ACKNOWLEDGMENTS

One of the authors (S. J. S.) wishes to thank the Department of Applied Mathematics of the Weizmann Institute of Science for a senior fellowship, and the Kurukshetra University for a study leave.

This research has been sponsored by the Environmental Science Services Administration of the U.S. Government Department of Commerce under contract 1-35138, and by the Cambridge Research Laboratories (AFCRL), United States Air Force under contract F44620-71-C-0120.

#### REFERENCES

- AKI, K. (1960). *J. Geophys. Res.* **65**, 729.
- AKI, K. (1961). *Bull. Egrthq. Res. Inst. Tokyo* **39**, 255.
- AKI, K. (1966). *Bull. Egrthq. Res. Inst. Tokyo* **44**, 73.
- AKI, K., and PRESS, F. (1961). *Geophys. J. Roy. Astron. Soc.* **5**, 292.
- ALSOP, L. E., and BRUNE, J. N. (1965). *J. Geophys. Res.* **70**, 6165.
- ALTERMAN, Z., JAROSCH, H., and PEKERIS, C. L. (1959). *Proc. Roy. Soc. Ser. A* **252**, 80.
- ANDERSON, D. L., and ARCHAMBEAU, C. B. (1964). *J. Geophys. Res.* **69**, 2071.
- ANDERSON, D. L., BEN-MENAHEM, A., and ARCHAMBEAU, C. B. (1965). *J. Geophys. Res.* **70**, 1441.

- BEN-MENAHEM, A. (1961a). Ph.D. Thesis, California Institute of Technology, Pasadena.
- BEN-MENAHEM, A. (1961b). *Bull. Seismol. Soc. Amer.* **51**, 401.
- BEN-MENAHEM, A. (1962). *J. Geophys. Res.* **67**, 345.
- BEN-MENAHEM, A. (1964). *Bull. Seismol. Soc. Amer.* **54**, 1323.
- BEN-MENAHEM, A. (1965). *J. Geophys. Res.* **70**, 4641.
- BEN-MENAHEM, A. (1972). *Geophys. J. Roy. Astron. Soc.* **25**, 307.
- BEN-MENAHEM, A., and ABOODI, E. (1971). *J. Geophys. Res.* **76**, 2674.
- BEN-MENAHEM, A., and HARKRIDER, D. G. (1964). *J. Geophys. Res.* **69**, 2605.
- BEN-MENAHEM, A., and SINGH, S. J. (1968a). *Bull. Seismol. Soc. Amer.* **58**, 1519.
- BEN-MENAHEM, A., and SINGH, S. J. (1968b). *Geophys. J. Roy. Astron. Soc.* **16**, 417.
- BEN-MENAHEM, A., and TOKSÖZ, M. N. (1963a). *J. Geophys. Res.* **68**, 5207.
- BEN-MENAHEM, A., and TOKSÖZ, M. N. (1963b). *Bull. Seismol. Soc. Amer.* **53**, 905.
- BEN-MENAHEM, A., SMITH, S. W., and TENG, T. L. (1965). *Bull. Seismol. Soc. Amer.* **55**, 203.
- BEN-MENAHEM, A., JAROSCH, H., and ROSENMAN, M. (1968). *Bull. Seismol. Soc. Amer.* **58**, 1899.
- BEN-MENAHEM, A., ROSENMAN, M., and HARKRIDER, D. G. (1970). *Bull. Seismol. Soc. Amer.* **60**, 1337.
- BEN-MENAHEM, A., ROSENMAN, M., and ISRAEL, M. (1972a). *Phys. Earth. Planet. Interiors* **5**, 1.
- BEN-MENAHEM, A., ISRAEL, M., and LEVITÉ, U. (1972b). *Geophys. J. Roy. Astron. Soc.* **25**, 407.
- BEINNDORF, H. (1905). *Mitt. Erdbeben-Komm. Wien [N.S.]* **114**, 1407.
- BERCKHEMER, H., and JACOB, K. H. (1968). "Scientific Report," No. 13. Inst. Meteorol. Geophys., Univ. of Frankfurt, Germany.
- BETTI, E. (1872). *Nuovo Cimento* [2] 7.
- BISWAS, N. N., and KNOPOFF, L. (1970). *Bull. Seismol. Soc. Amer.* **60**, 1123.
- BOLLINGER, G. A. (1968). *J. Geophys. Res.* **73**, 785.
- BOLLINGER, G. A. (1970). *J. Geophys. Res.* **75**, 955.
- BROMWICH, T. J. I'A. (1916). *Proc. London Math. Soc.* [2] **15**, 401.
- BRUNE, J. N. (1961). *Publ. Dominion Observ., Ottawa* **24**, 373.
- BRUNE, J. N. (1968). *J. Geophys. Res.* **73**, 777.
- BRUNE, J. N., and ALLEN, C. R. (1967). *Bull. Seismol. Soc. Amer.* **57**, 501.
- BULLEN, K. E. (1953). "An Introduction to the Theory of Seismology." Cambridge Univ. Press, London and New York.
- BURRIDGE, R., LAPWOOD, E. R., and KNOPOFF, L. (1964). *Bull. Seismol. Soc. Amer.* **54**, 1889.
- BYERLY, P. (1926). *Bull. Seismol. Soc. Amer.* **16**, 209.
- CAGNIARD, L. (1939). "Réflexion et réfraction des ondes séismiques progressives." Gauthier-Villars, Paris.
- CHANDER, R., and BRUNE, J. N. (1965). *Bull. Seismol. Soc. Amer.* **55**, 805.
- CHANDRA, U. (1970). *Bull. Seismol. Soc. Amer.* **60**, 639.
- CHINNERY, M. A. (1963). *Bull. Seismol. Soc. Amer.* **53**, 921.
- CURTIS, A. R., and SHIMSHONI, M. (1970). *Bull. Seismol. Soc. Amer.* **60**, 1077.
- DAVIES, J. B., and SMITH, S. W. (1968). *Bull. Seismol. Soc. Amer.* **58**, 1503.
- DEBYE, P. (1909). *Math. Ann.* **67**, 535.
- DE HOOP, A. T. (1958). D.Sc. Thesis, Delft.
- DORMAN, J., EWING, M., and OLIVER, J. (1960). *Bull. Seismol. Soc. Amer.* **50**, 87.
- EWING, M., and PRESS, F. (1954). *Bull. Seismol. Soc. Amer.* **44**, 471.
- FILSON, J., and McEVILLY, T. V. (1967). *Bull. Seismol. Soc. Amer.* **57**, 1245.
- GARVIN, W. W. (1956). *Proc. Roy. Soc., Ser. A* **234**, 528.

- GILBERT, F., and MACDONALD, G. J. F. (1960). *J. Geophys. Res.* **65**, 675.
- GUTENBERG, B. (1952). *Trans. Amer. Geophys. Un.* **33**, 573.
- HANSEN, W. W. (1935). *Phys. Rev.* **47**, 139.
- HARKRIDER, D. G. (1964). *Bull. Seismol. Soc. Amer.* **54**, 627.
- HARKRIDER, D. G. (1970). *Bull. Seismol. Soc. Amer.* **60**, 1937.
- HASKELL, N. A. (1953). *Bull. Seismol. Soc. Amer.* **43**, 17.
- HASKELL, N. A. (1960). *J. Geophys. Res.* **65**, 4147.
- HASKELL, N. A. (1962). *J. Geophys. Res.* **67**, 4751.
- HASKELL, N. A. (1964). *Bull. Seismol. Soc. Amer.* **54**, 377.
- HEALY, J. H. (1963). *J. Geophys. Res.* **68**, 5777.
- HIRASAWA, T. (1965). *J. Phys. Earth.* **13**, 35.
- HIRASAWA, T., and STAUDER, W. (1965). *Bull. Seismol. Soc. Amer.* **55**, 237.
- HODGSON, J. H. (1957). *Bull. Geol. Soc. Amer.* **68**, 611.
- ISACKS, B., and MOLNAR, P. (1971). *Rev. Geophys. Space Phys.* **9**, 103.
- JACKSON, W. H., STEWART, S. W., and PAKISER, L. C. (1963). *J. Geophys. Res.* **68**, 5767.
- JAROSCH, H. (1962). Ph.D. Thesis, University of London.
- JAROSCH, H., and ABOODI, E. (1970). *Geophys. J. Roy. Astron. Soc.* **21**, 513.
- JEANS, J. H. (1923). *Proc. Roy. Soc., Ser. A* **102**, 554.
- JEFFREYS, H. (1923). *Proc. London Math. Soc. [2]* **23**, 428.
- JEFFREYS, H. (1931). *Mon. Notic. Roy. Astron. Soc., Geophys. Suppl.* **2**, 407.
- JEFFREYS, H. (1970). "The Earth," Cambridge Univ. Press, London and New York.
- JEFFREYS, H., and BULLEN, K. E. (1967). "Seismological Tables." Brit. Ass. Advan. Sci., Gray Milne Trust, Burlington House, London.
- JEFFREYS, H., and LAPWOOD, E. R. (1957). *Proc. Roy. Soc., Ser. A* **241**, 455.
- KARAL, F. C., and KELLER, J. B. (1959). *J. Acoust. Soc. Amer.* **31**, 694.
- KELVIN, LORD (Sir W. Thomson). (1848). *Cambridge & Dublin Math. J.*
- KHATTRI, K. N. (1969a). *Bull. Seismol. Soc. Amer.* **59**, 615.
- KHATTRI, K. N. (1969b). *Bull. Seismol. Soc. Amer.* **59**, 691.
- KNOPOFF, L., and GILBERT, F. (1960). *Bull. Seismol. Soc. Amer.* **50**, 117.
- KNOTT, C. G. (1899). *Phil. Mag. [5]* **48**, 64.
- LAMB, H. (1904). *Phil. Trans. Roy. Soc. London, Ser. A* **203**, 1.
- LANDISMAN, M., SATO, Y., and NAFF, J. (1965). *Geophys. J. Roy. Astron. Soc.* **9**, 439.
- LANGER, R. E. (1937). *Phys. Rev.* **51**, 669.
- LAPWOOD, E. R. (1949). *Phil. Trans. Roy. Soc. London, Ser. A* **242**, 63.
- LOVE, A. E. H. (1903). *Proc. London Math. Soc. [2]*, **1**, 291.
- LOVE, A. E. H. (1911). "Some Problems of Geodynamics," Cambridge Univ. Press, London and New York.
- LORENTZ, L. (1861). *J. Math. (Crelle)* **58**.
- MARUYAMA, T. (1964). *Bull. Earthq. Res. Inst. Tokyo* **42**, 289.
- MORSE, P. M., and FISHBACH, H. (1953). "Methods of Theoretical Physics," McGraw-Hill, New York.
- NAKANO, H. (1923). *Seismol. Bull. Centr. Math Obs. Japan* **1**, 92.
- NESS, N. F., HARRISON, J. C., and SLICHTER, L. B. (1961). *J. Geophys. Res.* **66**, 621.
- NOWROOZI, A. (1970). Private communication.
- PEKERIS, C. L. (1955). *Proc. Nat. Acad. Sci. U.S.*, **41**, 629.
- PEKERIS, C. L., and JAROSCH, H. (1958). In "Contributions in Geophysics in Honor of Beno Gutenberg," p. 171. Pergamon, Oxford.
- POINCARÉ, H. (1910). *Palermo Rend.* **29**, 169.
- RAYLEIGH, LORD (1885). *Proc. London Math. Soc. [1]* **17**, 4.
- RAYLEIGH, LORD (1906). *Sci. Pap.* **5**, 300.

- ROLLER, J. C., and HEALY, J. H. (1963). *J. Geophys. Res.* **68**, 5837.
- SAITO, M. (1967). *J. Geophys. Res.* **72**, 3689.
- SAVAGE, J. C. (1965). *Bull. Seismol. Soc. Amer.* **55**, 263.
- SEZAWA, K. (1927). *Bull. Earthq. Res. Inst. Tokyo* **3**, 43.
- SHIMSHONI, M., and BEN-MENAHEM, A. (1970). *Geophys. J. Roy. Astron. Soc.* **21**, 285.
- SINGH, S. J. (1970). *J. Geophys. Res.* **75**, 3257.
- SINGH, S. J., and BEN-MENAHEM, A. (1969a). *Geophys. J. Roy. Astron. Soc.* **17**, 151.
- SINGH, S. J., and BEN-MENAHEM, A. (1969b). *Geophys. J. Roy. Astron. Soc.* **17**, 333.
- SINGH, S. J., and BEN-MENAHEM, A. (1969c). *J. Acoust. Soc. Amer.* **46**, 655.
- SINGH, S. J., and BEN-MENAHEM, A. (1969d). *Bull. Seismol. Soc. Amer.* **59**, 2039.
- SMIRNOV, V., and SOBOLEV, S. (1932). *Publ. Inst. Seismol. Acad. Sci. URSS* **20**.
- SOMIGLIANA, C. (1885). *Nuovo Cimento* [3] **17**.
- SOMMERFELD, A. (1909). *Ann. Phys. (Leipzig)* [4] **28**, 665.
- SOMMERFELD, A. (1949). "Partial Differential Equations in Physics." Academic Press, New York.
- STEKETEE, J. A. (1958). *Can. J. Phys.* **36**, 192.
- STOKES, G. G. (1849). *Trans. Cambridge Phil. Soc.* **9**.
- STRATTON, J. A. (1941). "Electromagnetic Theory." McGraw-Hill, New York.
- TENG, T. L., and BEN-MENAHEM, A. (1965). *J. Geophys. Res.* **70**, 5157.
- THOMSON, W. T. (1950). *J. Appl. Phys.* **21**, 89.
- TOKSÖZ, M. N., BEN-MENAHEM, A., and HARKRIDER, D. G. (1964). *J. Geophys. Res.* **69**, 4355.
- VOIGT, W. (1892). *Ann. Phys. Chem.* [3] **47**, 671.
- VOLTERRA, V. (1907). *Ann. Sci. Ec. Norm. Supér., Paris*, **24**, 401.
- WATSON, G. N. (1918). *Proc. Roy. Soc., Ser. A* **95**, 83.
- WEYL, H. (1919). *Ann. Phys. (Leipzig)* [4] **60**, 481.
- WICKENS, A. J., and HODGSON, J. H. (1967). *Publ. Dominion Observ., Ottawa* **1**, 33.
- WU, T., and BEN-MENAHEM, A. (1965). *J. Geophys. Res.* **70**, 3943.
- WYSS, M., and BRUNE, J. N. (1968). *J. Geophys. Res.* **73**, 4681.
- ZOEPPRITZ, K., GEIGER, L., and GUTENBERG, B. (1912). *Nachr. Kgl. Ges. Wiss., Göttingen, Math.-Phys. Kl.* p. 121.

# Author Index

Numbers in italics refer to the pages on which the complete references are listed.

## A

- Aboodi, E., 350, 352, 353, 373, 374  
Aboudi, J., 47, 55, 65, 126, 128, 152, 162, 173, 175, 176, 229  
Abramovici, F., 58, 65, 66, 76, 111, 112, 119, 126, 128, 129, 135, 162  
Abramowitz, M., 172, 184, 190, 194, 195, 212, 213, 229  
Aki, K., 346, 351, 352, 372  
Alexander, S. S., 132, 162, 166, 167, 168, 178, 179, 180, 186, 198, 212, 216, 220, 222, 229, 230  
Allen, C. R., 373  
Alsop, L. E., 91, 127, 163, 183, 229, 350, 372  
Alterman, Z., 37, 43, 47, 55, 58, 65, 66, 76, 85, 86, 88, 106, 109, 110, 111, 112, 126, 128, 129, 135, 152, 162, 162, 163, 170, 171, 175, 176, 229, 314, 364, 372  
Anderson, D. L., 152, 164, 168, 229, 249, 254, 266, 290, 298, 334, 343, 372  
Ansell, J. H., 166, 175, 179, 229  
Archambeau, C. B., 55, 162, 290, 298, 334, 343, 372  
Arkani-Hamed, J., 152, 164  
Arnold, E. P., 290, 298

## B

- Backus, G. E., 168, 198, 199, 206, 207, 229, 235, 236, 237, 240, 243, 244, 246, 266, 266  
Baker, D. W., 268, 298  
Ben-Menahem, A., 173, 229, 301, 303, 305, 308, 311, 313, 322, 323, 336, 341, 342, 343, 346, 347, 348, 349, 350, 351, 352, 353, 358, 364, 372, 373, 375  
Benndorf, H., 308, 373  
Berckheimer, H., 340, 347, 348, 350, 351, 373

Betti, E., 300, 373

Biot, M. A., 181, 229

Birch, F., 215, 229

Biswas, N. N., 322, 373

Bollinger, G. A., 347, 348, 351, 352, 373

Bolt, B. A., 167, 219, 229, 251, 266, 290, 298

Boore, D. M., 43, 163

Bremmer, H., 68, 163, 166, 175, 178, 230

Bridgman, P. W., 268, 298

Bromwich, T. J. I'A., 301, 373

Brune, J. N., 127, 128, 163, 250, 266, 321, 335, 350, 352, 361, 372, 373, 375

Buchbinder, G., 163

Budden, K. G., 191, 193, 196, 209, 229

Bullen, K. E., 132, 133, 163, 166, 167, 210, 212, 220, 230, 236, 249, 252, 266, 289, 298, 340, 341, 347, 373, 374

Burridge, R., 106, 109, 162, 163, 301, 350, 373

Byerly, P., 349, 373

## C

Cagnaird, L., 114, 163, 301, 373

Carder, D. S., 250, 251, 254, 266

Cathles, L. M., 166, 187, 211, 213, 216, 220, 222, 230

Červený, V., 2, 7, 15, 33, 132, 163

Chander, R., 352, 373

Chandra, U., 347, 350, 351, 373

Chapman, C. H., 166, 167, 177, 178, 179, 183, 190, 211, 213, 214, 220, 229

Chinnery, M. A., 152, 164, 352, 373

Clawson, G. E., 290, 298

Cleary, J., 217, 229

Clebsch, A., 172, 229

Craggs, J. W., 201, 230

Cumming, G. L., 11, 34

Curtis, A. R., 340, 341, 373

**D**

- Dahlen, F. A., 167, 229  
 Dana, S. W., 133, 163  
 Danes, Z. F., 133, 163  
 Davies, J. B., 347, 351, 373  
 De Bremaecker, J. C., 90, 163  
 Debye, P., 175, 229, 300, 373  
 de Hoop, A. T., 301, 373  
 Denson, M. E., 136, 163  
 Derr, J. S., 201, 229  
 Dorman, J., 233, 266, 322, 373  
 Dunford, N., 236, 266  
 Dunkin, J. W., 208, 229  
 Duwalo, G., 132, 163, 166, 175, 178, 179,  
 211, 229

**E**

- Eckersley, T. L., 212, 229  
 Engdahl, E. R., 234, 251, 266, 290, 298  
 Erdélyi, A., 196, 229  
 Ergin, K., 132, 133, 136, 163  
 Espinosa, A. F., 290, 298  
 Evison, F. F., 268, 298  
 Ewing, W. M., 65, 76, 92, 114, 163, 164,  
 168, 198, 229, 233, 266, 322, 352, 373

**F**

- Feschbach, H., 172, 174, 189, 230, 272, 298,  
 303, 374  
 Filson, J., 352, 373  
 Forester, R. D., 136, 163  
 Forsythe, G., 254, 266  
 Freedman, H. W., 290, 298  
 Friedman, B., 213, 229  
 Fuchs, K., 43, 163

**G**

- Gantmacher, F. R., 205, 206, 207, 229  
 Garvin, W. W., 55, 86, 163, 301, 373  
 Geiger, L., 308, 375  
 Gerver, M. L., 235, 249, 266

- Gilbert, F., 115, 131, 132, 163, 166, 167,  
 168, 198, 199, 201, 206, 207, 229, 230,  
 235, 236, 237, 239, 240, 243, 244, 266,  
 266, 301, 364, 374  
 Gordon, D. W., 250, 251, 254, 266, 290,  
 298  
 Greenfield, R. J., 152, 163  
 Griggs, D. T., 268, 298  
 Gutenberg, B., 131, 132, 135, 136, 137, 163,  
 166, 230, 232, 266, 308, 346, 374, 375

**H**

- Hales, A. L., 234, 252, 266, 290, 298  
 Handin, J., 268, 298  
 Hansen, W. W., 303, 374  
 Harkrider, D. G., 322, 323, 352, 353, 373,  
 374, 375  
 Harrison, J. C., 335, 374  
 Haskell, N. A., 179, 183, 230, 322, 323, 344,  
 374  
 Heading, J., 191, 212, 222, 230  
 Healy, J. H., 346, 374  
 Helmberger, D. V., 1, 2, 34  
 Herglotz, G., 232, 266  
 Herrera, I., 183, 230  
 Herrin, E., 250, 266, 290, 298  
 Hirasawa, T., 340, 348, 351, 374  
 Hodgson, J. H., 349, 350, 374, 375  
 Honda, H., 268, 298  
 Hron, F., 2, 7, 12, 15, 19, 34  
 Huta, A., 199, 230

**I**

- Isaacson, E., 199, 230  
 Isacks, B., 297, 298, 350, 374  
 Israel, M., 364, 373

**J**

- Jackson, W. H., 346, 374  
 Jacob, K. H., 340, 347, 348, 350, 351, 373  
 Jacobs, J. A., 132, 163, 166, 175, 178, 179,  
 211, 229  
 Jardetzky, W. S., 76, 114, 163, 168, 198, 229

Jarosch, H., 162, 162, 170, 171, 176, 229,  
309, 310, 314, 350, 353, 364, 365, 372,  
373, 374  
Jeans, J. H., 301, 374  
Jeffreys, B. S., 59, 163  
Jeffreys, H., 59, 72, 132, 133, 135, 136, 163,  
166, 167, 230, 232, 252, 266, 301, 333,  
335, 340, 341, 347, 374  
Johnson, L. R., 167, 230, 234, 250, 266  
Jordan, J. N., 250, 251, 254, 266  
Julian, B. R., 249, 254, 266

**K**

Kanamori, L., 163  
Kanasewich, E. R., 2, 7, 11, 12, 19, 34  
Karal, F. C., 37, 55, 112, 152, 162, 349,  
374  
Kawasumi, H., 268, 298  
Keller, H. B., 199, 230  
Keller, J. B., 349, 374  
Kelvin, Lord, 300, 374  
Khattri, K. N., 351, 374  
Knight, C. A., 152, 164  
Knopoff, L., 131, 132, 163, 166, 230, 283,  
284, 292, 293, 294, 297, 298, 301, 322,  
350, 373, 374  
Knott, C. G., 300, 374  
Kornfeld, P., 65, 128, 135, 162  
Kosminskaya, I. P., 31, 34

**L**

Lamb, H., 300, 374  
Lanczos, C., 206, 230  
Landisman, M., 65, 164, 173, 176, 230, 374  
Langer, R. E., 301, 374  
Lapwood, E. R., 43, 72, 88, 89, 135, 163,  
301, 350, 373, 374  
Laster, S. J., 115, 163  
Lehmann, I., 131, 136, 163  
Levité, U., 364, 373  
Lobdell, J. L., 250, 266, 290, 298  
Loewenthal, D., 43, 86, 88, 106, 109, 110,  
162, 163  
Lorentz, L., 300, 374  
Love, A. E. H., 300, 309, 374

**M**

MacDonald, G. J. F., 364, 374  
McEvilly, T. V., 352, 373  
McGarr, A., 91, 163  
Markushevich, V. M., 235, 249, 266  
Martner, S. T., 163  
Maruyama, T., 300, 374  
Masse, R., 173, 176, 230  
Miller, H. J., 290, 298  
Mitchell, A. R., 201, 230  
Mohorovicic, A., 232, 266  
Moler, C., 254, 266  
Molnar, P., 297, 298, 350, 374  
Morris, G. B., 1, 2, 34  
Morse, P. M., 170, 172, 174, 189, 230, 274,  
298, 303, 374  
Müller, G., 2, 34, 76, 163

**N**

Nafe, J. E., 127, 163, 374  
Nakano, H., 112, 163, 349, 374  
Ness, N. F., 335, 374  
Nowroozi, A., 370, 374  
Nussenzveig, H. M., 166, 174, 175, 177,  
194, 230  
Nuttli, O., 290, 298

**O**

Oldham, R. D., 231, 266  
Oliver, J., 92, 163, 233, 266, 322, 373  
Orowan, E., 268, 298

**P**

Pakiser, L. C., 346, 374  
Pekeris, C. L., 162, 162, 170, 171, 176, 229,  
301, 309, 310, 314, 364, 372, 374  
Petrashen, G. I., 6, 7, 14, 15, 34  
Phinney, R. A., 132, 162, 166, 167, 168,  
178, 179, 180, 186, 187, 190, 198, 207,  
211, 212, 213, 214, 216, 220, 222, 229,  
230

- Pitteway, M. L. V., 207, 230  
 Poincaré, H., 301, 374  
 Porra, K., 217, 229  
 Press, F., 76, 92, 114, 163, 168, 198, 229,  
     346, 352, 372, 373  
 Pugach, A. D., 8, 34
- R**
- Ralston, A., 201, 230  
 Randall, M. J., 252, 266, 268, 269, 272, 275,  
     276, 278, 279, 283, 284, 292, 293, 294,  
     297, 298  
 Ravindra, R., 15, 33  
 Rayleigh, Lord, 300, 309, 374  
 Reed, L., 217, 229  
 Reid, H. F., 267, 298  
 Richards, P. G., 166, 169, 173, 188, 189,  
     214, 217, 230, 234, 266  
 Richter, C. F., 132, 133, 135, 137, 163, 164,  
     166, 230  
 Riecker, R. E., 268, 298  
 Ringwood, A. E., 268, 298  
 Roberts, J. L., 234, 252, 266  
 Roever, W. L., 115, 164  
 Roller, J. C., 346, 375  
 Romney, C., 290, 298  
 Rooney, T. P., 268, 298  
 Rosenman, M., 323, 350, 353, 364, 373  
 Rotenberg, A., 43, 55, 85, 162  
 Rykunov, L. N., 132, 164
- S**
- Saito, M., 364, 375  
 Sarafyan, D., 199, 230  
 Satô, R., 127, 135, 164, 173, 177, 230  
 Satô, Y., 65, 164, 173, 176, 230, 374  
 Savage, J. C., 340, 375  
 Scheffé, H., 286, 298  
 Scheid, F., 198, 230  
 Scholte, J. G. J., 68, 132, 133, 164, 166,  
     175, 178, 179, 187, 230  
 Schwartz, J. T., 236, 266  
 Sezawa, K., 301, 333, 375
- Shanks, E. B., 199, 230  
 Sheppard, R. M., 152, 163  
 Shimamura, H., 127, 135, 164, 167, 230  
 Shimshoni, M., 340, 341, 342, 373, 375  
 Singh, S. J., 301, 303, 305, 308, 311, 313,  
     330, 349, 364, 373, 375  
 Slichter, L. B., 335, 374  
 Smirnov, V., 301, 375  
 Smith, S. W., 343, 346, 347, 350, 351, 373  
 Sobolev, S., 301, 375  
 Somigliana, C., 300, 375  
 Sommerfeld, A., 301, 312, 375  
 Spencer, T. W., 2, 13, 34  
 Starr, A. T., 107, 164  
 Stauder, W., 268, 298, 348, 374  
 Stegun, I. A., 172, 184, 190, 194, 195, 212,  
     213, 229  
 Steketee, J. A., 301, 330, 375  
 Stewart, S. W., 346, 374  
 Stokes, G. G., 191, 230, 300, 375  
 Stratton, J. A., 303, 375  
 Strick, E., 115, 164  
 Stoneley, R., 114, 164  
 Sutton, G. H., 290, 298
- T**
- Taggart, J. N., 234, 250, 251, 266, 290, 298  
 Teng, T. L., 166, 183, 217, 230, 343, 346,  
     347, 350, 351, 373, 375  
 Thomson, W. T., 322, 375  
 Todd, J., 206, 230  
 Toksöz, M. N., 152, 164, 348, 352, 373, 375  
 Tucker, W., 250, 266, 290, 298
- U**
- Usami, T., 65, 164, 173, 176, 230
- V**
- Van der Pol, B., 166, 175, 178, 230  
 Vavilova, T. I., 6, 8, 34  
 Vining, T. F., 115, 164  
 Voigt, W., 300, 333, 375  
 Volterra, V., 300, 301, 375

## W

Watson, G. N., 166, 173, 212, 230, 301, 320, 375  
Yosiyama, R., 268, 298

## Y

Weyl, H., 300, 375  
Wickens, A. J., 350, 375  
Wiechert, E., 232, 266  
Wiggins, R. A., 203, 204, 215, 230  
Wilkinson, J. H., 254, 266  
Wu, T., 350, 375  
Wyss, M., 352, 375  
Zöppritz, K., 232, 266, 308, 375  
Z

# Subject Index

## A

Acoustic scattering, 175, 212

Airy integral, 192

Alberta model, 10, 13, 29

Anelasticity, 333

Arrangement of balls, 32

Attenuation, 168, 198, 219, 280, 290, 333, 342

## B

Backus-Gilbert method, 235

Bromwich, integral, 62

Bullen's model B, 162

Byerly's method, 349

## C

Cagniard's technique, 111

Computers, types of, 32

Condition T-p $\Delta$ , 248

Converted waves, 11

Core phases, 135, 137, 167, 178, 203, 217, 234, 250, 251, 263

caustic point, 136

Corner problems, 43

Coupled ray segment, 4

Cracks, 106

Crustal structure, 283, 344

Cubic splines, 341

Curvature of earth, effect on waves, 126

## D

Decay constant, 219, 222

$\delta$ -ness criteria, 241

Diffraction, 85, 108, 167, 177

Directivity function, 358

Dislocations, 276, 301, 340, 347, 362, 366

Dispersion curves, 322

Divergence coefficient, *see* Geometric spreading

Doppler effect, 336, 358

Double couple, 297

## E

Earth models, 29, 162, 176, 215, 219, 232, 253, 346, 366

Earthquakes, 292

Chilean, May 22, 1960, 335

deep focus, 106, 268, 280, 289, 350

large magnitude, 363

San Francisco, April 18, 1906, 267

Shallow focus, 350

Equalization of seismic waves, 350, 354

Errors, 243, 247, 253, 259

## F

Fault-plane solutions, 269, 297, 349

Faulting, 269

dip-slip, 109, 308

rupture, 338, 351

strike-slip, 308, 386

Finiteness factor, 348

Finite differences, 36, 47, 206

Focal sphere, 270, 288

Fréchet kernel, 236, 249

## G

Geometric spreading, 284, 308, 340

$G_n$  waves, *see* Love waves

Gravity effect, 167, 310

Green's tensor, 310

Group velocity, 126

## H

Hamming's method, 198, 205

Haskell method, 208, 323

Head waves, 4, 14

Helmholtz equation, 303  
 Herglotz-Wiechert inversion, 234, 248  
 Heterogeneity, 153, 305, 349

**I**

Illuminated zone, 216, 224  
 Inversion, 232, 236, 248, 254

Poles, 63, 320  
 diffraction, 177, 211, 213, 216  
 resonance, 177  
 Pulses, 275  
 diffracted, 130  
 PKP, 130  
 quarter plane, 81

**Q****K**

"Quelling," 246

Kronecker's theorem, 207

**R****L**

Layered half-space, 37  
 Least squares, 237, 285  
 Legendre equation, 170, 365  
 Line spectra, 364  
 Love waves, 322, 328, 352, 357  
 Low velocity zones, 234  
 Lyapunov transformations, 206

**M**

Mantle-core boundary diffraction, 131  
 Monte Carlo experiments, 288  
 Multi-poles, 273, 285, 303

$R_n$  waves, *see* Rayleigh waves  
 Rainbow expansion, 175, 178, 186  
 Ray analysis, 58, 65, 209, 210  
 Ray theory, 2, 66, 166, 335  
 Rayleigh waves, 84, 85, 89, 111, 127, 179,  
 322, 324, 352, 357  
 Refracted waves, 113  
 Resolving power, 254, 257  
 Response integral, 187, 208  
 Riemann sheets, 115, 170, 196  
 Root finding, 201  
 Runge-Kutta method, 198, 202, 205, 208,  
 365  
 Rupture parameters, 338, 340, 351, 353

**S****N**

Navier equation, 168, 309  
 Normal modes, 58, 309

**P**

P waves, 181, 205, 214, 234, 250, 257, 273,  
 290, 307, 341, 344  
 pP waves, 132, 135, 284, 290, 292  
 Pascal's triangle, 20, 21  
 PcP waves, 132, 154, 178, 182, 203, 214,  
 234, 250  
 Polar phase shift, 321

S waves, 55, 90, 180, 205, 234, 250, 261,  
 273, 307, 341, 345  
 ScS, *see* S waves  
 Seismic waves  
 diffracted, 108  
 dynamic analogs, 3, 6  
 "H" waves, 4  
 kinematic analogs, 3  
 "R" waves, 5  
 simply converted wave, 11  
 transmission coefficients, 91, 203, 212  
 Seismograms, 81, 110, 347  
 Seismograph, 269, 283, 290, 361  
 Shadow boundary, 216  
 Shear invariant, 278

**Smothing**, 287, 341

**Sources**

- depth effect, 112
- dislocation, 276
- Garvin, 56, 83
- impulsive, 55, 66, 280
- initial pulse, 129
- off-diagonal, 87
- phase transition, 268, 297
- point, 171
- polarity, 350
- radiation pattern, 292, 347, 353
- strength, 189, 279

**Spectral amplitudes**, 216, 222, 224, 305,  
320, 322, 331, 350, 352

**Spherical coordinates**, 47

**Spheroidal oscillations**, 65, 311, 317, 365

**Stability conditions**, 51, 54, 206, 254

**Steepest descent**, 70

**Stokes phenomena**, 191, 196, 204

**Stoneley waves**, 83, 91, 114, 127, 179

**Strain**, 48, 268

**Stress drop**, 352

**Surface waves**

- higher modes, 128
- spectral analysis, 352

## T

**Terrestrial interferometry**, 358

**Toroidal oscillations**, *see* Torsional oscillations

**Torsional oscillations**, 65, 311, 316, 370

**Transfer function**, 344

**Travel-time curves**, 132, 250, 290, 347

## U

**Unconverted waves**, 4, 5

codes, 26

subroutines, 19

**Unfolding travel time curves**, 248

**Uniqueness**, 232, 240

## V

**Variances**, 237, 286

**Velocity distribution**, 167, 219, 232

**Volterra relation**, 301, 312

## W

**Watson transformation**, 173, 176, 320

**Wedge problems**, 43, 153

**WKBJ solutions**, 173, 187, 212

**WWSSN (World-Wide Standard Seismographic Network)**, 280

# Contents of Previous Volumes

## Volume 1: Statistical Physics

The Numerical Theory of Neutron Transport  
*Bengt G. Carlson*

The Calculation of Nonlinear Radiation Transport by a Monte Carlo Method  
*Joseph A. Fleck, Jr.*

Critical-Size Calculations for Neutron Systems by the Monte Carlo Method  
*Donald H. Davis*

A Monte Carlo Calculation of the Response of Gamma-Ray Scintillation Counters  
*Clayton D. Zerby*

Monte Carlo Calculation of the Penetration and Diffusion of Fast Charged Particles  
*Martin J. Berger*

Monte Carlo Methods Applied to Configurations of Flexible Polymer Molecules  
*Frederick T. Wall, Stanley Windwer, and Paul J. Gans*

Monte Carlo Computations on the Ising Lattice  
*L. D. Fosdick*

A Monte Carlo Solution of Percolation in the Cubic Crystal  
*J. M. Hammersley*

AUTHOR INDEX—SUBJECT INDEX

## Volume 2: Quantum Mechanics

The Gaussian Function in Calculations of Statistical Mechanics and Quantum Mechanics  
*Isaiah Shavitt*

Atomic Self-Consistent Field Calculations by the Expansion Method  
*C. C. J. Roothaan and P. S. Bagus*

The Evaluation of Molecular Integrals by the Zeta-Function Expansion  
*M. P. Barnett*

Integrals for Diatomic Molecular Calculations  
*Fernando J. Corbató and Alfred C. Switendick*

Nonseparable Theory of Electron-Hydrogen Scattering  
*A. Temkin and D. E. Hoover*

Estimating Convergence Rates of Variational Calculations  
*Charles Schwartz*

AUTHOR INDEX—SUBJECT INDEX

**Volume 3: Fundamental Methods in Hydrodynamics**

Two-Dimensional Lagrangian Hydrodynamic Difference Equations  
*William D. Schulz*

Mixed Eulerian-Lagrangian Method  
*R. M. Frank and R. B. Lazarus*

The Strip Code and the Jetting of Gas between Plates  
*John G. Trulio*

CEL: A Time-Dependent, Two-Space-Dimensional, Coupled Eulerian-Lagrange Code  
*W. F. Noh*

The Tensor Code  
*G. Maenchen and S. Sack*

Calculation of Elastic-Plastic Flow  
*Mark L. Wilkins*

Solution by Characteristics of the Equations of One-Dimensional Unsteady Flow  
*N. E. Hoskin*

The Solution of Two-Dimensional Hydrodynamic Equations by the Method of Characteristics  
*D. J. Richardson*

The Particle-in-Cell Computing Method for Fluid Dynamics  
*Francis H. Harlow*

The Time Dependent Flow of an Incompressible Viscous Fluid  
*Jacob Fromm*

AUTHOR INDEX—SUBJECT INDEX

**Volume 4: Applications in Hydrodynamics**

Numerical Simulation of the Earth's Atmosphere  
*Cecil E. Leith*

Nonlinear Effects in the Theory of a Wind-Driven Ocean Circulation  
*Kirk Bryan*

Analytic Continuation Using Numerical Methods  
*Glenn E. Lewis*

Numerical Solution of the Complete Krook-Boltzmann Equation for Strong Shock Waves  
*Moustafa T. Chahine*

The Solution of Two Molecular Flow Problems by the Monte Carlo Method  
*J. K. Haviland*

Computer Experiments for Molecular Dynamics Problems  
*R. A. Gentry, F. H. Harlow, and R. E. Martin*

Computation of the Stability of the Laminar Compressible Boundary Layer  
*Leslie M. Mack*

Some Computational Aspects of Propeller Design  
*William B. Morgan and John W. Wrench, Jr.*

Methods of the Automatic Computation of Stellar Evolution  
*Louis G. Henyey and Richard D. Levée*

Computations Pertaining to the Problem of Propagation of a Seismic Pulse in a Layered Solid  
*F. Abramovici and Z. Alterman*

AUTHOR INDEX—SUBJECT INDEX

**Volume 5: Nuclear Particle Kinematics**

Automatic Retrieval Spark Chambers  
*J. Bouin, R. H. Miller, and M. J. Neumann*

**Computer-Based Data Analysis Systems***Robert Clark and W. F. Miller***Programming for the PEPR System***P. L. Bastien, T. L. Watts, R. K. Yamamoto, M. Alston, A. H. Rosenfeld,  
F. T. Solmitz, and H. D. Taft***A System for the Analysis of Bubble Chamber Film Based upon the Scanning  
and Measuring Projector (SMP)***Robert I. Hulsizer, John H. Munson, and James N. Snyder***A Software Approach to the Automatic Scanning of Digitized Bubble  
Chamber Photographs***Robert B. Marr and George Rabinowitz***AUTHOR INDEX—SUBJECT INDEX****Volume 6: Nuclear Physics****Nuclear Optical Model Calculations***Michael A. Melkanoff, Tatsuro Sawada, and Jacques Raynal***Numerical Methods for the Many-Body Theory of Finite Nuclei***Kleber S. Masterson, Jr.***Application of the Matrix Hartree-Fock Method to Problems in Nuclear  
Structure***R. K. Nesbet***Variational Calculations in Few-Body Problems with Monte Carlo Method***R. C. Herndon and Y. C. Tang***Automated Nuclear Shell-Model Calculations***S. Cohen, R. D. Lawson, M. H. Macfarlane, and M. Soga***Nucleon-Nucleon Phase Shift Analyses by Chi-Squared Minimization***Richard A. Arndt and Malcolm H. MacGregor***AUTHOR INDEX—SUBJECT INDEX****Volume 7: Astrophysics****The Calculation of Model Stellar Atmospheres***Dimitri Mihalas*

Computational Methods for Non-LTE Line-Transfer Problems  
*D. G. Hummer and G. Rybicki*

Methods for Calculating Stellar Evolution  
*R. Kippenhahn, A. Weigert, and Emmi Hofermeister*

Computational Methods in Stellar Pulsation  
*R. F. Christy*

Stellar Dynamics and Gravitational Collapse  
*Michael M. May and Richard H. White*

AUTHOR INDEX—SUBJECT INDEX

**Volume 8: Energy Bands of Solids**

Energy Bands and the Theory of Solids  
*J. C. Slater*

Interpolation Schemes and Model Hamiltonians in Band Theory  
*J. C. Phillips and R. Sandrock*

The Pseudopotential Method and the Single-Particle Electronic Excitation Spectra of Crystals  
*David Brust*

A Procedure for Calculating Electronic Energy Bands Using Symmetrized Augmented Plane Waves  
*L. F. Mattheiss, J. H. Wood, and A. C. Switendick*

Interpolation Scheme for the Band Structure of Transition Metals with Ferromagnetic and Spin-Orbit Interactions  
*Henry Ehrenreich and Laurent Hodges*

Electronic Structure of Tetrahedrally Bonded Semiconductors: Empirically Adjusted OPW Energy Band Calculations  
*Frank Herman, Richard L. Kortum, Charles D. Kuglin, John P. Van Dyke, and Sherwood Skillman*

The Green's Function Method of Korringa, Kohn, and Rostoker for the Calculation of the Electronic Band Structure of Solids  
*Benjamin Segall and Frank S. Ham*

AUTHOR INDEX—SUBJECT INDEX

**Volume 9: Plasma Physics**

The Electrostatic Sheet Model for a Plasma and Its Modification to Finite-Sized Particles

*John M. Dawson*

Solution of Vlasov's Equation by Transform Methods

*Thomas P. Armstrong, Rollin C. Harding, Georg Knorr, and David Montgomery*

The Water-Bag Model

*Herbert L. Berk and Keith V. Roberts*

The Potential Calculation and Some Applications

*R. W. Hockney*

Multidimensional Plasma Simulation by the Particle-in-Cell Method

*R. L. Morse*

Finite-Size Particle Physics Applied to Plasma Simulation

*Charles K. Birdsall, A. Bruce Langdon, and H. Okuda*

Finite-Difference Methods for Collisionless Plasma Models

*Jack A. Byers and John Killeen*

Application of Hamilton's Principle to the Numerical Analysis of Vlasov Plasmas

*H. Ralph Lewis*

Magnetohydrodynamic Calculations

*Keith V. Roberts and D. E. Potter*

The Solution of the Fokker-Planck Equation for a Mirror-Confined Plasma

*John Killeen and Kenneth D. Marx*

AUTHOR INDEX—SUBJECT INDEX

**Volume 10: Atomic and Molecular Scattering**

Numerical Solutions of the Integro-Differential Equations of Electron-Atom Collision Theory

*P. G. Burke and M. J. Seaton*

Quantum Scattering Using Piecewise Analytic Solutions

*Roy G. Gordon*

Quantum Calculations in Chemically Reactive Systems

*John C. Light*

**Expansion Methods for Electron-Atom Scattering***Frank E. Harris and H. H. Michels***Calculation of Cross Sections for Rotational Excitation of Diatomic Molecules by Heavy Particle Impact: Solution of the Close-Coupled Equations***William A. Lester, Jr.***Amplitude Densities in Molecular Scattering***Don Secrest***Classical Trajectory Methods***Don L. Bunker***AUTHOR INDEX—SUBJECT INDEX****Volume 11: Seismology: Surface Waves and Earth Oscillations****Finite Difference Methods for Seismic Wave Propagation in Heterogeneous Materials***David M. Boore***Numerical Analysis of Dispersed Seismic Waves***A. M. Dziewonski and A. L. Hales***Fast Surface Wave and Free Mode Computations***F. A. Schwab and L. Knopoff***A Finite Element Method for Seismology***John Lysmer and Lawrence A. Drake***Seismic Surface Waves***H. Takeuchi and M. Saito***AUTHOR INDEX—SUBJECT INDEX**